Transactions of the ASME®

Technical Editor
H. D. NELSON (2001)

Associate Technical Editors
Advanced Energy Systems
M. J. MORAN (1999)
G. REISTAD (2002)
Fuels and Combustion Technologies
S. GOLLAHALLI (2001)
Gas Turbine (Review Chair)
D. WISLER (2001)
Gas Turbine
D. COOKE (1999)
M. MIGNOLET (2002)
J. PETERS (1999)
Internal Combustion Engines
D. ASSANIS (1999)
Nuclear
R. DUFFEY (2001)
Power
D. LOU (2002)

BOARD ON COMMUNICATIONS
Chairman and Vice President
R. K. SHAH

OFFICERS OF THE ASME
President, **R. E. NICKELL**
Executive Director, **D. L. BELDEN**
Treasurer, **J. A. MASON**

PUBLISHING STAFF
Managing Director, Engineering
CHARLES W. BEARDSLEY
Director, Technical Publishing
PHILIP DI VIETRO
Managing Editor, Technical Publishing
CYNTHIA B. CLARK
Managing Editor, Transactions
CORNELIA MONAHAN
Production Coordinator
COLIN MCATEER
Production Assistant
MARISOL ANDINO

Transactions of the ASME, Journal of Engineering for Gas Turbines and Power (ISSN 0742-4795) is published quarterly (Jan., April, July, Oct.) for $215.00 per year by The American Society of Mechanical Engineers, Three Park Avenue, New York, NY 10016. Periodicals postage paid at New York, NY and additional mailing offices. POSTMASTER: Send address changes to Transactions of the ASME, Journal of Engineering for Gas Turbines and Power, c/o THE AMERICAN SOCIETY OF MECHANICAL ENGINEERS, 22 Law Drive, Box 2300, Fairfield, NJ 07007-2300.
CHANGES OF ADDRESS must be received at Society headquarters seven weeks before they are to be effective. Please send old label and new address.
PRICES: To members, $40.00, annually: to nonmembers, $215.00. Add $40.00 for postage to countries outside the United States and Canada.
STATEMENT from By-Laws. The Society shall not be responsible for statements or opinions advanced in papers or ... printed in its publications (B7.1, par. 3).

INDEXED by Applied Mechanics Reviews and Engineering Information, Inc. Canadian Goods & Services Tax Registration #126148048

Journal of Engineering for Gas Turbines and Power

Published Quarterly by The American Society of Mechanical Engineers

VOLUME 121 • NUMBER 4 • OCTOBER 1999

TECHNICAL PAPERS

(Contents continued on outside back cover)

This journal is printed on acid-free paper, which exceeds the ANSI Z39.48-1992 specification for permanence of paper and library materials. ♾™
♻ 85% recycled content, including 10% post-consumer fibers.

(Contents continued)

Gas Turbines: Manufacturing Materials and Metallurgy

Gas Turbines: Structures and Dynamics

Internal Combustion Engines

Power

ANNOUNCEMENTS

Multixial Creep Life Prediction of Ceramic Structures Using Continuum Damage Mechanics and the Finite Element Method

O. M. Jadaan
University of Wisconsin-Platteville,
College of Engineering,
Platteville, WI 53818

L. M. Powers
Case Western Reserve University,
Cleveland, OH 44106

J. P. Gyekenyesi
NASA Lewis Research Center,
Cleveland, OH 44135

High temperature and long duration applications of monolithic ceramics can place their failure mode in the creep rupture regime. A previous model advanced by the authors described a methodology by which the creep rupture life of a loaded component can be predicted. That model was based on the life fraction damage accumulation rule in association with the modified Monkman-Grant creep rupture criterion. However, that model did not take into account the deteriorating state of the material due to creep damage (e.g., cavitation) as time elapsed. In addition, the material creep parameters used in that life prediction methodology, were based on uniaxial creep curves displaying primary and secondary creep behavior, with no tertiary regime. The objective of this paper is to present a creep life prediction methodology based on a modified form of the Kachanov-Rabotnov continuum damage mechanics (CDM) theory. In this theory, the uniaxial creep rate is described in terms of stress, temperature, time, and the current state of material damage. This scalar damage state parameter is basically an abstract measure of the current state of material damage due to creep deformation. The damage rate is assumed to vary with stress, temperature, time, and the current state of damage itself. Multiaxial creep and creep rupture formulations of the CDM approach are presented in this paper. Parameter estimation methodologies based on nonlinear regression analysis are also described for both, isothermal constant stress states and anisothermal variable stress conditions. This creep life prediction methodology was preliminarily added to the integrated design code named Ceramics Analysis and Reliability Evaluation of Structures/Creep (CARES/Creep), which is a postprocessor program to commercially available finite element analysis (FEA) packages. Two examples, showing comparisons between experimental and predicted creep lives of ceramic specimens, are used to demonstrate the viability of this methodology and the CARES/Creep program.

Introduction

Ceramic structural materials, such as silicon nitrides and silicon carbides, are continuously being developed and improved in response to demands for higher operating temperatures and load bearing capacity. Such demands are desirable for applications including gasoline, diesel, gas turbine engine components, and auxiliary power units. These systems are expected to survive for many thousands of hours, which necessitates subjecting them to low stress levels. The combination of high temperatures and low stresses typically causes failure of monolithic ceramics to be due to creep rupture (Wiederhorn et al., 1994).

Two previous papers by the authors (Jadaan et al., 1997; Powers et al., 1996) described a deterministic damage based approach and the structure of an integrated design code, named Ceramics Analysis and Reliability Evaluation of Structures/Creep (CARES/Creep), to predict the lifetimes of structural components subjected to creep loading. This approach utilized commercially available FEA packages and took into account the effect of stress redistribution. In this approach the creep life of a component was discretized into short time steps, during which, the stress distribution is assumed constant. The damage, calculated using Robinson's linear damage rule (Robinson, 1952), was then computed for each time step based on a creep rupture criterion. The creep rupture models used in the code are the Monkman-Grant (Monkman and Grant, 1956), and the modified Monkman-Grant (Menon et al., 1994) criteria. Failure was assumed to occur when the normalized accumulated damage at any point in the component is greater than or equal to unity. The corresponding time would be the creep rupture life for the component.

The combination of the methodology described above, and the constitutive laws (Norton and Baily-Norton) used to describe the material creep deformation behavior, have three shortcomings. The first shortcoming is with regards to the constitutive law. The Baily–Norton rule (Kraus, 1980; Norton, 1929; Boyle and Spence, 1983) relates the creep rate to stress, time, and temperature in the primary and secondary regions of a typical creep curve. For ceramics that display no tertiary creep behavior, this rule was proven satisfactory for describing both the material's creep deformation behavior, and life prediction (Jadaan et al., 1997; Powers et al., 1996). However, some ceramics such as SN88 silicon nitride (French and Wiederhorn, 1996; Luecke and Wiederhorn, 1997), PY6 silicon nitride (Ferber and Jenkins, 1992), and Si_3N_4-$6Y_2O_3$-$2Al_2O_3$ (Todd and Xu, 1989) do display tertiary creep behavior. For such materials, a more general constitutive creep law capable of describing the entire creep curve, including the tertiary creep regime, is necessary. Second, the linear damage summation approach in combination with the Monkman–Grant creep rupture criterion used to predict rupture in the methodology described above, did not take into account the instantaneous damaged state of the material as time elapsed. It assumes that a material loaded well

Contributed by the International Gas Turbine Institute (IGTI) of THE AMERICAN SOCIETY OF MECHANICAL ENGINEERS for publication in the ASME JOURNAL OF ENGINEERING FOR GAS TURBINES AND POWER. Paper presented at the International Gas Turbine and Aeroengine Congress and Exhibition, Stockholm, Sweden, June 2–5, 1998; ASME Paper 98-GT-489.

Manuscript received by IGTI March 26, 1998; final revision received by the ASME Headquarters June 23, 1999. Associate Technical Editor: R. Kielb.

into its creep design life displays the same creep characteristics as a virgin material. A more general and accurate approach, such as CDM, would incorporate the current damaged state of the material into the constitutive creep law. The third shortcoming of the methodology described above is due to the separation between the creep constitutive law (Baily–Norton) and the creep rupture criterion (Monkman–Grant). This could lead to reduced accuracy of life prediction due to accumulated error induced by fitting (regressing) two separate sets of data. A more coherent theory, such as CDM which already incorporates the damaged state of the material into the constitutive law, would have both creep deformation and rupture embedded into one law.

Therefore, the objective of this paper is the development of a multiaxial creep life prediction methodology, based on a modified form of the continuum damage mechanics theory. This modified CDM based approach has the following advantages: (1) generalized capability of describing a given material's creep deformation behavior whether or not it displays a tertiary creep regime; (2) takes into account the effect of the current damaged state of the material on the deformation and rupture of the component through a scalar damage state variable, ω; and (3) the rupture criterion is incorporated directly into the creep constitutive law. This methodology utilizes commercially available FEA packages (ANSYS), and takes into account stress redistribution.

Similar to the main concept of life prediction described by the authors in their previous two papers, the creep life of a component is discretized into short time steps, during which, the stress and temperature distributions are assumed constant. Rupture life is determined using Robinson's linear damage summation rule (Robinson, 1952). Robinson's rule is the creep version of the Palmgren–Miner linear damage summation rule for fatigue (Miner, 1945). Namely, the damage is computed for each time step through dividing the time duration for that time step by the predicted rupture life based on the current stress/temperature state and CDM theory. The cumulative damage is subsequently calculated as time elapses and failure is assumed to occur when the normalized cumulative damage at any point in the component reaches unity.

Background (Uniaxial Steady State Model)

CDM has evolved into a very useful method to analyze the effect of damage accumulation in a component subjected to thermomechanical loading. A characteristic feature of CDM is the incorporation into the constitutive equations of one or more, scalar or tensorial, state (internal) variables as measures of the degradation of the material (Hault, 1987). What is meant by an internal damage variable, is that it can not be measured directly (Penny and Marriott, 1995). CDM, which is a phenomenological approach, can be thought of as a counterpart to fracture mechanics (FM). While FM deals with structures containing one or more cracks of finite size embedded in a nondeteriorating material, the aim of CDM is to predict the behavior of structures subject to material damage evolution (Hault, 1987).

One CDM model that stands out, is the phenomenological theory developed by Kachanov (1958, 1986) during the 1950s, and later expanded upon by Rabotnov (1969), Hayhurst et al., (1975, 1984a, 1984b), Leckie and Hayhurst, (1977), Othman and Hayhurst, (1990), and Dunne et al., (1990). This model contains one scalar damage parameter, ω, that describes the collective effect of deterioration in the material. It was developed to describe the process of brittle creep rupture in metals. At low loads, in metals, the deformation may be small leading to essentially no variation in the cross sectional area with time. As time elapses, the material deteriorates as microcracks and cavities form. As these defects enlarge and ultimately coalesce, they would form macrocracks that lead to brittle failure. The aim of this paper is to reformulate this theory, proposed originally by Kachanov for metals, into a model that can be used with ceramics.

Kachanov elected to represent the damage via loss in material cross-section, due to cavitation. Consequently, the internal effective stress, σ, corresponding to a constant externally applied stress, σ_0, will increase with time as damage increases. He assumed that damage can be represented by a parameter he named the "continuity", ψ, which is defined as the ratio of the remaining effective area, A, to the original area, A_0. As damage accumulates, the resulting effective stress, σ, increases from its initial value σ_0 at time $t = 0$, to a value $\sigma = \sigma_0 A_0/A$. Subsequently, Rabotnov replaced the continuity with the damage parameter, ω, such that $\omega = 1 - \psi = 1 - (A/A_0)$. This leads to the relationship between the effective stress, σ, and the applied stress, σ_0, being $\sigma = \sigma_0/(1 - \omega)$. At $t = 0$, $A = A_0$, and thus $\omega = 0$. As time elapses, ω increases until it reaches a critical value ω_f, and failure occurs. Kachanov, Rabotnov, and Hayhurst and co-workers, dealing with creep of metals, assumed that $\omega_f = 1$.

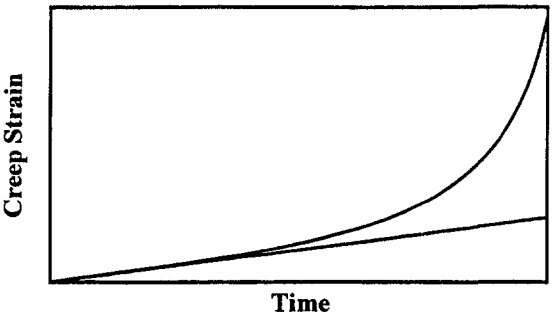

Fig. 1 Schematic creep curve representation using Kachanov's CDM model

The damage rate, $\dot{\omega}$, is expressed in terms of the applied stress, σ_0, and the current state of damage, ω, as (Kachanov, 1986; Hayhurst, et al., 1975)

$$\dot{\omega} = \frac{C\sigma_0^x}{(1 - \omega)^\phi}, \tag{1}$$

where C, x, and ϕ are material constants. Integrating Eq. (1) using the conditions that $\omega = 0$ at $t = 0$, and $\omega = 1$ at $t = t_f$, where t_f is the uniaxial failure time, yields

$$t_f = \frac{\sigma_0^{-x}}{C(1 + \phi)}. \tag{2}$$

The instantaneous damage state, $\omega(t)$, can be derived to be

$$\omega = 1 - \left[1 - \frac{t}{t_f}\right]^{1/(1+\phi)}. \tag{3}$$

For uniaxial stress states, Kachanov (1958) proposed a modified form of Norton's creep rate equation. In order to reflect the effect of the current state of damaged material on the creep rate, he replaced the applied stress σ_0 with the effective stress $\sigma = \sigma_0/(1 - \omega)$, which resulted in the following steady state creep rate formula:

$$\dot{\epsilon}_s = G\sigma^n = G\left[\frac{\sigma_0}{1 - \omega}\right]^n, \tag{4}$$

where G and n are material parameters. Upon substituting equation (3) into Eq. (4) and integrating, the following two equivalent expressions for the creep strain, ϵ, are obtained:

$$\epsilon(t) = G\sigma_0^n t_f \frac{1 + \phi}{1 + \phi - n}\left(1 - \left[1 - \frac{t}{t_f}\right]^{(1+\phi-n)/(1+\phi)}\right) \tag{5}$$

or

$$\epsilon(t) = G\sigma_0^n t_f \frac{1 + \phi}{1 + \phi - n}(1 - [1 - \omega(t)]^{1+\phi-n}). \tag{6}$$

Figure 1 shows a schematic representation of a typical creep

curve as described by the isothermal steady-state constitutive equations (5) and (6) (Penny and Marriott, 1995). It is apparent from the curve that the steady-state CDM model as described by Kachanov (1986) includes the features of tertiary creep following an initial minimum creep rate that remains essentially constant for the first 25 percent of life. At time zero, when $\omega = 0$, Eq. (4) indicates that the steady state creep rate reduces to the Norton equation. As time elapses and the damage ω increases, the creep rate increases accordingly. Hence, due to the incorporation of the current damage state into the model, the steady-state creep rate does not remain constant but rather tends to infinity as $t \rightarrow t_f$, and, hence, $\omega \rightarrow \omega_f = 1$. According to Penny and Marriott (1995), when using the Kachanov model, most of the damage occurs later than 80 percent of life.

Theory and Damage Laws

Generalized Anisothermal Uniaxial Constitutive Model. The Kachanov model presented above was derived to describe the creep brittle rupture of metals, assuming isothermal steady-state conditions. In addition, this model assumes that at failure a complete loss of integrity of the material occurs, which corresponds to $\omega_f = 1$. This condition results in the creep rate tending to infinity as $t \rightarrow t_f$.

In ceramics where tertiary creep behavior is observed, the creep rate increases as the failure time is approached, but does not go to infinity. In addition, the assumption that a complete state of damage given by the condition that $\omega_f = 1$ is not observed experimentally in ceramics or even in many metals. Menon et al. (1994) observed that in a tensile silicon nitride NT-154 specimen tested at 1400°C and failed at a strain of 2.5 percent, the ratio of cavitated area to the total area of the specimen was 5.5 percent. Penny and Marriott (1995) state that there are good reasons why ω at failure should be less than unity and devoted an appendix in their book to prove that point. Stamm and von Estorff (1992) who used ultrasonic techniques to determine cavity densities in steels concluded that the value of ω at failure is no where near unity, as was assumed by Kachanov. Hazime and White (1996) formulated a phenomenological damage model containing a hardening variable used to capture the continuous drop in creep rates with strain that observed in many ceramics. In this model they assumed that failure occurs when the damage reaches a critical value ω_f, which is predetermined experimentally.

In this section, a generalized anisothermal CDM model that takes into account temperature variation and models the entire creep curve, including the primary and tertiary creep regions, will be derived. This model will take into account the effect of the current state of damage on the creep strain and strain rate accumulation. In addition, this model is generalized to capture the creep behavior of materials across the spectrum, starting with materials that display absolutely no tertiary creep characteristics, and ending with those showing severe tertiary behavior. Unlike the Hazime model, this generalized formulation does not require ω_f to be measured or known apriori, but rather is computed as a material parameter via nonlinear regression using standard creep data.

Primary creep can be taken into account by multiplying the damage rate and creep rate (Eqs. (1) and (4)) by the term t^m, where t is the time and m is a material parameter. Additionally, temperature dependence can be accounted for by multiplying Eqs. (1) and (4) by an Arrhenius type temperature formulation. Hence, the damage rate and creep rate can be described as

$$\dot{\omega} = \frac{d\omega}{dt} = \frac{Ct^m e^{-(Q_D/RT)}}{(1-\omega(t))^{\phi}} \sigma_0^x \tag{7}$$

$$\dot{\epsilon} = \frac{d\epsilon}{dt} = Gt^m e^{-(Q_C/RT)} \left(\frac{\sigma_0}{1-\omega(t)} \right)^n, \tag{8}$$

where C, x, m, ϕ, Q_D, G, n, and Q_C are material constants to be determined via nonlinear regression of creep data, R is the gas constant (8.31 J/mol.K), and T is the absolute temperature. The parameters Q_D and Q_C represent the activation energies for damage and creep, respectively. The stress exponent, n, should be a positive number, while the time exponent, m, is generally negative.

Integrating Eq. (7), and using the conditions that at time zero the damage $\omega = 0$ and at the time of failure (t_f) the damage reaches a critical value ω_f, results in the following formula for the time to failure:

$$t_f = \left\{ \frac{(1+m)e^{Q_D/RT}}{C(1+\phi)\sigma_0^x} [1-(1-\omega_f)^{1+\phi}] \right\}^{1/(1+m)}. \tag{9}$$

Equation (9) can be rewritten to obtain an expression describing ω_f in terms of stress, temperature, and the time to failure:

$$\omega_f = 1 - \left\{ 1 - \frac{C(1+\phi)e^{-Q_D/RT} t_f^{1+m}}{(1+m)} \sigma_0^x \right\}^{1/(1+\phi)}. \tag{10}$$

A function describing the current state of damage as a function of time, $\omega(t)$, can be derived by integrating Eq. (7), or by substituting t for t_f in Eq. (10):

$$\omega(t) = 1 - \left\{ 1 - \frac{C(1+\phi)e^{-Q_D/RT} t^{1+m}}{(1+m)} \sigma_0^x \right\}^{1/(1+\phi)}. \tag{11}$$

Another useful expression for the current state of damage can be derived by combining Eqs. (9) and (11):

$$\omega(t) = 1 - \left\{ 1 - \left(\frac{t}{t_f} \right)^{1+m} [1-(1-\omega_f)^{1+\phi}] \right\}^{1/(1+\phi)}. \tag{12}$$

Now that the damage evolution has been derived, we will turn our attention to the creep strain accumulation and the effect of the current state of damage on it. The creep rate expression was given earlier in Eq. (8). Substituting Eq. (12) into Eq. (8) yields the following alternative expression for the creep rate:

$$\dot{\epsilon} = Gt^m \sigma_0^n e^{-Q_C/RT} \left\{ 1 - \left(\frac{t}{t_f} \right)^{1+m} [1-(1-\omega_f)^{1+\phi}] \right\}^{-n/(1+\phi)}. \tag{13}$$

Finally, upon integration of Eq. (13), an expression describing how the creep strain varies with time, temperature, and stress is derived:

$$\epsilon(t) = \frac{\left(\frac{1+\phi}{1+\phi-n} \right) Gt_f^{1+m} \sigma_0^n e^{-Q_C/RT}}{(1+m)[1-(1-\omega_f)^{1+\phi}]} \left\{ 1 - \left[1 - \left(\frac{t}{t_f} \right)^{1+m} \times [1-(1-\omega_f)^{1+\phi}] \right]^{(1+\phi-n)/(1+\phi)} \right\}. \tag{14}$$

Equation (14) describes the entire creep curve, including the primary, secondary, and tertiary regions. Depending on the value for ω_f, Eq. (14) can simulate creep curves with severe tertiary behavior ($\omega_f \rightarrow 1$) as well as creep curves displaying no tertiary characteristics ($\omega_f \rightarrow 0$). This behavior can be visualized by setting $\omega = \omega_f$ in the creep rate Eq. (8), which results in formulation for the creep rate at failure. The creep strain Eq. (14) can be rewritten in terms of the current state of damage $\omega(t)$ as follows:

$$\epsilon(t) = \frac{\left(\frac{1+\phi}{1+\phi-n} \right) Gt_f^{1+m} \sigma_0^n e^{-Q_C/RT}}{(1+m)[1-(1-\omega_f)^{1+\phi}]} \{ 1 - (1-\omega(t))^{1+\phi-n} \}. \tag{15}$$

An expression for the rupture strain, ϵ_f, can be obtained by setting $\omega = \omega_f$ in Eq. (15):

$$\epsilon_f = \frac{\left(\frac{1+\phi}{1+\phi-n}\right) G t_f^{1+m} \sigma_0^n e^{-Q_C/RT}}{(1+m)[1-(1-\omega_f)^{1+\phi}]} \{1-(1-\omega_f)^{1+\phi-n}\}. \quad (16)$$

Note that all the equations derived in this section will collapse to Kachanov's isothermal steady-state formulation if the activation energies and the time exponent parameters (Q_D, Q_C, m), are set to zero, and $\omega_f = 1$.

A worthwhile discussion at this point is one that relates the damage accumulation using the Robinson's (1952) time fraction rule, D, and the CDM current state of damage, ω. This is necessary because under conditions of varying temperature and/or stress, Robinson's linear damage summation rule is utilized to predict creep rupture. In order to accomplish this task of comparing these two formulations, let us first rewrite Eq. (12) into the following form:

$$D = \frac{t}{t_f} = \left[\frac{1-(1-\omega)^{1+\phi}}{1-(1-\omega_f)^{1+\phi}}\right]^{1/(1+m)}. \quad (17)$$

The term D represents the damage due to creep deformation after time t and is given by the time fraction t/t_f. For conditions in which constant uniaxial stress states exit, it can be seen that at the time of failure, when $\omega = \omega_f$ and $t = t_f$, $D = 1$. It is also apparent from Eq. (17) that the damage as defined by the life fraction term, t/t_f, does not equal the current state of damage, ω. For constant stress and temperature conditions, either the condition $D = 1$ or the condition $\omega = \omega_f$ can be used to predict rupture.

However, for varying stress (stress relaxation) and/or temperature conditions, the linear damage summation rule should be utilized. For such conditions, the design life of the component is discretized into short time steps. The damage is computed for each time step through dividing the time duration for that time step, t_i, by the predicted rupture life, t_{fi}, based on the current stress and temperature states and CDM theory (Eq. (9)). The cumulative damage, $D = \Sigma D_i = \Sigma(t_i/t_{fi})$, is subsequently calculated. Failure is assumed to occur when the normalized cumulative damage, D, at any point in the component reaches unity.

Other forms of creep damage assessment have recently been suggested. One such formulation is based on the concept of ductility exhaustion (Zamrik and Davis, 1990; Hales, 1988). Ductility exhaustion is similar in concept to Robinson's life fraction rule except that it uses strain fraction. Failure occurs when the cumulative strain reaches a critical value, usually assumed equal to the ductility in a constant load creep test (Penny and Marriott, 1995). Hence, the condition for failure is $D = \Sigma(\epsilon_i/\epsilon_{fi}) = 1$.

Multiaxial Stress Formulation. Engineering structures are seldom subjected to uniaxial stress states. Hence, it is necessary to extend the unixial CDM formulation presented in the previous section to the multiaxial case. CDM multi-axial stress development for isothermal steady state conditions, and assuming that $\omega_f = 1$ at failure, have been described by Kachanov (1958), Leckie and Hayhurst (1977), Hayhurst et al. (1983, 1984), Penny and Marriott (1995), and Krajcinovic (1987).

The uniaxial creep strain and damage laws were given by Eqs. (8) and (7), respectively. In the absence of damage the multiaxial creep rate equation is usually stated in the Von Mises form. A similar creep rate law taking into account the effect of damage can be stated as

$$\dot{\epsilon}_{ij} = \frac{d\epsilon_{ij}}{dt} = \frac{3}{2}\frac{\dot{\epsilon}_e}{\sigma_e} S_{ij} = \frac{3}{2}\frac{G t^m e^{-Q_C/RT} \sigma_e^{n-1}}{(1-\omega(t))^n} S_{ij}, \quad (18)$$

where $d\epsilon_{ij}/dt$ is the creep strain rate tensor, S_{ij} is the deviatoric stress tensor, ϵ_e is the effective creep strain, and σ_e is the Von Mises effective stress. The effective creep rate is obtained by replacing the uniaxial stress with the effective stress in Eq. (8). Similarly, the damage law for the multiaxial stress condition can be written as (note that the damage is a scalar term)

$$\dot{\omega} = \frac{d\omega}{dt} = \frac{C t^m e^{-Q_D/RT}}{(1-\omega(t))^\phi} \sigma_{eq}^x, \quad (19)$$

where σ_{eq} is the equivalent stress. Integrating Eq. (19), and assuming that σ_{eq} remains constant, yields the following equation describing the current state of damage in a multiaxial stress state:

$$\omega(t) = 1 - \left[1 - \frac{C(1+\phi) e^{-Q_D/RT} t^{1+m}}{(1+m)} \sigma_{eq}^x\right]^{1/(1+\phi)}. \quad (20)$$

Solving for the rupture time using Eq. (20) by setting $\omega = \omega_f$ (this corresponds to $t = t_f$), results in

$$t_f = \left\{\frac{(1+m) e^{Q_D/RT}}{C(1+\phi)\sigma_{eq}^x}[1-(1-\omega_f)^{1+\phi}]\right\}^{1/(1+m)}. \quad (21)$$

The equivalent stress term, σ_{eq}, correlates the damage under uniaxial tension with the damage under multiaxial stress states. Kachanov (1958) proposed setting the equivalent stress equal to the maximum normal tensile stress, $\sigma_1 (\sigma_{eq} = \sigma_1)$. Hayhurst, on the otherhand, proposed the following mixed criterion for the equivalent stress:

$$\sigma_{eq} = \alpha\sigma_1 + (1-\alpha)\sigma_e, \quad (22)$$

where α is a factor to be determined from two sets of creep tests, each carried out under a different multiaxial stress state (Hayhurst et al., 1984). Two extreme material classifications can be seen through Eq. (22). The first category corresponds to material failure governed by the maximum principal tensile stress criterion ($\alpha = 1$); the behavior of copper is described by this criterion. For the second category, the creep rupture time is governed by maximum effective (Von Mises) stress criterion ($\alpha = 0$); the behavior of aluminum is described by this criterion. Unfortunately, for ceramics no comprehensive multi-axial creep database exists. Thus, in this paper the equivalent stress will be set to either σ_1 or σ_e whichever results in the shorter life to failure.

In our life prediction methodology, FEA is used to perform the stress and creep deformation analysis. The ANSYS FEA package was utilized for this purpose. The ANSYS program allows the user to define his/her creep constitutive law through its user defined creep subroutine. This capability was used and described in more detail by the authors (Jadaan et al., 1997; Powers et al., 1996) in previous publications. The CDM creep rate and damage laws (Eqs. (18), (20), and (22)) were programmed into ANSYS to compute the creep strain rate tensor, and consequently the stress and deformation history for the component in question.

The CARES/Creep code developed by the authors (Powers et al., 1996; Jadaan et al., 1997) to predict the creep rupture life of ceramic components based on the modified Monkman–Grant creep rupture criterion, was expanded to add the capability of predicting rupture based on CDM. In summary, the CARES/Creep code is made up of two modules and is currently customized to run as a post-processor to the ANSYS FEA code. The first module is a parameter estimation program used to compute the creep material parameters. Parameter estimation for the CDM laws will be discussed in the next section. The second module contains the coding for calculating the cumulative damage as a function of time at each node/element of the meshed component, and thus its creep rupture life. The methodology used in this module is described next.

As was stated earlier, to carry out a creep life prediction analysis for a given component the creep life of the component is divided into short time steps, t_i, during which the stress state is assumed constant. This is done because even for constant load/temperature conditions, the stress state can vary with time due to creep deformation. During each time step and at each node/element, the time to failure, t_{fi}, is calculated using Eq. (21) and the existing stress/temperature state. Subsequently, the damage for each time step and at each node/element based on Robinson's time fraction rule, $D_i = t_i/t_{fi}$, is computed. Damage summation as a function of time, $D = \Sigma D_i = \Sigma(t_i/t_{fi})$, is then performed at each node/element. Failure

commences when the damage, D, at any node/element reaches unity.

Parameter Estimation

The CDM model presented in this paper contains nine material parameters to be determined form creep tensile data. These parameters are G, n, m, ϕ, Q_C, ω_f, C, x, and Q_D. Due to the nonlinear nature of the model, nonlinear regression using, the IMSL routine DRNLIN, was used to compute these constants. This routine utilizes a modified Levenberg–Marquardt (Press et al., 1989) least squares method.

The IMSL nonlinear regression routine requires the user to provide initial guesses for the parameters to be determined. The routine would then use these guesses as starting values and search in the space surrounding them for optimized parameters that would minimize the sum of square errors (SSE). Due to the large number of parameters to be determined in this model, the routine often did not converge. For the trials when the IMSL routine converged, it often converged to a local minimum, yielding values close to what was initially guessed or values that did not make physical sense such as zero activation energies or negative stress exponents. This dependence of converged parameter values on the initial guesses causes two problems. The first is that different users making different initial guesses can have different creep parameters. This will result in different life predictions for the same component. The second problem is that the accuracy of the computed parameters depends on the quality of the initial guesses made.

In order to alleviate these problems, and to automate the nonlinear regression parameter estimation procedure in such a way that all users would converge to the same parameters, the following parameter estimation methodology was devised:

1 Use the Baily-Norton constitutive creep model to obtain initial guesses for the four CDM creep parameters, G, n, m, and Q_C. The Baily-Norton model is a relatively simple one, the parameters of which can be obtained via simple multiple linear regression analysis. The Baily–Norton creep rate equation is given by

$$\dot{\epsilon} = C_1 \sigma^{C_2} t^{C_3} e^{-C_4/T}, \tag{23}$$

where C_1 through C_4, are material constants that can be determined via multiple linear regression analysis. The parameter estimation module within CARES/Creep is used to compute these parameters (Powers et al., 1996; Jadaan et al., 1997). Comparing the CDM and the Baily–Norton creep rate Eqs. (8) and (23), it can be seen that the parameters G, n, m, and Q_C/R have the same correspondence and physical interpretation as the Baily–Norton parameters, C_1, C_2, C_3, and C_4, respectively. Therefore, these C_1 through C_4 parameters are used as good initial guesses for the four CDM parameters, G, n, m, and Q_C/R, respectively.

2 From Eqs. (14) and (15), it is apparent that ϕ should be greater than $n - 1$, in order to obtain positive tensile strains in response to positive tensile stresses. In order to automate the parameter estimation process, the initial guess for ϕ is set randomly equal to $n + 2$. The critical damage state parameter must remain within the range $0 < \omega_f \leq 1$. Again, in order to automate the process, ω_f is set equal to 0.1 for materials displaying very little or no tertiary creep behavior, and 0.9 for materials displaying significant tertiary creep behavior. Another alternative available to the user is to set ω_f to a default intermediate value of 0.5, and let the nonlinear regression routine shift it up or down depending on whether or not the creep data displays tertiary creep characteristics. Now that we have good starting guesses for the six parameters G, n, m, Q_C, ϕ, and ω_f, the IMSL nonlinear regression routine DRNLIN is used to fit the creep data to the creep strain Eq. (14). This curve fitting requires that the creep strain and the corresponding time, stress, temperature, and time to failure for tensile creep specimens be available. This step of the parameter estimation methodology should ultimately result in convergence for the six CDM parameters stated above.

3 Finally, nonlinear regression is applied to Eq. (9) in order to obtain the last three parameters C, x, and Q_D. Note that this equation describes the time to failure as a function of stress and temperature, and, thus, uses one data point per creep curve. This data point obviously corresponds to that at the point of rupture. Equation (9) contains the already determined parameters m, ϕ, and ω_f. Therefore, these parameters are used as known constants for this procedure.

Due to the relatively few number of constants to be determined in this step (C, x, and Q_D), the nonlinear regression routine associated with reasonable starting guesses for these parameters is generally stable. In order to assure convergence and automate the process, the following procedure for choosing starting values for these three parameters is suggested. First, the parameters C and x are set equal to 1. Subsequently, these initial guesses for C and x, and the already known values for m, ϕ, and ω_f in association with any creep rupture data point (t_f, σ, T) are substituted into Eq. (9) to compute a corresponding starting guess for Q_D. Now, the nonlinear regression procedure is applied to Eq. (9), using these three starting guesses for C, x, and Q_D. This results in convergence to a set of parameters corresponding to minimized SSE.

To test the methodology described above and make sure that different users would obtain the same results, two of the authors of this paper applied this procedure, independently from each other, to three different sets of actual creep data. Two of these creep data sets will be presented in the next section. They both converged to the same parameters, which proved to describe the creep curves well.

Examples

Two benchmark examples of creep life prediction for ceramic components under multiaxial and uniaxial loading conditions are presented in this section to validate the CDM based approach and the CARES/Creep program. The first example is a silicon nitride NCX-5100 notched tensile specimen, which was analyzed as a part of Saint–Gobain/Norton advanced heat engine applications program. A multiaxial stress state exists at the notch root where creep rupture is predicted to occur. Hence, this example represents the application of the theory presented in this paper to multiaxial stress conditions. The second example involves the application of the theory to uniaxial tensile SN88 silicon nitride specimens. This example is used to demonstrate the ability of the CDM theory in representing the creep curves for materials displaying tertiary creep behavior.

Notched NCX-5100 Tensile Specimen. The aim of this example is to predict the multiaxial creep rupture behavior of silicon nitride NCX-5100, using creep data obtained from testing uniaxial smooth tensile specimens. All experimental creep data used in this example were obtained from reports published by Sundberg et al. (1994), Wade et al. (1994), and White et al. (1995). These creep data were part of a study on the joining of silicon nitride to silicon nitride for advanced heat engine applications. The creep tests were conducted on two types of specimens. First, smooth tensile specimens were tested under creep conditions to characterize the creep response of the NCX-5100 material. Second, experiments on notched tensile bars were performed. This specimen configuration yields a multiaxial stress state in the vicinity of the notch root, where creep rupture is expected to initiate.

The uniaxial smooth tensile test geometry consists of a flat dog-bone specimen with tapered holes to account for the relief of out-of-plane alignment. The creep characteristics of the NCX-5100 silicon nitride material when isothermally loaded in uniaxial tension at temperatures in the 1275–1425°C range were investigated. The creep curves corresponding to these tests were provided to the authors for analysis.

Using the parameter estimation methodology described above,

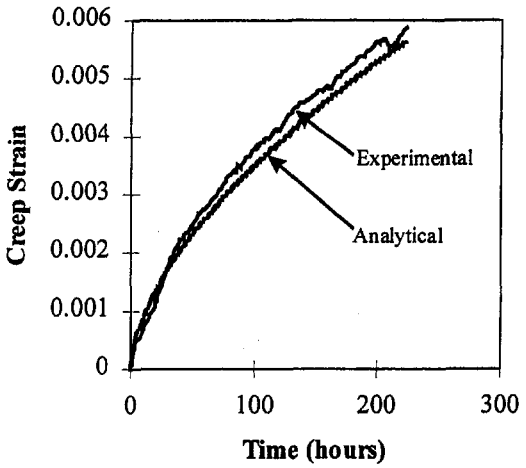

Fig. 2 Comparison between experimental and analytical creep curves for the NCX-5100 material at 1350°C and 175 MPa

the nine CDM parameters were computed to be $G = 5944$, $n = 1.53$, $m = -0.422$, $Q_C/R = 41300$, $\omega_f = 0.048$, $\phi = 1.53$, $C = 0.347 \times 10^{-5}$, $x = 2.83$, and $Q_D/R = 13{,}760$. These parameters are based on units of MPa, hours, and °K. The initial guesses for G, n, m, and Q_c/R when running the nonlinear regression routine, were obtained from the Baily–Norton model using the existing CARES/Creep multiple linear regression parameter estimation module. These parameters were found to be $C_1 = 3211$, $C_2 = 1.3$, $C_3 = -0.374$, and $C_4 = 38700$°K. The NCX-5100 material displays no tertiary creep behavior, which explains why ω_f is so small. Interestingly, the value $\omega_f = 4.8$ percent is very close to a measurement of 5.5 percent, conducted by Menon et al. (1994) using image analysis of the fraction of cavitated area after creep rupture of an NT-154 silicon nitride tensile specimen tested at 1400°C. The NT-154 material also displays no tertiary creep behavior.

Figure 2 shows a comparison between experimental and analytical creep curves for smooth tensile NCX-5100 material. The analytical creep curves was calculated using Eq. (14). As can be seen from the figure, the CDM constitutive creep model was successful in describing the creep behavior for the NCX-5100 material.

The FEM mesh for the notched specimen is shown in Fig. 3. Due to symmetry, analysis can be performed using one-quarter of the bar. The ANSYS model contains 598 axisymmetric elements (PLANE82). The notch is on the outside of the bar and its radius is 20 percent of the radius of the tensile specimen gage section. The mesh is refined near the notch root so that the stress state in that region can be more accurately characterized. The nonlinear transient creep FEM stress results obtained by the authors were very close to those reported by Foley et al. (1992) and White et al. (1995), thus yielding confidence in the FEM creep stress analysis performed in both studies.

Four notched bars were tested at 1370°C (Sundberg, et al., 1994). The reduced section average stresses were 105, 120, 135, and 150 MPa. Table 1 compares the experimental and predicted lives for these specimens as a function of their reduced section stress. As can be seen from the table, the predicted lives for these specimens using the CDM methodology described in this paper and computed via CARES/Creep compare well with the experimental failure times.

The maximum principal stress distributions for the 120 MPa reduced average section stress specimen, as a function of time, are shown in Fig. 4. Figures 4(*a*), and 4(*b*) are the maximum principal stresses at 0 and 50 hours, respectively. A multiaxial stress state exists in the vicinity of the notch root, which reduces to a uniaxial stress state away from the notch. When the load is initially applied at time = 0, the maximum principal stress at the notch root is

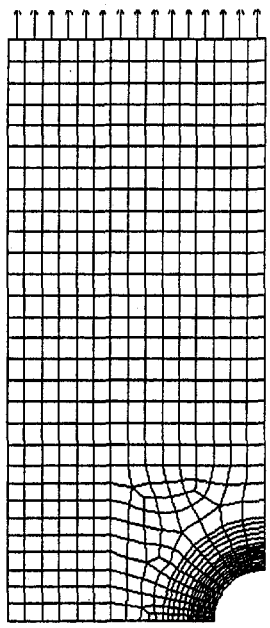

Fig. 3 Axisymmetric finite element mesh for the notched specimen

computed to be 258 MPa. As time progresses (Fig. 5) the stress relaxes at the notch root due to creep deformation, and decays to approximately 209 MPa after 50 hours. It is expected that given enough time, the maximum stress location would displace to the interior of the specimen. In a previous study conducted by the authors (Powers et al., 1996) and based on steady-state creep analysis using the Norton's model, it was found that at the time of failure the location of the maximum principal stress was a short distance within the specimen from the notch root. That finding concurred with that of White et al. (1995) who conducted similar steady-state analysis. Stress relaxation directly influences damage calculations, and, thus, the predicted time and location of creep rupture. This is because the location of the maximum cumulative damage could displace as the stress redistributes with time. In the current study, which takes into account the primary creep effect and is based on CDM, the locations of both the maximum tensile stress and the maximum cumulative damage were at the notch root. This prediction concurs with fractographic examinations (White et al., 1995) conducted on the failed notched specimens and found them all to have failed at the surface of the notch root. Figure 6 shows a cumulative damage map for the 120 MPa bar after 50 hours. Figure 7 displays the evolution of damage as a function of time at the notch root where rupture is predicted to occur. It can be seen from Fig. 6 and Fig. 7 that the damage reaches unity after 44 hours, which corresponds to rupture, at the notch root.

The maximum principal stress rather than the equivalent stress was used to predict the creep rupture life for the notched specimens. This was done, based on the discussion advanced in the multiaxial stress section of this paper, since the maximum principal stress resulted in the most conservative estimate for the creep rupture life (shorter life).

Table 1 Predicted and experimental creep rupture results for the notched tensile creep specimens tested at 1370°C

Reduced Section Average Stress (MPa)	Experimental Failure Time (hours)	Predicted Failure Time Using CDM (hours)
105	314	94
120	44	47
135	39	25
150	3.5	13.5

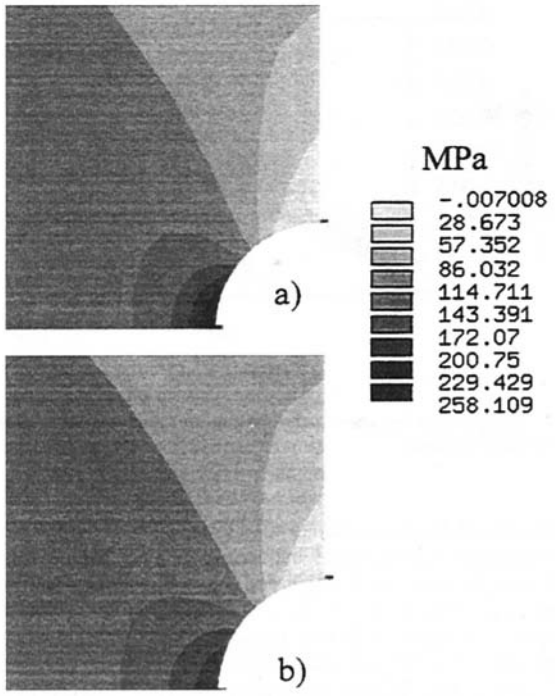

Fig. 4 Maximum principal stress distribution in the notched tensile specimen tested at a reduced section stress of 120 MPa at time equal to (*a*) zero and (*b*) 50 hours

Smooth SN88 Tensile Specimen. This example is used to demonstrate the capability of the CDM model in capturing the tertiary creep behavior for isothermal constant stress tensile ceramic specimens. The SN88 silicon nitride material (NGK Insulators, Nagoya, Japan) was selected for this purpose because it displays tertiary creep behavior, and because some of the data was available in the open literature (Luecke et al., 1997; French et al., 1996). The full data corresponding to the entire creep curves were supplied to the authors by Luecke. Five different laboratories were involved in testing a total of 24, 76-mm long SN88 tensile creep specimens at 1400°C under a 150 MPa stress.

The CDM equations presented in this paper thus far, were derived taking into account temperature and stress dependence. In other words, in order to compute the parameters in these equations, several creep tests conducted at various temperature and stress levels should be performed. Often, it is required to fit constitutive equations to isothermal constant stress creep curves such as in this example. Therefore, the CDM equations presented above should be reformulated to describe the creep behavior of specimens tested at the same temperature and stress levels. These isothermal and constant stress CDM equations are described next.

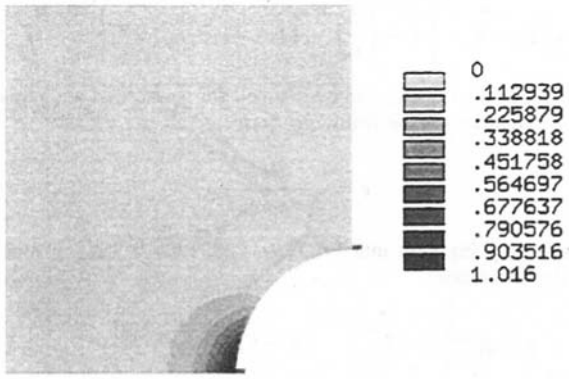

Fig. 6 Cumulative damage distribution in the notched tensile specimen tested at a reduced section stress of 120 MPa

Since the stress and temperature in Eq. (7) are constant, then that equation describing the damage rate can be rewritten as

$$\dot{\omega} = \frac{At^m}{(1-\omega)^{\phi}}, \tag{24}$$

where A, m, and ϕ are material constants. Note that the stress and temperature terms were incorporated into the A constant. Upon integration of Eq. (24) from $t = 0$ to $t = t_f$, the following formula describing the time to failure is obtained:

$$t_f = \left\{ \frac{(1+m)}{A(1+\phi)} \left[1 - (1-\omega_f)^{1+\phi} \right] \right\}^{1/(1+m)}. \tag{25}$$

Inversely, Eq. (25) can be rewritten in terms of the critical damage at failure, ω_f, as

$$\omega_f = 1 - \left\{ 1 - \frac{A(1+\phi)t_f^{1+m}}{(1+m)} \right\}^{1/(1+\phi)}. \tag{26}$$

The damage at a given time t can be obtained by replacing t_f with t in Eq. (26):

$$\omega(t) = 1 - \left\{ 1 - \frac{A(1+\phi)t^{1+m}}{(1+m)} \right\}^{1/(1+\phi)}. \tag{27}$$

Combining Eqs. (26) and (27), yields the following alternative form for $\omega(t)$:

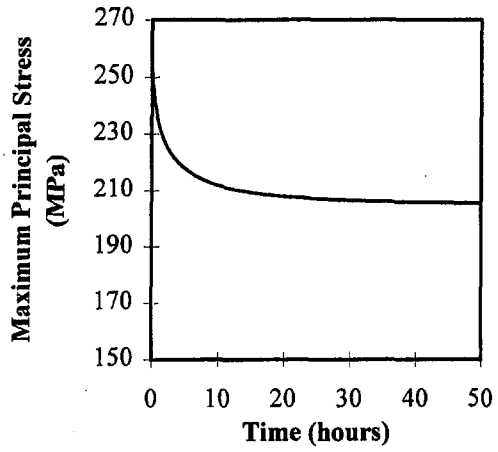

Fig. 5 Maximum principal stress relaxation at the notch root for the 120 MPa reduced section stress specimen

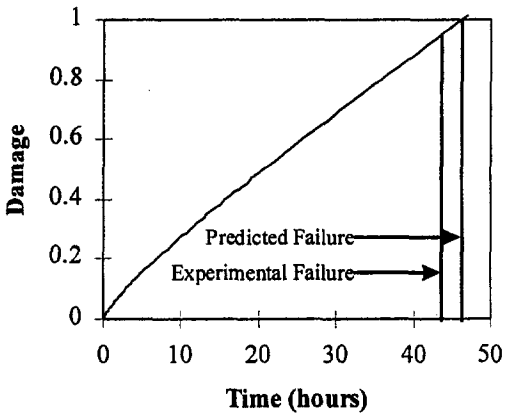

Fig. 7 Evolution of damage as a function of time at the notch root for the tensile specimen tested at a reduced section stress of 120 MPa

$$\omega(t) = 1 - \left\{ 1 - \left(\frac{t}{t_f}\right)^{1+m} [1 - (1 - \omega_f)^{1+\phi}] \right\}^{1/(1+\phi)}. \quad (28)$$

The creep rate Eq. (8), can be restated for isothermal and constant stress condition in the following form:

$$\dot{\epsilon} = \frac{Bt^m}{(1 - \omega(t))^n}. \quad (29)$$

Substituting Eq. (28) into Eq. (29), yields the following function for the creep rate:

$$\dot{\epsilon} = Bt^m \left\{ 1 - \left(\frac{t}{t_f}\right)^{1+m} [1 - (1 - \omega_f)^{1+\phi}] \right\}^{-n/(1+\phi)}. \quad (30)$$

Integrating Eq. (30) results in the following equation describing the creep strain as a function of time:

$$\epsilon(t) = \frac{\left(\frac{1+\phi}{1+\phi-n}\right) Bt_f^{1+m}}{(1+m)[1-(1-\omega_f)^{1+\phi}]} \left\{ 1 - \left[1 - \left(\frac{t}{t_f}\right)^{1+m} \times [1 - (1 - \omega_f)^{1+\phi}] \right]^{(1+\phi-n)/(1+\phi)} \right\}. \quad (31)$$

Combining Eqs. (28) and (31), results in the following equation describing the creep strain as a function of the current state of damage:

$$\epsilon(t) = \frac{\left(\frac{1+\phi}{1+\phi-n}\right) Bt_f^{1+m}}{(1+m)[1-(1-\omega_f)^{1+\phi}]} \{1 - (1 - \omega(t))^{1+\phi-n}\}. \quad (32)$$

Assuming that $\phi = n$, which implies that the damage accumulation affects the damage rate in a similar fashion as it affects the creep rate, Eq. (31) simplifies to the following form:

$$\epsilon(t) = \frac{B(1+\phi)t_f^{1+m}}{(1+m)[1-(1-\omega_f)^{1+\phi}]} \left\{ 1 - \left[1 - \left(\frac{t}{t_f}\right)^{1+m} \times [1 - (1 - \omega_f)^{1+\phi}] \right]^{1/(1+\phi)} \right\}. \quad (33)$$

The assumption that $\phi = n$ is very reasonable based on nonlinear regression parameter estimation results. Note that for the NCX-5100 material, the parameters, n and ϕ, converged to the same value. The same result was found by the authors for the NT154 silicon nitride material, which is not shown in this paper.

The SN88 creep parameters were computed using the same parameter estimation methodology described previously. Nonlinear regression applied to Eq. (33) was used to determine the four parameters B, m, ϕ, and ω_f. They were found to be: $B = 0.000838$, $m = -0.456$, $\phi = 1878$, and $\omega_f = 0.0007$. Subsequently, Eq. (25) was regressed to obtain the last parameter A. It was calculated to be $A = 2.01 \times 10^{-5}$. These values are based on units of hours.

Figure 8 shows the experimental creep curves for several SN88 tensile specimens tested at 1400°C under a 150 MPa stress. In addition, this figure displays the corresponding predicted creep curve plotted using the creep parameters listed above. The X sign shown at the end of the predicted creep curve indicates the predicted time to failure for this specimen. It is obvious from Fig. 8 that some scatter exists among the various creep curves. The predicted creep curve falls in the middle of the experimental creep curves and displays tertiary creep behavior. The predicted time to failure also compares very well with the measured rupture times (end of experimental creep curves). These results show that the CDM model described above is capable of representing entire creep curves including the tertiary creep regime.

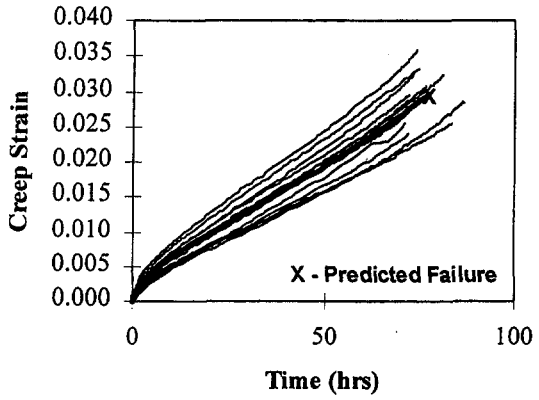

Fig. 8 Comparison between experimental and analytical creep curves for the SN88 material

The critical damage parameter, ω_f, was found to be low for the SN88 material even though it displays tertiary creep behavior. This is because the increase in the creep rate within the tertiary creep regime is a function of $(1 - \omega)^{\phi}$, and, thus, the parameters ω and ϕ. Since the exponent ϕ was found to be a large number, this compensated for the low value computed for ω_f. The nonlinear regression routine through its iterative procedure converges to the optimum set of parameters that would minimize the SSE for the data set in question.

Conclusions

A creep life prediction methodology based on the continuum damage mechanics theory was described. In this theory, the uniaxial creep rate is described in terms of stress, temperature, time, and the current state of material damage. The damage rate is assumed to vary with stress, temperature, time, and the current state of damage itself. Multiaxial creep and creep rupture formulations of the CDM approach were presented. Parameter estimation methodologies based on nonlinear regression analysis were also described for both, isothermal constant stress states and anisothermal variable stress conditions. Several advantages are apparent to the creep rupture life methodology presented in this paper. First, this methodology yields a cumulative damage map for the component showing the critical locations where failure would originate. This capability is very helpful for practical design applications. Through viewing such a damage map, the user can change the design parameters to reduce the damage at the critical locations and optimize the design. In creep type loading applications, it is not a trivial task to predict the location of failure since the multiaxial stress components get redistributed as time elapses. Thus, failure will not necessarily occur at the location where stresses are highest at the beginning of loading or at the time of failure, but can take place elsewhere. Second, this methodology is capable of incorporating the effects of primary and tertiary creep on rupture. Third, any equivalent stress criterion can be used to predict the component's life. Fourth and perhaps most importantly, this methodology takes into account the effect of instantaneous damage on the deformation and rupture of the component. This creep life prediction methodology was added to the integrated design code ceramics analysis and reliability evaluation of structures/creep (CARES/Creep), which is a postprocessor program to commercially available finite element analysis (FEA) packages. Two examples, showing comparisons between experimental and predicted creep lives of ceramic specimens, were used to demonstrate the viability of this methodology and the CARES/Creep program.

References

Boyle, J., and Spence, J., 1983, *Stress Analysis for Creep*, Butterworth & Co., London.

Dunne, F. P. E., Othamn, A. M., Hall, F. R., and Hayhurst, L. M., 1990, "Repre-

sentation of Uniaxial Creep Curves Using Continuum Damage Mechanics," *International Journal of Mechanical Science,* Vol. 32, No. 11, pp. 945–957.

Ferber, M. K., and Jenkins, M. G., 1992, "Empirical Evaluation of Tensile Creep and Creep Rupture in a HIPed Silicon Nitride," in *Creep: Characterization, Damage and Life Assessment,* ASM International Woodford, D. A., Townley, C. H. A., and Ohnami, M., eds., pp. 81–90.

Foley, M., Rossi, G., Sundberg, G., Wade, J., and Wu, F., 1992, "Analytical and Experimental Evaluation of Joining Silicon Carbide to Silicon Carbide and Silicon Nitride to Silicon Nitride for Heat Engine Applications," final report, Ceramic Technology for Advanced Heat Engines, Oak Ridge National Lab.

French, J. D., and Wiederhorn, S. M., 1996, "Tensile Specimens from Ceramic Components," *Journal of the American Ceramic Society,* Vol. 79, No. 2, pp. 550–552.

Hales, R., 1988, "Physical Mechanisms of Fracture in Combined Creep and Fracture," Proceedings, Inst. Metals Conference on Materials and Engineering Design, London.

Hault, J., 1987, "Introduction and General Overview," *Continuum Damage Mechanics Theory and Applications,* D. Krajcinovic, and J. Lemaitre, eds., Springer-Verlag, New York.

Hayhurst, D. R., Dimmer, P. R., and Cheruka, M. W., 1975, "Estimates of the Creep Rupture Lifetime of Structures Using the Finite Element Method," *Journal of Mechanical Physics of Solids,* Vol. 23, pp. 335–355.

Hayhurst, L. M., Dimmer, P. R., and Morrison, C. J., 1984a, "Development of Continuum Damage in the Creep Rupture of Notched Bars," *Phil. Trans. R. Soc. Lond.,* Vol. 311, pp. 103–129.

Hayhurst, L. M., Brown, P. R., and Morrison, C. J., 1984b, "The Role of Continuum Damage in Creep Crack Growth," *Phil. Trans. R. Soc. Lond.,* Vol. 311, pp. 131–158.

Hazime, R. M., and White, C. S., 1996, "An Internal Variable, Creep Damage Model of a Silicon Nitride," submitted for publication in *Materials Science and Engineering.*

Jadaan, O. M., Powers, L. M., and Gyekenyesi, J. P., 1997, "Creep Life Prediction of Ceramic Components Subjected to Transient Tensile and Compressive Stress States," ASME Paper 97-GT-319.

Kachanov, L. M., 1958, "On Creep Rupture Time," Izv. Acad. Nauk SSSR, Otd. Tech. Nauk, No. 8.

Kachanov, L. M., 1986, *Introduction to Continuum Damage Mechanics,* MartinusNijhof, Boston.

Kraus, H., 1980, *Creep Analysis,* John Wiley and Sons Inc., New York.

Leckie, F. A., Hayhurst, L. M., 1977, "Constitutive Equations for Creep Rupture," *Acta Metallurgica,* Vol. 25, pp. 1059–1070.

Luecke, W. E., and Wiederhorn, S. M., 1997, "Interlaboratory Verification of Silicon Nitride Tensile Creep Properties," *Journal of the American Ceramic Society,* Vol. 80, No. 4, pp. 831–838.

Menon, M., Fang, H., Wu, D., Jenkins, M., and Ferber, M., 1994, "Creep and Stress Rupture Behavior of an Advanced Silicon Nitride: Part III, Stress Rupture and Monkman-Grant Relationships," *Journal of the American Ceramic Society,* Vol. 77, pp. 1235–1241.

Miner, M. A., 1945, "Cumulative Damage in Fatigue," ASME *Journal of Applied Mechanics,* Vol. 12, pp. A159–A164.

Monkman, F., and Grant, N., 1956, "An Empirical Relationship Between Rupture Life and Minimum Creep Rate in Creep-Rupture Test," Proceedings, American Society for Testing and Materials, Vol. 56, pp. 593–620.

Norton, F., 1929, *The Creep of Steel at High Temperatures,* McGraw-Hill, New York.

Othman, A. M., and Hayhurst, L. M., 1990, "Multi-Axial Creep Rupture of a Model Structure Using a Two Parameter Material Model," *International Journal of Mechanical Science,* Vol. 32, No. 1, pp. 35–48.

Penny, R. K., and Marriott, D. L., 1995, *Design for Creep,* Chapman & Hall, London.

Powers, L. M., Jadaan, O. M., and Gyekenyesi, J. P., 1996, "Creep Life of Ceramic Components Using a Finite Element Based Integrated Design Program (CARES/Creep)," ASME Paper 96-GT-369.

Press, W. H., Flannery, B. P., Teukolsky, S. A., and Vetterling, 1989, *Numerical Recipes,* Cambridge University Press, Cambridge.

Rabotonov, Yu. N., 1969, *Creep Problems in Structural Members,* North-Holland, Amsterdam.

Robinson, E. L., 1952, "Effect of Temperature Variation on the Long-Time Rupture Strength of Steels," *Trans. ASME 74,* pp. 777–780.

Stamm, H., and von Estorff, U., 1992, "Determination of Creep Damage in Steels," Proceedings, 5th International Conference on Creep of Materials, FL.

Sundberg, G., Vartabedian, A., Wade, J., and White, C., 1994, "Analytical and Experimental Evaluation of Joining Silicon Carbide to Silicon Carbide and Silicon Nitride to Silicon Nitride for Advanced Heat Engine Applications Phase II," final report, Ceramic Technology Project, Oak Ridge National Lab.

Todd, J. A., and Xu, A.-Y., 1989, "The High Temperature Creep Deformation of Si_3N4-$6Y_2O_3$-$2Al_2O_3$," *Journal of Materials Science,* Vol. 24, pp. 4443–4452.

Wade, J., White, C., and Wu, F., 1994, "Predicting Creep Behavior of Silicon Nitride Components Using Finite Element Techniques," in *Life Prediction Methodologies and Data for Ceramic Materials,* ASTM STP 1201, C. Brinkman, and S. Duffy, eds., American Society for Testing and Materials, Philadelphia, PA, pp. 360–372.

White, C., Vartabedian, A., Wade, J., and Tracey, D., 1995, "Notched Tensile Creep Testing of Ceramics," *Materials Science and Engineering,* Vol. A203, pp. 217–221.

Wiederhorn, S., Quinn, G., and Krause, R., 1994, "Fracture Mechanism Maps: Their Applicability to Silicon Nitride," *Life Prediction Methodologies and Data for Ceramic Materials,* ASTM STP-1201, C. R. Brinkman, and S. F. Duffy, eds., American Society for Testing and Materials, Philadelphia, PA, pp. 36–61.

Zamrik, S. Y., and Davis, D. C., 1990, "A Ductility Exhaustion Approach for Axial Fatigue-Creep Damage Assessment Using Type 316 Stainless Steel," ASME PVP 215.

Ceramic Stationary Gas Turbine Development Program—Fifth Annual Summary

J. R. Price

O. Jimenez

L. Faulder

B. Edwards

V. Parthasarathy

Solar Turbines Incorporated,
2200 Pacific Highway,
San Diego, CA 92186

A program is being performed under the sponsorship of the United States Department of Energy, Office of Industrial Technologies, to improve the performance of stationary gas turbines in cogeneration through the selective replacement of metallic hot section components with ceramic parts. The program focuses on design, fabrication, and testing of ceramic components, generating a materials properties data base, and applying life prediction and nondestructive evaluation (NDE). The development program is being performed by a team led by Solar Turbines Incorporated, and which includes suppliers of ceramic components, U.S. research laboratories, and an industrial cogeneration end user. The Solar Centaur 50S engine was selected for the development program. The program goals included an increase in the turbine rotor inlet temperature (TRIT) from 1010°C (1850°F) to 1121°C (2050°F), accompanied by increases in thermal efficiency and output power. The performance improvements are attributable to the increase in TRIT and the reduction in cooling air requirements for the ceramic parts. The ceramic liners are also expected to lower the emissions of NOx and CO. Under the program uncooled ceramic blades and nozzles have been inserted for currently cooled metal components in the first stage of the gas producer turbine. The louvre-cooled metal combustor liners have been replaced with uncooled continuous-fiber reinforced ceramic composite (CFCC) liners. Modifications have been made to the engine hot section to accommodate the ceramic parts. To date, all first generation designs have been completed. Ceramic components have been fabricated, and are being tested in rigs and in the Centaur 50S engine. Field testing at an industrial co-generation site was started in May, 1997. This paper will provide an update of the development work and details of engine testing of ceramic components under the program.

Introduction

Because of their superior high temperature durability, the application of ceramics as structural materials for gas turbine hot section components will enable a significant increase in the turbine rotor inlet temperature (TRIT) of current all-metal industrial gas turbines, resulting in improved thermal efficiency, greater output power, and reduced emissions of NOx and CO. The U.S. Department of Energy (DOE), Office of Industrial Technologies (OIT), therefore, initiated in September of 1992 a program aimed at developing and demonstrating a ceramic stationary gas turbine (CSGT) for cogeneration operation. Solar Turbines Incorporated (Solar) is the prime contractor on the program which includes participation of major ceramic component suppliers, nationally recognized test laboratories, and an industrial cogeneration end user.

Phase I of the program, started in September of 1992, involved concept and preliminary engine and component design, ceramic materials selection, technical, and economic evaluation, and concept assessment. The work in Phase II, started in April of 1993, focuses on detailed engine and component design, ceramic specimen and component procurement, testing, and the development of appropriate nondestructive technologies for part evaluation, and component life prediction. Phase III of the program revolves around two consecutive engine tests at an industrial cogeneration site.

Previous summaries of the work performed under the CSGT program have been reported (van Roode et al., 1993, 1994, 1995, 1996, 1997). This paper summarizes the recent Phase II development work, in-house ceramic component engine testing and field testing at ARCO Western Energy in Bakersfield, California.

Technical Approach

The technology base for the CSGT program is provided by the advancements in ceramic component fabrication knowledge developed under past ceramic turbine programs, such as the Advanced Gas Turbine (AGT) Program and the Advanced Turbine Technology Applications Program (ATTAP) of the U.S. Department of Energy, Office of Transportation Technologies. The program strategy provides a strong focus on near-term ceramic turbine technology demonstration and lowering barriers for its acceptance by the marketplace. Applications include retrofitting existing gas turbine installations and incorporating ceramic component technologies in future engine designs. The ceramic turbine technology under development in this program is a key enabling technology to realize the performance and environmental goals of the advanced turbine systems (ATS) program, a broad initiative of the U.S. Department of Energy, Office of Fossil Energy, and Office of Energy Efficiency and Renewable Energy, to develop the next generation of high performance gas turbines for utility and industrial applications (U.S. Department of Energy, 1994).

Figure 1 is a schematic of the Solar Centaur 50S, the engine selected for ceramic insertion under the CSGT program. The baseline metal engine has a rated shaft thermal efficiency of 29.6 percent and an electrical output rating of 4144 kW and is fitted with a SoLoNOx dry, low NOx combustion system. The gas producer turbine of the all-metal Centaur 50S has two stages

Contributed by the International Gas Turbine Institute and presented at the International Gas Turbine and Aeroengine Congress and Exhibition, Stockholm, Sweden, June 2–5, 1998. Manuscript received by the ASME Headquarters April 1, 1998. Paper No. 98-GT-181. Associate Technical Editor: R. Kielb.

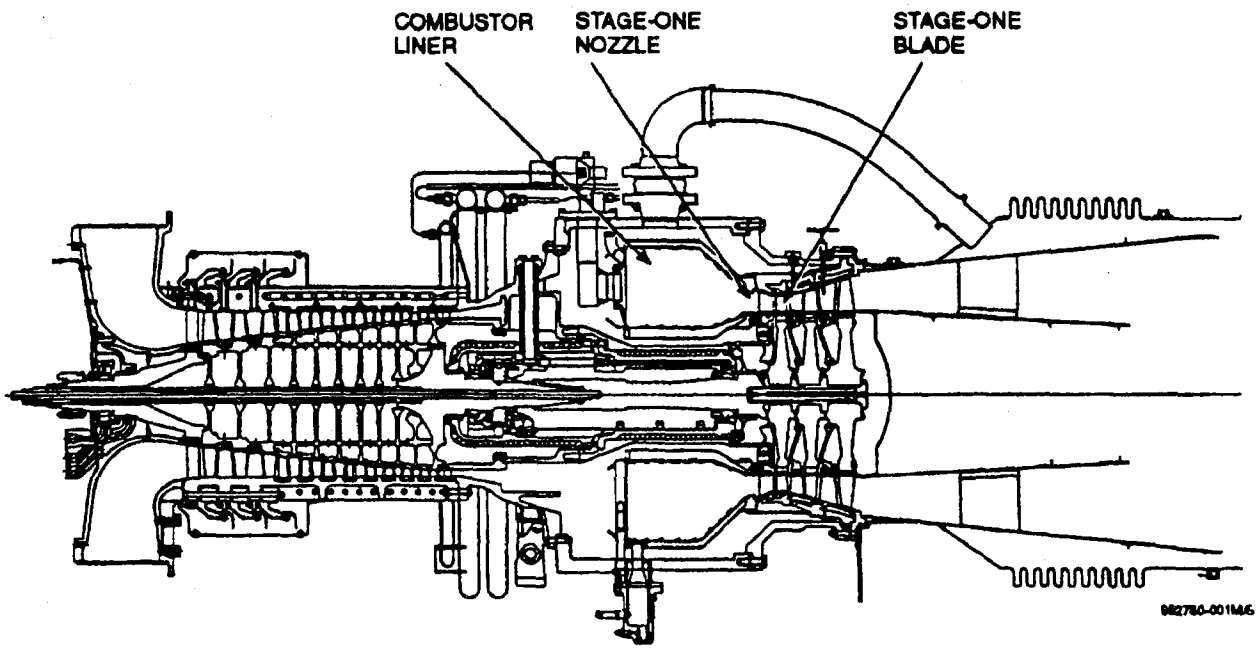

Fig. 1 Solar 50S gas turbine with components targeted for ceramic insertion

and the power turbine has one stage. A single-shaft configuration was selected for the development engine.

The Centaur 50S is being retrofitted with first stage ceramic blades and nozzles, and a ceramic combustor liner. The engine hot section is being redesigned to adapt the ceramic parts to the existing metallic support structure. Accompanying the ceramic insertion the Centaur 50S is being uprated from its current TRIT of 1010°C (1850°F) to a TRIT of 1121°C (2050°F). The performance improvement goals include a relative increase in the electrical thermal efficiency of 5.6 percent in simple cycle and 5.3 percent in cogeneration, and an increase in the electrical output from 4144 kW to 5217 kW, representing a relative increase of about 25.9 percent. Newer engines of the all-metal Centaur 50S meet NOx emissions levels of 25 ppmv over the 50 to 100 percent load range. Under the program NOx emission levels of 25 ppmv or below must be demonstrated and have the potential for NOx levels of 10 ppmv or better. No CO target level was required for the program, but Solar has set a CO target of 25 ppmv. Predicted engine performance data have been reported previously (van Roode et al., 1994).

Solar's approach to incorporating ceramics for industrial gas turbine design attempts to minimize the risks inherent in a still immature technology by using a set of guidelines which are consistent with current ceramic design practice. These include limiting the number of ceramic components, using proven ceramic design practice from past programs, selecting well characterized, and promising candidate ceramic materials with potential for cost-effective scale up to production applications, iterative testing with stepwise increases in firing temperatures to a modest final design TRIT, and minimizing transient and steady-state stresses in the ceramic components and adjacent metal structures. The CSGT program aims to achieve early demonstration of component designs in an engine rig which duplicates all the conditions the ceramic components will experience during actual engine operation.

Solar's industrial gas turbines must be able to operate continuously without interruptions other than those resulting at scheduled maintenance for 30,000 hours which is the typical time before overhaul (TBO). Ceramic components must therefore have design lives consistent with the expected TBO life. Since

Nomenclature

AGT = advanced gas turbine
ARCO = Atlantic Richfield Company
AS-800 = AlliedSignal Ceramic Components Silicon Nitride
ATTAP = Advanced Turbine Technology Applications Program
BFG = B.F. Goodrich Aerospace
CARES = Ceramics Analysis and Reliability Evaluation of Structures, NASA Life Prediction Code
CARES/LIFE = uprated version of CARES
CAT TC = The Caterpillar Technical Center
CC = AlliedSignal Ceramic Components
Centaur 50S = Solar Model Centaur 50 Gas Turbine with SoLoNOx Combustor
CFCC = continuous fiber-reinforced ceramic composites
CO = carbon Monoxide
CSGT = ceramic stationary gas turbine
DLC = Dupont Lanxide composites
DOE = United States Department of Energy
FPI = fluorescent penetrant inspection
HIP = hot isostatic pressing
KICC = Kyocera Industrial Ceramics Corporation
NASA = National Aeronautic and Space Administration
NDE = nondestructive evaluation
NGK = NGK Insulators, Ltd.
NOx = oxides of Nitrogen
OIT = Office of Industrial Technologies
ORNL = Oak Ridge National Laboratory
ppmv = parts per million by volume
TBO = time before overhaul
TRIT = turbine rotor inlet temperature

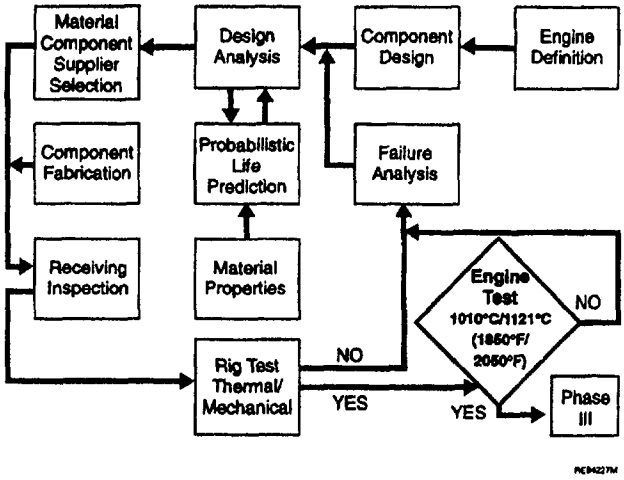

Fig. 2 Integrated design and test philosophy of the CSGT program

the ultimate field test goal for the program was 4000 hours, and to minimize the materials and design changes to the current metal engine, a design life target of 10,000 hours was selected for the engine and its components for the program.

Figure 2 illustrates the integrated design and test philosophy of the CSGT program. In this design approach, design analysis was iterated with life prediction, testing, and post-test component evaluation. In the first stage simulated components were tested in rigs to prove key design concepts such as blade and nozzle attachment configuration, blade root compliant layers, and interfacing of ceramics to metallic support structures. In the second stage the findings from these tests were fed back into the design of first ceramic component prototypes which were then tested in a Centaur 50S engine modified to accept the ceramic parts. The results of the engine tests were then used to modify the ceramic part designs to the extent desired. In the final stage second generation parts with superior performance are being used for the field testing in Phase III of the program.

Engine/Component Design and Material Selection

Figure 3 shows a cross section of the hot section of a Centaur 50S gas turbine, the gas turbine selected for ceramic insertion under the CSGT program, with a ceramic composite combustor liner, ceramic nozzles, and ceramic blades. Detailed design information regarding these components has been presented in prior papers (Norton et al., 1995; van Roode et al., 1995, 1996, 1997).

Combustor Design. The use of a ceramic gas turbine combustor is associated with two advantages over a conventional metal combustor: firing temperature can be increased without degrading combustor durability, and emissions from lean premixed gas turbine combustors can be reduced using a "hot wall" (Smith et al., 1996, 1997). Air saved from reduced cooling requirements for the combustor wall can be used to lean out the flame in the primary zone resulting in lower emissions of NOx. A second emission benefit is a reduction in CO quenching near the combustor wall.

The existing SoLoNOx combustor of the Centaur 50S engine was modified by integrating the ceramics in the linear sections of the combustor. The ceramic combustor was designed to be fully interchangeable with the production Centaur 50S dry low-NOx, lean-premix (SoLoNOx) combustor. The all-metal combustor is an annular, axial flow combustor that utilizes twelve premixing natural gas injectors. Through lean premixed combustion, NOx and CO emissions are limited to less than 25 ppmv and 50 ppmv, respectively, at the 1010°C design turbine rotor inlet temperature (TRIT) of the Centaur 50S engine.

The ceramic hot section layout of Fig. 3 shows the main design features. The combustor is comprised of a metallic dome section at the upstream end, two concentric ceramic cylinders (in metal housings) that form the combustor primary zone, and two conical, metallic exit sections. The dome and exit sections are film cooled and are essentially identical to their all-metal production engine counterparts. A layer of compliant insulation between the ceramic liners parts and the metal housing minimizes radial contact stresses. All pressure loads are carried by the metal housing. The inner and outer ceramic cylindrical liners

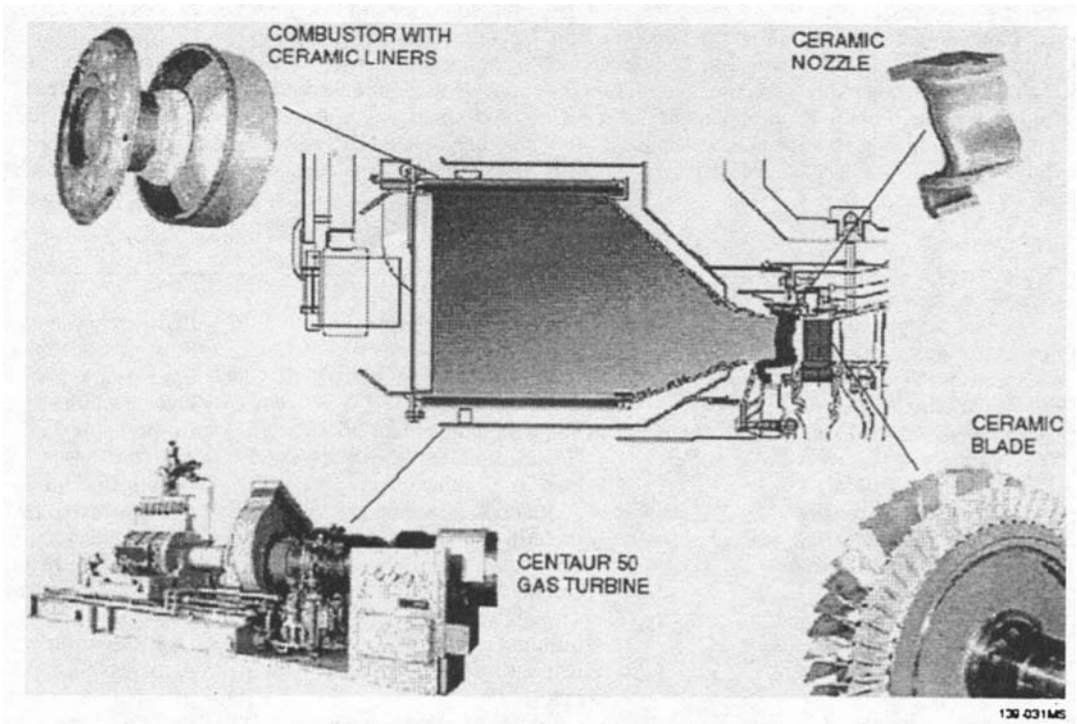

Fig. 3 Ceramic components in gas turbine hot section

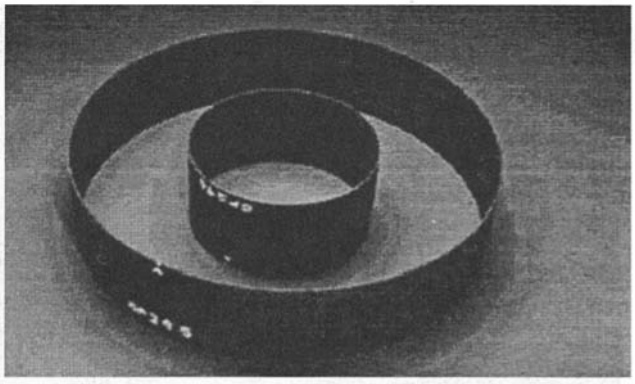

Fig. 4 Enhanced SiC/SiC CFCC Combustor liners fabricated by DuPont Lanxide Composites

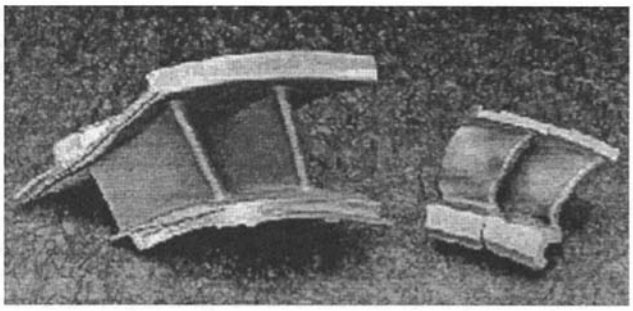

Fig. 5 Cooled FS-414 metal and uncooled SN-88 ceramic nozzles for Centaur 50S

are 33 cm and 75 cm in diameter, respectively, and are 20 cm long. Their wall thickness is approximately 0.2–0.3 cm. The ceramic liners replace louvre-cooled Hastelloy X liners in the Centaur 50S combustor.

The material of choice for the ceramic liners was a continuous fiber-reinforced ceramic composite (CFCC) with a silicon carbide based fiber (Nicalon) fabricated by Nippon Carbon Company of Japan as reinforcement in a silicon carbide matrix incorporated by chemical vapor infiltration. CFCC's were selected because of their superior fracture toughness, which gives them a distinct advantage over monolithics for large structures such as the combustor liners of the Centaur 50S engine. The current combustor liner material is the enhanced SiC/SiC CFCC of Dupont Lanxide Composites, Inc. (DLC). A set of these enhanced SiC/SiC CFCC liners, shown in Fig. 4, was acceptance tested for 100 hours in the CSGT Centaur 50s gas turbine, in preparation for field testing at ARCO Western Energy in Bakersfield, California. The actual materials selection process and supporting subscale component testing has been described elsewhere (van Roode, et al., 1996, Simpson, et al., 1997).

Nozzle Design. Under the CSGT program first stage all metal FS-414 nozzles are being replaced with ceramic parts. The cooled nozzles are coated with a Pt, Rh-aluminide diffusion coating. The ceramic nozzle design is significantly different from the metal nozzle. It is uncooled and single vane compared to the two-vane cooled metal nozzle, and the tip seal has been decoupled (a metal tip seal is attached to the nozzle case). These design changes were made to simplify the fabrication of the ceramic components. The nozzle attachment has been modified to accommodate the ceramic-to-metal interface to the first stage diaphragm. The number of nozzles was increased from 15 two-vane segments to 42 single-vane segments based on the results of a vibration analysis.

The ceramic nozzle airfoil is different from the metal airfoil as well. Finite element stress/temperature analysis and life prediction showed that replacing the metal airfoils with a ceramic vane of the same geometric configuration would result in an unacceptably high stress level incompatible with long service life. The airfoil chord was therefore reduced in half and the airfoil was bowed axially and tangentially compared to the current cooled metal nozzle. The redesign resulted in a significant drop in the maximum steady-state stress levels from about 480 MPa to about 162 MPa at the estimated "hot spot" temperature at the vane trailing edge of 1288°C (2350°F). The stress levels were calculated using SN-88 silicon nitride (NGK Insulators, Ltd.), the material selected for nozzle fabrication. The cooled metal FS-414 nozzle and the SN-88 silicon nitride nozzle are shown in Fig. 5. SN-88 was selected since it met the design requirements for slow crack growth and creep which are believed to be life limiting. A nine hour test was successfully conducted on 42 SN-88 nozzles in the CSGT Centaur 50S developmental gas turbine at Solar. A second test of the nozzle with minor design modifications is planned for March 1998.

Blade Design. In accordance with the low-risk design strategy of the CSGT program only the first stage of turbine blades was replaced with ceramic parts. The all-metal Centaur 50S engine has 62 first stage cooled equiaxed MAR-M247 blades coated with a Pt-aluminide diffusion coating for oxidation protection. The CSGT blade design has an airfoil shape that is almost identical to that of the metal blade, except for the absence of cooling passages. The fir tree attachment of the metal blade has been replaced with a conventional dovetail. A compliant layer between blade root and disk buffers the ceramic/metal interface. Maximum steady-state stress in the dovetail blade design was estimated at 214 MPa at the blade root neck under the platform at a temperature of 682°C (1260°F).

Based on critical materials properties and life prediction considerations, AS-800 (AlliedSignal Ceramic Components) and SN-281 (Kyocera Industrial Ceramics Corporation) silicon nitride materials were selected for engine testing. Figure 6 shows the cooled metal first stage MAR-M247 blade and an uncooled AS-800 silicon nitride blade. The AS-800 blades were tested for a 100 hours acceptance test in the CSGT Centaur 50S gas turbine in preparation for field testing at ARCO Western Energy in Bakersfield, California.

A significant difference between operation of the Centaur 50S engine with metal and ceramic blades is clearance control. The metal blade is designed for a hot clearance of 0.5 mm which is achieved by applying a rub-tolerant coating to the first stage nozzle tip seal. The ceramic blade has a design hot clearance of 1.3 mm, and is designed to operate with open clearances. Operating the engine with this wide clearance results in a performance loss. To fully realize the benefits of operating the engine

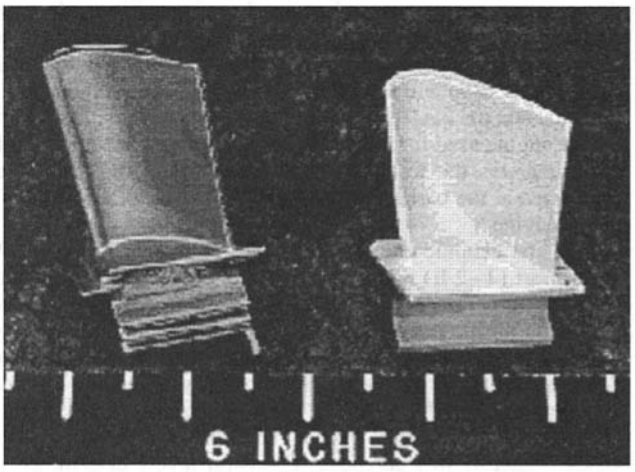

Fig. 6 Cooled MAR-M247 metal and uncooled AS-800 blades for Centaur 50 engine

with ceramic blades and nozzles will require the development of tip seals with abradable coatings that can accommodate a rub by ceramic blade tips. Development of abradable coatings is ongoing under other Solar development programs.

Secondary Component Design. A significant redesign effort was performed for the secondary components interfacing with the ceramic parts. The redesign effort involved the incorporation of rim seals on the first stage disk, changes to the first stage diaphragm and attachment of the first stage nozzle at the inner shroud, and changes to seals and related parts interfacing with the nozzle outer shroud. The design changes have been detailed elsewhere (van Roode et al., 1996, 1997).

In-House Component and Engine Testing

Component Testing. All ceramic components were tested extensively in laboratory rigs prior to engine testing. For example, the blade root configurations were evaluated in an attachment tensile test to establish the optimal blade root angle and compliant layer system. Full blades were tested in a cold spin test at 125 percent of design load to ensure that they were free of life limiting defects. Nozzles were proof tested in a thermal gradient proof test rig and a mechanical attachment test rig in which stress levels in excess of those in service eliminated defective parts. Details of the proof testing have been previously reported (van Roode et al., 1996, 1997).

The initial screening of candidate combustor liner materials was performed using a subscale liner test in which key elements of the full scale combustor design are evaluated in a cost effective but representative geometry. Full scale combustor rig testing was performed with an atmospheric combustor rig to establish that full scale liners can operate under the conditions of temperature that are anticipated in the engine environment. Subsequently, the liners were also tested in a pressurized full scale combustor rig to obtain an early assessment of emissions reduction potential. The liners were subsequently tested in the Centaur 50S engine. Emissions of NOx and CO were promising based on subscale and full scale test data. At full load in the high pressure rig, NOx and CO levels were determined to be <25 ppmv and <5 ppmv, respectively.

Engine Testing. The engine test strategy is based on initially evaluating each ceramic component separately, before testing the components in combination, in the Centaur 50S engine. This methodology minimizes the possibility of secondary damage to downstream prototype ceramic components in the case of an upstream ceramic component failure. The engine tests are initially performed at the baseline TRIT of 1010°C (1850°F) for each ceramic component system prior to testing these components in combination. In subsequent testing, ceramic components are being combined, and the engine is operated again at the baseline TRIT. The final test at a TRIT of 1121°C (2050°F) will be conducted with all three ceramic components, i.e., the blade, the nozzle, and a set of combustor liners.

The engine used for in-house testing is shown in Fig. 7. Table 1 summarizes the test data obtained to date. The tests were conducted at the baseline TRIT of 1010°C (1850°F) of the all-metal engine.

The first ceramic engine tests which started in August 1995 were short (1–2 h) and were intended to validate the dovetail blade design. The tests were performed with NT164 and GN-10 silicon nitride dovetail blades. The ceramic components and interfacing secondary components performed as expected and demonstrated good durability. Subsequently, an engine test was conducted with BFG SiC/SiC CFCC liners for a total of 12 h at full load over several cycles. This test established that the CFCC material was adequate. Emission levels determined in that test were very promising. NOx levels <15 ppmv and CO levels around 5 ppmv were typically measured at a 3 percent

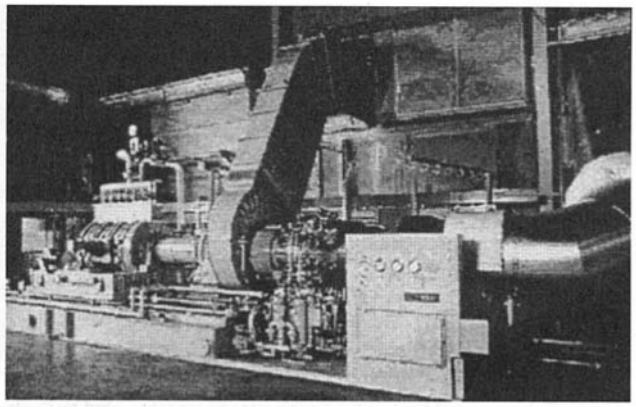

Fig. 7 CSGT Centaur 50S gas turbine

pilot fuel setting (Smith et al., 1996, 1997). The measured emission levels were well below the CSGT program goals of 25 ppmv NOx and 50 ppmv CO. The CFCC liners were in good condition following the tests.

These initial successful tests with a single ceramic component were followed by engine testing of both ceramic blades and combustor liners simultaneously. A 100 hour endurance test of 62 AS-800 (CC) dovetail blades and enhanced SiC/SiC (DLC) CFCC combustor liners was initiated in November 1996. Two compliant layer blade attachment systems were evaluated in the test. After 58 hours of cyclic testing, the engine shut down due to failure of the first stage blades. Failure analysis indicated that the origin of the failure was in one of the compliant layer attachment systems which caused the dovetail to pinch in the disk following cyclic engine testing. The alternate blade attachment system remained free in the disk. The attachment system was modified to further eliminate the risk of pinching, and the failed compliant layer system was eliminated (Jimenez et al., 1998).

A second 100 hour endurance test of 62 AS-800(CC) blades and enhanced SiC/SiC (DLC) CFCC liners was initiated in April 1997. The test included the modifications to the ceramic blade attachment system. The test was performed over a number of days incorporating cold and hot restarts. A total of 12 cold starts and 15 hot restarts were accumulated over the 100 hrs duration of the test. Final inspection revealed the ceramic and interfacing metal parts to be in excellent condition. This engine configuration was then used for the first field test in May 1997. Figure 8 shows the rotor assembly with AS-800 first stage blades prior to engine testing. Figure 9 shows the CFCC outer and inner liners of the combustor following the 100 h engine test.

Recently, the first test was also conducted in which the SN-88 ceramic nozzle was evaluated. The test lasted for 9 h, 1 h of which was at full load. Some minor chipping was found at the inner and outer shroud areas contacting the metal suggestive of a localized excessive contact stress condition. Redesign efforts are currently underway to alleviate this stress condition (Faulder et al., 1998). The next engine test of the SN-88 nozzles is planned for March 1998. The main focus of the engine testing will be to combine all three ceramic components, CFCC combustor liners, first stage blades, and first stage nozzles in the engine builds, and to operate the engine at the ultimate design TRIT of 1121°C (2050°F). A final 100 h test will be conducted prior to the final 4000 h field test scheduled for Phase III of the program.

Field Testing

In May 1997 the CSGT program experienced its most significant accomplishment to date. The CSGT T5901 Centaur 50

Table 1 Centaur 50S in house engine test summary

	Blades	Nozzle	Combustor Liners
Ceramics	NT-164, GN-10, AS-800, SN-281*	SN-88	BFG SiC/SiC DLC SiC/SiC
Total Test Time	325 hrs	9 hrs	252 hrs
Time at Full Load	284 hrs	1 hr	197 hrs
Max. Time on Single Build at Full Load	100 hrs (AS-800)	1 hr	100 hrs (DLC)
Nominal TRIT	1010°C (1850°F)	1010°C (1850°F)	1010°C (1850°F)
*To be tested in April 1998.			

SoLoNOx engine retrofitted with DLC enhanced SiC/SiC CFCC combustor liners and CC AS-800 first stage ceramic turbine blades was shipped to ARCO Western Energy Bakersfield enhanced oil recovery site for the first field test of ceramic hot section components in an industrial gas turbine engine. This engine replaced one of ARCO's existing gas turbines, a model T5501 Centaur 50, operated with water injection for NOx control. ARCO's control system was upgraded to allow operation in the SoLoNOx mode.

The field test started on May 21. A view of the test engine at the field test site is shown in Fig. 10. The engine operated at the 1010°C (1850°F) TRIT of the standard all-metal engine to demonstrate performance under typical industrial operating conditions. The CSGT engine was fully operational with normal steam and electrical power production. Boroscope inspections, conducted after 212 hs and 533 h showed no change in the appearance of the CFCC combustor liners and first stage ceramic turbine blades as compared to the appearance after the 100 h acceptance test at Solar. The field test duration was scheduled for 2000 h of maximum load operation with periodic boroscope inspections.

On July 1, 1997, after 948 h of full load operation, the CSGT engine shut down due to turbine underspeed. After several failed attempts to restart the engine, a boroscope inspection revealed that the 62 turbine blade airfoils had failed during service, which has now been attributed to impact damage from a locating pin from the inner liner of the combustor. ARCO's water-injected Centaur 50 T5501 was reinstalled and the CSGT engine was returned to Solar for failure analysis.

Failure analysis of the blades indicated that all of the fractures were above the blade platform and none of the dovetails were pinched in the disk (which was the cause of the previous blade failure), indicating that the redesign of the dovetail attachment was successful. The compliant layer attachment system appeared to have performed as designed. There was no evidence of contact on the first stage tip shoes. During teardown of the combustor, a locating pin (0.75 in. × 0.375 in. diam. tool steel) used during assembly of the combustor dome was found to be missing for the inner liner. The missing pin was at the bottom dead center location. Witness marks inside the housing of the inner liner indicated that the pin had moved to the aft end of the liner to a location near the 0.400 dilution holes. It was determined that the pin exited one of the dilution holes and

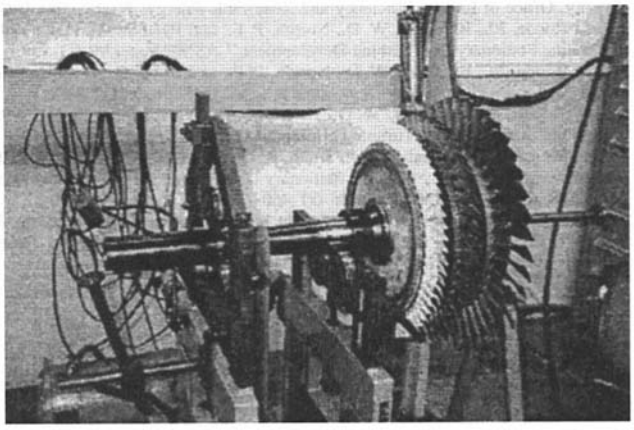

Fig. 8 CSGT rotor with AS-800 first stage blades prior to 100 hr engine test

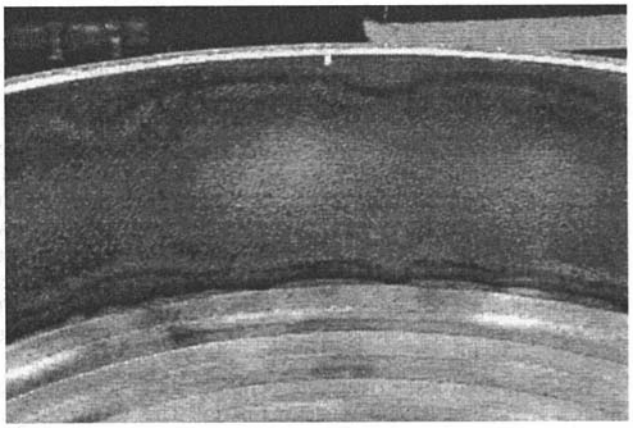

Outer Liner

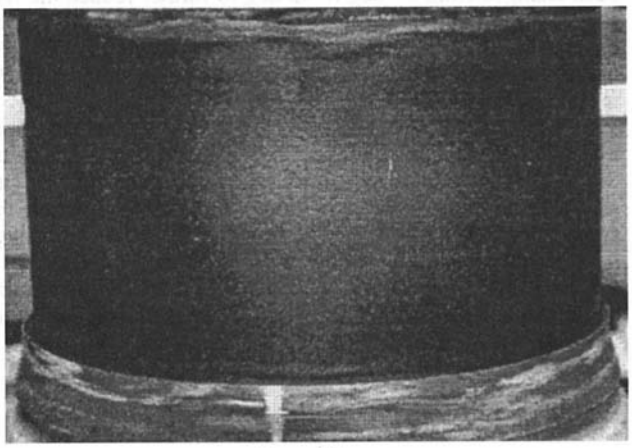

Inner Liner

Fig. 9 DLC SiC/SiC CFCC outer and inner liners following the 100 hr engine test

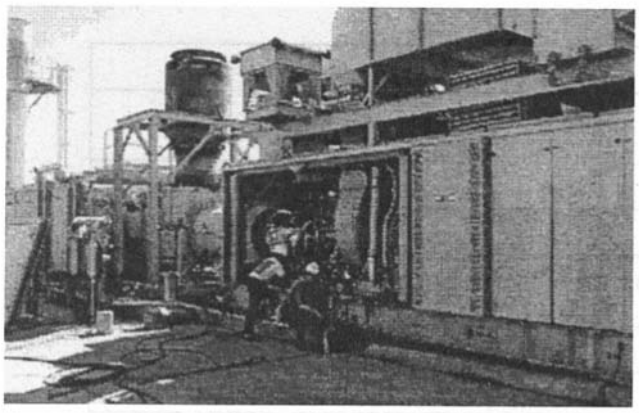

Fig. 10 CSGT Centaur-50S engine at Arco field test site

continued through the first stage nozzles into the ceramic turbine blades. Selected AS-800 blade roots from the ARCO field test failure were sent to ORNL for examination of the fracture surfaces. Evaluations to date have shown no sign of slow crack growth in the remaining blade airfoil.

The ceramic combustor liners remained intact following the engine shutdown. Over 1000 h of cumulative engine test data (test cell and field test data) to date have demonstrated that a simple modification to the Centaur 50S SoLoNOx combustor, involving replacement of the currently louvre-cooled metal liners with uncooled liners fabricated from continuous fiber-reinforced ceramic composite (CFCC) materials, results in significantly improved levels of NOx and CO at the 1010°C (1850°F) TRIT of the Centaur 50S engine. This reduction in emissions is a significant milestone for the program, as well as for future gas turbines, and becomes particularly important as the drive to reduce "greenhouse gases" increases. NOx levels from 10–15 ppmv and CO levels of around 5 ppmv have routinely been measured over the 50–100 percent load range for the CSGT engine operating on natural gas at ARCO. The outer CFCC combustor liner showed minor indications of oxidation following the field test. The inner CFCC liner exhibited a higher degree of uniform oxidation which will limit the life of the liner. The maximum inner liner temperature measured was 1188°C (2170°F), which was about 37.8–65.6°C (100–150°F) higher than the outer liner.

The next field test of ceramic components is scheduled for March 1, 1998 at ARCO Western Energy. This test will again contain 62 AS-800 (CC) dovetail blades and enhanced SiC/SiC (DLC) CFCC combustor liners. The dovetail angle has been changed from 55 deg to 45 deg to further reduce the risk of pinching. A 100 hour engine acceptance test of the 45 degree dovetail AS-800 blade was completed in January 1998. The blades appear in excellent condition, showing no signs of pinching in the disk.

Several changes have ben made to the CFCC combustor liner system in an attempt to reduce the oxidation of the enhanced SiC/SiC liners experienced during the field test at ARCO. Design changes to the metallic portion of the liners to improve the conduction path from the CFCC liners to the metallic housings have resulted in a temperature drop of about 54.4°C (130°F) for the CFCC liners. Material changes to the CFCC liners include using Hi-Nicalon fibers (which are stronger and more stable at higher temperatures and have higher thermal conductivity than the previous ceramic-grade Nicalon fibers), increasing the density of the CFCC liners, and doubling the thickness of the protective seal coat used for the CFCC liners. The liners will be tested in Solar's atmosphere rig in late January in preparation for the next 2000 hour field test at ARCO.

Summary

A Solar Turbines Incorporated Centaur 50S gas turbine is being retrofitted with ceramic first stage blades, first stage nozzles, and combustor liners for improved performance and lower emissions. The component designs have been completed and have been validated in rig and engine testing. A Centaur 50S engine with ceramic first stage blades and combustor liners started a 2000 h field test on May 21 at the baseline TRIT of 1010°C (1850°F) of the all metal engine. The engine field test accumulated 948 hours of full load operation prior to engine shutdown due to foreign impact damage of the first stage AS-800 turbine blades. The impact damage occurred due to a metallic locating pin used during combustor assembly impacting the first stage blades. The metallic locating pin has been eliminated and a second 2000 hour field test of ceramic blades and a modified CFCC combustion liner system has been scheduled for March 1998. Additional field testing of CFCC combustor liners, ceramic blades, and ceramic nozzles at an increased TRIT of 1121°C (2050°F) is planned for late 1998.

Acknowledgments

The work for this program was performed under DOE Contract DE-AC02-92CE40960. The authors wish to recognize the programmatic and technical guidance of Mr. Stephen Waslo, DOE Chicago Operations Office Technical Manager, and of Ms. Patricia Hoffman of the DOE Office of Industrial Technologies.

References

Faulder, L., McClain, J., Edwards, B., and Parthasarathy, V., "Ceramic Stationary Gas Turbine Development Program—Design and Test of a First Stage Ceramic Nozzle," ASME Paper 98-GT-528.

Jimenez, O., McClain, J., Edwards, B., and Parthasarathy, V., 1998, "Ceramic Stationary Gas Turbine Development Program—Design and Test of a Ceramic Turbine Blade," ASME Paper 98-GT-529.

Norton, P. F., Frey, G. A., Bagheri, H., Fierstein, A., Twardochleb, C., Jimenez, O., and Saith, A., 1995, Ceramic Stationary Gas Turbine Development Program—Design and Life Assessment of Ceramic Components," ASME Paper 95-GT-383.

Simpson, J. F., and Fahme, and Hossain, M. M., 1997, "Testing of Ceramics for Gas Turbine Combustor Applications," presented at the 1997 American Ceramic Society ECD Meeting, Cocoa Beach, Florida, Jan 12–16, 1997.

Smith, K. O., and Fahme, A., 1996, "Experimental Assessment of the Emissions Benefits of a Ceramic Gas Turbine Combustor," ASME Paper 96-GT-318.

Smith, K. O., and Fahme, A., 1997, "Testing of a Full Scale Low Emissions, Ceramic Gas Turbine Combustor," ASME Paper 97-GT-156.

U.S. Department of Energy, 1994, *Comprehensive Program Plan for Advanced Turbine Systems,* report to Congress, U.S. Department of Energy, Office of Fossil Energy, Office of Energy Efficiency and Renewable Energy, Washington, D.C.

van Roode, M., Brentnall, W. D., Norton, P. F., and Pytanowski, G. P., 1993, "Ceramic Stationary Gas Turbine Development," ASME Paper 93-GT-309.

van Roode, M., Brentnall, W. D., Norton, P. F., and Boyd, G. L., 1994, "Ceramic Stationary Gas Turbine Development," ASME Paper 94-GT-313.

van Roode, M., Brentnall, W. D., Norton, P. F., and Edwards, B. D., 1995, "Ceramic Stationary Gas Turbine Development," ASME Paper 95-GT-459.

van Roode, M., Brentnall, W. D., Smith, K. O., Edwards, B. D., Faulder, L. J., and Norton, P. F., 1996, "Ceramic Stationary Gas Turbine Development—Third Annual Summary," ASME Paper 96-GT-460.

van Roode, M., Brentnall, W. D., Smith, K. O., Edwards, B. D., McClain, J., and Price, J. R., 1997, "Ceramic Stationary Gas Turbine Development—Fourth Annual Summary," ASME Paper 97-GT-317.

Feedstock Blending Studies With Laboratory Indirectly Heated Gasifiers

A. E. S. Green

J. P. Mullin

Departments of Mechanical Engineering and Nuclear and Radiological Engineering,
P. O. Box 112050
University of Florida,
Gainesville, FL 32611-2050

To support the further development of indirectly heated gasifiers intended to provide fuels for advanced gas turbines, several indirectly heated laboratory gasifiers were constructed. During many comparative tests, advantages and problems with each system were observed. The most useful systems make use of laboratory tube furnaces in conjunction with temperature, time, and pressure or volume yield measuring systems and a gas chromatograph with a thermal conductivity detector. In this paper, high temperature pyrolysis results obtained with the latest system are presented. Contrasting feedstocks suitable for commercial systems separately or in blends are used. Yield versus time measurements are used to determine relevant rate constants and outputs. Since the rate constants are mainly reflective of heat transfer effects, cylindrical dowel sticks of varying radii were volatilized. The data set leads to an analytic heat transfer model that considers the hemicellulose, cellulose, and lignin components of the dowels. Also developed from the dowel experiments is an approximate procedure for estimating the proportionate releases of CO, CO_2, CH_4, and H_2 for any type of biomass whose component proportions are known.

Introduction

In 1981, the Clean Combustion Technology Laboratory (CCTL) at the University of Florida initiated studies on cofiring natural gas and coal in boilers designed for oil (Green et al., 1981; 1984; 1986). What evolved was a general focus on blending domestic fuels for various energy and environmental objectives (Green et al., 1988; 1989; 1991; 1993). Collaborations evolved with plant technologists in studying the efficiency of co-combustion and the emissions from a starved air incinerator cofiring institutional waste and biomass, biomass and coal, and other combinations of domestic fuels.

During this period, gas turbines (GTs) emerged as the best means for transforming heat to mechanical energy and are now the key component of the most efficient electrical generating systems. To take advantage of these high efficiencies the CCTL has been attempting to develop a science and technology for feedstock blending in indirectly heated gasifiers (IHGs) (Green et al., 1986; 1991; 1995; 1996A; 1996B; 1997). The overall objective is to produce middle heating value fuels suitable for advanced GTs.

The dismal state of the basic understanding of the pyrolysis of solid fuels, the initial stage of combustion, gasification and liquid fuel conversion, unfortunately, is a serious obstacle to applying IHGs. A comprehensive 1992 survey of coal pyrolysis (Solomon et al., 1992) calls attention to the fact that reaction rates for first order mass loss processes reported by different research groups of identical coal samples at identical temperatures frequently differ by factors of 100. The situation is generally worse for biomass pyrolysis which has had much less attention than coal. To pursue fuel blending in gasifiers, a much better understanding is needed of the heat transfer and pyrolysis characteristics of individual solid fuels and various blends under conditions similar to those in commercial IHGs.

Increased interest in biomass-to-energy conversion has developed recently as a result of world-wide concern for global warming, the growth of oil use in transportation, utility deregulation, and broader recognition of cases where dual or multiple benefits can be achieved. Paper production technology, municipal solid waste conversion to energy, and sugar production with bagasse use for energy are practical examples of dual or multiple benefit cases. Thus far these examples have mostly been pursued using boiler-steam turbine technology and efficiencies achieved are rather low. Gas turbine powered electricity generation technology is under aggressive pursuit by some of the world's highest technology companies. To take advantage of these advances, a strong effort is now needed to advance biomass gasification technology, in particular to understand the heat transfer and pyrolysis characteristics involved in the conversion of material derived from plants to suitable GT fuels.

IHGs that use one combustion chamber to provide the heat for an air free gasification of the feedstock in a second chamber (Paisley and Anson, 1997; Mansour et al., 1995; Carboni, 1995) have many advantages over traditional gasifiers based upon substoichiometric combustion in a single chamber. Like the starved air stage of incinerator systems, starved air gasifiers yield a low heating value producer gas, mostly H_2, CO, and CH_4 diluted with nitrogen and carbon dioxide. Dilution with atmospheric nitrogen can be avoided by using an oxygen blown gasifier to achieve a medium heating value gas, but with the capital and operating cost of an oxygen plant. On the other hand, IHGs that basically "cook" biomass at high temperatures in their own gaseous vapors directly produce a medium heating value gas.

CCTL Laboratory IHGs

Towards the goal of developing a science and technology of high temperature "cooking" of solid fuels the CCTL has designed and constructed several laboratory IHGs. Completed units include a gasifier simulator (GS), two horizontal batch mini-gasifiers (MG1 and MG2), and a microgasifier (MicG) to visually observe the evolution of the gaseous and liquid pyrolysis products of various materials. Most recently two vertical mini-gasifiers (MG3 and MG4) with volumetric yield measuring systems have been constructed.

The gasifier simulator can be operated in the downdraft or

Contributed by the International Gas Turbine Institute (IGTI) of THE AMERICAN SOCIETY OF MECHANICAL ENGINEERS for publication in the ASME JOURNAL OF ENGINEERING FOR GAS TURBINES AND POWER. Paper presented at the International Gas Turbine and Aeroengine Congress and Exhibition, Stockholm, Sweden, June 2–5, 1998; ASME Paper 98-GT-574.

Manuscript received by IGTI March 30, 1998; final revision received by the ASME Headquarters June 23, 1999. Associate Technical Editor: R. Kielb.

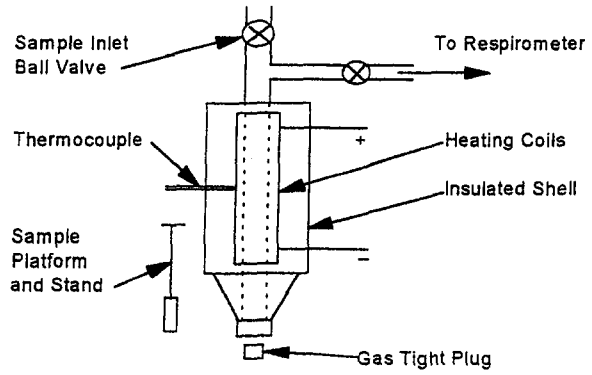

Fig. 1 Schematic of MG3

updraft mode and was, in part, designed to simulate the operation of conventional biomass gasifiers. Yields with the GS are based upon flow meter readings in relation to calibrated feed rates for each feedstock for various auger settings. Unfortunately with this GS only one condition could usually be investigated in a day.

To speed up data acquisition and sharpen yield determinations, two horizontal batch type IHG's were constructed. With MG1 and MG2, a measured quantity of feedstock material contained in a cylindrical paper capsule could be injected into the high temperature zone of a horizontal tube reactor. The gasifier pressure was then recorded with time at intervals of approximately 5 seconds. Some of the results with these systems have already been reported (Green et al., 1996a; 1996b; 1997) and will be augmented here. Results of catalyst blending studies will be reported in a separate paper (Peres and Green, 1998).

Problems with gas leakage in MG1 and MG2 at higher pressures motivated a search for an alternate yield measuring system. This search led to the acquisition of a 9 liter Collins Respirometer. With the respirometer, gas yield measurements were based on volume rather than pressure, providing the ability to (1) eliminate pressure dependent leaks, (2) have chart records of the time dependence of the gaseous volume yield, (3) simplify the minigasifier system, (4) develop simpler and less expensive gas sampling and gas analyzing procedures, (5) assemble data much more rapidly, (6) develop mass balance tests involving gas yields and char weights, and (7) conduct liquid yield studies at lower temperatures.

MG3, as shown in Fig. 1, is a vertical adaptation of MG2 that is also externally heated via electric heating elements. The replaceable heated tube is stainless steel with a 2.35 cm ID and a 2.70 cm OD, and has a total length of about 60 cm. The heating coils radiate onto a 28 cm long section of the tube. A removable platform rests inside the heating tube at a location about 18 cm down from the top of the heated region, or about 10 cm up from the bottom of the heated region. The platform is supported by a gas tight plug which is inserted at the bottom of the heating tube. Sample materials contained in a cylindrical paper capsule are dropped into the furnace from the top through a ball valve. The capsule falls onto the platform which approximately centers the sample in the furnace tube.

Connected in line with the gasifier is the Collins respirometer which has been modified to directly measure the volumetric gaseous yields of pyrolysis as a function of time. The influx of gases causes a water-sealed bell of constant cross section to displace upward and an ink pen to displace proportionately downward. The pen leaves a trace on a drum which rotates at constant speed. Thus, the device provides a direct measurement of the gas yield versus time while containing the gas mixture in a sealed chamber. The gas mixture can then be rerouted into a sampling container for gas analysis.

Composition Assessment

Gas samples collected from the mini-gasifiers are analyzed with a Varian 3700 gas chromatograph (GC) with a thermal conductivity detector (TCD). One hundred microliters of the gas sample is injected into the GC and separated into the component species through a 60/80 Carboxen-1000 15′ × $\frac{1}{8}$″ stainless steel column. The column temperature starts at 45°C, held for 6 min and then ramped at 20°C/min to a final temperature of 210°C and held for 12 min. After calibration oxygen, nitrogen, carbon monoxide, methane, carbon dioxide, acetylene, ethylene, and ethane are measurable using helium as the carrier gas. For hydrogen, an additional sample injection must be made using argon as the carrier.

Output from the GC is processed with a computer program to determine the volume of each species detected, the total volume detected, the percent volumes of each species, and the overall gas density and heating values. For all MG3 samples analyzed to date, the reported total volume of gas detected based on the calibration has been within 5 percent of the actual injected volume. Thus, it is expected that the primary constituents of the gas mixtures are those that are quantifiable with the GC apparatus used. The presence of other species, i.e., C3+ compounds, are neglected.

The gas analysis was performed twice for each sample. The first analysis was for the gas mixture as collected in order to determine the total detected volume of gas. In the second analysis, oxygen and nitrogen were ignored to determine the appropriate density and heating values since it was assumed that neither of these gases were generated by the pyrolysis of the solid feedstock. This procedure was necessary since dilution with air is difficult to avoid with this type of batch process unit.

A further correction to the gas analysis was the removal of the contribution of the paper capsule that can be accomplished using the average values for the bond paper gas composition, density, heating value, and total yield (Mullin, 1998).

Table 1 (below) gives the adjusted percent volumes of each constituent gas species, the adjusted density (ρ, in kg/m$_n^3$), and the higher heating value (HHV, in MJ/m$_n^3$) for the gaseous yields of sugar cane bagasse (B), melaluca (M), leucaena (L), elephant grass (EG), crushed wood pellets (WP) from sawdust waste, pine bark (PB), and lignin powder (LP) when pyrolyzed in MG3 at 1000°C. The data in Table 1 has been corrected for the contribution of the bond paper capsule.

Pressure measurements with MG1 and MG2 were taken at 1 psig increments, which occurred approximately every five seconds. The leakage in these system was determined as the pressure dropped with time from the maximum recorded value. By iterative

Table 1 Gas yield compositions and the corresponding density (kg/m_n^3) and higher heating value (kJ/m_n^3) for various biomass species volatized at 1000°C

	H_2	CO	CH_4	CO_2	C_2H_2	C_2H_4	C_2H_6	ρ	HHV
B	23.98	39.73	13.83	16.50	0.47	5.11	0.47	0.911	15.58
M	23.61	39.45	15.48	14.86	0.95	5.20	0.51	0.896	16.43
L	24.71	38.07	14.85	16.82	0.47	4.72	0.45	0.900	15.61
EG	23.42	36.32	15.25	18.11	0.47	5.82	0.69	0.920	16.17
WP	25.29	43.21	13.28	13.01	0.25	4.46	0.58	0.877	15.52
PB	30.29	39.81	12.66	13.18	0.53	3.44	0.15	0.829	14.79
LP	27.97	35.30	21.98	9.61	0.50	4.35	0.38	0.786	17.98

modeling, an approximate maximum pressure could be calculated as if the system were leakage-free. Figure 2 shows the pressure development with time using MG1 for gasification of 5 gram samples of shredded bagasse, pulverized bituminous coal, and a 50/50 blend of the bagasse and coal, all at 1000°C. The data includes the contribution of the paper capsule which has mass of approximately 0.4 g, for a total sample mass of about 5.4 grams. The lower points are the original data. The upper points are the corresponding data with corrections for leakage. The smooth curves will be described in the following section.

The modeling approach given in the next section also applies to the yield versus time data provided by the respirometer. In this case, the pressure variable is simply replaced by the volumetric yield. Figure 3(*a*) shows the volume yield versus time for a collection of biomass species volatized at 1000°C in MG3 with the respirometer. Figure 3(*b*) shows volume yields for a selection of feedstocks relevant to MSW issues.

Phenomenological Modeling of Data

The data obtained with the MG's undoubtedly are the result of a complex interplay of heat transfer, phase change, dissociation, chemical decomposition and diffusion processes. In modeling cellulose mass loss versus temperature with standard thermogravimetric apparatus under constant heating rate conditions (Green et al., 1997) it was found that some of the best representations can be achieved by assuming the mass loss obeys a p^{th} order reaction. Undoubtedly, these results are due to the net effect of some combination of the processes identified above. When applied to data acquired with the CCTL MG's expressed as m versus time where $m = M(t)/M_0$ and M_0 is the initial mass the counterpart equation is

$$-dm/dt = km^p \quad \text{or} \quad dm/m^p = -kdt. \tag{1}$$

Integrating both sides of the second equation gives

$$m(t) = 1/[1 + (p - 1)kt]^{1/(p-1)} \rightarrow \exp - kt, \tag{2}$$

where the arrow points to the result for the usual $p = 1$ case. When $p > 1$, $m(t)$ declines monatonically, going to zero asymptotically as $(kt)^{-1/(p-1)}$. When $p < 1$ it is more convenient to write

$$m(t) = [1 - (1 - p)kt]^{1/(1-p)} = [1 - (kt)/q]^q, \tag{3}$$

where $q = 1/(1 - p)$. In this case when $t = q/k$ the mass is exhausted and $m(t)$ at later times has no meaning.

For the first quantitative yield measurements, the observed pressure versus time data, the known gasifier volume, and the average temperature of the gas yield were used to estimate the volumetric gaseous yield versus time and total yield. Details will be described

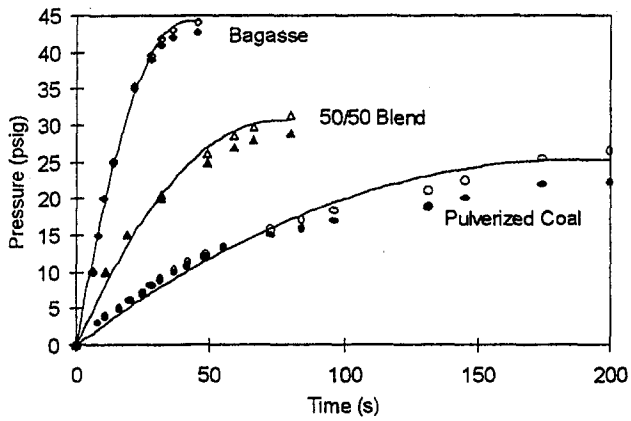

Fig. 2 Pressure versus time data (dark points) and data corrected for leakage (open points). Solid curves are quadratic fits to the corrected data.

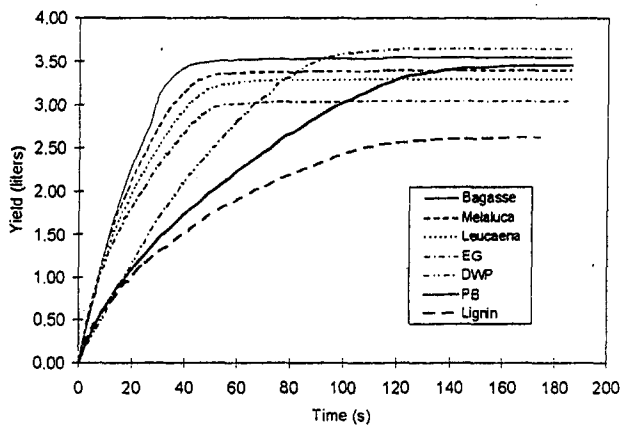

Fig. 3(*a*) Representative yield versus time data obtained with MG3 for various types of biomass

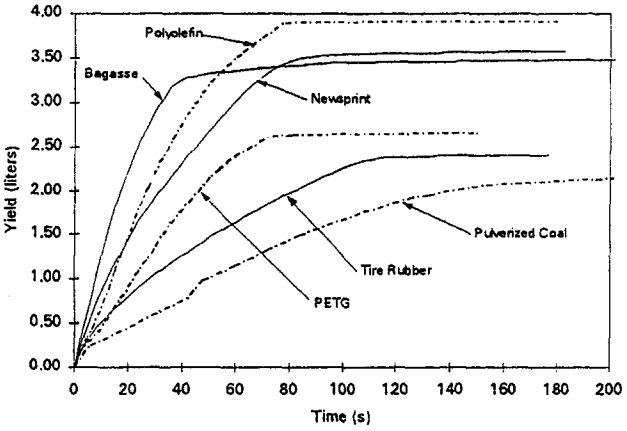

Fig. 3(*b*) MG3 yield versus time data for various wastes and coal

in a separate paper (Peres and Green, 1998). To assign an asymptotic Y_m one may write

$$Y(t) = Y_m[1 - m(t)] = Y_m\{1 - [1 - (kt)/q]^q\}. \tag{4}$$

In fitting data it has been found that a simple quadratic dependence upon time without a constant term, (i.e., $Y = at - bt^2$) usually provides a very good representation. This is equivalent to using the value $p = \frac{1}{2}$ in Eqs. 1–3 or $q = 2$ in Eq. 4 which becomes

$$Y(t) = Y_m[kt - (kt)^2/4] = at - bt^2 \tag{5}$$

where

$$a = Y_m k \tag{6}$$

and

$$b = Y_m k^2/4. \tag{7}$$

Accordingly, if a least square program is used to fit the yield versus time data to determine a and b, the maximum yield and an effective rate constant can be obtained by solving Eqs. 6 and 7 for $Y_{m \text{ and } k}$. Figures 4(*a*) and 4(*b*) show the data and quadratic fits obtained for bagasse and coal at 800°C, 900°C, and 1000°C. Table 2 gives rate constants derived from recent measurements in the equivalent forms

$$k = A \exp - E/RT = k_o \exp \alpha - \beta u$$
$$= k_o \exp \alpha[(1 - (T_t/T)], \tag{8}$$

where $k_o = 1/\text{s}$, $\alpha = \ln A/k_o$, $u = 1000\ \text{K}/T$, $\beta = E/1000$ R and $T_t = E/\alpha R$. Also given are $F = k_o \exp(\alpha - \beta)$, the value of k at 1000 K that might be viewed as a measure of reactivity. From the

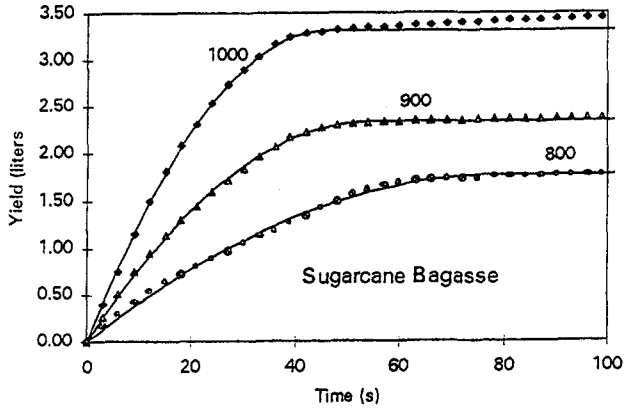

Fig. 4(*a*) Bagasse yield versus time at three temperatures

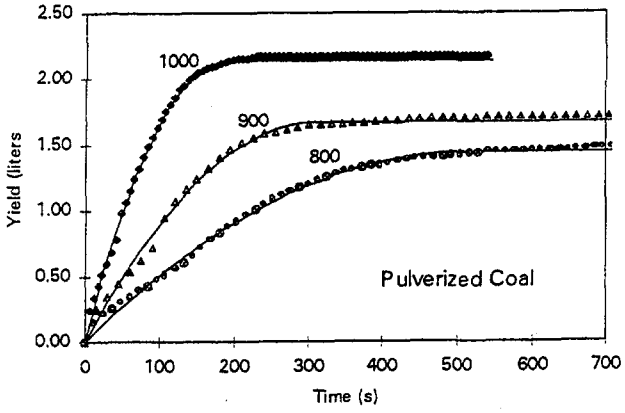

Fig. 4(*b*) Yield versus time for coal at three temperatures

T_i and F values it is clear that bagasse reacts at the lowest temperature and is the most reactive. Coal requires the highest temperature and is the least reactive. The others feedstocks are in between.

Heat Transfer Model and Dowel Experiments

A recent analysis of cellulose pyrolysis data (Green et al., 1997) and a number of prior articles (Miller and Bellan, 1996; 1997; Di Blasi, 1996; Lede, 1994) indicate heat transfer rather than chemistry dominates the time dependence of many pyrolysis experiments. For a cylindrical geometry the basic equation of heat transfer is

$$(1/r)\partial T/\partial r + \partial^2 T/\partial r^2 = (1/\alpha)\partial T/\partial t, \quad (9)$$

where $\alpha = \kappa/\rho C$ with ρ, the density, C_p, the specific heat, and κ, the thermal conductivity of the solid cylinder. Standard models of heat transfer to an infinite cylinder at an initial temperature T_i exposed at time $t = 0$ to a high temperature T_∞ give the temperature $T(t, r, R)$ at any radius r within the cylinder of radius R and subsequent time t (Lede, 1994; Ozisik, 1993; Heisler, 1947; Boelter et al., 1965). For such calculations engineers usually use the so-called Heisler charts based upon the leading term in the Bessel function expansion of the solution to the heat transfer equation, i.e.,

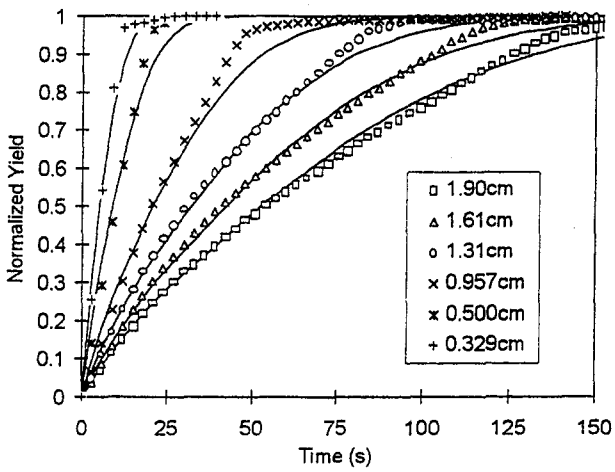

Fig. 5 Normalized yield curves for spruce dowels of various diameters. Points represent data and the curves are based upon Eq. 13.

$$\Theta = (T_\infty - T)/(T_\infty - T_i) = CJ_o(\zeta x)\exp(-\zeta^2 F) = G/E, \quad (10)$$

where $F = \alpha t/R^2$, $x = r/R$, $E = \exp \zeta^2 F$ and $G = CJ_o(\zeta x)$. It is customary to give the constant C and the parameter ζ for any Biot number in tabular form and $J_o(\zeta x)$ and $\exp(-\zeta^2 F)$ in graphical form. For infinite Biot numbers (simple conduction) $\zeta^2 \sim 5.6$ and $C \sim 2.3$. Unfortunately Heisler charts are not accurate for values of F less than 0.2 which, because of the low conductivity of biomass, turns out to be the main domain of interest. Another limitation is that the initial temperature T_i is not satisfied at $t = 0$ for all values of r. In an effort to remedy both problems Eq. 11 is modified to (Green and Burki, 1974)

$$\Theta = G/(G - 1 + E), \quad E = \exp \gamma t, \quad \gamma = 5.6\alpha/R^2, \quad (11)$$

which insures that at $t = 0$, $\Theta = 1$ for all r as required. Eq. 11 will be applied in an empirical mode to organize yield versus time data.

To use a physically well defined feedstock, exploratory experiments have been conducted at 1000°C with solid spruce (SP) dowels, each 4.85 cm in length with radii varying from 0.1 cm to 1 cm. The points in Fig. 5 are the measured gaseous yields normalized to $Y_m = 1$ for six representative cases of the dowel experiments.

Wood can be decomposed into the major components: hemicellulose (Hm = $n_1C_5H_{10}O_5$), cellulose (Cl = $n_2C_6H_{10}O_5$) and lignin (Lg = $n_3C_5H_6O_2$), plus an ash residue. Tables of the Hm, Cl, and Lg fractions of various woods give rather varied results. However, the choices $W_1 = 30$ percent, $W_2 = 45$ percent, and $W_3 = 25$ percent for the mass percentages of these components of spruce are not unreasonable. To assign the experimental gas yields one must allow for the percentages of the three components that go into the

Table 2 Specific yield (SY) for various materials volatized in MG3 at 1000°C and Arrhenius rate parameters derived from quadratic fits to yield versus time data at 800, 900, and 1000°C

Material	SY (liters/g)	α	β	F	A (s^{-1})	E_a/R	T_i
Sugarcane Bagasse	0.64	4.39	3.70	1.988	80.4	3700	843
Newsprint	0.64	3.84	4.01	0.840	46.3	4009	1045
Bituminous Coal	0.37	5.64	7.06	0.242	282	7062	1252
Polyolefin	0.73	4.61	4.88	0.764	101	4881	1058
PETG	0.47	3.68	3.76	0.931	39.8	3755	1019
Tire Rubber	0.42	3.55	3.92	0.687	34.7	3922	1106

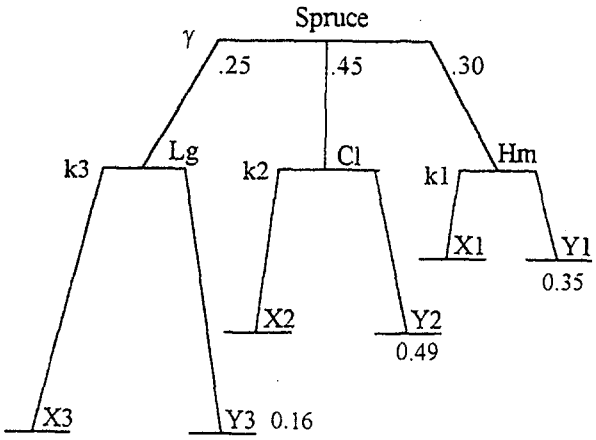

Fig. 6 Two step decay scheme illustrating mass branching ratios and volume fractions

gas phase. From the experiments at 1000°C with cellulose, lignin and spruce wood specific yields were obtained of 0.82 liters/g, 0.47 liters/g, and 0.75 liters/g, respectively. Thus, with the assumed mass proportions 0.30, 0.45, and 0.25 and the additivity rule, a specific yield of 0.88 liters/g was determined for hemicellulose. Accordingly, volume fractions might be assigned as $w_1 = 0.35$, $w_2 = 0.49$, and $w_3 = 0.16$. Figure 6 gives a very simplistic decay scheme for the gaseous yield system showing the originally assumed decomposition of the spruce into Hm, Cl, and Lg, and the final decomposition of spruce into the noncondensable gases (Y_i) and char-tar-ash (X_i).

In attempting to systematize the gas yield versus time data for the dowel experiments, many models have been examined. These were chosen in consideration of previous pyrolysis modeling efforts (Green et al., 1984; 1986; Miller and Bellan, 1996; 1997; Di Blasi, 1996; Lede, 1994). The most advanced treatments set up partial differential equations that allow for the heat transfer, phase change, diffusion, and chemical decomposition processes. Since the consequences of the numerical solutions are not readily visualized, in this work the primary focus was on developing a plausible analytic model that might be expected to give similar results. The decay scheme illustrated in Fig. 6 shows a two step process in which the first step, the effective separation at 1000°C of the spruce into Hm, Cl, and Lg, is the time to reach the ablation temperature for hemicellulose. For this purpose it is reasonable to use a thermal temperature-time function $Y_{th} = 1 - \Theta$, where Θ is given by Eq. 11. The result can be rearrange to the form

$$Y_{th} = 1 - [G/(G - 1 + E)]$$
$$= [1 - \exp - \gamma t]/[1 + (G - 1) \exp - \gamma t]. \quad (12)$$

Now G will be treated as a lumped parameter associated with each wood component that is still a function of R but no longer a function of r. Next, it is assumed that the time evolution of Y_{th} is slow compared to the time for the decomposition steps that change each wood component to a gas and a residue (X). Identifying $i = 1$ with Hm, $i = 2$ with Cl, and $i = 3$ with Lg and assuming the evolution of Hm, Cl, and Lg is governed by Y_{th}, the kinetics solution for the total gaseous yield is

$$Y_t = \Sigma w_i[1 - \exp - k_i t]$$
$$\times [1 - \exp - \gamma t]/[1 + (G_i - 1) \exp - \gamma t]. \quad (13)$$

A good overall representation of the exploratory dowel experiments has been achieved using the experimentally determined w_i along with four nominal parameters: $k_i = k = 1$, $G_1 = 1$, $G_2 = 10$, $G_3 = 100$; and two adjusted parameters: $g = 0.035$ and $p = 4/3$ in $\gamma = g/R^p$. The thin lines in Fig. 5 show the fits according to Eq. 13.

Molecular Decomposition Models

A molecular model has been developed to organize the specific gas yields obtained from the decomposition of spruce at 1000°C in a manner compatible with the gas yields obtained for cellulose and lignin. In this effort it was helpful to identify minimum sized molecular units for SP, Cl, Lg, and indirectly Hm consistent with their known CHO ratios and experimental volume and weight assignments. The first four columns of Table 3 summarize this model.

As a first step in assigning specific gas yields, consideration was given to the unique theoretical decomposition of these molecules into the gases CO and H_2 plus the residual C. As a second step some of the CO and H_2 were diverted into CH_4O as a surrogate condensable liquid to the point that the mass percentage of gas with respect to the original wood mass agreed approximately with experimental results. As a third step some molecular CO and H_2 were converted into CH_4 and CO_2 to extents compatible with gas chromatographic measurements of spruce, cellulose, and lignin yields. The hemicellulose gas composition was determined by difference. As a fourth and final step the carbon atoms and liquid molecules were consolidated into a hypothetical char-tar molecule and minor readjustments were made in the major gaseous molecular assignments to achieve compatibility with observed mass and volume percentages. The final result is a specific system of molecular splitting that satisfies mass and atomic balances and is consistent with experimental results at 1000°C.

Table 3 also gives the assumed mass fractions (m_f) of the components of "wood," the chemical formula used, and the molecular weight corresponding to the chemical formula. The "theoretical" rows give the number of molecules of a gas component as determined by a theoretical decomposition of the original molecule. To the right of the number of molecules (in the same cell), followed by a slash is the corresponding percent volume. This value was arrived at by dividing the number of gas molecules for the corresponding component by the total number of gas molecules. Based on the theoretical breakup, values for percent conversion to gas on a mass basis (%G) and the specific yield (volume of gas per mass of solid) were calculated. The specific yield values (SY_n) are normalized to SP (approx. 0.7 liters per gram average). For SP, Cl, and Lg, Table 3 also gives experimentally determined values for percent volumes of the gas components, the percent mass converted to gas (%G) and values for the specific yield

Table 3 Assumed compositions for wood dowels and dowel gas yields

	m_f	Formula	Molec. Wt.	H_2	CO	CH_4	CO_2	%G	SY_n
Wood-theo.	100%	$C_{59}H_{94}O_{43}$	1490	10/24	19/43	8/18	7/16	66	1.00
Wood-exp.				23	44	16	16	68	1.00
Cellulose-theo.	45%	$4 \cdot (C_6H_{10}O_5)$	648	4/20	11/55	3/15	2/10	70	1.05
Cellulose-exp.				22	53	17	8	70	1.14
Lignin-theo.	25%	$4 \cdot (C_5H_6O_2)$	450	3/33	3/33	2/22	1/11	42	0.78
Lignin-exp.				30	35	23	12	38	0.71
Hemicell.-theo.	30%	$3 \cdot (C_5H_{10}O_5)$	392	3/20	5/33	3/20	4/27	82	1.12
Hemicell.-'exp.'				19	33	19	29	90	1.03

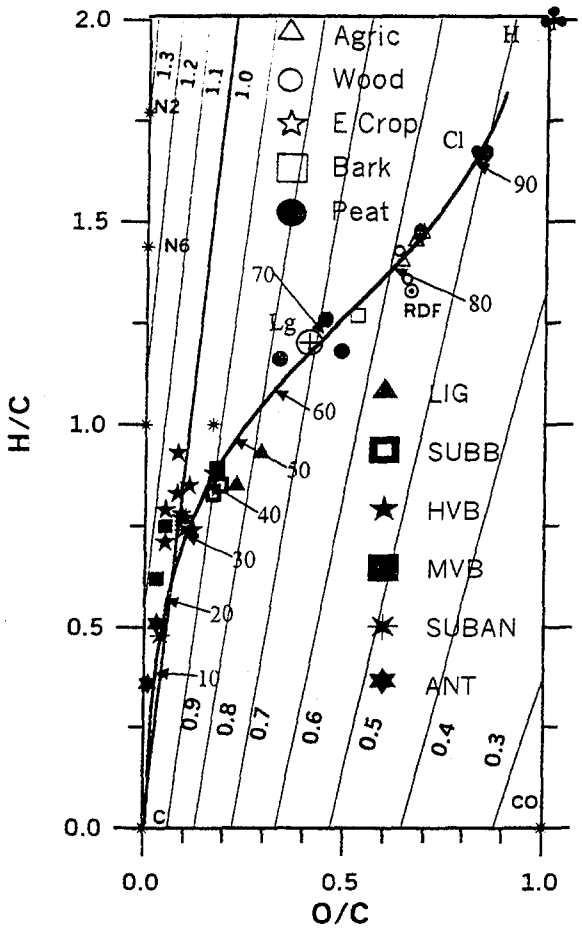

Fig. 7 ***H/C*** **versus** ***O/C*** **for various coals and biomass species**

normalized to that of SP. Hemicellulose "experimental" values were determined by difference.

The overview "coalification" diagram in Fig. 7 (Green et al., 1997) shows the $y = H/C$ and $x = O/C$ positions of fossil fuels ("aged biomass") as well as biomass fuels ("prenatal coal"). The contour lines give ratios of HHV to that of carbon as calculated from the Dulong law. The tick marks along the coalification curve give standard volatility assignments. The new entries on this figure are the positions of the three components (Hm, Cl, and Lg) of biomass. Every type of biomass might be viewed as a unique feedstock blend of these three major components.

Discussion and Conclusions

From the results of experimental measurements with identical inputs it is clear that the laboratory IHGs are capable of good reproducibility. From work with varying types of inputs, a differentiation is observed in the effective yields and rate constants for different samples. The ability of the laboratory IHG system to provide a gaseous sample for GC-TCD analysis greatly enhances the type of information obtainable with respect to the standard ASTM method of measuring biomass volatility based upon mass loss at 950°C. The time needed for most of the biomass experiments in MG3 and MG4 are of the order of one to three minutes. This is to be compared with TGA measurements which usually take 1 to 3 hours.

On the interpretive side it is clear that heat transfer rather than chemistry dominates the time dependence of gaseous release in the MG's as in commercial IHGs. The exploratory experiments with spruce dowels at 1000°C have been particularly illuminating. While Eqs. 12 and 13 were inferred from simple heat transfer considerations fortuitously they appears to provide an approximate way of allowing for phase change temperature delays. The assignment $G_1 = 1$ might, in effect, nullify the delay for hemicellulose because the time to reach the ablation temperature is already represented by the numerator (i.e., $1 - \exp - \gamma t$). The assignment $G_2 = 10$ might be attributed to the stabilization of temperature while the hemicellulose is volatizing before the temperature rises again and the cellulose volatizes. The $G_3 = 100$ could represent the delay time due to cellulose volatizing before the temperature rises again and the lignin starts to volatize. Note also that k, the chemical decomposition rate constant, is reasonably large as compared to the thermal rate constant γ. Most of the parameters used with Eq. 13 were coarsely estimated since these were simply exploratory measurements. Clearly further adjustment of parameters and the assignment of separate $k_i s$ and possibly the $\gamma_i s$ should refine the fits.

The results suggest that CO_2 components arising from hemicellulose is higher than in cellulose or lignin. The CO yield of cellulose is highest. The char-tar weight percentage is highest in lignin. From the residual compositions derived for the char-tars one might expect to get higher gaseous yields at higher temperatures.

The molecular modeling efforts point to a possible way of anticipating the major gas output from any wood whose weight percentages of Hm, Cl, and Lg are known by reproportioning the results given in Table 3. Note that one cannot conclude that these experiments display a simple additivity rule—since in effect such a rule was assumed in inferring the decomposition products of hemicellulose. By conducting independent experiments with hemicellulosic material, departures from the additivity rule and even useful synergies may be found. Pending this study it is not unreasonable to use given molecular decompositions to infer yields of other forms of biomass with differing ratios of Hm, Cl, and Lg.

These encouraging results from exploratory measurements strongly suggest that a broader series of dowel measurements at a number of temperatures be made using pure Hm, Cl, and Lg and dowels made from several different woods. Such a data set would check the additivity rule and provide a general way of estimating the gaseous yields of any biomass and at any temperature.

Indirectly heated gasifiers basically "cook" the feedstock at high temperatures in an anoxic environment. In carbon rich cases steam is often used although under some circumstances green biomass might do as well. Biomass has the advantage with respect to coal of easier convertibility to gaseous form but the disadvantage of lower heating value. The ideal feedstock blend for IHGs is one in which the char residue is just sufficient that when separated and combusted could provide the gross heat necessary for the pyrolysis or gasification process. Calculations in a previous study (Green et al., 1996a) suggested that the peat region of Fig. 7 was an optimum region. Thus 70 percent of the mass is readily volatized and the remaining mass in the form of char is adequate to provide the heat for gasification and the carbon needed to transform the carbon dioxide and water vapor to carbon monoxide and hydrogen. Lignin is in this advantageous same H/C–O/C neighborhood. The promise of feedstock blending is that many combinations of feedstocks might also satisfy these requirements. What is needed now is the development of a predictive science of high temperature cooking that considers the involvement of the various physical and chemical properties of available domestic feedstocks or the forms they can inexpensively be converted to by physical or chemical processing before the gasifier.

A number of attempts have been made recently to deal with the heat transfer, phase change, chemistry, and diffusion in the pyrolysis of biomass (Miller and Bellan, 1996; 1997; Di Blasi 1996; Lede, 1994). It is hoped that this combination of experiment and phenomenological modeling will also help in reaching the day when pyrolysis of biomass becomes a predictive science.

More immediately, the mini-gasifiers can be used as surrogates for commercial IHGs just entering the market to test various feedstocks, feedstock blends, various temperatures, particle sizes, the relationships between the constituents of the input and the constituents of the

output gases, in rapid screening of potential catalysts and in examination of other potential applications of IHGs.

Acknowledgments

The support of CCTL cogasification studies by the Mick A. Naulin Foundation and the College of Engineering is gratefully acknowledged. Thanks are due to Professor Michael Pollock and Ms. Linda Garzarella for the loan of the respirometer that had an important impact on this work; Dr. Robert Coldwell, Gordon Prine, Donald Post, William Pickering, and Sergio Peres for advice and materials; Professor C. K. Hsieh for his comments; Gregory Schaefer and Russell Auld for their technical assistance; and Elisa Lockhart and Alan Hill for their thermal conductivity measurements.

References

Boelter, L., Cherry, V., Johnson, H., and Martinelli, R., 1965, *Heat Transfer Notes,* McGraw Hill Book Co., New York.

Carboni, R., 1995, "Furnace Turns Biomass Into Clean Fuel and Feedstocks," *Environmental Engineering World,* Jan./Feb., pp. 37–39.

Di Blasi, C., 1996, "Influences of Model Assumptions on the Predictions of Cellulose Pyrolysis in the Heat Transfer Controlled Regime," *Fuel,* Vol. 75, pp. 58–66.

Green, A., ed., 1981, *Alternative to Oil, Burning Coal with Gas,* Univ. Presses of Fla., Gainesville, pp. 1–140.

Green, A., 1986, "Proposed Institute for Gasification Studies with Campus Cogenerating Plant," report, University of Florida, Gainesville, FL.

Green, A., ed., 1988, *Co-Combustion,* ASME FACT Vol. 4, New York, NY.

Green, A., ed., 1991, *Solid Fuel Conversion for the Transportation Sector,* ASME FACT Vol. 12, New York, NY.

Green, A., 1993, *Co-Combustion 93,* Proceedings, ASME IJPGC FACT Vol. 17, New York, NY.

Green, A., and Burki, J., 1974, "A Note on Survival Curves with Shoulders," *Radiation Research,* Vol. 60, pp. 536–540.

Green, A., and Pamidimukkala, K., 1984, "Synergistic Combustion of Coal with Natural Gas," *Energy,* Vol. 9, pp. 477–484.

Green, A., Wagner, J., et al., 1986, "Coal-Water-Gas, An All American Fuel for Oil Boilers," Proceedings, 11th Intern. Conf. on Slurry Technology, Hilton Head, SC, Slurry Technology Assoc., Washington, DC, pp. 251–262.

Green, A., Rockwood, D., Prine, G., et al., 1989, "Co-Combustion of Waste, Biomass and Natural Gas," *Biomass,* Vol. 20, pp. 249–262.

Green, A., Peres, S., Mullin, J., and Xue, H., 1995, "Cogasification of Domestic Fuels," Proceedings, ASME IJPGC FACT Vol. 1, Minneapolis, MN, ASME-FACT New York, NY.

Green, A., Zanardi, M., Peres, S., and Mullin, J., 1996a, "Cogasifying Biomass with other Domestic Fuels," presented at Bioenergy '96, Nashville, TN.

Green, A., Zanardi, M., Jurczyk, K., Peres, S., and Mullin, J., 1996b, "Cogasifying Solid Fuels," Proceedings, ASME FACT Vol. 1, Houston, TX, ASME, New York.

Green, A., Peres, S., Mullin, J., and Anderson, R., 1997, "Solid Fuel Gasification for Gas Turbines," ASME Paper 97-GT-062.

Green, A., Zanardi, M., and Mullin, J., 1997, "Phenomenological Models of Cellulose Pyrolysis," *Biomass and Bioenergy,* Vol. 13, pp. 15–24.

Heisler, M. P., 1947, "Temperature Charts for Induction and Constant Temperature Heating," *Trans ASME,* Vol. 69, pp. 227–236.

Lede, J., 1994, "Reaction Temperature of Solid Particles Undergoing an Endothermal Volatilization Application to the Fast Pyrolysis of Biomass," *Biomass and Bioenergy,* Vol. 7, pp. 49–60.

Mansour, M., Voelker, G., and Durai-Swamy, K., 1995, "MTCI/Thermochem Steam Reforming Process for Solid Fuels for Combined Cycle Power Generation," Proceedings, ASME IJPGC Vol. 1, Minneapolis, MN, ASME-FACT New York.

Miller, R. S., and Bellan, J., 1996, "Analysis of Reaction Products and Conversion Time in the Pyrolysis of Cellulose and Wood Particles," *Comb. Sci. Tech.,* Vol. 119, pp. 331–373.

Miller, R. S., and Bellan, J., 1997, "A Generalized Biomass Pyrolysis Model Based on Superimposed Cellulose, Hemicellulose, and Lignin Kinetics," *Comb. Sci. Tech.,* Vol. 126, pp. 97–137.

Mullin, J. P., 1998, "High Temperature Pyrolysis of Selected Solid Wastes," M.S. thesis, M. E. Dept., University of Florida; Gainesville, FL.

Ozisik, M. N., 1993, *Heat Conduction,* 2nd ed., Wiley, New York.

Paisley, M., and Anson, D., 1997, "Biomass Gasification for Gas Turbine Based Power Generation," ASME Paper 97-GT-005.

Peres, S., and Green, A., 1997, "Gasification of Bagasse Blended With Various Catalysts," Proceedings, ASME IGTI Turbo Expo '98; see also Peres, S., 1997, Ph.D. thesis, M. E. Dept., University of Florida, Gainesville, FL.

Solomon, P. R., Serio, M., and Suuberg, E., 1992, "Coal Pyrolysis: Experiments, Kinetic Rates and Mechanisms," *Prog. Energy Combust. Sci.,* Vol. 18, pp. 135–220.

LM2500 Gas Turbine Fuel Nozzle Design and Combustion Test Evaluation and Emission Results With Simulated Gasified Wood Product Fuels

C. E. Neilson

D. G. Shafer

General Electric Aircraft Engines,
General Electric Co.,
One Neumann Way,
Cincinnati, OH 45241

E. Carpentieri
CHESF/DEFA,
Recife-PE-Brazil

The Brazilian Wood Biomass Demonstration Project (WBP) Phase II was contracted with the United Nations Development Programme-PNUD, Setor Comerical Norte, Quadra 2-BLOCO A, EDF. Corporation-7º Andar, Brasilia-DF Brasil 70712-900 and General Electric Marine and Industrial Engines to develop the gas turbine equipment necessary to utilize fuel produced by the gasification of wood products. The program included performance studies, control specification requirements, bleed and fuel valve specifications, a modified dual gas fuel nozzle for fuel delivery to the combustor and results of two combustor component tests utilizing biomass simulated fuel. This paper will deal primarily with the fuel nozzle design elements, the setup and evaluation of the component combustor tests and resulting emissions produced by the simulated Biomass fuel. Details of the combustor test arrangement, facilities and special test equipment needed to complete the evaluation will be presented. In addition, background on the two types of combustor testing will be discussed.

Introduction

Advances in biomass gasification technology using renewable resources, such as wood, and the abundant availability of this resource in developing countries created renewed interest in this type of fuel as a basis for electrical power generation. In such areas where coal, natural gas, and water power are not readily available or already consumed, gasified wood products could promote continued economic growth and development with affordable electric power.

This paper evaluates combustion systems that are able to successfully burn low Btu fuel with minimum impact to the host gas turbine. The Brazilian Biomass WBP Project (phase II) was the venue to enhance the fuel nozzle design, evaluate combustor operation and to define a gas turbine system which can operate of low Btu fuel.

The design of the fuel nozzle is an adaptation of current dual fuel nozzle concepts in which two types of fuel are introduced into the combustor by the same fuel nozzle. This dual circuit design allows the introduction of different gas compositions in each circuit which integrates a fuel change over from starting fuel to biogas fuel with no affect on the gas turbine operation. Both component combustor tests utilized this fuel nozzle system for changing from starting fuel to biogas fuel.

The first combustion test was a 1 atmosphere test. Key performance characteristics evaluated by this test included combustion light-off and blow-out, low speed delta T, exit temperature profile, pattern factor and flammability limits. The purpose of this test was to compare biomass fuel burning characteristics to current production combustor systems.

The second combustion test was a high pressure sector test. The sector was a 5 fuel nozzle portion (60 deg sector) of a normal combustor. The object of this test was to obtain flammability, efficiency and emissions information about the proposed biomass fuels.

Combustor and Fuel Nozzle System

The General Electric LM2500 marine and industrial gas turbine is a derivative of the TF-39/CF6-6 family of engines. The LM2500 engine is used extensively in military marine, commercial marine, and industrial applications. The LM2500 operates on both natural gas and liquid fuels and has amassed over 22 million operational hours on over 1500 gas turbines in service worldwide. The combustion system contains a full annular combustor shown in Fig. 1 with film cooled liners and a multi-swirler dome for atomizing and mixing the fuel and air in the combustor primary zone. Several fuel nozzle designs exist (biomass fuel nozzle shown) to support the large variety of gaseous and liquid fuels needed for engine operation.

In 1983, General Electric demonstrated successful combustion system operation on low Btu fuels derived from coal or nonfossil fuel gasification processes (Bahr et al., 1985; Sabla and Kutzko, 1985). These gases typically have a lower heating value in the range of 100 (3.72 MJ/m^3) to 250 (9.3 MJ/m^3) Btu/SCF. Combustibles were chiefly hydrogen (H_2), methane (CH_4), and carbon monoxide (CO) with large proportions of CO_2 and N_2. Based on these earlier tests stable operation to 100 Btu/SCF is expected provided there is 10 percent of H_2 in the fuel mixture (Sabla and Kutzko, 1985).

The Brazilian WBP project represents the first LM2500 engine demonstration on low Btu gas. Listed in Table 1 is the expected makeup of the Brazilian biomass fuels. Fuel "A" is the product of a low pressure gasification process and fuel "B" the product of a pressurized system.

Based on the results of the 1983 testing, low Btu fuel LFHV can impact the ability of the fuel to sustain flame. The percentage of H_2 plus CO of the combustibles in the fuel is an indicator of this fuel flammability. Reproduced in Fig. 2 are the results from the 1983

Contributed by the International Gas Turbine Institute (IGTI) of THE AMERICAN SOCIETY OF MECHANICAL ENGINEERS for publication in the ASME JOURNAL OF ENGINEERING FOR GAS TURBINES AND POWER. Paper presented at the International Gas Turbine and Aeroengine Congress and Exhibition, Stockholm, Sweden, June 2–5, 1998; ASME Paper 98-GT-337.

Manuscript received by IGTI March 18, 1998; final revision received by the ASME Headquarters June 23, 1999. Associate Technical Editor: R. Kielb.

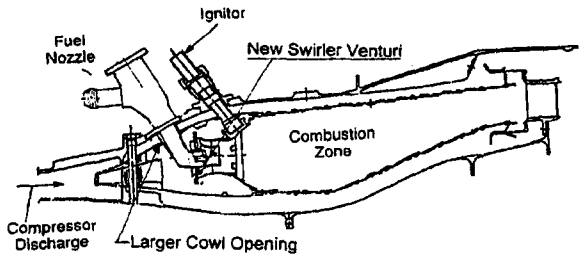

Fig. 1 LM2500 combustor with biomass fuel nozzle

test which showed that if the sum of H_2 and CO in the fuel exceeded 80 percent and the LFHV was equal to or greater than 100 Btu/SCF (3.72 MJ/m^3), combustion could be sustained in an LM2500 configured combustor at all power levels. The various levels of flammability are compared at different combustor inlet temperatures ranging to maximum power. For both fuels the combination is above the minimum value to sustain flame. Considering this, General Electric predicted that the LM2500 should operate successfully on both fuels.

Fuel Nozzle Design Criteria. Engine operation on the proposed biomass and start fuel compositions requires a dual gas fuel nozzle as shown in Fig. 3. This design concept is capable of handling the voluminous biomass fuel flows required at full power. The start fuel was vaporized commercial grade liquid petroleum (LPG).

The following were fuel nozzle design criteria:

(1) Size the fuel nozzle tip outer diameter to fit the LM2500 Dual Fuel Steam combustor configuration shown in Fig. 1. It features a larger swirler bore than the standard configuration. Flow splits of the primary and secondary air swirler remain the same.
(2) Design separate gas circuits. Startup to be accomplished when high energy start gas flows through the inner circuit. Full power operation should be achievable on the start gas. Full power operation on biomass gas fuel will utilize both fuel nozzle circuits to flow the biomass fuel.
(3) Operation to full power on high energy start fuel is required. Off engine purge of the outer biogas circuit is required to avoid combustion gas back flow.
(4) Set the fuel nozzle tip pressure ratio (Pr = FMP/Ps_3) at full power equal to that used by General Electric Marine & Industrial Engines in successful natural gas applications.
(5) Demonstrate transition from start fuel to biomass fuel at or above 2 MW's of output power, corresponding to power just above synchronous idle of generator to power grid.

All of the design requirements were met in the proposed design. Listed in Tables 2 and 3 are the important design characteristics of the fuel nozzle. Pressure ratio is listed instead of pressure drop (Delta P) in Table 3. All of the values listed for pressure ratio fall within the experience bands of successful LM2500 engine operation on various gaseous fuels.

Table 1 Fuel compositions, percent by volume

Constituent	Formula	Fuel "A"	Fuel "B"
Hydrogen	H_2	16.5	11.2
Carbon Monoxide	CO	23.45	17.4
Methane	CH_4	3.94	6.0
Ethane	C_2H_6	0.05	0.0
Ethylene	C_2H_4	1.45	0.0
Nitrogen	N_2	37.76	43.6
Carbon Dioxide	CO_2	12.05	13.2
Water Vapor	H_2O	4.75	8.6
Total		99.95	100.0
LFHV Btu/SCF (MJ/m^3)		179.4 (6.67)	141.6 (5.27)
% H_2 + CO in Combustibles =100 x (H_2+CO) / (H_2+CO+CH_4+C_2H_6+C_2H_4)		88.0	82.7

Combustion System Test Evaluation

Full Annular One Atmosphere Test. Important design features of combustion systems can be evaluated at atmospheric conditions. The approach is to scale engine operating conditions to atmospheric conditions by maintaining the correct combustor inlet Mach number, inlet temperature and fuel air ratio. This approach provides good correlation to gas turbine experience, reduces test complexity and saves cost as compared to testing at high pressure. Both new development and current production designs are tested in the same manner to confirm that key characteristics are within General Electric experience.

Key performance characteristics evaluated in the Biomass atmospheric test included combustor light-off, and blow out, low speed delta T, exit temperature profile, pattern factor and flammability limits.

The test was conducted in an improved and updated test facility compared to the facility used for the prior low Btu fuel tests in the mid 1980's (Sabla and Kutzko, 1985). The new combustion test facility began operation *n* 1994.

Atmospheric Test Vehicle. The test utilized the CF6/LM2500 test vehicle which has been used for many years to test this family of combustors. The combustor casing is mounted in a test dolly to facilitate vehicle build up, transport, and installation into the test cell.

The test vehicle includes two manifolds: the 6 inch (152.4 mm) biomass fuel manifold and the 3 inch (76.2 mm) start gas manifold. The biomass fuel manifold is hooked up to the outer circuit of the 30 fuel nozzles through 38.1 mm ($1\frac{1}{2}$") diameter flexible jumper tubes. The start fuel manifold is hooked up to the inner nozzle circuits through 19.05 mm ($\frac{3}{4}$") diameter flexible jumper tubes. The biomass and start gas manifolds are connected together by the transfer system. This system allows biomass fuel to transfer into

Nomenclature

Ps3 = combustor inlet static pressure, psi (kPa)
Wf = fuel flow, lbs/hour (kg/h)
FAR = fuel-air ratio
Tt3 = combustor inlet temperature, °F (°C)
Pt3 = combustor inlet pressure, psi (kPa)
Tt4 Avg. = combustor average exit temperature, °F (°C)
Tt4 Local Max. = combustor maximum exit temperature, °F (°C)
Delta T = combustor temperature rise
Pt4 = combustor exit pressure, psi (kPa)
Pr = pressure ratio
Ae = effective area, in^2 (mm^2)
ppm = parts per million
LFHV = lower fuel heating value, Btu/SCF (MJ/m^3)
FMP = fuel manifold pressure, psi (kPa)
W = mass flow, lbs/s (kg/s)

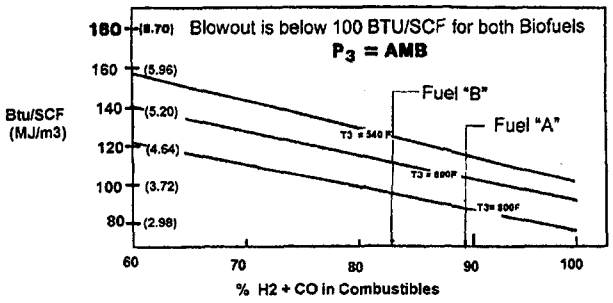

Fig. 2 Flammability results of LM2500 combusttor

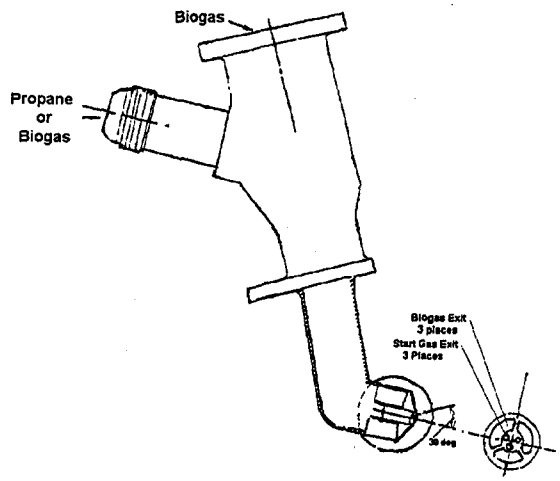

Fig. 3 Biomass fuel nozzle

the start gas manifold and hence to the inner circuit of the fuel nozzles when the rig is running on biomass fuel.

The test vehicle is equipped with an inlet instrumentation plane measuring *Pt*, *Ps*, and *Tt* with simple rakes. The discharge plane is more complex and consists of four, seven element temperature rakes and four, three element pressure rakes mounted on a traversing ring. Each temperature and pressure rake captures data in a 90 deg sector. The automatic traverse control drives the ring in $1\frac{1}{2}$ degree steps and data is captured from all eight rakes at each step. This amounts to 1680 individual temperatures being recorded over a complete traverse for exit temperature profile determination.

An air purge system is incorporated that allows purging of the biomass fuel manifold with air from the vehicle inlet. Both manifolds are also supplied with high pressure N_2 inputs that allow purging of flammable gases during shut down as a safety precaution.

Test Air Supply. Pressurized test air (shown in Fig. 4) is

Table 2 Biomass fuel nozzle—tip area characteristics

Description	Units	Inner	Outer
Tip Effective Area = Ae	In^2. $(mm)^2$	0.0192 (12.387)	0.2112 (136.26)
Biomass Fuel Flow Splits	Percent	8.3	91.7

Table 3 Biomass fuel nozzle—pressure ratio characteristics

Description	Fuel "A"	Fuel "B"	Start Gas (LPG)	Experience
Tip Pr @ Max Power	1.16	1.29	1.1	1.05 - 1.30
FMP @ Max Power psi (kPa)	299 (2062)	304 (2096)	239 (1648)	330 (2275)
Tip Pr @ Idle	N/A	N/A	1.06	1.025 Min

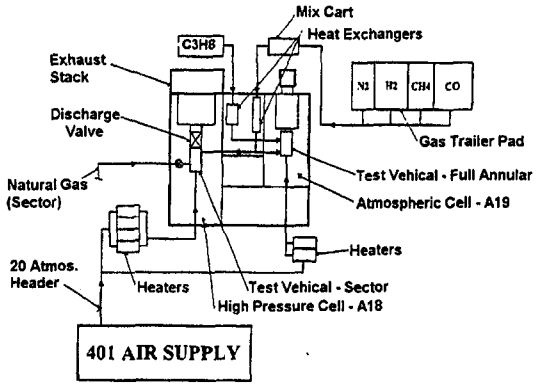

Fig. 4 Air and fuel supply sketch

routed from the air supply building. Heating of test air, if required to simulate compressor discharge air, is by gas fired heat exchangers located just outside the test cell. Measurement of inlet air to the vehicle is by a choked, circular arc venturi installed in the inlet piping.

Two separate, controlled, and metered bleed systems, powered by air ejectors, were available. One of the bleed systems, simulating the gasifier pressure requirements, was used to pull bleed from the test rig. The second bleed simulated normal gas turbine cooling.

Biomass Fuel System. Shown in Table 4 are the test fuel compositions used in the component tests. The proposed biomass fuels, fuel "A" and fuel "B", contain carbon dioxide (CO_2) and water vapor (H_2O) as shown in Table 1. The substitution of nitrogen (N_2) for CO_2 and H_2O for the test fuels was made to simplify the component tests. The substitution of N_2 for H_2O should have no impact on the results. The substitution of N_2 for CO_2 could produce less conservative results on flammability. However, based on results from earlier low Btu tests (Bahr et al., 1985), the impact was not expected to adversely affect the results by more than 5 percent. Fuel "B" also has a small amount of ethylene (C_2H_4) that was replaced with an equivalent heat content of methane (CH_4). This, likewise, was not expected to impact the results.

Figure 4 shows the biomass fuel delivery system. Tube trailers were hooked up to delivery piping that supplied the flammable gases to the test cell. Nitrogen was supplied from a truck mounted liquid nitrogen plant. A nitrogen tube trailer was located on the same pad and tied into the system to act as an accumulator.

The constituent gases in the biomass fuel mixture were controlled, metered, and mixed in a Mixer Cart. Constituent flow was controlled by an appropriately sized V-ball valve with diaphragm actuator and positioner. Each flow was measured with an ASME orifice run. Each control and meter run is also equipped with a remote operated shut off valve and check valve. The gases were mixed in a Koch mixer.

The mixed biomass fuel was piped to an air/fuel heat exchanger shown in Fig. 4 where it was heated to the required test temper-

Table 4 Test fuel compositions percent by volume

Constituent	Formula	Fuel "A" Test	Fuel "B" Test
Hydrogen	H_2	16.5	11.2
Methane	CH_4	6.4	6
Carbon Monoxide	CO	23.5	17.4
Nitrogen	N_2	53.6	65.4
Total		100	100
LFHV Btu/SCF		179.4	141.6
(MJ/m^3)		(6.67)	(5.27)

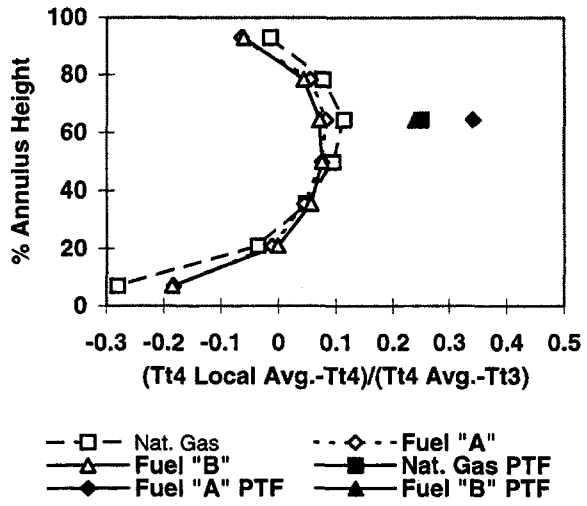

Fig. 5 Typical profile and pattern factor (PTF)

ature. The required fuel temperature was supplied by each gasifier as the expected temperature result from the gasification cleanup processes and delivered to the gas turbine. The heated, mixed biomass fuel was then piped into the test cell and into the fuel manifold on the test rig.

The start fuel for the atmospheric test was propane, similar to that proposed for use in Brazil. The fuel was processed in a vaporizer and delivered to the manifold at 300°F (149°C).

Performance Results. The biomass configuration uses the dual fuel steam combustor described in Fig. 1. The specific combustor tested during the biomass program was performance tested on standard fuels in November of 1993. The results from that test and the General Electric data base form the basis for comparison to the current test results.

Performance testing determines the combustor exit radial temperature profile, pattern factor and pressure loss at simulated maximum power operating conditions. Some special definitions are required to explain the results of the multiple temperature measurements and to show how these data are used to evaluate combustor performance.

$$\text{combustor pressure loss} = \frac{(\text{Pt3} - \text{Pt4})}{\text{Pt3}} * 100\%$$

Combustor exit temperature profile is calculated as follows: ((the arithmetic average of all combustor exit thermocouple temperature readings at each given radial immersion) − (Tt4 Avg.))/(Tt4 Avg. − Tt3).

$$\text{combustor pattern factor} = \frac{(\text{Tt4 local max.} - \text{Tt4 avg.})}{(\text{Tt4 avg.} - \text{Tt3})}$$

Profile and Pattern factor characterize the combustor exit temperature (see Fig. 5). Profile represents the average of the temperatures at selected radial locations in the combustor exit. Profile factor is an index of the maximum average temperature at a given radial position. Pattern factor represents the highest individual temperature measured at any of the selected radial locations. Profile could impact downstream rotating parts whereas pattern factor could affect the stationary parts downstream of the combustor.

Shown in Table 6 and Fig. 5 are the maximum results from the biomass performance test and data from the General Electric data base. The General Electric data base (section 1 of Table 6) consists of data from LM2500 combustors with standard size fuel nozzle swirler bores tested at consistent parameter conditions.

The audit power setting represents a generic set of test conditions used during combustor production quality audits. Data recorded at audit conditions are compared to the data base as a "go, no go" evaluation of a combustor. Data falling within two sigma bands of the average are acceptable.

Table 5 LM2500 biomass atmospheric ignition and efficiency results

	Current Test	Data Base	
Fuel	Propane	JP5	Nat. Gas
Ignition - Wf @ 8 lbs/s air flow (3.63kg/s)	*272 lbs/hr 123.4kg/hr*	*430 195*	*269 122*
Low Speed Efficiency = Delta T @ Wa = 8 (3.63) FAR=0.024)	1700 °F (389 °C)	1104 °F (613 °C)	1675 °F (931 °C)

The results from the Nov. 93 test (section 2 of Table 6) on natural gas were within the two sigma bands of the data base average. This test confirmed that the larger fuel nozzle swirler bore had no impact on combustor performance.

The current series of tests evaluated the impact on profile factor, pattern factor and pressure drop using biomass simulated fuel. Results for the biomass fuels are shown in section 3a and 3b of Table 6. Test conditions simulated the actual maximum engine operating conditions expected in Brazil. This included modifying the atmospheric test rig to flow the high bleed flows requested by the gasifiers of up to 12 percent of the engine flow rate. Bleed flow simulated either gasifier requested pressurization for startup of system or to balance the stall margin at high power operation.

Profile and profile factor were acceptable for all of the configurations tested and are not a concern. The expected profile factor is 10 percent based on General Electric historical data. The biomass fuels have a smaller profile factor of 7.6 to 8.2 percent or a flatter Tt4 profile across the annulus than the base fuels (JP5 and natural gas).

Operation with simulated fuel "A" resulted in a high pattern factor of 0.341. This may be due, in part, to the increased mass flow of fuel plus engine air flow where the fuel flow of low Btu fuels could be 5 to 7 times that of natural gas. This results in poorer mixing in the combustor and some gas reaching the combustor exit at a higher absolute temperature (Bahr et al., 1985; Sabla and Kutzko, 1985). The pattern factor affect may also be offset by the reduced turbine inlet temperature compared to standard LM2500 operation. The significant added mass flow of the fuel contributes to the total power delivered by the gas turbine, requiring less Delta T to attain the same power output.

Conversely, operation with fuel "B" gas resulted in a low pattern factor of 0.239. This result is surprising based on the low Btu tests conducted in 1983 (Bahr et al., 1985; Sabla and Kutzko, 1985). A high pattern factor was expected for both biomass fuels. Although it is a positive result, and somewhat more consistent with the data base for audit tests, the reason for the lower pattern factor on fuel "B" will require further analysis an is beyond the scope of this paper.

Pressure drop on fuels "A" and "B" were both low at 3.95 percent and 3.56 percent, respectively. This represents a potential concern to the high pressure turbine nozzle vanes. A large combustor exit pressure level increases the potential for nozzle gas side back flow into the vane cooling circuit, since the cooling pressur-

Table 6 LM2500 biomass atmospheric test performance results

Section	1	2	3a	3b
Date	Data Base	Nov.93	May-95	May-95
Power Setting	Audit	Audit	Max Brazil	Max Brazil
Combustor Swirler	Standard	Large	Large	Large
Fuel	JP5	Nat. Gas	Fuel "A"	Fuel "B"
Profile Factor	0.101	0.113	0.082	0.076
Pattern Factor	0.219	0.25	0.341	0.239
Combustor Press Loss	4.85	4.84	3.95	3.56

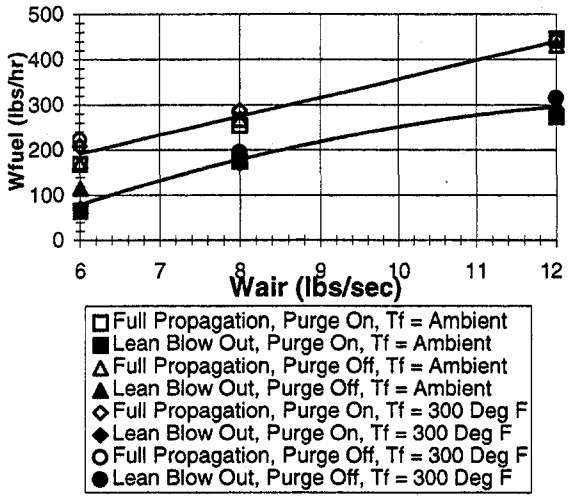

Fig. 6 Sea level ignition results on propane

ization is supplied by the compressor discharge pressure (Ps3). These results indicate that biomass fuels will require further study as to the impact on the service durability of hot section components of the high pressure turbine. A conservative estimate of the hot section overhaul interval for the smaller pressure drop only is between 12,500 and 25,000 hours which corresponds to General Electric experience with liquid and natural gas fuel with steam augmentation on hot section intervals. Actual estimates will be dependent on other factors including contaminants in the resultant fuel delivered to the gas turbine. When the prototype project is launched this impact will be evaluated as part of the next phase engineering effort.

Sea Level Ignition and Low Speed Temperature Rise. Tests were conducted using propane to simulate the start fuel. Listed in Table 5 are the test results and data from the General Electric data base. For comparisons, General Electric quotes ignition and low speed combustor temperature rise (delta T) results at 8 lbs/s (3.63 kg/s) of combustor airflow and FAR = 0.024. This approximates the actual engine airflow.

Figure 6 shows the data recorded at 6, 8, and 12 lbs/s (2.72, 3.63, 5.44 kg/s respectively) for ignition. Ignition was evaluated with ambient and 149°C (300°F) propane as well as purge of the biomass manifold.

Light-off on propane at 3.63 kg/s (8 lbs/s) is good at an average of 23.4 kg/hr (272 lbs/hr). Heated fuel and purge (on or off) did not significantly impact the results. Purge media is used, from an independent supply source, to protect the biomass circuit from back flow of combustion gases.

Figure 7 shows the data recorded at 2.72, 3.63, 5.44 kg/s (6, 8, and 12 lbs/s respectively) for low speed delta T. The figure also contains comparison data for natural gas and JP5. Delta T was evaluated with 149°C (300°F) propane and purge (normal engine operation). Delta Temperature of 944°C (1700°F) is excellent at 3.63 kg/s (8 lbs/s) airflow and FAR = 0.024.

Sector Tests

To control costs, General Electric uses both low pressure and high pressure sector testing in conjunction with full annular tests. It also allows the use of facilities that are flow limited when the objective is to test at actual engine operating conditions. Sectors can range from one cup to as many as fifteen in triple annular combustors. A 5-cup sector with air cooled side walls was used in the biomass program. The primary objectives of the high pressure test were to obtain flammability, efficiency and emissions information about the two simulated biomass fuels.

Sector Test Vehicle. The test vehicle was the LM2500 5-cup sector rig. The 5-cup sector is housed within a portion of the engine flow path and is contained in a pressure vessel designed for 20 atmospheres of pressure service. The vehicle is mounted in a test dolly to facilitate build-up, transport and installation into the test cell.

Sector Test Air Supply and Fuel System. The biomass 5-cup high pressure sector test (see Fig. 5) was conducted in the same facilities as the earlier tests. This test cell shares the same air supply, building and control room as the atmospheric test cell. Test air is available in the test cell at up to 40 atmospheres of pressure, 113.4 kg/s (250 lbs/s) flow and 760°C (1400°F) temperature.

The biomass fuel system was the same as that used for the one atmosphere test. Biomass mixture control operated the same as the previous test.

Sector Starting Fuel System. The fuel system was the same as the one atmosphere test. High pressure natural gas was supplied to the test rig in place of propane for start up and re-light purposes. This was done to minimize the cost of the test. However, some propane test data was taken to capture low power efficiency up to the facility capability.

Sector Instrumentation. The vehicle had pressure and temperature rakes at the inlet. Four, four element gas sampling rakes and one temperature rake were installed at the combustor discharge for emissions, pressure, and temperature readings.

The emissions analysis system (EAS) located in the control room acquired the gas sampling data. This system gives near real time gas analysis data that is merged with the steady-state data readings as they are taken. The data system and control system were the same as the atmospheric test.

Flammability Test Results. The sector test determined flammability limits and combustion efficiencies when operating on "A" and "B" fuels. Determination of flammability limits was made by

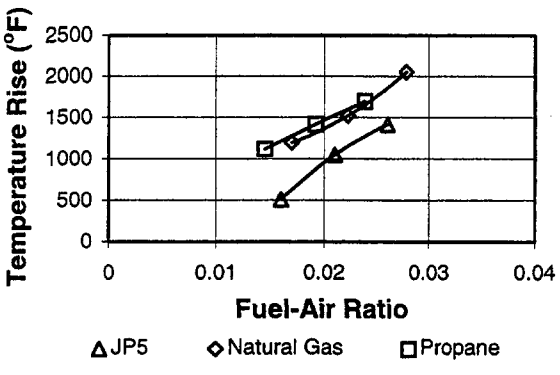

Fig. 7 Low speed efficiency at 8 lbs/s

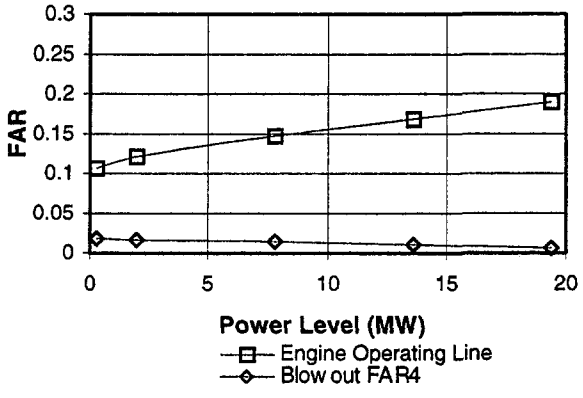

Fig. 8 Fuel "A" fuel air blowout

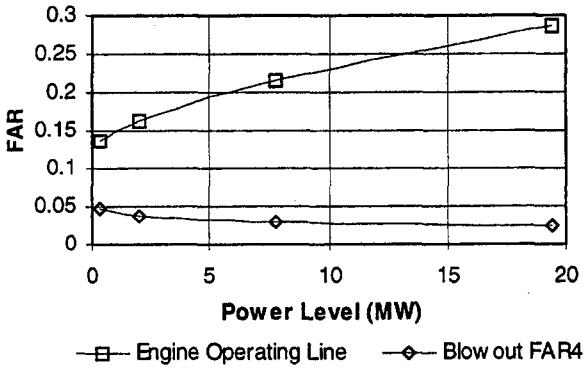

Fig. 9 Fuel "B" fuel air blowout

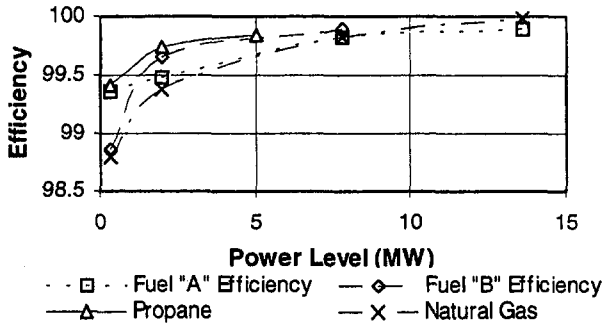

Fig. 10 Combustor efficiency versus power level

reducing both the overall fuel air ratio and the lower fuel heating value to blowout. Lean blowout tests were conducted by each of the following two methods: (1) decrease fuel flow while holding constant mix until lean blowout; (2) increase N_2 flow until lean blowout.

Lean blowout occurs when the fuel mixed with the compressor discharge air flow does not contain enough energy to sustain a flame. A loss of and/or decrease in the fuel pressure or any large reduction in fuel heating value could cause a lean blowout and corresponds to the two test methods respectively. Both test fuels have tolerance margin for the expected variation in fuel quality and supply pressure. The overall fuel air ratio was reduced by maintaining the combustor air flow constant while reducing the fuel "A" and "B" flow. The results are shown in Figs. 8 (fuel "A") and Fig. 9 (fuel "B"). The two biomass fuels have robust fuel air ratio blowout margins across the entire operating range. At core idle, blowout margins for fuel "A" and "B" were 83 percent and 66 percent, respectively.

The results at maximum power were from the one atmosphere tests. Full power conditions could not be set during the sector test. Regardless, the results at full power would be expected to be better in the sector test due to the beneficial effects of increased pressure.

The lower fuel heating value was reduced to blowout by maintaining the combustible flows while increasing the nitrogen flow. Listed in Table 7 are the results at core idle, 2 MW and 7.8 MW. The nitrogen system did not have the capacity to evaluate higher power levels.

Lower fuel heating value (LFHV) margin at core idle for fuel "A" and fuel "B" were 49 percent and 15 percent, respectively. The LFHV quoted by the gasifier vendor can vary on the low side by nearly 25 percent. This much variation would prevent transition of fuel at gas turbine idle for fuel "B". The blowout margin increases to 28 percent at 2 MW and to 34 percent at 7.8 MW. The blowout margins for both fuels would continue to increase up to full power and is not a concern.

Test results confirmed pretest predictions that transition from propane to biomass fuel can occur at a power level of 2 MW's or above for either fuel.

Combustion Efficiency Results. As expected, fuels "A" and "B" have good combustion efficiencies at part power operation as shown in Fig. 10. This is driven by the significant amount of H_2 in the fuels. Natural gas and propane efficiencies are shown for comparison.

Emissions Test Results. Listed in Table 8 are the emissions measured during the sector test on the simulated fuels. The NOx values in Table 8 apply to the thermal NOx produced by the simulated fuel. The test fuel did not contain any other forms of fuel Nitrogen, such as Ammonia, that would be present in a biomass fuel gas. The data followed expected trends.

NOx is primarily an exponential function of the fuel adiabatic flame temperature. Higher flame temperatures produce higher NOx emissions. In the sector test, natural gas had the highest flame temperature, followed by Fuel "A" and Fuel "B", respectively. The data aligns in the correct relative order across the operating range as shown in Fig. 11. A conservative extrapolation of the data indicates that a 50 percent reduction in NOx, compared to a standard LM2500 operating on natural gas, can be expected with the biomass fuels at maximum power.

Review of CO emissions data indicates that a large CO level was measured at the same power level that provided the reduced NOx emissions (see Fig. 12). The CO levels seem to be unaffected by the burning of biomass simulated fuels. CO levels may be 10–15 times higher than the NOx level when operated on low Btu fuel at maximum power. Actual emissions levels will be determined during the site demonstration and commissioning phase.

Conclusions

The LM2500 will likely operate successfully on either Fuel "A" or Fuel "B" biomass fuels. Combustor exit temperature profile should not be a concern for any of the proposed fuels tested.

Table 7 LM2500 biomass sector blowout results

	Baseline LFHV Btu/SCF (MJ/m^3)	Core Idle Blowout Btu/SCF (MJ/m^3)	2 MW Blowout Btu/SCF (MJ/m^3)	7.8 MW Blowout Btu/SCF (MJ/m^3)
Fuel "A"	179.4 (6.66)	91 (3.39)	85 (3.16)	N_2 Limited
Fuel "B"	141.6 (5.25)	121 (4.50)	102 (3.79)	93.9 (3.44)

Table 8 LM2500 biomass sector NOx ppm (Ref. 15% O2) emissions results

	Core Idle	2 MW	7.8 MW	13.6 MW
Natural Gas	36.1	44.9	69.2	105
Fuel "A"	10.4	12.7	22.6	27.4
Fuel "B"	5	6.7	9.1	---

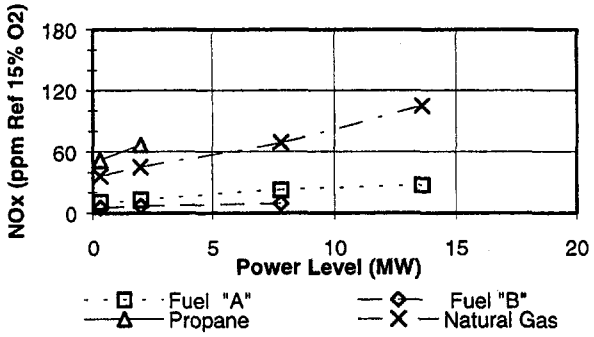

Fig. 11 NOx emissions versus power level

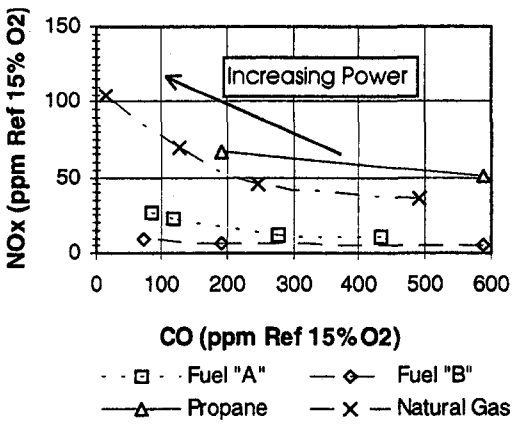

Fig. 12 NOx verses CO emissions

The combination of high pattern factors and low combustor pressure drops may represent a concern for the high pressure turbine hot section. The temperature level may be suppressed due to the greater fuel flow rate, but the pressure drop could affect the cooling capability of the turbine blades and nozzles. This combined characteristic may influence hot section installed service time.

The two proposed biomass fuels should have wide flammability limits for stable operation down to 2 MW. The biomass fuels (fuel "A" and fuel "B") seem to have excellent combustion efficiencies.

A 50 percent reduction in NOx emissions should be expected at full power using biomass fuels compared to the same power using natural gas. This does not include the negative impact of NH_3 to NOx conversion.

CO emissions will likely increase 10–15 times the NOx values at full power on the biomass fuels. Exhaust stack scrubbing or other emission improvements may be required. Actual emissions levels should be determined during site commissioning.

Acknowledgments

Contributions to this report came from the following: Doug Fortuna, GEAE Combustor COE; and Eric Kress, GEAE Combustor COE; General Electric Co., Cincinnati, OH.

References

Bahr, D. W., Sabla, P. E., and Vinson, J. W., 1985, "Small Industrial Gas Turbine Combustor Performance With Low BTU Gas Fuels," ASME Paper 85-IGT-125.

Battista, R. A., Pandalai, R. P., and Hilt, M. B., "Low Heating Value Fuel Burning Capabilities of General Electric Industrial Gas Turbines," ASME Paper 82-GT-255.

Sabla, P. E., and Kutzko, G. G., 1985, "Combustion Characteristics of the GE LM2500 Combustor With Hydrogen—Carbon Monoxide Based Low BTU Fuels," ASME Paper 85-GT-179.

The Application of Expert Systems and Neural Networks to Gas Turbine Prognostics and Diagnostics

H. R. DePold
depoldhr@pweh.com
United Technologies,
Pratt & Whitney,
400 Main Street,
East Hartford, CT 06108

F. D. Gass
gassfd@pwfl.com
United Technologies,
Pratt & Whitney,
West Palm Beach, FL 33410

Condition monitoring of engine gas generators plays an essential role in airline fleet management. Adaptive diagnostic systems are becoming available that interpret measured data, furnish diagnosis of problems, provide a prognosis of engine health for planning purposes, and rank engines for scheduled maintenance. More than four hundred operations worldwide currently use versions of the first or second generation diagnostic tools. Development of a third generation system is underway which will provide additional system enhancements and combine the functions of the existing tools. Proposed enhancements include the use of artificial intelligence to automate, improve the quality of the analysis, provide timely alerts, and the use of an Internet link for collaboration. One objective of these enhancements is to have the intelligent system do more of the analysis and decision making, while continuing to support the depth of analysis currently available at experienced operations. This paper presents recent developments in technology and strategies in engine condition monitoring including: (1) application of statistical analysis and artificial neural network filters to improve data quality, (2) neural networks for trend change detection, and classification to diagnose performance change, and (3) expert systems to diagnose, provide alerts and to rank maintenance action recommendations.

Introduction

Years of accumulation of knowledge of jet engine diagnostics has led to an understanding of the processes, rules of thumb, diagnostic fingerprints, and hierarchies for ranking, and fault isolation techniques. Effective and timely diagnostics and prognostics now necessitates that the users of diagnostic tools exercise considerable judgment and experience in applying this accumulated knowledge. A minimum of one week of intensive training is required to apply this knowledge, but effective utilization of current tools requires years of experience.

A critical mass of diagnostics knowledge has been achieved to permit the effective use of artificial intelligent systems such as neural networks and knowledge based systems, to emulate much of the required judgment and experience.

Overview of Diagnostic Processes

The diagnostic process (Fig. 1) is modular and begins with propulsion system data, and applies data validity analysis to convert the data to more usable information. It then extracts the knowledge of performance and mechanical trends from the information. Then it compares the extracted knowledge to several knowledge bases, and completes a diagnosis or prognosis of the propulsion system's health. Finally it alerts the operator to any important findings, and constructs a hierarchy of potential actions to correct any problems it uncovered.

A robust diagnostic process uses competing strategies with alternative analytical processes that operate in parallel. It considers from the outset, more than one possible explanation for any trends it discovers. By using knowledge of the measurement uncertainties and the fingerprints for the possible explanations, it identifies and ranks the suspected root causes. It can carry the recommendations further by consulting additional knowledge bases and providing check procedures and maintenance procedures.

Adaptive Diagnostics

The computational engine of a diagnostic system is an adaptive performance model of the gas turbine being analyzed. The model's primary function is to normalize data so that every data point is evaluated at effectively the same flight condition, power setting, system power off-takes and bleed off-takes. This is accomplished by running the model to each input data condition and computing the difference between the model and the data.

Adaptive diagnostics requires that the model be able to adapt itself to reasonably match revenue service data. Models now have the capability of thermodynamically scaling their component maps to close with early engine revenue service data. The closer the thermodynamic match of the baseline model, the better the normalization of the data.

Data Validity

Statistical analysis is essential for evaluating the quality of the data. Rolling averages typically waste the initial data points and are slow in responding to trend changes. Several data validation improvements have been developed.

First the rolling average method is replaced by an exponential memory retention method. An exponential average equivalent of a ten point rolling average requires the storage of only the exponential average, not the ten preceding points. With each new data point 15 percent of the remembered average is replaced by new data. Therefore, the old data is forgotten 15 percent at a time, resulting in an exponential decline in its usage. In a ten point rolling average the old data is 100 percent recalled until it is 11 points old. Then it is 100 percent forgotten. The exponential equivalent of the 10 point moving average is given by the following:

Contributed by the International Gas Turbine Institute (IGTI) of THE AMERICAN SOCIETY OF MECHANICAL ENGINEERS for publication in the ASME JOURNAL OF ENGINEERING FOR GAS TURBINES AND POWER. Paper presented at the International Gas Turbine and Aeroengine Congress and Exhibition, Stockholm, Sweden, June 2–5, 1998; ASME Paper 98-GT-101.

Manuscript received by IGTI March 2, 1998; final revision received by the ASME Headquarters March 23, 1999. Associate Technical Editor: R. Kielb.

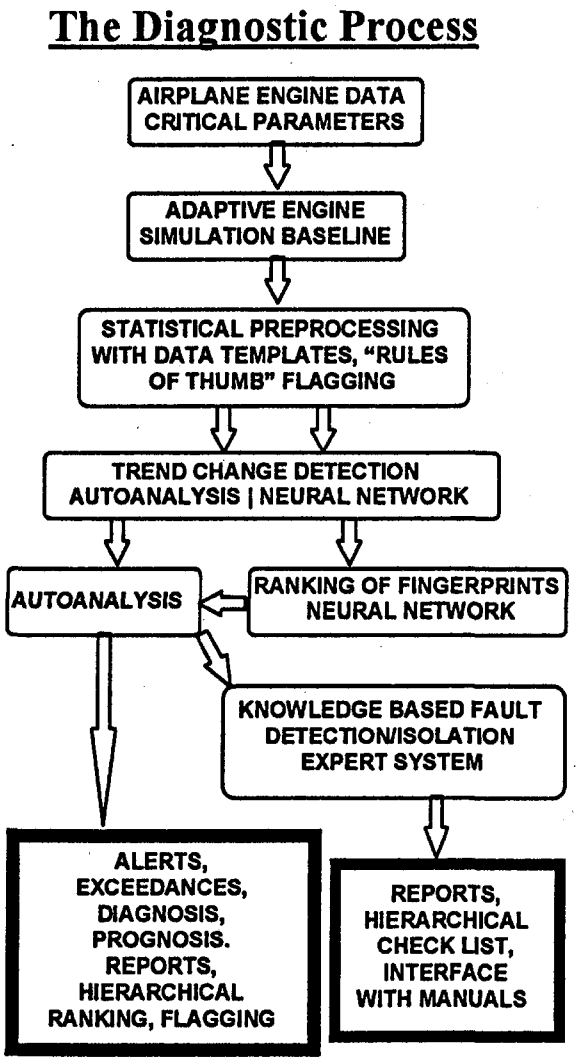

Fig. 1

$$\text{EXP\_Average}(t)_{10} = \text{Exp\_Average}(t-1)^{*}_{10}0.85 + \text{New\_Data}*0.15$$

With each new data point a fraction of the memory of the older data is replaced. This means that since only the last average is retained, the exponential averages can respond instantaneously to step changes in trends.

Figure 2 shows the response of the two methods to a 2 percent step increase with ±1.5 percent random scatter. The exponential has an equivalent or better response and definition. As soon as a trend is detected the exponential average can be incremented to show the step change.

Similarly, the exponential averaging method allows statistical bands to be carried with little overhead. That allows the statistical analysis to adapt quickly to changes in data quality. Therefore, the diagnostics automatically adapt to the data quality of each airline reducing the likelihood of false alarms. Unlike a moving average, an exponential average can be changed at the moment of the trend change detection, so the statistical bands also show the discontinuity.

If care were not taken, pure statistical analysis disregards trend changes presuming them to be bad data. Therefore, earlier diagnostic systems kept the bad data and gave the analyst a warning flag and a few rules to evaluate the data validity. A neural network (Fig. 3) is a system of computations plus logical tests that can be used to recognize patterns. The input to the network is the instantaneous average value and standard deviation of each critical parameter. The neurons apply the knowledge and experience that the analyst would normally consider. The network can act as templates to eliminate bad data much the same as analysts would with their rules of thumb.

These templates (Fig. 3) identify spurious TAT, EPR, input errors, and large instrumentation errors. The first two ANN templates identify errors that result in all four parameters being either high out of statistical limits or low out of statistical limits. The remaining four ANN templates detect single parameter limit exceedences that are not physically possible.

When five key jet engine parameters (EPR, EGT, *WF*, *N*2, *N*1) are considered, six basic templates can be defined which correct approximately 9 percent of typical data (example Fig. 4). In this typical example, 9 percent of the data caused 26 percent to 63 percent of the raw data measurement uncertainty. A separate report is generated so that the raw and corrected data are both available.

The test case selected was a recent event where a JT3D combustor crack occurred. The weightings for each of the four engine parameters entering the first two template ANN nodes were set equal to one another and then optimized. The optimum node threshold limit was found to be 1.4 sigma for four parameters. That is the equivalent of more than 2.5 sigma for a single parameter statistical test.

The weightings for the other four template nodes were individually optimized because JT3D experience showed *N*2 to be the most reliable parameter and *WF* to be the least reliable. The optimum relative weightings for this case were found to be, *N*2 (1.30), EGT (0.96), *N*1 (0.93), and *WF* (0.81).

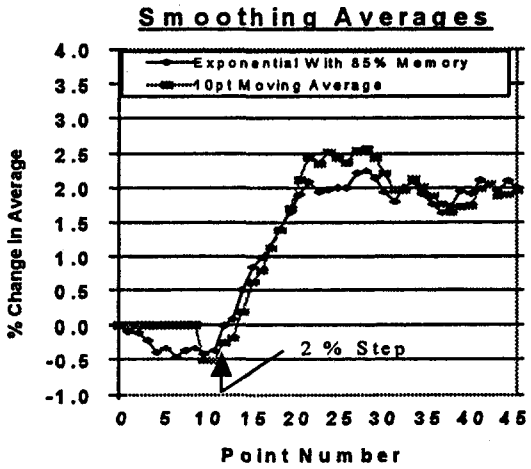

Fig. 2

Nomenclature

EPR = engine pressure ratio
EGT = cor. turbine temperature
WF = cor. engine fuel flow
*N*2 = cor. high rotor speed
N1 = cor. low rotor speed
T3 = cor. HPC exit temp
HPT = high pressure turb.
LPC = low pressure compres.
μ = exponential average
σ = standard deviation about μ
ANN = artificial neural network
B = bias applied to a neuron
W = weighting of neuron input
TAT = total air temperature
HPC = high pressure compres.
LPT = low pressure turb.
TCC = turbine case cooling

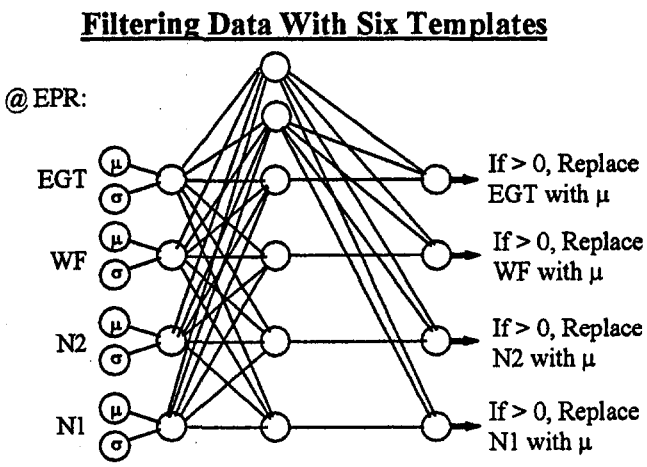

Fig. 3

Several training cases are typically used to determine the ANN weightings. However, the direct knowledge of the individual engine's current data scatter is an available and useful alternative for a diagnostic system that adapts to the data being analyzed. As processes are improved and data quality improves, the improvement is measured and the sensitivity of the diagnostic system adapts.

Over the range of the 44 points before the event, the templates reduced $N2$ scatter 49 percent (Fig. 5), EGT scatter by 34 percent, $N1$ scatter by 26 percent, and WF scatter by 63 percent. The preprocessing of the data with statistical analysis applied through ANN templates improved the data validity significantly thereby improving the accuracy of all the downstream processes.

Trend Change Detection—Neural Networks

Figure 5 shows that the current system required six data points collected over a period of six days before the sample trend change was detected and the engine was removed. $N2$ was the most reliable parameter for detecting this trend change. That is characteristic of the data acquired from JT3D and JT8D engines. EGT is the most reliable parameter for high bypass engines such as PW2000, PW4000, and JT9D engines. Having four or more parameters for detection improves the reliability of the prediction.

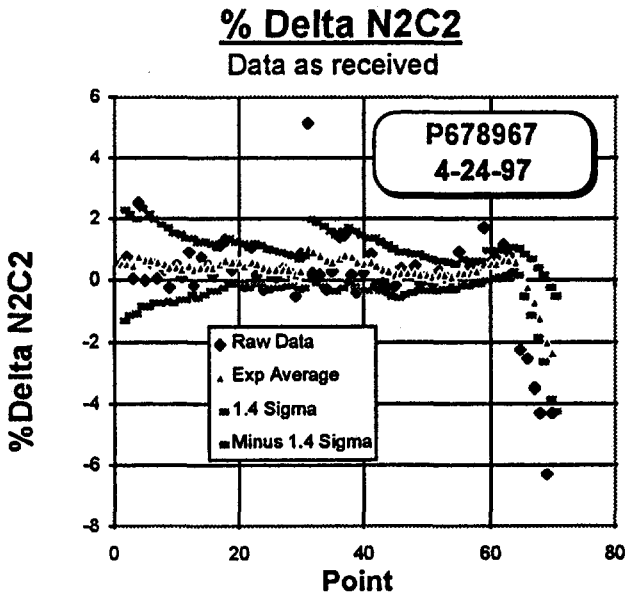

Fig. 4

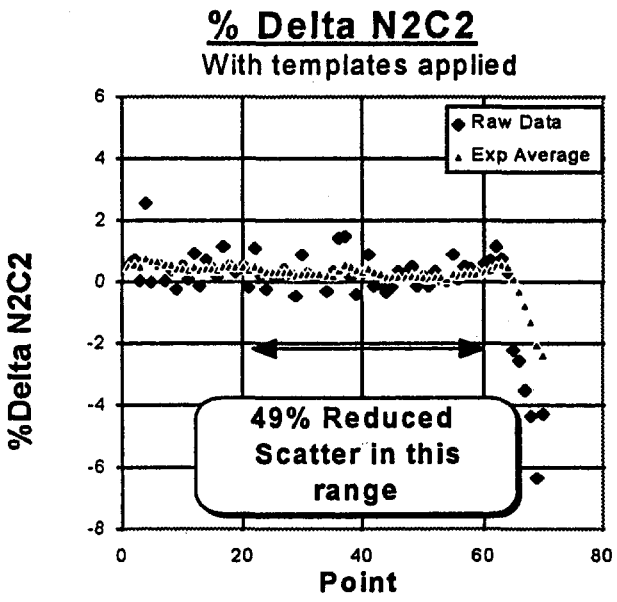

Fig. 5

Therefore the detection system can be used on all the key parameters to improve the confidence level. It is quite likely that as experience is gained with intelligent diagnostic systems, that calculated parameters such as efficiencies and flow capacities will be used for detecting trend changes. Synthesized non-dimensional parameters may also come into use.

In this example (Fig. 6) we use an ANN that evaluates three different exponential averages for corrected $N2$, the equivalents of 3 pt, 5 pt, and 10 pt moving averages.

The ANN is trained with trend changes in the positive direction and then used to process the trend twice to account for both positive and negative trend changes. A separate calculation of the magnitude is computed based on the relationships between the moving averages and the response of the detection system. The calculation is a weighted sum of the three averages trained separate from the neural network. The magnitude of the change is a criteria to filter out spurious detection. The filter is applied to inhibit trend change detection when the change detected is less than one third the data's noise level. It is very important to inhibit potential false alerts. It is preferable to miss a detection than to give a premature alert. For that reason three detection systems are used, the first to detect significant changes within two to three data points, the second to detect subtler significant changes within five or six data points, and the third to detect 1 percent or greater moves in ten data points.

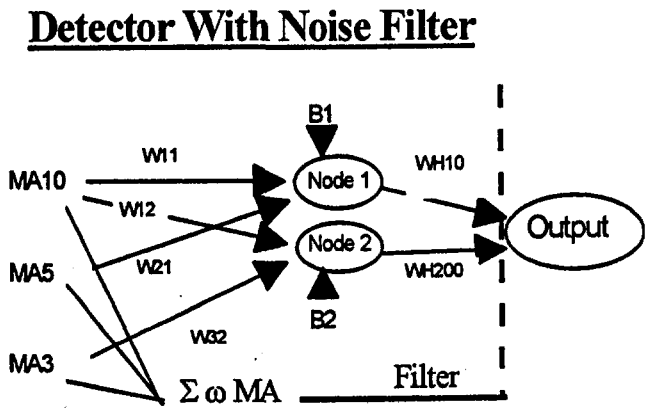

Fig. 6

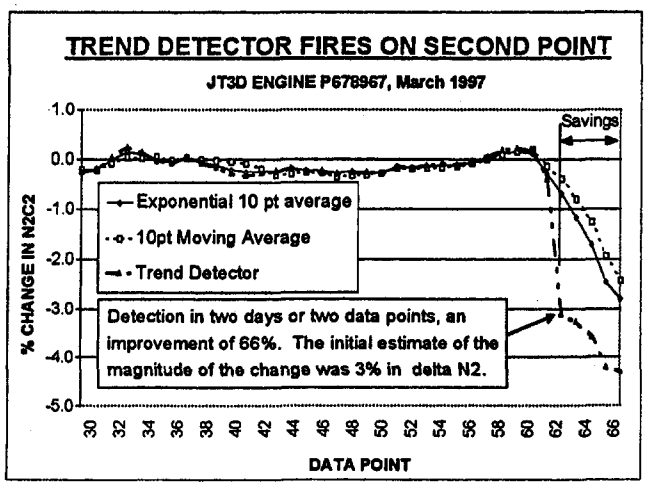

Fig. 7

Figure 7 shows the trend detection system applied to the filtered $N2$ data. A 66 percent improvement in detection time response was achieved using the ANN/filter detection system in this example. The initial estimate of the step change was −3 percent, and settled at about a 4 percent decrease in corrected $N2$.

Trend Change Detection—AutoAnalysis

AutoAnalysis is an analytical tool developed by Pratt & Whitney to assess changes in the performance of engine components. The AutoAnalysis process is an independent, parallel analytical process for detecting trend changes. For gradual changes it does a modular analysis of performance retention. It uses a Kalman filter which makes it adaptive to the quality of the data being analyzed [2].

The Kalman filter attempts to model and explain the data. When an abrupt change in performance occurs, the change is first perceived as a large sensor error. A persistent sensor error term is therefore used for trend change detection.

Trend Change Root Cause Determination—Neural Networks

The root cause of performance trend shifts needs to be determined to make recommendations for corrective action. Measurement uncertainty and the similarities of some problem symptoms does not always yield high confidence in the most probable root cause. Typically three alternative assessments are needed to encompass the true root cause. Neural networks provide easy access to other possible root causes. The computations of the output neurons of a neural network can be intercepted. That reveals the most probable alternatives and allows them to be ranked in the order of the strength of their signals.

Each neural network node represents a line that partitions the data [1]. The slope of the partitioning line is given by the ratio of the two input parameter weightings (Fig. 8). That ratio can be determined from gas generator influence coefficients. Therefore all the node weights for hidden layers in this particular network can be calculated and require no training or optimization. Each data phase space was partitioned into high ratio (>), low ratio (<), and intermediate ratio regions. Nodes based on ambivalent gas generator parameter ratios that could easily change signs were removed.

There are two design strategies for neural networks. The most common strategy is to use a symmetric matrix of neurons and train them with specific cases using an error back propagation technique. This method can provide the best fit of the data with the least number of neurons. However this method provides solutions that are for the most part incomprehensible, and non adaptive. This method can also provide the best fit of the data with the greatest number of neurons. However, again the network tends to be incomprehensible and the data over fitted.

Another strategy is to partition the problem into key elements and independently optimize those neural network sub functions. Adaptability then becomes a part of the solution. For instance, in the detection system previously discussed (Fig. 6), the neuron bias terms were made a linear function of the standard deviation of the data, and of the magnitude of the deviation of the data from the model baseline. The network was then first optimized for one signal to noise ratio, with no deviation of the data from the baseline, and with constant neuron bias terms. The neuron thresholds were then independently optimized as a variable accounting for different signal to noise ratios, different moving averages, and different deviations between the data and the baseline. It was found that as uncertainty increased, the threshold required for firing the neurons also increased. This method that applies first principles and physical insight, is easier to understand and to optimize [3].

A useful feature applied in these networks was the implementation of gains as transfer functions, so that the use of classical sigmoid functions were not necessary. The sigmoid functions are continuous functions that increase the uncertainty of the input data. The gains on the other hand are analogous to the biological neuron function and allow the output of the nodes to be variables. Therefore, if the node's input barely meets the threshold, the node's output is calculated to be less than 1.0. If the input greatly exceeds the threshold then the node output carries a percentage (typically 20 percent used) of the amount by which the input exceeded the threshold. The gain is kept small so that the network is stable.

The input parameters were normalized for the data uncertainty by dividing each input parameter by its respective standard deviation. The standard deviations were exponential averages that continuously adapted to changing data quality.

The network weights between the hidden layer and the output root causes, are independent and are trained one root cause at a time.

The symptoms or fingerprints of the root causes of the performance trend shifts have the efficiencies, flow capacities, and effective areas of the modules coupled the way the problems usually occur. That improves the effectiveness of separation of root causes such as the HPC versus HPT deterioration. During development, false positive indications are minimized by treating no-fault found (NFF) results as faults.

The focus of this paper is on diagnostics for a minimum case of four measured key engine parameters (EGT, WF, $N1$, and $N2$) at constant EPR. However, typically as many as nine parameters are monitored. $T3$ is shown to indicate how additional measured data is used in areas where they can improve the separation of root causes of performance changes. In Fig. 9, $T3$ is shown to be used to separate a 2.5 bleed from a 2.9 bleed problem, or an HPC from an HPT problem.

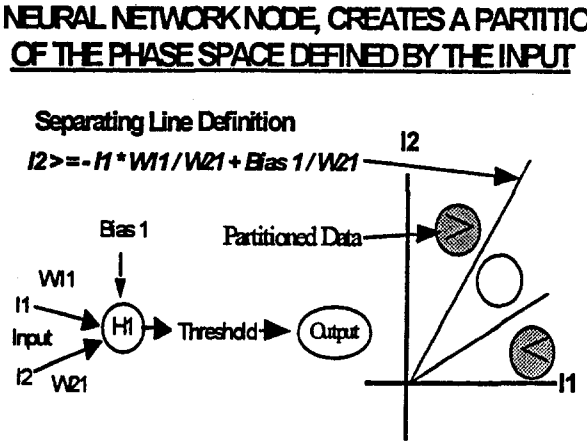

Fig. 8

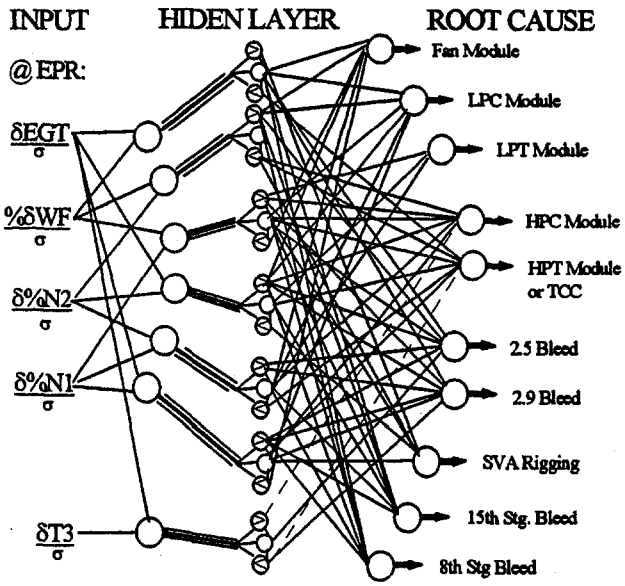

Fig. 9

In addition to engine modular changes, it is necessary to identify systematic sensor errors or changes to instrumentation. They too can trigger trend detection logic. These changes are not quickly detected by the rules of thumb data filter templates because they are repeated and are gradually accepted as significant. Systematic sensor errors can be of three types, aircraft instrumentation errors (total air temperature, Mach number, and altitude), engine instrumentation errors (all measured parameters), and changes that can result from installation of new sensors or equipment.

Systematic airplane related instrumentation changes and errors affect all engines equally. When the root cause of a trend shift is found to be the same for all the engines on the aircraft, then the aircraft instrumentation is identified as the actual root cause.

Systematic engine related instrumentation changes and errors usually affect one engine, and often only one parameter. When an engine instrumentation change or error is responsible for a trend change, the affected instrumentation shows the change and is therefore identified.

The neural network can determine the alternative root causes, but the magnitudes of the root causes are best determined using AutoAnalysis. The aerothermal diagnosis is ranked in order of probability in Table 1.

Trend Change Root Cause Determination—AutoAnalysis

AutoAnalysis includes a Kalman sensor error analysis followed by a statistical determination of the root causes. It uses the instrumentation uncertainties and an adaptive engine model to generate a matrix of influence coefficients. AutoAnalysis independently assesses the most probable root cause as well as its magnitude [4].

In addition, AutoAnalysis accepts the alternative root causes determined from the neural network, and computes the magnitudes of the alternative root causes. In Table 2, 2.3 percent high turbine distress is the most probable root cause to explain the performance loss. A 100 percent TCC failure or a 2 percent burner pressure loss are possible alternative root causes.

Table 1 Trend change detection 5-18-87, JT9D-7Q, P702143

	Probability
Boroscope HPT	74%
Check TCC system	62%
Boroscope Burner	30%

Table 2 Trend change detection 5-18-87, JT9D-7Q, P702143

	Probability	Magnitude
Boroscope HPT (%EFF/FC)	74%	2.0/15.%
Check TCC system (%TCA)	62%	100%
Boroscope Burner (%DP)	30%	2%

The AutoAnalysis assessments provide detailed modular breakouts suitable for engineering analysis. In addition, a knowledge based expert system is used to provide the flight line recommended checks and maintenance procedures.

Knowledge Based Expert System for Fault Detection and Isolation

The knowledge based expert system diagnostics provides the maintenance mechanic with "What's wrong and how to fix it," value analysis based task optimization.

The expert system integrates the aerothermal input from AutoAnalysis with onboard control status and maintenance words (codes) for additional fault detection and isolation with maintenance recommendations. It is an object oriented system [6] designed to emulate the human thought process. The control identifies faults in scheduled system switches, valves, and indicators. The root cause assessment of AUTOANALYSIS is compared and linked with the control fault analysis providing a specific check list. The reasoning is temporal in that it considers not only the facts, but the order in which the facts occur [7]. A Bayesian type statistical evidence approach is used to reflect the uncertainties in the rule based analysis.

Value analysis considers the probability that the diagnosis is correct, and the cost required to check the hardware and verify the diagnosis. An alert is issued with the recommended corrective action whenever a significant trend change occurs (Table 3).

The maintenance recommendations provide 'Answers-not-Data' type of results. The information will be available in a hand held computer for powerplant analysis or line maintenance groups. Substantial maintenance cost saving and reduced down time are predicted for the quicker, and more accurate diagnostics [5].

Symptoms of open clearances or Hot Section Distress

Maintenance word indicates TCC valves powered.
Action: Check function of valves

If valves are functional, then
Action: Check for system cracks and loose fittings

If TCC system OK, then
Action: Boroscope HPT looking for distress

If HPT system OK, then
Action: Boroscope burner looking for distress

The expert system prognostics module integrates the aerothermal input from AUTOANALYSIS with module configuration information and the fault detection maintenance information from the control.

Knowledge Based Expert System for Prognosis

The knowledge based expert system prognostics provides the quality assurance, reliability engineering, maintenance support,

Table 3 Trend change detection 5-18-87, JT9D-7Q, P702143 (for illustration only)

	Probability	Magnitude	Cost	Rank
Boroscope HPT (%EFF/FC)	74%	2.0/1.5%	$260	2
Check TCC system (%TCA)	62%	100%	$60	1
Boroscope Burner (%DP)	30%	2%	$220	3

Table 4 Workscope 5-19-87, JT9D-7Q, P702143 (for illustration only)

	Probability	Value	Cost	Rank
Replace TCC valve	100%	1.5%/15C	$1523	1
Replace 2.5 Bseal	100%	0.3%/4C	$2022	2
Waterwash engine	20%	0.5%/5C	$535	3

flight operations, and fleet management teams with projections and advice based on the expected long term behavior of the engine with the diagnosed condition.

Having isolated the cause of the fault(s), the expert system presents a prognosis. A critical fault could result in the prognosis that requires the engine immediately be removed from the wing or that the engine be grounded until a critical part is replaced.

If the isolated fault is noncritical such as a missing bleed seal or a TCC valve failure, the prognosis may (depending on other conditions) be, that the fault need only be corrected at the next scheduled maintenance, or that the aircraft can safely fly to the overhaul facility.

A fault occurring as the normal maintenance cycle approaches may result in the prognosis that the aircraft can continue to operate between city pairs in cooler climates where the engine operates at cooler internal temperatures.

Another prognosis could advise if overhaul can be postponed or if overhaul should be pulled forward.

With a prognosis for all engines in the fleet, scheduling of fleet maintenance as well as the ordering of spare parts can be planned. This information can be used for asset management to assure that spare parts are available on site on time.

Expert System for Integration of Flight and Test Cell Data Analysis

Flight data can be used with or in lieu of tested-as-received-data for workscope value analysis. The probabilities are set to 100 percent when inspections and checks verify the causes of the trend changes. In the following case the certainty of the TCC and 2.5 bleed seal involvement make them highest ranked for maintenance and repair (Table 4).

Conclusions

A modular intelligent and adaptive system is presented for gas turbine diagnostic and prognostic analysis.

The system uses adaptive intelligent diagnostics to improve data quality, detect trend changes, interpret data, furnish diagnosis of problems, provide a prognosis of future engine behavior for planning purposes, and provide corrective actions on the basis of value. Artificial intelligence is used to automate, improve the quality of the analysis, provide timely alerts, and to integrate flight data and test cell data analysis for workscope and value analysis.

A robust dual approach is taken combining the attributes of neural networks, Kalman filters, statistical analysis, Bayesian/Evidence based decision making, and rule based analysis. An expert system is used to integrate the analysis and to perform value analysis in making recommendations.

Significant improvements in accuracy, quality of analysis, timeliness and usefulness of reporting are shown.

Further development is underway to provide additional system enhancements. Diagnostics will be expanded to include vibration and oil systems to detect blade damage, schedule trim balance/lubrication, detect shifts in SVS schedule or rigging, detect bearing thrust balance changes, improve fatigue analysis, and possibly enable safe life analysis.

Other enhancements include the use of artificial intelligence and value analysis to do more of the decision making for asset management, and to predict part lives, shop visits, work scopes, and inventory requirements. Improvements are also planned for sensors, real time telemetry of data, data links, and secure Internet collaboration.

Maintenance costs can be reduced by

—early detection for prevention of collateral damage.
—reduced in flight shut downs
—reduced down time
—improved planning and asset management

References

1 Vachtsevanos, G., 1995, "Neuro-Fuzzy Tools For Modeling, Optimization, and Control of Complex Systems," Georgia Institute of Technology, Intelligent Control Laboratory, Atlanta, GA.

2 Volponi, A., 1994, "Sensor Error Compensation In Engine Performance Diagnostics," ASME Paper 94-GT-58.

3 Jaw, L., 1997, "Neural Network Modeling of Engine Tip Clearance," presented at the 33rd AIAA/ASME/SAE/ASEE Joint Propulsion Conference & Exhibit, Session 24-ASME-7 Smart Engine Technology.

4 Urban, L., and Volponi, A., 1992, "Mathematical Methods of Relative Engine Performance Diagnostics," SAE Technical Paper 922048.

5 Miller, B., 1997, "AMOSS May Stem Rising Maintenance Costs," *Overhaul & Maintenance, September–October,* Vol. 3, No. 5, McGraw-Hill Companies, New York, pp. 51–56.

6 Rumbaugh, J., 1991, "Object-Oriented Modeling and Design," Prentice-Hall Inc., Englewood Cliffs, NJ.

7 Fikes, R., and Keller, T., 1985, "The Role of Frame-Based Representation in Reasoning," *Communications of the ACM,* Vol. 28, No. 9, Sept.

Gas Turbine Parameter Corrections

A. J. Volponi
United Technologies Corporation,
Hamilton Standard,
One Hamilton Road, MS 3-2-A6,
Wondsor Locks, CT 06092

The various parameters appearing along an engine's gas path, such as flows, pressures, temperatures, speeds, etc., not only vary with power condition but also with the ambient conditions at the engine's inlet. Since a change in inlet temperature and/or pressure will contribute to an attendant change in a gas path parameter's value, it would be difficult to characterize the aero-thermodynamic relationships between gas turbine engine parameters, (even at a constant engine operating point) unless the ambient conditions are somehow accounted for. This is usually accomplished through the use of corrected engine parameters. Although most of these corrections are well known by practitioners in the industry, knowledge of their origin does not appear to be as commonplace. The purpose of this paper is to fill that gap and furnish a summary of the commonly used corrections for the "major" gas path parameters that are used in performance analysis, diagnostics, and control design, and to offer a derivation of these corrections. We will suggest both an analytic approach as well as an empirical approach. The latter can be used to establish the correction for parameters not directly addressed in this paper, as well as to fine tune the correction factors when actual engine data is available.

Historical Perspective

The use of corrected parameters to describe the performance of a gas turbine appears to be as old as the machine itself (Warner, 1945; Sanders, 1946; Shepherd, 1949). Earlier works (e.g., Capon, 1930) reference many of the same parameters as applied to more general aero-thermodynamic machines such as air compressors. These typically take the form of so-called dimensionless quantities derivable from dimensional analysis, which has been the primary technique for establishing what I will refer to as the classical parameter corrections. Since this technique is somewhat old and is not necessarily known to all, the analytic derivations that are provided in this paper will use a more general method which relies only on a knowledge of basic calculus and a handful of thermodynamic principles. Since dimensional analysis has played such an important historical role in establishing these corrections, we will describe (briefly) its principle and derive a particular correction as an illustrative example. The following description follows that given by (Buckingham, 1914).

Let us assume that we have a physical relationship to be represented by n physical quantities $Q_1, Q_2, \ldots, Q_n$. Without any loss of generality, we may write this relationship as

$$f_1(Q_1, Q_2, \ldots, Q_n) = 0. \tag{1}$$

Since physical quantities are measured in physical units (feet, seconds, lbs, degrees, etc.) or some algebraic combination of units, it can be shown that the above general relationship must have the form

$$\sum M Q_1^{b_1} Q_2^{b_2} \ldots Q_n^{b_n} = 0,$$

where M is a dimensionless number and each of the products being summed must have the same units (otherwise you could not add them together). If we divide both sides by any one term in the sum, the expression takes the form

$$\sum N Q_1^{a_1} Q_2^{a_2} \ldots Q_n^{a_n} + 1 = 0,$$

where each product in the sum is a dimensionless quantity. If we represent each of these terms by π_i, then we may rewrite this equation as

$$f_2(\pi_1, \pi_2, \ldots, \pi_n) = 0. \tag{2}$$

Loosely stated, the Buckingham π-Theorem declares that the number of dimensionless products π_i necessary for Eq. (2) to represent Eq. (1) is $n - k$, where k is the number of fundamental dimensions used to define the variables.

Applying the above principles, let us assume that we have a single spool turbojet engine having the following independent parameters (and dimensions)

Parameter		Dimension
N	spool speed (rpm)	$1/t$
T_1	ambient temperature	T
P_1	ambient pressure	$M/(Lt^2)$
v	aircraft velocity	L/t
D	compressor diameter	L
R	gas constant	$L^2/(t^2T)$

and dependent variable

Fn	Thrust	ML/t^2,

where t = time, T = temperature (degrees), M = mass, and L = length. The total number of fundamental dimensions in this case is four.

Thus, if we assume that we have a relationship of the form $Fn = f(N, T_2, P_2, v, D, R)$, which implies an implicit form $f(Fn, N, T_2, P_2, v, D, R) = 0$, involving 7 quantities. By virtue of the π-theorem, we may express the relationship in terms of $7 - 4 = 3$ dimensionless quantities as follows:

$$\varphi(\pi_1, \pi_2, \pi_3) = 0,$$

where

$$\pi_1 = N P_2^a T_2^b D^c R^d, \quad \pi_2 = v P_2^e T_2^f D^g R^h, \quad \pi_3 = F_n P_2^k T_2^m D^n R^r.$$

The π_i terms are dimensionless, and, hence, their units must be equal to $L^0 M^0 T^0 t^0$. For example,

Contributed by the International Gas Turbine Institute (IGTI) of The American Society of Mechanical Engineers for publication in the ASME Journal of Engineering for Gas Turbines and Power. Paper presented at the International Gas Turbine and Aeroengine Congress and Exhibition, Stockholm, Sweden, June 2–5, 1998; ASME Paper 98-GT-347.

Manuscript received by IGTI March 19, 1998; final revision received by the ASME Headquarters June 23, 1999. Associate Technical Editor: R. Kielb.

$$\pi_1 = \left(\frac{1}{t}\right)\left(\frac{M}{Lt^2}\right)^a T^b L^c \left(\frac{L^2}{t^2 T}\right)^d = L^0 M^0 T^0 t^0$$

$$= L^{c+2d-a} M^a T^{b-d} t^{-1-2a-2d}$$

$$\therefore$$

$$0 = a$$

$$0 = c + 2d - a$$

$$0 = b - d$$

$$0 = 1 + 2a + 2d$$

which implies

$$a = 0$$

$$b = d = -1/2$$

$$c = -1.$$

This yields a parameter of the form

$$N/(L\sqrt{RT_2}).$$

Repeating this process for the other dimensionless quantities yields the following relationship:

$$\frac{F}{P_2 A} = f_1\left(\frac{N}{D\sqrt{RT_2}}, \frac{v}{\sqrt{RT_2}}\right),$$

and if we assume a constant geometry (A = const, D = const) we obtain

$$\frac{F}{P_1} = f_2\left(\frac{N}{\sqrt{T_2}}, Mn\right) \Rightarrow \frac{F}{\delta} = f_3\left(\frac{N}{\sqrt{\theta}}, Mn\right),$$

which would imply that the appropriate corrections for net thrust and spool speed are F/δ and $N/\sqrt{\theta}$, respectively.

Introduction

In the sequel, we will assume a two shaft, mixed flow, turbofan engine with station numbers as depicted in Fig. 1 below. This reference is made for convenience only, and all corrections that are given in this paper can be applied equally to all gas turbine engines.

For any gas path parameter $\mathcal{P}$, the equivalent corrected parameter will be denoted by $\mathcal{P}^*$ throughout this discussion. In general, a change in the engine inlet conditions T_2 and P_2 will be accompanied by an attendant change in any downstream gas path parameter $\mathcal{P}$. A corrected parameter $\mathcal{P}^*$ would be constant regardless of the change in inlet condition and represents the value the parameter $\mathcal{P}$ would have at some fixed reference inlet condition. This reference condition can be whatever you like, however, it is common practice to select standard day conditions (T_2 = 518.67 deg R, P_2 = 14.696 psia) for this purpose. Thus, we can assume without loss of generality that $\mathcal{P} = f(T_2, P_2, \mathcal{P}^*)$. Thus, it follows that

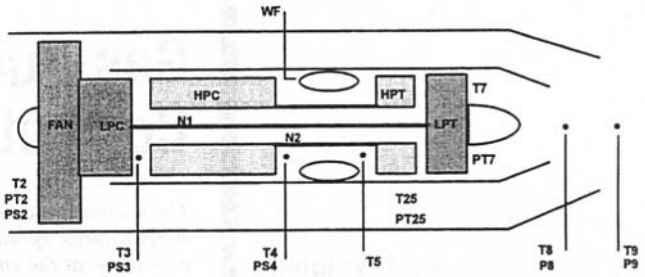

Fig. 1 Twin spool mixed flow turbofan

$$d\mathcal{P} = \left(\frac{\partial \mathcal{P}}{\partial T_2}\right) dT_2 + \left(\frac{\partial \mathcal{P}}{\partial P_2}\right) dP_2 + \left(\frac{\partial \mathcal{P}}{\partial \mathcal{P}^*}\right) d\mathcal{P}^*$$

$$\therefore$$

$$\frac{d\mathcal{P}}{\mathcal{P}} = \left(\frac{\partial \mathcal{P}/\mathcal{P}}{\partial T_2/T_2}\right)_{\substack{P_2=\text{const} \\ \mathcal{P}^*=\text{const}}} \frac{dT_2}{T_2} + \left(\frac{\partial \mathcal{P}/\mathcal{P}}{\partial P_2/P_2}\right)_{\substack{T_2=\text{const} \\ \mathcal{P}^*=\text{const}}} \times \frac{dP_2}{P_2} + \left(\frac{\partial \mathcal{P}/\mathcal{P}}{\partial \mathcal{P}^*/\mathcal{P}^*}\right)_{\substack{P_2=\text{const} \\ T_2=\text{const}}} \frac{d\mathcal{P}^*}{\mathcal{P}^*}.$$

Now if we make the simplifying assumption that the first two partials are constant (the third clearly is constant and equal to unity) and denote them by a and b, respectively, then

$$\frac{d\mathcal{P}}{\mathcal{P}} \approx a\frac{dT_2}{T_2} + b\frac{dP_2}{P_2} + \frac{d\mathcal{P}^*}{\mathcal{P}^*}.$$

If we now define, the dimensionless parameters $\theta = T_2/518.67$ and $\delta = P_2/14.696$, then we arrive at

$$\frac{d\mathcal{P}^*}{\mathcal{P}^*} \approx \frac{d\mathcal{P}}{\mathcal{P}} - a\frac{d\theta}{\theta} - b\frac{d\delta}{\delta} \Rightarrow \mathcal{P}^* \approx \frac{\mathcal{P}}{\theta^a \delta^b}. \quad (3)$$

Nomenclature

A = area
c_p = specific heat @ constant pressure (BTU/lbm°R)
c_v = specific heat @ constant volume (BTU/lbm°R)
D = diameter
Fn = net thrust (lbs)
g = acceleration constant (32 ft/sec^2)
H = heat transfer coefficient (BTU/hr ft^2°R)
HP = horsepower
h = enthalpy
I = moment of inertia
J = mechanical equivalent of heat (778 ft-lbs/BTU)
k = ratio of specific heats (c_p/c_v)
m = mass (lbm)
N = speed (rpm)
P = pressure (psia)
$\mathcal{P}$ = arbitrary gas path parameter
$\mathcal{P}^*$ = arbitrary gas path parameter corrected to standard day conditions
Q = torque
R = gas constant
S = entropy
T = temperature (degrees R)
Wa = air mass flow (lbs/sec)
Wf = fuel mass flow (lbs/sec)
θ = nondimensional temperature (ratio)
δ = nondimensional pressure (ratio)
ρ = density
κ = fluid thermal conductivity
v = fluid velocity
μ = fluid viscosity
η = adiabatic efficiency
Γ = flow capacity

Subscripts

1, 2, 3, . . . = Engine station number
s = Static quantity
t = Total quantity

Superscripts

* = Corrected quantity

Table 1 Common gas turbine parameter corrections

Parameter	a	b	Corrected Symbol
Rotor Speed	0.5	0	$N^* = \frac{N}{\sqrt{\theta}}$
Airflow	-0.5	1	$Wa^* = \frac{Wa\sqrt{\theta}}{\delta}$
Fuelflow	a (classical: 0.5)	1	$Wf^* = \frac{Wf}{\theta^a \delta} = \frac{Wf}{\sqrt{\theta}\,\delta}$
Thrust	0	1	$Fn^* = \frac{Fn}{\delta}$
HorsePower	0.5	1	$HP^* = \frac{HP}{\sqrt{\theta}\,\delta}$
Torque	0	1	$Q^* = \frac{Q}{\delta}$
Temperature	a (classical:1.0)	0	$T^* = \frac{T}{\theta^a} = \frac{T}{\theta}$
Pressure	0	1	$P^* = \frac{P}{\delta}$
Acceleration	0	1	$\dot{N}^* = \frac{\dot{N}}{\delta}$
Metal Temp Rate	0.74	0.8	$\dot{T}_m^* = \frac{\dot{T}_m}{\theta^{0.74}\delta^{0.8}}$

Thus, a corrected parameter maintains the same units and is calculated by means of theta and delta exponent corrections. We might mention at this juncture, that Eq. (3) is not only approximate for the reasons already alluded to, but, in addition, some gas path parameters such as fuel flow (Wf), for example, are also corrected for humidity and fuel heating value. The impact of changes in viscosity with altitude (Reynolds effects) or changes in the gas composition and their impact on gas path parameters will not be considered in this paper. A discussion of these types of corrections are beyond the scope of this presentation and thus, we will assume the above form (Eq. 3) for all corrected parameters $\mathcal{P}^*$.

In general, the values for a and b will vary with engine type and cycle; however, there are some values which might be considered standard classical corrections and are approximations which are commonly used in practice for all gas turbines. Table 1 depicts many of the common gas path parameters and their standard day corrections. In the sequel we will attempt to develop all of these and show the classical value as a special case, where applicable.

Derivations

In the sequel, we shall attempt to supply some rationale for these corrections. Most will be motivated from simple thermodynamic relationships and simplifying assumptions and do not require an extensive knowledge of either thermodynamics or gas turbine operation. Where applicable we will attempt to supply the required definitions.

The most extensively used and perhaps the simplest correction of all is the correction for temperatures, and is the first one which we shall consider.

Corrected Temperature: T/θ. As a general rule, it seems reasonable that engine inlet temperature (T_2) should have a direct effect on downstream temperatures in the engine's gas path. It seems natural, for example, that at a given operating condition, increasing T_2 would in turn increase T_3, which in turn would increase T_4, etc. To motivate this concept, we need to consider the T-S diagram. To be definite, let us consider the compression induced by the Fan and LPC from station 2 to station 3 of our sample engine in Fig. 1. Without loss of generality, an isentropic compression has been assumed. Figure 2 depicts a compression from P_2 to P_3 starting at different temperatures (T_2 and T_2^*).

At this point we will note two properties of the T-S diagram which we will state without proof. (The reader can derive these for him/herself, armed only with the elementary laws of thermodynamics.) The relationships are

1 the curves of constant pressure are monotonically increasing with S
2 the constant pressure curves diverge from one another with increasing S

These properties suggest that the * quantities are larger in magnitude than their nonstarred counterparts and that $(T_3 - T_2) < (T_3^* - T_2^*)$. What we will now show, however, is that the ratio of T_3 over T_2 is approximately equal to T_3^* over T_2^*!

To accomplish this we need one more relationship from basic thermodynamics (which follows from the definition of entropy and the perfect gas law).

$$dS = \frac{dh}{T} - R\frac{dP}{P},$$

where S, h, T, P, and R denote entropy, enthalpy, temperature, pressure and the gas constant, respectively. Integrating this relationship between states 2 and 3 and assuming constant specific heat, yields,

$$0 = \int_2^3 dS = \int_2^3 \frac{dh}{T} - R\int_2^3 \frac{dP}{P} = c_p \int_2^3 \frac{dT}{T} - R\int_2^3 \frac{dP}{P}$$

$$= c_p \ln\left(\frac{T_3}{T_2}\right) - R\ln\left(\frac{P_3}{P_2}\right)$$

$$\Rightarrow$$

$$\frac{T_3}{T_2} = \left(\frac{P_3}{P_2}\right)^{R/c_p}.$$

Likewise, integrating between 2* and 3* with the same assumption on specific heats, provides

$$\frac{T_3^*}{T_2^*} = \left(\frac{P_3}{P_2}\right)^{R/c_p}$$

$$= \frac{T_3}{T_2}$$

$$\Rightarrow$$

$$T_3^* = \frac{T_3}{(T_2/T_2^*)} = \frac{T_3}{\theta}$$

as required.

Corrected Pressure: P/δ. The pressure changes experienced at various stations throughout the engine's gas-path are the effect of either compressions or expansions resulting from the action of the engine's turbomachinery. For purposes of motivating the cor-

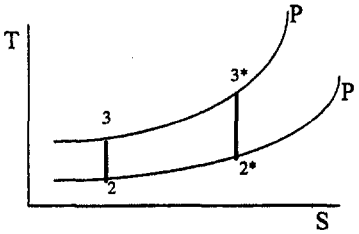

Fig. 2 Compression T-S diagram

rection for pressure, we can consider without loss of generality, a compression process; the argument for expansion pressures would be similar.

Let us consider, for example, the pressure P_3 at the exit of the LPC. This pressure is related to temperature and pressure by virtue of the following relationship:

$$\frac{T_3}{T_2} = \left(\frac{P_3}{P_2}\right)^{(k-1)/k\eta}$$

where η = polytropic efficiency, and $k = c_p/c_v$ = ratio of specific heats.

Thus, since T_3/θ = constant implies T_3/T_2 = constant, we have that P_3/P_2 = constant, which in turn implies that P_3/δ = constant, which establishes the correction at station 3. Implicit in this argument is that the ratio of specific heats k and efficiency η do not change. Moving downstream to station 4 we have that

$$\frac{P_4}{P_3} = \left(\frac{T_4}{T_3}\right)^{k\eta/(k-1)} = \left(\frac{T_4/\theta}{T_3/\theta}\right)^{k\eta/(k-1)} = \text{const.}$$

$$\therefore$$

$$\frac{P_4}{\delta} = \frac{P_4}{P_3}\frac{P_3}{\delta} = \text{const}$$

Thus, we proceed downstream and establish in general that P/δ = constant = P^*.

Corrected Mass Flow: $W_a\sqrt{\theta}/\delta$. Consider flow W_a (in pps) moving with uniform velocity v through a pipe having cross sectional area A (ft^2). Then,

$$W_a = \rho A v = \text{density (lbs/ft}^3) \times \text{area (ft}^2) \times \text{velocity (ft/sec)}.$$

For an ideal gas, we also know that $P_s = \rho RT$, from which it follows that

$$\frac{W_a}{A} = \rho v = \frac{P_s}{RT_s} v$$

and from the definition of mach number M_n,

$$M_n = v/\sqrt{gkRT_s},$$

we obtain the relationship

$$\frac{W_a}{A} = \frac{P_s M_n \sqrt{gkRT_s}}{RT_s} \Rightarrow \frac{W_a\sqrt{T_t}}{AP_t} = \left(\frac{P_s}{P_t}\right)\sqrt{\frac{T_t}{T_s}} M_n \sqrt{\frac{gk}{R}}.$$

We know, however, that for an isentropic process

$$\frac{T_t}{T_s} = 1 + \frac{k-1}{2} M_n^2 \quad \text{and} \quad \frac{P_t}{P_s} = \left(1 + \frac{k-1}{2} M_n^2\right)^{k/(k-1)}.$$

Substituting, we obtain

$$\frac{W_a\sqrt{T_t}}{AP_t} = \sqrt{\frac{gk}{R}} M_n \left(1 + \frac{k-1}{2} M_n^2\right)^{(k+1)/(2(1-k))},$$

and multiplying both sides by $(\theta/T_t)^{1/2}/(\delta/P_t)$ to get the proper units (pps) yields

$$\frac{W_a\sqrt{\theta}}{\delta} = \frac{A}{P_t/\delta}\sqrt{\frac{gk(T_t/\theta)}{R}} M_n \left(1 + \frac{k-1}{2} M_n^2\right)^{(k+1)/(2(1-k))}$$

$$= \text{constant}$$

for M_n = const., thus providing a corrected quantity.[1]

[1] T/θ and P/δ are corrected parameters and, hence, constant by virtue of the previous derivations.

Corrected Fuel Flow: $W_F/\delta\sqrt{\theta}$. Consider the (simplified) energy equation bounding the combustor

$$\frac{BTU}{\text{sec}} = \eta_b q W_F = (W_a + W_F)\Delta h = (W_a + W_F)(h_5 - h_4),$$

where h denotes enthalpy, q denotes the heating value of the fuel, and η denotes the adiabatic efficiency of the combustor. If we assume that (at a given operating point) efficiency and fuel heating value are constant, then if we take logs of both sides and differentiate, we obtain

$$\frac{dW_F}{W_F} = \frac{d(W_a + W_F)}{(W_a + W_F)} + \frac{d(\Delta h)}{\Delta h}$$

$$= \left(\frac{W_a}{(W_a + W_F)}\right)\frac{dW_a}{W_a} + \left(\frac{W_F}{(W_a + W_F)}\right)\frac{dW_F}{W_F} + \left(\frac{c_{p5}T_5}{\Delta h}\right)\frac{dT_5}{T_5} - \left(\frac{c_{p4}T_4}{\Delta h}\right)\frac{dT_4}{T_4},$$

and a little algebraic manipulation gives

$$\left(\frac{W_a}{W_a + W_F}\right)\frac{dW_F}{W_F} = \left(\frac{W_a}{(W_a + W_F)}\right)\frac{dW_a}{W_a} + \left(\frac{c_{p5}T_5}{\Delta h}\right)\frac{dT_5}{T_5} - \left(\frac{c_{p4}T_4}{\Delta h}\right)\frac{dT_4}{T_4}.$$

Now, at a given operating point, we can assume that the following relationships hold:

$$\frac{W_a\sqrt{\theta}}{\delta} = \text{const} \Rightarrow \frac{dW_a}{W_a} + \frac{1}{2}\frac{dT_4}{T_4} - \frac{dP_4}{P_4} = 0$$

$$\frac{T_4}{\theta} \quad \text{and} \quad \frac{T_5}{\theta} = \text{const} \Rightarrow \frac{dT_4}{T_4} = \frac{dT_2}{T_2} = \frac{dT_5}{T_5}$$

$$\frac{P_4}{\delta} = \text{const} \Rightarrow \frac{dP_4}{P_4} = \frac{dP_2}{P_2}.$$

Thus,

$$\frac{dW_F}{W_F} = \frac{dP_2}{P_2} - \frac{1}{2}\frac{dT_2}{T_2} + \left(\frac{W_a + W_F}{W_a}\frac{c_{p5}T_5}{\Delta h}\right)\frac{dT_2}{T_2} - \left(\frac{W_a + W_F}{W_a}\frac{c_{p4}T_4}{\Delta h}\right)\frac{dT_2}{T_2}$$

$$= \frac{dP_2}{P_2} + \underbrace{\left[\left(1 + \frac{W_F}{W_a}\right)\left(\frac{c_{p5}T_5}{\Delta h} - \frac{c_{p4}T_4}{\Delta h}\right) - \frac{1}{2}\right]}_{x}\frac{dT_2}{T_2}$$

$$= \frac{dP_2}{P_2} + x\frac{dT_2}{T_2}$$

$$\Rightarrow \frac{W_F}{\delta\theta^x} = \text{const.} \tag{5}$$

Furthermore, if we make the assumption that specific heats are constant, i.e., $c_{p4} = c_{p5}$ then the exponent x reduces to $\frac{1}{2}$ + Fuel-Air Ratio = (*approximately*) $\frac{1}{2}$ and we obtain the classical normalization

$$W_F^* \approx \frac{W_F}{\delta\sqrt{\theta}}.$$

Corrected Net Thrust: F_n/δ. Expressions for the net thrust produced by a gas turbine engine will depend upon the configuration of the engine, i.e., whether it is a turbojet or a turbofan, mixed flow or nonmixed flow, as well as an expression for ram drag as a function of mach number. To keep the derivation as

simple as possible, we will assume a static thrust expression, i.e., mach = 0, no ram drag and, we will once again refer to our sample engine configuration which is that of a mixed flow turbofan. It should be noted that derivation that follows can be repeated (in spirit) with more complicated expressions for net thrust for other engine types and flight conditions to arrive at similar representations for corrected thrust.

The thrust produced by this engine depends on the momentum of the air ejected from the exhaust nozzle as well as the net force (due to pressure) acting across the total area of the nozzle. In symbols,

$$F_n = \frac{W_9}{g} v_9 + A_9(P_9 - P_{s9}),$$

where

$W_9 = W_8$ = total airflow at nozzle
A_9 = nozzle area
P_9 = nozzle exit total pressure
$P_{s9} = P_2$ = nozzle exit static pressure (ambient)
$v_9 = \sqrt{2gJ(h_9 - h_{s9})}$ = velocity at exhaust nozzle
h_9 = total (stagnation) enthalpy at exit
h_{s9} = static enthalpy at exit
J = mechanical equivalent of heat (778 ft-lbs/BTU).

The expression for the exit velocity follows directly from the definition of stagnation (total) enthalpy. Similarly, there is an expression for the velocity at station 8 (mixer) involving total and static enthalpies at station 8. The flow from station 8 to 9 (through a nozzle) we will assume to be adiabatic, i.e., no work done, no heat added. By conservation of energy, the total enthalpies are equal ($h_8 = h_9$). If we denote the change in enthalpy $(h_9 - h_{s9}) = (h_8 - h_{s9}) = \Delta h$, then we may rewrite the above expression for thrust as

$$F_n = \frac{W_8}{g} \sqrt{2gJ\Delta h} + A_9(P_9 - P_{s9}).$$

Taking logs of both sides and differentiating produces

$$\frac{dF_n}{F_n} = \frac{(W_8/g)\sqrt{2gJ\Delta h}}{F_n}\left[\frac{dW_8}{W_8} + \frac{1}{2}\frac{d\Delta h}{\Delta h}\right] + \frac{A_9(P_9 - P_{s9})}{F_n}\left[\frac{dA_9}{A_9} + \left(\frac{P_9}{P_9 - P_2}\right)\frac{dP_9}{P_9} - \left(\frac{P_2}{P_9 - P_2}\right)\frac{dP_2}{P_2}\right]$$

$$= \frac{(W_8/g)\sqrt{2gJ\Delta h}}{F_n}\left[\frac{dW_8}{W_8} + \left(\frac{h_8}{2\Delta h}\right)\frac{dh_8}{h_8} - \left(\frac{h_{s9}}{2\Delta h}\right)\frac{dh_{s9}}{h_{s9}}\right] + \frac{A_9(P_9 - P_{s9})}{F_n}\left[\underbrace{\frac{dA_9}{A_9}}_{\text{zero (fixed geometry)}} + \left(\frac{P_9}{P_9 - P_2}\right)\frac{dP_9}{P_9} - \left(\frac{P_2}{P_9 - P_2}\right)\frac{dP_2}{P_2}\right]$$

$$= \frac{(W_8/g)\sqrt{2gJ\Delta h}}{F_n}\left[\frac{dW_8}{W_8} + \left(\frac{c_{p8}T_8}{2\Delta h}\right)\frac{dT_8}{T_8} - \left(\frac{c_{p9}T_{s9}}{2\Delta h}\right)\frac{dT_{s9}}{T_{s9}}\right] + \frac{A_9(P_9 - P_{s9})}{F_n}\left[\left(\frac{P_9}{P_9 - P_2}\right)\frac{dP_9}{P_9} - \left(\frac{P_2}{P_9 - P_2}\right)\frac{dP_2}{P_2}\right].$$

Now, at a given engine operating point (steady state), the following conditions hold:

$$\frac{W_8\sqrt{\theta_8}}{\delta_8} = \text{constant} \Rightarrow \frac{dW_8}{W_8} + \frac{1}{2}\frac{dT_8}{T_8} - \frac{dP_8}{P_8} = 0$$

$$\frac{T_8}{\theta_2} = \text{constant} \Rightarrow \frac{dT_8}{T_8} - \frac{dT_2}{T_2} = 0$$

$$\frac{T_{s9}}{\theta_2} = \text{constant} \Rightarrow \frac{dT_{s9}}{T_{s9}} - \frac{dT_2}{T_2} = 0$$

$$\frac{P_8}{\delta_2} = \text{constant} \Rightarrow \frac{dP_8}{P_8} - \frac{dP_2}{P_2} = 0$$

$$\frac{P_9}{\delta_2} = \text{constant} \Rightarrow \frac{dP_9}{P_9} - \frac{dP_2}{P_2} = 0.$$

Substituting, we obtain

$$\frac{dF_n}{F_n} = \frac{(W_8/g)\sqrt{2gJ\Delta h}}{F_n} \times \left[\frac{dP_8}{P_8} + \underbrace{\left(\frac{c_{p8}T_8}{2\Delta h} - \frac{c_{p9}T_{s9}}{2\Delta h} - \frac{c_{p9}T_{s9}}{2\Delta h} - \frac{1}{2}\right)}_{x}\frac{dT_2}{T_2}\right] + \frac{A_9(P_9 - P_{s9})}{F_n}\frac{dP_2}{P_2}$$

$$= \underbrace{\frac{(W_8/g)\sqrt{2gJ\Delta h}}{F_n}}_{y_1}\left[\frac{dP_8}{P_8} + x\frac{dT_2}{T_2}\right] + \underbrace{\frac{A_9(P_9 - P_{s9})}{F_n}}_{y_2}\frac{dP_2}{P_2}$$

$$= (y_1 + y_2)\frac{dP_2}{P_2} + y_1 x\frac{dT_2}{T_2} = \frac{dP_2}{P_2} + y_1 x\frac{dT_2}{T_2}$$

$$\Rightarrow \frac{F_n}{\delta_2\theta_2^{y_1 x}} = \text{constant}.$$

Since the specific heats at station 8 and 9 are approximately equal (since $T_8 \approx T_{9s}$), we may assume a common specific heat c_p. In this case, the theta exponent x reduces to 0 (since $\Delta h = c_p\Delta T$). Thus, we arrive at the classical correction for thrust, namely

$$F_n^* = \frac{F_n}{\delta_2}.$$

Corrected Horsepower: $HP/\delta\sqrt{\theta}$. Horsepower required (or developed) by a compressor (or turbine) is given by

$$HP = \frac{J}{550} W_a c_p \Delta h \approx \frac{J}{550} W_a c_p \Delta T \quad \text{where}$$

$J = 778.17$ ft lb/BTU.

A corrected horsepower will not vary with inlet temperature and pressure, and, thus, can be written as above with corrected flow and temperature, i.e.,

$$HP^* = \frac{J}{550} W_a^* c_p \Delta h^* \approx \frac{J}{550} W_a^* c_p \Delta T^*$$

$$= \frac{J}{550}\frac{W_a\sqrt{\theta}}{\delta} c_p \frac{\Delta T}{\theta}$$

$$= \frac{\frac{J}{550} W_a c_p \Delta T}{\delta\sqrt{\theta}}$$

$$= \frac{HP}{\delta\sqrt{\theta}}.$$

Corrected Rotational Speeds: $N/\sqrt{\theta}$. Tangential velocity is related to rotational speed (rpm) by the radius of the object (compressor or turbine blade) in question. It is also related to acoustic velocity by Mach number and the square root of temperature.

Mathematically, we have

$$v = rN = M_n\sqrt{gkRT},$$

where v is the velocity in ft/s, r is the radius (ft), N is the rotational speed (rpm), g, k, and R are constants (gravity, ratio of specific heats and the gas constant respectively), and M_n is Mach number. Taking logs and differentiating, we obtain

$$\frac{dN}{N} = \frac{dM_n}{M_n} + \frac{1}{2}\frac{dT}{T} = \frac{1}{2}\frac{dT}{T} \quad \text{since Mach} = \text{constant}$$

$$\Rightarrow \frac{dN}{N} - \frac{1}{2}\frac{d\theta}{\theta} = 0$$

$$\Rightarrow \frac{N}{\sqrt{\theta}} = \text{constant}.$$

Corrected Torque: Q/δ. The correction for torque follows from corrections for speed and horsepower, since horesepower is the product of torque and speed. It follows that a corrected horsepower should be a product of corrected torque and corrected speed, i.e.,

$$HP^* = Q^*N^*$$

$$= \frac{HP}{\delta\sqrt{\theta}} = Q^*\frac{N}{\sqrt{\theta}}$$

$$\Rightarrow$$

$$Q^* = \frac{HP}{N\delta} = \frac{Q}{\delta}.$$

Corrected Acceleration Ndot: $\dot{N}/\delta$. From Newton's law, torque (force) = moment of inertia (I) × acceleration:

$$Q = I\dot{N}$$

$$\therefore \quad Q^* = I\dot{N}^* \Rightarrow \frac{Q}{\delta} = I\dot{N}^*$$

$$= I\frac{\dot{N}}{\delta}$$

$$\Rightarrow \dot{N}^* = \dot{N}/\delta$$

Corrected Metal Temperature Rate $T_m dot$: $(\dot{T}_m/\theta^{.74}\delta^{.8})$. The (time) rate of change of a metal temperature is typically modeled as a 1st order lag heat transfer between the gas path temperature T and the metal temperature T_m. In symbols,

$$\dot{T}_m = \frac{1}{\tau}(T - T_m), \tag{3}$$

where time constant $\tau = (mc_p/HA)$.

The McAdams correlation for turbulent flow over a flat plate (Shepherd, p. 254) is given by

$$\text{Nu} = 0.023(\text{Re})^{0.8}(\text{Pr})^{0.4},$$

where Nu, Re, and Pr are the Nusselt's, Reynold's, and Prandtl's numbers, respectively, which are defined as follows:

$$\text{Nu} = \frac{HD}{\kappa}, \quad \text{Re} = \frac{\rho vD}{\mu}, \quad \text{Pr} = \frac{c_p\mu}{\kappa}.$$

Substituting and re-arranging terms we can obtain the following form:

$$H = 0.023\frac{\kappa}{D}\left(\frac{\rho vD}{\mu}\right)^{0.8}\left(\frac{c_p\mu}{\kappa}\right)^{0.4}$$

$$= 0.023\frac{\kappa^{0.6}c_p^{0.4}}{D^{0.2}}\frac{\rho^{0.8}v^{0.8}}{\mu^{0.4}}$$

$$= \left(\frac{0.023\kappa^{0.6}}{c_p^{0.6}\mu^{0.6}}\right)\frac{c_p\mu^{0.2}\rho^{0.8}v^{0.8}}{D^{0.2}}$$

$$= \left(\frac{0.023}{\text{Pr}^{0.6}}\right)\frac{c_p\mu^{0.2}\rho^{0.8}v^{0.8}}{D^{0.2}}$$

$$\approx 0.027\frac{c_p\mu^{0.2}\rho^{0.8}v^{0.8}}{D^{0.2}}, \tag{4}$$

where the final approximation is obtained by noting that Prandtl's number is approximately constant in the range of interest (Shepherd, p. 254). At this juncture we may recall that mass flow $W_a = \rho A v$ was corrected by square root of theta over delta. Combining these observations, we have

$$\frac{W_a}{A} = \frac{W_a^*\delta}{\sqrt{\theta}} = \rho v.$$

Therefore,

$$(\rho v)^{0.8} = (W_a^*)^{0.8}\delta^{0.8}\theta^{-0.4}.$$

Using the approximation at the end of Eqs. (4) to define the reference condition H^* and noting that $D = D^*$, we can write the ratio

$$\frac{H^*}{H} = \left(\frac{c_p^*}{c_p}\right)\left(\frac{\mu^*}{\mu}\right)^{0.2}\left(\frac{\rho^* v^*}{\rho v}\right)^{0.8}$$

$$= \left(\frac{c_p^*}{c_p}\right)\left(\frac{1}{\theta^n}\right)^{0.2}\left(\frac{\sqrt{\theta}}{\delta}\right)^{0.8}$$

$$= \left(\frac{c_p^*}{c_p}\right)\theta^{0.4-0.2n}\delta^{-0.8},$$

where we have assumed that the ratio μ^*/μ is solely a function of temperature (θ). Now using Eq. (3) to define $\dot{T}_m^*$ in a similar manner, we can form the appropriate ratio and use the above relationship to simplify the expression.

$$\frac{\dot{T}_m^*}{\dot{T}_m} = \left(\frac{H^*}{H}\right)\left(\frac{c_p}{c_p^*}\right)\frac{T^* - T_m^*}{T - T_m}$$

$$= \theta^{0.4-0.2n}\delta^{-0.8}\frac{\left(\frac{T}{\theta}\right) - \left(\frac{T_m}{\theta}\right)}{T - T_m}$$

$$= \theta^{-0.6-0.2n}\delta^{-0.8}$$

$$\Rightarrow$$

$$\dot{T}_m^* = \frac{\dot{T}_m}{\theta^{0.6+0.2n}\delta^{0.8}}.$$

The value of n appearing in the theta exponent can be determined experimentally by correlating viscosity with temperature from which it is observed that n varies from 0.8 at low temperature to 0.6 at high temperature. These values provide a theta exponent ranging from 0.76 to 0.72, respectively. The average value of 0.74 is recommended, thus providing the requisite correction.

$$\dot{T}_m^* = \frac{\dot{T}_m}{\theta^{0.74}\delta^{0.8}}.$$

Determining Correction Factors

The methods for obtaining appropriate corrections for gas path parameters depends in part on the application at hand as well as the amount and type of information (data) available. These methods can be split into essentially the following two groups: (1) analyt-

Table 2 Nonlinear engine simulation data

Parameter		Station 4	Station 5	Units
k		1.39801	1.30214	ft-lb/deg R
h		300.297	657.18	BTU
T		1235.18	2436.52	deg R
W_a		23.2613	23.7252	pps
Wf	0.4639			pps
Δh	356.883			
Wf/W_a	0.019943			
cp		0.24081	0.29542	
$cp\,T/\Delta h$		0.83346	2.01690	
$1+Wf/W_a$	1.019943			
Exponent	0.707			

ical and (2) empirical. In practice, it is more than likely that a combination of both types of techniques will be utilized. We will briefly illustrate both of these approaches.

Analytical Methods. As a practical application of how to utilize some of the above information to determine a theta correction for Wf in a turbo-fan engine from engine simulation information, consider the information contained in Table 2. This data was obtained from a nonlinear aero-thermodynamic representation of a small turbofan engine. In order to avoid introducing new station numbers, we will use the corresponding station numbers of our sample engine in Fig. 1. The thermodynamic deck provides the following information at station 4 (HPC exit) and station 5 (HPT inlet) at one engine operating point.

Applying these values to the Wf, Eq. (5) yields a value of 0.707 for the theta exponent "x". The actual value used for this engine is 0.69. Presumably, the above calculation would yield slightly different results at differing engine operating points, the average of which is probably around 0.69.

This type of analytic approach could be made by applying some of the intermediate equations used in the derivations for various gas path parameters in much the same way as in the above example. Another analytic method would be to construct a complete differential model of the engine (Volponi and Urban, 1992). Models of this type provide sensitivities to percentage changes in independent parameters (T_2 is one such) to corresponding percentage changes in dependent engine parameters (such as Wf, for example). The difference between this and what was done in the derivation of the Wf correction, is that the latter would be one of many differential equations (usually around 40) that would relate all the independent and dependent parameters at various engine stations interrelated through the laws of thermodynamics, energy, and flow conservation. The simultaneous solution of these 40 equations would produce (for example) a sensitivity of T_2 on spool speeds (N), fuel flow (Wf), temperatures at various stations, etc. These sensitivities give an indication of the (theta) correction to be applied.

An example of such an approach is illustrated in the sensitivity matrix in Table 3 below.

The sensitivities of engine inlet temperature and pressure are given in the last two columns for all of the dependent parameters listed in the 1st column. For example, the dependent parameter N1C2 which is corrected low spool speed has a sensitivity of -0.0105 with Tam. This means that the following is true:

$$\frac{dN1c2}{N1c2} = \frac{dN1}{N1} - \frac{1}{2}\frac{dT2}{T2} = -0.0105\,\frac{dT2}{T2} \Rightarrow$$

$$\frac{dN1}{N1} - 0.4895\,\frac{dT2}{T2} = 0,$$

which implies that the correction for $N1$ is $N1/\theta^{.4895}$ instead of $N1/\theta^{0.5}$. Likewise, the correction for $N2$ is .4833 instead of square root. Now if we choose some raw parameters such as $T3$, $T4$, and $T7$, we see that the suggested theta exponents are 0.9816, 0.9291, and 0.9746, respectively, and not 1.0 as the classical correction would dictate. Fuel flow is demanding an exponent of 0.6014, instead of 0.5. All of these theta exponents derivable from a differential model will provide a correction that is closer to the truth than the classical (providing the model is reasonably correct) and can be used as a good first guess for the correction to be used. The fidelity of these corrections will of course depend on the fidelity of the underlying differential model. For general analysis, classical corrections often suffice. Several parameters may require a finer correction. Wf is typically one of those parameters and it is not uncommon to see theta exponents ranging from 0.5 to 0.7 for this parameter. Such a refinement is required for work demanding greater accuracies, such as diagnostics, and for these purposes it is customary to use corrections such as those given in the sensitivity matrix above, and when actual engine data becomes available, to adjust these first guesses empirically. This leads us to our next topic.

Empirical Methods. Empirical methods utilize actual engine data collected over a temperature range and comprise more of a statistical approach to the subject of parameter normalization and as such, do not require any in-depth knowledge of gas turbines or their operation. It has become a generally accepted practice among engine performance diagnosticians to perform some sort of empirical analysis to verify the validity of the correction factors being used. Neglecting to do so exposes the diagnostic procedure to greater error which may render the diagnostics entirely useless.

There are many techniques that can be put forward to analyze engine data for normalization purposes, however, we will restrict our discussion to a simple formula (derived by this author, circa 1980), suggest several alternative approaches, and finally offer some Monte Carlo simulation results that suggest that all of the above produce roughly the same result.

For simplicity, we will consider only temperature (θ) corrections; pressure (δ) corrections can be handled in an analogous manner. Let $P^* = P/\theta^x$, where x denotes the true (sought)

Table 3 Sensitivity matrix

	TAM	PAM
N1C2	-0.0105	0.0077
N2C2	-0.0167	0.0021
WF	0.6014	0.9933
FN	0.0123	1.0035
P3/P2	-0.0119	0.007
P4/P3	-0.014	-0.003
P7/P2	0	0
T3	0.9816	0.0037
T4	0.9291	0.0025
T5	0.9265	-0.005
T6	0.9542	-0.005
T7	0.9746	-0.006
P3	-0.0119	1.007
P4	-0.0259	1.0037
P5	-0.0224	1.0031
P6	-0.0073	1.0024
WA	-0.5076	1.0056
T2	1	0
P2	0	1

exponent and let α be a theta exponent used to normalize a set of data $\{P_i\}_{i=1,\ldots,n}$. Let us further assume that each datum P_i (for all i) was obtained at an inlet condition represented by θ_i and that we have available, the nominal value of this parameter for the engine operating condition(s) at which the parameters P_i were obtained. Let us denote this uncorrected nominal value by P_{NOM}. Then

$$\frac{P_i}{\theta^{\alpha}} = \frac{P_{\text{NOM}}}{\theta^{x}}\left(1 + \frac{\Delta G_i}{100}\right),$$

where ΔG_i represents the percentage of point delta from nominal (for all i). Now if we plot these deltas against θ, then if α were the true correction exponent, we would expect to see a scatter plot that would have zero correlation, i.e., a linear regression line fit horizontal with the theta axis. An upward or downward trend, however, would indicate the extent to which the exponent α was deficient. If we let m and b, denote the regression slope and intercept, respectively, then we have a defined linear relationship as follows:

$$\Delta G = m\theta + b \quad \text{where} \quad b = \Delta\bar{G} - m\bar{\theta}$$

$$= \frac{1}{n}\sum_{i=1}^{n}\Delta G_i - m\left[\frac{1}{n}\sum_{i=1}^{n}\theta_i\right]$$

and

$$m = r\frac{s_{\Delta G}}{s_{\theta}},$$

where r is the correlation coefficient and $s_{\Delta G}$ and s_{θ} are the sample standard deviations for ΔG and θ, respectively. Thus, for arbitrary θ, we have

$$\frac{P}{P_{\text{NOM}}}\theta^{x-\alpha} \approx 1 + \frac{m\theta + b}{100} \Rightarrow \frac{P}{P_{\text{NOM}}} \approx 1 + \frac{m + b}{100} \quad (\theta = 1)$$

and

$$\frac{P}{P_{\text{NOM}}}\bar{\theta}^{x-\alpha} \approx 1 + \frac{m\bar{\theta} + b}{100} \quad (\theta = \bar{\theta});$$

therefore,

$$\bar{\theta}^{x-\alpha} \approx \left[1 + \frac{m\bar{\theta} + b}{100}\right] \Big/ \left[1 + \frac{m + b}{100}\right].$$

Taking natural logs of both sides and applying the relationship that $\ln(1 + x) \approx x$ for small x, we obtain an expression for the new exponent in terms of the old exponent, namely,

$$x \approx \alpha + \frac{m(\bar{\theta} - 1)}{100 \ln(\bar{\theta})}. \tag{6}$$

We see from this equation, that if the slope of the regression line is positive, then the exponent will be raised. Likewise, it will be lowered when the slope is negative. If the data sample was such that the mean theta was standard day (i.e., =1), then note that the limit of $(\theta - 1)/\ln(\theta)$ as $\theta \to 1$, is 1, and the equation reduces to

$$x \approx \alpha + \frac{m}{100}. \tag{7}$$

The form of these equations is particularly simple and allows a rapid check for corrections when engine data is available. The reader should note that the above can be applied just as well to pressure corrections (i.e., the δ exponent) where the relationships would be identical except for replacing θ with δ).

There are, of course, other empirical paths which one can take in pursuit of the proper correction. For instance, one could determine the exponent which minimizes the standard deviation ($\sigma_{\Delta G}$) of the parameter deltas $\{\Delta G_i\}$, or to minimize the covariance ($\sigma_{\Delta G,\theta}$) between the deltas $\{\Delta G_i\}$ and $\{\theta_I\}$, or the correlation coefficient ($r_{\Delta G,\theta}$). Monte Carlo simulations indicate, however, that the results are approximately the same for all of these techniques. The differences obtained for theta exponents using these four methods are well within the limits of measurement noise and are not statistically significant. The three minimization methods that we have just alluded to do carry a substantial computational overhead in that each of these methods are iterative in nature and require that a complete statistical analysis be performed at each newly chosen exponent, where the exponent is modulated in small increments over some range. After that is completed, the minimum statistic is isolated and the corresponding exponent is selected as the winner. In this regard, the simple formula(s) given in Eqs. (6) and (7) above are superior in that they return essentially the same exponent but require only one statistical analysis.

Table 4 Monte Carlo simulation

		Slope Method		Min Std Deviation Method	
TRUE Exp	Reduction Exp	Exp	Error	Exp	Error
0.710	0.789	0.707	-0.0035	0.705	-0.005
0.702	0.899	0.710	0.0085	0.710	0.0082
0.953	0.756	0.954	0.0008	0.950	-0.0028
0.773	0.864	0.768	-0.0046	0.775	0.0025
0.866	0.827	0.866	0.0006	0.865	-0.0005
0.964	0.710	0.986	0.0218	0.980	0.0158
0.743	0.936	0.734	-0.0086	0.735	-0.0075
0.749	0.706	0.763	0.0135	0.760	0.0109
0.953	0.701	0.950	-0.0023	0.950	-0.0025
0.708	0.809	0.711	0.0027	0.715	0.0071
0.791	0.787	0.784	-0.0072	0.785	-0.0063
0.961	0.747	0.956	-0.0045	0.960	-0.0008
0.775	0.893	0.738	-0.0366	0.740	-0.0347
0.860	0.934	0.850	-0.0098	0.855	-0.0052
.	.	.	.	.	.
.	.	.	.	.	.
0.920	0.988	0.913	-0.0079	0.915	-0.0054
0.729	0.703	0.727	-0.0017	0.725	-0.0039
0.821	0.729	0.844	0.0223	0.845	0.0237
0.867	0.972	0.862	-0.005	0.865	-0.0018
0.774	0.943	0.770	-0.0039	0.770	-0.0035
0.864	0.811	0.864	-0.0007	0.865	0.0007
0.927	0.711	0.929	0.0021	0.930	0.003
0.978	0.986	0.976	-0.0017	0.975	-0.0029
0.756	0.796	0.757	0.0004	0.755	-0.0012
		Mean Error =	-0.0011		-0.00053

As an illustration, Table 4 below presents the results of a Monte Carlo simulation comparison of the slope formula method and the minimum standard deviation method. This table contains 50 randomly chosen true exponents between 0.7 and 1.0. For each exponent a set of 200 deltas $\{\Delta G_i\}$ were randomly generated. These deltas were selected from a normal population where the variance for each of the 50 $\{\Delta G_i\}$ sets was also selected randomly. Thus, we have created a set of data where we have differing true exponent magnitudes and as well as differing variation in the deltas (simulating different measurement accuracies and/or engine to engine variation levels). For each of these 50 true exponents sets, we set a fixed corrected parameter level P^* and generate 200 θ_i's and calculate a set of 200 uncorrected parameters $\{P_i\}$ by applying both the theta correction (in reverse) using the true exponent, as well as the % delta $\{\Delta G_i\}$. This produces a set of data that simulates 200 raw measurements, each at a different temperature, each with a different (measurement/engine) bias ($\{\Delta G_i\}$). The $\{P_i\}$ are now corrected using one of 50 randomly chosen incorrect reduction theta exponents. Using this set of falsely corrected parameters, the aforementioned two methods are

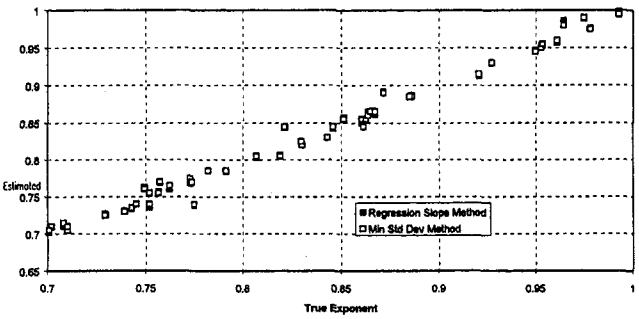

Fig. 3 Monte Carlo simulation experiment

applied and an estimate for the true exponent determined. This is repeated for each of the 50 samples exponents. Table 4 contains a sampling of the data generated. Figure 3 below summarizes the results of all 50 sets in graphical form.

As can be seen by perusing the table, a reasonably accurate assessment of the proper exponent can be obtained using the empirical method described above. In addition, both methods used in this example return exponents which are essentially the same. The slope method, however, offers the additional advantage of requiring far less computational effort.

Summary

We have summarized the traditional standard day corrections for most of the commonly encountered gas path parameters such as temperatures, pressures, speeds and flows as well as providing a derivation for each utilizing only simple thermodynamic relationships and fundamentals of the calculus. The topic of dimensional analysis was also mentioned as a matter of historical perspective in the treatment of nondimensional quantities and their relationship to corrected parameters. Other model dependent analytical methods were also discussed and illustrated. Finally, and perhaps most importantly, the practical aspects of determining the theta-delta exponents empirically from samples of engine data was discussed and a computationally simple method was derived and illustrated.

Acknowledgment

The author wishes to thank Richard Meisner formerly of Pratt & Whitney Aircraft for his insightful critique of this paper as well as for the many hours of phone conversations, communications and suggestions relating to this general topic. I would also like to acknowledge my long time friend and colleague Louis A. Urban, for introducing me to my first corrected parameter.

References

Buckingham, E., 1914, "On Physically Similar Systems: Illustrations of the Use of Dimensional Equations," *Physical Review,* Vol 4.

Capon, R. S., and Brooke, G. V., 1930, "The Application of Dimensional Relationships to Air Compressors," Aer. Res. Comm., Reports and Memoranda No. 1336.

Sanders, N. D., 1946, "Performance Parameters for Jet-Propulsion Engines," NACA Technical Note No. 1106.

Shepherd, D. G., 1949, *An Introduction to the Gas Turbine,* Constable and Company, Ltd., London.

Volponi, A. J., and Urban, L. A., 1992, "Mathematical Methods of Relative Engine Performance Diagnostics," *Journal of Aerospace,* SAE 1992 Transactions, Vol. 101, Technical Paper 922048.

Warner, D. F., and Auyer, E. L., 1945, "Contemporary Jet-Propulsion Gas Turbines for Aircraft," *Mech. Eng.,* Vol. 67, No. 11, pp. 707–714.

High Temperature Silicon Integrated Circuits and Passive Components for Commercial and Military Applications

R. R. Grzybowski
United Technologies Research Center,
411 Silver Lane, MS 129-32,
East Hartford, CT 06108

B. Gingrich
Honeywell Solid State Electronics Center,
12001 State Hwy. 55,
Plymouth, MN 55441

Advances in silicon-on-insulator (SOI) integrated circuit technology and the steady development of wider band gap semiconductors like silicon carbide are enabling the practical deployment of high temperature electronics. High temperature civilian and military electronics applications include distributed controls for aircraft, automotive electronics, electric vehicles and instrumentation for geothermal wells, oil well logging, and nuclear reactors. While integrated circuits are key to the realization of complete high temperature electronic systems, passive components including resistors, capacitors, magnetics, and crystals are also required. This paper will present characterization data obtained from a number of silicon high temperature integrated evaluated over a range of elevated temperatures and aged at a selected high temperature. This paper will also present a representative cross section of high temperature passive component characterization data for device types needed by many applications. Device types represented will include both small signal and power resistors and capacitors. Specific problems encountered with the employment of these devices in harsh environments will be discussed for each family of components. The goal in presenting this information is to demonstrate the viability of a significant number of commercially available silicon integrated circuits and passive components that operate at elevated temperatures as well as to encourage component suppliers to continue to optimize a selection of their product offerings for operation at higher temperatures. In addition, systems designers will be encouraged to view this information with an eye toward the conception and implementation of reliable and affordable high temperature systems.

Introduction

Advances in silicon-on-insulator (SOI) integrated circuit technology and the steady development of wider band gap semiconductors like silicon carbide are enabling high temperature electronics to be practically employed. High temperature civilian and military electronics applications include distributed controls for aircraft, automotive electronics, electric vehicles and instrumentation for geothermal wells, oil well logging, and nuclear reactors [1]. High temperature electronic systems will require semiconductor devices as well as passive components including resistors, capacitors, magnetics, and crystals. This paper will present characterization data obtained from a number of selected SOI devices being developed by Honeywell Solid State Electronics Center (SSEC) as well as from passive components evaluated over a range of elevated temperatures or aged at a selected high temperature. The collection and sharing of this type of device characterization data among designers and manufacturers of harsh environment components is crucial for several reasons. Primarily, it is necessary to evaluate whether specific components or families of components will perform well and how their performance degrades over temperature and over time at temperature. Secondly, this testing is required to identify failure modes specific to the components being evaluated so that component manufacturers can improve their processes and materials selection criteria used to realize harsh environment components. Component failure modes must also be understood in order to predict the reliability of a design when subjected to the intended harsh environmental stresses. Finally, extensive characterization data is required to perform valid circuit simulations and a worst case circuit analysis of any design destined for harsh environment operation.

The goal in presenting this information is to demonstrate the viability of a significant number of commercially available components to operate at elevated temperatures as well as to encourage component suppliers to continue to optimize a selection of their product offerings for operation at higher temperatures. In addition, systems designers are encouraged to view this information with an eye toward the conception and implementation of reliable and affordable high temperature systems.

It is acknowledged in advance that the data presented in this paper does not reflect the life of any component in a thermal cycling environment. Thermal cycling can be a large part of a design operating environment which will generally be much more stressful than static operation at an elevated temperature. A significant amount of work is being conducted at the United Technologies Research Center to characterize passive components in thermal cycling environments. The results of this work will be presented at a later time.

High Temperature Integrated Circuits

Integrated circuits are being developed specifically for applications requiring reliable high temperature operation such as aircraft turbine engine instrumentation and control. The analog circuits being developed use a 1.25 micron 2 layer metal CMOS (complementary metal oxide semiconductor) process with silicon on insulator, SOI, substrates. A similar 0.8 micron 3 layer metal CMOS SOI process is used for the digital parts. The analog process and

Contributed by the International Gas Turbine Institute (IGTI) of THE AMERICAN SOCIETY OF MECHANICAL ENGINEERS for publication in the ASME JOURNAL OF ENGINEERING FOR GAS TURBINES AND POWER. Paper presented at the International Gas Turbine and Aeroengine Congress and Exhibition, Stockholm, Sweden, June 2–5, 1998; ASME Paper 98-GT-362.

Manuscript received by IGTI February 21, 1998; final revision received by the ASME Headquarters June 23, 1999. Associate Technical Editor: R. Kielb.

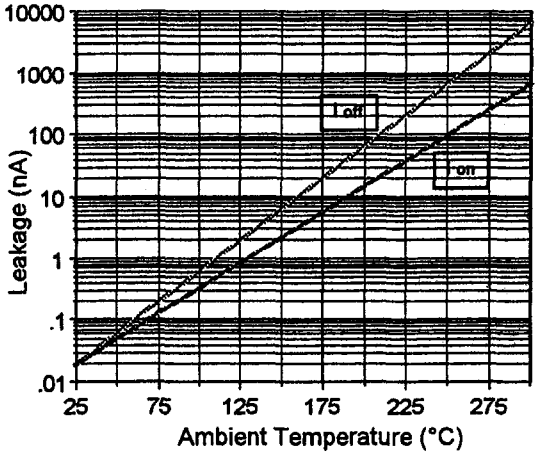

Fig. 1 Analog switch leakage current versus temperature

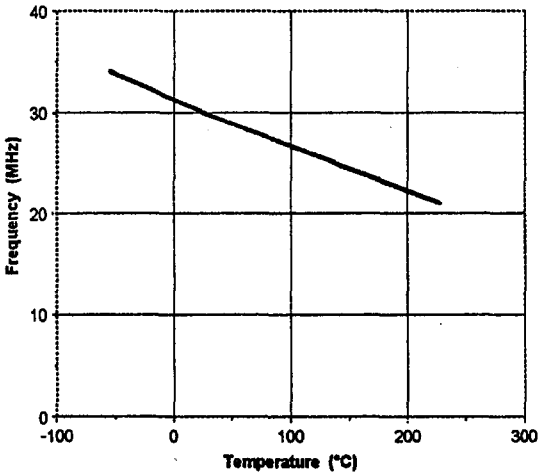

Fig. 3 Microcontroller frequency versus temperature

first circuits developed have been presented previously [2, 5], as has the digital process and first digital circuits [2, 3]. The performance of these parts over temperature has been characterized and shown to meet the requirements of instrumentation and control applications at temperatures up to 300°C. The parts are tested to data sheet specifications at 225°C after a burn-in at 250°C.

In Fig. 1 the leakage current of a quad analog switch is shown over temperature. The SOI technology provides extremely low leakage current even at high temperatures. This feature allows the SOI switch to perform well above the normal military temperature range (−55°C to +125°C) where conventional silicon circuits are no longer viable. The operational amplifier circuit designed in SOI shows similar high temperature performance in Fig. 2. Both circuits have been designed in the analog SOI process and have been optimized for performance over a very large temperature range. As seen in Fig. 2, the 225°C gain and bandwidth are evenly matched to the room temperature values for typical frequencies of operation. This allows the designer to maintain precise operation over a very large temperature range.

The performance of the digital SOI process can be seen in Figs. 3 and 4. In Fig. 3 the maximum clock frequency is plotted versus temperature for a 83C51 microcontroller. In Fig. 4 the read access time and write access time are plotted versus temperature for a 32 K × 8 SRAM (static random access memory). Both of these parts utilize the SOI digital process and have been designed to optimize their high temperature operation. The clock frequency degradation from −55°C to 225°C is only 40 percent for the 83C51 shown in Fig. 3. Similarly the increase in access time of the SRAM is less than 80 percent from −55°C to 225°C. This compares to similar bulk CMOS parts that degrade at a rate of 50 percent for clock frequency for every 100°C increase in temperature. Similarly the access time of military temperature range SRAMs will increase by 100 percent for every 100°C increase in temperature.

Additional high temperature SOI circuits are currently in various stages of development and evaluation. A voltage reference is in evaluation at this time. The design of the reference uses a standard PMOS transistor layout with the body contact open and not tied to the source. This configuration can then be used as a lateral PNP transistor with the PMOS (p-channel MOSFET) body contact acting as the base contact. The lateral PNP transistor is then configured as a traditional band gap reference circuit. Again, the SOI technology with its reduced leakage and high temperature design techniques provides a stable reference voltage at extreme temperature ranges well beyond the limits of traditional band gap circuits. The characterization of this part has started and the output voltage of several untrimmed devices is shown in Fig. 5.

In production the output voltage will be trimmed to provide a 5 volt output reference. As seen in Fig. 5, the output is stable over the full temperature range with an overall error of less than ±0.25 percent. The design specification for this part is ±0.5 percent over temperature. At this time the parts have not completed burn-in or drift with time testing. The use of the voltage reference in conjunction with the operational amplifier shown earlier will meet instrumentation and control requirements in a typical engine environment with ±0.5 percent accuracy.

In addition to being used to realize integrated circuits, the SOI

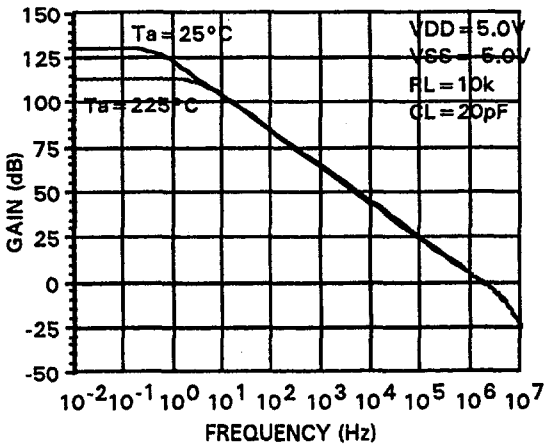

Fig. 2 Op amp gain versus frequency

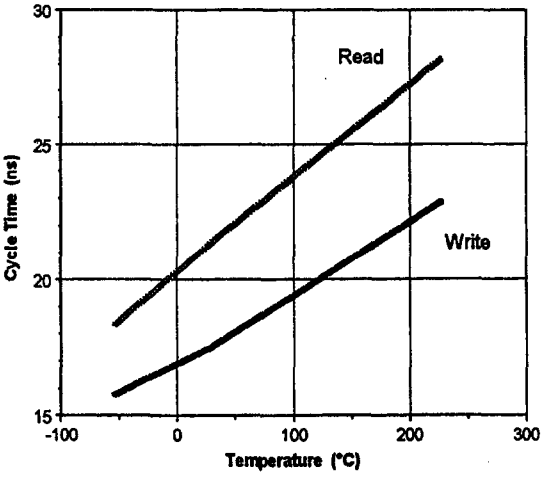

Fig. 4 SRAM access time versus temperature

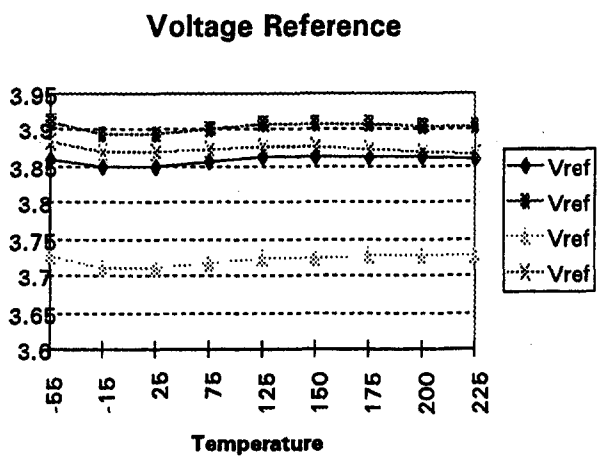

Fig. 5 Voltage reference output versus temperature

process can be used to fabricate P and N-type DMOS (depletion mode MOSFET) transistors. Figure 6 shows an I-V plot for a P-channel DMOS transistor and Fig. 7 shows an I-V plot for an N-channel DMOS transistor. Both devices are shown with a drain to source voltage of 40 volts. These transistor structures can be used to meet modest power switching requirements in applications such as torque motor drivers, solenoid drivers, and voltage regulator circuits. The practical output current limit for these types of structures in SOI between 0.5 and 1 ampere. DMOS SOI Structures have been presented previously [4] for high temperature applications.

Capacitors

Of all the passive devices that will be required in the above mentioned applications, perhaps none is as problematic as the capacitor. Because capacitance will often change significantly with increasing temperature (due to temperature dependent values of the dielectric constant), as will the equivalent series resistance (ESR) and dissipation factor, capacitors were identified years ago as a challenging passive component requiring development for reliable high temperature operation. In addition, the volumetric efficiency of capacitors fabricated with dielectric systems more compatible with high temperature operation is generally quite low. For example, capacitors properly prepared with an NPO dielectric have been shown to be very stable to temperatures as high as 500°C [6]. However, NPO capacitors are seldom seen with values of more than 0.22 uF because they become so physically large that the stresses they encounter within a few thermal cycles will cause them to crack and fail. These shortcomings are even more evident in large value capacitors of several microfarads or more, like those required for power conditioning circuits associated with electric motors and power switching applications. Even more problematic for power supply circuits required to operate at high temperatures is the fact that large value capacitors like wet tantalum components suffer from higher values of ESR. This often requires relinquishing more package volume or substrate area so that these capacitors can

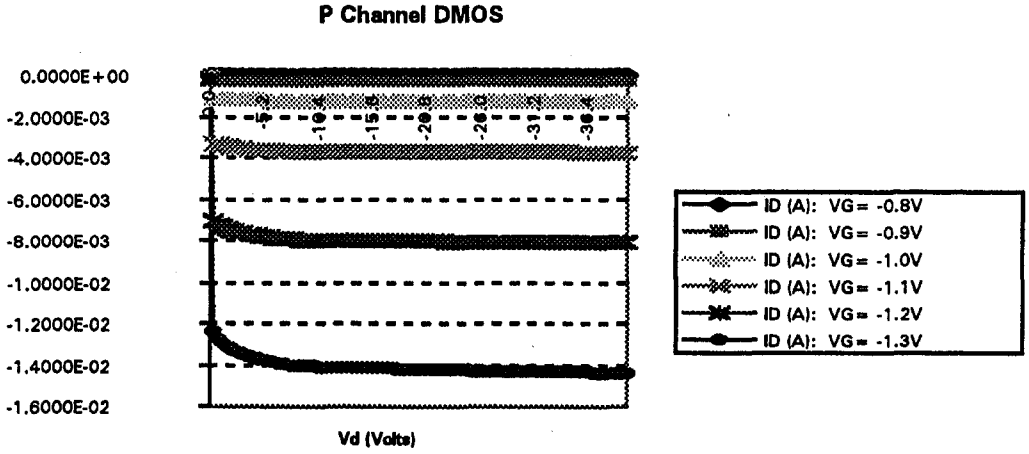

Fig. 6 I-V curve for an SOI P-channel DMOS device

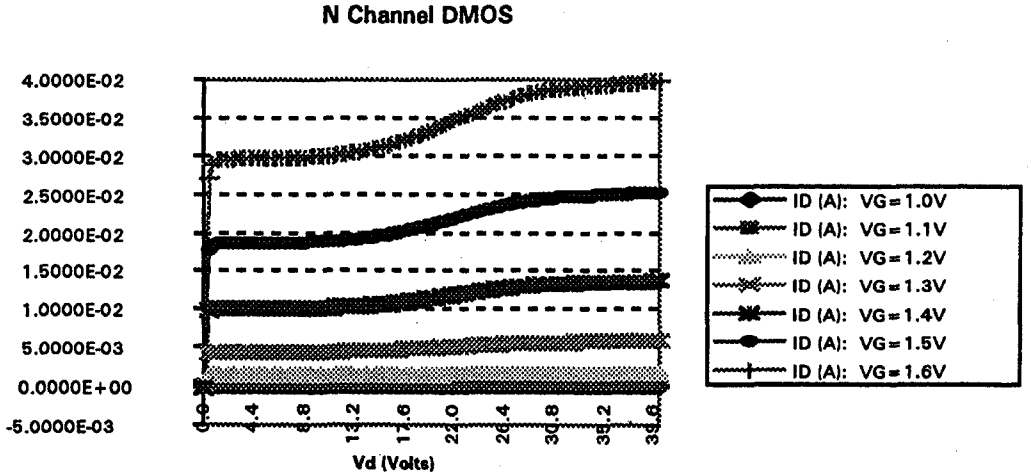

Fig. 7 I-V curve for an SOI N-channel DMOS device

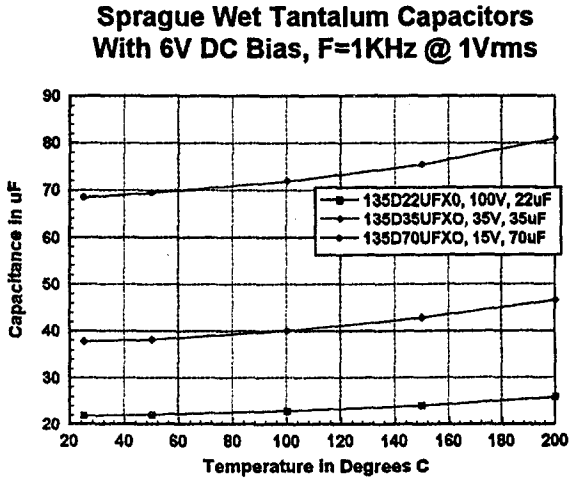

Fig. 8 Capacitance versus temperature for three different Sprague wet tantalum capacitors

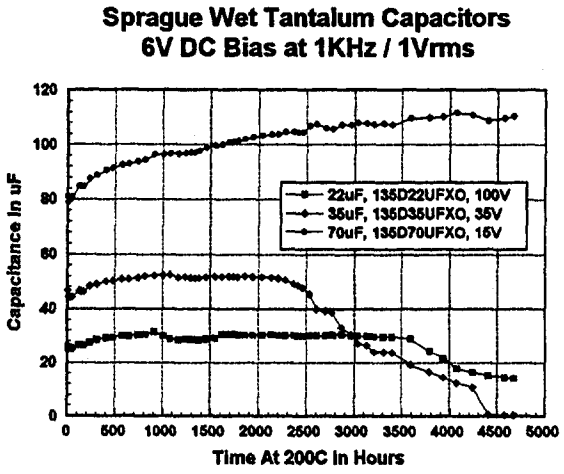

Fig. 9 Capacitance versus time at 200°C for three different Sprague wet tantalum capacitors

be connected in parallel to reduce the effective ESR value. Electrolytic capacitor are traditionally employed in these applications, but devices that will operate reliably at temperatures greater than 150°C do not commonly exist. This is because the dielectric films employed in the fabrication of these devices break down at these temperatures. Alternative films have been developed [7], however, they are not widely employed in the manufacture of commercially available devices.

The relative merit or failure of all of these characteristics, however, is very application dependent. That is to say that, what is a liability in one instance may be an asset in another. Careful circuit design and component selection is even more critical in harsh environment applications than is in those expected to operate over traditional military temperature ranges—but far from impossible. The rest of this section will present sample data to support this assertion.

Since small values of capacitance (less than 0.1 uF) are commonly available in the form of ceramic devices made with NPO, X7R, or X8R dielectrics, larger values of capacitance employing tantalum based material systems will first be considered. Wet tantalum capacitors are available from several companies including Sprague and Tansitor. Figure 8 presents sample capacitance versus temperature data obtained from three different wet tantalum capacitors manufactured by Sprague. Since manufacturers typically specify their components over the military temperature range (−55 to 125°C) only data that covers the higher temperature ranges is presented here. Figure 9 presents capacitance versus time at 200°C characterization data for the same three devices.

From these two figures it may be observed that there is a gradual, easily modeled positive shift in capacitance versus temperature for these fairly large value devices. In addition, the aging characteristics for the first 2000 hours at 200°C, while not insignificant, are relatively graceful. This is really quite extraordinary for a complex wet chemical capacitor family like this in which one of the capacitor plates is a liquid electrolyte which has to be hermetically sealed within the capacitor body.

The loss of integrity of this hermetic seal is one of the most frequent failure modes for these devices. The shift in capacitance value with time at elevated temperatures is most probably attributable to the gradual leaking of the liquid electrolyte through an imperfect seal. The wet electrolyte permits a certain amount of self-healing to occur within the device. If a certain area of TaO_5 dielectric breaks down for any reason, the liquid electrolyte will aid the regrowth of the damaged area. However, as the quantity of electrolyte is lost through an imperfect hermetic seal, this ability to heal defects in the TaO_5 is reduced. Figure 9 shows evidence of this on the 35 μF device occurring after approximately 2200 hours at 200°C and on the 22 μF device after approximately 3500 hours at 200°C. As will be seen, the critical importance of device packaging on the reliability of electronic components is a recurrent theme. Very often, the basic materials systems are quite robust. However, joining, sealing and other packaging related shortcomings prove to be hurtles to be overcome by manufacturers of harsh environment passive components.

The performance of several solid tantalum components will now be considered. Figure 10 presents sample capacitance versus temperature data obtained from five solid tantalum capacitors manufactured by Matsuo. Figure 11 presents capacitance versus time at 200°C characterization data for the same five devices.

Here again, from Fig. 10, it may be observed that there is a gradual, easily modeled positive shift in capacitance versus temperature for these device that are fairly large for solid tantalum components. From Fig. 11 it may be noted that there is an aging phenomena during the first 1100 hours that first causes the capacitance to rise by approximately 4 percent, level off and finally settle back down to within a couple of percent of where it started. For the remaining time of the test, however, the capacitance of the devices remain relatively constant.

In contrast to the tantalum devices just examined, some large value capacitors fabricated with an X7R ceramic dielectric material will be considered. Figure 12 presents sample capacitance versus temperature data obtained from two X7R capacitors manufactured by NOVACAP. Figure 13 presents capacitance versus time at 200°C characterization data for the same two devices.

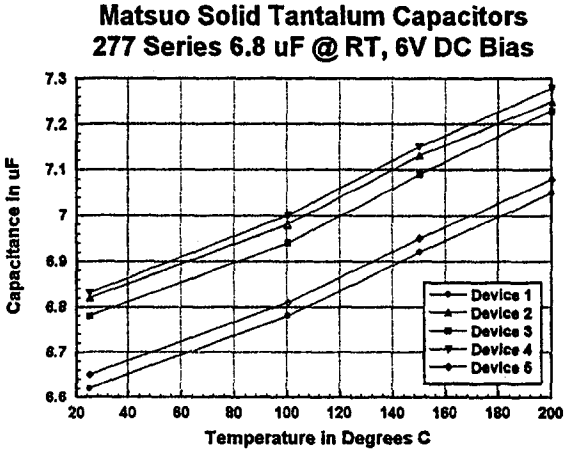

Fig. 10 Capacitance versus temperature for five Matsuo solid tantalum capacitors

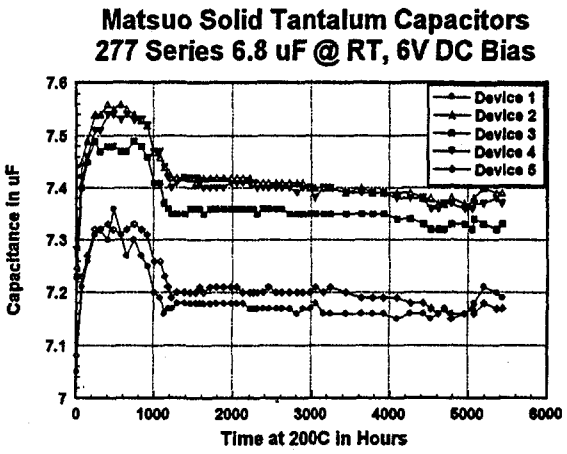

Fig. 11 Capacitance versus time at 200°C for five Matsuo solid tantalum capacitors

Figure 12 shows the capacitance versus temperature that is typical of components that employ X7R as a dielectric [6, 7]. From Figure 13 it may be seen that after the first 500 hours at 200°C, the components were brought to room temperature, and then returned to 200°C for the several thousand more hours. During this temperature transient, some fatiguing of the solder joints may have accounted for the step change in the capacitance values measured. What should be noted here is the relative stability of the capacitance values with time at 200°C.

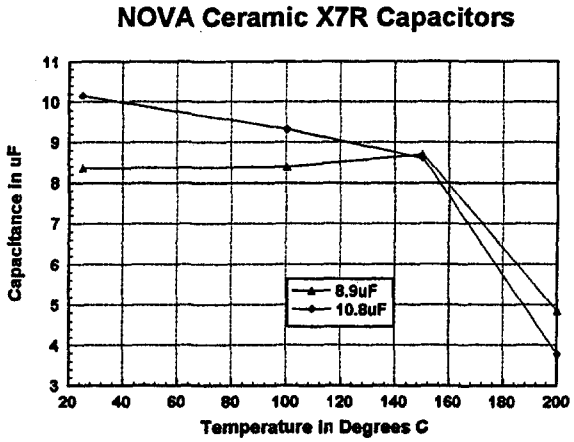

Fig. 12 Capacitance versus temperature for two NOVACAP X7R capacitors

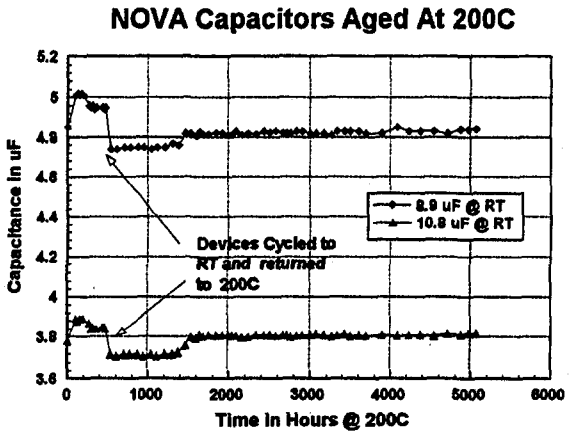

Fig. 13 Capacitance versus time at 200°C for two NOVACAP X7R capacitors

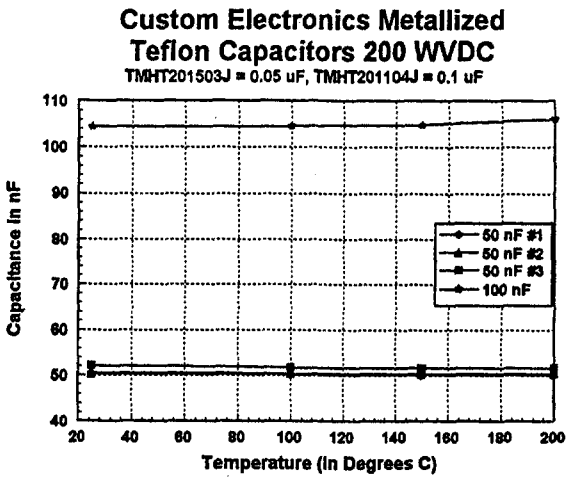

Fig. 14 Capacitance versus temperature for several Teflon electrostatic capacitors

The final capacitor type touched upon is the Teflon electrostatic capacitor. Teflon is a dielectric that has been demonstrated to be very stable over temperature. Figure 14 is a plot of capacitance versus temperature of several electrostatic devices manufactured using teflon by Custom Electronics. From this figure it is clear that this type of capacitor is very stable from room temperature to 200°C. Although the devices represented by this figure do not have very large values of capacitance (0.05 and 0.1 μF) larger devices are commercially available and development work is ongoing to optimize these devices for very high dV/dT applications like snubber capacitors. The drawbacks associated with Teflon capacitors are that they are often custom ordered and not commonly available in a wide variety of capacitance values, and the values that are available are small and costly. There are, however, a number of programs underway to produce much larger capacitance value components at a lower cost.

Resistors

Resistors are the least complex of the passive components needed for high temperature systems applications. However, obtaining stable resistor values over wide temperature ranges once again requires careful component selection. A selection of wire wound power resistors manufactured by Dale Electronics will be considered first. Wire wound resistors tend to be very stable over wide temperature ranges because the resistance is determined simply by the material properties of a resistive wire wound around a ceramic core. Since power resistors are generally expected to run very hot in typical applications, the packaging materials employed are usually selected to be compatible with each other over wide temperature ranges as well. To keep the energized devices from exceeding the use temperature of the packaging materials, specifically the silicone based potting material, the power dissipation of these devices was limited to 20 percent of their room temperature ratings. Figure 15 presents resistance versus time at 300°C characterization data obtained from a selection of Dale wire wound components reported earlier [8]. The change in resistance is plotted as a normalized shift using the following formula:

$$\text{Norm. Shift } (\%) = \frac{\text{Value} - \text{Init Value}}{\text{Init Value}} \times 100\% \qquad (1)$$

Each point is based on the average of the five measurements. The transient at 4520 occurred when the test chamber was shutdown for three weeks. A significant jump in resistance was noted in the 10 KΩ/5 W and the 1 Ω/5 W. The 1 Ω/5 W returned to pre-shutdown values very quickly, but the 10 KΩ/5 W had a permanent shift associated with the shutdown. With the exception of the

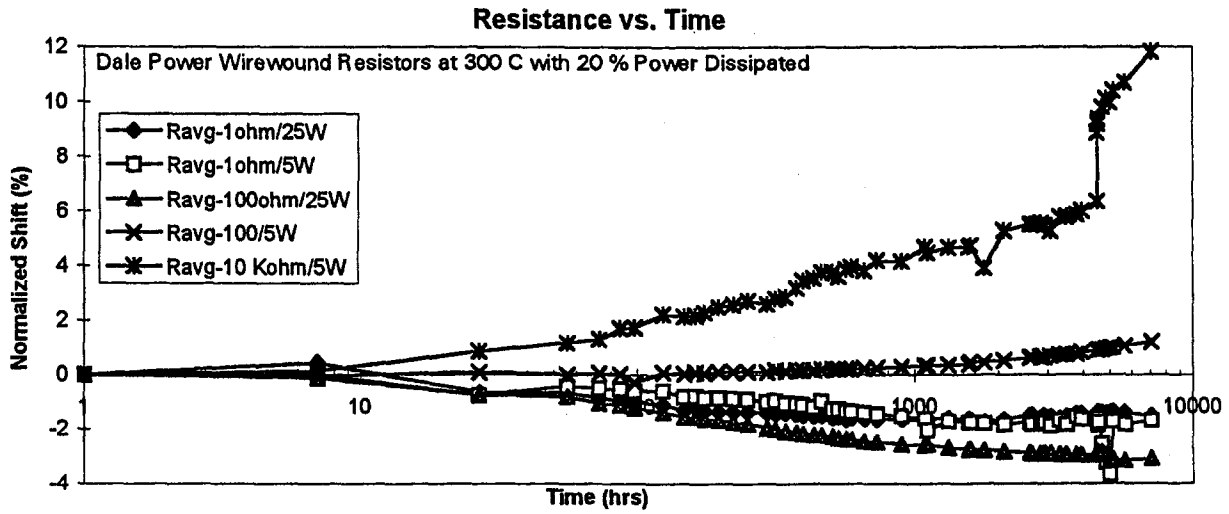

Fig. 15 Resistance versus time at 300°C for a selection of Dale wire wound resistors

10 KΩ/5 W resistor, all shifts in resistance value were less than 4 percent.

Small signal resistors with power ratings from 0.1 watt to 1 watt are also commercially available for high temperature applications that require stable values of resistance. Sample resistance versus temperature characterization data for $\frac{1}{4}$ watt wire wound components manufactured by Caddock is presented in Fig. 16. Aging characteristics similar to those shown in Fig. 15 have been observed in these devices as well. One caveat to bear in mind when specifying wire wound resistors, especially with tight tolerances, is the method used by the manufacturer to trim the resistor values. Very often, rather than adjusting the length of the resistance wound around the ceramic core, the resistance value is trimmed by putting a notch in the wire. For harsh environment applications, this notch will serve as a nucleation site for wire fatigue damage to collect. This aggregate damage at this site is the usual failure mechanism for these components.

Thick film resistors are typically rated over the military temperature range of −55°C to +125°C. For higher temperature applications Heraeus-Cermalloy developed the 900 Series resistor inks [6, 7]. These inks are formulated with a higher softening point glass that makes them useful at higher temperatures. In addition, the temperature coefficient of resistance (TCR) minimum was shifted to approximately 150°C. Figure 17 presents normalized resistance shift versus temperature characterization data, reported earlier [8], obtained from thick film resistors fabricated using Heraeus-Cermalloy 931 (1 KΩ/□) paste with a Heraeus-Cermalloy (C1003) palladium-silver termination conductor printed on 96 percent alumina substrates. From this figure it may be noted that the expected minimum resistance is in the 150–200°C temperature range. In addition, the resistor geometry had little effect on the TCR below 300°C. The change in resistance with temperature was generally less than ±1 percent below 300°C.

Figure 18 presents characterization data for the normalized shift in resistance versus time at 500°C for these same components. From this figure it may be noted that the resistor geometry has a significant effect on resistance drift with time at 500°C. Shifts were less than 3 percent throughout the test duration shown, however, longer resistors drifted more than shorter ones.

Conclusions

As stated at the outset, the goal of this paper is to present information that demonstrates the viability of a significant number of commercially available passive components and SOI integrated circuits that operate at elevated temperatures. Performance data versus temperature obtained from both digital and analog IC's developed at Honeywell SSEC was presented. Characterization data obtained from capacitors, with a number of substantially

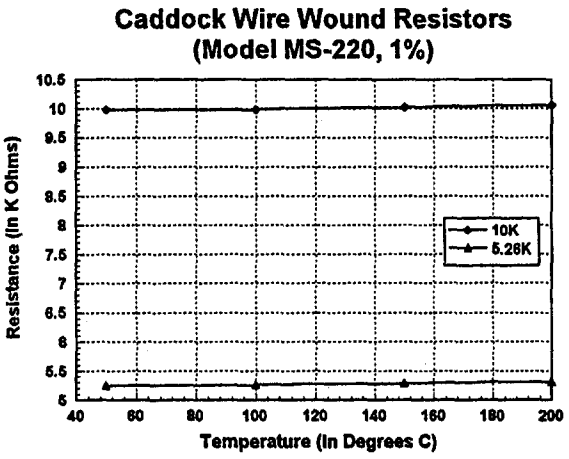

Fig. 16 Resistance versus temperature for a selection of Caddock wire wound resistors

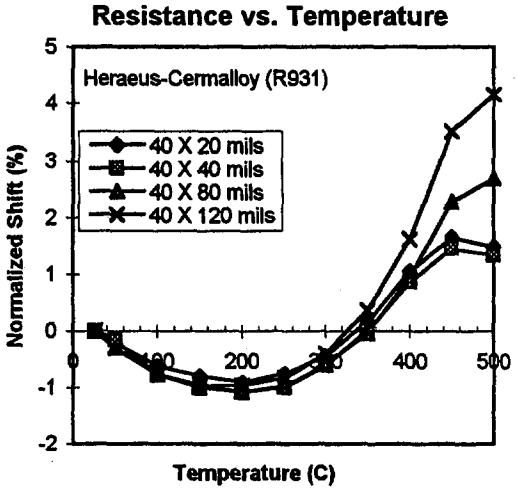

Fig. 17 Normalized resistance shift versus temperature for a selection of thick film resistors

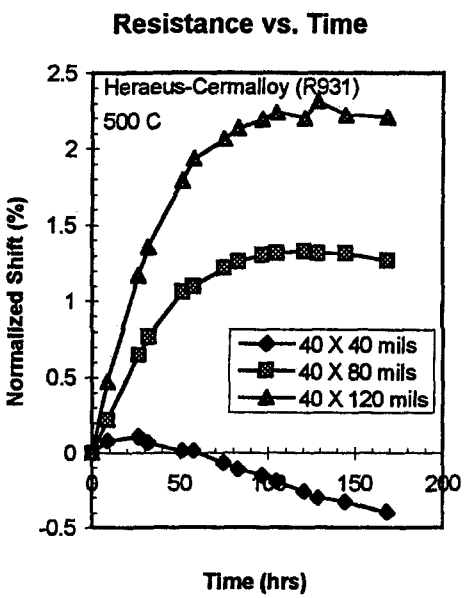

Fig. 18 Normalized resistance shift versus time at 500°C for a selection of thick film resistors

different dielectric families represented, was presented. Capacitance values versus temperature as well as versus time at temperature substantiated the claim that components capable of operating in high temperature applications were commercially available. Resistors were examined in the same fashion. This information should encourage designers to consider innovative approaches to tough technical problems that involve harsh environments and higher temperatures than have been encountered in the past. Furthermore, the authors want to encourage component suppliers to optimize some of their product offerings for operation at higher temperatures for these applications. Finally, even a high reliability application that does not require high temperature operation will benefit from the use of components designed to operate at higher temperatures because of the inherent additional reliability achievable from devices that are designed and packaged to operate at high temperatures.

References

1 Shorthouse, G., and Lande, S., 1996, "The Global Market for High Temperature Electronics," *Transactions of the 3rd International High Temperature Electronics Conference,* June 1996, Albuquerque, New Mexico, p. I-3-8.

2 Brusius, P. G., et al., 1996, "SOI Devices for High Temperature Applications," Proceedings, Third International High Temperature Electronics Conference, June 1996.

3 Swenson, G., 1997, "8-Bit Microcontroller and 32Kx8 SRAM Launch HTMOS™ Digital Product Offerings," Transactions HITEN '97, Manchester, England, Sept. 97.

4 McKitterick, J. B., et al., 1996, "An SOI Smart-Power Solenoid Driver for 300°C Operation," Proceedings, Third International High Temperature Electronics Conference, June 1996.

5 Swenson, G. M., and Ohme, B., 1996, "HTMOS™: Affordable High Temperature Product Line," Proceedings, Third International High Temperature Electronics Conference, June 1996.

6 Grzybowski, R. R., 1993, "Characterization and Modeling of Ceramic Multilayer Capacitors to 500°C and Their Comparison to Glass Dielectric Devices," Proceedings, Thirteenth Capacitor and Resistor Technology Symposium (CARTS), pp. 157–162.

7 McCluskey, F. P., Grzybowski, R. R., and Podlesak, T., 1996, *High Temperature Electronics,* CRC Press, New York, NY, pp. 113–114.

8 Naefe, J. E., Palmer, J., Lankford, M. A., Johnson, R. W., and Grzybowski, R. R., 1997, "High-Temperature Characterization of Heraeus-Cermalloy Thick Film and Dale Power Wirewound Resistors," Proceedings, Seventeenth Capacitor and Resistor Technology Symposium (CARTS), pp. 244–250.

B. G. Vroemen

H. A. van Essen
h.a.v.essen@wtb.tue.nl

A. A. van Steenhoven

J. J. Kok

Eindhoven University of Tehnology,
Department of Mechanical Engineering,
P. O. Box 513,
5600 MB Eindhoven,
The Netherlands

Nonlinear Model Predictive Control of a Laboratory Gas Turbine Installation

The feasibility of model predictive control (MPC) applied to a laboratory gas turbine installation is investigated. MPC explicitly incorporates (input and output) constraints in its optimizations, which explains the choice for this computationally demanding control strategy. Strong nonlinearities, displayed by the gas turbine installation, cannot always be handled adequately by standard linear MPC. Therefore, we resort to nonlinear methods, based on successive linearization and nonlinear prediction as well as the combination of these. We implement these methods, using a nonlinear model of the installation, and compare them to linear MPC. It is shown that controller performance can be improved, without increasing controller execution-time excessively.

Introduction

Gas turbines can be found, for instance, in jet engines and in the field of power generation. The laboratory installation is a scale model (400 kW thermal power input) of a true gas turbine and differs from a gas turbine in the traditional sense, in the fact that compressor and expander are separated by a buffer-tank, as will be depicted in Fig. 2. This setup is used to validate general purpose dynamic simulation models of turbomachines, and to investigate the control of such systems.

The gas turbine's operation is limited by some undesirable effects, which we will incorporate as output constraints. Furthermore, limits on actuator operation impose input constraints. It is especially these constraints which have resulted in choosing MPC for a control strategy. Apart from explicit constraint handling, the advantages of MPC include anticipation to future setpoint changes (and possibly known disturbances), and the ability to handle dead-time responses and interactions in multivariable systems.

MPC uses a model of the process to predict future system response. Through minimizing the difference between desired and predicted outputs, the future inputs (or manipulated variables) can be determined. Standard linear MPC incorporates linear models both for prediction and optimization. Although it is successful in controlling linear and mildly nonlinear processes, performance degradation and instability often occur in the presence of strong nonlinearities. During the past decade, the number of nonlinear predictive control algorithms has increased significantly. A comprehensive review of nonlinear control is provided by Bequette (1991). However, the excessive computational requirements of such methods remain a serious obstacle to industrial implementation in spite of the advances made in developing efficient algorithms. Also, little progress has been made in understanding their stability and performance properties (Gattu, 1992).

For our purposes, we need an algorithm which handles nonlinearities adequately, but is guaranteed not to require computation-times in excess of that which is allowable for real-time implementation. This limit is set at approximately 1 sec. per sample. Furthermore, a strategy must be developed to handle infeasibilities during the optimization phase.

This paper addresses three different approaches, which are then compared to linear MPC. The first approach we will look into, uses a linearization of the nonlinear model, obtained at each sampling time. This linear model is used to compute the effect of previous control moves, as well as to optimize future manipulated variables. A second approach uses a nonlinear model for prediction and again a linear model for optimization but does not repeat the linearization. Combining nonlinear prediction and successive linearization results in the third approach. A major advantage of these approaches is that they allow the use of proven linear optimization algorithms to be used on a nonlinear problem. The third approach was utilized earlier by Garcia (1984) and has been refined by Gattu (1992) and Lee (1993) to include an Extended Kalman Filter. We do not linearize repeatedly within the prediction horizon, something which is done, e.g., by Brengel (1989), Li (1989), and De Oliveira (1995). These methods are expected to increase computational demands substantially, since they incorporate an iterative (SQP) optimization problem instead of a single QP problem.

The main objective of this paper is to asses the feasibility (stability, real-time performance, robustness) and benefits of MPC on a system as fast as the gas turbine installation. We evaluate situations where our nonlinear model perfectly describes the plant, as well as situations where parametric plant/model mismatch is introduced. In a larger context, one of the goals is to implement the control algorithm in a real-time situation. This paper only describes results from simulations, which were obtained using PRIMACS, the MPC-implementation developed by TNO-TPD at Delft. Experiments will be performed shortly and reported in a successor of this paper. Initial experimental results are encouraging.

The paper is organized as follows: It starts with a short description of the gas turbine installation and some key aspects of the model we developed. In the following section we elucidate the concept of MPC as it is implemented in PRIMACS and describe the nonlinear methods that were newly developed and added to the package. The concluding sections present and discuss simulation results, respectively.

The Gas Turbine Installation

A gas turbine produces mechanical (shaft) power by expansion of compressed gas—usually air—through an expander. The required pressure ratio is provided by a compressor. Compressor and expander are mounted on the same shaft and the expander powers the compressor. To overcome losses and develop useful power, energy has to be added by raising the temperature of the compressed air prior to expansion. This is accomplished in a combustion chamber which is positioned between compressor and expander.

Contributed by the International Gas Turbine Institute (IGTI) of THE AMERICAN SOCIETY OF MECHANICAL ENGINEERS for publication in the ASME JOURNAL OF ENGINEERING FOR GAS TURBINES AND POWER. Paper presented at the International Gas Turbine and Aeroengine Congress and Exhibition, Stockholm, Sweden, June 2–5, 1998; ASME Paper 98-GT-100.

Manuscript received by IGTI March 2, 1998; final revision received by the ASME Headquarters March 23, 1999. Associate Technical Editor: R. Kielb.

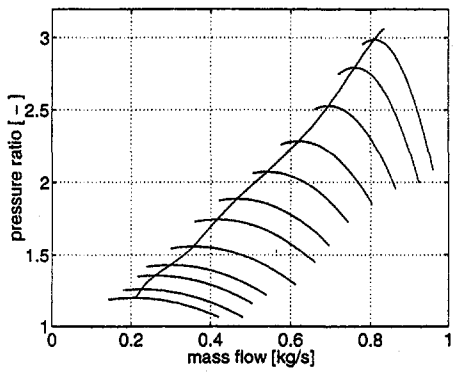

Fig. 1 Compressor characteristic

Of special interest to us are the restrictions to the operation of the gas turbine. Operating points are determined by the combination of the characteristics of the comprising components. Operation restrictions are therefore related to these components. Furthermore, since the compressor appears to be the most critical component, the operating points of the overall gas turbine are usually represented in the compressor characteristic, which is depicted in Fig. 1.

In this characteristic, curved lines represent the relationship between pressure ratio over, and mass flow through the compressor for various rotational speeds. The extrema of these lines are connected by what we refer to as the surge line.

Being the most severe restriction, surge denotes the phenomenon associated with violent limit cycle oscillations of mass flow and pressure rise, which originate in the compressor and are transmitted throughout the gas turbine. Surge is likely to happen when the mass flow through the compressor decreases enough to enter the part of the compressor characteristic where a decrease in mass flow will be accompanied by a fall of delivery pressure, i.e., where the lines of constant speed exhibit a positive slope. In the compressor characteristic this corresponds to passing the surge line, which more or less separates the stable zone from the unstable zone.

The second limitation we consider is the expander inlet temperature which may not exceed some maximum value. Beyond this temperature the life-time of the rotor decreases dramatically. In practice, this is the limitation we encounter most, especially when the fuel valve is opened rather quickly. Doing so causes the inlet temperature of the expander to rise instantaneously, only to decrease again after mass flows—being governed by larger timescales—have risen also.

The Laboratory Setup. Figure 2 schematically depicts the laboratory installation. It comprises a BBC turbocharger, which consists of a single stage radial compressor and a single stage axial expander. Also a combustion chamber and a buffer-tank can be recognized. The main function of the buffer-tank is to decouple the flows out of the compressor and into the expander, enabling the isolation of physical phenomena in both components. Other components are the blow-off valve, the throttle valve and the fuel valve, which are all powered by electric drives. The blow-off valve directly influences the ratio of mass flows through compressor and expander, while the throttle valve influences the ratio of compressor delivery and expander inlet pressure. The fuel valve controls the power supplied to the gas turbine. These three valves are used to reach different operating points of the installation. A compressed air facility is employed in start-up procedures. For detailed information about the laboratory installation, the reader is referred to Essen (1995).

Control Objectives. In a practical gas turbine application, objectives (other than surge avoidance) one can think of are operating at constant rotational speed for generator purposes, or, if the gas turbine is to be used as a power supply for some external load it might be important to deliver constant power. Of course, this should still be true if disturbances, such as varying ambient conditions, are present. Also, operating at maximum efficiency can be of significant importance, so as to minimize fuel consumption.

In this paper, we will not primarily seek to meet these real-life control objectives. Instead we will specify objectives that in one way or another "challenge" the controller. We will focus on setpoint control and constraint handling.

The outputs we wish to control are formed by the three variables which determine the position of the operating point of the gas turbine in the compressor characteristic. These are the pressure ratio over the compressor, the mass flow through the compressor and the rotational speed. Of course, we will never seek to control all these three variables at the same time, because this would result in an inherently over-determined problem: two out of these three variables fully determine the position in the compressor characteristic.

In order to specify the surge line constraint in MPC, we define a dummy output. To avoid surge, the distance (in terms of mass flow) between operating point and surge line must be kept greater than zero. The second output constraint stems from the expander inlet temperature, which is not allowed to (continuously) exceed the bound of 900° K.

Furthermore, valves should be constrained not to operate beyond their saturations. Just as importantly, maximum moving rates should be specified, since real-life actuators cannot simply move with arbitrarily high speed. In MPC this is realized by specifying the maximum move size per sample period.

Modeling the Gas Turbine. We developed a model in which components of the installation like compressor, valves, and expander are represented by a set of (nonlinear) quasi-steady, algebraic, equations. This implies that the component characteristics are used as static impulse balances to determine the mass flow through the components. This type of modeling of turbomachines has been widely accepted, see, e.g., Botros (1991).

Two successive components are coupled by a volume, in which the dynamic behaviour is lumped. In our model three volumes, corresponding to the compressor plenum, the buffer tank, and the combustion chamber volume, are applied. For each of these, instationary mass and energy conservation laws are used to obtain state equations for pressure (p) and temperature (T):

$$\frac{dp}{dt} = \frac{\gamma R}{V}\left[\dot{m}_{\text{in}} T_{\text{in}} - \dot{m}_{\text{out}} T\right]$$

$$\frac{dT}{dt} = \frac{RT}{pV}\left[\gamma(\dot{m}_{\text{in}} T_{\text{in}} - \dot{m}_{\text{out}} T) - T(\dot{m}_{\text{in}} - \dot{m}_{\text{out}})\right],$$

with $\dot{m}_{\text{in}}$ and $\dot{m}_{\text{out}}$ mass flows in and out of the volume (V), and T_{in} the inlet temperature. γ and R denote the quotient of specific heat

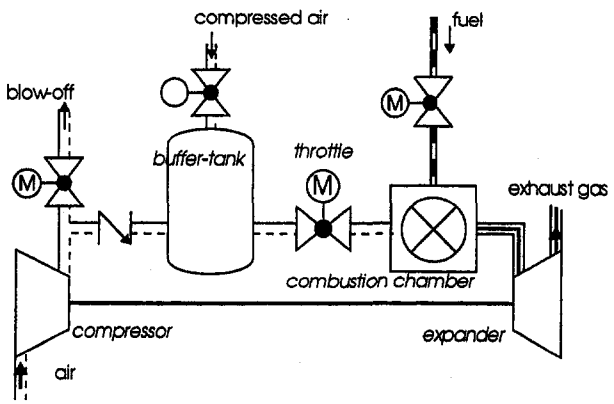

Fig. 2 Laboratory gas turbine installation

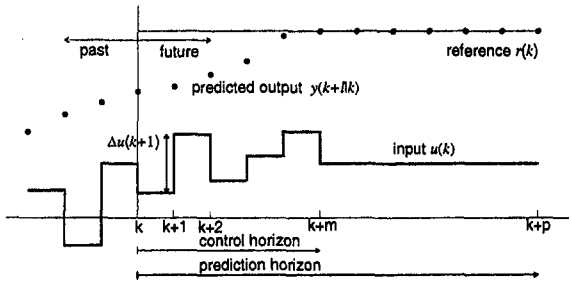

Fig. 3 Basic concept of MPC

capacities (c_p/c_v) and the gas constant, respectively. In the combustion chamber an additional power input term represents the energy of combustion.

These equations are valid under the assumptions of a homogeneous, adiabatic volume, and an ideal gas. In the combustion chamber volume additional power terms are introduced, representing the combustion process. In the present model the (isentropic) efficiencies of compressor, expander, and combustion chamber are assumed to be constant.

Using a power balance between compressor and expander, a state equation for rotational speed (N) is obtained:

$$\frac{dN}{dt} = [\dot{m}_e c_{p,e}(T_{\text{in},e} - T_{\text{out},e}) - \dot{m}_c c_{p,c}(T_{\text{out},c} - T_{\text{in},c})] \frac{1}{NI},$$

where subscripts e and c denote *e*xpander and *c*ompressor, while I stands for shaft inertia.

The model thus obtained has 7 states and 3 inputs (the positions of the control valves). More information on the specifics of this model can be found in Vroemen (1997).

Model Predictive Control

Model predictive control uses a model of the process to predict the outputs up to a certain time-instant, based on the inputs to the system and the most recent process measurements. For example, consider Fig. 3. At the present time k, the response of the output $y(k)$ to changes in the manipulated variables $u(k)$ is predicted over the prediction horizon p. The manipulated variables are allowed to vary over the control horizon m and can be computed such that future deviations of the output from a desired target $r(k)$ are minimized.

Of the computed optimal control moves, only the values for the first sample are actually implemented. This way the most recent process measurements can be used to calculate a new sequence of control moves. This mechanism is known as a moving (or receding) horizon. A comprehensive treatment on linear MPC is provided by Morari (1991).

To minimize future deviations of the controlled variables from their setpoints, while preventing the inputs from changing inadmissibly fast, we use the quadratic objective function

$$\min_{\Delta u(k+1)\ldots\Delta u(k+m)} \{\sum_{l=2}^{p} \|\Gamma_l^y[y(k+l|k) - r(k+l)]\|^2 + \sum_{l=1}^{m} \|\Gamma_l^u[\Delta u(k+l)]\|^2\}, \quad (1)$$

where weights are included to express the relative importance of outputs following their reference trajectory on the one hand and trading this off with reducing the action of manipulated variables on the other. In this notation Γ_l^y and Γ_l^u represent the output and input-weightings, respectively. Furthermore, $y(k+l|k)$ denotes the estimate of $y(k+l)$ obtained at k, taking into account all measurement information up to k. Note that, at the current sample k, input moves Δu are optimized starting from sample $k+1$, so as to minimize predicted output deviations from their setpoints, from sample $k+2$ onwards. This way, the computational delay is accounted for, with the inherent implication that $y(k+1|k)$ can never be influenced at sample k.

The solution to this unconstrained problem can be obtained analytically with relatively little effort. In general, though, constraints will always be present at one time or another, be it output constraints, input constraints or input move constraints. Incorporating these constraints leads to a quadratic program (QP) of the following form:

$$\min_{\Delta\mathcal{U}(k+1)} \tfrac{1}{2}\Delta\mathcal{U}(k+1)^T\mathcal{H}^u\Delta\mathcal{U}(k+1) - \mathcal{G}(k+2|k)^T\Delta\mathcal{U}(k+1)$$

such that

$$\mathcal{C}^u\Delta\mathcal{U}(k+1) \geq \mathcal{C}(k+2|k),$$

where $\Delta\mathcal{U}(k+1)$ contains the control moves $\Delta u(k+1)\ldots\Delta u(k+m)$, whereas $\mathcal{H}^u$ and $\mathcal{G}(k+2|k)$ are the Hessian matrix and gradient vector. $\mathcal{C}^u$ and $\mathcal{C}(k+2|k)$ depend on the constraints on manipulated variables, change in manipulated variables, and outputs.

Constraint Handling. The QP may not always have a solution, which is why a strategy must be specified to handle these infeasibilities. In PRIMACS, a strategy is adopted where constraint violations are included into the optimization criterion, once infeasibility occurs. This way, violations are kept from becoming inadmissibly large. It is implemented by simply adding the ℓ_1-norm of the (suitably weighted) constraint violations ϵ ($\epsilon \geq 0$) to the optimization criterion, which will then look like

$$J_{\text{modified}} = J + \rho^T\epsilon,$$

where J denotes the unmodified optimization criterion, and ρ the vector with weights on the constraint violations. The ℓ_1-norm is chosen over the ℓ_2-norm for its guaranteed open-loop stability when the unconstrained system is stable.

The total constraint handling strategy can now be summarized as follows:

1 Solve the unconstrained problem. If constraints are violated, go to step 2. Else, implement the controller moves and return to step 1.
2 Find a solution to the QP problem. If infeasible, go to step 3. Else, implement the controller moves and return to step 1.
3 Include constraint violations into the QP, and solve this modified problem. Implement the controller moves and return to step 1.

Internal Model. We assume that the internal model (the model MPC uses for its computations) is expressed through the following nonlinear differential equations:

$$\dot{x}(t) = f(x(t), u(t)) \quad (2)$$

$$y(t) = g(x(t), u(t)) + d(t), \quad (3)$$

where $x(t)$ are the model states, $u(t)$ the manipulated variables, $y(t)$ the outputs, and $d(t)$ unmeasured disturbances. We adopted the same output disturbance model Garcia (1984) uses, where disturbances are added directly to each output.

In order to handle nonlinearities adequately, we will look into three nonlinear extensions to linear MPC, which we will denote as successive linearization, nonlinear prediction and the combination of these, nonlinear prediction, and successive linearization. Eventually, we will compare the results of these methods to those obtained with linear MPC.

Successive Linearization. This method linearizes the nonlinear model at each sampling instant. The linear model thus obtained

is expected to describe the dynamics better than the one, obtained from linearizing only once.

Using the first-order Taylor expansion of (2)–(3), we obtain the following set of linear equations:

$$\dot{x}(t) = \dot{x}_0 + \dot{\tilde{x}}(t) = f(x_0, u_0) + A\tilde{x}(t) + B\tilde{u}(t)$$

$$y(t) = y_0 + \tilde{y}(t) = g(x_0, u_0) + C\tilde{x}(t) + D\tilde{u}(t) + d(t),$$

where x_0, u_0 are the nominal states and inputs around which we linearize, and $\tilde{x}(t)$, $\tilde{u}(t)$ the deviations from these nominal values. Furthermore,

$$A := \left.\frac{\partial f(x, u)}{\partial x}\right|_{x=x_0, u=u_0} \qquad B := \left.\frac{\partial f(x, u)}{\partial u}\right|_{x=x_0, u=u_0}$$

$$C := \left.\frac{\partial g(x, u)}{\partial x}\right|_{x=x_0, u=u_0} \qquad D := \left.\frac{\partial g(x, u)}{\partial u}\right|_{x=x_0, u=u_0}$$

Let Φ, Γ (C and D) denote the discrete-time versions of these matrices. Similarly, $[f(x_0, u_0)]_d$ denotes the discrete-time version of $f(x_0, u_0)$, which is obtained by integrating (2) for one sample interval with the initial condition of $x = x_0$ and constant inputs u_0.

This yields the discrete-time model representation

$$\begin{bmatrix} x(k+1) \\ d(k+1) \end{bmatrix} = \begin{bmatrix} \Phi & 0 \\ 0 & I \end{bmatrix} \begin{bmatrix} x(k) \\ d(k) \end{bmatrix} + \begin{bmatrix} \Gamma \\ 0 \end{bmatrix} u(k) + \begin{bmatrix} 0 \\ K_F \end{bmatrix} q(k) + \begin{bmatrix} [f(x_0, u_0)]_d \\ 0 \end{bmatrix}$$

$$y_m(k+1) = \begin{bmatrix} C & I \end{bmatrix} \begin{bmatrix} x(k+1) \\ d(k+1) \end{bmatrix} + Du(k) + g(x_0, u_0)$$

$$q(k) = y_p(k) - y_m(k),$$

which includes an output disturbance filter. The output disturbances $d(k+1)$ are obtained from a first-order integrating filter K_F with $q(k)$ as input, with K_F taken to be a diagonal matrix. Furthermore, y_p are the process output measurements, and y_m the corresponding model outputs. All of our regulated variables are assumed to be measured, and no system or measurement noise is assumed to be present.

The elements of K_F should be chosen somewhere between 0 and 1. Taking these filter constants close to 1 is useful only if the process measurements are quite accurate. We chose to take the filter gains equal to 0.1, to allow for some difference between model and process.

We obtain x_0 and u_0 from $x(k)$ and $u(k)$, but one could also choose to reconstruct x (and u) from process measurements y_p, naturally in conjunction with a noise filter.

Nonlinear Prediction. This approach uses a nonlinear model to predict the output response to previous control moves, but is no different from linear MPC otherwise. Though formally not correct, this approach (and the following) relies on the premise that the superposition theorem—which is valid for linear systems—still holds to a reasonable extent. The method requires execution-times, which—depending on the efficiency of the nonlinear integration algorithm—more or less severely exceed those of the method of successive linearization.

Nonlinear Prediction and Successive Linearization. Computationally even more demanding is the combination of nonlinear prediction and successive linearization. This approach should combine the benefits of using an updated linear model to perform the optimizations on the one hand, and obtaining output predictions from the nonlinear model on the other.

Results

In this section we present results obtained with the various methods we described. We compare these results to those obtained with linear MPC, and state execution times. In all figures, 1 × lin stands for linearizing once (=linear MPC), sl is short for successive linearization, nlp denotes the case where nonlinear prediction is used, and nlp + sl refers to the combination of nonlinear prediction and successive linearization. Furthermore, the solid (step-shaped and straight) lines correspond to setpoints and temperature constraint. We assume this to become clear from the accompanying text. Throughout the simulations, the prediction and control horizon were chosen to be 15 and 4 samples, respectively. Finally, we mention the fact that valve positions can vary between 0 (closed) and 1 (fully opened).

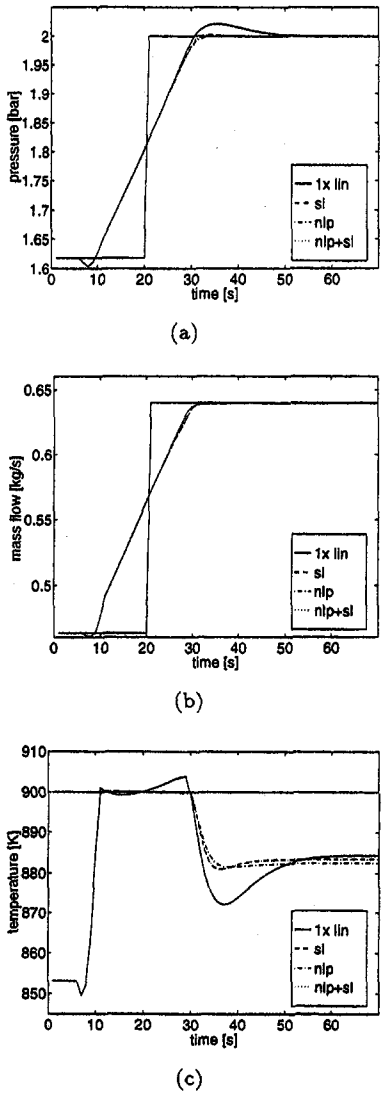

Fig. 4 Compressor pressure (*a*), compressor mass flow (*b*), and expander inlet temperature (*c*) response to setpoint rises in pressure and mass flow

Simple Setpoint Change. Figure 4 shows the response to setpoint changes in compressor pressure from 1.62 to 2.00 (bar), and in compressormass flow from 0.464 to 0.640 (kg/s), both at $t = 20$ (s). Corresponding valve-positions are shown in Fig. 5. All approaches give satisfactory results, although the pressure response obtained with linear MPC displays quite some overshoot. Indeed, all controllers anticipate to future set-point changes. Note, however, that all controllers make the outputs move initially in the wrong direction, so as to make the rises as steep as possible. This effect has been seen to decrease if larger control horizons are used. Also note that these setpoints can be attained with different combinations of inputs. Due to blow-off, the mass flows through

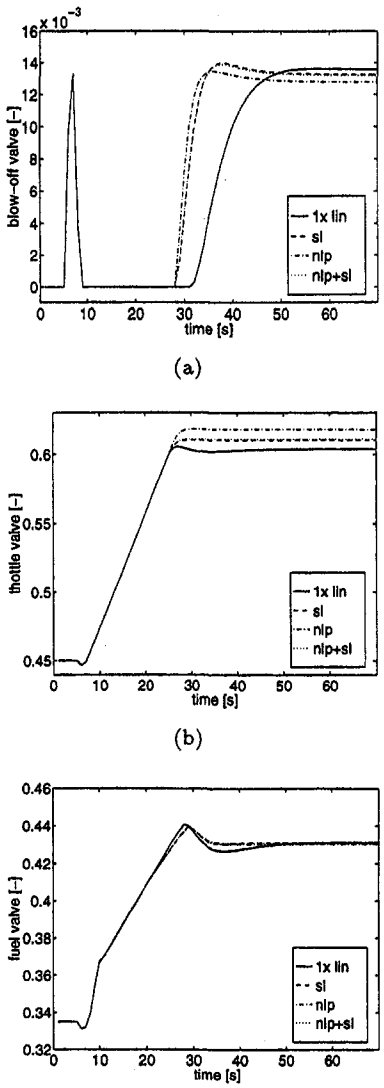

Fig. 5 (*a*) Blow-off, (*b*) throttle, and (*c*) fuel valve for setpoint rises in pressure and mass flow

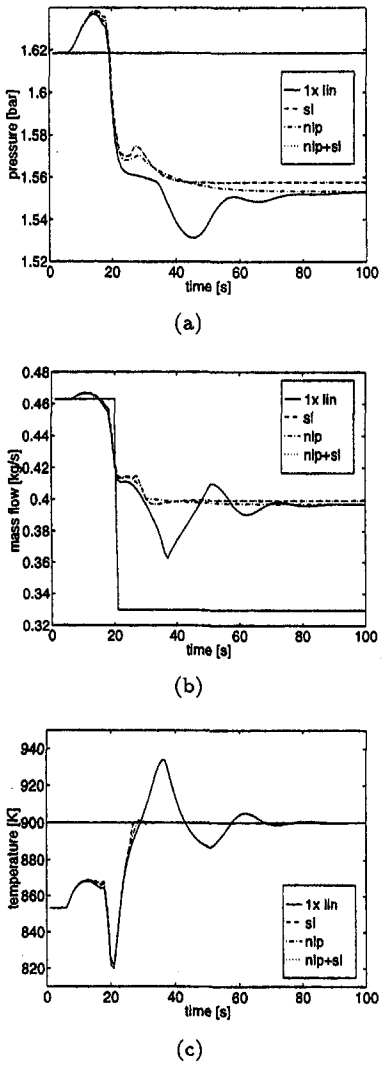

Fig. 6 (*a*) compressor pressure, (*b*) compressor mass flow, and (*c*) expander inlet temperature, response for "unreachable setpoint"

compressor and expander may not be the same, resulting in, for instance, different stationary temperatures. An interesting situation, in this sense, arises if gas turbine efficiency is required to be maximal. In this case, this can quite easily be achieved by imposing a constraint upon the blow-off valve (or similarly, the mass flow through this valve) at 0. This causes the blow-off valve to remain fully closed most of the time, while the steady-state fuel valve position drops from 0.43 to 0.42 (not shown).

The temperature constraint is violated by linear MPC only, though not by the model output—only by the process output. Of course, the process output is really all we are interested in, but this does explain the fact that in the constraint handling strategy, as stated in the previous section, step 3 is never executed in this simulation.

The three nonlinear methods we incorporated do not outperform one another, although they take different execution times, see Table 1. Although the nonlinear methods require execution-times in excess of that which is available for real-time implementation (1 (s)), one must bear in mind that these results were obtained on a Pentium133/32 Mb. Especially the two methods which incorporate successive linearization yield results very much alike. All this suggests that it is of significant importance to predict outputs by using some ("semi") nonlinear model. Furthermore, if successive linearization is used for the optimization, results are hardly dependent on the method of prediction (successive linearization or nonlinear).

Table 1 Maximum controller execution-time per sample

	1× lin	sl	nlp	nlp+sl
execution-time [s]	0.5	1.2	2.3	3.0

Unreachable Setpoint. We next specify a combination of setpoint changes, which simply cannot be realized. Mass flow is supposed to drop to 0.330 (kg/s), while keeping a constant pressure. This point would not only result in a temperature constraint violation, but also in surge. Figure 6 shows the resulting responses. Of course, in all cases pressure does not retain its initial value, whereas mass flow does not decrease as far as we wanted it to. This is exactly what we expected from the controller, in order not to violate constraints. However, linear MPC encounters serious trouble, as it cannot keep expander inlet temperature from reaching values in excess of 930° K. The surge constraint is almost reached (not shown), but is kept from doing so by the controller actions which serve to prevent temperature constraint violations. Again, sl and nlp + sl are hardly distinguishable.

Simple Setpoint Change With Model Errors. Finally, we repeat the "simple setpoint change" simulation, but different in the

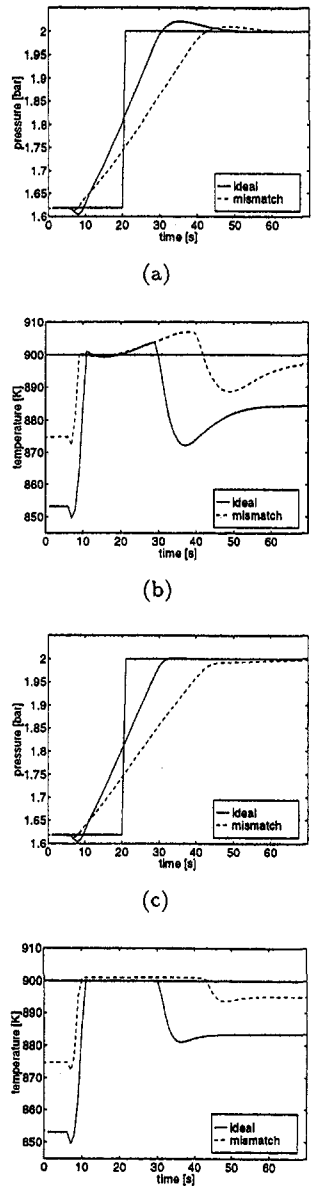

Fig. 7 Effect of model error on compressor pressure and expander inlet temperature response to setpoint changes as in Fig. 4; 1 × lin: *(a, b), sl: (c, d), respectively*

fact that we introduced parametric plant/model mismatch. This is not a rigorous test of robustness, but gives one an idea of the sensitivity of each method to modeling errors. We changed some of the most important parameters (such as compressor efficiency) by 5 to 20 percent. Figure 7 shows that both linear and nonlinear MPC yield results which are acceptable. Here we compared linear MPC to successive linearization only, considering the close resemblances we already experienced in the previous simulations.

Note that, even in case of successive linearization, the temperature constraint is slightly violated for some time, which is due to the fact that filter actions cannot adequately compensate for the differences between model and process, because controller actions in this time interval ($t \in [10, 42]$) are still quite severe (not shown). This situation would not occur if the expander temperature in this time interval corresponded to a (nearly) stationary situation.

Discussion

We presented three nonlinear extensions to linear model predictive control, the last of these resulting in the same approach Garcia (1984) used. We also incorporated the same output disturbance model encountered in that paper, and stress that—though not especially relevant to our problem—this strategy may not perform well in controlling integrating processes and may lead to instabilities when applied to open-loop unstable processes. To prepare for real-time implementation, we are currently researching the incorporation of a Kalman filter in the on-line optimization, to allow for reconstruction of unmeasured variables as well as to handle measurement noise.

The three nonlinear methods all offer improvements over linear MPC, with results in fact almost identical most of the time. This conclusion would favour whichever approach is computationally the least demanding. Most likely, the method which incorporates successive linearization, but refrains from nonlinear prediction, requires the least computational effort. Nevertheless, the execution-times stated should be viewed with scepticism, since the various algorithms involved can probably all be made more efficient, one way or another. For instance, using a more efficient integration routine would speed up the methods using nonlinear prediction, whereas a more efficient QP solver would contribute to reducing the requirements for successive linearization.

Judging from the simulations, it is concluded that, if no measurement noise is present and if the model describes the process fairly well, linear MPC is suited to control the gas turbine installation most of the time, requiring execution-times within the prespecified limit of 1 (s) per sampling period. The benefits MPC offers, such as anticipation, input/output constraint handling, were shown to hold for all approaches investigated. Still, some situations may cause linear MPC to perform significantly worse, situations where nonlinear extensions offer considerable improvements. However, for the time being, none of these nonlinear methods can be made to require execution-times within the limit of 1 (s), although sl is not far from achieving this goal. In practice, the somewhat arbitrarily set bound of 1 (s) might be slightly increased or, alternatively, a faster computer may be used to render at least sl 'feasible'.

It should still be investigated if the approaches mentioned can be guaranteed to improve controller performance at all times, especially in a real-time application, where measurement noise is present and robustness of the control algorithm becomes increasingly important. Although the various methods were shown to possess some kind of robustness, more rigorous tests should point out if this result holds for a larger class of model uncertainties.

Acknowledgment

The authors gratefully acknowledge TNO-TPD at Delft for their support and for providing the PRIMACS software.

References

Bequette, B. W., 1991, "Nonlinear Control of Chemical Processes: A Review," *Ind. Eng. Chem. Res.*, Vol. 30, No. 7, pp. 1391–1413.

Brengel, D. D., and Seider, W. D., 1989, "Multistep Nonlinear Predictive Controller," *Ind. Eng. Chem. Res.*, Vol. 28, No. 12, pp. 1812–1822.

Botros, K. K., Campbell, P. J., and Mah, D. B., 1991, "Dynamic Simulation of Compressor Station Operation Including Centrifugal Compressor and Gas Turbine," ASME JOURNAL OF ENGINEERING FOR GAS TURBINES AND POWER, Vol. 113, pp. 300–311.

De Oliveira, N. M. C., and Biegler, L. T., 1995, "An Extension of Newton-Type Algorithms for Nonlinear Process Control," *Automatica*, Vol. 31, No. 2, pp. 281–286.

Garcia, C. E., 1984, "Quadratic Dynamic Matrix Control of Nonlinear Processes: An Application to a Batch Reaction Process," presented at the 1984 AIChE Annual Meeting, San Francisco, CA.

Gattu, G., and Zafiriou, E., 1992, "Nonlinear Quadratic Dynamic Matrix Control With State Estimation," *I & EC Res.*, Vol. 31, No. 4, pp. 1096–1104.

Lee, J. H., and Ricker, N. L., 1993, "Extended Kalman Filter Based Nonlinear Model Predictive Control," Proceedings, Amer. Contr. Conf., pp. 1895–1899.

Li, W. C., and Biegler, L. T., 1989, "Process Control Strategies for Constrained Nonlinear Systems," *Ind. Eng. Chem. Res.*, Vol. 27, No. 8, pp. 1421–1433.

Morari, M., Garcia, C. E., Lee, J. H., and Prett, D. M., 1991, "Model Predictive Control," *Prentice-Hall*, Englewood Cliffs, NJ.

van Essen, H. A., 1995, "Design of a Laboratory Gas Turbine Installation," ISBN 90-5282-452-5, Eindhoven University of Technology.

Vroemen, B. G., 1997, "Model Predictive Control of a Gas Turbine Installation," technical report WFW 97.002, Eindhoven University of Technology.

CO_2 Emission Abatement in IGCC Power Plants by Semiclosed Cycles: Part A—With Oxygen-Blown Combustion

P. Chiesa

G. Lozza

Dipartimento di Energetica,
Politecnico di Milano,
Piazza Leonardo da Vinci 32,
Milan, 20133, Italy

This paper analyzes the fundamentals of IGCC power plants where carbon dioxide produced by syngas combustion can be removed, liquefied and eventually disposed, to limit the environmental problems due to the "greenhouse effect." To achieve this goal, a semiclosed-loop gas turbine cycle using an highly-enriched CO_2 mixture as working fluid was adopted. As the oxidizer, syngas combustion utilizes oxygen produced by an air separation unit. Combustion gases mainly consist of CO_2 and H_2O: after expansion, heat recovery and water condensation, a part of the exhausts, highly concentrated in CO_2, can be easily extracted, compressed and liquefied for storage or disposal. A detailed discussion about the configuration and the thermodynamic performance of these plants is the aim of the paper. Proper attention was paid to: (i) the modelization of the gasification section and of its integration with the power cycle, (ii) the optimization of the pressure ratio due the change of the cycle working fluid, (iii) the calculation of the power consumption of the "auxiliary" equipment, including the compression train of the separated CO_2 and the air separation unit. The resulting overall efficiency is in the 38–39 percent range, with status-of-the-art gas turbine technology, but resorting to a substantially higher pressure ratio. The extent of modifications to the gas turbine engine, with respect to commercial units, was therefore discussed. Relevant modifications are needed, but not involving changes in the technology. A second plant scheme will be considered in the second part of the paper, using air for syngas combustion and a physical absorption process to separate CO_2 from nitrogen-rich exhausts. A comparison between the two options will be addressed there.

1 Introduction

The increasing concern about climatic changes, due the dispersion in the atmosphere of "greenhouse" gases produced by human activities, poses a formidable challenge to the power industry. Fossil fuels will remain the largest source of primary energy for many decades, according to any reasonable long-term projection. Therefore, carbon dioxide will be largely produced in the future, but its dispersion to the atmosphere can be avoided, provided that it is separated from other combustion products, collected and then ducted to underground storage or to deep sea for absorption. This objective can be pursued by various processes, all requiring a substantial amount of energy (thus reducing the conversion efficiency) and of additional equipment (thus increasing costs). Most studies (including the present paper) were devoted to coal-fired power stations, because coal is (i) the most widely used fossil fuel for power generation, (ii) the most abundant in terms of worldwide resources, (iii) a large CO_2 producer, if compared to natural gas.[1] Three methodologies have been proposed up to now:

— removal of CO_2 from exhausts of conventional power stations, for instance by means of ammine chemical absorption (Smelser et al., 1991), cryogenic distillation (U.S. Department of Energy, 1993), membrane separation (Van der Sluijs et al., 1992)

— coal gasification followed by catalytic shift, producing CO_2 and H_2 from CO and H_2O: therefore, CO_2 can be separated by relatively low-cost physical absorption systems before being ducted to the gas turbine, which essentially uses hydrogen as fuel (Schütz et al., 1992; Chiesa and Consonni, 1999)

— cycles using enriched CO_2 mixtures as working fluid, usually employing pure oxygen as oxidizer: in this case, after condensation of water produced by combustion, the remaining working fluid is essentially carbon dioxide which can be easily removed and disposed (De Ruyck, 1992; Mathieu and DeRuyck, 1993; Ulizar and Pilidis, 1996, 1997; Chiesa and Lozza, 1997b). Oxygen combustion can be also applied to conventional boilers (Nakayama et al., 1992)

At present, little information is available to fully understand the merits and the drawbacks of each solution. However, according to McMullan et al. (1995), solutions based on gasification and gas turbine-derived cycles are of particular interest. This paper, divided into two parts, will consider two plant configurations: the first one (part A) fully belongs to the third group exposed above, while the second one (part B), using air as oxidizer rather than oxygen and including a physical absorption system to remove CO_2 from moderately enriched exhausts, represents a connection point between the two latter concepts.

The latter plant scheme represents a novel proposal, the former has already been addresses by some of the authors quoted above. We will consider here the power cycle, the complete gasification process, the oxygen production, and the CO_2 separation and compression as a whole, accounting for their interactions. Therefore, we will be able to assess the overall coal-to-electricity conversion

[1] Coal produces about 0.35 kg of CO_2 per kWh of thermal energy (a correct value depends on its actual composition), a figure 70 percent higher than natural gas. In terms of electricity the difference is larger due the higher conversion efficiency obtainable by combined cycles versus steam plants.

Contributed by the International Gas Turbine Institute (IGTI) of THE AMERICAN SOCIETY OF MECHANICAL ENGINEERS for publication in the ASME JOURNAL OF ENGINEERING FOR GAS TURBINES AND POWER. Paper presented at the International Gas Turbine and Aeroengine Congress and Exhibition, Stockholm, Sweden, June 2–5, 1998; ASME Paper 98-GT-384.

Manuscript received by IGTI March 23, 1998; final revision received by the ASME Headquarters June 23, 1999. Associate Technical Editor: R. Kielb.

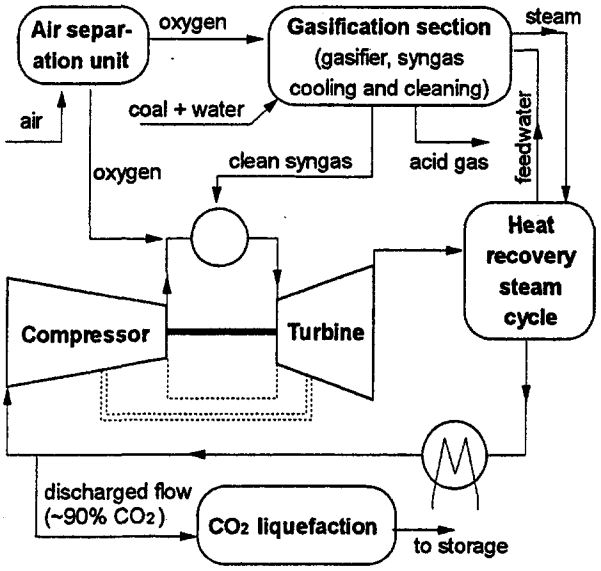

Fig. 1 Conceptual overview of the semiclosed cycle here analyzed, with oxygen combustion

efficiency, in power plants producing CO_2 as a separated stream, available for disposal without further energy expenses.

2 Conceptual Plant Configuration

To better understand the cycle concept here referred (semiclosed cycle with oxygen combustion), let's first consider Fig. 1, showing a very simplified scheme. The blocks of the figure perform the following tasks:

- a complete coal gasification section produces clean syngas from coal under the "usual" conditions of an IGCC plant: therefore, this block consists of a coal treatment plant, a gasifier, a syngas cooling system, and various syngas filtering devices (wet scrubbing, acid gas removal, sulfur plant)
- syngas is burned into the gas turbine combustor using oxygen as the oxidizer: combustion products mainly consist of CO_2 and H_2O
- after turbine expansion and heat recovery steam generator (feeding the steam cycle), combustion gases are cooled to remove H_2O by condensation: the remaining stream is almost pure CO_2 (about 90 percent mass fraction)
- part of this stream, such to conserve the mass balance of the cycle, exits the power cycle; the remainder is recycled, after compression, as a diluting agent to gas turbine combustion
- the stream removed from the cycle is compressed up to liquefaction of CO_2, rendering it available for storage or disposal
- oxygen necessary to gasification and to syngas combustion is produced by a double-column air-separation-unit (ASU)

Carbon dioxide is the main component of the cycle working medium: the virtual absence of nitrogen in the combustion process leads to negligible NO_x formation, while sulfur is very efficiently captured in the IGCC process. Therefore, being CO_2 sequestrated, the plant is virtually free of any kind of air pollution.

Before addressing with more detail the plant configuration, let us recall briefly the main features of the method of calculation used for predicting the on-design overall performance and the energy balance of the plant. It was described in previous papers, with reference to the gas turbine model (Macchi et al., 1991; Consonni, 1992), the steam plant model (Lozza, 1990), and the system used to analyze gasification processes (Lozza et al., 1996). Its main features are (i) capability of reproducing very complex plant schemes by assembling basic modules, such as turbine, compressor, combustor, steam section, chemical reactor, heat exchanger, etc., (ii) built-in correlations for efficiency prediction of turbomachines, as a function of their operating conditions, (iii) built-in correlations for predicting cooling flows of the gas turbine, and (iv) calculation of gas composition at chemical equilibrium. A peculiarity of the present method is its ability to reproduce a whole IGCC process in a single computer run, without any need of "matching" results coming from different computational tools: it enables the possibility of studying heavily integrated processes and of performing a complete second law analysis of the entire plant. To preserve this peculiarity, a new module was added to consider the compression of a gas mixture in which CO_2 is treated as a real gas (including phase change). Therefore, ideal gas behaviour is assumed for all gaseous species, with the exceptions of water/steam in the steam cycle module and of carbon dioxide during its final compression and liquefaction. More details are given in 3.4.

The assumptions used for calculating the performance of the various components are fully reported in a recent paper (Chiesa and Lozza, 1997a). During the next chapter, we will recall and discuss the most important assumptions for each plant section.

3 Detailed Plant Description and Assumptions

Once discussed the basics, a deeper understanding of the plant configuration is necessary to perform a comprehensive thermodynamic analysis. Figure 2 provides a complete overview of the various plant sections and of their interaction. Let us now discuss the arrangement of the various blocks, by outlining the main assumptions necessary to calculate their performance.

3.1 Air Separation Unit. We will refer to conventional ASU processes, consisting of an air intercooled compressor (exit pressure was assumed as 4.8 bar, according to Rao (1993), compatible with a 95 percent oxygen purity in large plants) and of a double separation column providing gaseous nitrogen (dispersed to the ambient) and gaseous oxygen at near-atmospheric pressure. Oxygen must be compressed before being used: we stipulated a maximum oxygen temperature of 340°C,[2] so the compression has to be partly intercooled. Due to the large oxygen requirement, the air compressor is directly driven by the gas turbine, to save expensive electric machinery and related power losses. Other ASU arrangements, sometimes found in IGCC plants (Smith et al., 1996), making use of compressed air from the gas turbine compressor, are not feasible here, due to the lack of oxygen in the cycle working fluid. The air compressor efficiency is relevant to the overall power balance: being its volume flow compatible with axial multi-stage machines, the general correlation for compressor polytropic efficiency estimation developed by the authors (Chiesa et al., 1995) was used.

3.2 Gasification Section. In this paper we will refer to an entrained-flow slurry-feed gasifier, reproducing the Texaco technology. Coal used is Illinois #6, with 3.4 percent sulfur content. The thermal input to the plant was set to 900 MW_{th} (36.25 kg/s of coal with LHV = 24.826 MJ/kg). Gasification pressure and temperature were assumed of 60 bar and 1600 K. Oxygen supply was calculated to actually obtain such a temperature with a gas composition imposed by the chemical equilibrium, considering a water/coal ratio in the slurry of 0.323. Raw syngas is cooled by radiative-convective syngas coolers, producing high pressure saturated steam and high temperature feedwater, the latter partly used to rise the temperature of clean syngas before combustion. Raw syngas is therefore cleaned by a wet scrubber. Low temperature

[2] The higher the temperature of oxygen for both combustion or gasification, the lower the fuel consumption to obtain the same combustion products. This overrides the larger compression work, increasing the cycle efficiency. However, a conservative value of oxygen temperature was stipulated to reduce hazards and risks of material corrosion.

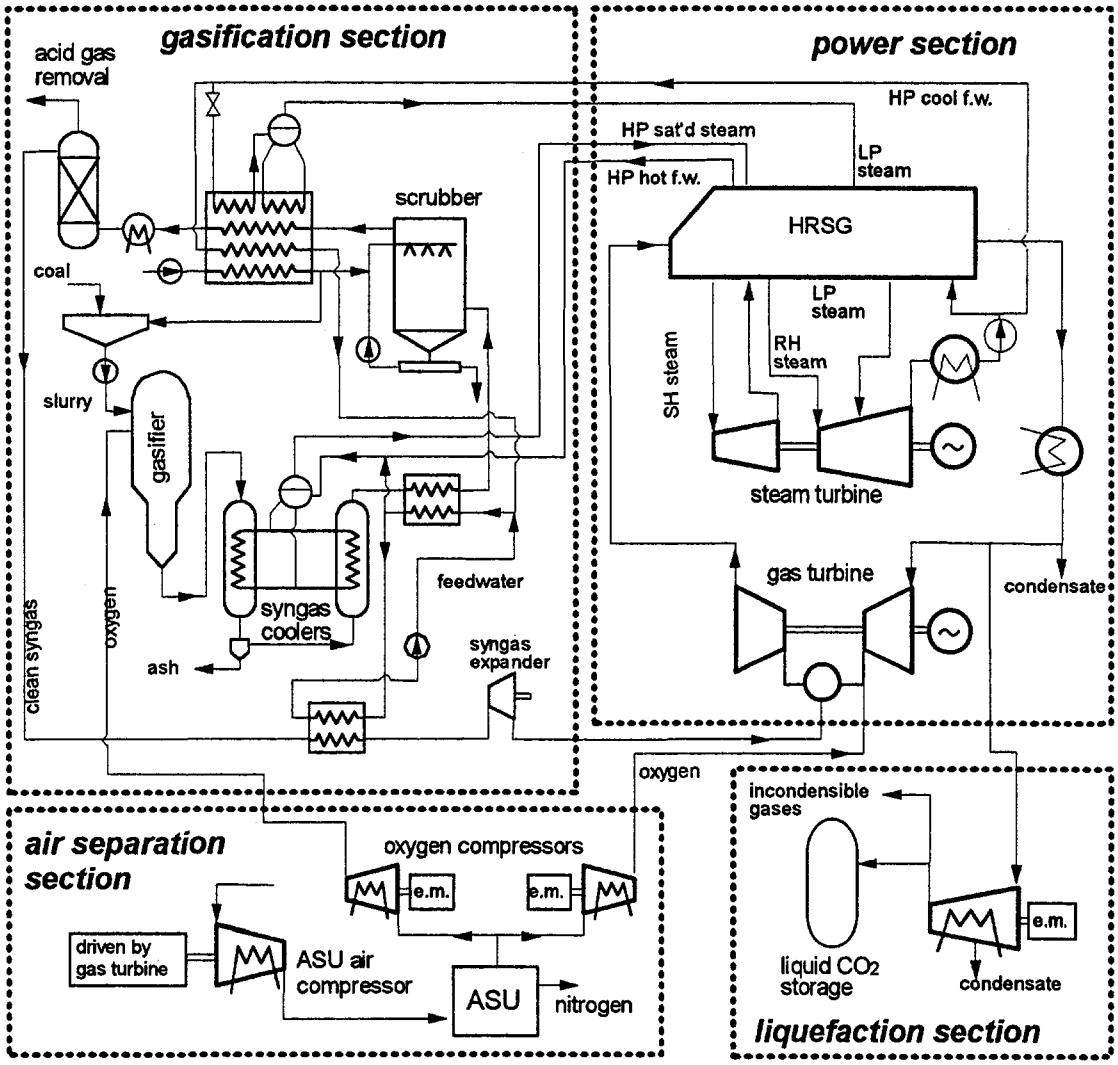

Fig. 2 Complete plant configuration of the semiclosed cycle with oxygen combustion here discussed

heat is recovered from syngas for various purposes (feedwater heating, make-up water heating, low pressure steam generation). Acid gases are removed from near-ambient temperature syngas and then treated to produce sulphur by means of processes well known in the IGCC practice. Clean syngas is preheated by the above quoted feedwater supply and therefore expanded, depending on the combustion pressure. Details on the calculation method and on the assumptions (heat exchangers effectiveness, pressure and thermal losses, etc.) have been quoted in previous papers (Lozza et al., 1996; Chiesa and Lozza, 1997a).

For this application, we did not consider any fuel dilution strategy for NO_x abatement (i.e., by moisturization or by nitrogen addition) due to the very low nitrogen concentration in the combustion region.

3.3 Power Plant. A semiclosed-cycle gas turbine is the key machine. Assumptions regarding its performance prediction (i.e., compressor and turbine polytropic efficiency, coolant requirement and cooled expansion modelization, pressure losses, etc.) have been calibrated during previous works (Macchi et al., 1991; Chiesa et al., 1995; Chiesa and Lozza, 1997a) to accurately reproduce the performance of modern gas turbines. We will make here reference to the today's proven technology of "F" industrial gas turbines: in particular, a TIT of 1280°C was stipulated for all considered solutions. In those conditions, a comparison between manufacturers' data and our predictions (with natural gas as fuel) shows a very close agreement,[3] confirming the reliability of the correlations when applied to open cycles.

We supposed here that the change of the working fluid will not affect the validity of the correlations used for calculating turbomachinery polytropic efficiency and cooling requirements of the hot parts of the turbine (Consonni, 1992; Chiesa et al., 1995). To be more clear, this does not mean that cooling flows and efficiencies remain constant between open and semiclosed cycle: the parameters governing the correlations are recalculated according to the actual values of volumetric flow, transport properties, etc.

However, the change of the working fluid claims for a novel optimization of the cycle. The most important parameter to be considered is the pressure ratio: the higher molecular mass and complexity of CO_2 mixtures versus air results in a lower temperature rise at the same pressure ratio. Since cycle performance mainly depends on the temperature history of the fluid, an higher pressure ratio will be required to obtain the same efficiency. To discuss this issue, the pressure ratio will be varied during the analysis from the basic value of 15, typical of large industrial "F" machines.

A possible variation to the scheme shown in Fig. 2 consists of

[3] For instance, calculations of the GE Fr.9FA with a TIT of 1288°C (Miller, 1996) show an error as low as 0.3 percent on power output, 0.3 points on efficiency, 2°C on turbine outlet temperature.

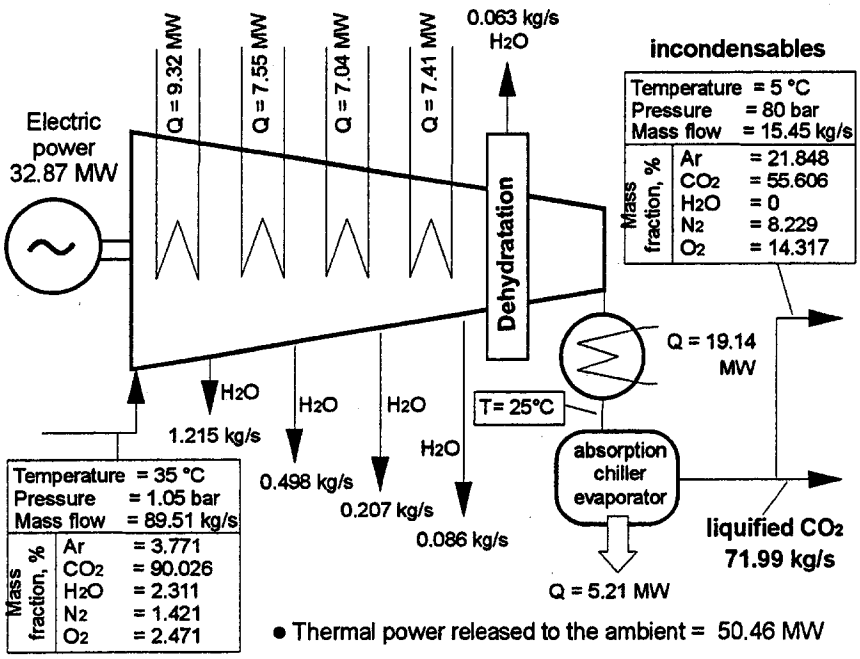

Fig. 3 Energy and mass balance of the carbon-dioxide compression/liquefaction train used for scheme A. Data are referred to a cycle pressure ratio of 30, with a thermal input of 900 MW (coal LHV).

moving the oxygen injection point from the compressor outlet to the compressor suction. In this mode, oxygen compression is performed by the same gas turbine compressor, rather than by a separated unit, with higher efficiency and lower plant complexity. However, the cooling flows, retrieved from the compressor, are enriched in oxygen, providing a lower CO_2 concentration in the exhausts: this increases the energy requirement for both air separation and CO_2 liquefaction. This issue was discussed in a previous paper (Chiesa and Lozza, 1997), showing a negligible influence on the overall efficiency, and will not be addressed further here.

The heat recovery steam cycle is a conventional combined cycle unit, based on a three-pressure reheat cycle. The method of calculation of the bottoming cycle and its optimization have been addressed by Lozza (1990 and 1993). Steam conditions here assumed are rather conservative: the maximum pressure is 110 bar, with SH and RH at 538/538°C and a condensing pressure of 0.05 bar. A somewhat better efficiency may be obtained by resorting to more elevated steam conditions (for instance, slightly supercritical pressure and 565 or 580°C, according to the above quoted papers and to the better steam technology): we decided here not to stress the technological issues in an already complicated and risky plant configuration. It must be also considered that the here adopted values are rather common even in the more advanced natural gas and coal gasification combined cycle presented up to now.

3.4 Carbon Dioxide Liquefaction. We will assume here that separated carbon dioxide must be available at the plant boundaries at a pressure of at least 80 bar and in liquid phase. This is necessary to allow for deep sea disposal without further energy expenses. The exhaust stream retrieved from the cycle can be simply compressed to achieve this goal. However, incondensable species (N_2, O_2, Ar) are present in this stream, increasing the compression power. Their amount depends on various parameters: (i) the above quoted position of the oxygen injection point, (ii) the oxygen purity, and (iii) the oxygen exceeding the stoichiometric combustion to ensure complete fuel oxidation. According to our calculations, an increase of the oxygen purity (beyond the assumed value of 95 percent) will require an higher ASU consumption, vanishing the savings in the liquefaction process. A 3 percent oxygen concentration by volume after combustion was stipulated, believing it sufficient to make CO production negligible. In addition to incondensables, water vapour is also present: its initial amount depends on the water partial pressure in the exiting stream, and particularly on its temperature, here assumed as 35°C after cooling of the entire exhaust flow. Under those assumptions, the exhaust composition is fixed and reported in Fig. 3, showing the energy and mass balance of the liquefaction system. Water is separated by condensation and by dehydration.

To improve CO_2 removal efficiency, the gaseous CO_2 fraction in the incondensables (wasted to the ambient) should be minimized. To achieve this goal, two ways are possible: (i) increasing the final pressure, thus the energy consumption; (ii) cooling down the stream. The compression train shown in Fig. 3 includes an absorption refrigerating unit, to obtain a final temperature of 5°C: the same removal efficiency (89.4 percent) would have required a final pressure of 132 bar (rather than 80) at 25°C, with a 10 percent higher power consumption. Low temperature heat needed by the absorption chiller (about 8 MW_{th}) can be easily retrieved from the compression train intercoolers without significant energy expenses. A further improvement of removal efficiency is possible: for instance, 96 percent can be achieved with a final pressure of 145 bar, requiring about 37 rather than 33 MW_e (approximately a 1 percent reduction of the plant net output).

About thermodynamic properties, the ideal gas assumption used for the power cycle cannot be realistic here. CO_2 properties were calculated by the corresponding state law (acentric factor = 0.239, Reid et al., 1988) with saturation curve from Casci et al. (1972). H_2O properties from Schmidt, 1982 (as used for the steam cycle). We assumed (i) ideal mixtures (i.e., mixing does not alter volumetric properties), (ii) Ar, N_2, O_2 as ideal gases, (iii) negligible liquid solubility in gases, and (iv) H_2O and CO_2 condensation rates according to the Raoult law.

4 Overall Plant Performance

4.1 General Overview. The results of the performance prediction are shown in Fig. 4 for various cycle pressure ratios. In the figure, two efficiency curves are shown: the upper dotted curve does not consider the power expenses for compression-

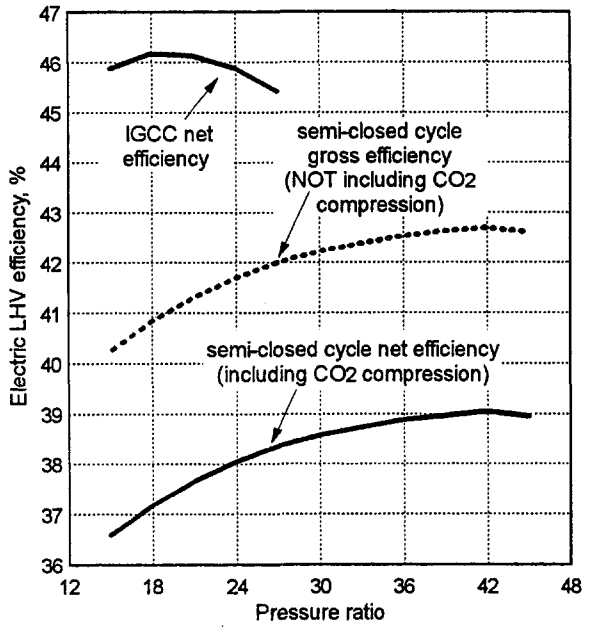

Fig. 4 Influence of the cycle pressure ratio on the efficiency of IGCC and semiclosed cycles

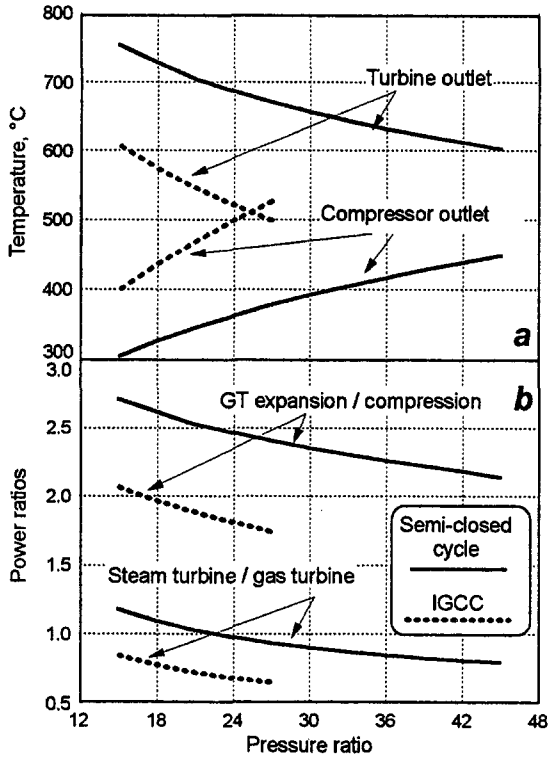

Fig. 5 Turbine and compressor outlet temperatures, expansion/compression and steam/gas turbine power ratios for IGCC and semiclosed cycles, as a function of the pressure ratio

liquefaction of carbon dioxide, the lower curve represents the overall net plant efficiency. In addition, Fig. 4 quotes, as a reference, the performance of IGCC cycles based on the same gasification and power cycle technology, but not including any CO_2 removal strategy.

The loss of efficiency resulting from the adoption of CO_2 capture systems is severe, from about 46 percent of IGCC to about 39 percent at optimum pressure ratio. We can justify the efficiency decay by the following three considerations:

(i) CO_2 separation itself yields to a power loss, even if carried out by a reversible process and even if the separated gases would be available at ambient pressure, rather than pressurized. The production of separated species is, as a matter of facts, another "thermodynamic asset" (in addition to electricity) generated by the cycle. Its value corresponds to the mechanical work required by the reversible separation (isothermal compression from the partial to the total pressure). Referring to the IGCC exhausts ($\beta = 15$), this work is 196.4 kJ/kg of CO_2 (90 percent removal efficiency), yielding to 14.1 MW consumption: this brings the efficiency of an IGCC with ideal separation to 44.3 percent versus the original 45.9 percent.

(ii) CO_2 is compressed up to 80 bar, by means of a real machine: therefore, ideal isothermal compression work plus losses due to irreversibilities during the process are to be considered. This power consumption corresponds, in terms of efficiency loss, to the "distance" between the continuous and the dotted line of Fig. 4.

(iii) Another relevant source is related to the large oxygen consumption, here about 2.6 times the one of an IGCC. Irreversibilities of the ASU process are therefore much more detrimental to the overall efficiency. In fact, the air separation unit requires 868 kJ/kg of oxygen produced (under our assumptions), rather than 197 needed by a reversible process.

4.2 Influence of the Cycle Pressure Ratio. The above mentioned losses are largely independent on the power cycle thermodynamics. As far as this issue is concerned, the most important parameter is the pressure ratio (β) of the gas turbine cycle. Its influence is clearly shown in Fig. 4. The best performance of an IGCC plant is obtained at $\beta = 18$: the use of a lower pressure ratio of 15 (often found in large commercial heavy-duties) does not impair the plant efficiency in a significant way. On the contrary, the present scheme requires a much larger pressure ratio: the best value is 42, while 2.4 points of efficiency would be lost at $\beta = 15$. The reason of this discrepancy is the change of the working fluid composition, i.e., the increase of the molecular mass due to higher CO_2 content. In fact, Fig. 5(a) shows that, at the same pressure ratio, the CO_2 cycle presents consistently lower compressor outlet temperature and higher turbine outlet temperature: higher pressure ratios are therefore required to optimize the cycle, obtaining the same temperature levels found in IGCC and gas turbine practice. More information is given by Fig. 5(b): the power ratios between plant components indicate that, at the same β, more percentage power is produced by the steam turbine and less percentage power is consumed by the compressor. This is not favourable: for instance, at $\beta = 15$ a turbine outlet temperature of about 750°C would lead to substantial heat transfer irreversibilities in feeding heat to the steam plant, unable to operate efficiently at high temperatures, while a low compressor outlet temperature of 300°C, even if reducing compressor power consumption, improves combustion irreversibilities. At the optimum pressure ratio, both temperature and power ratios are similar to the ones of IGCCs.

In this discussion, the minimum cycle pressure was kept at near-atmospheric values, but it can be subject of optimization in a semiclosed cycle. We will address this issue in the second part of the paper, together with the cycle proposal discussed there.

4.3 Discussion of the "Reference" Scheme. In the following we will make reference to a pressure ratio of 30, as a compromise between performance and utilization of existing technologies ($\beta = 30$ is already used by aero-derived engines and by a modern reheat industrial unit). A pressure ratio of 15 was assumed for the IGCC case used for comparisons. The main characteristics of the selected plant are shown in Fig. 6. Together with information provided by Fig. 3 and by Table 1, reporting the electric power balance, we can comment that:

— the ASU air compressor has an inlet volume flow of 267 m^3/s, versus 328 of the cycle compressor: the two machines have a comparable size, justifying their single-shaft arrangement

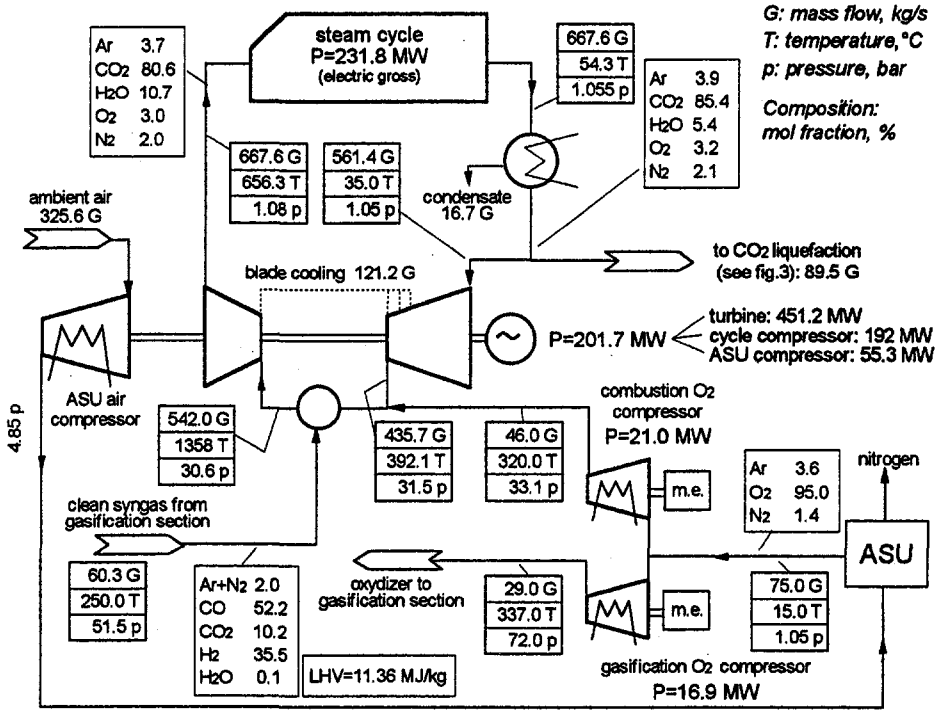

Fig. 6 Energy and mass balance of the power cycle and air separation components of the semiclosed cycle with oxygen combustion at a pressure ratio of 30

- the turbine mass flow is 19 percent higher than the one of the compressor (versus 10 percent for IGCC and 2 percent for natural gas machines), due to oxygen addition
- the CO_2 volume fraction is 85 percent (90 percent by weight): water and incondensables are not negligible during the liquefaction process, affecting the power requirement
- large part of the gross output is recycled into the process, because of the consumption of the air and oxygen compressors and of the liquefaction train (Table 1)
- a relevant part of the heat released to the ambient comes from the intercoolers of those compressors (114.8 MW_{th}, versus 365.7 from the condenser and 52.1 from the exhaust cooler). The total heat released to cooling waters is therefore 532.6 MW_{th}, i.e. 153 percent of the net electric power produced (the same percentage is 85 percent for the IGCC plant, due to its higher efficiency and to direct heat discharge at the stack)

Table 1 Electric power balance between the various plant components for the reference IGCC and the semi-closed cycle here addressed, for a thermal input of 900 MW by coal LHV

Plant type / Electric power, MW	Open IGCC, β=15	Semi-closed, β=30
Gas turbine gross output	247.8	257.0
Steam turbine gross output	209.5	231.8
Syngas expander	11.4	-
ASU air compressor	-23.7	-55.3
Oxygen compressor(s)	-16.9	-37.9
Power cycle auxiliaries	-5.7	-6.3
Gasification auxiliaries	-9.5	-9.3
CO_2 compression/liquefaction	-	-32.9
Net power output	412.9	347.1
Net LHV efficiency, %	45.88	38.57

5 Turbomachinery Design and Development

The plant economics cannot be fully discussed at the present status of the knowledge. However, the investment cost, compared to the one of IGCCs, will depend on two basic issues: (i) can the main equipment be derived from machines now present in the market? (ii) how many additional equipment will be required? We will discuss this matter by comparing the basic design specifications for the largest turbomachines included in the cycles, with particular regard to the main gas turbine engine. In fact, the change of the working fluid and of the pressure ratio poses some concern about the extent of modifications required to gas turbines developed for natural gas or, at most, for IGCC applications. Comparing the IGCC and the semi-closed cycle here proposed (Table 2), we can comment that:

- enthalpy rise/drop for both turbine and compressor differ by about 10 percent from the ones of IGCC: this difference may become negligible by selecting a pressure ratio slightly higher than 30 (improving the efficiency). This implies that the stage number and stage loading will remain unchanged. However, the velocity of sound of the CO_2 mixture is about 20 percent lower than for air: more detailed analyses are therefore needed, especially for highly loaded compressor stages.
- the changes of volume flow through the machines are very different: lower blade height (up to about one half) in high pressure stages will be necessary for CO_2 machines.
- the volume flow is significantly smaller for the same thermal input: more compact (and cheaper) machines can be adopted.
- the turbine cooling flows are 10–20 percent larger. This is due to the larger pressure and density: a more detailed discussion will be given in part B. However, the rate of increase is modest and remains within technical feasibility limits.

Extended modifications are therefore required, but a real change in the gas turbine technology is not necessary. Combustor design will also require adaptations, but a real advantage comes from the elimination of any NO_x control strategy, due to the virtual absence of nitrogen.

Table 2 also reports some data about the other compressors included in the cycles. The ASU air compressor results 2.6 times larger than for the IGCC, as already discussed, but, apart from size,

Table 2 Specifications involved in turbomachinery design, for the reference IGCC and semi-closed cycle

Plant type (input = 900 MW by coal LHV)	Open IGCC, β=15	Semi-closed, β=30
Gas turbine compressor		
Inlet volume flow, m^3/s	507.9	328.3
Inlet/outlet volume flow ratio	7.262	15.975
Isentropic enthalpy rise, kJ/kg	337.9	305.5
ASU air compressor		
Inlet volume flow, m^3/s	103.2	266.9
Real compression work, kJ/kg	176.7	169.4
CO_2 compressor		
Inlet volume flow, m^3/s	-	52.34
Real compression work, kJ/kg	-	335.6
Gas turbine		
Outlet volume flow, m^3/s	1633.9	1182.5
Turbine outlet / compressor inlet volume flow	3.217	3.602
First nozzle throat area, m^2	0.4433	0.1817
Turbine inlet / compressor inlet volume flow	0.351	0.1827
Isentropic enthalpy drop (cooled expansion), kJ/kg	1062	974.2
First nozzle cooling flow / gas flow (volume)	0.0256	0.0309
First rotor cooling flow / gas flow (volume)	0.0243	0.0265

it is a very conventional unit. The CO_2 compressor is an unconventional machine, but its development should not present particular technological issues.

6 Conclusions

The discussion here developed outlines the negative impact of CO_2 removal on the conversion efficiency and on the plant complexity, compared to the already capital-intensive and complicated IGCC stations. On another side, a virtually emission-free power production from coal can be realized, resorting to well-known technologies, with an efficiency very similar to the one of conventional steam power stations. A realistic economic study cannot be drawn at present, due to the difficulties of estimating the investment costs of components not available in the market. Among them, critical issues are the modified gas turbine, operating with an enriched CO_2 mixture, and the unusually large air separation unit. The necessity of adopting such components can be eliminated by using air rather than oxygen for syngas combustion and by introducing a separation process. The second part of the paper will discuss this concept and a comparison between the two plants, together with some final considerations, will be addressed.

References

Casci, C., Macchi, E., and Angelino, G., 1972, "Thermodynamic Properties of Carbon Dioxide," Tamburini Editore, Milan, Italy, (in Italian).

Chiesa, P., Lozza, G., Macchi, E., and Consonni, S., 1995, "An Assessment of the Thermodynamic Performance of Mixed Gas-Steam Cycles. Part A: Intercooled and Steam-Injected Cycles. Part B: Water-Injected and HAT Cycles," ASME JOURNAL OF ENGINEERING FOR GAS TURBINES AND POWER, Vol. 117, pp. 489–508.

Chiesa, P., and Lozza, G., 1997a, "Intercooled Advanced Gas Turbines in Coal Gasification Plants, with Combined or "HAT" Power Cycle," ASME Paper 97-GT-039.

Chiesa, P., and Lozza, G., 1997b, "Coal Power Plants with Semi-Closed Combined Cycle for CO_2 Removal: A Preliminary Study," Proceedings IX National Congress *Tecnologie e Sistemi Energetici Complessi—Sergio Stecco,* Milan, Italy, pp. 165–181, (in Italian).

Chiesa, P., and Consonni, S., 1999, "Shift Reactors and Physical Absorption for Low-CO_2 Emission IGCCs, " ASME JOURNAL OF ENGINEERING FOR GAS TURBINES AND POWER, Vol. 121, pp. 295–305.

Consonni, S., 1992, "Performance Prediction of Gas/Steam Cycles for Power Generation," Ph.D. thesis n. 1893-T, MAE Dept., Princeton University, Princeton, NJ.

De Ruick, J., 1992, "Efficient CO_2 Capture Through a Combined Steam and CO_2 Gas Turbine Cycle," *Energy Convers. Mgmt.,* Vol. 33, pp. 397–404.

Lozza, G., 1990, "Bottoming Steam Cycles for Combined Gas-Steam Power Plants: A Theoretical Estimation of Steam Turbine Performance and Cycle Analysis," Proceedings, 4th ASME Cogen-Turbo, New Orleans, LA, pp. 83–92.

Lozza, G., 1993, "Steam Cycles for Large-Size High-Gas-Temperature Combined Cycles," Proceedings, 1993 ASME Cogen-Turbo Power Symposium, Bournemouth, UK, pp. 435–444.

Lozza, G., Chiesa, P., and DeVita, L., 1996, "Combined Cycle Power Stations Using Clean-Coal-Technologies: Thermodynamic Analysis of Full Gasification versus Fluidized Bed Combustion With Partial Gasification," ASME JOURNAL OF ENGINEERING FOR GAS TURBINES AND POWER, Vol. 118, pp. 737–748.

Macchi, E., Bombarda, P., Chiesa, P., Consonni, S., and Lozza, G., 1991, "Gas-Turbine-Based Advanced Cycles for Power Generation. Part A: Calculation Model. Part B: Performance Analysis of Selected Configurations," Proceedings, 1991 Yokohama Int'l Gas Turbine Congress, Vol. III, Yokohama, Japan, pp. 201–219.

Mathieu, P., and De Ruick, J., 1993, "CO_2 Capture in CC and IGCC Power Plants Using a CO_2 Gas Turbine," IGTI-Vol. 8 ASME Cogen-Turbo, ASME, New York.

McMullan, J. T., Williams, B. C., Campbell, P., McIlveen-Wright, D., and Bemtgen, J. M., 1995, "Techno-Economic Assessment Studies of Fossil Fuel and Fuel Wood Power Generation Technologies," in "R&D in Clean Coal Technology," Report to the European Commission, Bruxelles, Belgium.

Miller, H. E., 1996, ""F" Technology—the First Half-Million Operating Hours," GE Company Report GER-3950, Schenectady, NY.

Nakayama, S., Noguchi, Y., Kiga, T., Miyamae, S., Maeda, U., Kawai, M., Tanaka, T., Koyata, K., and Makino, H., 1992, "Pulverized Coal Combustion in O_2/CO_2 Mixtures on a Power Plant for CO_2 Recovery," *Energy Convers. Mgmt.,* Vol. 33. pp. 379–386.

Rao, A. D., et al., 1993, "HP Integrated versus Non-Integrated ASU in Destec IGCC," Proceedings, Twelfth EPRI Conference on Gasification Power Plants, San Francisco, CA.

Reid, R. C., Prausnitz, J. M., and Poling, B. E., 1988, *The Properties of Gases and Liquids,* 4th ed., McGraw-Hill, New York.

Schmidt, E., 1982, *Properties of Water and Steam in S.I. Units,* Springer-Verlag, Berlin.

Schütz, M., Daun, M., Weinspach, P. M., Krumbeck, M., and Hein, K. R. G., 1992, "Study on the CO_2-Recovery From an IGCC Plant," *Energy Convers. Mgmt.,* Vol. 33., pp. 357–364.

Smelser, S. C., Stock, R. M., and McCleary, G. J., 1991, "Engineering and Economic Evaluation of CO_2 Removal From Fossil-Fuel-Fired Power Plants—Volume 1 Pulverized-Coal-Fired Power Plants," EPRI Report IE-7365.

Smith, A. R., Klosek, J., and Woodward, D. W., 1996, "Next-Generation Integration Concepts for Air Separation Units and Gas Turbines," ASME Paper 96-GT-144.

Ulizar, I., and Pilidis, P., 1996, "A Semiclosed Cycle Turbine with Carbon Dioxide-Argon as Working Fluid," ASME Paper 96-GT-345.

Ulizar, I., and Pilidis, P., 1997, "Design of a Semiclosed Cycle Gas Turbine with Carbon Dioxide—Argon as Working Fluid," ASME Paper 97-GT-125.

U.S. Department of Energy, 1993, "The Capture, Utilization and Disposal of Carbon Dioxide from Fossil Fuel-Fired Power Plants," U.S. Department of Energy Report, Contract DE-FG02-92ER30194.

Van der Sluijs, J. P., Hendriks, C. A., and Blok, K., 1992, "Feasibility of Polymer Membranes for Carbon Dioxide Recovery from Flue Gases," *Energy Convers. Mgmt.,* Vol. 33, pp. 429–436.

CO_2 Emission Abatement in IGCC Power Plants by Semiclosed Cycles: Part B—With Air-Blown Combustion and CO_2 Physical Absorption

P. Chiesa

G. Lozza

Dipartimento di Energetica,
Politecnico di Milano,
Piazza Leonardo da Vinci 32,
Milan, 20133, Italy

This paper analyzes the fundamentals of IGCC power plants with carbon dioxide removal systems, by a cycle configuration alternative to the one discussed in Part A (with oxygen-blown combustion). The idea behind this proposal is to overcome the major drawbacks of the previous solution (large oxygen consumption and re-design of the gas turbine unit), by means of a semiclosed cycle using air as the oxidizer. Consequently, combustion gases are largely diluted by nitrogen and cannot be simply compressed to produce liquefied CO_2 for storage or disposal. However, CO_2 concentration remains high enough to make separation possible by a physical absorption process. It requires a re-pressurization of the flow subtracted from the cycle, with relevant consequences on the plant energy balance. The configuration and the thermodynamic performance of this plant concept are extensively addressed in the paper. As in the first part, the influence of the pressure ratio is discussed, but values similar to the ones adopted in commercial heavy-duty machines provide here acceptable performance. Proper attention was paid to the impact of the absorption process on the energy consumption. The resulting net overall efficiency is again in the 38–39 percent range, with assumptions fully comparable to the ones of Part A. Finally, we demonstrated that the present scheme enables the use of unmodified machines, but large additional equipment is required for exhausts treatment and CO_2 separation. A final comparison between the two semiclosed cycle concepts was therefore addressed.

1 Introduction

The separation of carbon dioxide from exhausts of power plants, followed by its disposal into underground cavities or by deep sea dispersion, can represent a significant contribution to reduce the concerns about climatic changes, due to the dispersion in the atmosphere of "greenhouse" gases produced by human activities. However, carbon dioxide concentration is rather poor in combustion products: from 4 percent in a natural gas-fired gas turbine, to 8 percent in an IGCC plant, to 12 percent in a conventional coal-fired boiler (all values, expressed by volume, are indicative). Therefore, to avoid processing huge gas flows with large energy consumption, carbon dioxide removal claims for measures to improve its concentration. The most radical solution is to use CO_2 as the main component of the working fluid in a semiclosed gas turbine cycle. It was the subject of the Part A of this paper and, as we discussed, such a solution requires pure oxygen for combustion and substantial modifications to the existing gas turbine engines. Now we will consider semiclosed cycles in which air is used as the oxidizer, characterized by a moderate CO_2 enrichment (about 20 percent by volume) and thus requiring a separation process.

The basic concept of the cycle is reported in Fig. 1. It includes a complete coal gasification section and a combined cycle power plant, similarly to the scheme discussed in part A (in the followings, we will shortly address the oxygen-blown plant of part A as "scheme A" and the present air-blown plant as "scheme B"). Differently from scheme A, oxygen, produced by an air separation unit (ASU), is supplied to the gasification section only. Ambient air enters the cycle to provide the minimum amount of oxidizer necessary to the syngas combustion process. Part of exhaust gases are recycled to the compressor, acting as diluting agent to obtain the desired turbine inlet conditions, rather than excess air as in open cycle gas turbines. As anticipated, exhausts are moderately enriched by carbon dioxide: the fraction exiting the cycle can be treated to remove CO_2 by a physical absorption process. Eventually, CO_2 is compressed and liquefied for disposal, while the remaining components of exhausts (mainly nitrogen) are dispersed toward the ambient.

The paper will firstly address the plant arrangement and the solutions found for the physical separation process. Then we will discuss its performance prediction, based on the same calculation method and assumptions reported in Part A, and we will finally address a comparison between the solutions presented in the two parts of this paper.

2 Detailed Plant Configuration

2.1 IGCC Sections. Figure 2 provides a complete overview of the various plant sections and of their interactions. The sections typical of IGCC plants are rather similar to the ones described at chapter 3 of Part A, and the assumptions used during the calculation are unchanged. In particular:

Air Separation Unit. As for scheme A, we will refer to a conventional ASU process, consisting of an intercooled air compressor and of a double separation column. The only difference is size, since the oxygen consumption of scheme A is 2.6 times the

Contributed by the International Gas Turbine Institute (IGTI) of THE AMERICAN SOCIETY OF MECHANICAL ENGINEERS for publication in the ASME JOURNAL OF ENGINEERING FOR GAS TURBINES AND POWER. Paper presented at the International Gas Turbine and Aeroengine Congress and Exhibition, Stockholm, Sweden, June 2–5, 1998; ASME Paper 98-GT-385.

Manuscript received by IGTI March 23, 1998; final revision received by the ASME Headquarters June 23, 1999. Associate Technical Editor: R. Kielb.

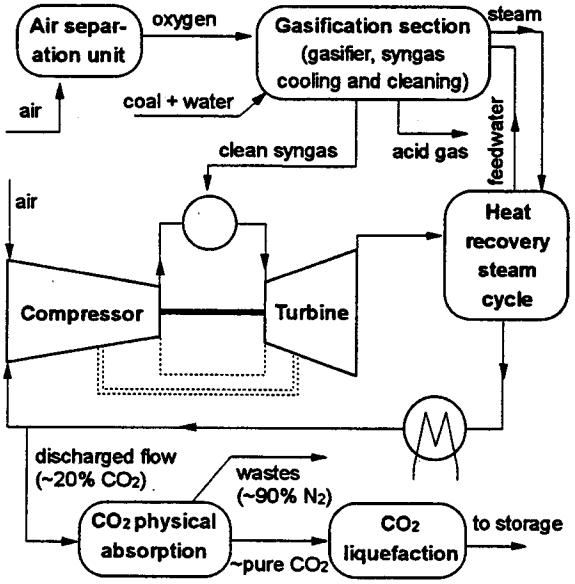

Fig. 1 Conceptual overview of the air-blown semiclosed cycles here analyzed, with physical absorption of CO_2

one of the present scheme. The reduced power consumption of the air compressor allows for an electric motor drive rather than direct drive by the gas turbine.

Gasification Section. We will refer again to an entrained-flow slurry-feed gasifier, reproducing the Texaco technology, with the same coal feedstock (Illinois #6) and gasification pressure and temperature (60 bar, 1600 K). The gasification section is mostly unchanged between scheme A and B. However, comparing Figs. 2 of part A and part B, two important differences can be outlined: (i) in scheme B, the convective syngas cooler, in addition to rising saturated HP steam, provides heat to the nitrogen stream exiting the absorption unit, before its expansion (see 2.2); (ii) a syngas saturator was introduced into scheme B, to contribute to NO_x abatement by fuel moisturization: warm water for saturation is produced from low temperature syngas cooling, substituting low pressure steam generation of scheme A. The adoption of NO_x control strategies requires some comment. It was unnecessary in scheme A, due to the virtual absence of nitrogen in the gas turbine combustion chamber. Here, nitrogen is abundantly present and fuel dilution by inert agents is advisable, even if not strictly necessary. Water saturation is a very effective method, not really affecting the efficiency, because of the correct thermodynamics of the process. On the contrary, the use of nitrogen as an inert diluent (available in the plant at sufficient pressure after the separation process) is not convenient, since it reduces the carbon dioxide fraction in the exhausts, increasing the CO_2 separation duty.

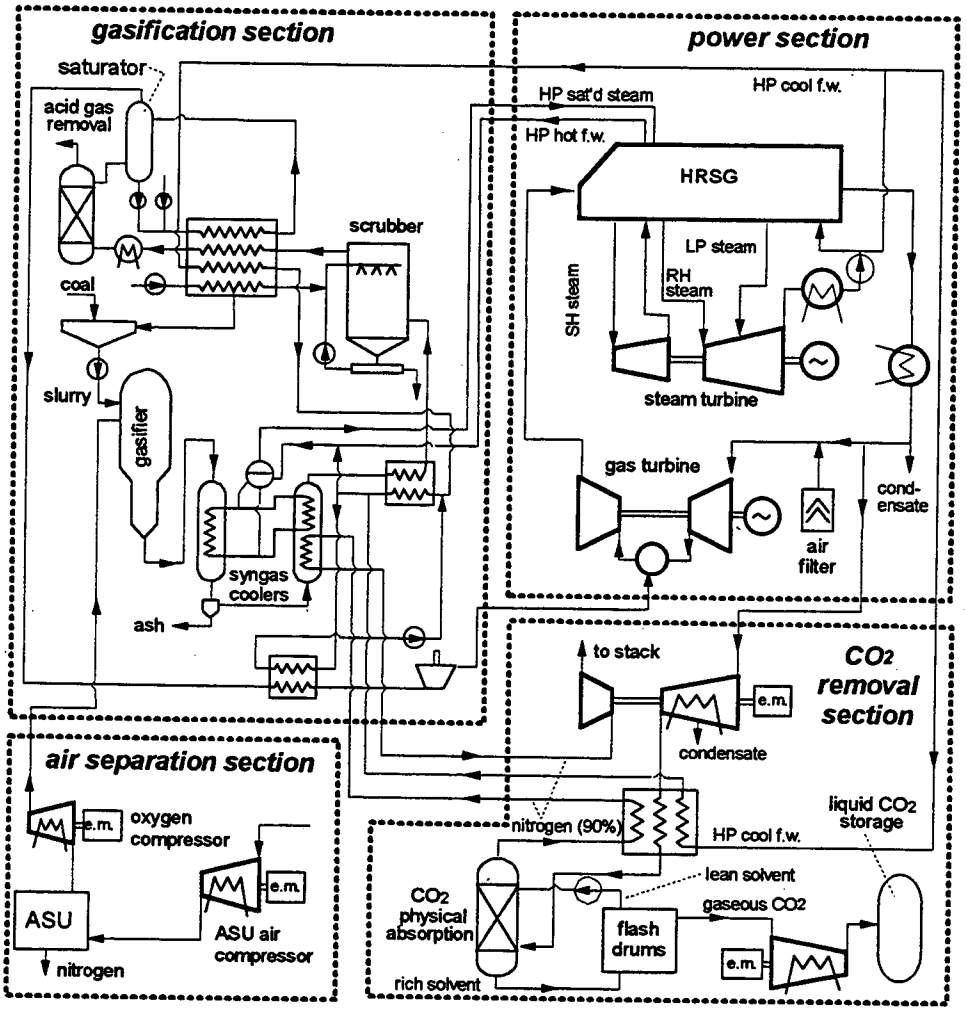

Fig. 2 Plant configuration of the semiclosed cycle with air-blow combustion (scheme B)

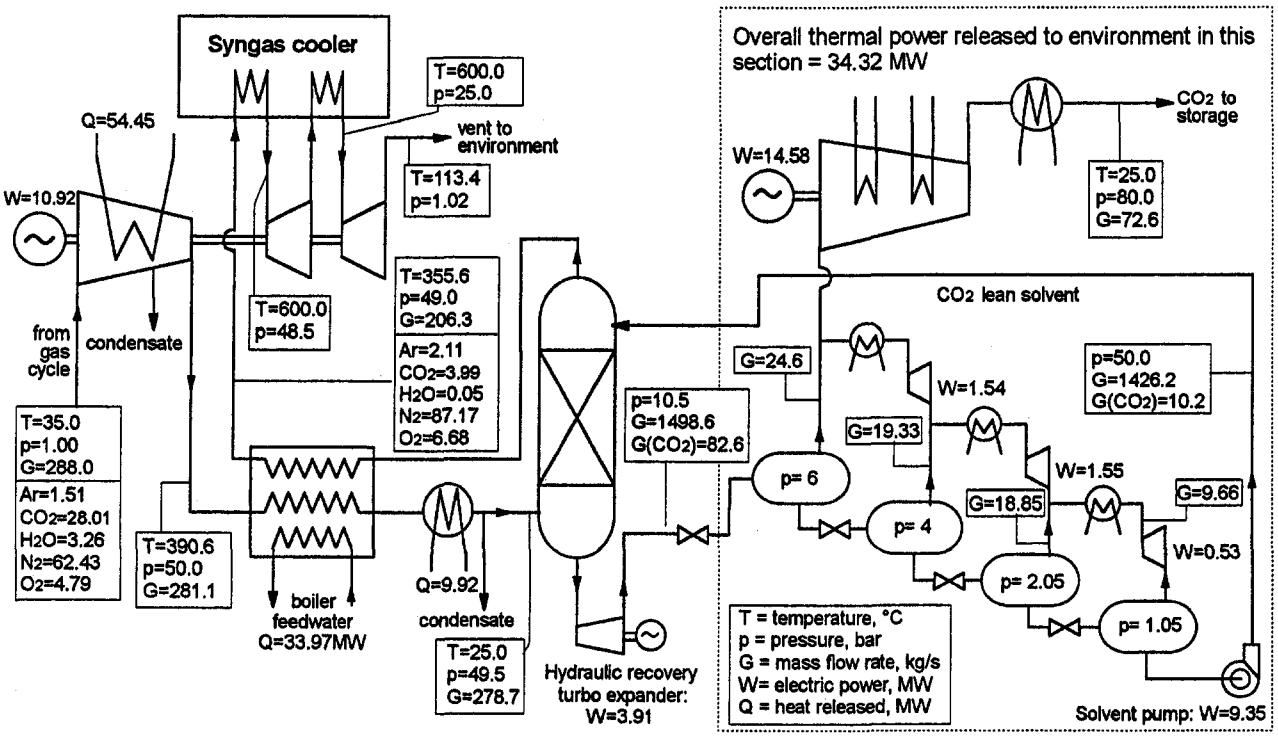

Fig. 3 Energy and mass balance of the carbon-dioxide physical separation process, including the compression/liquefaction train, for a cycle pressure ratio of 15 and a thermal input of 900 MW (LHV). Gas compositions in mass percentage fraction.

Power Plant. Apart from the change of the working fluid composition, no conceptual modifications are introduced from scheme A, both for the gas turbine technology (adopting a TIT of 1280°C as in "F" industrial machines) and for the heat recovery steam cycle. It can be anticipated that, in the present case, the composition of the fluid evolving within the semiclosed cycle is much more similar to the one of open cycle gas turbines: as we will discuss later, this allows for minimal modifications to the engine with respect to market-available units.

2.2 Carbon Dioxide Separation. The major differences between scheme A and B are concentrated in the treatment of the stream retrieved from the gas turbine. For scheme A a simple mechanical compression process was sufficient to make CO_2 available at the liquid state and at a pressure necessary for disposal without further energy expenses (here stipulated as 80 bar). For scheme B, the situation is much more complicated, since carbon dioxide must be separated from nitrogen-diluted exhausts.

CO_2 separation from gaseous mixtures can be carried out by means of different processes: among them, the most common ones are chemical and physical absorption (Kohl and Riesenfeld, 1985). In the first process capture of CO_2 is mainly due to chemical bonds created in the adsorber between CO_2 and solvent (usually aqueous solutions of ethanol-ammines). CO_2 is then stripped from solvent by breaking the chemical bonds and, since this operation is endothermic, large amounts of thermal energy are required for its accomplishment. On the contrary physical absorption relies upon the selective solubility of gases into a solvent and upon its variation with pressure: CO_2 is absorbed in the solvent at high pressure within a counter-current packed tower and then released by reducing the pressure of the CO_2-rich solvent stream. In this case, since CO_2 is removed from a mixture largely diluted with N_2, the solvent has to present a much larger solubility for the former substance compared to the latter one. The Selexol solvent, commercialized by Union Carbide, results very suitable for the purpose since, for the same partial pressure and temperature, about 0.01 mols of N_2 are captured for each mol of CO_2 (Bucklin and Schendel, 1984).

The theoretical energy requirement is relatively low (power for pumping the solvent stream and for recompression of the separated gas), compared to the large low temperature heat requirement of chemical absorption processes. This does not imply any evaluation of chemical versus physical absorption, being the thermodynamic value of power and heat very different: chemical absorption can be the subject of future works.

Figure 3 shows the complete plant arrangement of the physical separation section (quoted values refer to the "reference" case described later). The operating pressure of the absorption tower depends on pressure selected for the last flash drum and on CO_2 concentration in the exhausted gaseous stream (i.e., CO_2 removal efficiency). In fact the former parameter brings about the purity of the solvent introduced at the top of the column; according to this purity, a minimum pressure can be determined to achieve the required CO_2 absorption, corresponding to an infinite tower height. In the scheme of Fig. 3, the last flash drum pressure has been assumed as 1.05 bar to operate the whole system above the atmospheric pressure. To achieve a 90 percent removal efficiency, 0.237 kmols of CO_2 per kmol of diluting gas must be captured. According with the solubility curves of CO_2 within Selexol (Bucklin and Schendel, 1984), a minimum operating pressure of 41 bar is needed. To obtain a reasonable driving force for mass transfer, absorption pressure was increased to 50 bar (see also Chiesa and Consonni, 1999, appendix A).

To achieve this pressure, a compressor processes the stream vented from the cycle at near-ambient pressure. The compression is partly intercooled, to limit the high pressure stage temperature within 400°C (similarly to gas turbine compressors). The pressurized stream is therefore cooled to near-ambient temperature, by a recuperative heat exchanger, and ducted to the absorption column. Within the column, CO_2 is captured by Selexol. The nitrogen-rich, CO_2-free stream, exiting the absorption column at high pressure (50 bar), must be heated and expanded, to recover its pressure content improving the energy balance. Heating is necessary to (i) keep the stream temperature above ambient at the expander cold end, to avoid freezing problems, and (ii) provide an enthalpy drop as high as possible, to drive the compressor. Heat is largely

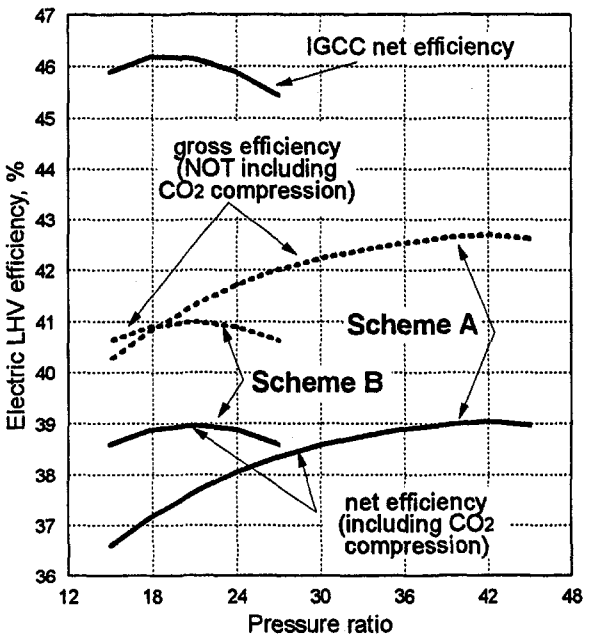

Fig. 4 Influence of the cycle pressure ratio on the efficiency of IGCC and of semiclosed cycles A and B. The dotted curves do not take into account the power consumption of the carbon dioxide compression/ liquefaction train.

available from cooling of the compressed stream before absorption (in fact, hot feedwater is produced in the heat exchanger to achieve a complete heat recovery), but at a temperature not sufficient for those duties. Therefore, following the recuperative heat transfer, an additional heating is required. The only available heat sources are the convective syngas cooler and, to a lesser degree, the HRSG. We will discuss this issue later (section 3.2): Fig. 3 shows the "reference" solution in which a double expansion with reheat was adopted (unfortunately increasing the plant complexity) with heat extracted from the syngas cooler at a maximum temperature of 600°C. Turbines and intercooled compressor are arranged on the same shaft; an electric motor provides the extra power needed to balance this shaft.

On the Selexol side, Fig. 3 shows that the rich solution, after absorption of CO_2, is flashed within sequential chambers, were CO_2 is gradually released as pressure decreases, in order to reduce the power required for re-compression of the separated CO_2. From the last flash chamber, at near-atmospheric pressure, lean Selexol is pumped back to the absorber. The pump consumption is rather large (2.7 percent of the net total output), due to huge flow of Selexol (1426 kg/s); an hydraulic expander improves the energy balance, making use of the pressure drop between the absorption column and the first flash chamber. Carbon dioxide, released at various pressures, is re-compressed to the pressure of the first chamber and then ducted to a compression-liquefaction train similar to the one described in 3.4 (part A). Its power requirement is substantially reduced because (i) CO_2 is already pressurized (6 bar), and (ii) CO_2 is almost pure, because nitrogen, oxygen, and argon solubilities within Selexol are negligible compared to the one of CO_2.

3 Overall Plant Performance

3.1 Influence of the Cycle Pressure Ratio. The results of the cycle calculations are shown in Fig. 4, reporting the efficiency versus pressure ratio (β) of the present scheme (B, air-blown) and of the ones addressed in part A (i.e., scheme A, oxygen-blown, and the reference IGCC not including any CO_2 removal strategy). In the figure, two efficiency curves are shown for plant schemes A and B: the upper dotted curves do not consider the power expenses for compression-liquefaction of carbon dioxide, the lower curves represent the overall net plant efficiency. Two basic considerations can be drawn:

(1) The optimum pressure ratio range is very similar between IGCC and scheme B, and substantially different from scheme A. In fact, the working fluid composition and molecular mass of the air-blown cycle are rather similar to the ones of an open cycle, due to the large nitrogen concentration (Fig. 5). The best performance of scheme B is obtained at $\beta = 21$, versus a optimum β of 18 for IGCC, while a β as large as 42 was required to optimize the efficiency of scheme A. For the former two plants the use of a lower pressure ratio of 15 (often found in large commercial heavy-duties) does not impair the plant efficiency in a significant way. This represents an important confirmation about the possibility of using these machines with a limited amount of modifications.

(2) At optimum pressure ratio, the overall efficiencies of schemes A and B are very similar (about 39 percent) and, thus, substantially lower from the IGCC one. However, reasons justifying the loss of efficiency are rather different from the ones outlined in part A. The gap between the continuous and the dotted lines represents the power consumption due to the need of providing pressurized CO_2 at the plant boundaries, rather than at atmospheric pressure. In scheme B, it includes the power requirement of the various CO_2 compressors represented in Fig. 3: the multiple flash chambers (together with the absence of incondensables) reduce their duty with respect to the unique compressor of scheme A. The major drawback of the present cycle is due to the necessity of compressing the exhaust stream up to the required absorption pressure of 50 bar. Even if a recovery of the pressure content of the separated gas is carried out, those processes (compression, expansion, heat transfer) are highly irreversible. Being the mass flow involved almost one half of the one of the power cycle, the associated exergy destruction is largely relevant to the whole energy balance. In fact, an additional power of 11 MW is needed to drive the turbo-compressor, and, mostly, a large amount of high temperature heat (82.8 MW) is subtracted from the syngas cooler, which in turn produces less steam, reducing the steam turbine power output. Those effects are mostly independent on the pressure ratio, because the separation process, at equal carbon input to the plant, involves the same CO_2 mass flow to be processed. We will therefore provide some more detail by addressing the reference scheme at $\beta = 15$.

3.2 Discussion of the "Reference" Scheme. In this section we will focus our discussion on the "reference" case with a pressure ratio of 15, selected to maintain the same value of the IGCC case. Its main characteristics are shown in Fig. 5: together with information provided by Fig. 3 and Table 1, a rather complete plant balance can be drawn. We can comment that

- about 45 percent of the gas turbine exhausts are ducted to the separation plant (the CO_2 fraction is 20 percent by volume—28 percent by mass): the size and cost of the turbo-compressor shown in Fig. 3, compared to the main gas turbine, is therefore of high relevance
- to better understand the above point let's say that (i) the compressor power is 141.8 MW (versus 222.5 of the one of the main engine), (ii) the reheat turbine power is 131.1 MW, and (iii) the thermal power coming from the syngas cooler is 82.8 MW, as already stated

To confirm the impact of this process on the power balance, let us consider the content of Table 1. Together with figures for open-cycle IGCC and "reference" scheme B, it addresses (last column) a semiclosed cycle at $\beta = 15$, similar to the one here discussed but deprived of the CO_2 removal section (therefore, producing full steam from the syngas cooler and directly venting to the ambient

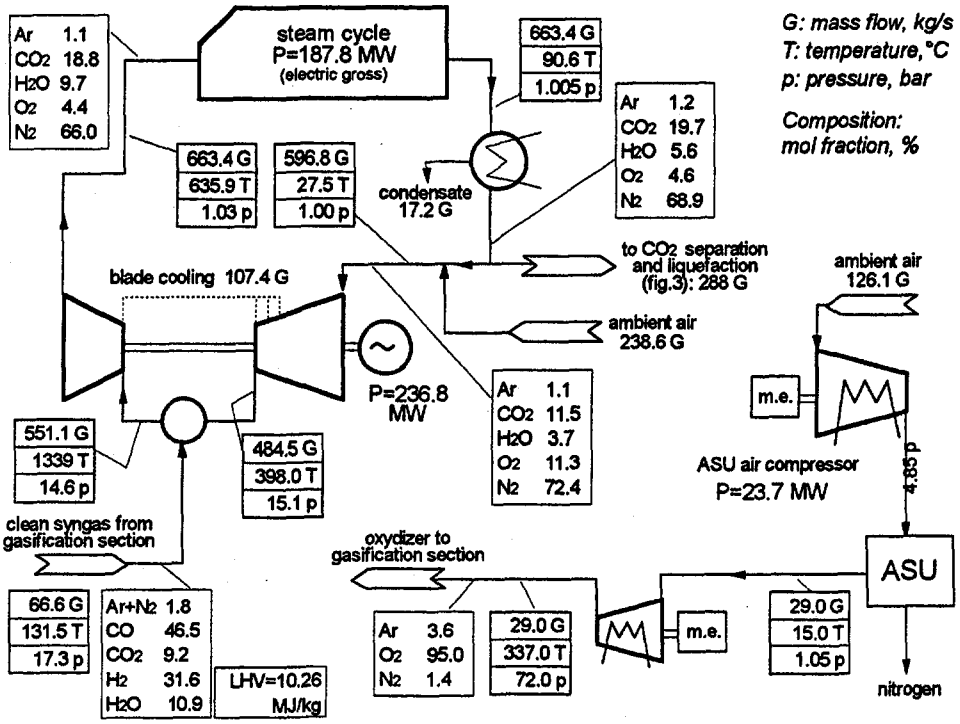

Fig. 5 Energy and mass balance of the power cycle and air separation components of the air-blown semiclosed cycle (scheme B) at a pressure ratio of 15

the stream extracted from the gas cycle). It can be noticed that the efficiency of this latter cycle is very close to the one of the IGCC. In fact, the differences on a thermodynamic point of view are rather limited: an higher turbine exit temperature (636°C versus 609°C, due to higher fluid molecular mass) provides a lower gas turbine output, recovered by the steam cycle; on the compressor side of the gas turbine, differences are negligible because the working fluid is largely diluted with air. Comparing this cycle to the one with CO_2 removal, a loss of steam turbine output of 33 MW, due to the vent stream heating, is clearly shown: together with the power consumption of the various devices reported in Fig. 3 (totaling 36.5 MW), the loss of overall efficiency (7 percentage points) is fully justified. The figures discussed up to now are based on a preheating of the vent stream up to 600°C by means of heat recovered from the convective syngas cooler. This temperature level was assumed in order to limit the thermal stresses in the heat exchanger to values comparable to the ones of reheaters in steam boilers. Being this assumption relevant to the cycle performance and being rather questionable (no references can be found relatively to the demanding environment of a syngas cooler), a sensitivity analysis was performed, whose results are shown in Table 2. By decreasing this temperature a rather relevant loss of efficiency is found, because of the higher power consumption of the electric motor driving the turbo-expander (partly balanced by the lower thermal power retrieved by the syngas cooler). The last row shows the temperature at which the vent stream should be heated to balance the turbo-expander (789°C): it is not realistically achievable by available metallic materials for heat exchangers.

Alternatively, preheating of the vent stream can make use of heat recovered by the HRSG (by using a clean gas stream at a moderate temperature) rather than by the syngas cooler (with higher erosion-corrosion and high-temperature stresses). In this case, larger heat transfer surfaces would be needed, due to the much lower temperature difference, complicating the HRSG design (parallel tube bundles for the vent stream heater and the steam superheater and reheater). However, at equal maximum temperature, the heat source (HRSG or syngas cooler) does not influence the thermodynamic performance, because in both cases the heat subtracted by vent stream heating would have been used to generate the same amount of HP steam.

Table 1 Electric power balance of the various plant components for the open-cycle IGCC, the reference air-blown semiclosed cycle (scheme B) and a semiclosed air-blown cycle not including the CO_2 removal section. Thermal input of 900 MW by coal LHV for all cycles.

Type of cycle (β=15)	Open	Semiclosed	
		CO2 removal	
Electric power, MW	IGCC	yes	no
Gas turbine gross output	247.8	236.8	236.8
Steam turbine gross output	209.5	187.8	220.7
Syngas expander	11.4	11.4	11.4
ASU air/oxygen compressors	-40.6	-40.6	-40.6
Auxiliaries	-15.2	-13.6	-14.9
Exhausts compressor/expander	-	-10.9	-
Selexol pump/expander	-	-5.4	-
CO_2 compression/liquefaction	-	-18.2	-
Net power output	412.9	347.3	413.4
Net LHV efficiency, %	45.88	38.59	45.93

Table 2 Influence of the vent stream temperature after heating in the syngas cooler (T_{rh}) for a semiclosed air-blown cycle with $\beta = 15$. Legend: η = overall LHV efficiency, P_{em} = power of the electric motor driving the turbo-expander, Q_{sc} = thermal power retrieved from the syngas cooler, p_{rh} = optimized reheat pressure of the vent stream, T_{st} = stack temperature. Results of the first three lines also apply to the case of heating in the HRSG.

T_{rh}, °C	η, %	P_{em}, MW	Q_{sc}, MW	p_{rh}, bar	T_{st}, °C
400	37.66	36.4	46.7	15	61.6
500	38.17	24.7	61.6	22	77.3
600	38.59	10.9	82.8	25	113.4
789	39.04	0.0	97.2	-	130.8

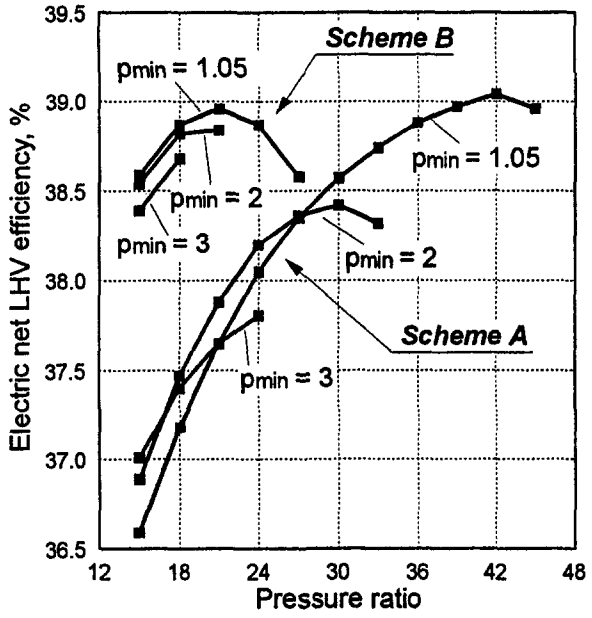

Fig. 6 Influence of the pressurization (p_{min} is the minimum cycle pressure) on the efficiency of semiclosed cycles A and B, at various pressure ratios

3.3 Influence of the Cycle Pressurization. Up to now, the minimum cycle pressure was kept close to the atmosphere, mainly for compatibility with open-cycle machines. In closed cycles this pressure can be freely selected. In semiclosed cycles, like the ones here considered (including part A), the influence of pressurization can be discussed by separating its effects on auxiliaries consumption and on cycle thermodynamics.

In scheme A (oxygen-blown), pressurizing the cycle obviously brings about a pressure increase at the O_2 compressor outlet, needing more power compared to the atmospheric option. In case that the available syngas pressure is not enough to inject the fuel in the combustor, an additional compressor (rather than an expander) is required and its electric consumption has to be considered. With a syngas pressure of 51 bar (before the syngas expander), cycle pressurization at 2 ÷ 3 bar necessarily requires this component for pressure ratios maximizing the efficiency. Similar considerations hold for cycle B where pressurization requires a large compressor to introduce fresh air into the cycle. In change of this additional work, the stream ducted to CO_2 absorption process is available at higher pressure decreasing the compression power requirements.

Nevertheless a restricted analysis, only considering the variation in consumption of the auxiliaries, leads to erroneous results because pressurization also has a significant influence upon the power cycle. As a first point, the turbomachines efficiency is influenced by "size," according to our correlations. Pressurization reduces the volumetric flow and negatively influences the efficiency. For large machines, this effect is rather limited (for instance, the compressor polytropic efficiency decreases of about 0.5 points at a minimum cycle pressure of 3 bar), but it is not negligible. In addition, pressurization has a great importance on the factors which control heat transfer in the hottest rows of the turbine. On the one side, increasing the operating pressure reduces volume flow and hence surfaces to be cooled. On the other side it increases the heat transfer coefficients on both sides of the cooling channels and hence the heat flux through the blade walls. It brings about an increase in the temperature drop due to conduction along the wall thickness which reduces the temperature rise available to the coolant in the inner blade channels. Therefore, larger coolant flows are required to remove the same thermal load. All these effects are taken into account by the cooling model here adopted, described by Consonni (1992).

Figure 6 depicts the overall effects of pressurization on the plant efficiency. In scheme A, at low pressure ratio where blade cooling is less demanding due to a lower coolant temperature, pressurization is beneficial to performance. On the contrary, pressurization becomes noxious at higher β, where cycle efficiency approaches its peak. The critical condition reached by the cooling system is attested by the curves' breaks which occur for pressure ratio lower and lower as pressurization increases, thus impairing the achievement of the best efficiency. Curves referred to scheme B follow the same trend, but the cooling system results critical even at low β: in fact, compressor outlet (i.e., coolant) temperatures are higher than for scheme A, due to the lower molecular mass of the working fluid (see Fig. 5 of Part A, keeping into account that compressor outlet temperatures of scheme B are very similar to the ones of IGCC). Hence, pressurization penalizes efficiency of scheme B in the whole pressure ratio range reported in Fig. 6.

Apart from efficiency, pressurization could give some benefits in the practice. It reduces the size of gas cycle turbomachinery and enhances heat transfer in the recovery steam generator. In scheme A, requiring some changes in gas turbine design, a moderate pressurization could allow some advantage on the economic viewpoint. With regard to scheme B, pressurization does not have the same appeal since it introduces a supplementary air compressor and modifies the gas turbine operating conditions, conflicting with the rationale supporting this configuration: the adoption of an unchanged current engine.

4 Turbomachinery Design and Development

In the previous discussion, we often stated that the present configuration (with air-blown combustion) may result attractive if it makes feasible the adoption of unmodified gas turbines, with respect to the one available in the market. Now, this statement can be confirmed by looking at Table 3, in which some relevant turbomachinery specifications are compared for the IGCC machine and for a semi-closed cycle having (i) the same compressor inlet volume flow, and (ii) the same turbine nozzle throat area. The first assumption brings about a thermal input of 917 MW rather than 900, the second one can be accomplished by selecting a pressure ratio of 14.8 rather than 15, with negligible consequences on the plant efficiency. These conditions were stipulated to verify if the same gas turbine unit can operate safely under the new conditions imposed by the change of the working fluid, without any need of blade design or blade height modification. The results shown in Table 3 indicate that (i) the volume flow rate at the last compressor stage is less than 1 percent lower than the one of the IGCC machine, eliminating any risk of stall-surge at HP stages, (ii) the compressor work variation is minimal, (iii) variations on the turbine side are very limited and cannot influence its performance, and (iv) improvements in cooling flows are minimal. Considering

Table 3 Specifications involved in turbomachinery design, for an IGCC and a semiclosed air-blown cycle characterized by the same compressor inlet volume flow and turbine nozzle area

Common design parameters Inlet volume flow = 507.9 m^3/s First nozzle throat area = 0.4433 m^2	Open IGCC, β=15	Semi-closed, β=14.8
Thermal input by coal LHV, MW	900	917
Gas turbine gross output, MW_{el}	247.8	243.0
Gas turbine compressor		
Inlet mass flow, kg/s	613.6	612.5
Inlet / outlet volume flow ratio	7.262	7.221
Isentropic enthalpy rise, kJ/kg	337.9	329.4
Gas turbine		
Outlet volume flow, m^3/s	1633.9	1645.5
Outlet / inlet volume flow ratio	9.165	9.495
Isentropic enthalpy drop (cooled expansion), kJ/kg	1062	1046
First nozzle cooling flow / gas flow (vol.)	0.0256	0.0260
First rotor cooling flow / gas flow (vol.)	0.0243	0.0249

that problems cannot be expected on the mechanical standpoint, due to a slightly reduced power output, it can be concluded, beyond any reasonable doubt, that the very same machine of open cycles can be used with the moderately CO_2 enriched fluid here addressed. Regarding other turbomachines included in the cycle, the ASU compressors are unchanged with respect to the IGCC, while the duty of the CO_2 liquefaction compressor is much reduced if compared to the one of scheme A (14.6 versus 32.9 MW, with an inlet volume flow of 6.82 versus 52.34 m^3/s). The real drawback of scheme B comes from the machines involved in the exhaust treatment and separation, especially as far as the main exhausts turbo-expander, pressurizing the absorption process, is concerned. This machine is about one-half the size of the main gas turbine, with an higher loading (larger stage number), intercoolers and reheat. It is a novel machine, resembling the characteristics of large process units. Its impact on the plant cost may represent a serious obstacle to the development of this class of plants. In addition, a polytropic efficiency lower than here estimated (on the basis of the same correlations used for gas turbine components) may seriously affect the cycle performance.

Other components to be considered are the absorption column, the flash chambers, the heat exchangers (the recuperative one shown in Fig. 3 and the gas heaters placed inside the convective syngas cooler), the Selexol turbo-pump and the minor CO_2 compressors connecting the flash chambers: they represent large pieces of additional equipment. The impact on the overall investment cost of the separation plant can therefore result prohibitive. A reliable cost prediction cannot be drawn at present, but a very rough estimation, based on limited data available to the authors, suggests a rise of 50–55 percent with respect to the already elevated plant costs of an IGCC having the same gasification capacity. It is authors' opinion that the proposal described in part A (oxygen blown) can be realized with lower costs (about 35 percent rise), assuming that the gas turbine development costs are scattered on a reasonable number of machines, to limit the cost rise of this component to a 30 percent. Considering the lower net output of these plants versus an IGCC (about 18 percent less), the estimated specific cost rise is substantially higher (in the range of 60 percent for scheme A and of 80 percent for scheme B, according to a very preliminary evaluation).

6 Final Comparisons and Conclusions

Figure 7 shows the efficiency decay of various plant types as a function of the specific CO_2 emission, for (i) the two schemes here discussed (including part A), (ii) the most efficient solution studied by Chiesa and Consonni (1999), based on syngas catalytic shift reaction, physical absorption of CO_2 and hydrogen-fueled gas turbine, (iii) a mix of conventional IGCC with a semiclosed CO_2 cycle (reference scheme A). The points representative of an IGCC, a coal-fired steam plant and a natural gas combined cycle are also reported. The figure shows that some improvements in the plant conversion efficiency can be achieved by reducing the CO_2 removal rate. For scheme A the final CO_2 pressure determines the amount of CO_2 condensed and therefore removed (see pressures quoted in Fig. 7). A pressure reduction brings about a very limited power saving, clearly demonstrating that such a scheme makes sense only if a very high removal rate is achieved. For scheme B, the efficiency of the CO_2 separation depends on the pressure drop between the absorber and the last flash chamber (see again pressures in Fig. 7): by operating the physical absorption at a lower pressure some efficiency gain may be obtained, but at a rather slow rate. The proposal from Chiesa and Consonni, being calculated under the same assumptions used in this paper and then fully comparable, shows about the same efficiency of our schemes at high removal rates (90 percent or higher) but achieves a substantially better efficiency at medium removal rate (50–70 percent), due to a lower consumption of high pressure steam needed by the shift reaction. At this intermediate rates, their performance is slightly better than the one achieved by a mix of IGCC + scheme A, with the additional advantage of the use of unmodified gas turbines and the disadvantage of unmodified NO_x emission (remember that scheme A is virtually NO_x free). A curve very similar to the one "IGCC + scheme A" can be also obtained by scheme B alone, if only a part of the stream exiting the power cycle is submitted to CO_2 separation (with the remainder vented to the atmosphere), due to the fact that IGCC and scheme B, without separation process, show the same net efficiency (see Table 1).

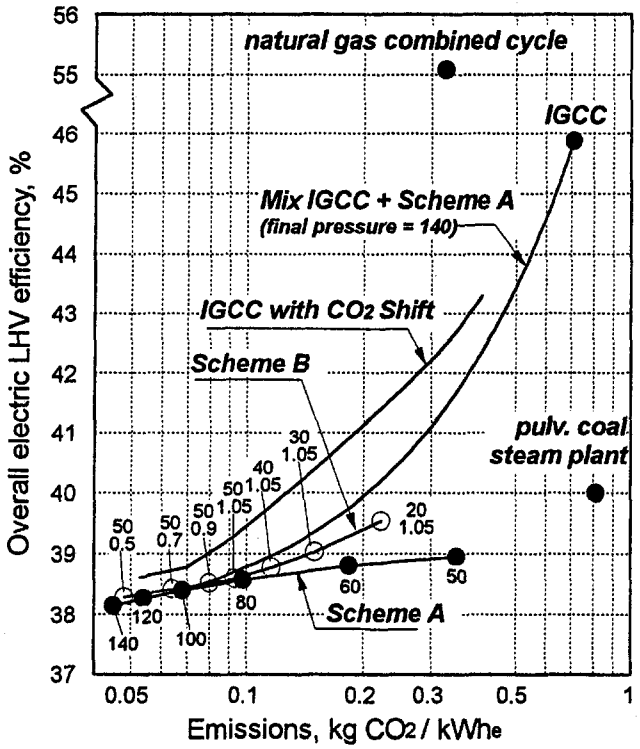

Fig. 7 Specific carbon dioxide emissions versus efficiency of various plant types. The numbers quoted for scheme A represent the final CO_2 delivery pressure (bar); for scheme B, they represent the pressure of the absorption column and of the last flash chamber.

The selection of the best strategy of CO_2 removal, keeping into account its progressive penetration into the market, is beyond the scope of the paper and would anticipate the necessary research and development studies. In fact, the discussion here developed outlines the negative impact of CO_2 removal on the conversion efficiency and on the plant complexity, compared to the already high capital-intensive and complicated IGCC stations, but demonstrates that a drastic abatement of CO_2 emissions is within today's technological capabilities. A realistic economic study cannot be drawn at present, due to the difficulties of estimating the investment costs when novel components are introduced. In addition, any cost estimation should take into account the avoided costs of "externalities," i.e., the social cost connected to pollutant emission (mainly CO_2 and NO_x). Nevertheless, we believe that the present analysis can be useful to provide the necessary basic information to develop such estimations and to assess the possibility of success of emission-free fossil-fueled power plants in a competitive energy market constrained by increasingly stringent global emission regulations.

References

Bucklin, R. W., and Schendel, R. L., 1984, "Comparison of Fluor Solvent and Selexol Processes," *Energy Progress,* Vol. 4, No. 3, pp. 137–142.

Chiesa, P., and Consonni, S., 1999, "Shift Reactors and Physical Absorption for Low-CO_2 Emission IGCCs," ASME JOURNAL OF ENGINEERING FOR GAS TURBINES AND POWER, Vol. 121, pp. 295–305.

Consonni, S., 1992, "Performance Prediction of Gas/Steam Cycles for Power Generation," Ph.D. thesis n. 1893-T, Princeton University, Princeton, NJ.

Kohl, A., and Riesenfeld, F., 1985, *Gas Purification,* 4th ed., Gulf Publishing Co., Houston, TX.

Off-Design Performance of Various Gas-Turbine Cycle and Shaft Configurations

T. Korakianitis

K. Svensson

Department of Mechanical Engineering,
Washington University,
Campus Box 1185,
One Brookings Drive,
St. Louis, MO 63130

The design-point performance of various gas turbine cycles such as simple, regenerative, and intercooled-regenerative, is well understood. It is also understood that more elaborate shaft arrangements such as one, two, or three concentric or nonconcentric shafts, and a separate power turbine shaft, provide better starting and operational flexibility, and wider plateaus of high off-design performance. However, the types of different off-design performance one can obtain with these different shaft arrangements has not been previously reported. In this paper we use a computer program to investigate the design-point and off-design-point performance of engines with the following: one single shaft joining the compressor, turbine and load; one shaft joining compressor and turbine, and one shaft for the power turbine; two shafts for compressor and turbine, and one shaft for the power turbine; and three shafts joining the compressor and turbine, and one shaft for the power turbine. This is done by specifying typical compressor and turbine maps, and computing various aspects of off-design performance. The advantages and disadvantages of the various arrangements are investigated and discussed.

Introduction

Two important parameters in thermodynamic cycles for shaft-power engines are thermal efficiency and specific power. Thermal efficiency is defined as

$$\eta_{th} \equiv \frac{\dot{W}}{\dot{\Omega}_F} \approx \frac{\dot{W}}{\dot{m}_F LHVF}. \quad (1)$$

The best simple-cycle thermal efficiencies are just over 0.4. Regenerative and intercooled-regenerative cycles of low pressure ratios can attain thermal efficiencies between 0.5 and 0.6. Specific power $\dot{W}'$, a nondimensional measure of the power density of the cycle, is defined as

$$\dot{W}' \equiv \frac{\dot{W}}{\dot{m}_A C_p T_{01}}, \quad (2)$$

where $T_{01} = T_{mn}$ is the minimum cycle temperature (at engine inlet, see Fig. 1). Cycle-performance maps indicate that substantially different thermodynamic-cycle parameter choices should be made for engines intended for different applications.

All shaft-power engines are designed considering very few points of operation, usually one point, called the design point. However, when these engines are coupled to different prime movers the engine needs to operate efficiently at several off-design points. Usually the power (or torque) versus speed operating map of the engine, occasionally with η_{th} contours superimposed, is called the engine performance map (with specific fuel consumption contours it is called the fuel map). Some performance (fuel) maps over limited regions of engine operation can be obtained from engine companies, but the limits of off-design performance are not readily available. As gas-turbine engines find ever wider applications (e.g., automotive, marine, space, etc.), we need a better understanding of the off-design performance expected from various thermodynamic cycles and shaft arrangements.

Contributed by the International Gas Turbine Institute (IGTI) of THE AMERICAN SOCIETY OF MECHANICAL ENGINEERS for publication in the ASME JOURNAL OF ENGINEERING FOR GAS TURBINES AND POWER. Paper presented at the International Gas Turbine and Aeroengine Congress and Exhibition, Stockholm, Sweden, June 2–5, 1998; ASME Paper 98-GT-386.

Manuscript received by IGTI March 23, 1998; final revision received by the ASME Headquarters June 23, 1999. Associate Technical Editor: R. Kielb.

Computer programs using component maps to predict the off-design performance of gas turbine engines have been published, for example, by Koenig and Fishbach (1972), Seldner et al. (1972), Shapiro and Caddy (1974) (whose program is called NEPCOMP and is used in this paper) and others. Dynamic simulations have also been modeled by various methods, for example Szuch (1974), Schobeiri and Haselbacher (1985), Korakianitis, Vlachopoulos and Zou (1994) and others. These programs have been used for individual engines of interest, for example Korakianitis and Beier (1994) used NEPCOMP to predict the off-design performance of two specific 1.12 MW regenerative marine gas turbines. However, the off-design performance of simple, regenerative, and intercooled-regenerative gas turbines using various shaft configurations has not been reported.

The purpose of this paper is to use component-performance maps typical of those used in production engines to study the performance of several thermodynamic-cycle and shaft configurations.

Approach

The thermodynamic cycles considered in this paper are the simple compressor-burner-expander (CBE) cycle, the regenerative cycle (CBEX, where the additional X denotes the heat exchanger) and the intercooled-regenerative cycle (CICBEX, where the additional I denotes the intercooler between two compressors). The types of shaft arrangements considered are the following: The single-shaft engine, 1S, which denotes one shaft connects the compressor, turbine, and load. The 1GPT arrangement, which denotes one shaft connects the gas-generator compressor and turbine (1G), and the power turbine and load are on a separate shaft (PT). The 2GPT and 3GPT arrangements, which denote that the cycle has a gas-generator arrangement with two and three concentric or nonconcentric shafts, respectively, and a power turbine connected to the load. In cases with multiple gas-generator spools we have the low, intermediate and high-pressure spools (*lp*, *ip*, and *hp* respectively). In principle any shaft arrangement could be used with any cycle, but as will be shown below for some thermodynamic cycles some arrangements make better sense than others. Figure 1 illustrates some of the component arrangements and thermodynamic points around the cycles for three typical engines (more types of engines and shaft arrangements than those shown in Fig. 1 have been investigated in the paper). CBE-1S is a

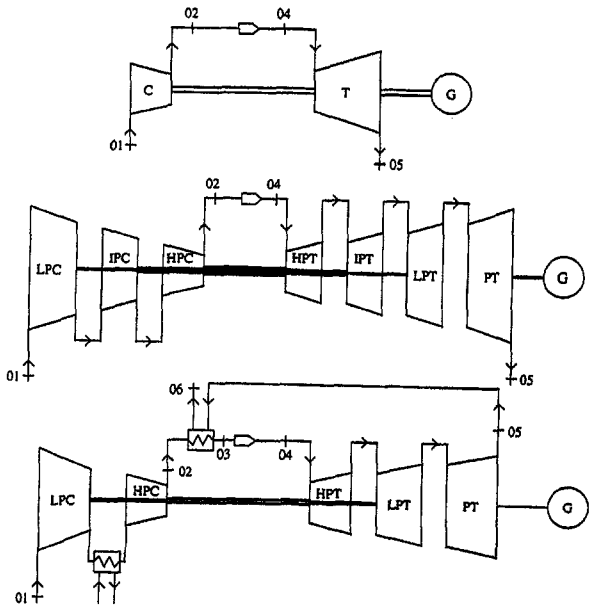

Fig. 1 Representative gas-turbine cycle and shaft arrangements. Top: CBE-1S. Middle: CBE-3GPT. Bottom: CICBEX-2GPT. Concentric shafts are shown in the figure, but the analysis is also valid for nonconcentric shafts.

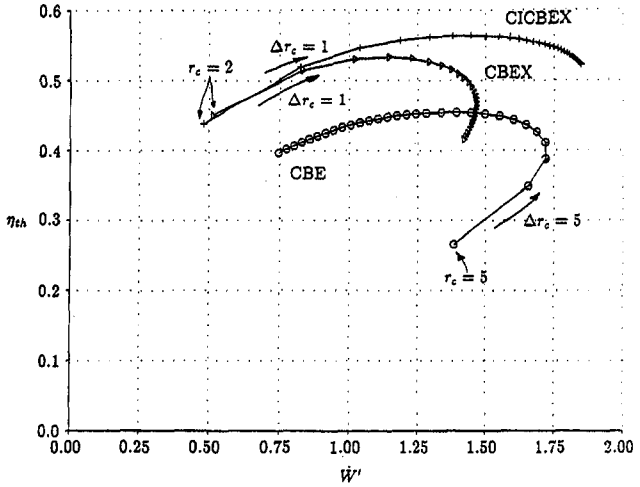

Fig. 2 Thermal efficiency η_{th} versus specific power $\dot{W}'$ as a function of compressor pressure ratio r_c and for $T' = 5.9$. Each point corresponds to the design-point performance of a different engine. Other inputs are described in the text

single-shaft CBE engine, with the compressor, turbine and load on the same shaft. CBE-3GPT is a CBE engine with high, intermediate and low pressure compressors and turbines on concentric (or nonconcentric) shafts, and a separate shaft for the power turbine that drives the load. CICBEX-2GPT is a CICBEX engine with high and low-pressure compressors and turbines on concentric (or nonconcentric) shafts, and a separate shaft for the power turbine that drives the load.

We made several initial choices for the cycles. Then the "optimum" pressure ratio for each cycle was evaluated from cycle parameter plots. Then representative component maps and NEPCOMP were used to evaluate the design-point and off-design performance of each cycle and shaft configuration.

Design-Point Performance

Many authors have illustrated that thermodynamic-cycle-parameter choices have a big effect on the thermal efficiency and specific power of gas-turbine cycles (e.g., Korakianitis and Wilson, 1994; Wilson and Korakianitis, 1998). Compressor and turbine design-point efficiencies decrease as the pressure ratio increases. Regenerative and intercooled-regenerative cycles have more flow passages and therefore higher pressure drops than simple cycles. The effect of turbine-rotor-inlet temperature, or of $T' \equiv T_{mx}/T_{mn} = T_{04}/T_{01}$ is dominant on cycle performance (T_{mx} and T_{mn} are the maximum and minimum temperatures of the working fluid, and T_{01} and T_{04} are shown in Fig. 1). In modern gas-turbine engines the turbine-rotor inlet temperature is between 1500 K and 1800 K. With ambient temperatures of about 288 K, $5.2 < T' < 6.2$. In regenerative gas turbines the regenerator effectiveness also has a pronounced effect on performance. Given these inputs, the optimum pressure ratios for maximum power and maximum thermal efficiency are different for CBE, CBEX, and CICBEX cycles. In order to make choices for the design-point performance of the cycles under consideration, we obtained the cycle-performance map shown in Fig. 2.

The computer programs presented by Korakianitis and Wilson (1994) were used to obtain Fig. 2, with the following inputs: the compressor and turbine stagnation-to-stagnation polytropic efficiencies are a function of pressure ratio, starting from 0.93 at a pressure ratio of 1, and reducing to about 0.85 at a pressure ratio of about 60. $T_{01} = 288\ K$, and $T' = 5.9$, or turbine rotor inlet temperature is $T_{04} = 1700\ K$. It was assumed that the blading material temperature is limited to 1300 K, and transpiration/impingement cooling was used, so that the resultant cooling mass-flow rate for the first turbine rotor and cooled blade rows further

Nomenclature

1S = one shaft (compressor, turbine and load)
1GPT = one-shaft gas-generator and power turbine
2GPT = two-shaft gas-generator and power turbine
3GPT = three-shaft gas-generator and power turbine
CBE = simple cycle
CBEX = regenerative cycle
CICBEX = intercooled-regenerative cycle
C_p = isobaric specific heat capacity
LHVF = lower heating value of the fuel
m, $\dot{m}$ = mass, mass-flow rate
N = percent of speed at design point
N = percent of speed at design point
p = pressure
r = pressure ratio
T, T' = temperature, temperature ratio
W, $\dot{W}$, $\dot{W}'$ = work, power, specific power
η_{th} = thermal efficiency
Ω = thermodynamic availability (exergy)

Subscripts

A = air
c = compressor
dp = design point
ex = engine exhaust
F = fuel
G = gas-generator
hp, ip, lp = high, intermediate, low pressure shaft
in = engine inlet
mn = minimum
mx = maximum
pt = power turbine
t = turbine

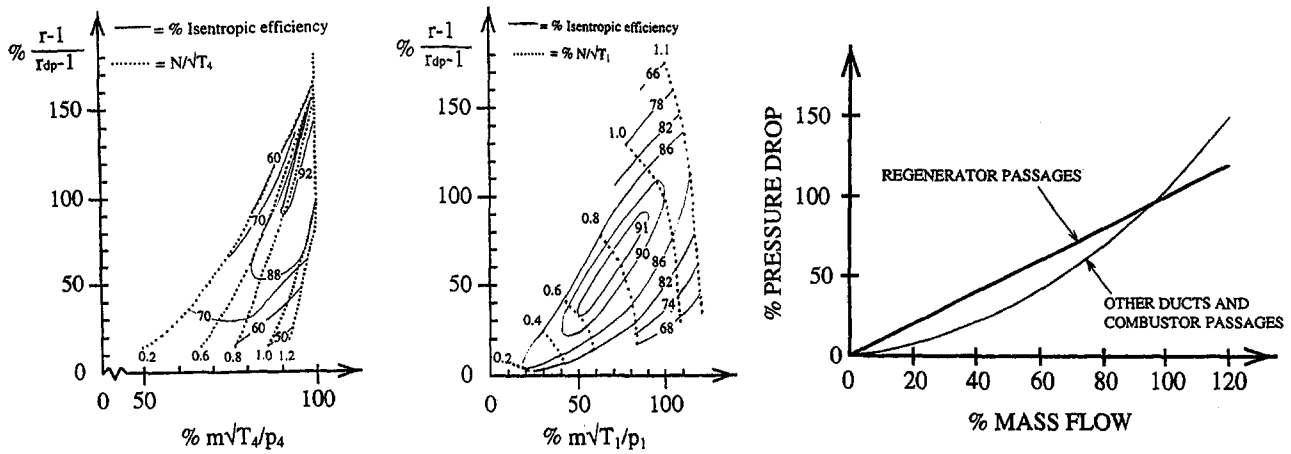

Fig. 3 Typical performance maps. Left: compressor map. Middle: turbine map. Right: pressure drop as a function of mass-flow rate, nondimensionalized with their values at design-point engine operation.

downstream is between 2 percent and 6 percent of the core flow. Pressure drops were 4 percent in the CBE cycle, 12 percent in the CBEX cycle, and 15 percent in the CICBEX cycle (increasing with the number of ducts). The heat exchanger effectiveness in the CBEX and CICBEX cycles was 0.95, and the intercooler effectiveness in the CICBEX cycle was 0.90. These choices were made as good compromises between larger components and high thermal efficiency for each cycle. Each cycle-performance point shown in Fig. 2 corresponds to a different engine. The optimum pressure ratio for thermal efficiency is different from the optimum pressure ratio for maximum power, and it is different for each cycle. The choice of cycle pressure ratio for each cycle is a compromise between thermal efficiency and specific power.

Based on Fig. 2 we chose design-point pressure ratios r_c of 25 for the CBE cycle, 6 for the CBEX cycle, and 10 for the CICBEX cycle. These pressure ratios make some shaft arrangements more desirable than others. The CBE cycle can use one high pressure ratio compressor in the CBE-1S and CBE-1GPT configuration. Alternatively, it can use two or three concentric or nonconcentric compressors of $r_c \approx 5$ in the CBE-2GPT and $r_c \approx 2.9$ in the CBE-3GPT arrangement. For the CBEX cycle (which is not shown in Fig. 1) the engine was restricted to CBEX-1S and CBEX-1GPT cycle because the pressure ratio of 6 is already low. For the CICBEX cycle we chose the single-shaft CICBEX-1S and CICBEX-1GPT with $r_c \approx 10$, and the CICBEX-2GPT engine with two compressors of $r_c \approx 3.2$ each, which allows for intercooling between the high and low pressure gas-generator shafts.

Off-Design Performance

The design-point and off-design performance of each cycle and shaft configuration, and of several cycle properties of interest, were obtained using the computer program NEPCOMP (Shapiro and Caddy, 1974). This computer program uses the design-point and off-design-point performance of various gas-turbine components, which are assembled and controlled in the proper sequence to simulate the operation of turbine engines.

The nondimensional compressor and turbine performance maps typical of large axial components shown in Fig. 3 were used. The isentropic stagnation-to-stagnation efficiency lines are shown solid (NEPCOMP uses isentropic efficiencies), and the nondimensional corrected speed lines (nondimensionalized with design-point speed) are shown dotted. These maps are intended to provide the performance trends in off-design operation of the components; they do not match exactly the design-point efficiency and power of the engine performance figures shown below with the cycle performance shown in Fig. 2. Based on Fig. 3, the pressure ratio and isentropic efficiency of each component used in each cycle and shaft configuration were adjusted to approximately match the polytropic efficiencies used to produce the performance plot of Fig. 2. The design-point pressure drops in the components of the CBE, CBEX, and CICBEX cycles mentioned above (4 percent, 12 percent, 15 percent) were used, but at off-design operation the pressure drops were modeled as a function of mass-flow rate as shown in Fig. 3 (shown nondimensionalized with the pressure drop and mass-flow rate at design point). We assumed that the laminar flow in the heat exchanger passages results in linear variation of pressure drop with mass-flow rate, and the turbulent flow in the combustor and ducts results in a square-law variation of pressure drop with mass-flow rate.

The performance of each engine is shown as contours of thermal efficiency η_{th}, $T' = T_{04}/T_{01}$ (it shows how hot the engine needs to run at each operating point), T_{ex}/T_{in} (it is a measure of the exergy wasted at engine exhaust), percent of compressor and turbine pressure ratio as a fraction of the pressure ratio of the component at design-point operation, gas-generator shaft speeds etc. A sufficient number of these figures to illustrate engine performance are shown in this paper. Each performance figure indicates the cycle and shaft combination to which it corresponds, and the performance parameter being plotted. Performance figures for several individual engines we studied have been reported by Svensson (1998).

Figs. 4 and 5 show representative performance plots for the CBE engines. Figure 6 and 7 similarly show representative performance plots for the CBEX and CICBEX engines. The design-point efficiency shown on these performance maps is slightly different from that shown in Fig. 2 because the design-point efficiency of the components when matched in the engine operate at slightly different points than the inputs in NEPCOMP runs, and the inputs used to produce Fig. 2.

Figures 8 and 9 show the direction in which engine and component operating points are "perturbed." Points north N, east E, south S, and west W correspond to "compass" points on the engine performance map. The figures are shown for CBE-1GPT and CBE-1S, but the trends are similar in all the other cycle and engine configurations. Points A are the design point of the engine; points B are at 100 percent engine speed and 30 percent to 40 percent engine power; and points C are at a lower-than-design point engine speed and power (in the 20 percent to 60 percent ranges, depending on the engine). The figures also show the directions in which the corresponding matched operating points move: on the compressor performance map; on the turbine performance map; and (for the power-turbine shaft arrangements) on the power-turbine performance map. The magnitude of the perturbation vectors on the component performance maps indicate the relative displacement of the corresponding point on the component performance maps.

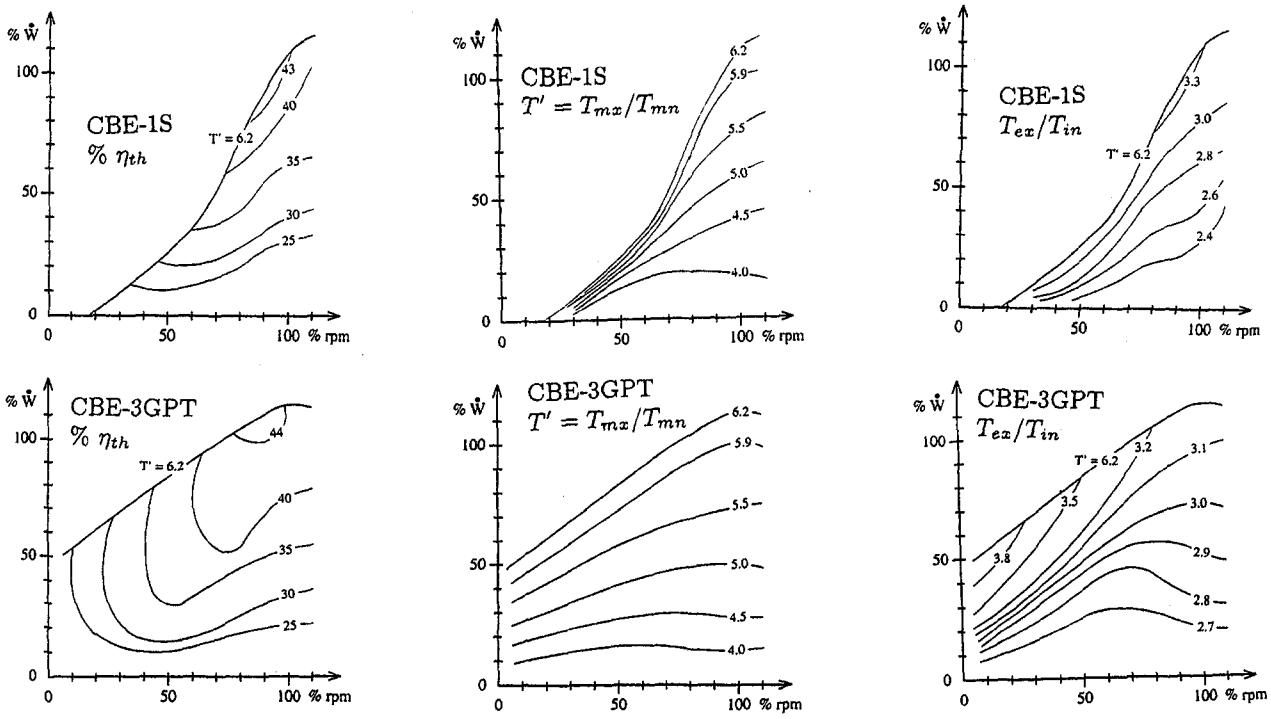

Fig. 4 Typical performance maps (ηth, T' and T_{ex}/T_{in}) for the CBE-1S engine (top) and the CBE-3GPT engine (bottom)

Discussion

As a general rule, the single shaft (1S) arrangements can only operate at speeds over 50 percent of design engine speed, because in these engines the compressor speed is coupled with the speed of the load (see the low-speed lines on the compressor map in Fig. 3). Also as a general rule, the multi-shaft engines with a separate power turbine can operate down to very low engine speeds at reasonable power. In the gas-generator/power-turbine arrangements the gas-generator speed is decoupled from that of the engine output shaft, enabling the components of the gas generator to operate at more efficient points than the 1S arrangement, or at points where the 1S arrangement can not operate. As the number of gas-generator shafts increases from 1G to 2G to 3G engine performance improves by small amounts, but the matching trends of the components in terms of pressure ratios, temperature ratios, and speeds do not change. For example, the speed maps of the

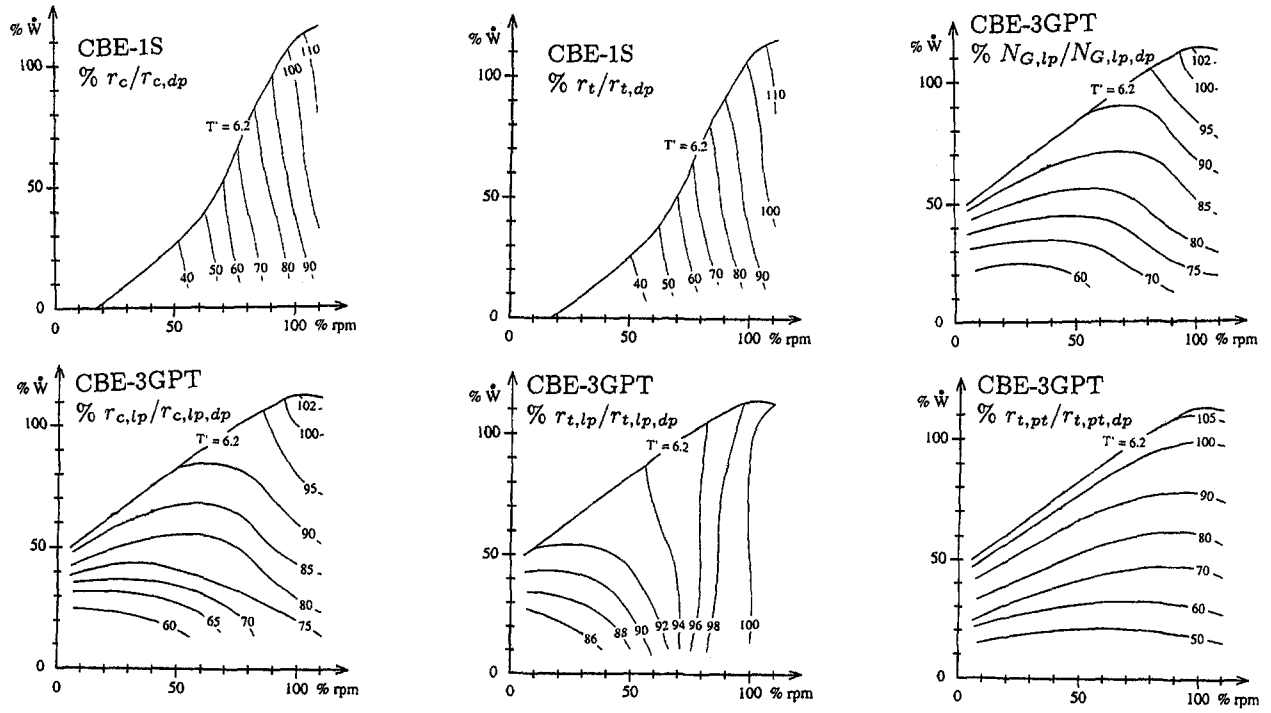

Fig. 5 Typical performance maps (r_c, r_t, $r_{t,pt}$ and $N_{G,lp}$) for the CBE-1S and the CBE-3GPT engine

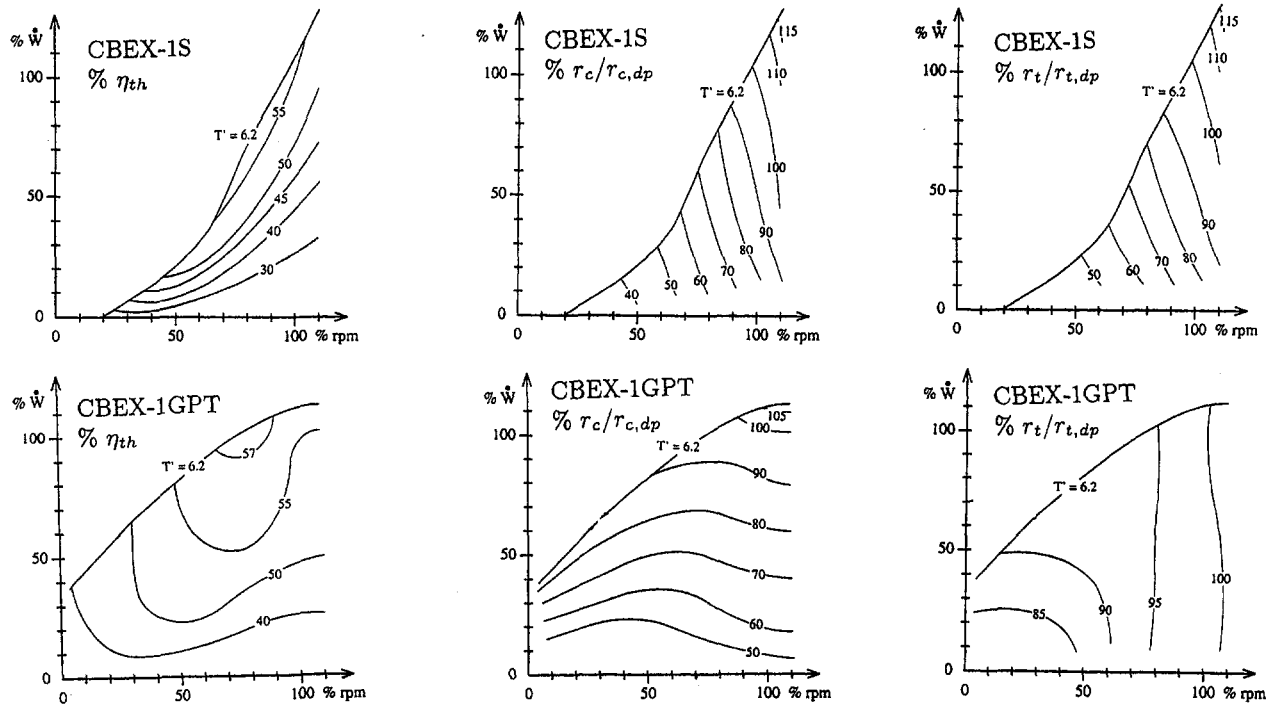

Fig. 6 Typical performance maps (ηth, and r_c and r_t) for the CBEX-1S engine (top) and the CBEX-1GPT engine (bottom)

gas-generator shafts ($N_{G,lp}$) shown for the CICBEX engine (Fig. 7) look similar to those of the *hp* and *ip* shaft of this cycle and to those of the CBE and CBEX cycles. Similarly, variable compressor or turbine geometry blading has a beneficial but less-pronounced effect than going from the single-shaft to the gas-generator/power-turbine shaft arrangement.

The thermal efficiency contours (Fig. 4 of the CBE-1S engine look similar to those of the CBE-3GPT engine in the off-design power-speed regions where both engines operate. However, the engine with the gas-generator shafts (3GPT) operates at lower than 50 percent speed with reasonable power. Of course, operating at low shaft speed while demanding some power would impose different design constraints on the engine bearings. Similarly the T_{mx}/T_{mn} and T_{ex}/T_{in} maps of the 1S and 3GPT shaft arrangements of the CBE cycle shown in Fig. 4 indicate similar trends at over 50 percent power and over 50 percent speed, but these trends are different at lower speeds and/or powers. The reasons for these differences are explained using Fig. 5.

Figure 5 shows the different trends in the compressor and turbine operating regimes of the engines. In the 1S arrangement the compressor and turbine pressure ratio lines are almost vertical, top left, and top middle of the figure. The remaining four performance plots of Fig. 5 are for the CBE-3GPT arrangement. While these four performance plots are substantially different from the 1S arrangement, they are similar to the plots for the 1GTP and 2GTP arrangements. Surprisingly, these trends of the CBE-cycle shaft arrangements look similar to the corresponding trends of the CBEX-cycle and CICBEX-cycle shaft arrangements as well. At each power-speed operating point the overall pressure ratio across all turbines and the pressure drops in the ducts must equal the overall pressure ratio produced by all compressors, but the gas-generator compressor and turbine pressure-ratio trends do not have to be identical because the balance is affected by the pressure ratio of the power turbine.

The off-design temperature trends (but not the exact values) for the CBEX and CICBEX cycles are similar to those shown in Fig. 4 for the CBE cycles. The T_{ex}/T_{in} plots indicate that at some off-design conditions the turbine-exhaust temperatures of the multi-shaft arrangements may exceed their values at design point. Unless the hot components of the engine and the regenerator are designed to account for these maximum temperatures that occur at off-design conditions, some of the multi-shaft engine arrangements may not be able to operate in the top band of the highest power regimes indicated in their performance maps.

The perturbation maps (Figs. 8 and 9) show the differences in matching trends between the components for the 1S and multi-

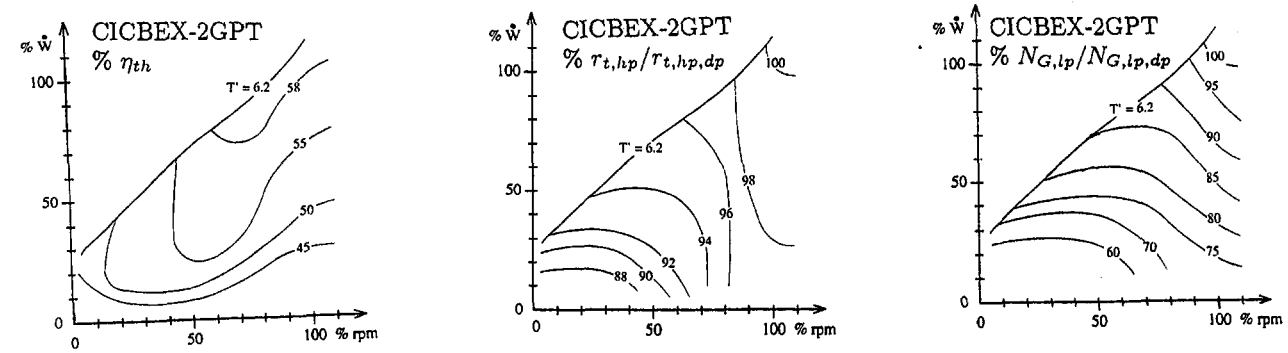

Fig. 7 Typical performance maps (ηth, $r_{t,hp}$, $N_{G,lp}$) for the CICBEX-2GPT engine

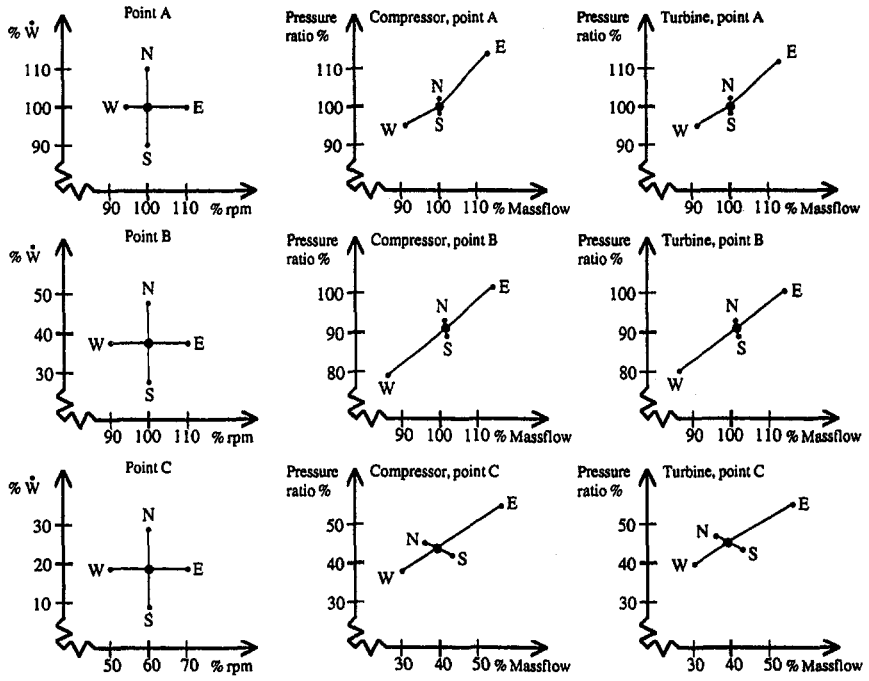

Fig. 8 Perturbations of operating point on the component map as a function of perturbation of operating points on the engine map at points A, B, and C for the CBE-1S engine

shaft configurations. Again, the differences between the CBE, CBEX, and CICBEX cycles are surprisingly small. The differences occur between the single shaft and multi-shaft arrangements.

Figure 8 shows the CBE-1S perturbations. Points N and S do not move significantly on the compressor and turbine maps, but points E and W move significantly. This means that changes in engine speed affect compressor and turbine pressure ratio more than changes in engine power. The same observation is true for points A, B and C; the observation is valid for different engine operating regimes.

Figure 9 shows the CBE-1GPT perturbations. In general, the resulting perturbations on the component maps are smaller than those in the CBE-1S configuration (the scales of the figures are different), and the trends have changed. In this case the bigger perturbations are "north and south," instead of "east and west," indicating that in this case changes in engine power affect compressor and gas-generator turbine pressure ratio more than changes in engine speed. The corresponding changes in power turbine are bigger than those in the gas-generator turbine. This is because the gas-generator match works to give a good operating point for

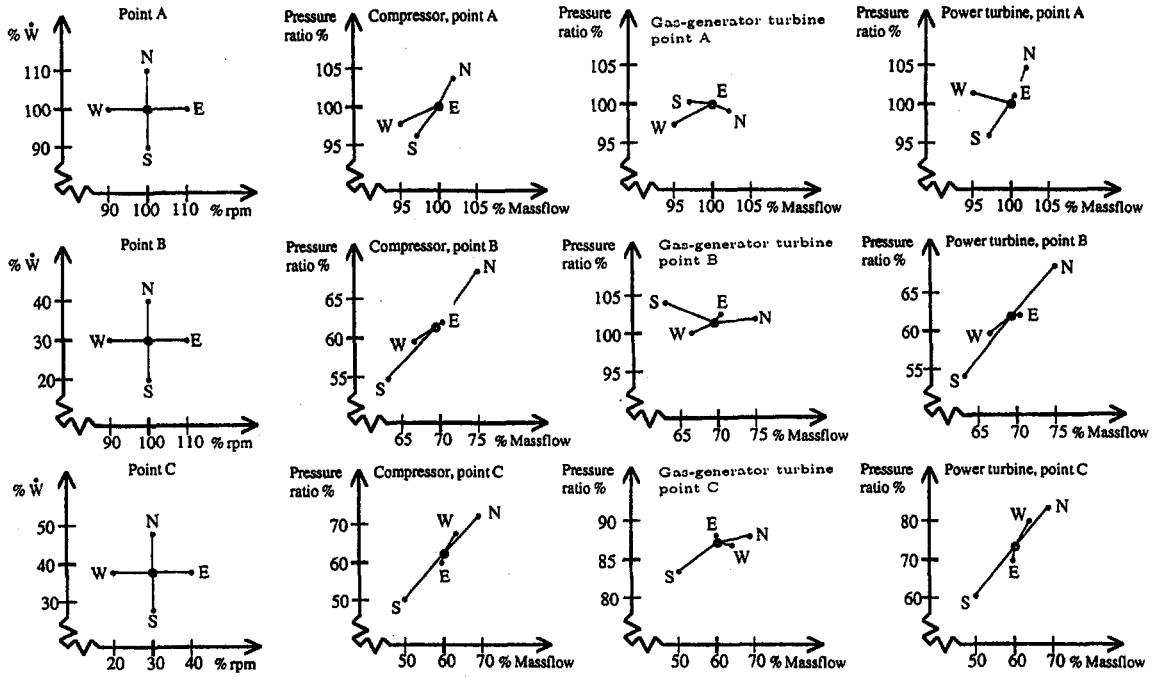

Fig. 9 Perturbations of operating point on the component map as a function of perturbation of operating points on the engine map at points A, B, and C for the CBE-1GPT engine

compressor efficiency at the desired mass flow, and the power turbine uses the remaining exergy at its inlet to produce shaft work.

As expected, the multi-shaft arrangements give wider plateaus of engine operation than the one-shaft engine. However, three other aspects of the results are surprising. First, increasing the number of shafts in the gas generator has a less pronounced effect than we expected, and the trends were very similar between the 1G, 2G, and 3G configurations. Of course the trends would have been significantly different if one of the gas-generator shafts (i.e., one of the compressors) was attached to the power turbine and load. Second, the trends were similar between the different cycles. Of course the CBEX and CICBEX cycles have higher efficiency than the CBE cycle. (Figures 1 and 2 indicate the T_{ex}/T_{in} figures of the CBEX and CICBEX cycle are lower than those of the CBE cycle; the CBEX and CICBEX cycles send fewer losses to the environment). However, the trends in the T', r_c, r_t, $r_{t,pt}$, $N_{G,lp}$, $N_{G,ip}$, and $N_{G,hp}$ are very similar across cycles and within each shaft configuration. The third surprising result is that wider power-turbine performance maps actually deteriorate engine performance at off design. This is not illustrated by the figures of this paper, but was repeatedly observed in the several engine performance maps obtained in the course of this investigation. The reason is that the engine would try to give the desired output power and speed, but because of the wider power-turbine performance map this would occur at a reduced power-turbine inlet pressure and mass-flow rate. As a result of the low cycle pressure and low mass-flow rate through the engine, the gas generator would converge to a low-power and low-speed point, where the performance of the gas-generator components is very low, or they simply do not match.

Conclusions

The design point and off-design performance of simple, regenerative, and intercooled-regenerative gas turbines have been presented. Different shaft configurations have been examined. The configuration in which the load, compressor and turbine are all on one shaft gives the narrowest operating regime. Shaft arrangements with a power turbine driving the load, and with gas generators with one, two or three concentric or nonconcentric shafts have also been examined. The addition of several concentric or nonconcentric shafts to the gas generator has a less pronounced effect than the addition of the power turbine. The trends in the performance figures look similar across the different cycles (the actual numbers are different as the regenerative and intercooled-regenerative engines are more efficient). The trends of corresponding shaft configurations across thermodynamic cycles also look similar.

Acknowledgments

Krister Svensson worked on this topic at Washington University in St. Louis in partial fulfillment of the requirements for his Masters Degree thesis, awarded by the Royal Institute of Technology, Stockholm, Sweden.

References

Koenig, R. W., and Fishbach, L. H., 1972, "GENENG," a program for calculating design point and off-design performance for turbojet and turbofan engines, NASA TN D-6552.

Korakianitis, T., and Wilson, D. G., 1994, "Models for Predicting the Performance of Brayton-Cycle Engines," ASME JOURNAL OF ENGINEERING FOR GAS TURBINES AND POWER, Vol. 116, pp. 381–388.

Korakianitis, T., Vlachopoulos, N. E., and Zou, D., 1994, "Models for the Prediction of Transients in Closed Regenerative Gas-Turbine Cycles With Centrifugal Impellers," ASME Paper 94-GT-342.

Korakianitis, T., and Beier, K., 1994, "Investigation of the Part-Load Performance of Two Regenerative Gas Turbines," ASME JOURNAL OF ENGINEERING FOR GAS TURBINES AND POWER, Vol. 116, pp. 418–423.

Schobeiri, T., and Haselbacher, H., 1985, "Transient Analysis of Gas Turbine Power Plants Using the Huntorf Compressed Air Storage Plant as an Example," ASME Paper 85-GT-197.

Seldner, K., and Mihailowe, J. R., and Blaha, R. J., 1972, "Generalized Simulation Technique for Turbojet Engine Systems Analysis," NASA TN D-6610.

Shapiro, S. R., and Caddy, M. J., 1974, "NEPCOMP—The Navy Engine Performance Program," ASME Paper 74-GT-83.

Svensson, K., 1998, "Off-design Performance of Several Gas-Turbine Arrangements," SM thesis, Royal Institute of Technology, Stockholm, Sweden.

Szuch, J. R., 1974, "HYDES," a generalized hybrid computer program for studying turbojet or turbofan engine dynamics, NASA TM X-3014.

Wilson, D. G., and Korakianitis, T., 1998, *The Design of High-Efficiency Turbomachinery and Gas Turbines*. Prentice Hall; Englewood Cliffs, NJ.

An Iterative CFD and Mechanical Brush Seal Model and Comparison With Experimental Results

L. H. Chen

P. E. Wood

T. V. Jones

Department of Engineering Science,
University of Oxford,
Parks Road, Oxford, United Kingdom

J. W. Chew
Mechanical Science Group,
Rolls-Royce plc.,
Moor Lane, Derby, United Kingdom

The position of the bristles within a brush seal is dictated by the pressure distribution within the seal, which is itself influenced by the position of the bristle matrix. In order to predict mass flows, pressure capabilities, bristle displacements, stresses, and contact loads at the rotor interface, a technique for iterating between a CFD and a mechanical model has been developed. The iterative technique is used to model the behavior of seals with an initial build clearance, where the application of pressure causes a change in the position of the bristle matrix. Frictional effects between neighboring bristles and at the backing ring influence the behavior of the bristles and these are accounted for within the mechanical part of the model. Results are presented and discussed for seals of both initial build clearance and interference. The mathematical predictions for flow, contact loads at the rotor interface, and the nature of the bristles displacements are compared with experimental results.

Introduction

Significant improvements in engine performance and efficiency can be obtained by replacing labyrinth seals with brush seals (Fig. 1) in gas turbine air to air sealing applications (e.g., Hendricks et al., 1994). Unlike labyrinth seals, brush seals do not require an inherent operating clearance between the seal and rubbing surface. Due to their compliant nature they can withstand radially outward excursions of the rubbing surface into the seal. Furthermore, due to an aerodynamic phenomena termed blow down (Wood and Jones, 1997) brush seals are capable of closing the clearance that would otherwise develop after excursions of the rubbing surface away from the seal.

The design of a brush seal is governed by two distinct objectives; leakage performance and life. Modeling activities focused on the former encompass many techniques from computational fluid dynamic (CFD) calculations (e.g., Turner et al., 1997) to one-dimensional porosity approaches (e.g., Chupp and Holle, 1994). The life of a seal is influenced by the contact pressure that exists between the bristle tips and rubbing surface. This contact pressure is determined by the distribution and magnitude of both aerodynamic and frictional forces in the seal, as well as the mechanical behavior of the bristle matrix and rubbing surface to seal relative movements. The principal challenge that is currently faced in brush seal application is to minimize ware and consequently extend seal life. In order to achieve this, it is necessary to reduce the effective stiffness of the seal to rotor relative movements and to ensure that the magnitude of bristle blow down is sufficient to cause closure of the seal after excursion but not so excessive as to produce unacceptable ware. Since brush seals are employed in a variety of engine applications, the optimum geometry for a given operating condition (pressure, leakage, excursion etc.) is likely to be unique. Given the array of design variables that influence the performance of the seal, the scope for employing a model that can predict the operation of a particular geometry is considerable.

In order to predict bristle displacements and contact pressures, it is therefore necessary to obtain estimates of the aerodynamic forces acting on the bristles and apply these to a mechanical model. Chew et al. (1995), developed a technique for applying the aerodynamic forces predicted by a CFD code to a mechanical model of the bristle matrix. Bristle movements, stresses, and bristle tip contact loads were predicted. Turner et al. (1997) developed the mechanical model of Chew et al. (1995) to consider frictional effects between the downstream bristle row and backing ring. Treating the bristle matrix as a single entity limits the accuracy of the mechanical model since movement is only considered between the downstream bristle row and backing ring face. The authors concluded that since, in clearance seals, the distribution of aerodynamic forces and the position of the bristle matrix were dependent on each other, there was a requirement for iteration between the CFD and mechanical parts of the model. The present study is a continuation of that of these previous workers. An iterative routine has been developed between the CFD and mechanical component of the model. Frictional effects are considered between neighbouring bristle rows as well as at the backing ring.

Model results for seals of both initial build clearance and interference are compared to experimental measurements obtained from tests conducted on the engine seal experimental test facility at the University of Oxford (Wood and Jones, 1997).

Numerical Modeling

Fluid Dynamics. The CFD model is described in detail in Chew et al. (1995). For completeness brief description is given here.

Outside the bristle pack, which is assumed to be a rectangle region, the Reynolds-averaged Navier-Stokes equations are used with a Prandtl mixing length model of turbulence. Uniform total temperature of the air is assumed. The conservation equations for mass and momentum are respectively,

$$\nabla \cdot (\rho \underline{u}) = 0 \tag{1}$$

$$\rho \underline{u} \cdot \nabla \underline{u} = \nabla \cdot \mu_e \nabla \underline{u} + \nabla \cdot \mu_e \nabla \underline{u}^T - \nabla p. \tag{2}$$

Contributed by the International Gas Turbine Institute (IGTI) of THE AMERICAN SOCIETY OF MECHANICAL ENGINEERS for publication in the ASME JOURNAL OF ENGINEERING FOR GAS TURBINES AND POWER. Paper presented at the International Gas Turbine and Aeroengine Congress and Exhibition, Stockholm, Sweden, June 2–5, 1998; ASME Paper 98-GT-372.

Manuscript received by IGTI March 22, 1998; final revision received by the ASME Headquarters June 23, 1999. Associate Technical Editor: R. Kielb.

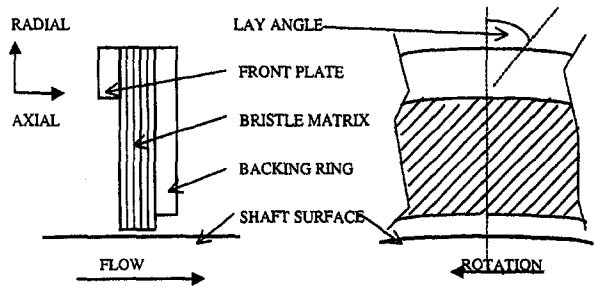

Fig. 1 Schematic of build clearance brush seal

Within the bristle matrix the right hand side of the momentum conservation equation (Eq. 2) is modified with the addition of a anisotropic, nonlinear resistance law (Eq. 2):

$$\underline{F_r} = -A\mu\underline{u} - B\rho|\underline{u}|\underline{u}$$

$$\rho\underline{u}\cdot\nabla\underline{u} = \nabla\cdot\mu_e\nabla\underline{u} + \nabla\cdot\mu_e\nabla\underline{u}^T - \nabla p + \underline{F_r}. \quad (3)$$

This represents the body force acting on the bristle matrix. **A** and **B** are the viscous and inertial resistance tensors:

$$A = a_n\underline{e_n}\underline{e_n} + a_s\underline{e_s}\underline{e_s} + a_z\underline{e_z}\underline{e_z}$$

$$B = b_n\underline{e_n}\underline{e_n} + b_s\underline{e_s}\underline{e_s} + b_z\underline{e_z}\underline{e_z}$$

The resistance coefficients, a_n, a_s, a_z, b_n, b_s, and b_z are defined in the principal directions, which are normal to the bristles in the $r-\theta$ plane ($\underline{e_n}$), aligned with the bristles in the $r-\theta$ plane ($\underline{e_s}$), and in the axial direction ($\underline{e_z}$) (see Fig. 1). The boundary conditions are the total pressure and flow angle at inlet, static pressure at outlet, and no-slip, no-penetration at the walls.

Mechanical Model. The mechanical model is developed from that employed by Turner et al. (1997) which only considered frictional effects between the downstream bristle row and backing ring.

In the bending calculation it is assumed that the bristle deflections are much smaller than the bristle length, and, therefore, axial deflections are independent of the forces and deflections in the orthogonal ($r-\theta$) plane. The equation underlying the model for both axial and orthogonal plane deflections is that for the flexion of a straight beam:

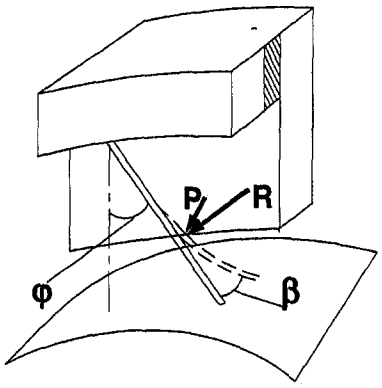

Fig. 2 The inclined prop effect

$$EI\frac{d^2y}{dx^2} = M, \quad (4)$$

where, x is the distance along the bristles, y is the deflection normal to the bristle, and M is the bending moment in the plane considered. Taking $x = 0$ at the free end of the bristle and $x = 1$ at the fixed end, the following boundary conditions apply:

$$y = \frac{dy}{dx} = 0 \quad \text{at} \quad x = 1. \quad (5)$$

For the axial bending calculation, the forces on the bristles include aerodynamic forces, reaction forces between contacting bristle rows and at the backing ring. An iterative solution method is used to obtain the reaction forces and deflections. Friction is neglected in the axial bending calculation.

The aerodynamic forces acting on the bristles are equal, but opposite in sign to the resistance forces for the fluid flow ($\underline{F_r}$ in Eq. 3), and are obtained from bilinear interpolation of the CFD results. The problem is discretised by defining a number of nodes along the length of the bristles and approximating all the forces on the bristle to point forces acting at the nodes. From the linear nature of the problem it follows that the principle of superposition may be used.

For bristle bending in the orthogonal plane, in addition to the aerodynamic forces, frictional effects between contacting bristle rows, at the backing ring and at the shaft interface are also considered. A mechanism termed the inclined prop effect (Fig. 2), can, in addition to the aerodynamic forces, be responsible for

Nomenclature

A, B = viscous and inertial resistance tensors
a, b = viscous and inertial resistance coefficients
c = normal bristle deflection at the tip
dr = build clearance
D = shaft diameter
$\underline{e}$ = unit vector
E = modulus of elasticity
$\underline{F_r}$ = resistance force per unit volume
I = moment of inertial
l = bristle length
k = coefficient of expansion for rotor
M = bending moment
p = static pressure
p_d = downstream pressure
p_r = pressure ratio (p_u/p_d)
p_u = upstream pressure
P = inclined prop force
r = radial co-ordinate
R = axial reaction force at the backing ring edge
S_n = tip force normal to bristle
S_r = shaft reaction normal to surface of shaft
t = torque
T = friction force
$\underline{u}$ = mean velocity vector
x = distance along bristle length (from tip)
y = normal bristle deflection
z = axial co-ordinate
α = coefficient of friction between the shaft and the bristle tips
β = axial deflection of bristle at backing ring (see Fig. 2.)
δr = radial expansion of the rotor
φ = bristle lay angle (0 degree for radial alignment)
λ = cohesion (friction) factor
μ = viscosity
θ = tangential co-ordinate
ρ = density
ω = shaft rotation speed

Subscripts

e = effective
j, i = bristle row j, location $x = x_i$
n = direction normal to the bristles in the $r-\theta$ plane
s = direction aligned with the bristles in the $r-\theta$ plane
t = turbulent
z = axial direction

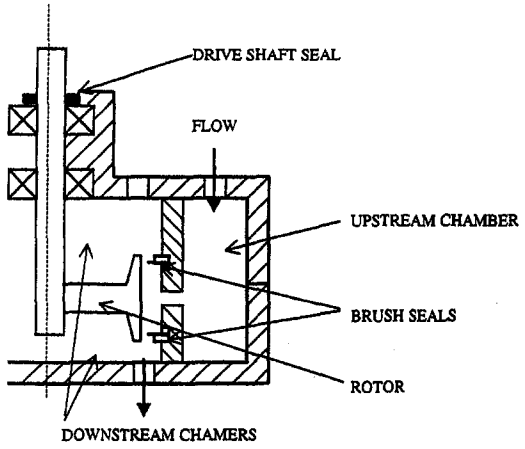

Fig. 3 Engine seal test facility

radially inward deflection of the bristles. It occurs as a consequence of the reaction force at the backing ring edge, which due to the axial bending of the bristles, has a component in the orthogonal plane (P):

$$P = R \tan \beta \times \tan \varphi,$$

where R is the axial reaction at the backing ring edge and β is the angle between the bristle and the backing ring face (which is zero when there is no axial deflection).

The friction forces are given by

$$T_{j,i} = \min (\lambda_j R_{j,i}, F_{j,i}),$$

where λ_j is the cohesion factor (or friction factor) between row j and row $j - 1$ or between the rear-most row and backing ring when $j = 1$. $R_{j,i}$ is the reaction force in the axial direction. $F_{j,i}$ is the force required to maintain the initial, relative position of bristle row j and row $j - 1$ at the point i. If $\lambda R > F$, static friction is dominant, and bristle row j is fixed in position in relation to row $j - 1$ at the point i. If $\lambda R < F$, then sliding friction opposes the bristle movement. The limiting cases are as follows: λ is large (e.g., $\lambda = 1$), where the bristles will lock together and move as a single entity; or $\lambda = 0$ (frictionless), where the bristles move independently without drag from adjacent rows.

For bristles in contact with the shaft a reaction force at the shaft surface is generated. This force is obtained from the restriction on bristle deflection. If c denotes normal bristle deflection at the tip (which will be negative for a radial closure) and the build clearance is dr, then

$$c \sin \varphi \geq -dr.$$

To satisfy this condition a point force S_n acting normal to the bristle may be required. The reaction force which is normal to the shaft surface (S_r) can be described in terms of the point force which is normal to the bristle tip:

$$S_r = S_n/(\sin \varphi + \alpha \cos \varphi),$$

where α is the coefficient of friction at the shaft surface. The torque produced by the seal on the shaft is the sum over all the bristle rows of the product of normal shaft reaction, coefficient of friction, shaft radius, and number of bristles per row:

$$t = \sum_{\text{rows}} \alpha S_r D/2$$

Apparatus

Design, instrumentation calibration and operation of the engine seal test facility is described in detail in Wood and Jones (1997). A brief description is given here.

Table 1 Averaged geometries for apparatus and seals

	Interference seal	clearance seal
bristle bore (mm)	327	328
backing ring diameter (mm)	329	330
rotor diameter (mm)	328	327

The working section is shown in Fig. 3. Two test seals are employed in a back to back configuration in order to minimize axial loading of the shaft and bearing assembly. The shaft is driven by a 100 kW air turbine. Approximate geometries for the test seals are given in Table 1.

The parasitic aerodynamic, air turbine and bearing torques are calibrated; this allows the torque produced by the seals to be inferred from the observed acceleration of the rotor.

A video system is used to observe and record the behavior of the seals. Cameras are coupled to two endoscopes which focus on a 5 cm circumference on the upstream side of the seal and a 1 cm circumference on the downstream side. These images are displayed in a split screen format. A third camera is used to superimpose speed and pressure readings onto this image.

Results

Interference Seal. Model predictions for mass flow at an upstream pressure of 6 bar abs. are compared to experimental results in Fig. 4. During the experiment the rotor is stationary and the pressure ratio across the seal is increased by manual operation of a downstream valve. Two sets of results, marked higher and lower resistance, are shown for the model. The "higher" set of results represents a seal in which the bristles are more closely packed. The resistance coefficients for the two cases are

higher: $a_n = a_z = 60a_s = 7.44 \times 10^{11}\ \text{m}^{-2}$,

$b_n = b_z = 2.8 \times 10^6\ \text{m}^{-1}$, $b_s = 0$

lower: $a_n = a_z = 60a_s = 5.317 \times 10^{11}\ \text{m}^{-2}$,

$b_n = b_z = 1.998 \times 10^6\ \text{m}^{-1}$, $b_s = 0$

The use of the lower resistance coefficients, predicts mass flows that are in agreement with the experiment data at pressure ratios below approximately 1.2 and over estimate mass flow by up to 20 percent at greater pressure ratios. The model results with higher resistance coefficients are in good agreement with the experimental data at the greater pressure ratios. The results indicate that

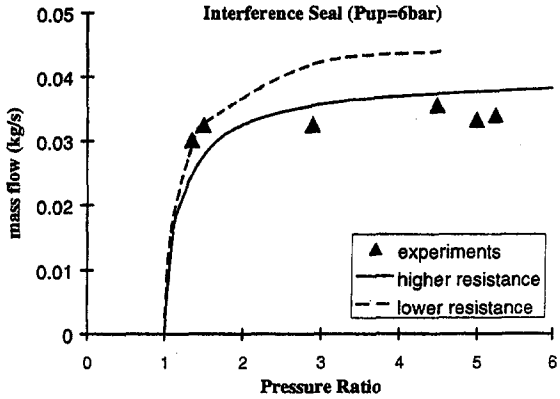

Fig. 4 Mass flow versus pressure ratio across seal

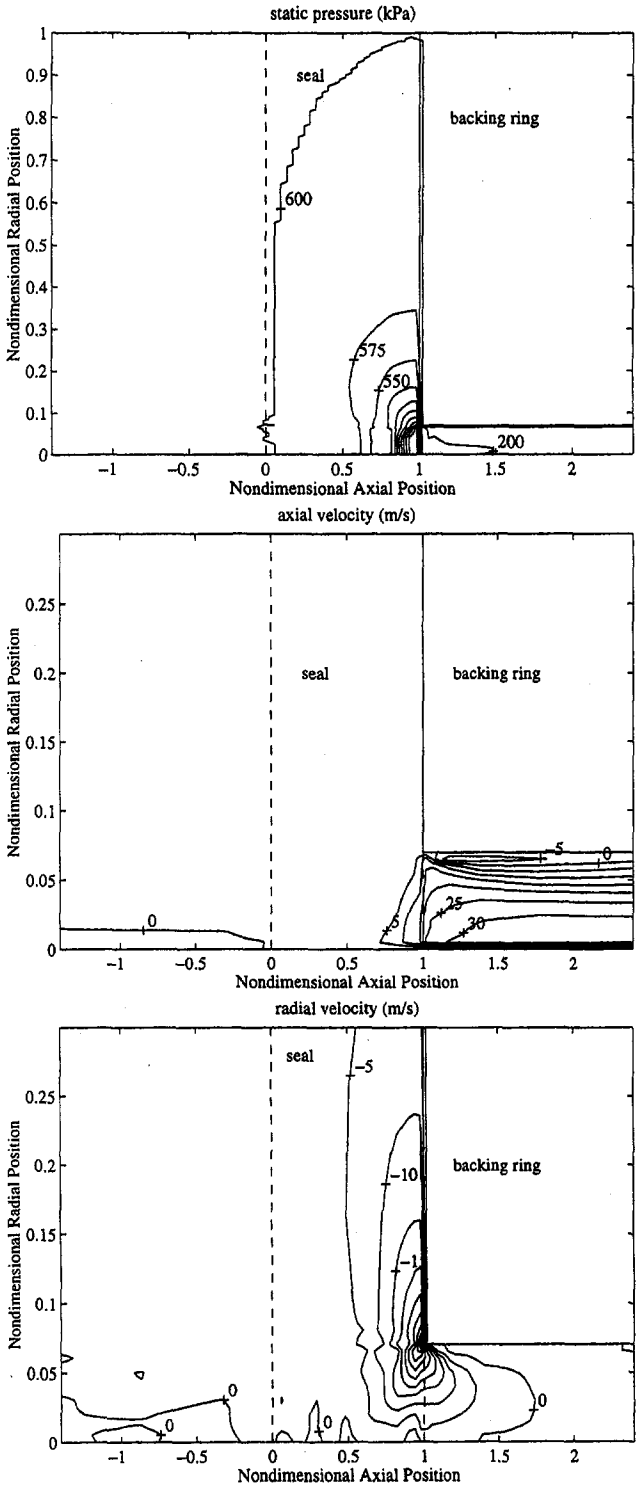

Fig. 5 Pressure and velocity contours for interference seal (Pr = 3.0)

closer packing of the bristle matrix is produced by an increase in differential pressure across the seal.

CFD predictions of static pressure, axial velocity and radial velocity are shown in Fig. 5. Upstream and downstream pressure are 600 kPa abs. and 200 kPa abs., respectively. The radial position is nondimensionalized by the radial bristle length. The axial position is nondimensionalized by the thickness of the bristle pack. The nondimensional axial position for the seal is between 0 and 1. Static pressure contours are at intervals of 25 kPa. and demonstrates, that as a consequence of compressibility, there is an increase in the pressure drop per unit length in the downstream region of the bristle matrix.

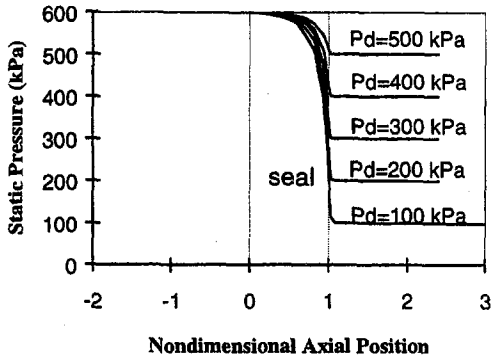

Fig. 6 Axial pressure distributions at shaft surface

Velocity contours are at intervals of 5 m/s. Radial velocity is positive when moving away from the shaft, axial velocity is positive in the direction from the upstream to the downstream. The magnitude of the radial velocity is greatest (−52.7 m/s) in the region which is adjacent to the corner formed by the upstream face and bore of the backing ring. There is a small reverse flow close to the backing ring bore immediately downstream of the bristle matrix. A reverse flow in the axial velocity distribution indicates the presence of a recirculation in this region. A maximum axial velocity of 34.8 m/s is predicted to occur at a position which is adjacent to the shaft surface and downstream of the bristle matrix. Similar velocity and pressure distributions are predicted for interference seals at an upstream pressure of 600 kPa and pressure ratios of 6, 2, 1.5 and 1.17.

For the test presented in Fig. 5 and at the other pressure conditions discussed above, predictions for the axial pressure distributions at the surface of shaft are shown in Fig. 6. As expected, as a consequence of compressibility, the pressure drop is observed to increase in the downstream direction. This is in disagreement with experiments conducted by Bayley and Long (1993), on seals in interference with a static rotor, where an almost linear pressure drop along the surface of the shaft was measured in the axial direction.

In order to predict the mechanical behavior of the seal, the CFD prediction for the aerodynamic forces was applied to the mechanical model. The mechanical model was then iterated from a specified position of the bristle matrix (termed "start position") until equilibrium of forces was established. As expected, this equilibrium position was found to be dependent on the specified start position; consequently, different solutions for contact pressure and consequently the torque exerted on the shaft were obtained. A start position in which the bristles are deflected by the mechanical interference with the shaft in the absence of frictional and aero-

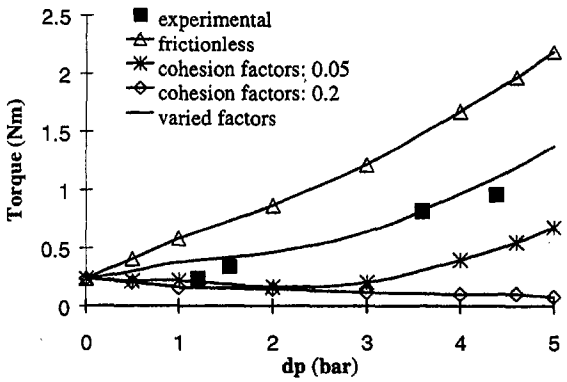

Fig. 7 Comparison of peak values of torque

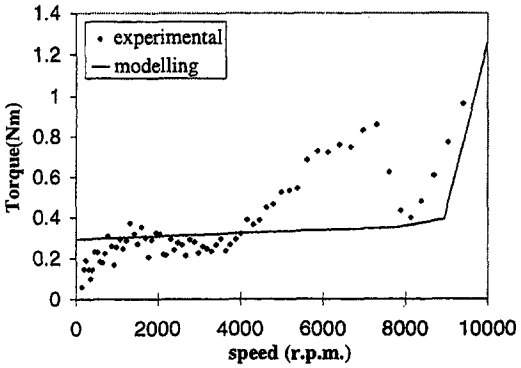

Fig. 8 Comparison of theoretical and experimental torque in a rundown test (Pr = 3.0)

dynamic forces within the seal was assumed in each case. In the present model the cohesion coefficients are time independent and therefore do not account for vibration of the bristles that might be induced by step changes in pressure or excitation from the rubbing surface. It should also be noted that the solution found by the mechanical model for a given start position may not be unique.

For a series of experiments conducted at an upstream pressure of 6 bar abs., the peak torque developed when pressure is initially applied to the seal is plotted against differential pressure in Fig. 7. Pressure is applied at a rotor speed of 10,000 rpm., torque is a maximum at this point and thereafter reduces as a consequence of frictional effects which restrict the ability of the bristles to follow the centrifugal contraction of the decelerating rotor. Various model predictions for torque are plotted along side the experimental data. The frictionless model, in which all the bristles deflect freely under the aerodynamic forces, gives the maximum possible torque for a specific differential pressure and overestimates the experimental data. Model results with cohesion factors of 0.05 and 0.2 demonstrate the effect of friction in limiting bristle blow down. Even at a cohesion factor of 0.05, which is significantly less than that which can be reasonably assumed for metal to metal contact, the model underestimates the experimental results. This is attributed to transient effects that occur with the initial application of pressure. For example, the bristles were observed to momentarily vibrate and a reduction in the influence of frictional effects would therefore be expected. To account for this, fictitiously low cohesion factors were assigned to the seal to model behavior in the transient phase. Good agreement with experimental results was obtained by assigning cohesion factors between neighboring rows in the upstream to downstream direction of 0.2, 0.2, 0.19, 0.17, 0.15, 0.13, 0.11, 0.09, 0.07, and 0.05; and a cohesion factor of 0.03 between the downstream row and backing ring. Since, in the unpressurized state the bristles are splayed axially, the varied cohesion factors represent the process by which the bristles are deflected into contact with neighboring rows when pressure is applied.

The torque produced by the seal in run down tests was modeled by considering the centrifugal change in the diameter of the rotor. Changes in the aerodynamic forces as a consequence of excursion of the shaft surface were ignored. The relationship between rotational speed ω and growth of shaft radius δr is

$$\delta r = k\omega^2, \tag{11}$$

in which the constant of proportionality (k) was derived from the measured radial growth of 0.05 mm at 10,000 rpm.

The peak torque, at the onset of pressure at the beginning of the test, was calculated by assuming varied cohesion factors. Subsequent torques at decreasing speed were calculated by assuming cohesion factors of 0.2 between adjacent rows and 0.06 between the downstream row and backing ring. Experimental results and model predictions for a test conducted at an upstream pressure of 6 bar abs. and mean pressure ratio of 3 are shown in Fig. 8. The general characteristic of the model is in reasonable agreement with the experiment in view of the approximations used. The temporary increase in the experimental measurement at approximately 7500 rpm. was attributed to instability of the bristles induced by rotation of the shaft (Wood and Jones, 1997), a time dependent effect which is not accounted for in the model.

Clearance Seal. Modeling of the clearance seal is complicated by the fact that the flow field is completely different between the initial clearance and blown down states. Turner et al. (1997) accounted for this by adjusting the resistance coefficients to cor-

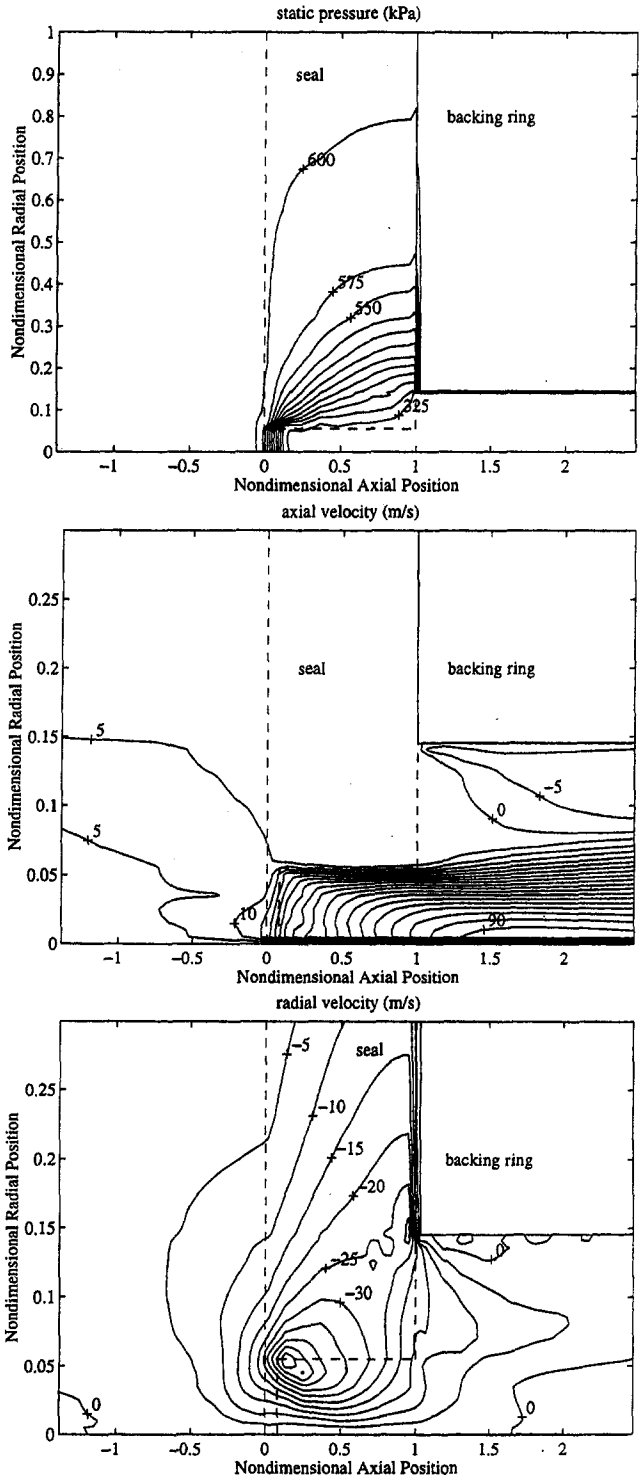

Fig. 9 Pressure and velocity contours for clearance seal (Pr = 2.0)

relate with experimental measurements of backing ring pressure distribution. In the present experiments, only the first 2 to 3 upstream bristle rows were observed to blow down, no movement was evident in the downstream rows, this was reflected in the bristle tip wear which was always confined to the first 2 to 3 upstream rows.

In order to simulate this movement of the bristle matrix, an iterative technique between the CFD and mechanical models was developed. The starting position for the iteration was the equilibrium position of the bristle matrix in the absence of frictional, aerodynamic and mechanical forces. The porous region which represents the bristle matrix in the CFD code was treated as a series of rectangles (representative of individual bristle rows). The position of these rectangular regions was adjusted in accordance with the deflections predicted by the mechanical model. Iteration was conducted between the CFD and mechanical models until the change in the flow field produced by changing the position of the bristle matrix was negligible. Displacement of the porous region was confined to that which occurs in the orthogonal plane, axial bending of the bristles was predicted by the mechanical model but assumed to have a negligible effect on the nature of the flow field.

The model was further complicated by experimental observations which revealed that the upstream rows did not deflect in a uniform manner. Typically, only 50 percent of the blown down bristles were in contact with the shaft and gaps were evident between adjacent groups of blown down bristles around the circumference of the seal. To account for this, the following lower resistance coefficients were employed in the blown down region of the bristle matrix:

$$a_n = a_z = 60a_s = 3.6 \times 10^{10}\ \mathrm{m}^{-2},$$

$$b_n = b_z = 1.2 \times 10^{5}\ \mathrm{m}^{-1}, \quad b_s = 0.$$

A cohesion factor of 0.2, between adjacent bristle rows and at the backing ring, is used in all of the clearance seal analyses. CFD predictions for static pressure and velocity, at an upstream pressure of 600 kPa and downstream pressure of 300 kPa are shown in Fig. 9. The maximum axial and radial velocities are 93.8 m/s and −53.8 m/s, respectively. Pressure contours are at intervals of 25 kPa and illustrate that the pressure drop is concentrated in the region of the blown down bristles.

Model predictions for mass flow are in good agreement with a series of experiments conducted at upstream pressure of 10 bar abs. (Fig. 10).

In Fig. 11, experimental results and model predictions are shown for the torque produced by the seal in an acceleration test. The upstream pressure was maintained as 10 bar. Pressure is applied to the seal whilst the rotor is stationary, the rotor is then accelerated. The model correctly predicts the increase in torque that results as a consequence of the shaft surface expanding into the bristle matrix. The frictional forces in the bristle matrix which resist radially outward deflection of the bristles, under expansion of the shaft, result in an increase in bristle tip contact pressure.

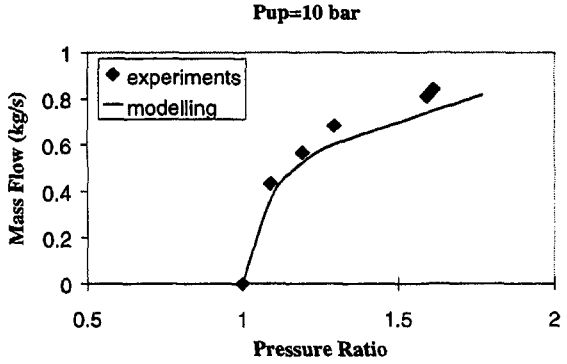

Fig. 10 Mass flow versus pressure ratio across seal

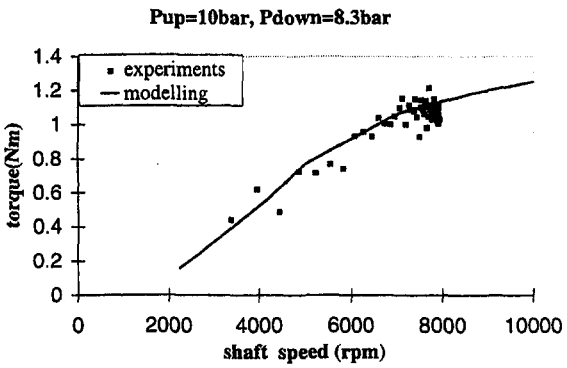

Fig. 11 Comparison of torque with an acceleration test

Conclusions

The study further demonstrates that the use of a non-Darcian resistance law can give good agreement with experimental measurements of leakage for both interference and clearance seals. Predictions for mass flow through interference seals demonstrate that the porosity of the bristle matrix is influenced by compression caused by the application of pressure. Currently, uniform resistance coefficients are assumed to exist in the interference seals, whereas two different uniform regions are assumed in the clearance seals. It should be possible to establish a relationship between the resistance coefficients and the pressure drop across the seal when more experimental data becomes available.

Frictional effects have been observed in static and dynamic experiments. In this paper, a simple frictional model has been introduced. Friction coefficients can be selected so that model predictions for bristle displacements and changes in torque during dynamic tests are in good agreement with experimental measurements and observations. However, it is apparent that the simple model does not capture the full complexity of brush seal behaviour. During pressure transients, the time-dependent process in which flow propagates through the bristle matrix is observed to have a significant effect on the mechanical performance of the seal and this area offers scope for improvement of the model.

The iterative CFD and mechanical model has given reasonable agreement with the observed and measured behavior of clearance seals. In this case, good agreement was obtained with the increase in seal torque due to shaft growth in an acceleration test.

The development of the model has generated a useful research tool for understanding and predicting complex brush seal behaviour. The ability to parametrically compare a variety of designs has greatly reduced the number of seal permutations that it is necessary to test at the pre production prototype stage. This has offered advantages in terms of cost, particularly in view of tooling requirements for bristle matrix production, and perhaps more importantly has allowed a number of alternative geometries, whose benefits might not be immediately obvious to the brush seal designer, to be investigated with relative ease.

Acknowledgments

Financial support for the work described in this paper was provided by the E.P.S.R.C. and Rolls-Royce plc. The authors would like to thank the directors of Rolls-Royce plc for their permission to publish.

References

Braun, M. J., and Kudriavtsev, V. V., 1995, "A Numerical Simulation of a Brush Seal Section and Some Experimental Results," *Journal of Turbomachinery*, Jan., Vol. 117, pp. 190–202.

Chew, J. W., Lapworth, B. L., and Millener, P. J., 1995, "Mathematical Modeling of Brush Seals," *Int. J. Heat & Fluid Flow*, Vol. 16, pp. 493–500.

Chupp, R. E., and Holle, G. F., 1994, "Generalising Circular Brush Seal Leakage Through a Randomly Distributed Bristle Bed," ASME Paper 94-GT-71.

Baylay, F. J., and Long, C. A., 1993, "A Combined Experimental and Theoretical Study of Flow and Pressure Distribution in a Brush Seal," ASME JOURNAL OF ENGINEERING FOR GAS TURBINES AND POWER, Vol. 115, No. 2, pp. 404–410.

Dowler, C. A., Chupp, R. E., and Holle, G. F., 1992, "Simple Effective Thickness Model for Circular Brush Seals," AIAA-92-3192.

Ferguson, J. G., 1988, "Brushes as High Performance Gas Turbine Seals," ASME Paper 88-GT-182.

Hendricks, R. C., Griffin, T. A., Kline, T. R., Csavina, K. R., Pancholi, A., and Sood, D., 1994, "Relative Performance Comparison Between Baseline Labyrinth and Dual Brush Compressor Discharge Seals in a T-700 Engine Test," ASME Paper 94-GT-266.

Turner, M. T., Chew, J. W., and Long, C. A., 1997, "Experimental Investigation and Mathematical Modeling of Clearance Brush Seals," ASME Paper 97-GT-282.

Wood, P. E., and Jones, T. V., 1997, "A Test Facility for the Measurement of Torques at the Shaft to Seal Interface in Brush Seals," ASME Paper 97-GT-184.

D. J. Maeng

J. S. Lee

Turbo and Power Machinery Research Center,
Department of Mechanical Engineering,
Seoul National University,
Seoul 151-742, Korea

R. Jakoby

S. Kim

S. Wittig

Lehrstuhl und Institut für Thermische
Strömungsmaschinen,
Universität Karlsruhe, Germany

Characteristics of Discharge Coefficient in a Rotating Disk System

The discharge coefficient of a long orifice in a rotating system is measured to examine the rotational effect on discharge behavior. The rotating system is comprised of a rotating disk and two stators on both sides of the rotating disk. Test rig is constructed to simulate the real turbine operating conditions. Pressure ratios between upstream and downstream cavities of the orifice range from 1.05 to 1.8, and rotational speed of the rotor disk is varied up to 10,000 rpm. The orifice hole bored through the rotor disk has length-to-diameter ratio of 10. For a better interpretation of discharge behavior, three-dimensional velocity field in the downstream and upstream cavities of the rotor is measured using a Laser Doppler Velocimetry. A new definition of the rotational discharge coefficient is introduced to consider the momentum transfer from the rotor to the orifice flow. Additional loss in the discharge coefficient due to pressure loss in the orifice hole at the inlet and exit regions is quantitatively presented in terms of the Rotation number and the compressibility factor. The effect of corner radiusing at the orifice inlet is also investigated at various rotational conditions.

Introduction

As compactness, lightness, and high efficiency are required in recent design of gas turbine, the internal air system is getting more and more important and complicated. Internal air is defined as the flow which does not directly contribute to the turbine power but performs several important functions such as blade and disk cooling, accessory unit cooling, bearing chamber sealing, prevention of hot gas ingestion into turbine disk cavities, control of bearing axial loads, and control of turbine blade tip clearances (*The Jet Engine*, 1986).

The internal air flow rate reaches up to more than 20 percent of the main flow rate from the compressor. This large amount of airflow supplied by additional compressor work directly affects the overall turbine efficiency. Consequently, it is demanded to supply an appropriate amount of airflow to each component of engines through an accurate estimation of the performance of various parts.

Since airflow passages are subject to numerous operating conditions, and the shape of orifice is far from the standardized one such as ASME orifice, numerous studies have been conducted to investigate the orifice discharge characteristics under various operating conditions.

Bragg (1960) considered the effect of compressibility on the discharge coefficient. He made a simplified assumption on the flow pattern at the upstream wall of an orifice, and compared his theoretical predictions with experimental results. Lichtarowicz et al. (1965) observed discharge behaviors in a wide range of length-to-diameter ratios, and obtained the critical discharge coefficient at large Reynolds numbers. Rohde et al. (1969) determined the effect of approaching angle of inlet flow relative to orifice axis. Hay et al. (1983) investigated the crossflow effect on the discharge coefficient. Their results show that the influence of crossflow is strong and complex, particularly on the inlet side. Hay et al. (1987) defined the additive loss due to the crossflow of orifice inlet and outlet, and described it with the momentum ratio between orifice jet and crossflow. Hay and Spencer (1992) studied the effect of radiusing and chamfering of orifice edge. They acquired about 10–30 percent increase in the discharge coefficient, and reported that the chamfered orifice shows more desirable performance. Recently, Hay and Lampard (1996) reviewed works on the discharge behavior of turbine cooling holes.

However, all of the studies mentioned above are limited to the stationary conditions, and, thus, there is a lack of information on a rotating system. Meyfarth and Shine (1965) focused on the discharge behavior of rotating orifices, but this study is confined to the orifice with very short length-to-diameter ratio, which is far from the mainly used orifice in the internal air system of gas turbine.

The internal airflow should pass inevitably through rotating components because a turbine system is composed of stationary and rotating parts. Recent development of design technology makes it possible to reach high rotational speeds. In this case, discharge behavior is easily expected to considerably deviate from stationary one. The effect of rotation thus should be estimated for a balanced supply of airflow to each component, and consequently for the reduction of overall amount of airflow.

In this study, a turbine disk system was constructed to simulate real operating conditions. The test rig is composed of a rotating disk with orifices and two stationary disks. Characteristics of the discharge behavior in the rotating disk system is scrutinized through measurements of the discharge coefficient under various rotating conditions in a wide range of pressure ratio between upstream and downstream of the orifice. The effect of corner radiusing of the orifice inlet is also investigated.

Experimental Apparatus and Procedure

Experimental Facility. Schematic diagram of the test facility is depicted in Fig. 1. This test rig is constructed at the Institut für Thermische Strömungsmaschinen, Universität Karlsruhe, Germany. Compressor of 85.3 kW power supplies airflow at a maximum mass flow rate of 0.5 kg/s. Supply pressure level can be controlled up to 4 bars by a bypass valve. Mass flow rate is precisely determined in an orifice-metering system, which consists of three orifices with different measurable ranges. Thermocouples and pressure taps are installed to monitor temperature and pressure around orifices and inside of pipes.

Contributed by the International Gas Turbine Institute (IGTI) of THE AMERICAN SOCIETY OF MECHANICAL ENGINEERS for publication in the ASME JOURNAL OF ENGINEERING FOR GAS TURBINES AND POWER. Paper presented at the International Gas Turbine and Aeroengine Congress and Exhibition, Stockholm, Sweden, June 2–5, 1998; ASME Paper 98-GT-266.

Manuscript received by IGTI March 8, 1998; final revision received by the ASME Headquarters June 23, 1999. Associate Technical Editor: R. Kielb.

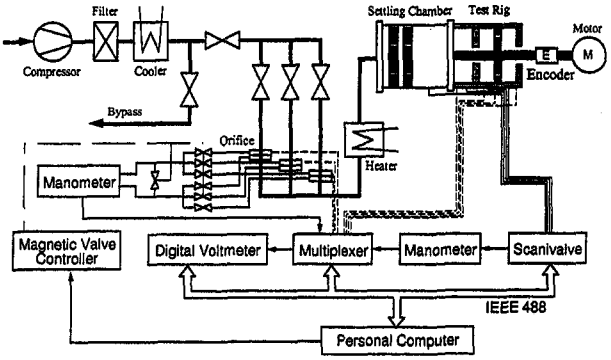

Fig. 1 Schematic diagram of experimental facility

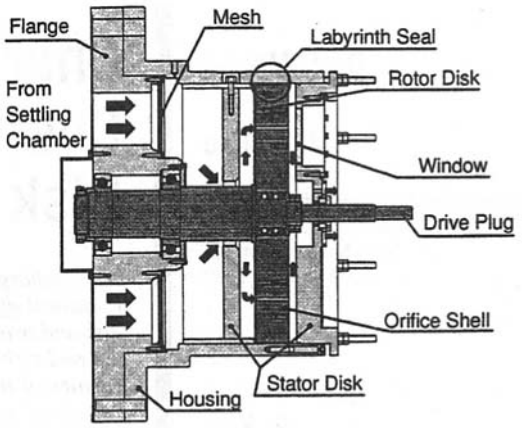

Fig. 2 Schematic diagram of test rig

The test rig is shown schematically in Fig. 2. A rotor disk where eight orifices are installed and two stator disks on each side of the rotor compose the turbine disk system. Turbulence mesh is positioned to remove large scale fluctuations from the settling chamber. Airflow comes into the upstream cavity through the inside annular slot, and then discharged into the downstream cavity through the rotating orifices. Dimensions of the rotating disk system are summarized in Table 1.

Due to the requirement of high rotational speed, high precision bearings are used, and labyrinth seal is adopted for sealing the gap between the rotor and housing. Gap distance is minimized to about 0.2 mm. The maximum allowable rotational speed is 10,000 rpm, which is equivalent to a circumferential velocity of 150 m/s at the outer edge of the rotor disk. An encoder which generates 4096 pulses per one revolution is attached on the shaft, and its signal is sent to a motor controller.

High flexibility considering geometrical variations is obtained by modular design of the rig. The orifices are bored into cylindrical shells. These are inserted into the disk to obtain easy modification of the geometry by replacing the shells. Furthermore, the distance of the stationary disks to the rotor disk can be continuously adjusted. Glass windows are installed on both front and rim sides of the test rig to acquire optical access for LDV measurements.

Two-dimensional velocity field in the upstream cavity, and three-dimensional velocity field in the downstream cavity are measured using an LDV system because the flow in the downstream cavity could be highly three-dimensional. The differential doppler technique for optical heterodyning is used in the back scatter mode of receiving optics.

A 10W Argon-Ion laser (Coherent INNOVA 90) is used in multi-mode operation as a light source. The multi-wavelength beam passes the transmitter box (Dantec), in which it is first split into two beams, one of which passes a bragg cell to be shifted with a frequency of 40 MHz for the detection of the flow direction. Subsequently, both of them are separated into the particular colors for two or three components (476.5 nm, 488 nm and 514.5 nm) and linked into two fiber probes (Dantec, 60 × 65; 60 × 67). Three channels of the burst spectrum analyzer (Dantec, 57N20, 57N35) are used to process simultaneously the multiplied signals. A commercial aerosol generator (Pallas AGF5.0) is used to seed the flow with atomized particles of DEHS solution. The mean diameter of the generated particles ranges from 0.21 to 0.27 μm. Detailed description of LDV system and signal processing procedures are well described in Jakoby et al. (1997). Statistical uncertainties in the measured velocity field are estimated using the procedures described by Snyder et al. (1984). The maximum uncertainty levels for each component of the axial and the circumferential velocities are estimated to be 2.8 percent and 2.5 percent, respectively, over the whole measured area.

Nomenclature

A = orifice cross-sectional area
C_d = discharge coefficient
$C_{d,\mathrm{rot}}$ = rotational discharge coefficient
C_{loss} = additional loss coefficient
c_p = specific heat at constant pressure
d = orifice hole diameter
f = compressibility factor ($=(p_s - p)/\frac{1}{2}\rho U^2$)
h = enthalpy
l = orifice hole length
Ma = Mach number of discharged jet ($=U/\sqrt{\gamma RT_\infty}$)
$\dot{m}$ = measured mass flow rate through orifice
$\dot{m}_{\mathrm{ideal}}$ = ideal mass flow rate through orifice
p_0 = static pressure at orifice inlet
p_s = stagnation pressure
p_t = rotational total pressure
R = gas constant
R_D = radius of rotor disk
R_h = pitch radius of orifice hole
Re = Reynolds number of discharged jet ($=Ud/\nu$)
Ro = Rotation number ($=\omega R_h/U$)
r = radial coordinate
r_c = corner radius of orifice inlet
s = gap distance between rotor and stator disks
T_0 = temperature at orifice inlet
T_∞ = temperature at orifice outlet
T_{rot} = rotational temperature ($=R_h^2\omega^2/2c_p$)
T_s = torque
T_t = rotational total temperature ($=T_0 + T_{\mathrm{rot}}$)
t = time
U = ideal exit velocity of discharge-ment
V_∞ = exit velocity of discharge considering rotational work transfer
$\bar{V}_\phi$ = averaged circumferential velocity component
W_s = shaft work
x = axial location from orifice outlet in the orifice flow direction
xx = axial location from orifice inlet in the direction opposite to the orifice flow

Greek Symbols

γ = specific heat ratio
ν = kinematic viscosity
Π = pressure ratio between upstream and downstream cavities ($=p_0/p_\infty$)
ϕ = circumferential coordinate
ω = rotational speed of rotor

Subscript

0 = orifice inlet
∞ = orifice outlet
rot = rotational
x = axial
ϕ = circumferential

Table 1 Dimensions of rotating disk system

	Parameter	Dimension
Orifice hole diameter	d (mm)	4
Orifice hole length	l (mm)	40
Corner radius of round inlet	r_c (mm)	2
Pitch circle radius of orifice	R_h (mm)	105
Rotor disk radius	R_D (mm)	160
Gap distance between rotor and stator	s (mm)	25

Measurement of Discharge Coefficient. Precise measurement of reference temperature and pressure, and mass flow rate through orifices in the rotor is essential to determine the discharge coefficient under various operating conditions. NiCr-Ni thermocouples and pressure taps are installed inside upstream and downstream cavities to identify inlet and exit conditions of the orifice. Static pressure taps of 1 mm diameter are drilled at right angle on disk surfaces, and thermocouple junctions are protruded by 2 mm from the disk surface to measure the fluid temperature. During the entire measurements, the orifice exit pressure is kept constant at 2 bars, and inlet pressure is changed according to the required pressure ratio.

In spite of the labyrinth seal, there is leakage flow through the gap between the rotor and housing. The amount of leakage mass flux should be considered for the exact evaluation of the discharge coefficient. The leakage mass flux, however, also changes with variation of experimental conditions such as rotational speed of the rotor, pressure ratio and geometric parameters. Thus, additional experiment for compensating the leakage flow is conducted. Waschka et al. (1992) found that the leakage flux of labyrinth seal can be determined by the inlet and exit conditions of the leakage and rotational speed. In each experiment, the leakage flux is measured with orifice shells being replaced by those with no orifice hole, keeping all other experimental conditions including rotational speed of rotor, pressure ratio, and geometric parameters the same as those in corresponding discharge coefficient measurement. The precise seal leakage rate as a function of pressure ratios and the rotor speeds is well described in Maeng (1998).

The discharge coefficient is defined as

$$C_d = \frac{\dot{m}}{\dot{m}_{\text{ideal}}}, \tag{1}$$

where $\dot{m}_{\text{ideal}}$ is the mass flux through the orifice in an ideal process.

In general, the following relation can be deduced for an ideal discharge system from energy conservation, entropy, and ideal gas relations:

$$T_0 = T_\infty + \frac{U^2}{2c_p}. \tag{2}$$

$\dot{m}_{\text{ideal}}$ can described in terms of inlet conditions using Eq. (2), which is given by

$$\dot{m}_{\text{ideal}} = \frac{p_0 A}{\sqrt{T_0}} \cdot \sqrt{\frac{2\gamma}{(\gamma-1)R}\left[\left(\frac{1}{\Pi}\right)^{2/\gamma} - \left(\frac{1}{\Pi}\right)^{(\gamma+1)/\gamma}\right]}. \tag{3}$$

Thus, the discharge coefficient can be defined as follows:

$$C_d = \dot{m} \cdot \frac{\sqrt{T_0}}{p_0 A} \Big/ \sqrt{\frac{2\gamma}{(\gamma-1)R}\left[\left(\frac{1}{\Pi}\right)^{2/\gamma} - \left(\frac{1}{\Pi}\right)^{(\gamma+1)/\gamma}\right]}. \tag{4}$$

Uncertainty in the measurement of the discharge coefficient is estimated less than 3.8 percent by Kline and McClintock's (1953) method for a single-sample experiment.

Results and Discussion

Flow Field in Upstream and Downstream Cavities. The coordinate system and disk configuration is depicted in Fig. 3. x, r, and ϕ are axial, radial, and circumferential coordinates, respectively, which are fixed at the rotor disk rotating in the clockwise direction viewed from the downstream face. The origin of x and xx coordinates are located on the disk surfaces facing downstream and upstream cavities, respectively. Three-dimensional velocity components are measured at a rotational speed of 6000 rpm and a pressure ratio of 1.05.

Figure 4 shows the velocity vectors in the x-ϕ plane from $\phi = -10$ to 20 degrees at a fixed radial location, $r = R_h$. Flow measurement near the rotor surface in upstream cavity cannot be made because of difficulty in probing. As shown in Fig. 4(b), flow in the region $xx/s > 0.5$ is relatively unidirectional which does not have the axial component. It seems that the flow only in the vicinity of the orifice is influenced by the orifice flow. On the other hand, the flow in the downstream cavity shows strikingly different structure from that in the upstream cavity, and shows strong three-dimensional behavior because jet-like orifice flow interacts with the downstream stator which is located at $x/s = 1$. The backward flow shown near the downstream stator is due to redirection of the flow after colliding with the stator. A rapid deceleration of the flow near the stator surface might occur because the velocity vector preserves its magnitude far down to the stator surface. Flow structure in the downstream cavity is described in detail by Jakoby et al. (1997).

Variation of circumferential velocity component along the radial direction is illustrated in Fig. 5. The circumferential velocity plotted in this figure is the averaged values over 360 deg in the circumferential direction. Figure 5(a) shows the variation of the circumferential velocity in the downstream cavity at the axial locations of $x/s = 0.40$ and 0.76. Note that the orifice center is

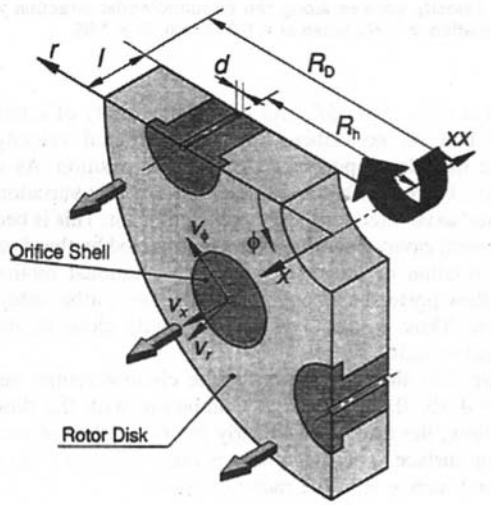

(a) rotor disk sector from downstream

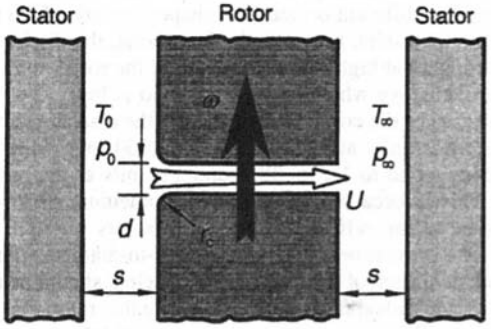

(b) orifice cross-section at the top of disks

Fig. 3 Configuration of the disks with coordinate system

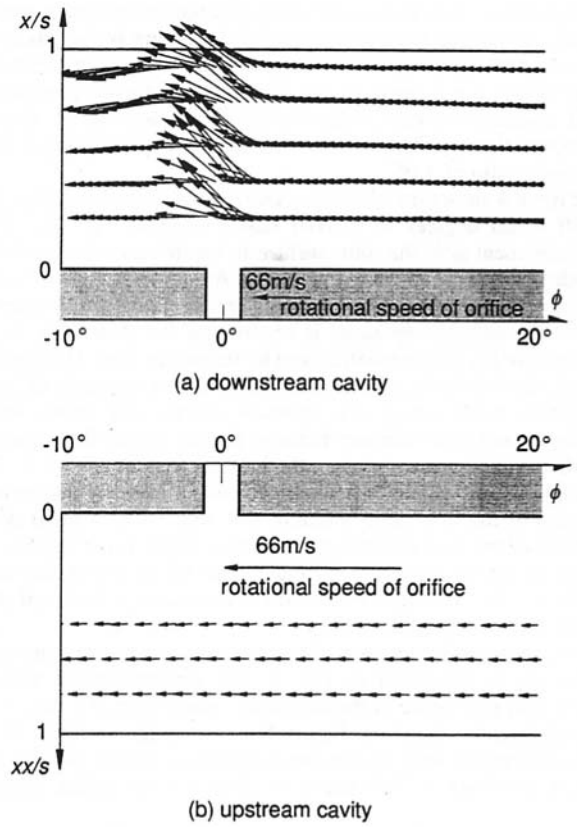

Fig. 4 Velocity vectors along the circumferential direction at a fixed radial location, $r = R_h$, when ω = 6,000 rpm, Π = 1.05

located at $r/R_D = 0.656$, and its linear velocity of rotation is 66 m/s. If there is no orifice, the circumferential velocity should increase linearly proportional to the radial position. As shown in Fig. 5(*a*), however, the circumferential velocity variation in both radial and axial directions appears insignificant. This is because the downstream cavity flow is not directly affected by the shear caused by the rotation of the disk but strong rotational motion of the orifice flow preserves its angular momentum further into the axial direction. Thus, it also has its magnitude close to the orifice rotational velocity, 66 m/s.

Figure 5(*b*) shows variation of the circumferential velocity at $xx/s = 0.50$, 0.66 and 0.82. Comparing with the downstream cavity flow, the flow shows nearly inviscid behavior except near the rotor surface. The magnitude is quite reduced from the rotor speed and increases in the radial direction.

Rotational Work Transfer from Rotor to Orifice Flow. The discharge coefficient C_d as a function of pressure ratio Π is plotted for different rotational speeds in Fig. 6. Figure 6(*a*) and Fig. 6(*b*) correspond to different orifice inlet shapes: square edged inlet and corner radiused inlet, respectively. In general, the discharge coefficient is higher at high rotational speed of the rotor, and this trend is more distinctive when the pressure ratio is low.

In the case of the corner radiused inlet, the discharge coefficient value exceeds unity at ω = 7500 and 10,000 rpm, which respectively correspond to $\bar{V}_\phi$ = 82.5 and 110 m/s at the orifice hole center. This is because the rotational momentum of the rotor is transferred to the orifice flow when it passes through the long orifice. The present orifice has the length-to-diameter ratio of 10. Thus, the definition of the discharge coefficient should be modified by reevaluating ideal mass flux considering this rotational momentum transfer. When energy balance is applied to a control volume including the orifice and its surroundings, energy equation is reduced as follows for a one-dimensional discharge system with adiabatic assumption.

$$\frac{dW_s}{dt} = \dot{m}\left(h_\infty + \frac{1}{2}V_\infty^2\right) - \dot{m}\left(h_0 + \frac{1}{2}V_0^2\right). \tag{5}$$

From the flow measurement data, the following assumption can be deduced:

$$\frac{V_0}{V_\infty} \cong \frac{V_{\phi,0}}{\sqrt{V_{x,\infty}^2 + (\omega R_h)^2}} \ll 1. \tag{6}$$

The shaft work transferred from the rotor can be determined by applying the angular-momentum theory. It follows that:

$$\frac{dW_s}{dt} = T_s \cdot \omega = \dot{m}\omega^2 R_h^2. \tag{7}$$

From Eq. (5)–(7), the energy relation can be rearranged as follows:

$$T_0 + \frac{R_h^2\omega^2}{2c_p} = T_\infty + \frac{V_{x,\infty}^2}{2c_p}. \tag{8}$$

When compared with Eq. (2), the second term on the left hand side is newly added because of the rotational energy transfer. This term can be defined as the rotational temperature T_{rot}, that is

$$T_{\text{rot}} = \frac{R_h^2\omega^2}{2c_p}. \tag{9}$$

With definition of T_{rot}, the rotational discharge coefficient considering the rotational work transfer, $C_{d,\text{rot}}$, can be written as follows:

$$C_{d,\text{rot}} = \dot{m} \cdot \frac{\sqrt{T_0}}{p_0 A} \Big/ \sqrt{\frac{2\gamma}{(\gamma-1)R}\left[\left(\frac{1}{\Pi}\right)^{2/\gamma}\left(1 + \frac{T_{\text{rot}}}{T_0}\right) - \left(\frac{1}{\Pi}\right)^{(\gamma+1)/\gamma}\right]}. \tag{10}$$

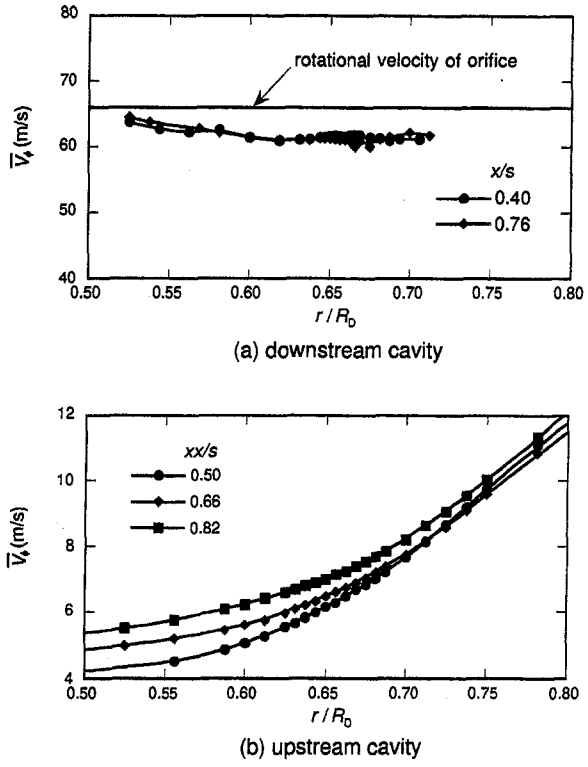

Fig. 5 Distribution of circumferential velocity in the radial direction when ω = 6,000 rpm, Π = 1.05

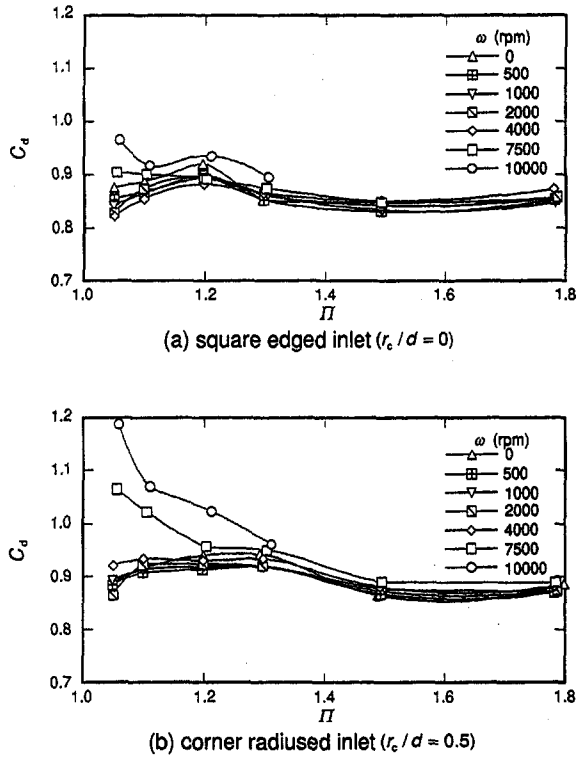

Fig. 6 Distribution of discharge coefficient

Meyfarth et al. (1965) described discharge behavior of a rotating system in terms of the velocity ratio of rotating orifice to discharged jet to take into account the rotational effect. In the present study, this velocity ratio is defined as the Rotation number, Ro, which is given by

$$\mathrm{Ro} = \frac{\omega R_h}{U}, \tag{11}$$

where U is the ideal exit velocity of discharge defined by Eq. (2) and (3) as follows:

$$U = \sqrt{\frac{2\gamma R T_0}{(\gamma - 1)}\left[1 - \left(\frac{1}{\Pi}\right)^{(\gamma-1)/\gamma}\right]}. \tag{12}$$

Figure 7 shows the variation of the rotational discharge coefficient $C_{d,\mathrm{rot}}$ for the square edged inlet with the Rotation number. Plotted are also the present data and data from Meyfarth et al. (1965) evaluated from the conventional definition of the discharge coefficient C_d. In the study of Meyfarth et al. (1965), their orifice is so short that the rotational work transfer effect is negligibly small. As can be seen in this figure, the rotational discharge coefficient now reasonably represents the discharge behavior which shows the same trend as Meyfarth et al. (1965). The rotational discharge coefficient, $C_{d,\mathrm{rot}}$, decreases with increasing Rotation number. The difference in the discharge coefficient values between present $C_{d,\mathrm{rot}}$, and Meyfarth et al. (1965) is owing to location of vena contracta. In the present study, vena contracta is located inside the long orifice hole, and thus the flow is reattached as it expands. *Visualized Flow* (1988) shows this for a stationary setup. The enlarged vena contracta leads to higher discharge coefficient than that of Meyfarth et al. (1965), because their orifice is very short.

Equation (10) can be rearranged into a similar form as the conventional definition of the discharge coefficient given by Eq. (4). The rotational total pressure in the isentropic process can be defined as follows:

$$\frac{p_t}{p_0} = \left(\frac{T_t}{T_0}\right)^{\gamma/(\gamma-1)} = \left(1 + \frac{T_{\mathrm{rot}}}{T_0}\right)^{\gamma/(\gamma-1)}. \tag{13}$$

The ideal mass flux considering rotational work transfer can be rewritten in terms of p_t and T_t as follows:

$$\dot{m}_{\mathrm{ideal,rot}} = \frac{p_t A}{\sqrt{T_t}}\sqrt{\frac{2\gamma}{(\gamma-1)R}\left[\left(\frac{1}{\Pi}\cdot\frac{p_0}{p_t}\right)^{2/\gamma} - \left(\frac{1}{\Pi}\cdot\frac{p_0}{p_t}\right)^{(\gamma+1)/\gamma}\right]}. \tag{14}$$

Finally, $C_{d,\mathrm{rot}}$ can be expressed in terms of the rotational pressure ratio, Π_{rot}, as

$$C_{d,\mathrm{rot}} = \dot{m}\cdot\frac{\sqrt{T_0}}{p_t A}\Big/\sqrt{\frac{2\gamma}{(\gamma-1)R}\left[\left(\frac{1}{\Pi_{\mathrm{rot}}}\right)^{2/\gamma} - \left(\frac{1}{\Pi_{\mathrm{rot}}}\right)^{(\gamma+1)/\gamma}\right]}, \tag{15}$$

where the rotational pressure ratio is defined as

$$\Pi_{\mathrm{rot}} = \Pi\,\frac{p_t}{p_0}. \tag{16}$$

Equation (15) has exactly the same formula as Eq. (4) if T_0, p_0 and Π are correspondingly replaced by T_t, p_t and Π_{rot}. It has been shown that the rotational work transfer in a rotating orifice system can be considered by introducing the rotational discharge coefficient $C_{d,\mathrm{rot}}$ which can be easily evaluated with the orifice exit and modified inlet conditions.

Figure 8 is a reproduction of Fig. 6 as a function of the rotational pressure ratio. Now the magnitude of the discharge coefficient can be presented in the reversed order, that is, it decreases with increasing rotational speed. It should also be noticed that in the case of the corner radiused inlet (Fig. 8(*b*)), the rotational discharge coefficient values are now meaningfully evaluated to be less than unity.

Additional Loss Due to Orifice Rotation. In addition to the rotational work transfer effect on the discharge behavior, an additional loss may be generated due to the relative motion of the orifice to upstream and downstream cavity flows. As shown in Fig. 7, results of both Meyfarth et al. (1965) and present $C_{d,\mathrm{rot}}$ diminish as the Rotation number increases. The additional loss can be generated at both inlet and outlet of the orifice. In the inlet region, flow separation bubble is getting larger as the Rotation number increases because the crossflow at the orifice inlet, which flows at right angle with respect to the orifice flow, is getting stronger, and consequently produces pressure loss. The pressure loss is also produced in the orifice exit region due to the interaction of the jet-like orifice flow and the stator, which is developed into a complex three-dimensional flow as shown in Fig. 4(*a*). This pressure loss is expected to result in the deficit of discharge coefficient.

In this section, it is attempted to systematically isolate the effect of the above pressure loss on the discharge behavior. To do this, the additional loss coefficient, C_{loss} is defined as follows:

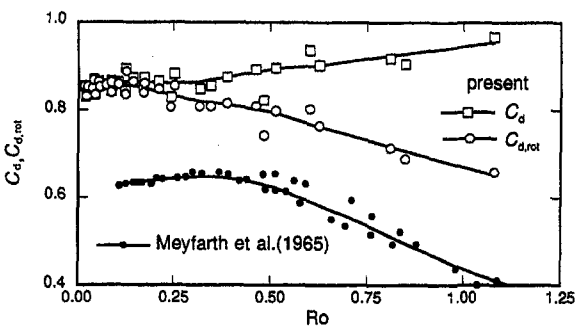

Fig. 7 Variation of discharge coefficients, C_d and $C_{d,\mathrm{rot}}$ with Rotation number ($r_c/d = 0$)

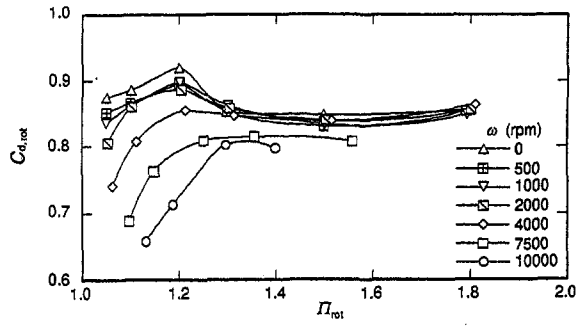

(a) square edged inlet ($r_c / d = 0$)

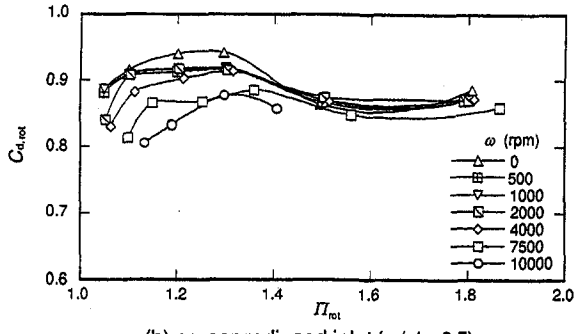

(b) corner radiused inlet ($r_c / d = 0.5$)

Fig. 8 Variation of rotational discharge coefficient with rotational pressure ratio

$$C_{loss}(\Pi_{rot}, \omega) = \frac{C_{d,rot}(\Pi_{rot}, \omega = 0) - C_{d,rot}(\Pi_{rot}, \omega)}{C_{d,rot}(\Pi_{rot}, \omega = 0)}, \quad (17)$$

where $C_{d,rot}(\Pi_{rot}, \omega = 0)$ and $C_{d,rot}(\Pi_{rot}, \omega)$ represent the curves at different rotational speeds shown in Fig. 8. The loss coefficient C_{loss} is determined in such a way that at a given rotational pressure ratio the difference between $C_{d,rot}(\Pi_{rot}, \omega = 0)$ and $C_{d,rot}(\Pi_{rot}, \omega)$ values are calculated from the data shown in Fig. 8 using an interpolation scheme proposed by Akima (1970), and then it is normalized by $C_{d,rot}(\Pi_{rot}, \omega = 0)$ value.

The loss coefficient as a function of the Rotation number is shown in Fig. 9. As expected the loss production increases with the Rotation number. This is because the higher Rotation number implies higher orifice rotational velocity compared relatively to the discharged orifice flow velocity at a given rotational pressure ratio. This fact agrees well with Hay et al. (1983) who observed the diminishing discharge coefficient of a long orifice, as the inlet or exit crossflow velocity increases.

However, the Rotation number alone is not sufficient to properly describe the loss characteristics because of the compressibility effect. Mach number of the present orifice jet, Ma, ranges from

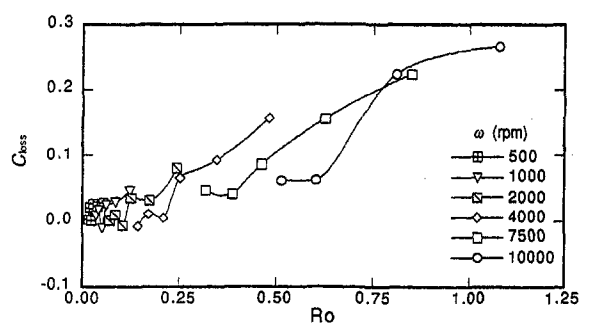

Fig. 9 Variation of additional loss coefficient with Rotation number ($r_c/d = 0$)

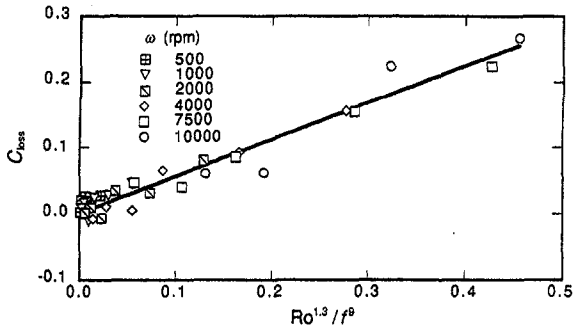

Fig. 10 Variation of additional loss coefficient with Rotation number and compressibility factor ($r_c/d = 0$)

0.26 to 0.88. As flow turns into the orifice hole, the streamline curvature is influenced by the compressibility. High compressibility results in an increase in turning angle of the streamline, which tends to enlarge the area of vena contracta. Such a change in the streamline curvature can be the primary cause of an increase in the discharge coefficient at high pressure ratio for a stationary orifice, as indicated by Bragg (1960). This effect is more pronounced in the presence of relative motion of surrounding flow. Furthermore, the exit velocity of dischargement increases in the presence of the wall friction, explained as Fanno process. This leads to the further flow expansion at a given mass flux.

In order to take into account the compressibility effect, another parameter should be introduced such as the dynamic pressure compressibility factor in addition to the Rotation number. The dynamic pressure compressibility factor, f, is defined as the ratio of the difference between stagnation pressure p_s and static pressure p_0 to the dynamic pressure as follows:

$$f = \frac{p_s - p}{\frac{1}{2}\rho U^2}. \quad (18)$$

The behavior of the dynamic pressure compressibility factor is related closely to the Mach number as described in Saad (1993). The loss coefficient is plotted in Fig. 10 including the compressibility effect. It looks very well correlated with $Ro^{1.3}/f^9$ regardless of the rotational speed ω. The exponents were determined by the least-error-square method.

Effect of Inlet Corner Radius. As shown in Fig. 6, the orifice with corner radiused inlet has higher discharge coefficient distribution than that of the square edged one in the entire experimental range. This is due solely to geometric difference of these two because the amount of the rotational work transfer for each inlet shape should be identical at the same experimental conditions. Thus, the difference in the rotational discharge coefficient results solely from flow interaction with surrounding near the orifice hole.

As previously explained, additional loss is related closely to the streamline curvature at the orifice inlet. Enlargement of vena contracta by inlet radiusing is well illustrated for the stationary orifice in *Visualized Flow* (1988). In a rotating system, vena contracta is reduced because the flow approaches asymmetrically with respect to the orifice axis. Thus, the discharge behavior can deviate from the stationary one, and can be more susceptible to corner radiusing.

Figure 8(*b*) depicts the rotational discharge coefficient distribution of the orifice with corner radiused inlet. It shows more uniform distribution compared with that of the square edged orifice (Fig. 8(*a*)).

The increment in the discharge coefficient due to inlet radiusing is shown in Fig. 11, where C_d is the discharge coefficient of the squared inlet and ΔC_d is the difference between the discharge coefficients of two different inlet shapes. The effect of inlet radiusing is well presented by a single parameter Ro, regardless of

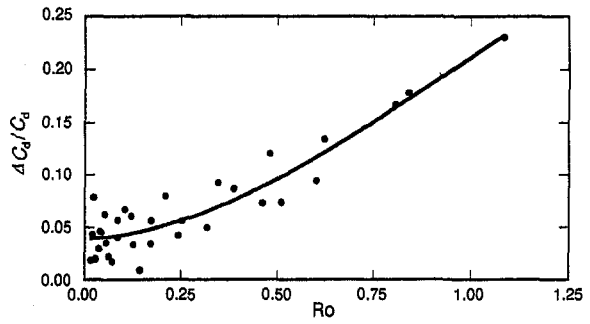

Fig. 11 Increment of discharge coefficient by inlet corner radiusing with Rotation number variation

pressure ratio and rotor speed. The increment amounts to more than 20 percent at high Rotation numbers.

Summary and Conclusions

Discharge characteristics of a long orifice with length-to-diameter ratio of 10 is investigated at various rotational conditions. The pressure ratio is in the range between 1.05 and 1.8, and rotational speed of the rotor up to 10,000 rpm. The Reynolds number based on the ideal exit velocity ranges from 45,650 to 152,500. Some important observations are noted and summarized below.

1 The discharge coefficient in a rotating system increases compared to the stationary one because of the rotational momentum transfer to the orifice flow from the rotor. The rotational discharge coefficient is introduced which can reasonably represent the discharge behavior of the rotating system.

2 The additional loss due to relative motion of the rotating orifice and surrounding flow is qualitatively presented by two parameters: the compressibility factor and the Rotation number.

3 The orifice with corner radiused inlet shows higher distribution of the discharge coefficient than that of the orifice with square inlet, and the difference increases with the Rotation number. The increase in the discharge coefficient can be predicted when the Rotation number is given.

References

Akima, H., 1970, "A New Method of Interpolation and Smooth Curve Fitting Based on Local Procedures," *Journal of Association for Computing Machinery,* Vol. 17, No. 4, pp. 589–602.

Bragg, S. L., 1960, "Effect of Compressibility on the Discharge Coefficient of Orifices and Convergent Nozzles," *Journal of Mechanical Engineering Science,* Vol. 2, No. 1, pp. 35–44.

Hay, N., and Lampard, D., 1996, "Discharge Coefficient of Turbine Cooling Holes: A Review," ASME Paper 96-GT-492.

Hay, N., Lampard, D., and Benmansour, S., 1983, "Effect of Crossflows on the Discharge Coefficient of Film Cooling Holes," *ASME Journal of Engineering for Power,* Vol. 105, pp. 243–248.

Hay, N., Khaldi, A., and Lampard, D., 1987, "Effect of Crossflows on the Coefficient of Discharge of Film Cooling Holes with Rounded Entries or Exits," Proceedings, 2nd ASME/JSME Thermal Engineering Conference, Hawaii, pp. 369–374.

Hay, N., and Spencer, A., 1992, "Discharge Coefficients of Cooling Holes with Radiused and Chamfered Inlets," *ASME Journal of Turbomachinery,* Vol. 114, No. 4, pp. 701–706.

Jakoby, R., Maeng, D. J., Kim, S., and Wittig, S., 1997, "3D LDA-Measurement in Rotating Turbine Disk Systems," Proceedings, 7th Int. Conf. Laser Anemometry Advances and Applications, pp. 255–262.

Kline, S. J., and McClintock, F. A., 1953, "Describing Uncertainties in Single-Sample Experiments," *Mechanical Engineering,* Vol. 75, pp. 3–8.

Lichtarowicz, A., Duggins, R. K., and Markland, E., 1965, "Discharge Coefficients for Incompressible Non-Cavitating Flow through Long Orifices," *Journal Mechanical Engineering Science,* Vol. 7, No. 2, pp. 210–219.

Maeng, D. J., 1998, "Flow Characteristics and Discharge Behaviors of Highly Rotating Turbine Cavity System with Discharge Holes," Ph.D. thesis, Seoul National University.

Meyfarth, P. F., and Shine, A. J., 1965, "Experimental Study of Flow Through Moving Orifices," *Journal of Basic Engineering,* Dec., pp. 1082–1083.

Saad, M. A., 1993, *Compressible Fluid Flow,* 2nd ed., Prentice-Hall, Inc., Englewood Cliffs, NJ.

Snyder, P. K., Orloff, K. L., and Reinath, M. S., 1984, "Reduction of Flow Measurement Uncertainties in Laser Velocimeters with Nonorthogonal Channels," *AIAA,* Vol. 22, No. 8, pp. 1115–1123.

Rohde, J., Richard, R., and Metger, G. W., 1969, "Discharge Coefficients for Thick Plate Orifices With Approach Flow Perpendicular and Inclined to Orifice Axis," NASA TND-5467.

Waschka, W., Scherer, T., Kim, S., and Wittig, S., 1992, "Influence of High Rotational Speeds on the Heat Transfer and Discharge Coefficients in Labyrinth Seals," *ASME Journal of Turbomachinery,* Vol. 114, pp. 462–468.

The Jet Engine, 1986, Rolls-Royce PLC publication, 4th ed.

Visualized Flow, 1988, The Japan Society of Mechanical Engineers, Pergamon Press, Inc., Tarrytown, NY.

Correlations of the Convection Heat Transfer in Annular Channels With Rotating Inner Cylinder

R. Jakoby[1]

S. Kim

S. Wittig

Lehrstuhl und Institut für,
Thermische Strömungsmaschinen,
Universität Karlsruhe (T.H.),
Kaiserstraße 12,
76128 Karlsruhe, Germany

In the internal air system of gas turbine engines or generators, a large variety of different types of annular channels with rotating cylinders are found. Even though the geometry is very simple, the flow field in such channels can be completely three-dimensional and also unsteady. From the literature it is well-known that the basic two-dimensional flow field breaks up into a pattern of counter-rotating vortices as soon as the critical speed of the inner cylinder is exceeded. The presence of a superimposed axial flow leads to a helical shape of the vortex pairs that are moving through the channel. For the designer of cooling air systems there are several open questions. Does the formation of a Taylor-vortex flow field significantly affect the convective heat transfer behavior of the channel flow? Is there a stability problem even for high axial Reynolds-numbers and where is the location of the stability boundary? After all, the general influence of rotation on the heat transfer characteristics has to be known. By the results of flow field and heat transfer measurements, the impact of rotation and the additional influence of Taylor-vortex formation on the heat transfer characteristics in annular channels with axial throughflow will be discussed. The flow field was investigated by time-dependant LDA-measurements, which revealed detailed information about the flow conditions. By a spectral analysis of the measured data, the different flow regimes could be identified. Based on these results, the heat transfer from the hot gas to the rotating inner shaft was determined with a steady-state method. Thus, the influence of the different physical phenomena such as rotation with and without Taylor-vortex formation or the flow development could be separated and quantified. Finally, correlations of the measured results were derived for technical applications.

1 Introduction

The efficiency and the performance characteristics of gas turbine engines strongly depend on the turbine inlet temperature and the pressure ratio of the working cycle. Remarkable improvements of engines for power generation or aeroengines in most cases are coupled to a further increase of the hot gas temperature and the pressure ratio. The turbine inlet temperature of present engines has already exceeded the admissible temperature level even of super alloys, which requires an efficient cooling system for the turbine blades, vanes, and disks. For this purpose, air is taken from the compressor and supplied to the turbine via an internal air system. Unfortunately, the compressor exit temperature also increases if the pressure ratio of the engine is raised, which leads to a reduction of the driving temperature difference for cooling purposes. As a consequence of these circumstances, the cooling air mass flow had to be raised significantly in the past years. As it currently can reach 20 percent of the total core mass flow, the design of the internal air system plays a key role for the whole engine. Since the pressurized cooling air does not directly contribute to the power output, those parasitic mass flows have to be reduced to an unavoidable minimum. To meet this demand, detailed data about the fluid flow and the heat transfer in the components of the internal air system is required.

At the Institut für Thermische Strömungsmaschinen of Karlsruhe University, a part of the research activities is focussed on the particular components of the internal air and oil system of turbomachines in order to enhance the comprehension of the fluid-mechanical phenomena and to provide data bases for improvements of the design. Within the last fifteen years, labyrinth seals (Waschka et al., 1991), rotating disks with orifices (Jakoby et al., 1997a; Wittig et al., 1996), rotor-stator systems (Jakoby et al., 1997b) and bearing chambers (Glahn et al., 1997) were analyzed using combinations of experimental and numerical methods. Furthermore, many efforts were directed towards the determination of the flow and heat transfer phenomena in annular channels with axial throughflow and with rotating inner cylinder. Such configurations are found in a large variety of different applications in gas turbine engines, steam turbines, or turbogenerators. Although, the geometry of annular channels is very simple, the flow field inside can be extremely complicated. If the critical speed of the rotor is exceeded, the axisymetric flow pattern breaks up into pairs of counter-rotating, helical vortices. Thus, the basic two-dimensional flow field turns into a completely three-dimensional and periodic flow, which exceeded the capabilities of experimental and numerical methods in the past years. Subsequently, there is a remarkable lack of information about the flow regimes and the heat transfer characteristics especially in the Reynolds and Taylor number range of technical applications.

The structure of such Taylor-vortex flow fields can be revealed since powerful nonintrusive measurement techniques like LDA have achieved a standard, where they can be applied even to difficult problems within reasonable time scales. The determina-

[1] Current address for correspondence: ABB Corporate Research Ltd., Department of Mechanical Engineering, Baden/Dätwil, Switzerland.

Contributed by the International Gas Turbine Institute (IGTI) of THE AMERICAN SOCIETY OF MECHANICAL ENGINEERS for publication in the ASME JOURNAL OF ENGINEERING FOR GAS TURBINES AND POWER. Paper presented at the International Gas Turbine and Aeroengine Congress and Exhibition, Stockholm, Sweden, June 2–5, 1998; ASME Paper 98-GT-97.

Manuscript received by IGTI February 28, 1998; final revision received by the ASME Headquarters June 23, 1999. Associate Technical Editor: R. Kielb.

tion of the flow field is essential because without the knowledge of the predominant flow regime, an analysis of the heat transfer characteristics is almost impossible.

This background gives the motivation for the present paper, which is to contribute to a better understanding of the flow phenomena and the heat transfer characteristics in annular channels at high Reynolds and Taylor numbers. In the following sections, the influence of Taylor vortices and the flow development on the heat transfer will be pointed out. Furthermore, the impact of the channel geometry is discussed. Finally, the results achieved by an experimental investigation are summarized by correlations in order to provide a design tool for technical applications.

2 Background

2.1 Taylor-Couette Flow Without Axial Throughflow. The study of fluid flows between concentric cylinders has a long tradition in engineering sciences. Already at the end of the last century, Couette (1890) and Mallock (1896) published the results of experimental investigations without axial throughflow.

The first theoretical analysis of instabilities in annuli was performed by Rayleigh (1916), who derived a stability criterion for inviscid flows. According to Rayleigh, the flow is stable, if the square of the circulation increases monotonically in the radial direction.

The first analytical solution for viscous flows was published by Taylor (1923) in a famous article. He solved the momentum equations and the continuity equation using Bessel functions. Subsequently, he calculated the critical speed and the velocity distributions for the two-dimensional and also the vortex flow field and gave an experimental verification of his theory. The so-called Taylor vortices are superimposed to the mainflow and consist of counter-rotating vortex pairs. The appropriate dimensionless Parameter (the Taylor number) describing the stability behavior of the flow can be defined as

$$\mathrm{Ta} = \left(\frac{U \cdot s}{\nu}\sqrt{\frac{s}{r_i}}\right)^2 = \mathrm{Re}_t^2 \cdot \frac{s}{r_i} = \frac{\omega_i^3 \cdot r_i \cdot s^3}{\nu^2} \qquad (1)$$

Ta can be interpreted as the ratio of centrifugal and frictional forces (cp. Bühler (1985)). In Eq. (1), U is the circumferential speed of the rotor, s denotes the height of the channel, and r_i is the radius of the inner cylinder. In the context it should be mentioned, that in the literature also other definitions of Ta using the square root of the right side of Eq. (1) are found.

At that time, the appearance of Taylor vortices was judged as a transition-phenomenon from laminar to turbulent flow. Nevertheless, Pai (1943) showed in his study that the macroscopic vortex structure persists even at Taylor numbers which are far above the stability boundary in the fully turbulent range. Furthermore, he detected two modes of the flow regime differing in the number and size of the vortices. In some cases, both modes could be observed for identical operating conditions. The appearance of a particular mode was found to depend upon the initial conditions, such as the acceleration of the rotor. The results of Pai (1943) were confirmed by flow visualizations of Schultz-Grunow and Hein (1956).

Coles (1965) analyzed the modes, which appear above the critical Taylor number. He detected not only two but more than 70 different modes of the flow in the range he investigated with his set-up. However the most important result of his study was the detection of a second stability boundary of the flow. Beyond the second stability boundary, the steady Taylor vortices turn into a periodic flow of wavy vortices.

The existence of a first and a second instability as well as the numerous modes of the flow are typical features of a nonlinear, dynamic system. A detailed analysis of the dynamic behavior of Taylor–Couette flow regimes was performed by Fenstermacher et al. (1979). They used an LDA-system for the measurement of the time-dependant flow velocities in the channel. A spectral analysis of the velocity data showed, that the second instability coincided with the appearance of a single, distinct frequency in the power spectrum. For high Reynolds numbers, a "double-periodic" flow regime characterized by two frequencies was found. Finally, the transition from laminar to turbulent vortex flow at twelve times the critical Reynolds number lead to a low frequent and broad band component that started to form in the spectrum just as the two distinct peaks began to fade away.

The references cited in this paragraph are based on a more or less academic interest for Taylor–Couette flows, which is expressed by a strong simplification of the configurations and the chosen range of the operating conditions. In many cases, laminar flows with liquids in enclosed channels were investigated. Since this is far away from real engine conditions, a second branch exists in the literature, where publications with a technical background are found.

2.2 Taylor-Couette Flow With Axial Throughflow. Detailed heat transfer measurements for laminar and turbulent flows were published by Gazley (1958). In accordance to the results of Fage (1938), he observed a stabilizing impact of the axial flow. He suggested to define the Reynolds number with an "effective velocity," which is calculated by an addition of the circumferential and the axial velocity vectors. For rotational flows, the heat transfer coefficients based on the effective velocity were higher than the corresponding values for purely axial flow. Gazley presumed a secondary flow to cause the difference of the results.

A very systematic and comprehensive study on Taylor–Couette flows was performed by Kaye and Elgar (1958). Their field of application was the cooling of electrical machines. The study included flow visualizations, time-dependant velocity measurements using a hot-wire anemometer and heat transfer measurements. They identified the basic flow regimes comprising

Nomenclature

a_o (—) = coefficient
a_u (—) = coefficient
b (—) = coefficient
c (—) = coefficient
$c_{ax,m}$ (m/s) = average axial velocity
c_{eff} (m/s) = resulting velocity
c_∞ (m/s) = free-stream velocity
f (s^{-1}) = characteristic frequency
L (m) = rotor length
m (—) = factor
n (min^{-1}) = rotational speed
n (—) = coefficient
Nu (—) = Nusselt number
Nu_l (—) = Nusselt number based on rotor length
r (m) = radius
r_i (m) = rotor radius
Re_{ax} (—) = axial Reynolds-number
$\mathrm{Re}_{\mathrm{eff}}$ (—) = effective Reynolds-number
Re_t (—) = tangential Reynolds-number
Re_x (—) = Reynolds-number based on x
s (m) = channel height
t (—) = coefficient
Str (—) = Strouhal number
Ta (—) = Taylor number
U (m/s) = rotor speed
x (m) = axial coordinate
y (m) = vertical coordinate

Greek Symbols

α (W/(m²K)) = local heat transfer coefficient
$\bar{\alpha}$ (W/(m²K)) = average heat transfer coefficient
λ_{gas} (W/(mK)) = thermal conductivity of the gas (air)
ν (m^2/s) = kinematic viscosity
ω_i (s^{-1}) = angular speed of the rotor

— laminar flow
— laminar flow with vortices
— turbulent flow and
— turbulent flow with vortices

In configurations without throughflow, the stability of the flow only depends on the Taylor number. Kaye and Elgar derived a quantitative stability map that demonstrated the additional influence of the axial discharge on the flow stability. The axial Reynolds number is defined as

$$\mathrm{Re}_{ax} = \frac{c_{ax,m} \cdot 2s}{\nu}. \qquad (2)$$

In Eq. (2), $c_{ax,m}$ is the average axial velocity in the channel.

Due to the axial flow, the basic axisymetric flow pattern breaks up into pairs of counter-rotating helical vortices, which are moving through the channel. Thus, a fully three-dimensional and periodic flow field appears as soon as the critical Taylor number is exceeded.

Recent investigations of annular channels were performed by Pfitzer and Beer (1992) who conducted flow velocity and heat transfer measurements for fully developed and steady flow regimes as well as numerical calculations. As the test facility with independently driven cylinders was operated at moderate rotational speeds, the appearance of Taylor vortices could not be detected. In a subsequent study, Rothe and Beer (1994) analyzed the developing region. However, questions of flow stability were not considered either.

Questions of flow stability were considered by Shih and Hunt (1994) for fully developed flows and high Taylor numbers. They performed flow velocity measurements using a hot-wire-anemometer in order to analyze the frequency spectrum.

Correlations on the heat transfer in annular channels are published for example by Tachibana and Fukui (1964), Kuzay and Scott (1977) or in the german VDI-Wärmeatlas (1984). In the first two references no information about the basic flow regime is available, whereas in the VDI-Wärmeatlas only static configurations are considered.

3 Experimental Setup

For the investigations of flow and heat transfer in annular channels, the test section sketched in Fig. 1 was used. It is connected to a settling chamber by the flange on the left side. Compressor air with a maximum flow rate of 0.5 kg/s is fed into the settling chamber through a piping system which includes three orifice meters in parallel connection for the massflow measurements and an electrical heater with a maximum power of 135 kW.

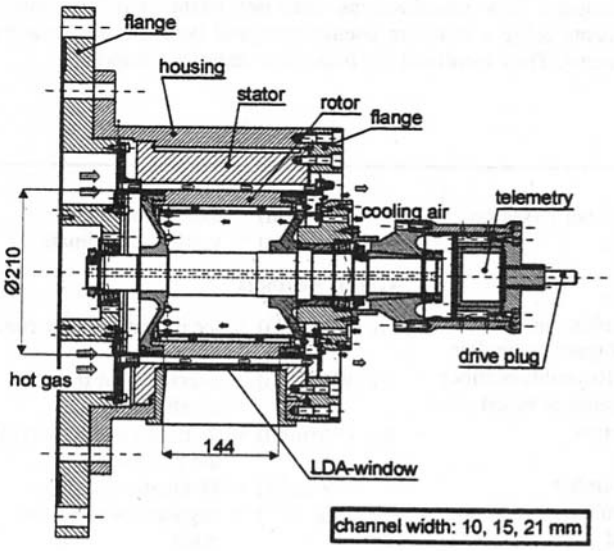

Fig. 1 Test section

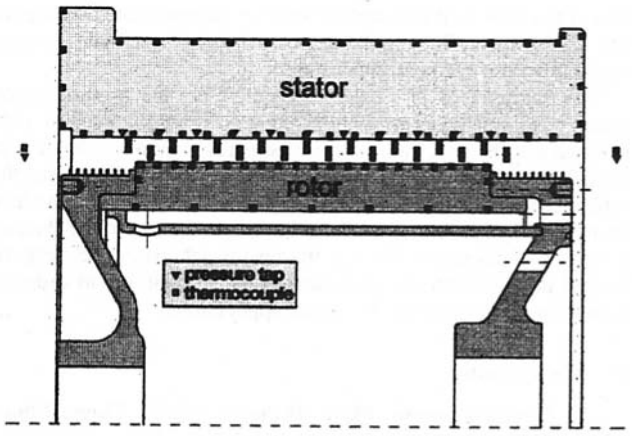

Fig. 2 Instrumentation

The heated air is discharged from the settling chamber through a flange and a small inlet section into the annulus with rotating inner and stationary outer cylinder. Through the second flange on the right side, the hot gas is exhausted into the environment. For the measurement of the convective heat transfer to the rotor, a steady-state method was applied. Therefore, a cooling system to maintain the temperature gradients across the rotor material is required. Cooling air is injected through the right hand flange and through orifices in the rotor side wall into the inner cavity of the rotor. On the left side of the cavity, the coolant flows into an annular channel by passing radial orifices in a cylindrical insert. Afterwards the air is also discharged into the environment.

The rotor has a diameter of 210 mm. The surface area which is exposed to the hot gas is 144 mm long. The channel width (s = 10; 15 and 21 mm) is varied by using stator sleeves with a different inner diameter. The rotor is driven by an electrical DC-motor which is connected to the plug on the right side by a flexible clutch. The maximum rotational speed is 10000 rpm, which corresponds to a circumferential velocity of 110 m/s on the outer diameter of the rotor. These high rotational speeds are achieved by the use of precision bearings, which are located in the two flanges of the test section. Since the left bearing is only protected by a cover from the hot gas, a water cooling system is installed (not sketched in Fig. 1).

For optical flow velocity measurements with a two-component laser Doppler anemometer (LDA), a glass window covering the rotating channel section is inserted into the stator. Thus, the axial and circumferential velocity components were measured. The LDA system comprises an Argon-Ion-Laser in multimode operation as the light source, a two-dimensional fibre probe, and a dantec flow velocity analyser (FVA) for the signal detection and processing. The axis of the fibre probe was arranged perpendicular to the rotational axis in order to perform measurements in backscatter-mode. To obtain time-dependant velocity profiles, the arrival time of each burst signal was recorded in addition to the velocity data (cp. Jakoby, 1996).

For the measurement of the heat transfer, a steady-state method was chosen. The temperature distribution on the rotor and stator surface as well as the gas temperature profiles are measured using NiCr-Ni-thermocouples (Fig. 2). For the transmission of the rotor temperature signals, a 32-channel telemetry is installed. By the large number of measuring locations, a good spatial resolution of the temperature profiles is achieved. The rotational symmetry of the temperature distribution is observed by additional thermocouples in different angular sections.

The convective heat transfer to the rotor wall is determined by using the measured temperature profiles around the rotor walls as boundary conditions for a finite element heat conduction calcula-

tion. Thus, the temperature distribution within the rotor material and the heat fluxes are obtained. Local heat transfer coefficients finally are calculated by the heat flux normal to the wall and the gas temperatures at 50 percent channel height. Averaged α and Nusselt numbers are achieved by an integration of the local heat transfer coefficients.

Measurements were conducted for three different channel heights (Fig. 1). The channel size was varied by exchanging the stator and maintaining the rotor.

As the length-to-height-ratio L/s for the particular configurations is rather small ($6.9 \leq L/s \leq 14.4$), the developing flow plays an important role for the convective heat transfer. Beneath the occurrence of Taylor vortices and the influence of the channel geometry, the discussion of the results will be focussed on the developing flow field.

In the first step, the velocity measurements will be briefly discussed in order to provide a basis for the analysis of local and average heat transfer coefficients and the derivation of the correlations.

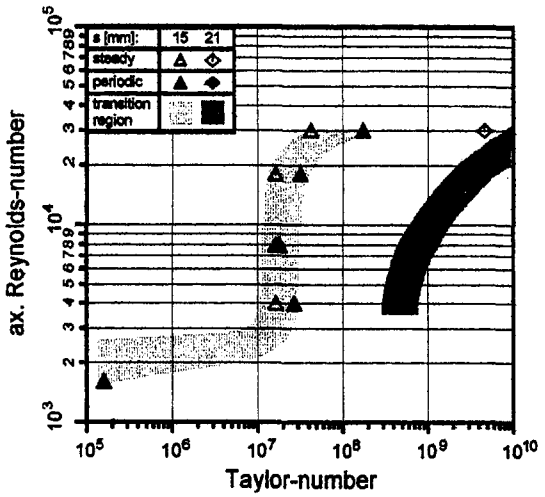

Fig. 4 Stability map

4 Results

4.1 Flow Field. The investigations of flow and heat transfer in annular channels were focussed on Taylor and Reynolds numbers, which are found in technical applications such as turbomachines or generators. The flow conditions belong to the turbulent regime, the axial Reynolds numbers are in the range of $1600 \leq \mathrm{Re}_{ax} \leq 30000$. The rotational speeds reached from $0 \leq n \leq 10000$ rpm, which is equivalent to a Taylor number range of $0 \leq \mathrm{Ta} \leq 10^{10}$.

When the critical Taylor number is exceeded by an increase of the rotational speed, perturbations in the flow are no longer damped but amplified. The flow becomes unstable, which at first leads to the formation of axial waves in the channel. The amplitudes of the waves increase with increasing rotational speed until a pattern of counter-rotating and unsteady vortex pairs is established (cp. Jakoby, 1996).

The transition from the basic steady and axisymetric flow regime into an unsteady and fully three-dimensional flow can be demonstrated by time-dependant LDA-measurements. In Fig. 3, the axial velocities for a single point at 53 percent channel height ($y/s = (r - r_i)/s = 0.53$, $x/s = 0.34$) are plotted in the left column for three different rotational speeds. The discharged mass-flow and, therefore, the axial Reynolds number were kept constant, whereas the rotational speed was increased up to 10000 rpm. The upper diagram ($n = 100$ rpm) represents the steady-state case with almost constant velocity over the time. Since each plot is based on 2000 data points, the number of deviating burst signals is very small, the distribution is almost uniform. The circumferential velocities look very similar, and, therefore, are not presented.

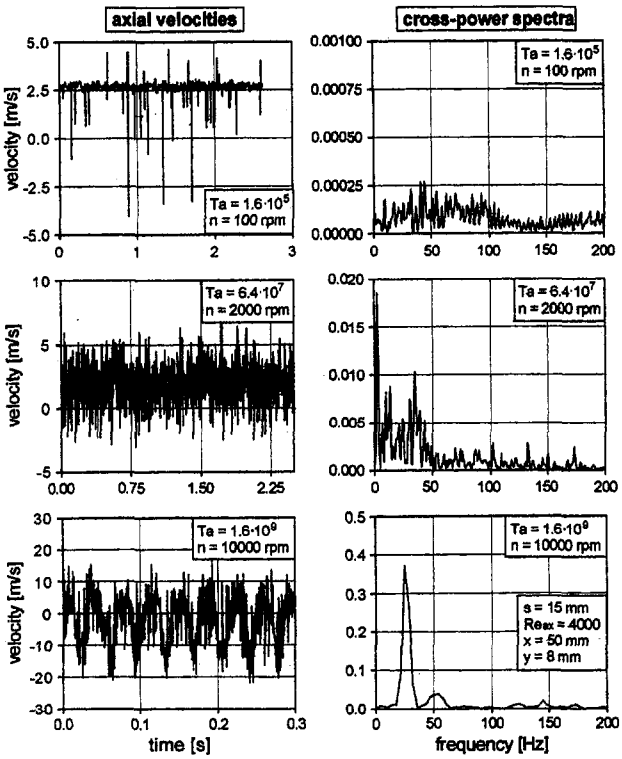

Fig. 3 Transition to turbulent Taylor-vortex flow—data processing

One of the major goals of the measurements was the determination of the stability boundary for the configurations of interest. The precise definition of a stability boundary is rather difficult because in contrast to cases without throughflow, there is no sharp stripline between the steady and the periodic flow regime. The transition occurs within a certain range of Taylor-numbers, which leads to the problem of an appropriate definition and detection of the boundary. Since the steady flow turns into a periodic regime, the appearance of a distinct frequency in the velocity signals was chosen as the criterion to identify the stability boundary. Therefore, the cross-power spectra were calculated from the axial and the circumferential velocities revealing the common frequencies in both components.

The corresponding power spectra to the velocities in Fig. 3 are shown in the right column. Due to the big differences of the maxima, different axes scales for the particular plots were chosen. For $n = 100$ rpm, only noise at a very low level can be observed, which is in agreement to the velocity distribution.

Increasing the rotational speed leads to an amplification of the noise in the velocity signals shown for a medium speed of $n = 2000$ rpm (second row of Fig. 3). The noise is obvious in the velocity distribution as well as in the power spectrum. However, the peaks in the frequency range below 50 Hz indicate that this is not only pure noise. A distinct frequency is found in addition. Consequently, this case was assigned to the transitional region between steady and periodic flow.

When the rotational speed is increased furthermore to $n = 10000$ rpm (third row), no spectral analysis is required to identify the periodic nature of the flow. In this case, the measured velocities alternate within a range of -20 m/s $\leq c_{ax} \leq 10$ m/s and with a predominant frequency f of approximately 26 Hz. The characteristic frequencies, which were detected for a considerable number of operating conditions can be described with the following equation:

$$\mathrm{Str} = \frac{f \cdot s}{c_{ax}} = m \cdot \frac{1}{4} \cdot \frac{U}{c_{ax}} \cdot \frac{s^2}{r_i \cdot L}; \quad m = 1; 2. \tag{3}$$

In Eq. (3), Str is the Strouhal number, which depends on U/c_{ax}, s/r_i, s/L and also on a factor m. During the measurements, two different modes of the flow leading to a period-doubling were observed. The period-doubling is considered by the introduction of m, which is equal to one or two, respectively.

By the spectral analysis demonstrated above, the stability map shown in Fig. 4 was derived for two configurations (s = 10; 15 mm). The transitional regions are depending on the axial Reynolds number and the Taylor number, respectively, and are outlined by the shaded areas. In comparison to the 15 mm channel, the stability boundary for s = 21 mm is shifted towards higher Taylor numbers. This is probably due to the smaller relative length of the 21 mm channel. Since the rotor length was kept constant, an increase of the channel width reduces the relative length. At the channel exit, the flow is not yet fully developed. The boundary layers in both cases have a different degree of development, which influences the onset of instabilities. Channels with smaller relative length are stable over a wider Ta number range.

The stability boundaries shown in Fig. 4 are the basis for the evaluation of secondary Taylor-vortex flows on the convective heat transfer. The intensity of the secondary flow and especially of the reversed fluid motion was found to be surprisingly high. Axial velocity fluctuations in the range of 30 m/s were observed for an average axial velocity of approximately 2.6 m/s. Under this point of view, the influence of Taylor vortices on the convective heat transfer is hard to assess. An evaluation will be given in the following section.

4.2 Heat Transfer. The results presented in this paper were achieved for configurations with a rather small ratio of channel-length-to-height L/s. Therefore, the development of the boundary layers in the channel significantly affects the convective heat transfer and has to be separated from other influences like rotation or secondary motions. Consequently, it will be discussed by an example with predominant axial flow. In Fig. 5, local heat transfer coefficients are plotted versus a nondimensional axial coordinate, which is normalized by the channel height. A constant axial Reynolds number of Re_{ax} = 30,000 was chosen in combination with a very low rotational speed. The symbols correspond to the α-numbers at the nodes of the finite element mesh, the lines are approximation functions. Since the geometry was varied by maintaining the channel length (L = 144 mm) and using stators with different inner diameter to change the channel height, the three curves have a different nondimensional length.

At the entrance into the channel (x/s = 0), high heat transfer coefficients are found due to the small boundary layer. With increasing length, a decrease of the α-numbers takes place until a local minimum in the range of $5.0 \le x/s \le 6.5$ is reached.

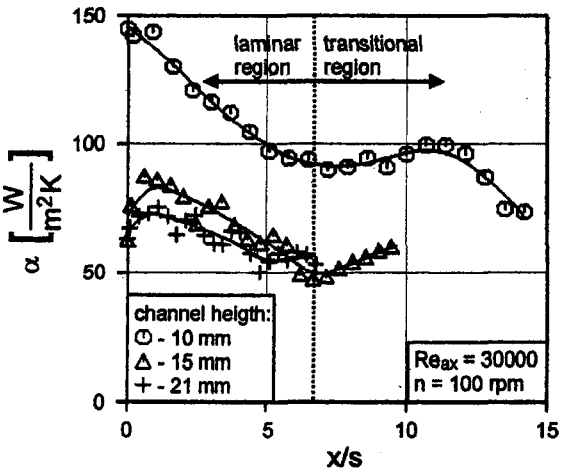

Fig. 5 Local heat transfer coefficients

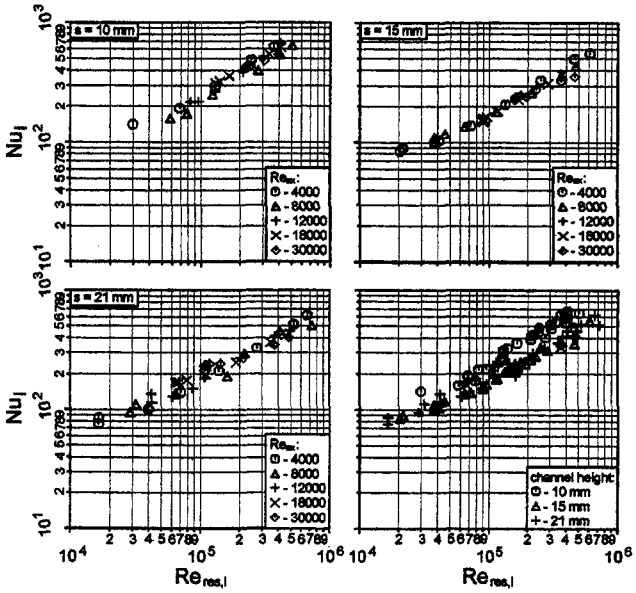

Fig. 6 Nusselt numbers (based on channel length)

As it is well-known from the literature, developing flows start with a laminar boundary layer even for high Reynolds numbers. If the stability point is passed, perturbations in the flow cause a laminar-turbulent transition. Within the transition region, an enhancement of the convective heat transfer takes place. In Fig. 5, the heat transfer enhancement is expressed by a second maximum of the α-numbers. For flat plates, the theoretical stability point is calculated to $\mathrm{Re}_x = c_\infty \cdot x/\nu \approx 6 \cdot 10^4$ (Jischa, 1982). In this equation, c_∞ is the free-stream velocity and x is the axial distance from the leading edge of the plate. Subsequently, for a given Re_x the axial location of the stability point can be calculated. By a comparison of the channel flow with the flat plate results, a rough estimation of the stability point location can be made. For Re_{ax} = 30,000 it is located at $x/s \approx 4$, which is in good agreement to the observed transition region. Even for flat plates, the laminar-turbulent transition region in most cases is found downstream of the theoretical point of instability (Jischa, 1982).

As shown by Fig. 5, the heat transfer to the rotor is influenced by regions with laminar, transitional and turbulent boundary layer, which is not a very surprising result but important for the interpretation of averaged heat transfer coefficients and the derivation of correlations.

For the analysis and the description of the heat transfer characteristics, appropriate dimensionless parameters have to be defined. For channel flows, the Reynolds numbers and the Nusselt number in many cases are based on the hydraulic diameter or the channel height as the characteristic length. This is useful with regard to fully developed flows, where the boundary layers at both cylinders are merged and the axial distance to the entrance is unimportant. If entrance effects have to be taken into account, the use of the channel length is more suitable, as shown by Fig. 5. The heat transfer coefficients significantly decrease with increasing channel height although the Reynolds number is constant for all cases. Here Re_{ax} is calculated by using the hydraulic diameter as the characteristic length. Constant Re_{ax} means constant massflow. Consequently, the axial velocities and the shear stresses decrease with increasing channel height, which, according to the Reynolds analogy, leads to a reduction of the α-numbers. As long as the boundary layers at the rotor and the stator are not merged, the influence of the axial length is much more crucial than the hydraulic diameter and should be used as the characteristic length.

The flow regime in annular channels with rotating walls is

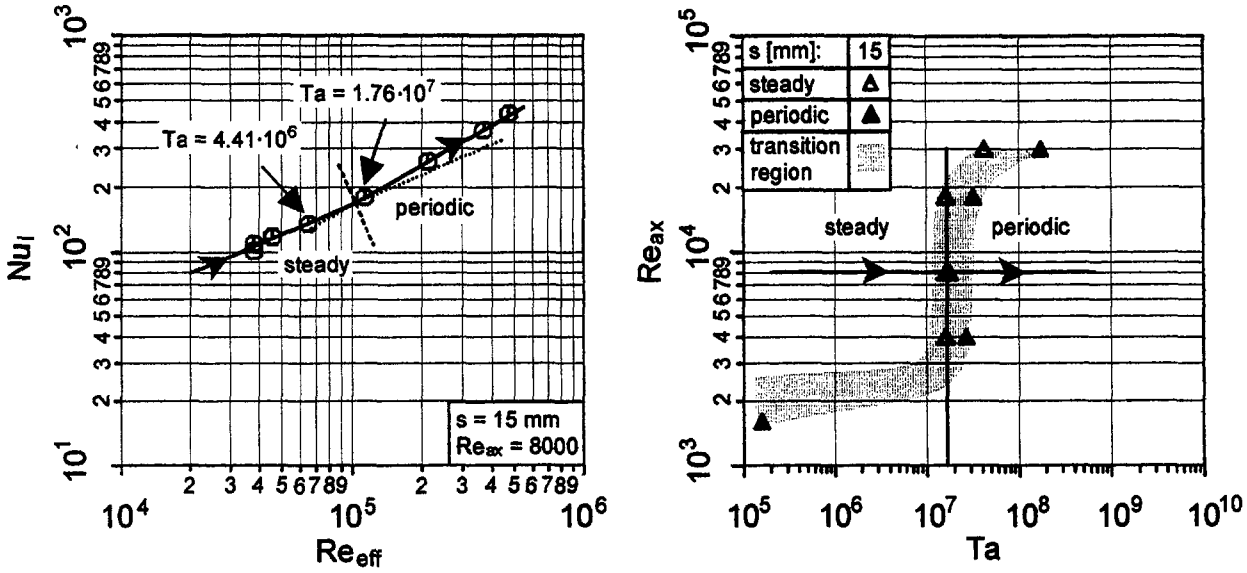

Fig. 7 Influence of Taylor vortices on the convective heat transfer

influenced by the combination of axial and circumferential main flows. Therefore, the question arises whether the separate use of a Taylor and an axial Reynolds number is required or if they can be combined into one dimensionless number, which is representative for the flow conditions. As already shown by Gazley (1958), a suitable description of the convective heat transfer is obtained by the use of a characteristic velocity, which is a combination of the average axial velocity and the rotor speed. Thus, an "effective" Reynolds number can be defined as

$$\mathrm{Re}_{\mathrm{eff}} = \frac{c_{\mathrm{eff}} \cdot L}{\nu} = \frac{\sqrt{c_{ax,m}^2 + U^2} \cdot L}{\nu} = \mathrm{Re}_{ax} \cdot \frac{c_{\mathrm{eff}}}{c_{ax,m}} \cdot \frac{L}{2s}. \quad (4)$$

This definition of the Reynolds number based on the "effective" velocity c_{eff} and the channel length will by used for the discussion of the averaged heat transfer coefficients, because it is a measure for the shear stresses at the rotor wall and provided the best correlation of the measured data.

In accordance with the Reynolds number, the Nusselt number is also modified by using the channel length

$$\mathrm{Nu}_l = \mathrm{Nu} \cdot \frac{L}{2s} = \frac{\bar{\alpha} \cdot L}{\lambda_{\mathrm{gas}}}. \quad (5)$$

In this equation, the average heat transfer coefficient $\bar{\alpha}$ is obtained by an integration of the local α-numbers.

Using the Nusselt and Reynolds number defined above, the average heat transfer coefficients for the three configurations are plotted in Fig. 6. For each channel geometry, a separate diagram is drawn. The symbols refer to different axial Reynolds numbers.

In addition to the three plots for constant geometry, the complete data base is summarised in the lower right diagram of Fig. 6. The Nusselt numbers of the particular configurations can be distinguished by the symbols. In these double-logarithmic plots, the symbols for each configuration seem to form straight lines depending on $\mathrm{Re}_{\mathrm{eff}}$. Varying the channel width leads to a shift of the Nu_l-numbers. For the smallest channel, the largest heat transfer numbers are found, because here the largest turbulent fraction of the boundary layer exists according to the discussion of the local heat transfer coefficients (Fig. 5). When the channel width is increased, the influence of the laminar fraction of the boundary layer on the average heat transfer coefficient predominates, which leads to a decrease of Nu_l.

When the data is analysed more in detail, different exponents n for $\mathrm{Nu}_l \sim \mathrm{Re}_{\mathrm{eff}}^n$ are found for the three configurations expressing the influence of the developing flow (cp. Fig. 9). Furthermore, the impact of Taylor-vortex secondary motions is revealed. One of the benefits of using $\mathrm{Re}_{\mathrm{eff}}$ is a general consideration of rotation by the characteristic velocity. Thus, the additional heat transfer enhancement caused by Taylor-vortex formations can be separated and quantified. However, as suggested by the results shown in Fig. 6, the influence of Taylor vortices is not as spectacular as expected by the discussion of the flow field.

With the stability map derived by a spectral analysis of the velocity data (section 4.1), the heat transfer coefficients can be assigned to steady or periodic flow conditions. When the basic flow regime is identified, the impact of Taylor vortices on the Nu_l numbers can be quantified as shown by the example in Fig. 7. The right diagram shows the stability map for $s = 15$ mm depending on Re_{ax} and Ta. When the axial Re number is kept constant and the rotational speed is increased, the transition region is crossed as indicated for $\mathrm{Re}_{ax} = 8000$. Within $10^7 < \mathrm{Ta} < 3 \cdot 10^7$, the basic flow turns into a periodic flow regime with turbulent Taylor vortices. The corresponding Nu_l numbers for $\mathrm{Re}_{ax} = 8000$ are plotted in the left diagram versus $\mathrm{Re}_{\mathrm{eff}}$. The arrows indicate the direction of increasing rotational speed. In this diagram, the left hand symbols lie on a straight line, whereas the right hand symbols can be connected by another straight line with a slightly higher gradient. The point of intersection (dashed line) is close to the data point for $\mathrm{Ta} = 1.76 \cdot 10^7$, which belongs to the transition region. Subsequently, the heat transfer enhancement due to Taylor vortices is expressed by different gradients within the steady and the periodic regime in this double-logarithmic plot. The influence of the secondary motion is rather small, because the circumferential

Table 1 Correlation coefficients

	steady flow		periodic flow	
	n	*c*	*n*	*c*
a_o	0.8	0.04	0.8	0.04
a_u	0.5	0.6	0.625	0.136
t	0.27	0.32	0.27	0.3
b	12.1	8.85	15.0	12.9

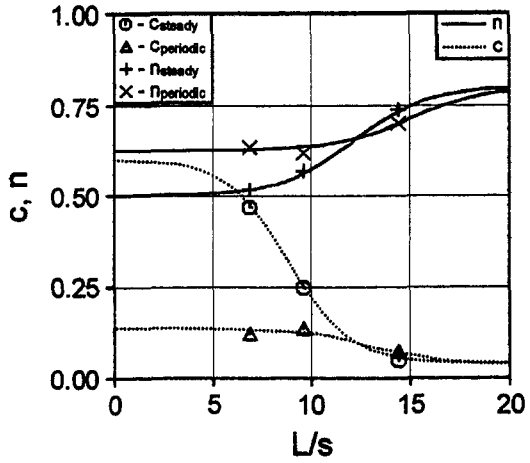

Fig. 8 Correlation coefficients

velocity field is predominant for the heat transfer. The effective velocities and therefore the gradients close to the wall first of all depend on the rotor speed. The additional motions and velocity fluctuations, which appear due to the formation of Taylor vortices, still are small compared to the circumferential speed of the inner cylinder.

Based on the results presented in the preceding paragraphs, correlations for the heat transfer numbers were derived. One of the goals was to use a simple approach with a minimum of constants. Since the data summarized in Fig. 6 can be divided into groups with linear connection in the double-logarithmic plot, the basic correlation function is

$$\mathrm{Nu}_l = c \cdot \mathrm{Re}_{\mathrm{eff}}^{n}. \tag{6}$$

Although the influence of periodic flow regimes on the heat transfer is not predominant, the data was subdivided into Nu_l numbers for steady and periodic flows. However, the error by neglecting secondary flow structures in most cases is acceptable.

In the next step, the constants c and n in Eq. (6) were calculated from the measured data. Thus, six different sets of constants were obtained for the three configurations and for steady and periodic flow regimes. As such discrete values are not suitable for the correlation of the results, appropriate approximation functions for the correlation coefficients have to be found. The general problem of using correlations is their restriction to the validity range of the basic data. However, in most cases an extrapolation of correlations is unavoidable, because the conditions of the particular applications often differ from the validity range of the correlations. Consequently, correlations should lead to reasonable results even if they are extrapolated. To meet this goal, the available data in the literature was used to determine the asymptotic behavior for channels with low and very large L/s ratio. With regard to the exponent n for example, the specifications in the literature are $n = 0.5$ for laminar flows (cp. Schlünder, 1983) and $0.75 \leq n \leq 0.8$ for turbulent flow regimes (e.g., Tachibana and Fukui, 1964) and fully developed flow. Due to the influence of transition, the exponents determined by this study lie in between this range (Fig. 8). Therefore, the approximation function should converge against 0.5 for small L/s, where the boundary layer is purely laminar. For very large L/s ratios, where the flow is turbulent and fully developed, a boundary value of 0.8 was chosen.

As a suitable approximation function, the hyperbolic tangent function was identified. It can be adjusted to meet the desired behavior with only four parameters. The correlation coefficients then can be described as

$$c\left(\frac{L}{s}\right);\ n\left(\frac{L}{s}\right) = \frac{a_o \cdot e^{t[(L/s)-b]} + a_u \cdot e^{t[-(L/s)+b]}}{e^{t[(L/s)-b]} + e^{t[-(L/s)+b]}} \tag{7}$$

The coefficients for c and n according to Eq. (7) are shown in Table 1. The upper and the lower boundary values are a_o and a_u, whereas t and b are used to match the experimental data. In Fig. 8, the hyperbolic tangent functions for c and n are plotted versus L/s. The experimental values are represented by the symbols. Thus, the good fit between the functions and the basic data is shown. Additionally, the convergence behavior for small and large L/s ratios is pointed out.

Finally, a comparison of the correlation and the measured data is shown in Fig. 9. In contrast to Fig. 6, the data for periodic flows is separated from the steady flow Nusselt numbers. For steady flows, the influence of the channel geometry is found to be more distinct than for periodic flows, where the Nu_l numbers are closer together. Nevertheless, the differences are not crucial. For most

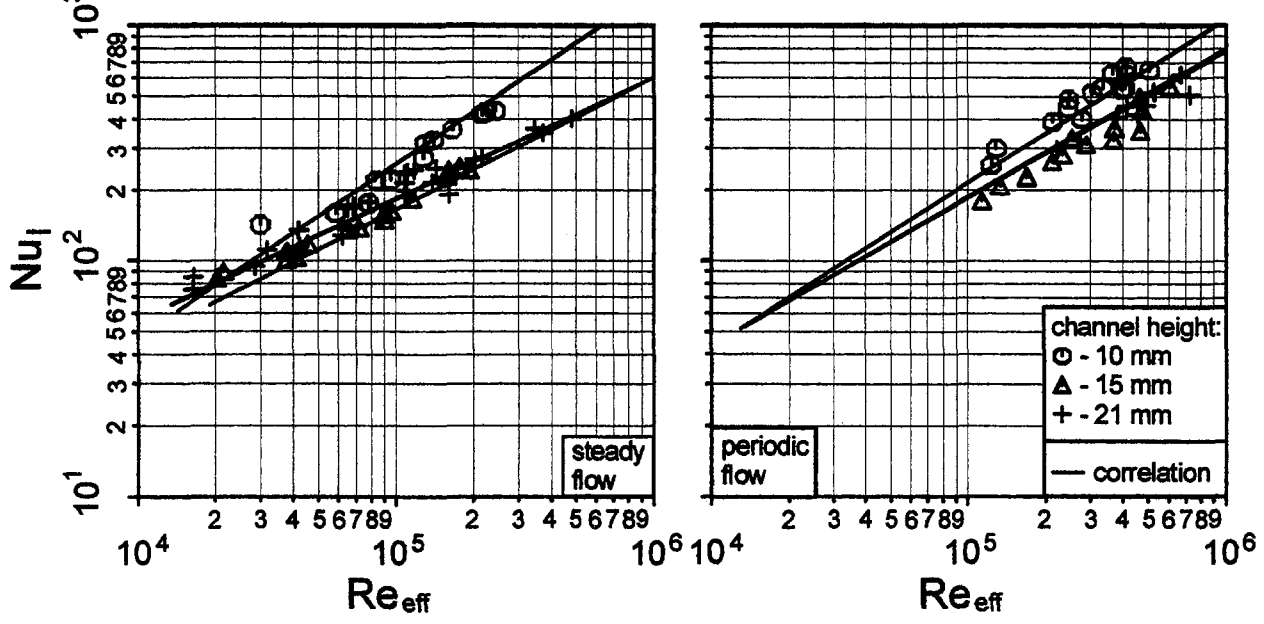

Fig. 9 Comparison of correlation and measured data

technical applications it is sufficient to use the correlation for steady flows, especially if the stability boundary is unknown.

5 Conclusions

This paper presents a study of the flow and heat transfer in annular channels with rotating inner cylinder and axial throughflow. Such configurations are found in the internal air system of turbomachines or generators. Although the geometry is very simple, the flow field becomes extremely complicated when the stability boundary is exceeded. The basic two-dimensional flow pattern breaks up into pairs of helical, counter-rotating Taylor vortices leading to a three-dimensional and periodic flow field. In the range of technical relevance, neither the stability boundary that depends on the axial Reynolds number and the Taylor number as well, nor the impact of Taylor vortices on the convective heat transfer usually is known. Since the length of the channels found in turbomachines in many cases is not sufficient to obtain a fully developed flow, the influence of the flow development must also be considered.

First of all, the basic flow regimes were investigated by two-component LDA-measurements. Thus, detailed data about the periodic and also the steady flow regime was achieved. The periodic flow field is characterized by extreme fluctuations of the instantaneous velocities compared to the average values. By a spectral analysis of the time-dependant velocity signals, the stability boundary was determined for the configurations of interest.

Based on the knowledge of the flow regimes, the heat transfer characteristics for air was analyzed in the next step. Local heat transfer coefficients were measured for the rotating inner cylinder, which revealed the development of the flow including the laminar-turbulent transition of the boundary layer. By an integration of the local numbers, the overall heat transfer characteristics was analyzed. For the description of the convective heat transfer, modified Reynolds and Nusselt numbers based on the channel length were used. Furthermore, an "effective" velocity was introduced into the definition of the Reynolds number. Using these numbers, the influence of Taylor vortices on the heat transfer could be pointed out. Surprisingly, the heat transfer enhancement due to secondary motions was found to be of minor importance as expected.

Finally, the experimental results were condensed into correlation functions. Thus, the influence of a combined axial and rotational flow, the development of the flow field and also the impact of secondary motions on the convective heat transfer are considered. With this tool, a contribution to an improvement of cooling air systems in turbomachines shall be made.

References

Bühler, K., 1985, *Strömungsmechanische Instabilitäten zäher Medien im Kugelspalt,* Vol. 7, No. 96, VDI-Verlag, Düsseldorf.

Coles, D., 1965, "Transition in Circular Couette Flow," *Journal of Fluid Mechanics,* Vol. 21, pp. 385–425.

Couette, M., 1890, "Etudes sur le frottement des liquides," *Ann. Chim. Phys.,* Vol. 6, No. 21, pp. 433–510.

Fage, A., 1938, "The Influence of Wall Oscillations, Wall Rotation and Entry Eddies on the Breakdown of Laminar Flow in an Annular Pipe," *Proceedings of the Royal Society of London,* No. A 165, pp. 501–529.

Fenstermacher, P. R., Swinney, H. L., and Gollub, J. P., 1979, "Dynamical Instabilities and the Transition to Chaotic Taylor Vortex Flow," *Journal of Fluid Mechanics,* Vol. 94, pp. 103–128.

Gazley, C., 1958, "Heat-Transfer Characteristics of the Rotational and Axial Flow Between Concentric Cylinders," *Journal of Turbomachinery,* Vol. 80, No. 1, pp. 79–90.

Glahn, A., Busam, S., and Wittig, S., 1997, "Local and Mean Heat Transfer Coefficients Along the Internal Housing Walls of Aero Engine Bearing Chambers," ASME Paper 97-GT-261.

Jakoby, R., 1996, "Untersuchung von Ringspaltströmungen mit Taylor-Wirbein und axialer Durchströmung," dissertation, Institut für Thermische Strömungsmaschinen, Universität Karlsruhe.

Jakoby, R., Kim, S., and Wittig, S., 1997, "Discharge Coefficients of Rotating Orifices With Radiused Inlet Corners," presented at the 13th International Symposium on Air Breathing Engines (ISABE), IS 137/GE 17, September 8–12, Chattanooga, Tennessee, USA.

Jakoby, R., Maeng, D. J., Kim, S., and Wittig, S., 1997, "3D LDA-Measurements in Rotating Turbine Disk Systems," presented at the 7th International Conference on Laser Anemometry—Advances and Applications, September 8–12, Karlsruhe, Germany.

Jischa, M., 1982, *Konvektiver Impuls-, Wärme- und Stoffaustausch,* F. Vieweg & Sohn, Braunschweig/Wiesbaden.

Kaye, J., and Elgar, C., 1958, "Modes of Adiabatic and Diabatic Flow in an Annulus with an Inner Rotating Cylinder," *Journal of Turbomachinery,* Vol. 80, pp. 753–765.

Kuzay, T. M., and Scott, C. J., 1977, "Turbulent Heat Transfer Studies in Annulus With Inner Cylinder Rotation," ASME *Journal of Heat Transfer.*

Mallock, A., 1896, "Experiments on Fluid Viscosity," *Philosophical Transactions A,* pp. 41–56.

Pai, S.-I., 1943, "Turbulent Flow Between Rotating Cylinders," NACA TN 892.

Pfitzer, H., and Beer, H., 1992, "Heat Transfer in an Annulus Between Independently Rotating Tubes with Turbulent Axial Flow," *International Journal of Heat and Mass Transfer,* Vol. 35, No. 3, pp. 623–633.

Rayleigh, O. M., F. R. S., 1916, "On the Dynamics of Revolving Fluids," *Proceedings of the Royal Society,* No. A93, pp. 148–154.

Rothe, T., and Beer, H., 1994, "An Experimental and Numerical Investigation of Turbulent Flow and Heat Transfer in the Entrance Region of an Annulus Between Rotating Tubes," presented at the Fifth International Symposium On Transport Phenomena and Dynamics Of Rotating Machinery (ISROMAC-5), May 8–11, Maui, Hawaii, USA.

Schlünder, E.-U., 1983, *Einführung in die Wärmeübertragung,* 4th ed., Friedrich Vieweg & Sohn, Braunschweig/Wiesbaden.

Schultz-Grunow, F., and Hein, H., 1956, "Beitrag zur Couette-Strömung," *Zeitung für Flugwissenschaften—ZFW,* No. 4, pp. 1–21.

Shih, A. C., and Hunt, M. L., 1994, "The Effect of Superimposed Axial Flow on Taylor-Couette Flow at Large Taylor Numbers," presented at the Fifth International Symposium On Transport Phenomena and Dynamics Of Rotating Machinery (ISROMAC-5), May 8–11, Maui, Hawaii, USA.

Tachibana, F., and Fukui, S., 1964, "Convective Heat Transfer of the Rotational and Axial Flow Between Two Concentric Cylinders," *Bulletin of JSME,* Vol. 7, No. 26.

VDI-Wärmeatlas, 1984, 4th ed., VDI-Verlag GmbH, Düsseldorf.

Waschka, W., Wittig, S., Scherer, T., and Kim, S., 1991, "Leakage Loss and Heat Transfer in High-Speed Rotating Labyrinth Seals: An Experimental Verification of Numerical Codes," presented at the Yokohama International Gas Turbine Congress, 91-Yokohama-IGTC-34.

Wittig, S., Kim, S., Jakoby, R., and Weißert, I., 1996, "Experimental and Numerical Study of Orifice Discharge Coefficients in High Speed Rotating Disks," *Journal of Turbomachinery,* Vol. 118, No. 2, pp. 400–407.

The Creep Damage Behavior of the Plasma-Sprayed Thermal Barrier Coating System NiCr22Co12Mo9-NiCoCrAlY-ZrO_2/7%Y_2O_3

U. T. Schmidt

O. Vöhringer

D. Löhe

Institute of Materials Science and Engineering,
University of Karlsruhe (TH),
Karlsruhe, 76128,
Germany

During creep loading metallic substrates impose deformation on deposited ceramic thermal barrier coatings (TBC). Strain accomodation of the TBC is not attained by plastic deformation, but by means of crack initiation, crack opening, crack propagation or sliding of adjacent crack faces. In technical applications a distinction is made between tolerated or desired cracks perpendicular to the surface, and detrimental cracks parallel to the substrate-coating interface. Thus, TBC can respond to creep deformation by segmentation or spallation, the latter being referred to as failure. The parameters influencing the probability of either segmentation or spallation are temperature, creep rate, magnitude of creep deformation, layer thickness, and microstructure of the TBC. It can be stated that spallation failure probability increases with increasing creep rate, creep deformation, and layer thickness. The presence of pores between single spraying layers also strongly augments the likelyhood of spallation. No significant influence of temperature on spallation failure probability can be found in the range from 850°C to 1050°C. Light microscopy and scanning electron microscopy investigations show that the microstructure of the ceramic TBC changes during creep, and that the density of cracks detected on micrographs with low magnification (×50) increases with increasing creep deformation. On the other hand, the density of microcracks visible with high magnification (×500) is constant, or even decreases with increasing creep deformation. These findings are explained by sintering processes enabled by stress relaxation due to formation of macroscopic cracks perpendicular to the surface as a response to creep deformation. A relationship between microstructural changes and the emission of acoustic signals recorded during creep is presented.

Introduction

Plasma sprayed thermal barrier coating systems composed of MCrAlY (M for Ni, Co, Fe) bond coat and a ZrO_2/Y_2O_3 thermal barrier coating (TBC) are now a state-of-the-art feature in modern combustion chambers for turbines in both aviation and power generation. Although much empirical knowledge is available about the optimization of the spray process in respect to the behavior under thermal cycling or thermo-shock, little is known about the failure mechanisms governing the degradation process of these coating systems. However, an understanding of these failure mechanisms is necessary for the modeling of coating degradation and life time prediction of coated engine parts.

Therefore elementary creep tests were carried out in order to separate basic parameters influencing the damage process and to determine their degree of influence. Creep tests were carried out at 850°C, 950°C, and 1050°C in air at constant load resulting in creep rates of approximately $\dot{\epsilon} = 5 \cdot 10^{-5}$ 1/s (fast) and $5 \cdot 10^{-7}$ 1/s (slow) and microstructures were investigated after 1 percent, 3 percent, and 5.5 percent creep strain. Furthermore, accompanying investigations using an acoustic emission technique were carried out to obtain more information of the damage behavior of the TBC.

Contributed by the International Gas Turbine Institute (IGTI) of THE AMERICAN SOCIETY OF MECHANICAL ENGINEERS for publication in the ASME JOURNAL OF ENGINEERING FOR GAS TURBINES AND POWER. Paper presented at the International Gas Turbine and Aeroengine Congress and Exhibition, Stockholm, Sweden, June 2–5, 1998; ASME Paper 98-GT-387.

Manuscript received by IGTI March 24, 1998; final revision received by the ASME Headquarters June 23, 1999. Associate Technical Editor: R. Kielb.

Results

During creep loading metallic substrates impose deformation on deposited ceramic thermal barrier coatings. Strain accomodation of the TBC is not attained by plastic deformation, but by means of crack initiation, crack opening, crack propagation or sliding of adjacent crack faces. Thermal barrier coatings can respond to creep deformation by segmentation or spallation, the latter being referred to as failure.

In Figs. 1 through 3 it is shown that segmentation and spallation can either occur separately or in a combined mode. Provided a strong bond between bond coat and TBC and between single layers of the TBC the coating system responds to creep strain in a mode depicted in Fig. 1. Here, an increase in creep strain (Fig. 1(*a*) to (*c*)) leads to the formation and growth of cracks perpendicular to both the coating plane and the strain direction.

The cracks perpendicular to the surface visible in Fig. 2 are caused by the spraying process and the subsequent cooling and temperature equilization rather than by creep deformation of the substrate. During spraying, usually performed in several layers, a temperature gradient develops which leads to a higher thermal contraction in the outermost layers and thus to a thermally induced crack initiation and crack growth. Despite of these cracks the coating system in Fig. 2 responds to creep deformation of the substrate by initiation and propagation of a single crack along a row of pores between the first and second layer of the TBC leading to a complete loss of the TBC above it.

A combination of these two extreme modes of failure is shown in Fig. 3. In this combined mode the cracks already existing after

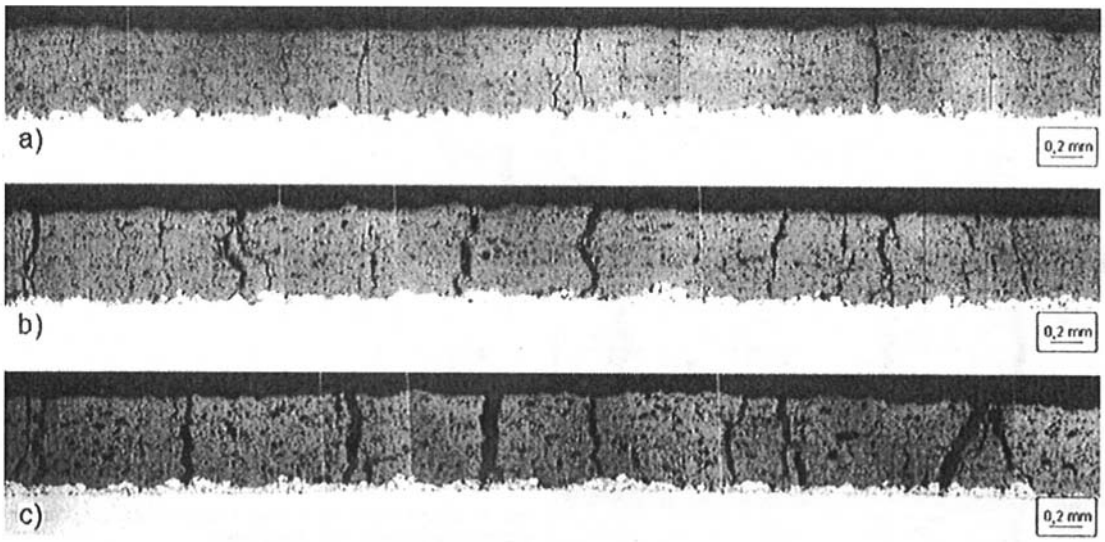

Fig. 1 Pure segmentation failure mode of plasma sprayed TBC (500 μm thickness, T = 1050°C, σ = 35 MPa); (*a*) ϵ = 1 percent, (*b*) ϵ = 3 percent, and (*c*) ϵ = 5.5 percent

the spraying process propagate from the surface towards the bond coat/TBC interface. The distance between these cracks is not a function of creep conditions but of spraying conditions. Thus, as an adaptation to creep temperature, creep rate and creep strain, additional cracks originate at the bond coat/TBC interface and propagate to the surface. Final failure, i.e., spallation, occurs provided the stress relief achieved by perpendicular cracks does not insure a subcritical shear stress distribution in the 1st/2nd layer interface.

It was found that increasing TBC thickness, creep strain and creep rate leads to a higher probability of spallation. Quantitative statements cannot be made due to the scatter in microstructure of the specimens. No influence of temperature on spallation failure probability was observed.

Quantitative information about the development of perpendicular cracks can be obtained from Fig. 4 for a 500 μm TBC. Crack density values were calculated by normalizing the number of intersection points of cracks and an intersection line to the length of this line. With increasing creep strain the density of cracks visible at 50-fold magnification, in the following referred to as macro cracks, increases tending to a saturation value. Only in very few cases did spallation occur in TBC of 500 μm thickness after 5.5 percent creep strain.

The failure behavior of a TBC of 1500 μm thickness is shown in Fig. 5. Distinction is made between big macro cracks clearly separating two neighboring segments and small macro cracks within a single segment and also between the locations near the surface (top), mid-coating thickness (center), and near the bond coat/TBC interface (bottom).

At the top position as the density of big macro cracks (Fig. 5(*b*)) increases with the same rate as the density of small macro cracks (Fig. 5(*a*)) decreases, it can be stated that no crack initiation takes place, which causes a constant total macro crack density (Fig. 5(*c*)) with increasing creep strain. Near the bond coat/TBC interface strain accomodation can only be obtained by formation of additional cracks, as can be seen in a steep increase in small macro crack density (Fig. 5(*g*)) with increasing creep strain. This formation of additional small macro cracks also causes an increase in total macro crack density (Fig. 5(*i*)), whereas the density of big macro cracks (Fig. 5(*h*)) shows the same dependence on creep strain as in the top section.

In the center section the density of small macro cracks (Fig. 5(*d*)) remains nearly constant. Therefore, new small macro cracks must form mainly as small macro cracks from the bottom section propagating upwards to the center to compensate the small macro cracks turning into big macro cracks (Fig. 5(*e*)).

Generally speaking it is observed that strain accomodation is accomplished by means of macro crack initiation and macro crack growth as well as macro crack opening which causes stress relief in the sections between the macro cracks.

As a consequence, micro cracks visible at 500-fold magnification within these sections are stress free. Figure 6 shows the density of micro cracks parallel and perpendicular to the surface as a function of creep strain. To separate the influence of the heating process and temperature equalization time prior to the application of the creep load from the influence of creep strain crack densities are normalized by subtracting the micro crack density after 1 percent creep strain. Within a considerable scatter band the general

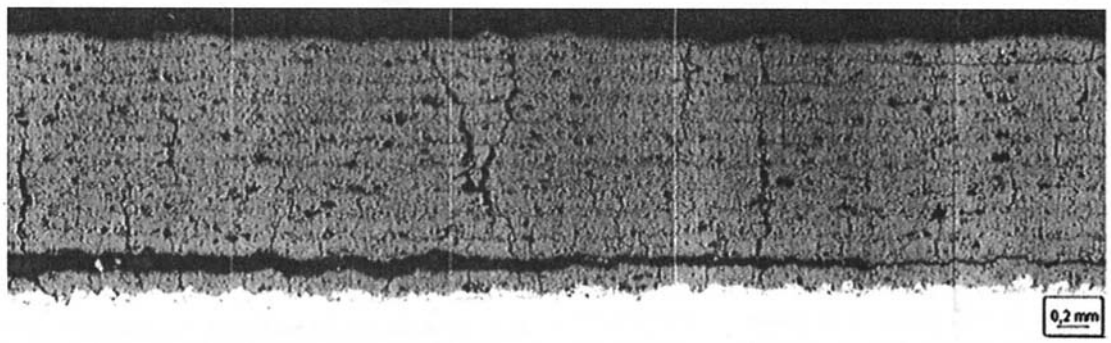

Fig. 2 Pure spallation failure mode of plasma sprayed TBC 1500 μm thickness T = 850°C, σ = 100 MPa, and ϵ = 5.5 percent

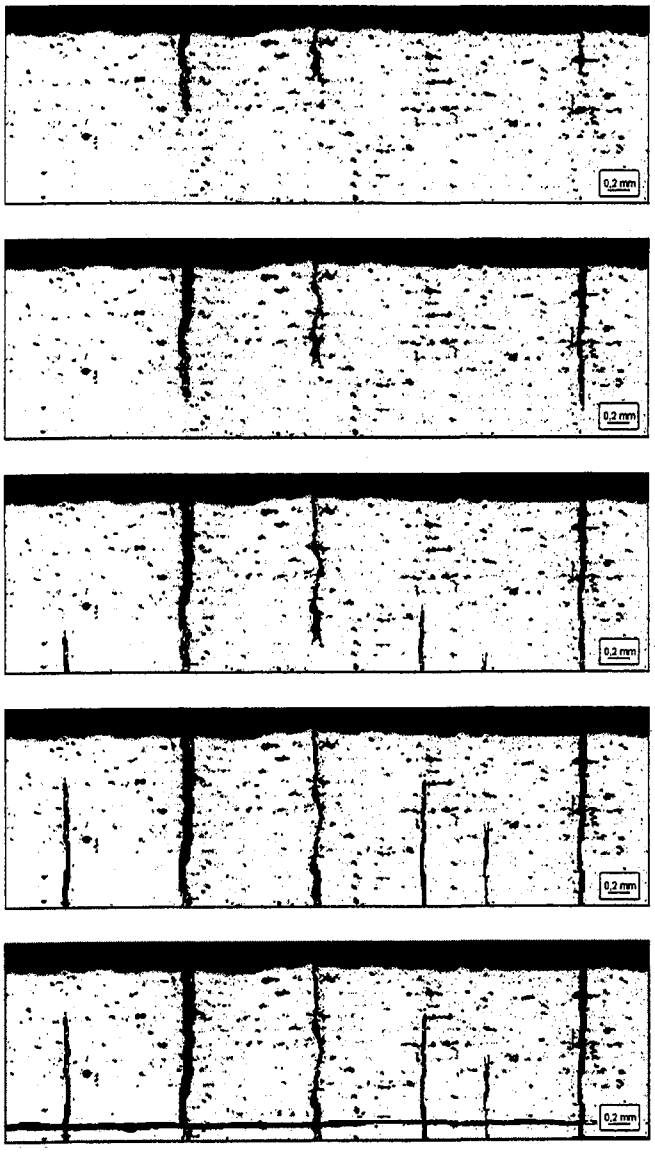

Fig. 3 Schematic depiction of combined segmentation/spallation failure mode of plasma sprayed TBC

tendency can be found that the micro crack density both in parallel and perpendicular direction decreases with increasing creep strain.

These findings which are obviously caused by sintering processes can also be observed within thermal barrier coatings in the as received condition detached by etching in hydrochloric acid as shown in Fig. 7. The micro crack density decreases with increasing annealing time and temperature even at a temperature as low as 850°C.

The afore mentioned microstructural processes such as crack initiation, crack propagation and also stick-slip movements of spalled segments relative to the substrate are all discontinuous processes at which elastic energy is set free at discrete times.

Thus an acoustic emission system was set up to detect record and analyse the emission of the elastic energy. In order to locate the sources of acoustic emission a linear chain arrangement of two piezoelectric transducers was coupled to the watercooled heads of the creep specimens using roller bearing grease as couplant. After the creep tests the recorded signals were analysed using logical filters such as location filters to separate acoustic signals which originated from the thermal barrier coating from acoustic or electromagnetic noise. Several characteristic parameters were used to analyse the acoustic emission data. A visualization of these parameters is given in Fig. 8.

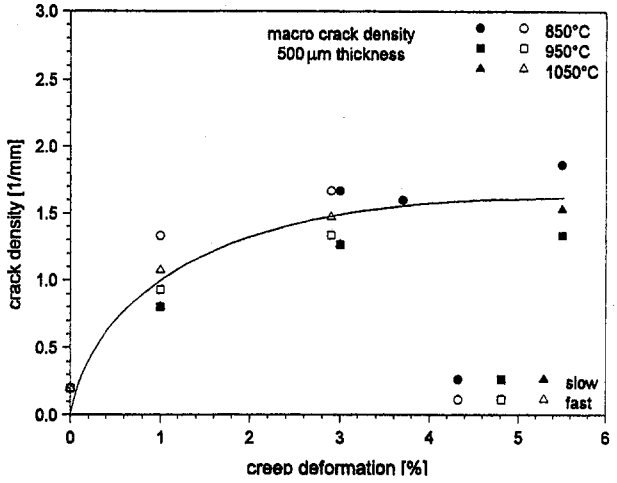

Fig. 4 Macro crack density as a function of creep strain for different creep temperatures and creep rates

Figure 9 shows a selection of cumulative frequencies of the parameter rise time, i.e., the time elapsed from the first threshold crossing to the arrival of the maximum peak. Cumulative frequencies of the total signals from beginning of the creep test, i.e., after complete application of creep load to 1 percent (solid line), 3 percent (dashed line), and 5.5 percent (dotted line) are presented for different temperatures and TBC thicknesses. It can be stated that an increase in creep strain causes an increase in rise time as the

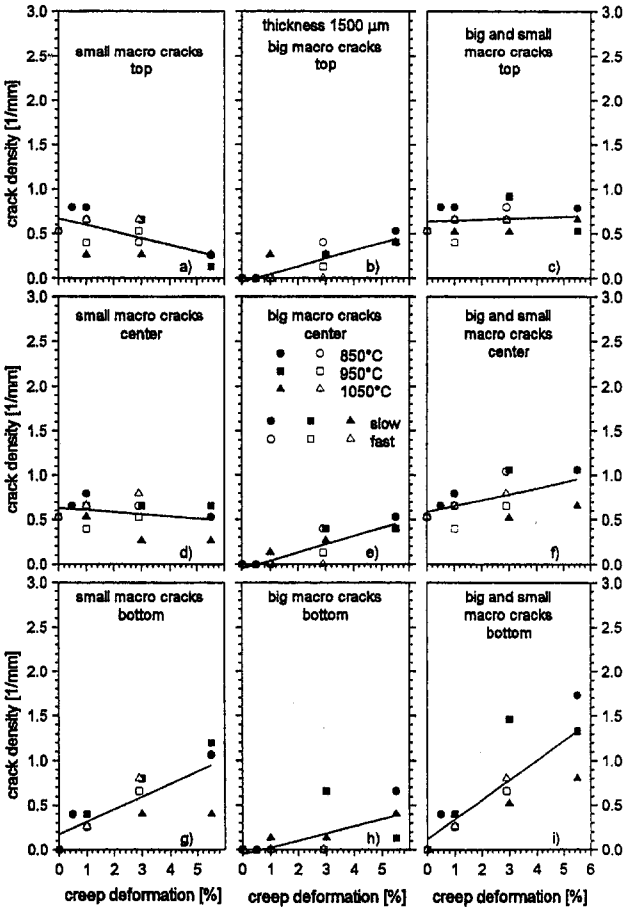

Fig. 5 Small ((*a*), (*d*), (*g*)) and big ((*b*), (*e*), (*h*)) macro crack density at the top ((*a*)–(*c*)), center ((*d*)–(*f*)), and bottom (*g*)–(*j*)) section as a function of creep strain for different creep temperatures and creep rates

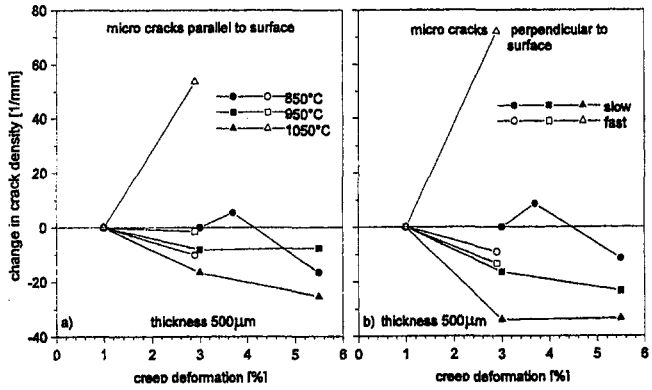

Fig. 6 Change of micro crack density as a function of creep strain for different creep temperatures and creep rates

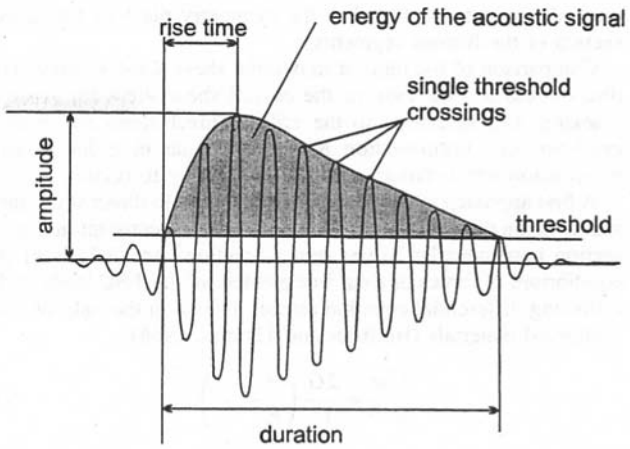

Fig. 8 Visualization of characteristic parameters to describe acoustic emission data

cumulative frequency shifts to higher rise time values. This increase in rise time is most significant for creep tests at 850°C or 1050°C and thin (300 μm) or thick (1500 μm) thermal barrier coatings.

Discussion

Creep strain of the substrate imposes stresses on applied thermal barrier coatings. However, these stresses are relatively low on a macroscopic scale compared to the creep stresses in the substrate because of the high density of pores, micro and macro cracks in plasma sprayed coatings and therefore do not influence the stress distribution in the substrate.

With this presumption the boundary conditions at the substrate coating interface can be formulated that the displacement of each point of the coating is equal to the creep displacement of the substrate. With increasing creep strain of the substrate a distribution of shear stresses and a distribution of direct stresses develops. These stresses are proportional to creep strain. The maximum shear stress is found at the end of the coated section or when segmentation already took place at the edge of segments, maxi-

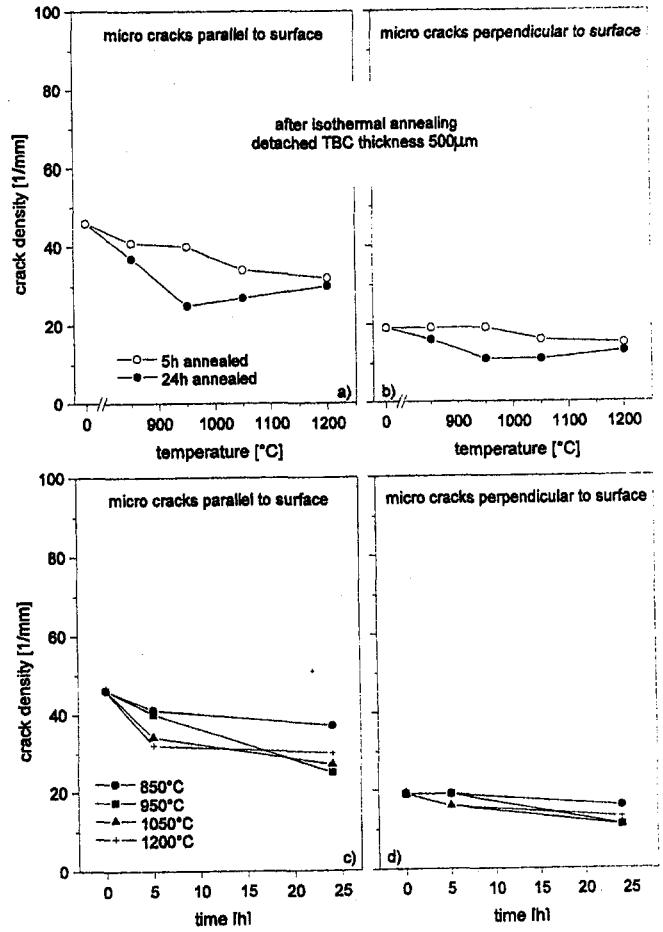

Fig. 7 Micro crack density of detached TBC as a function of annealing temperature and annealing time

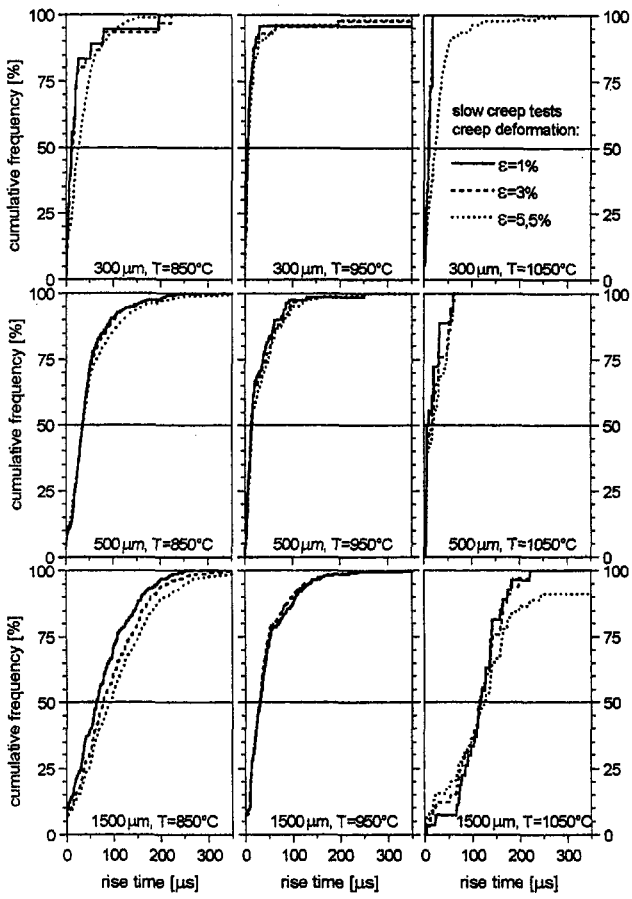

Fig. 9 Cumulative frequencies of rise time distributions as a function of creep strain for different creep temperatures and TBC thicknesses

mum direct stress is found in the symmetry plain of the coated section or the formed segments.

Comparison of the ratio of maximum shear stress to maximum direct stress and the ratio of the critical shear stress for mode II cracking, i.e., spallation to the critical direct stress for mode I cracking, i.e., segmentation has to be made in order to gain information which failure mode is more likely to occur.

A first approach to calculate the shear stress to direct stress ratio was done on the assumption that direct stress is constant in a cross section perpendicular to the strain direction. An analysis of the equilibrium of forces of a cut free element of the TBC leads to the following differential equation already known in the field of fibre reinforced materials (Hollister and Thomas, 1966):

$$\frac{\partial^2 \sigma}{\partial x^2} = \frac{2G}{t^2}\left(\frac{\sigma}{E} - \epsilon_0\right) \tag{1}$$

or

$$\frac{\partial^2 \tau}{\partial x^2} = \frac{2G}{t^2}\frac{\tau}{E}, \tag{2}$$

where x = distance from the symmetry plane of the coated section or segment, t = thickness of the TBC, ϵ_0 = creep strain of the substrate, E = Young's modulus of the TBC, and G = shear modulus of the TBC. Equation (1) and Eq. (2) can be solved by using

$$\sigma(x) = \sigma_0 \cosh(ax) + c \tag{3}$$

and

$$\tau(x) = \sigma_0 ta \sinh(ax) \tag{4}$$

with σ_0, a, and c as integration constants.

Thus the maximum stress ratio becomes

$$\frac{\tau_{\max}}{\sigma_{\max}} = \frac{\tau\left(x = \frac{w}{2}\right)}{\sigma(x = 0)} = \frac{ta \sinh \frac{aw}{2}}{1 + \frac{c}{\sigma_0}} \tag{5}$$

with w = width of the coated section or segment.

The boundary condition

$$\sigma\left(x = \frac{w}{2}\right) = 0 \tag{6}$$

leads to

$$\frac{c}{\sigma_0} = -\cosh\left(\frac{aw}{2}\right). \tag{7}$$

Substituting Eq. (7) in Eq. (5),

$$\frac{\tau_{\max}}{\sigma_{\max}} = \frac{ta \sinh \frac{aw}{2}}{1 - \cosh \frac{aw}{2}}. \tag{8}$$

From Eq. (7) it can be seen that the maximum shear stress to maximum direct stress increases with increasing TBC thickness. Further statements about the maximum stress ratio are difficult because the integration constant a shows a high order dependence on both thickness and width.

The strong dependence of the maximum stress ratio on TBC thickness found in the analytical approach is confirmed by the experimental findings. An increase in TBC thickness strongly augments the fault probability of spallation. Another experimental finding is that spallation occurs along a row of pores between the first and second spraying layer. This can be discussed as a locally very low critical shear stress to critical direct stress ratio. The influence of creep rate on spallation failure probability has to be explained by the ability of the bond coat to relax the shear stress peaks due to its very low creep strength. This effect is not included in the basic stress model presented in this paper. The missing temperature influence is either caused by a constant critical shear stress to critical direct stress ratio or is the result of the interplay of different mechanisms such as change in critical stress ratio, maximum stress ratio, oxidation and creep strength of the bond coat.

As long as segmentation is the governing failure mode an increase in creep strain causes an increase in direct stress above the critical value relieved by cracking. With decreasing segment width the bond coat gains more and more the ability to relax the stresses in the TBC so that a saturation value as shown in Fig. 4 is aspired.

The investigation shows that stress relief is basically achieved by means of macro cracking and that the influence of pores and micro cracks has to be discussed as an influence on macroscopic Young's modulus and shear modulus as well as an influence on critical direct stress and critical shear stress. The latter is quite obvious when looking at the rows of pores between single spraying layers as a major location of severe spalling.

As stress is relieved by macro cracks the observed sintering processes even in specimens under creep load can be understood. This finding is supported by investigations of Thurn (1997) and Thurn et al. (1997) who detected a shrinkage of detached plasma sprayed TBC in the first heating cycle in a differential dilatometer.

The changes in acoustic emission characteristics are explained by the changes in microstructural damage behavior during creep. Both segmentation close to the point of saturation and spallation cause a decrease in crack initiation and crack propagation activity. These acoustic events are related to single distinguished signals graphically described as a click. As this acoustic activity fades other events come to the fore such as a stick-slip movement of adjacent crack faces parallel to the surface. This grating stick-slip movement emits cascades of single bursts that cannot be distinguished. Thus the time between first threshold crossing and arrival of the highest amplitude oscillation of a subsequent burst can be significantly high, which leads to a shift of the rise time distribution to higher values.

The increase of the frequency of the low rise time signals in the creep test of the 1500 μm TBC systems at 1050°C (Fig. 9(*i*)) is related to cracking of the oxide scale growing underneath the spalled TBC. The growth rate of the oxide scale is the highest because under these conditions (high temperature/thick TBC) premature spalling causes a loss of oxidation protection by the TBC and the oxidation attack is strongest.

Acknowledgment

The research work was done within the framework of the Sonderforschungsbereich 167 "Hochbelastete Brennräume-Stationäre Gleichdruckverbrennung" of the Deutsche Forschungsgemeinschaft (DFG). The support of the investigations by the DFG is gratefully acknowledged.

References

Holister, G. S., and Thomas, C., 1966, *Fibre Reinforced Materials,* Elsevier Publishing Co. LTD., Amsterdam, p. 15.

Thurn, G., Schneider, G. A., and Aldinger, F., 1997, "High-Temperature Deformation of Plasma-Sprayed ZrO_2 Thermal Barrier Coatings," *Materials Science and Engineering,* Vol. A233, pp. 176–182.

Thurn, G., 1997, "Hochtemperatureigenschaften und Schädigungsverhalten plasmagespritzter ZrO_2-Wärmebarrieren," Doctoral thesis, University of Stuttgart, Germany.

A Metallographic Technique for High Temperature Creep Damage Assessment in Single Crystal Alloys

P. Henderson
Vattenfall Energisystem AB,
P. O. Box 528,
162 16 Stockholm,
Sweden

J. Komenda
Swedish Institute for Metals Research,
Stockholm, Sweden

The use of single crystal (SX) nickel-base superalloys will increase in the future with the introduction of SX blades into large gas turbines for base-load electricity production. Prolonged periods of use at high temperatures may cause creep deformation and the assessment of damage can give large financial savings. A number of techniques can be applied for life assessment, e.g., calculations based on operational data, nondestructive testing or material interrogation, but because of the uncertainties involved the techniques are often used in combination. This paper describes a material interrogation (metallographic) technique for creep strain assessment in SX alloys. Creep tests have been performed at 950°C on the SX alloy CMSX-4 and quantitative microstructural studies performed on specimens interrupted at various levels of strain. It was found that the strengthening γ′-particles, initially cuboidal in shape, coalesced to form large plates or rafts normal to the applied stress. The γ-matrix phase also formed plates. CMSX-4 contains ~70 vol % γ′-particles and after creep deformation the microstructure turned itself inside out, i.e., the gamma "matrix" became the isolated phase surrounded by the γ′-"particles." This can cause problems for computerized image analysis, which in this case, were overcome with the choice of a suitable measurement parameter. The rafts reached their maximum length before 2 percent strain, but continued to thicken with increasing strain. Although of different dimensions, the aspect ratios (length/thickness ratio) of the gamma-prime rafts and the gamma plates were similar at similar levels of strain, increasing from ~1 at zero strain to a maximum of ~3 at about 1–2 percent strain. Analysis of microstructural measurements from rafting studies on SX alloys presented in the literature showed that the aspect ratios of the γ and γ′-phases were similar and that at a temperature of 950–1000°C a maximum length/thickness ratio of about 2.5–3.5 is reached at 1 to 2 percent creep strain. Measurement of gamma-prime raft or (or gamma plate) dimensions on longitudinal sections of blades is thus a suitable method for high temperature creep damage assessment of SX alloys. This gives a considerable advantage over conventional Ni-base superalloys whose microstructures are usually very stable with respect to increasing creep strain.

Introduction

The use of single crystal (SX) nickel-base superalloys will increase in the future with the introduction of SX blades into large gas turbines for base-load electricity production. Prolonged periods of use at high temperatures may cause creep deformation and the assessment of damage can give large financial savings. For example, blades exhibiting large amounts of creep strain in localized areas can be taken out of service before failure occurs, so avoiding widespread damage and unplanned outages. Alternatively, it may be found that blades can be run for significantly longer than their original design lives.

In wrought or conventionally cast turbine blades and vanes thermal fatigue cracking is often a cause of premature failure, although creep is an important design criterion. As a first step towards understanding the deformation of an SX alloy which could be used in industrial gas turbines it was decided to study the creep of CMSX-4.

In SX alloys the γ′-particles agglomerate during creep at high temperatures to form large plates (rafts) normal to the applied stress [1–7]. The rafts form in the early stages of creep, gradually increasing in length until a constant raft length is reached [3, 4]. A previous study of CMSX-4 showed that while no rafts occurred during creep at 800°C, rafting occurred at low stresses (long times) at 950°C and at all stress levels at 1100°C [7]. In spite of the large number of experiments where rafting has been observed there have been few quantitative microstructural studies of SX alloys reported in the literature. This was the motivation for the work reported here.

Experimental

Material and Mechanical Testing. The SX alloy used in the study, CMSX-4, was received in the form of fully heat treated 16 mm diameter bars, having deviations of 3.5 to 12 deg from the [001] orientation. The bars had been cast and heat-treated by Howmet Exeter Casting, UK. The solution treatment was a multi-step process in which the temperature was raised from 1277°C to 1321°C. The aging treatment was a two stage process, viz. 6 h at 1140°C, argon fan quench, 20 h at 870°C, air cool. CMSX-4 contains ~70 vol % γ′-particles. The chemical compositions of the master batches from which the crystals were grown are given in Table 1.

Creep testing was performed in air under constant load at 950°C/155 MPa. The testpieces were not allowed to spend more

Contributed by the International Gas Turbine Institute (IGTI) of THE AMERICAN SOCIETY OF MECHANICAL ENGINEERS for publication in the ASME JOURNAL OF ENGINEERING FOR GAS TURBINES AND POWER. Paper presented at the International Gas Turbine and Aeroengine Congress and Exhibition, Stockholm, Sweden, June 2–5, 1998; ASME Paper 98-GT-488.

Manuscript received by IGTI March 25, 1998; final revision received by the ASME Headquarters June 23, 1999. Associate Technical Editor: R. Kielb.

Table 1 Composition in weight % of the CMSX-4 used for creep testing

Crystal no.	Cr	Co	Mo	W	Ta	Re	Al	Ti	Hf	Ni
V6, V9	6.4	9.7	0.6	6.4	6.5	2.9	5.7	1.0	0.1	Bal
V1, V2, V5	6.5	9.6	0.6	6.4	6.5	2.9	5.6	1.0	0.1	Bal

than three hours or less than one hour at the testing temperature before being loaded. The tests were interrupted at specified levels of strain before failure occurred and allowed to cool under load.

Metallography. Creep specimens were sectioned longitudinally along the gauge length and prepared for microstructural examination. One creep specimen (deformed to 8.4 percent at 950°C) was also examined directly outside the gauge length where the stress (and therefore strain) were lower, but the temperature and creep testing time were the same. The specimens were lightly etched in glyceregia containing 10 ml HNO_3, 20 ml HCl, and 20 ml glycerol. Particle shapes and sizes were measured from micrographs taken in a scanning electron microscope (SEM) and quantified by automatic image analysis using a Kontron IBAS 2000 image analysis system. A number of particle parameters were measured, but many were found to be unsuitable. A major drawback to quantifying the γ'-particle/γ-matrix microstructure is that initially, before creep testing, the γ'-particles are discrete and the γ-matrix is the continuous phase. However, after 0.5 percent creep the matrix is the isolated phase and the γ'-phase is continuous in the form of interlocking rafts. A computerized image analysis system thus measures one γ'-particle as filling an entire measurement frame. The mean chord size was found to be the most suitable parameter for characterizing the particles and the matrix. Chord size is defined in Fig. 1.

Results

Creep Testing. Creep curves are shown in Figs. 2 and 3. There was no primary creep and the creep curve was dominated by the tertiary stage as seen in Fig. 2. Figure 3 shows, however, that there is a small amount of steady-state creep, about 0.5 percent, before the start of tertiary. Although small in percentage terms, the steady-state creep stage extends for about 50 percent of the lifetime.

Microstructural Changes During Creep. The mean values of the particle and matrix dimensions are given in Table 2. Four areas, each of dimensions 29 μm × 29 μm were examined for each specimen. There is a fall in the number of particles measured when rafting begins from 1225 particles at 0 percent strain to 10 at 0.5 percent strain, even though the area measured for each specimen is the same. This is because the particles form an interlocking network of rafts and one particle can fill an entire measurement frame. There is also a corresponding increase in the perimeter from 1.6 μm at 0 percent strain to 1451 μm at 2 percent strain. The lengths and widths were obtained from chord sizes (see Fig. 1 for an explanation of chord size). With chord measurements a large number can be sampled and this method is therefore more suitable. The rafts reached their maximum length between 0.5 and 2 percent strain, but continued to thicken throughout the creep test. Specimen V5, which reached 0.5 percent strain after 2876 hours showed similar raft dimensions to V1x, which reached ~0.5 percent strain after 5028 hours. Specimens V1 and V1x both spent the same amount of time at 950°C (5028 h), but experienced different levels of strain and showed different raft dimensions. These two observations show that the raft dimensions depend on the strain rather than time. Figure 4 shows the original microstructure and after rafting at 0.5 percent strain. The aspect ratios (length/thickness) of the γ' and the γ-phases are plotted as a function of strain in Fig. 5. It can be seen that they are similar, reaching a maximum at 0.5–1.0 percent strain.

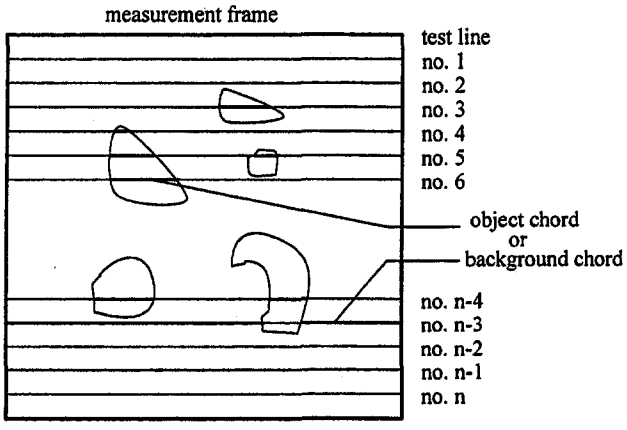

Fig. 1 Definition of chord size. Each measuring frame was divided into 50 tests lines. The length of intersection of the test lines within each particle is called a chord. The mean chord size of all lines within particles is reported. Test lines were produced in the horizontal and vertical directions and the chord size was measured in the matrix and the particles.

Discussion

Measurements of γ'-rafting in an SX alloy at 982°C have been presented in [3] and rafted microstructures from an interrupted creep test on SC16 at 950°C have been presented in [15]. The aspect ratios

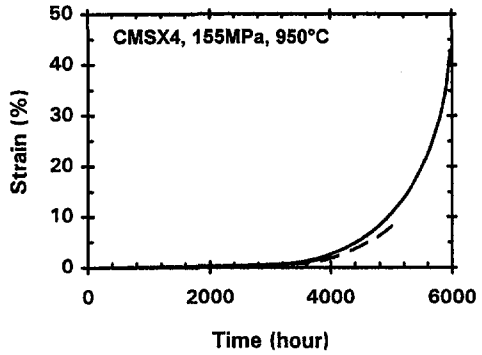

Fig. 2 Creep curves of the investigated specimens. A large amount of tertiary creep.

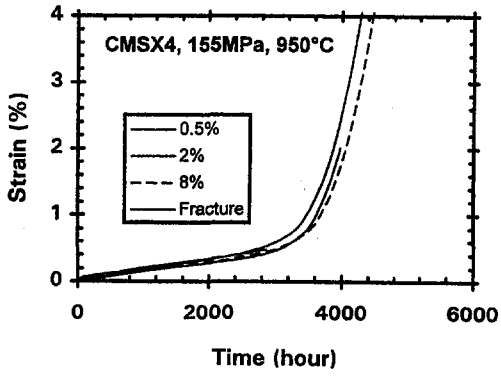

Fig. 3 Same as Fig. 2, but showing the first part of the creep curves in more detail. A small amount of steady-state creep (~0.5 percent strain) can be seen.

Table 2 Microstructural measurements taken from longitudinal sections of creep tested specimens. The creep testing conditions were 950°C/155 MPa. Four areas, each of dimensions 29 μm × 29 μm (a total area of 3364 μm^2) were examined for each specimen. The length is defined as the direction perpendicular ($\perp^r$) to the stress direction and the thickness is the direction parallel ($\|^{el}$) to the stress.

Test conditions		Gamma prime particle measurements		Particle/raft dimensions, chord measurements (μm)				Matrix dimensions, chord measurements (μm)			
Specimen no.	Elongation (%)	No.	Perimeter (μm)	No. $\perp^r$	Length $\perp^r$ stress	No. $\|^{el}$	Thickness $\|^{el}$ stress	No. $\perp^r$	Length $\perp^r$ stress	No. $\|^{el}$	Thickness $\|^{el}$ stress
V6	0 untested	1225	1.6	2037	0.34 ± 0.004	2229	0.31 ± 0.004	2072	0.46 ± 0.016	2222	0.43 ± 0.016
V5	0.5	10	335	2532	1.64 ± 0.038	7622	0.54 ± 0.003	2441	0.68 ± 0.016	7523	0.22 ± 0.001
V2	2.0	6	1451	2263	1.94 ± 0.043	5945	0.74 ± 0.006	2159	0.66 ± 0.014	5828	0.25 ± 0.001
V1	8.4	5	1365	2425	1.80 ± 0.034	4241	1.03 ± 0.012	2329	0.62 ± 0.011	4144	0.40 ± 0.002
V1x # (97 MPa)	~0.5%	22	443	2640	1.49 ± 0.038	6831	0.59 ± 0.004	2570	0.72 ± 0.016	6755	0.27 ± 0.001
V9* rupture	30*	7	805	2515	1.73 ± 0.030	3072	1.42 ± 0.019	2422	0.61 ± 0.011	2972	0.49 ± 0.004

measurements were made immediately outside the gauge length of Spec. V1 between the extensometer ridges and the threaded ends where the stress and therefore strain were lower (denoted Spec. V1x). The stress was 97 MPa and the strain (reduction in area) was about 0.5%.

* the microstructure of the ruptured specimen V9 was quantified away from the fracture at an area of uniform deformation along the gauge length. The strain (reduction in area) was in this case 30% at 950°C. The maximum reduction in area and the elongation of V9 were 46% and 44% respectively.

of the γ'-particles during creep at 982°C were calculated from length, thickness, time and strain information presented in [3] and replotted as aspect ratio versus strain in Fig. 6. The aspect ratios of the γ and γ'-phases from [15] were measured by chord measurements on micrographs presented in [15] and the results are shown in Fig. 7. They show a similar trend to the aspect ratio results reported here (see Fig. 5) although the maximum aspect ratio is reached at a slightly higher level of strain. In Fig. 7, 2 percent strain was reached after only 238 h, whereas in Fig. 5 0.5 percent and 2 percent strain were reached after 2876 h and 3978 h respectively.

As rafting is a process which depends on diffusion and needs a finite amount of time to occur, it is likely that the maximum aspect ratio will be shifted to higher strain levels if the strain rate is high. It is known, for example, that rafting does not occur during conventional high temperature tensile tests on SX alloys. In industrial gas turbines the strain rate is slow and so rafting will be strain controlled.

The use of microstructural changes to predict the remanent life of nickel-base superalloys is less advanced than in ferritic alloys. In wrought Ni-base alloys grain boundary cavitation occurs in much the same way as in ferritic steels [8]. In cast alloys the situation is more complex: cavities can occur and rafting may occur to a limited extent [8, 9]. Particle growth, precipitation of carbides, and the precipitation of topologically close packed phases like σ also occurs [8–11]. In some cases the most noticeable change in the microstructure was the increase in dislocation density and this required the use of transmission electron microscopy [12, 13].

SX alloys tolerate higher temperatures than conventional Ni-base superalloys and rafting is more likely to occur because: (a) the magnitude of the γ/γ' misfit is larger (more negative) at higher temperatures, (b) in commonly used $\langle 001 \rangle$ crystals all the γ'-particles are oriented with some faces normal to the stress, and (c) in modern SX alloys the γ' volume fraction is 0.5–0.7, which means that particle impingement is easier.

Although the rafting process is not totally understood it is thought that plastic strain is a prerequisite for rafting [6, 14]. The results from this study show that the raft dimensions depend on the amount of creep strain and thus it seems that high temperature creep damage will

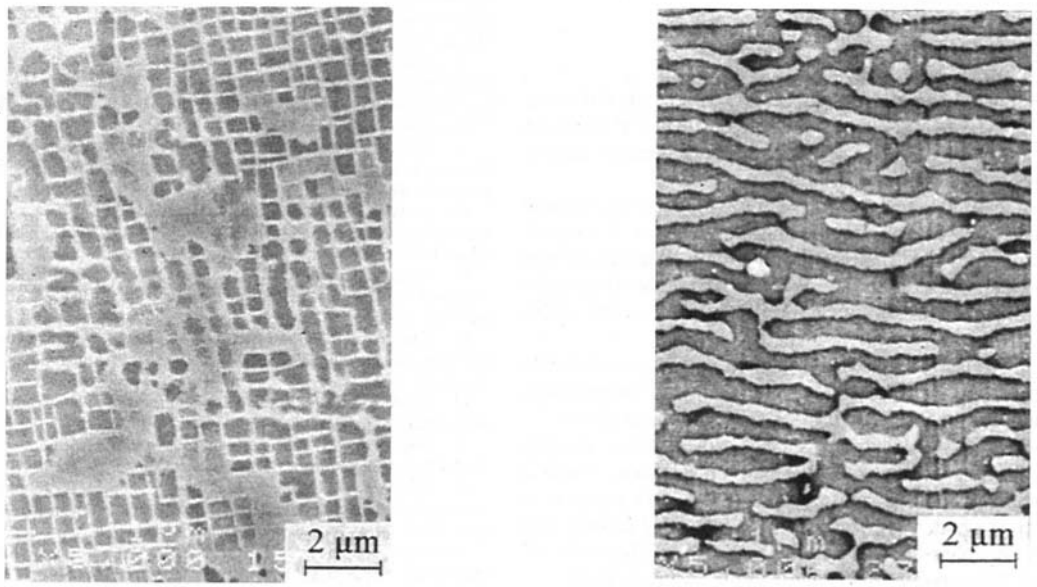

Fig. 4 Original microstructure before creep testing (left). Microstructure after 0.5 percent strain (right). Secondary electron image. Stress direction vertical. γ' is the dark phase. Before creep the γ-matrix is the continuous phase, but after creep the γ'-phase is continuous.

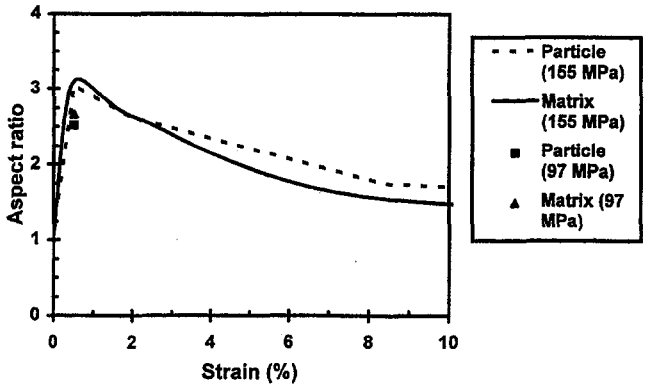

Fig. 5 The aspect ratio (length/thickness ratio) of γ'-particles and the γ-matrix as a function of creep strain at 950°C and 155 MPa

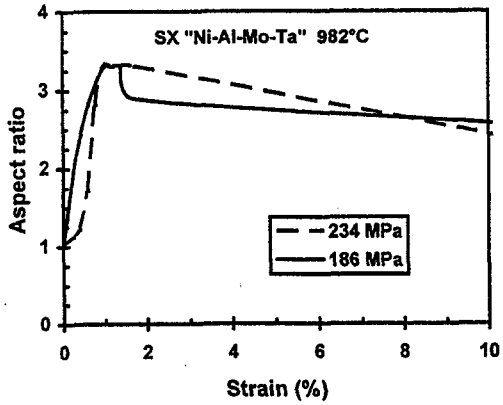

Fig. 6 The aspect ratio (length/thickness ratio) of γ'-particles versus creep strain for an SX alloy tested at 982°C. The aspect ratios have been calculated from length and thickness versus time information and from time-strain creep curves presented in [3].

be easier to assess in SX alloys than in their conventionally cast counterparts. It must be stressed that no rafts have been seen after low temperature (750–800°C) creep of CMSX-4 [7, 16] and other methods will have to be developed to estimate creep damage at these temperatures. Preliminary results indicate that rafting occurs in low temperature creep strained material after a suitable post-creep high temperature heat treatment [17].

Conclusions

Creep tests have been performed on the single crystal alloy CMSX-4 at 950°C and the changes occurring in the γ' particles have been quantified to provide a basis for creep damage assessment of single crystal turbine components.

Before creep testing, the γ'-particles (~70 vol %) were cuboidal and discrete and the γ-matrix was the continuous phase. However, after 0.5 percent creep the "matrix" became the isolated phase and the γ'-phase formed a continuous network of interlocking rafts. The rafts reached their maximum length before 2 percent strain, but continued to thicken throughout the test.

Chord length measurements were found to be the most suitable method of quantifying the microstructure by automatic image analysis, because they can be used for discrete and continuous phases.

Although of different dimensions, the aspect ratios (length/thickness ratios) of the γ'-rafts and the γ-matrix plates were similar at the same levels of strain, increasing from 1 at zero strain to a maximum of 3 at about 1 percent strain. Analysis of rafting data presented in the literature showed that this was also true for other SX alloys provided that enough time is allowed for rafting to occur.

Measurement of γ' raft (or matrix plate) aspect ratios on longitudinal sections of SX turbine blades is a method suitable for creep strain assessment.

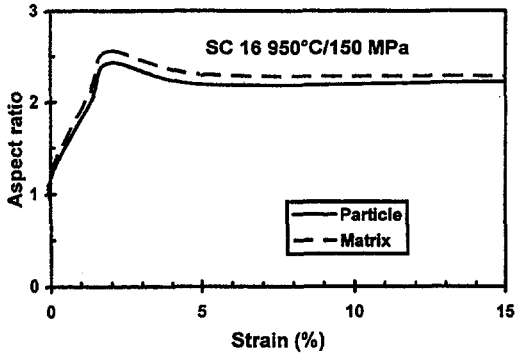

Fig. 7 The aspect ratios of particles and matrix measured from micrographs presented in [15]. SC16 contains ~40 vol % γ'-particles.

Acknowledgments

The creep testing and microscopy were performed at the Swedish Institute for Metals Research. We thank Joakim Lindblom and Facredin Seitisleam for experimental help and Leif Berglin (ABB STAL, Finspång, Sweden) for useful discussions. The research was entirely funded by Värmeforsk (The Swedish Thermal Power Research Foundation) and additional financing was provided by Vattenfall Värmekraft AB (Vattenfall Thermal Power). The financial support is gratefully acknowledged.

References

1 Pearson, D. D., Lemkey, F. D., and Kear, B. H., 1980, "Stress Coarsening of γ' and Its Influence on Creep Properties of a Single Crystal Superalloy," Proceedings, 4th Int. Symp. on Superalloys, J. K. Tien et al., eds., ASM, OH, pp. 513–519.

2 MacKay, R. A., and Ebert, L. J., 1983, "The Development of Directional Coarsening of the γ' Precipitate in Superalloy Single Crystals," *Scripta Metall.*, Vol. 17, pp. 1217–1222.

3 MacKay, R. A., and Ebert, L. J., 1985, "The Development of γ-γ' Lamellar Structures in an Nickel-Base Superalloy During Elevated Temperature Mechanical Testing," *Metall. Trans. A*, Vol. 16A, pp. 1969–1982.

4 Nathal, M. V., and Ebert, L. J., 1983, "Gamma Prime Shape Changes During Creep of a Nickel Base Superalloy," *Scripta Metall.*, Vol. 17, pp. 1151–1154.

5 Pollock, T. M., and Argon, A. S., 1994, "Directional Coarsening in Nickel-Base Single Crystals with High Volume Fractions of Coherent Precipitates," *Acta Metall. Mater.*, Vol. 42, pp. 1859–1874.

6 Nathal, M. V., and MacKay, R. A., 1987, "The Stability of Lamellar γ-γ' Structures," *Mater. Sci. and Eng.*, Vol. 85, pp. 127–138.

7 Mughrabi, H., Schneider, W., Sass, V., and Lang, C., 1994, "The Effect of Raft Formation on the High Temperature Creep Deformation Behaviour of the Monocrystalline Nickel-Base Superalloy CMSX-4," Proceedings, ICSMA-10, Oikawa et al., eds., JIM, Sendal, pp. 705–708.

8 Karlsson, S.-Å, Persson, C., and Persson, P.-O., 1995, "Metallographic Approach to Turbine Blade Lifetime Prediction," Proceedings, BALTICA III Int. Conf. on Plant Condition and Life Management, S. Hietanen and P. Auerkari, eds., VTT, Espoo, Finland, pp. 333–349.

9 Persson, C., and Persson, P.-O., "Evaluation of Service Induced Damage and Restoration of Cast Turbine Blades," Proceedings, Superalloys 1992, S. D. Antolovich et al., eds., TMS, pp. 867–876.

10 Castillo, R., Koul, A. K., and Immarigeom, J-P. A., 1988, "The Effect of Service Exposure on the Creep Properties of Cast IN 738 LC," Proceedings, Superalloys 1988, S. Reichman et al., eds., TMS, pp. 805–814.

11 Koul, A. K., and Castillo, R., 1988, "Assessment of Service Induced Microstructural Damage and its Rejuvenation in Turbine Blades," *Met. Trans.*, Vol. 19A, pp. 2049–2066.

12 Henderson, P. J., and McLean, M., 1985, "Microstructural Changes During the Creep of a Directionally Solidified Nickel-Base Superalloy," *Scripta Metall.*, Vol. 19, pp. 99–104.

13 Henderson, P. J., 1988, "Dislocations at γ/γ' Interfaces During the Creep of Nickel-Base Superalloys," *Scripta Metall.*, Vol. 22, pp. 1103–1107.

14 Veron, M., and Bastie, P., 1997, "Strain Induced Directional Coarsening in Nickel Based Superalloys," *Acta Mater.*, Vol. 45, pp. 3277–3282.

15 Mukherji, D., Gabrisch, H., Chen, W., Fecht, H. J., and Wahi, R. P., 1997, "Mechanical Behaviour and Microstructural Evolution in the Single Crystal Superalloy SC16," *Acta Metall.*, Vol. 45, pp. 3143–3154.

16 Henderson, P. J., and Komenda, J., 1997, "Changes in the Microstructure During the Creep of a Single Crystal Alloy," Proceedings, Advances in Turbine Materials, Design, and Engineering, A. Strang et al., eds., The Institute of Materials, London, UK, pp. 663–678.

17 Henderson, P., Berglin, L., and Jansson, C., 1999, *Scripta Metall.*, Vol. 40, pp. 229–234.

Influence of an Aluminide Coating on the TMF Life of a Single Crystal Nickel-Base Superalloy

E. E. Affeldt
MTU Motoren und Turbinen Union München,
Postfach 50 06 40,
80976 München,
Germany

TMF tests were conducted with bare and aluminide coated single crystal nickel-based superalloy specimens. Temperature cycling was between 400°C and 1100°C with a phase shift (135 deg) that is typical for damaged locations on turbine blades. Stress response is characterized by a constant range and the formation of a tensile mean stress as a result of relaxation in the high temperature part of the cycle which is in compression. Bare specimens showed crack initiation from typical oxide hillocks. Coated specimens showed life reduction with respect to the bare ones caused by brittle cracking of the coating in the low temperature part of the cycle. Isothermal bending tests of coated specimens confirmed the low ductility of the coating at temperatures below 600°C but quantitative correlation with the TMF test results failed.

Introduction

Aero-engine turbine blades and vanes experience strong cyclic thermal mechanical loading combined with hot corrosive attack. Single crystal nickel-base superalloys are widely used as blade and vane materials because of their excellent resistance to high temperature deformation. Tuning of their chemical composition focuses primarily towards improving their high temperature strength but guarantees no sufficient oxidation resistance. Sufficient oxidation resistance is achieved in a high percentage of blades through coatings based on the formation of nickel aluminide by a diffusion process or by plasma spraying of a MCrAlY coating on the outer surface of the blades. Such coatings, especially the diffusion coatings, show brittle behavior at low and ductile behavior at high temperatures, with a transition at temperatures around 600°C. Thus isothermal cyclic testing at low temperatures may be shortened by brittle cracking of the coating, but as LCF life is much higher at low temperatures (Fleury, 1990) can result in an unrealistic long fatigue life. Testing at high temperatures will result in a more realistic number of cycles to failure, but may avoid the detrimental influence of brittle cracks in the coating. That underlines the necessity of anisothermal testing which can account for the interaction of low and high temperature damage mechanisms for the design of coated blades and vanes.

Experimental Details

The substrate material was a single crystal nickel-based superalloy. Its chemical composition is given in Table 1. Following the solution heat treatment of the 25 mm diameter single crystal blanks, these were machined into TMF test specimens. The aluminide coated specimens were given a coating diffusion treatment of 3 h at 1080°C in vacuum. The crystallographic orientation of the longitudinal axis of the test specimens was within 15 deg of ⟨001⟩.

The thermo-mechanical fatigue tests were carried out on a computer controlled servohydraulic testing machine. The test specimen is heated by means of direct induction. The TMF test specimen has a cylindrical end geometry and a solid gauge length with a rectangular cross section of 12 mm × 4 mm. The edges of the gauge length section are rounded in order to promote good adherence of the coating and to reduce thermal gradients. Coated specimens are tested in the as-received condition without any further surface modification treatment. The sample temperature is controlled by means of a thermocouple spot welded to the specimen surface in the gauge length. If the main crack initiated at or near to the thermocouple during testing, the results were disregarded. Strains were measured by means of a longitudinal extensometer, with the limbs spanning a gauge length of 12 mm. All tests were carried out in total strain control symmetrically (R-ratio of $R_\epsilon = -1$) between mechanical strain limits. The temperature is varied linearly with time and synchronously with a 135 deg phase lag with respect to the mechanical strain. Prior to each TMF test the thermal expansion of the specimen is recorded as a continuous function of the temperature while heating and cooling the specimen at the same rate as in the actual TMF test. To obtain a constant mechanical strain rate the calculated thermal expansion is added to the mechanical strain and the sum is used as the control signal for the total strain. The minimum cycle temperature was 400 °C, the maximum temperature 1100 °C. Specimen heating and cooling rates were set at 10°C/s which required forced cooling during the end of the downward branch of the cycle. The maximum temperature gradient over the gauge length was ±15°C. All tests were started at 400°C. As a result of the tests the stress range remains constant until cracks reduce the specimen compliance. Based on this observation TMF-"life" was defined as the cycle number corresponding to a decrease of the stress range to 70 percent of the range measured after cycle number 10.

In addition to the TMF tests, isothermal three point bending tests were performed to evaluate the fracture strain of the aluminide coating on the single crystal substrate. The specimens had dimensions of 5 mm × 5 mm × 50 mm and are coated on that side which experienced tension under bending loads. Two batches were coated to account for the influence of scatter in the coating procedure. The specimens were loaded to a maximum strain which was 10 percent higher than that strain which corresponds to the yield strength. The coating fracture strain was evaluated during the test by acoustic emission measurements and after the test by optical inspection. A small bending apparatus was used to load the specimen to half of the maximum load experienced during testing to enhance the resolution of the cracks under the microscope. The

Contributed by the International Gas Turbine Institute (IGTI) of THE AMERICAN SOCIETY OF MECHANICAL ENGINEERS for publication in the ASME JOURNAL OF ENGINEERING FOR GAS TURBINES AND POWER. Paper presented at the International Gas Turbine and Aeroengine Congress and Exhibition, Stockholm, Sweden, June 2–5, 1998; ASME Paper 98-GT-318.

Manuscript received by IGTI March 16, 1998; final revision received by the ASME Headquarters June 23, 1999. Associate Technical Editor: R. Kielb.

Table 1 Composition of the nickel base alloy (in wt.%)

Ni	Co	Cr	Mo	W	Ta	Al	Hf	Re
bal	10.0	5.0	2.0	6.0	9.0	5.6	0.1	3.0

strain value in the coating decreases linearly with the distance from the middle of the specimen. Thus after testing cracks are found in the middle of the specimen till the distance from the middle reduces the strain below the coating fracture strain. Those cracks which had the largest distance to the middle of the specimen were evaluated and the corresponding strain at that location was taken as a measure of the coating fracture strain.

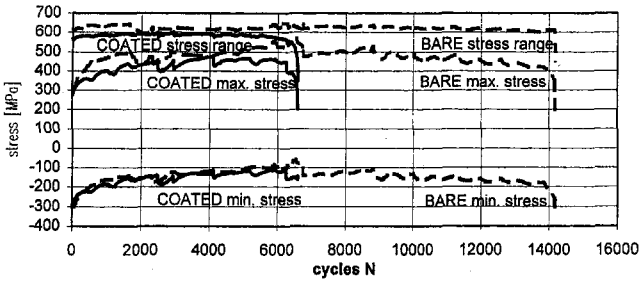

Fig. 1 Evolution of the maximum stress, minimum stress and stress range as a function of the cycle number for TMF with a strain range of 0.8 percent

Results

TMF Stress Response. The stress response of the strain-controlled experiments is shown in Fig. 1, which describes the behavior of the maximum stress, the minimum stress, and the stress range as a function of the number of cycles experienced. The stress range remains constant despite minor fluctuations. The small kinks at about 3000 and 6000 cycles are caused by experimental problems; the signal of the thermocouple showed irregularities caused by oxide surrounding the thermocouples. This led to automatic test interruption requiring spotwelding a new thermocouple to the specimen and a restart of the test. For the test conditions shown (which is a long-term test, requiring about 15,000 cycles to specimen failure) the maximum stress and the minimum stress are about symmetrical at the start with an absolute value of about 300 MPa and shift by about 200 MPa, which is two thirds of the absolute start conditions. It indicates that a tensile mean stress was formed by relaxation at the high temperature branch of the cycle were the specimen is in compression. At the end of the test the stress range drops, indicating that the size of cracks causes a noticeable reduction of the specimen compliance. The stress response is unaffected by the coating but as coating can accelerate cracking the specimen compliance can be reduced at a lower number of cycles.

TMF Life. The number of cycles to failure of the specimens are shown in Fig. 2. The lives of the bare specimen as well as the coated specimen show a clear relationship with the applied strain range, indicating minor scatter. The lives of the coated samples as compared to the comparable to the extrapolated life of the bare specimen. The test was terminated and the specimen was investigated, but no cracks were found.

Figure 3 shows typical examples of the crack initiation sites on the side surface of a bare specimen in the gauge length. Several oxide hillocks were found which were typically broken, and cracks propagate on both sides and into the interior of the specimen. Figure 4 shows the fracture surface of the same specimen. Local crack initiation and penny-shaped propagation are observed.

The side surface of the coated specimens is exemplified in Fig. 5. It shows the formation of a typical wavy surface roughness with alignment perpendicular to the loading axis. Additionally, very sharp and straight cracks were found hardly visible on the picture of the side surface given. These cracks propagate in a straight line from the side surface, indicating a different propagation mode than for the bare specimen. Figure 6 shows a cross section along the loading axis perpendicular to the side surface. The wavy surface roughness of the coating is partly visible as well as a crack in the coating. It shows extended oxidized regions in the interdiffusion zone expanding over the width of that zone and extending to both sides of the crack. Only part of the coating cracks extend into the substrate (as the crack in Fig. 6) as comparably sharp cracks with minor oxidation on both sides.

Crack Initiation in the Coating. The results of the isothermal bending tests are given in Fig. 7. The coating fracture strain is given as a function of the temperature. Whereas there is a small increase with temperature below 600°C, the cracking strain raises rapidly to the maximum strain applied at temperatures higher than 600/650°C, and no cracks were found at higher temperatures.

Discussion

TMF. The stress response of the above reported investigations is characterised by a constant stress range and a time/cycle dependant formation of a tensile mean stress. That formation is caused by relaxation in the high temperature part of the cycle, which is under compressive stresses. A simple comparison with isothermal tests is expected to fail based on literature (Vasseur, 1994) and on the apparent fact, that the stress strain relationship is described by the Young's modulus in the elastic regime, which is temperature dependant and changes by 50 percent in the investigated range. Incorporation of the temperature dependence of the Young's modulus enables to describe the stress range/strain range relationship of the first cycle satisfactorily. The formation of the mean stress, however, underlines the importance of time-dependant processes.

The behavior of the bare specimen is characterised by oxide hillocks which were build up on the surface of the specimen and cause localised crack initiation and propagation of semi-ellipitical cracks. This mechanism was reported in several references for different alloys, e.g., (Chataigner, 1996; Fleury, 1990; Bressers, 1996a; Bressers, 1996b). It was often shown to be associated with preferred oxidation of carbides or casting porosity in the interdendritic zones, which is discussed in detail in Johnson (1997). This leads to many oxide hillocks and cracks on the specimen surface, which means that there are many sites of comparable varied behavior on one specimen surface. It is expected that the behavior of different specimens is as comparable as that of different locations on one specimen causing small scatter in the results. That is contrary to the LCF behavior of several nickelbase alloys at

Nomenclature

TMF = thermomechanical fatigue test technique

MCrAlY = an overlay coating containing chromium, aluminum, yttrium and nickel and/or cobalt

R_ϵ = ratio of lower strain/upper strain in a strain controlled test

LCF = low-cycle fatigue test technique

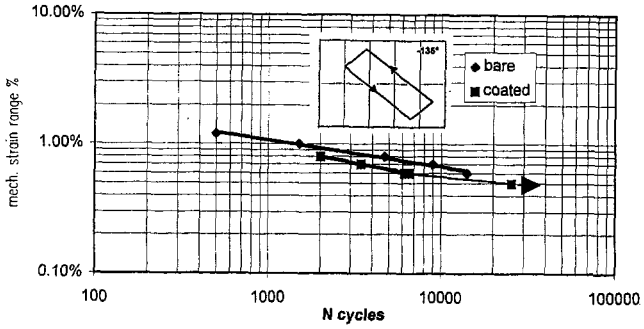

Fig. 2 Number of cycles to failure for bare and Al-coated specimen. Arrow indicates test termination without failure.

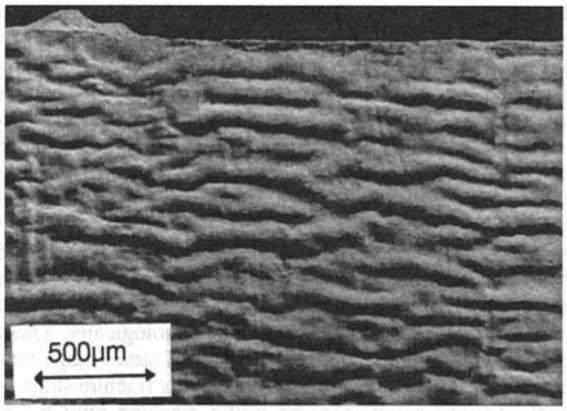

Fig. 5 Side surface of a coated specimen with wavy surface structure *indicating plasticity of the coating*

intermediate and low temperatures, which is often controlled by the existence and size of one inhomogenity in the specimen.

As far as the mechanistic understanding is concerned it is clear that all conditions causing faster oxidation lead to localisation which is true for the interdendritic region and for carbides. Because the fracture resistance of the oxides is very small (Martinez, 1996) it is realistic to assume that it will be broken in every cycle. Carbides and pores can additionally act as stress concentrator. That intensifies the breakage of the oxides and causes acceleration of oxidation by access to new surface. That forces the localization of oxidation and causes the formation of oxide spikes.

Cyclic propagation of cracks necessitates to overcome the threshold of fatigue crack propagation. Thereafter, life is controlled by (thermomechanical) fatigue crack propagation. To overcome the threshold a mechanism of crack propagation is necessary which extends the crack length. It is assumed that the localization of oxidation and the cyclic breakage of that oxide is able to elongate the crack sufficiently. That means it is not only a mechanism of initiation but also of propagation till threshold is overcome. Thus crack propagation is controlled by two different consecutive mechanisms, first the cyclic build-up and breakage of oxides and second fatigue crack propagation by cyclic plasticity.

Lives of Coated Specimen and Coating Fracture. Coating reduced the life of the specimen at strain ranges higher than 0.6 percent. The fracture and the side surface of the specimens showed that straight line coating cracks spanning over the whole specimen width were initiated and propagated through the substrate. Such behavior indicates unstable cracking of the coating by exceedance

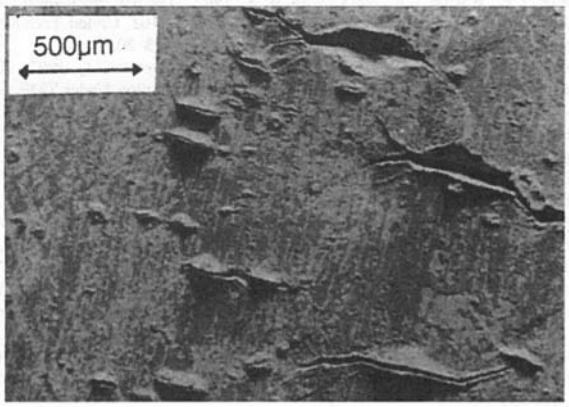

Fig. 3 Side surface of a bare specimen showing brocken oxide hillocks with cracks

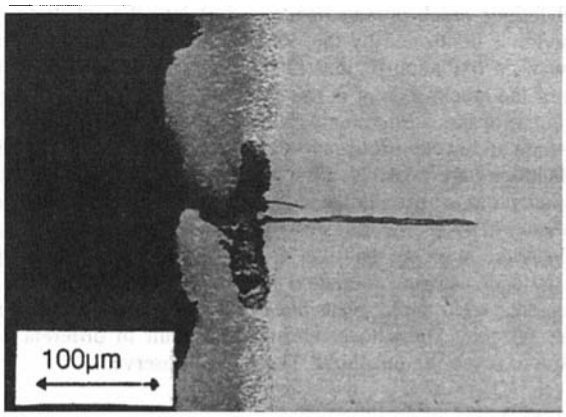

Fig. 6 Cross section of a coated specimen with wavy coating. A coating crack extends in the substrate showing oxidized region in the diffusion zone.

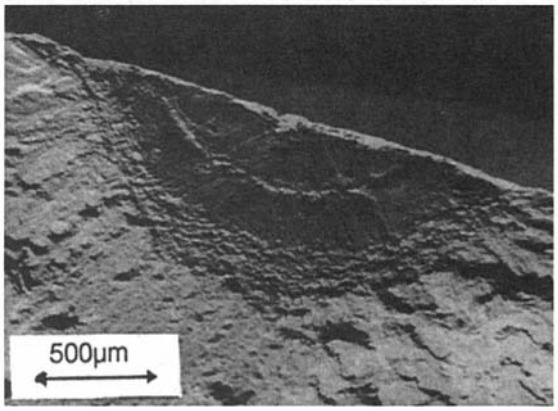

Fig. 4 Fracture surface or bare specimen showing penny-shaped crack propagation

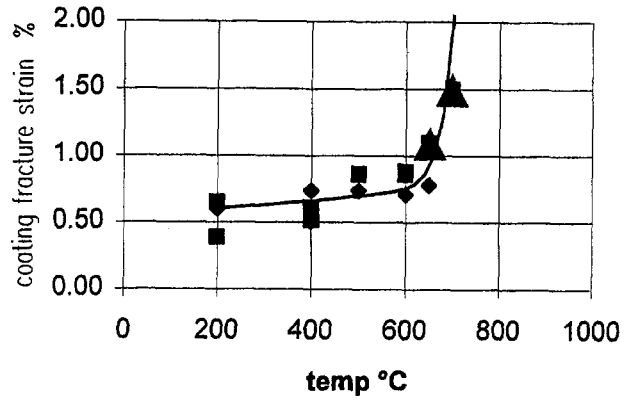

Fig. 7 Coating fracture strain as function of the temperature. Triangles indicate max. strain applied without cracks in the coating.

of the fracture toughness. Comparable observations are reported by Bressers (1996a), Bressers (1996b, Martinez (1996) for TMF; by Totemeier (1996) for isothermal LCF. In contrast, Chataigner (1996) and Linde (1994) reported no life reduction for TMF testing of a comparable alloy coating system. As shown by the bending tests the fracture strain of the coating substrate combination of our investigation shows a brittle behavior at low temperatures and a transition to a ductile behavior at a temperature of about 600°C. Such behavior is often reported in the literature (Totemeier, 1993; Heine, 1989). Simple correlation of the fracture behavior of the coating with TMF testing postulates brittle cracking of the coating by the strain versus temperature path crossing the fracture strain of the coating which is confirmed phenomenologically. Quantitatively for symmetric cycling ($R = -1$), the strain range must be greater then 1.2 percent according to a coating fracture strain of 0.6 percent. But our results showed brittle cracking until the strain range decreases to less than 0.7 percent. At a strain range of 0.6 percent, brittle cracking of the coating was no longer observed, and the life tends to reach that for uncoated tests. Totemeier et al. (1996) reported a comparable behavior. They attributed it to a volume effect based on the different amount of coating defects in different specimen types. Another point may be emphasized. TMF loading first leads to compressive strains at high temperatures before is reaches tensile strains able to crack the coating in the brittle temperature regime. That clearly will influence the residual stresses in the coating. Plastic deformation of the coating at the higher temperatures is confirmed by the wavy surface appearance of the coating after termination of the test.

Comparing bare and coated specimens it is apparent that the brittle cracking reduces life. But, from a mechanistic point of view, which steps in lifing are influenced by (brittle cracking of) the coating? Clearly the crack initiation is different. The heavily oxidized regions in the interdiffusion zone additionally show that oxidation and breakage of oxide drives the crack through that zone until fatigue crack propagation can start into the substrate. This behavior is confirmed by the observation that all coating cracks show wide oxidation regions in the interdiffusion zone but only part of the cracks extend in the substrate. These oxidized regions end more or less at the boundary between interdiffusion zone and substrate and cyclic propagation starts at that boundary. Different explanations are possible. First it may be accidentally, that the boundary has a thickness which correspond to the crack depth necessary to overcome the threshold of crack propagation. Another explanation may be that the interdiffusion zone has a higher threshold or a higher oxidation rate than the substrate. The last argument seems more plausible because different strain ranges cause different stress level and should result in different crack depths to reach the threshold. That is not observed.

Conclusion

In summary the coating enhances oxidation resistance but also causes initiation of cracks by brittle cracking of the coating. The fracture behavior of the coating under TMF cycles is different from that under isothermal bending that may be attributed to size effects, but surely is influenced by the plastic deformation of the coating in the high temperature regime of the first TMF cycle. Coating cracks seem to stop in the interdiffusion zone and extend by alternating oxidation and breakage of the oxide. Only part of that cracks extend in the substrate. If they do so they look like fatigue cracks driven by cyclic plasticity with minor influence of oxidation. Detailed understanding of the interaction of coating and substrates to optimize the balance of beneficial effect on oxidation and detrimental effects on TMF life are a key issue in turbine blade development.

Acknowledgments

I would like to thank J. Ritter for performing the TMF tests and J. Haug for the evaluation of the results of the bending tests.

References

Bressers, J., Timm, J., Williams, S. J., Affeldt, E. E., and Bennett, A., 1996a, "Effects of Cycle Type and Coating on the TMF Lives of CMSX6," AGARD-CP-569, advisory group for aerospace research and development, Neuilly-sur-Seine, France, pp. 9-1–9-10

Bressers, J., Timm, J., Williams, S. J., Bennett, A., and Affeldt, E. E., 1996b, "Effects of Cycle Type and Coating on the TMF Lives of a Single Crystal Nickel Based Gas Turbine Blade Material," ASTM STP 1263, M. J. Verrilli, and M. G. Castelli, eds., American Society for Testing and Materials, Philadelphia, PA, pp. 56–67.

Chataigner, E., and Remy, L., 1996, "Thermomechanical Fatigue Behavior of Coated and Bare Nickel-Based Superalloy Single Crystals," ASTM STP 1263, M. J. Verrilli and M. G. Castelli, eds., American Society for Testing and Materials, Philadelphia, PA, pp. 3–26.

Fleury, E., and Remy, L., 1990, "Thermal Mechanical Fatigue of AM1 Superalloy Single Crystals," *High Temperature Materials for Power Engineering 1990,* E. Bachelet et al., eds., Kluwer Academic Publishers, London, pp. 1007–1016.

Heine, J. E., Warren, J. R., and Cowles, B. A., 1989, "Thermal Mechanical Fatigue of Coated Blade Materials," Report No. WRDC-TR-87-4102, United Technologies Corporation, Pratt & Witney, West Palm Beach, FL, pp. 13–20.

Johnson, P. K., Arana, M., Ostolaza, K. M., and Bressers, J., 1997, "Crack Initiation in a Coated and an Uncoated Nickel-Base Superalloy Under TMF Conditions," *J. of Eng. Materials and Technology,* to be published.

Linde, L., and Henderson, P. J., 1994, "Thermo-Mechanical and Low Cycle Fatigue of a Coated Nickel-Base Superalloy," *Materials for Power Engineering, Part II,* E. Bachelet et al., eds., Kluwer Academic Publishers, London, pp. 1367–1376.

Martinez-Esnaola, J. M., Arana, M., Bressers, J., Timm, J., Bennett, A., and Affeldt, E. E., 1996, "Crack Initiation in an Aluminide Coated Single Crystal During Thermomechanical Fatigue," ASTM STP 1263, M. J. Verrilli and M. G. Castelli, eds., American Society for Testing and Materials, Philadelphia, PA, pp. 68–81.

Totemeier, T. C., Gale, W. F., and King, J. E., 1993, "Fracture Behaviour of an Aluminide Coating on a Single Crystal Nickel Base Superalloy," *Materials Science and Engineering,* Vol. A169, pp. 19–26.

Totemeier, T. C., King, J. E., 1996, "Isothermal Fatigue of an Aluminide-Coated Single-Crystal Superalloy: Part I," *Metallurgical and Materials Transactions A,* Vol. 27A, pp. 353–361.

Vasseur, E., and Remy, L., 1994, "High Temperature Low Cycle Fatigue and Thermal-Mechanical Fatigue Behaviour of an Oxide-Dispersion-Strengthened Nickel-Base Superalloy," *Mat. Science and Engng.,* A184, pp. 1–5.

Rotor Power Losses in Planar Radial Magnetic Bearings—Effects of Number of Stator Poles, Air Gap Thickness, and Magnetic Flux Density

P. E. Allaire
Mechanical, Aerospace, and Nuclear Engineering, University of Virginia, Charlottesville, VA 22901

M. E. F. Kasarda
Mechanical Engineering Department, Virginia Polytechnic Institute and State University, Blacksburg, VA 24061

L. K. Fujita
Mechanical, Aerospace, and Nuclear Engineering, University of Virginia, Charlottesville, VA 22901

Rotor power losses in magnetic bearings cannot be accurately calculated at this time because of the complexity of the magnetic field distribution and several other effects. The losses are due to eddy currents, hysteresis, and windage. This paper presents measured results in radial magnetic bearing configurations with eight pole and 16 pole stators and two laminated rotors. Two different air gaps were tested. The rotor power losses were determined by measuring the rundown speed of the rotor after the rotor was spun up to speeds of approximately 30,000 rpm, DN = 2,670,000 mm-rpm, in atmospheric air. The kinetic energy of the rotor is converted to heat by magnetic and air drag power loss mechanisms during the run down. Given past publications and the opinions of researchers in the field, the results were quite unexpected. The measured power losses were found to be nearly independent of the number of poles in the bearing. Also, the overall measured rotor power loss increased significantly as the magnetic flux density increased and also increased significantly as the air gap thickness decreased. A method of separating the hysteresis, eddy current and windage losses is presented. Eddy current effects were found to be the most important loss mechanism in the data analysis, for large clearance bearings. Hysteresis and windage effects did not change much from one configuration to the other.

Introduction

Rotor power losses in magnetic bearings are very important for many applications but are not well understood. Recently there have been a number of power loss studies in magnetic bearings published in the open literature. Some of the indications in the literature of how iron power losses should vary in different stator configurations appear to be directly contradicted by the results of the measurements in this paper. The purpose of this study is to provide fundamental information of critical importance on rotor iron power losses to the magnetic bearing industry.

A primary concept in the previous literature was that the rotor iron power losses (eddy current and hysteresis) were expected to be roughly proportional to the number of poles or edges in the stator that the rotor would pass as it rotated. Matsumura et al. (1988) presented a paper discussing power loss in magnetic bearings including a partial Fourier analysis of magnetic flux as seen by the rotor as it passes each pole edge in the rotor. The implication is that the eddy current power loss should be approximately proportional to the number of poles in the bearing. Another implication of the Fourier analysis presented in this work is that the shape of the pole edge may be very important in the rotor iron power loss. Matsumura and Hatake (1992) discussed a Fourier analysis of fringing and leakage effects on eddy current losses, indicating that pole edge effects may be the most important consideration. Kasarda et al. (1996b, 1999) discussed power loss measurements in an eight pole bearing and an analytical/empirical model which used a frequency dependent effect based upon the number of poles passed by the rotor.

Allaire et al. (1997) presented results on an eight pole magnetic bearing for the power loss variation with respect to air gap flux density and air gap thickness. It was found that, overall, the power loss varied with the rotational speed squared. Also, the power loss is approximately proportional to the air gap flux squared and inversely proportional to the air gap thickness. The effect of the air gap thickness was not predicted by previous studies reported in the literature. Rockwell et al. (1997) presented a finite element model of the same bearing to calculate the eddy current loss component of these losses.

This paper reports the first results where rotor power losses were directly measured in both an 8 pole and 16 pole stator with the same pole face area, and with other geometric parameters kept as compatible as possible. The tests were run with different bias flux densities and air gaps using the same rotor. Most unexpectedly, the power loss measurements for the eight pole and 16 pole bearings were nearly identical, when other parameters were held constant. This contradicts the expectations of all previous publications in regard to the effect of the number of stator poles on the iron losses.

Test Rig

Figure 1 shows a schematic of the test rig. It consists of a shaft with two magnetic bearings and two induction motors located at the shaft ends. The two electric motors drive the rotor up to peak operating speed and then they are shut off. Kasarda et al. (1994) discussed the design of the high speed test rig in some detail and gave a sensitivity analysis of the loss modeling based upon the theoretical parameters involved. The test rig has been designed to measure the power losses in magnetic bearings by accurately measuring the conversion of the rotor's kinetic energy into heat. This is done by measuring the time it takes for the rotor to run

Contributed by the International Gas Turbine Institute (IGTI) of THE AMERICAN SOCIETY OF MECHANICAL ENGINEERS for publication in the ASME JOURNAL OF ENGINEERING FOR GAS TURBINES AND POWER. Paper presented at the International Gas Turbine and Aeroengine Congress and Exhibition, Stockholm, Sweden, June 2–5, 1998; ASME Paper 98-GT-316.

Manuscript received by IGTI March 16, 1998; final revision received by the ASME Headquarters June 23, 1999. Associate Technical Editor: R. Kielb.

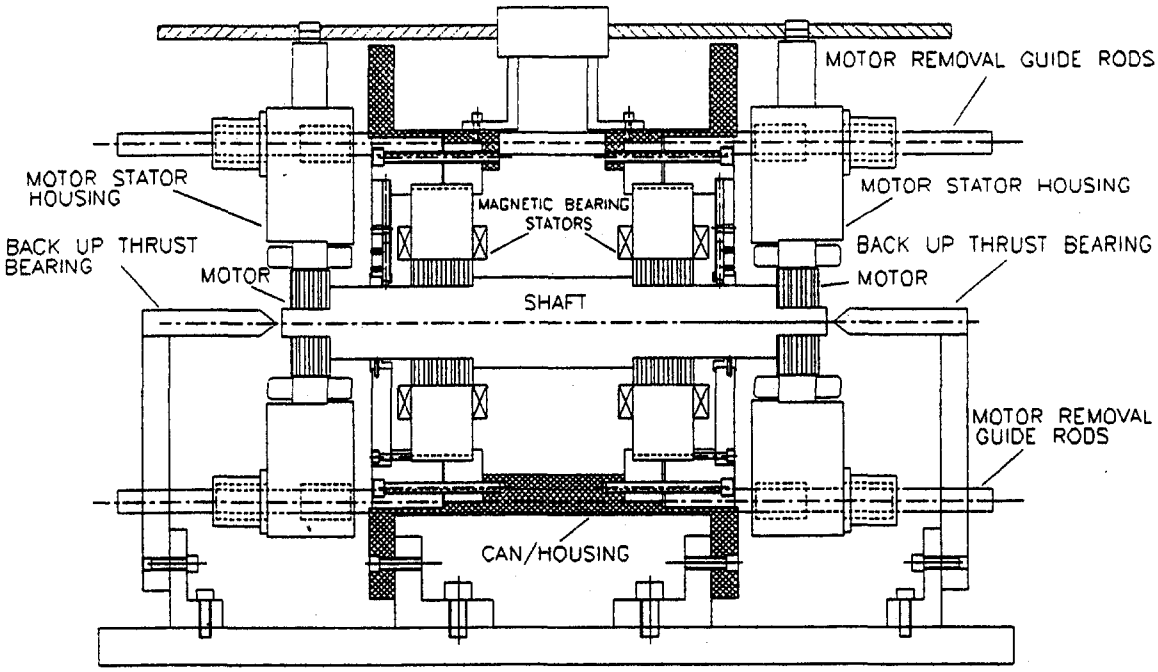

Fig. 1 Diagram of magnetic bearing loss test rig

down from one speed to another. The rotor kinetic energy due to rotation is $E_k = J\omega^2/2$, where ω is the rotational speed of the rotor in rad/s. PID control was used.

The power loss is the time derivative of the kinetic energy

$$P_k = J\omega \frac{d\omega}{dt} = \left(\frac{\pi}{30}\right)^2 JN \frac{dN}{dt}$$

$$= P_h + P_e + P_w. \quad (1)$$

Here the polar moment of inertia is easily determined from a calculation, and $N(t)$ is easily measured from the rundown tests. On the right hand side of this equation, the power loss is written as the sum of the power loss due to hysteresis, P_h, the power loss due to eddy currents, P_e, and the power loss due to windage, P_w. It has been shown in previous work by Kasarda et al. (1996a, b, c) that the power loss can be written in terms of frequency dependent parameters as

$$P_k = C_h\omega + C_e\omega^2 + C_w\omega^{2.8} \quad (2)$$

based upon analytical/empirical models. In this formula, the skin effects are neglected (Kasarda, 1996b).

The outer diameter of the bearing journals is approximately 89.0 mm (3.5 in) and the test rig is designed to operate up to 50,000 rpm resulting in a DN of 4.5×10^6 mm-rpm. However, the yield strength of the current silicon iron bearing limits the peak speed to 32,000 rpm. The rotor first bending critical speed is at approximately 84,000 rpm so the rotor is considered rigid. Additional details of the test rig design are given in (Kasarda, 1994).

Magnetic Bearing Properties

Two magnetic bearing stators have been used in these tests: S1—an eight pole radial planar (heteropolar) bearing stator and S2—a 16 pole bearing stator. Stator dimensions for both designs have an OD = 196.2 mm (7.726 in) and axial length L = 43.6 mm (1.715 in) (without coils). In the eight pole bearing stator, the radial length of each leg is 31.8 mm (1.253 in) and the circumferential width of each leg is 21.1 mm (0.79 in). In the 16 pole bearing stator, the circumferential width of each leg is 10.6 mm (0.395 in). Each pole has a coil winding of 94 turns. The stators were constructed of 0.356 mm (0.014 in) 3 percent silicon iron laminations. Each of the two stators has a total pole face area which covers 53 percent of the journal surface area. The eight pole radial bearing geometry is shown in Fig. 2 and the 16 pole bearing geometry is shown in Fig. 3. It should be noted that these bearings were designed to be comparable to one another to provide an

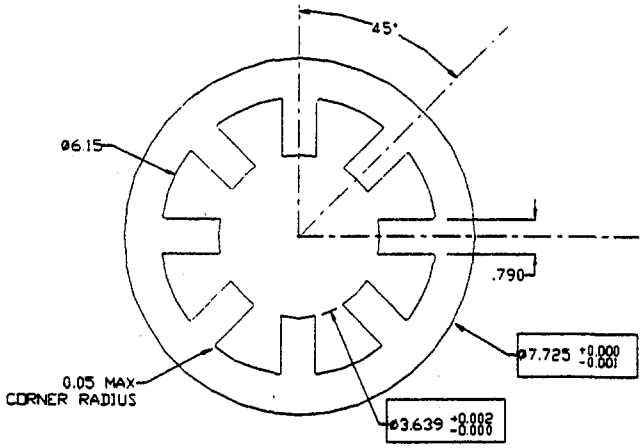

Fig. 2 8 Pole radial bearing stator S1 geometry

Nomenclature

b = loss coefficient
C = loss coefficient
d = lamination thickness (mm)
f = frequency
J = polar moment of inertia (N-s^2-m)
N = rotor speed (rpm)
P_k = power loss (watts)
V = volume
ω = rotor speed (rad/sec)

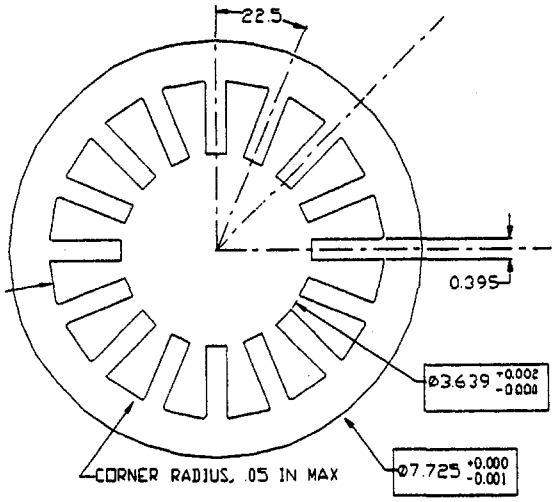

Fig. 3 16 Pole radial bearing stator S2 geometry

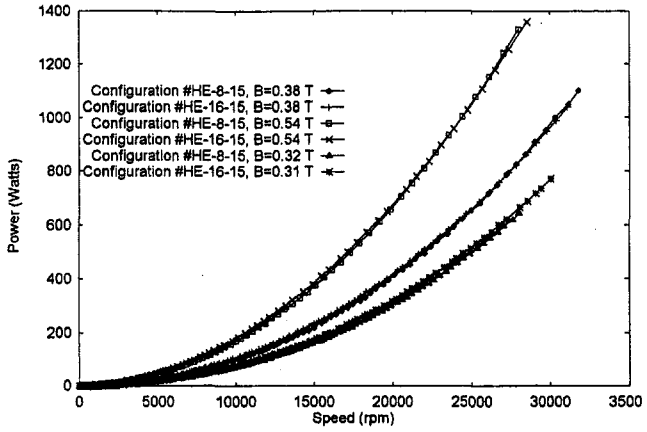

Fig. 4 Measured magnetic bearing power loss versus speed at three bias flux density values for HE-8-15 and HE-16-15

"apples to apples" comparison between bearings but are not designed to be low loss bearings.

The bearing rotor lamination stack diameters have an approximate OD = 89.0 mm (3.50 in), shaft OD = 50.8 mm (2.0 in), and axial length of 4.36 mm (1.72 in) and are shrunk fit onto a 50.8 mm (2.0 in) diameter shaft. They are constructed of 3 percent silicon iron laminations with a thickness of 0.356 mm (0.014 in). The laminations are stacked axially along the shaft to restrict the development of eddy currents moving in the axial direction. Two test rotor assemblies have been built with two different air gaps at the bearings; Rotor R1 had an air gap of 0.762 mm (0.030 in) and Rotor R2 had an air gap of 0.381 mm (0.015 in). The different gap thicknesses were obtained by using two different rotor lamination outer diameters. The polar moment of inertia of the first rotor is $J_1 = 8.10$ N-s^2-mm (7.02 $\times$ 10^{-2} lbf-s^2-in) and for the second rotor $J_2 = 8.16$ N-s^2-mm (7.08 $\times$ 10^{-2} lbf-s^2-in). The difference is primarily due to the addition of a small collar in rotor R2 to prevent the laminations from separating. The relative permeability of the rotor and stator material is estimated at 3000.

Data Reduction

The measured data was recorded as speed (in rpm) versus time (in seconds). The rundown data dN/dt was evaluated using the following model:

$$\frac{dN}{dt} = b_1 + b_2 N + b_3 N^{1.8}, \tag{3}$$

where the coefficients are defined as

$$b_1 = \frac{C_h}{J(\pi/30)^2}$$

$$b_2 = \frac{C_e}{J(\pi/30)^2}$$

$$b_3 = \frac{C_w}{J(\pi/30)^2} \tag{4}$$

from (1) and (2). An analytical expression for the actual speed curve was determined for each case and minimized using a simplex search method (Kasarda, 1997). The calculated power loss components were then determined from (1) and (4).

Measured Power Losses for Air Gap = 0.381 mm (0.015 in)

Figure 4 gives six measured power loss curves for two bearings. Three curves are for bearing No. HE-8-15 (eight pole stator S1 and rotor R2 with air gap of 0.381 mm (0.015 in)), for static flux levels of 0.32, 0.38 and 0.54 T, versus speeds up to 28,000 rpm. The next three curves are for bearing No. HE-16-15 (16 pole stator S2 and rotor R2 with air gap of 0.381 mm (0.015 in)), for static flux levels of 0.31, 0.38, and 0.54 T, also versus rotational speed from 0 to 28,000 rpm. In each case, there were numerous actual runs made to provide better statistical results. For example, for the HE-8-15 magnetic bearing, the number of runs for the bias flux levels of 0.32 T, 0.38 T, and 0.54 T were 4, 4, and 3 runs respectively. The runs were consistent to within a few percent in each data set (Kasarda, 1997).

The quite unexpected result is that the losses are nearly identical for each value of air gap magnetic flux density. The bearings have been designed to have exactly the same surface area under the poles, the same air gap length, and the static bias flux level (Kasarda, 1997). Air gap flux levels were measured statically and were not expected to be significantly different at running speed

Table 1 Power loss coefficients for magnetic bearings data for bearings HE-8-15 and HE-16-15

	HE-8-15			HE-16-15		
Loss Coefficient	B= 0.32 T	B= 0.44 T	B= 0.54 T	B= 0.31 T	B= 0.46 T	B= 0.54 T
Hysteresis b_1 (rpm/s)	-10.0	-15.7	-21.8	-11.6	-21.5	-24.3
Eddy Current b_2 (1/s)	-5.5 x10^{-3}	-1.0 x10^{-2}	-1.6 x10^{-2}	-6.3 x10^{-3}	-1.3 x10^{-2}	-1.8 x10^{-2}
Windage b_3 (1/rpm$^{0.8}$s)	-9.2 x10^{-7}	-6.7 x10^{-7}	-6.4 x10^{-7}	-7.9 x10^{-7}	-5.5 x10^{-7}	-2.47 x10^{-7}

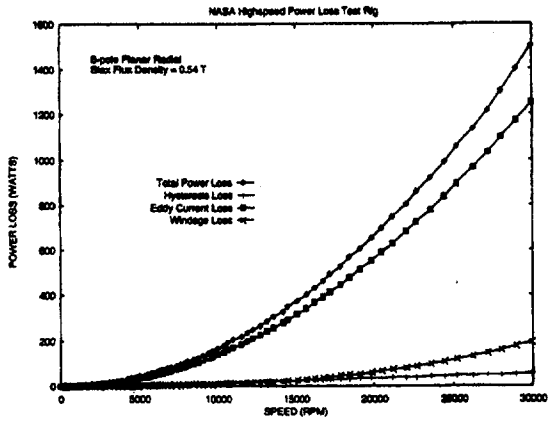

Fig. 5 Eddy current, hysteresis, and windage loss components in bearing HE-8-15 for flux density 0.54 *T*

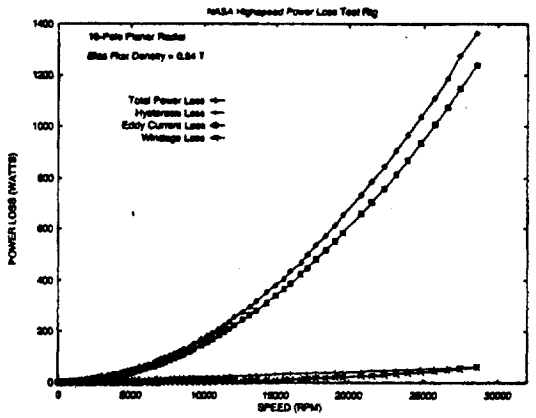

Fig. 6 Eddy current, hysteresis, and windage loss components in bearing HE-16-15 for flux density 0.54 *T*

although they were not measured due to the difficulties of working with Hall probes under rotating conditions (Kasarda, 1997). The tip clearance to air gap thickness ratio is 22 for the eight pole stator and 44 for the 16 pole stator but it is felt that the difference in these two numbers is not particularly important. Obviously the number of poles or edges differs by a factor of two in stator S1 versus S2 but the measured power loss is nearly the same.

The coefficients b_1, b_2, and b_3 are given in Table 1 for some of the data in Fig. 4 for bearings HE-8-15 and HE-16-15. The effect of various mechanisms on power loss are indicated by the coefficients in Table 1 for some of the data in Fig. 4 and some other data at an air gap magnetic flux level of 0.44 *T* (Kasarda, 1997). This model of the loss components is not perfect, implying that there is some error in the reduction process from the overall power loss measured values to the three components, but is the best that has been found to date.

The hysteresis coefficients are similar for both bearings at a given value of flux density indicating that the hysteresis effects are nearly the same for each bearing. The eddy current coefficients are also similar for both bearings. Figures 5 and 6 show the calculated loss components for the two bearings for a bias flux of 0.54 *T* based upon (2). In Fig. 5 for the HE-8-15 bearing, the results show that the eddy current losses are much larger than the hysteresis losses at all speeds. The eddy current losses are proportional to the square of the speed so they will be even larger as the speed continues to increase. Similar trends are seen in Fig. 6 for the HE-16-15 bearing, where the eddy current losses are much larger than the other two components. Comparing the windage losses for both cases, the windage loss is quite a bit higher for the HE-8-15 bearing than the HE-16-15. This indicates that the model for separating the losses is not as accurate as desired.

The windage coefficients are comparable for the two bearings when the bias flux density is the same. Trends in the windage loss terms are not equal but are within approximately 28 percent. The windage power losses should be independent of the bias flux. More work needs to be done on a better statistical separation of losses into the components and will be reported in future work.

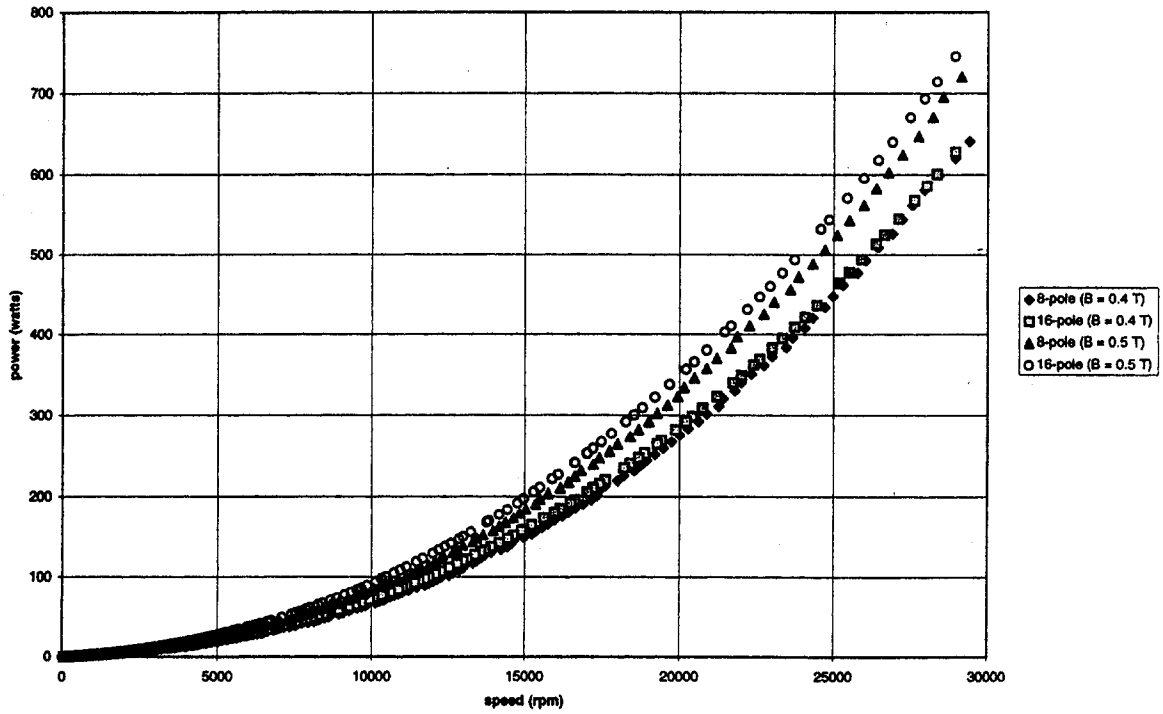

Fig. 7 Measured magnetic bearing power loss versus speed at three bias flux density values for HE-8-30 and HE-16-30

Table 2 Power loss coefficients for magnetic bearings data presented in Fig. 7 for bearings HE-8-30 and HE-16-30

	HE-8-30		HE-16-30	
Loss Coefficient	B= 0.44 T	B= 0.54 T	B= 0.42 T	B= 0.50 T
Hysteresis b_1 (rpm/s)	-17.9	-21.5	-18.6	-23.8
Eddy Current b_2 (1/s)	-4.5 $x10^{-3}$	-6.3 $x10^{-3}$	-5.3 $x10^{-3}$	-7.2 $x10^{-3}$
Windage b_3 (1/rpm$^{0.8}$s)	-9.1 $x10^{-7}$	-7.3 $x10^{-7}$	-7.1 $x10^{-7}$	-5.9 $x10^{-7}$

Measured Power Losses for Air Gap = 0.762 mm (0.030 in)

Measured power losses were also obtained for a different rotor with twice the air gap thickness. Figure 7 gives four measured power loss curves for bearing No. He-8-30 (eight pole stator S1 and rotor R1 with air gap of 0.762 mm (0.030 in)) for static flux levels of 0.44 and 0.54 T and bearing No. He-16-30 (16 pole stator S2 and rotor R1 with air gap of 0.762 mm (0.030 in)) for static flux levels of 0.44 and 0.50 T versus rotational speed from 0 to 30,000 rpm.

Again, the result is that the losses are nearly identical for each comparable value of air gap flux. The stators are the same as in the cases plotted in Fig. 4 and the rotor is different only in the air gap thickness. The number of poles or edges differs by a factor of two in stator S1 versus S2 but the measured power loss in Fig. 7 is nearly the same in each case confirming the results presented in Fig. 4.

The power losses were separated into components based upon (2). The numerical values of the coefficients are given in Table 2. The loss components are plotted in Figs. 8 and 9 for the two bearings for a bias flux level of 0.54 T for the HE-8-30 bearing and 0.50 for the HE-16-30 bearing. The flux levels for for these two plots are not exactly equal but the calculated values illustrate significant differences between the smaller clearance bearings in Figs. 5 and 6. In each of plots 8 and 9, the eddy current losses are clearly dominant over the hysteresis losses by a factor of approximately 2.5 to 4.0. If it is desired to design a low loss bearing, the air gap thickness will be selected as large as possible. The eddy currents will be the largest component of the iron losses by a large factor, unless greatly reduced by employing very thin laminations.

The windage losses in Figs. 8 and 9 are within approximately 15 percent of one another. This indicates that the windage loss model is acceptable but an improved formula is needed. Future work will be done with this test rig in a vacuum chamber to eliminate the windage term.

Analytical/Empirical Model

One approach to evaluating the eddy current losses, which are normally the highest of the loss components for high speed applications, is to use a formula adopted from transformer and motor loss models (Kasarda and Allaire, 1996). The most commonly employed formula for the eddy current losses, without skin effects, is

$$P_e = \frac{\pi^2 d^2 B_{\max}^2 f_{\text{eff}}^2 V_{\text{eff}}}{6\rho}, \tag{5}$$

where d is the lamination thickness, $B_{\max}$ is the maximum flux density in the rotor, f_{eff} is the effective frequency, V_{eff} is the effective volume of the rotor, and ρ is the resistivity of the material. Previous calculation models have employed a factor for the effective frequency based upon the number of poles in the bearing stator. The measured power loss values presented in Figs. 4 and 7 indicates that the use of eddy current power and hysteresis loss formulas based upon this effective frequency factor are not accurate.

Conclusions

Magnetic bearing rotor power loss variations with speed, bias flux density, air gap thickness, and number of poles were studied

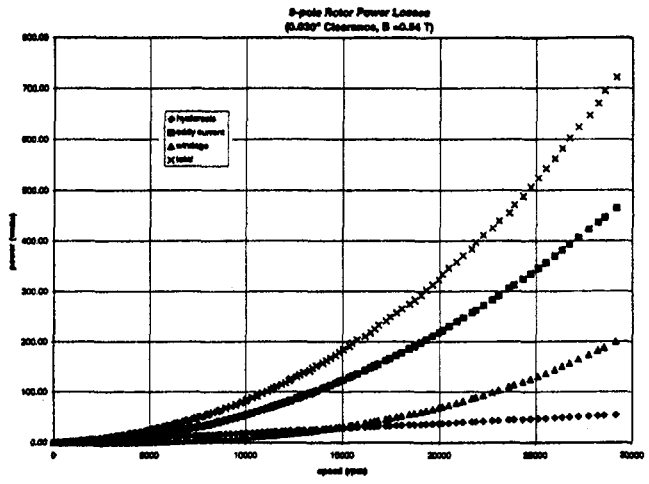

Fig. 8 Eddy current, hysteresis, and windage loss components in bearing HE-8-30 for 0.54 T

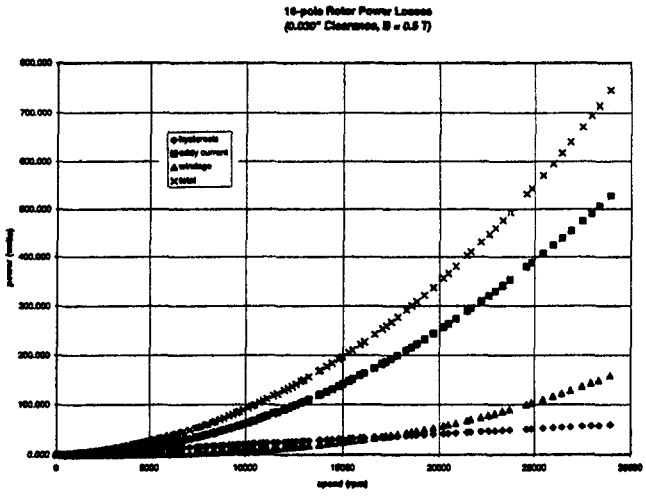

Fig. 9 Eddy current, hysteresis, and windage loss components in bearing HE-16-30 for 0.50 T

for four different planar radial (heteropolar) bearing configurations. The unexpected result was that the measured rotor power losses for comparable bearings, with the same pole face area, air gap flux, and air gap thickness for both eight and 16 pole stators were nearly identical. The windage losses in these bearings have been found to be largely independent of the number of poles indicating that the iron losses (eddy current and hysteresis) must be nearly identical. These measured results contradict expected results, that the power loss should be approximately proportional to the number of poles or edges seen in passing by the rotor material, as reported in the literature. While this result is clear for heteropolar bearing designs, it may or may not be true for homopolar designs. Only further testing will determine this. This may also imply that, since the number of pole edges is not a major factor in heteropolar bearings, the shape of the pole edges is also not a critical factor.

A power loss model including hysteresis, eddy current, and windage losses was applied to the data. Values of hysteresis, eddy current, and windage coefficients were obtained from the measured data. Eddy current effects were found to be the largest loss component.

Acknowledgment

This work was supported in part by NASA Lewis Research Center with Dr. Gerald Brown and Andrew Provenza as Project Monitors.

References

Allaire, P. E., Kasarda, M. E. F., Maslen, E. H., and Gillies, G. T., 1996, "Rotor Power Loss Measurements for Heteropolar and Homopolar Magnetic Bearings," Proceedings, 5th Inter. Conf. on Magnetic Bearings, Kanazawa, Japan, pp. 271–276.

Allaire, P. E., Kasarda, M. E. F., Maslen, E. H., Gillies, G. T., and Fujita, L. K., 1997, "Flux Density and Air Gap Effects on Rotor Power Loss Measurements in Planar Radial Magnetic Bearings," ASME Paper 97-GT-17.

Kasarda, M. E. F., Allaire, P. E., Maslen, E. H., and Gillies, G. T., 1994, "Design of a High Speed Rotating Loss Test Rig For Radial Magnetic Bearings," Proceedings, Fourth International Symposium on Magnetic Bearings, ETH Zurich.

Kasarda, M. E., and Allaire, P. E., 1999, "Experimentally Measured and Improved Calculated Losses in Planar Radial Magnetic Bearings," *STLE Transactions.*

Kasarda, M. E. F., Allaire, P. E., Maslen, E. H., Brown, G. R., and Gillies, G. T., 1996a, "High Speed Rotor Losses in a Radial 8-Pole Magnetic Bearing, Part 1: Experimental Measurement," ASME Paper 96-GT-470.

Kasarda, M. E. F., Allaire, P. E., Maslen, E. H., Brown, G. R., and Gillies, G. T., 1996b, "High Speed Rotor Losses in a Radial 8-Pole Magnetic Bearing, Part 2: Analytical/Empirical Models and Calculation," ASME Paper 96-GT-471.

Kasarda, M. E. F., 1997, "The Measurement and Characterization of Power Losses in High Speed Magnetic Bearings," Ph.D. thesis, University of Virginia, Charlottesville, VA.

Matsumura, F., Fujita, M., and Ozaki, Y., 1988, "Characteristics of Friction on Magnetic Bearings," *Trans. IEE of Japan,* 108-D, No. 5, pp. 462–468.

Matsumura, F., and Hatake, K., 1992, "Relation between Magnetic Pole Arrangement and Magnetic Loss in Magnetic Bearing," Proceedings, Third Inter. Conf. on Magnetic Bearings, Alexandria, Virginia, USA, pp. 274–283.

Rockwell, R. D., Allaire, P. E., and Kasarda, M. E. F., 1997, "Radial Planar Magnetic Bearing Analysis with Finite Elements Including Rotor Motion and Power Losses," ASME Paper 97-GT-503.

M. E. F. Kasarda
Department of Mechanical Engineering,
Virginia Polytechnic Institute and
State University,
Blacksburg, VA 24061-0238

P. E. Allaire

P. M. Norris

Mechanical, Aerospace, and Nuclear
Engineering Department,
University of Virginia,
Charlottesville, VA 22901

C. Mastrangelo
Department of Systems Engineering,
University of Virginia,
Charlottesville, VA 22901

E. H. Maslen
Mechanical, Aerospace, and Nuclear
Engineering Department,
University of Virginia,
Charlottesville, VA 22901

Experimentally Determined Rotor Power Losses in Homopolar and Heteropolar Magnetic Bearings

The identification of parameters that dictate the magnitude of rotor power losses in radial magnetic bearings is very important for many applications. Low loss performance of magnetic bearings in aerospace equipment such as jet engines and flywheel energy storage systems is especially critical. Two basic magnetic bearing designs are employed in industrial practice today: the homopolar design, where the flux paths are of a mixed radial/axial orientation, and the heteropolar design, where the flux paths are primarily radial in nature. The stator geometry and flux path of a specific bearing can have a significant effect on the rotor losses. This paper describes the detailed measurement of rotor losses for experimentally comparable homopolar and heteropolar designs. The two test bearing configurations are identical except for geometric features that determine the direction of the flux path. Both test bearing designs have the same air gap length, tip clearance ratio, surface area under the poles, and bias flux levels. An experimental test apparatus was used where run down tests were performed on a test rotor with both bearing designs to measure power losses. Numerous test runs where made for each bearing configuration by running multiple levels of flux density. The components of the overall measured power loss, due to hysteresis, eddy currents, and windage, were determined based on theoretical expressions for power loss. It was found that the homopolar bearing had significantly lower power losses than the heteropolar bearing.

Introduction

The increased interest in applying magnetic bearings in a variety of applications dictates the need to better understand and quantify loss mechanisms associated with the electromagnetic phenomena in the bearings. Generally, it is desired to reduce loss mechanisms in all components of devices such as aircraft gas turbines, space devices, or energy storage flywheels to minimize energy consumption. Excessive heating from magnetic bearings can also be a problem in other machines such as large compressors, electric motors, textile spindles, turbine generators and artificial heart pumps, if the rotor power losses are high.

Two basic radial magnetic bearing designs are employed in industrial practice today: the homopolar design, where the flux paths are of a mixed radial/axial orientation, and the heteropolar design, where the flux paths are primarily radial in nature. Figure 1 shows typical design configurations for the homopolar and heteropolar bearing. There has been considerable discussion in the magnetic bearing community as to which of the two basic magnetic bearing designs has the lower rotor power losses: the homopolar design or the heteropolar design.

Researchers have investigated the performance of homopolar magnetic bearing arrangements. Studer (1978) was one of the first to discuss a homopolar bearing design which involved a four pole bearing. Sortore et al. (1990) reported on the design of a high speed homopolar bearing design employed in a flexible rotor but did not report on any measured rotor power loss results. Meeks (1989) discussed homopolar bearing designs employed for industrial applications.

Experimental power loss studies in magnetic bearings published in the open literature discussing theoretical or experimental homopolar and heteropolar bearing losses have been very limited. Kasarda et al. (1994) discussed the design of a high speed power loss test rig in some detail and gave a sensitivity analysis of the loss modeling based upon the theoretical parameters involved. The test rig is capable of testing both homopolar and heteropolar bearing configurations. Kasarda et al. (1996b) presented high speed loss results, using the same test rig employed for the work in this paper, for an 8 pole radial bearing constructed of silicon iron laminated materials. The rotor operated at a top speed of about 32,000 rpm, corresponding to a DN value of 2.9×10^6 mm-rpm. Variations in pole winding configuration (NNSS versus NSNS pole magnetization) and bias flux were examined. Bias flux was found to be very significant while pole winding was found to have only a minor effect in the tests studied.

The purpose of this paper is to report on detailed rotor power loss measurements from the test rig data taken for comparable radial bearings of the two different geometries. The homopolar bearings and heteropolar bearings tested here have been designed to have the same air gap length, tip clearance ratio, surface area under the poles, and bias flux level. A preliminary report of one homopolar bearing test result was presented in Allaire et al. (1996) with additional tests presented in Kasarda et al. (1997). This paper contributes to earlier work by expanding the discussion and evaluation of hysteresis, eddy current, and windage power loss components from the experimental data for each of the bearing designs.

Experimental Apparatus

The basis for the apparatus used to measure power losses is a shaft with two magnetic bearings and two induction motors located at the shaft ends, as shown in Fig. 2. It has been designed to measure the power losses in magnetic bearings by accurately

Contributed by the International Gas Turbine Institute (IGTI) of THE AMERICAN SOCIETY OF MECHANICAL ENGINEERS for publication in the ASME JOURNAL OF ENGINEERING FOR GAS TURBINES AND POWER. Paper presented at the International Gas Turbine and Aeroengine Congress and Exhibition, Stockholm, Sweden, June 2–5, 1998; ASME Paper 98-GT-317.

Manuscript received by IGTI March 16, 1998; final revision received by the ASME Headquarters June 23, 1999. Associate Technical Editor: R. Kielb.

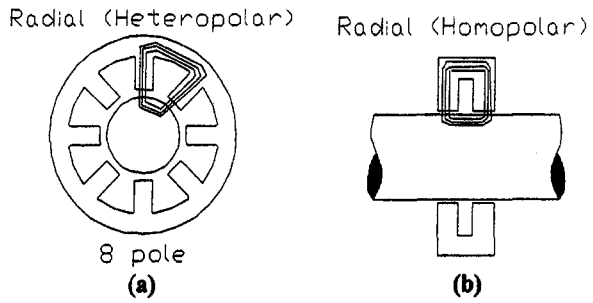

Fig. 1 (a) Heteropolar flux path; (b) homopolar flux path

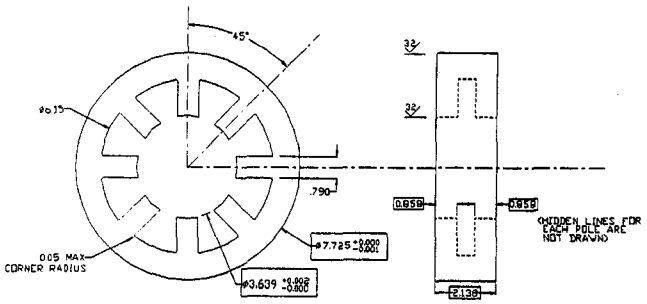

Fig. 3 16 pole (8-pole per plane) homopolar stator

measuring the conversion of the rotor's kinetic energy into heat. This is done by measuring the time it takes for the rotor to run down from one speed to another. The rotor kinetic energy due to rotation is

$$E_k = \tfrac{1}{2} J\omega^2, \tag{1}$$

where ω is the rotational speed (rad/s), and J is the rotor mass moment of inertia (N-s^2 mm). The power loss is the time derivative of the kinetic energy

$$P_k = \frac{dE_k}{dt} = J\omega \frac{d\omega}{dt} + \frac{\omega^2}{2}\frac{dJ}{dt}. \tag{2}$$

The second term is small for this test because the rotor does not have large dimensional changes so this expression reduces to

$$P_k = J\omega \frac{d\omega}{dt} = \left(\frac{\pi}{30}\right)^2 JN \frac{dN}{dt} = P_h + P_e + P_w, \tag{3}$$

where the polar moment of inertia is easily determined from a calculation and $N(t)$ (rpm) is easily measured from the rundown tests. On the right hand side of this equation, the power loss is written as the sum of the power loss due to bulk hysteresis, P_h, the power loss due to eddy currents, P_e, and the power loss due to windage, P_w.

It has been shown in previous work by Kasarda et al. (1996a, 1996b) that the power loss can be written in terms of frequency dependent parameters as

$$P_k = C_h\omega + C_e\omega^2 + C_w\omega^{2.8} \tag{4}$$

based upon analytical/empirical models of the specific loss components. The material hysteresis effects can be divided into alternating hysteresis and rotating hysteresis. As shown in previous tests, both of these effects are expected to vary linearly with speed and so the two terms are lumped together for statistical analysis as a bulk hysteresis term.

Eddy currents are sometimes evaluated as the sum of two terms: a standard eddy current term and the first term of a series expansion representing skin effects (Kasarda et al., 1996b). However, as detailed in Kasarda et al. (1996b), the skin effect term which is expected to be small and vary with rotor speed to the fourth power is not clearly separable from the windage loss component which varies with rotor speed to the 2.8 power in the measured data. Therefore, the skin effect term is not included in Eq. (4). Future work, including vacuum rundown data to eliminate windage losses, will address the skin effect issue in more depth.

The test apparatus has been designed so that the only significant loss mechanisms come from the magnetic bearings: eddy current losses, hysteresis losses, and air drag. As shown in Fig. 2, the test rotor consists only of a shaft with two radial magnetic bearings and two motors. There are no thrust bearings and reluctance centering effects of the radial bearings maintain good axial alignment. The two electric induction motors drive the rotor up to peak operating speed and are then shut off and rotor rundown measurements recorded. The presence of the motor stators have been shown to have no significant residual magnetic drag or any effect on windage losses during run down (Kasarda et al., 1996b).

Homopolar Bearing Geometry

The homopolar bearing tested has a total of 16 poles, eight poles per axial plane. The poles are wound so that there are eight north poles in one axial plane and eight south poles in the other axial plane. For the purposes of this study, this bearing is designated #HO-16-15. It should be noted that neither the homopolar or heteropolar bearings have been designed to optimize for low losses but rather, for the experimental investigation of specific parameter effects on power losses in magnetic bearings. In this manner, the homopolar bearing was designed to have the same number of poles located in a plane radially around the shaft as the heteropolar design yet it is still representative of a viable commercial design. A drawing of the homopolar stator design is given in Fig. 3. The inner diameter of the stator is 92.43 mm (3.639 in) and the total axial length of the two poles is 43.56 mm (1.715 in). The radial air gap is 0.381 mm (0.015 in). Each stator pole has a leg width and length of 20.1 mm (0.79 in) and 31.8 mm (1.25 in), respectively.

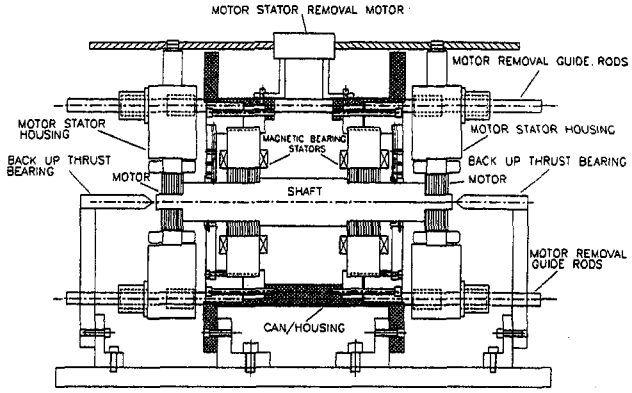

Fig. 2 Test rig assembly drawing

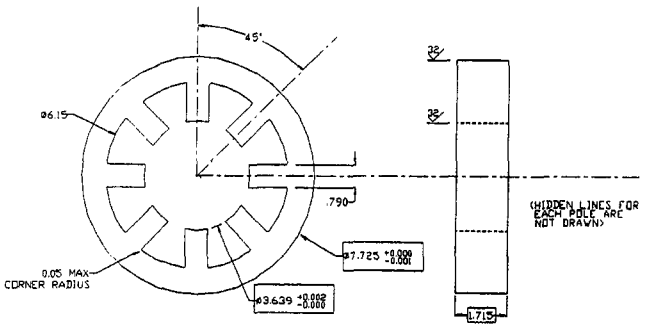

Fig. 4 8-pole heteropolar stator

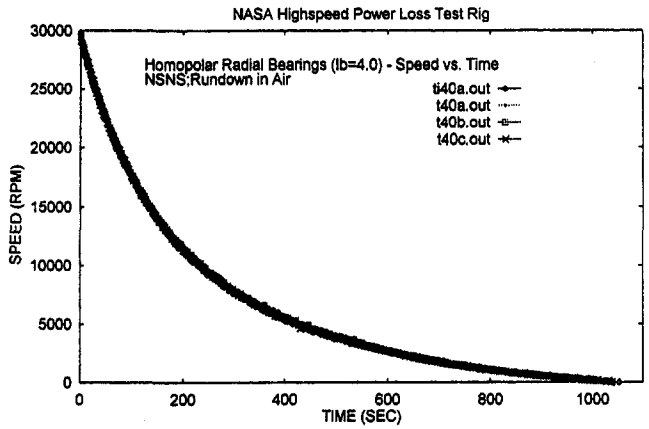

Fig. 5 Typical rundown data—configuration #HO-16-15-B = 0.40 *T* (homopolar)

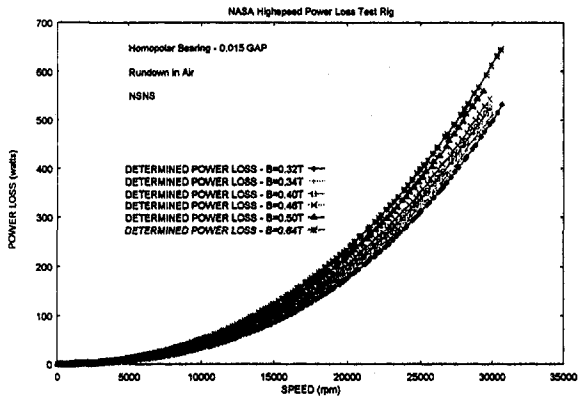

Fig. 6 Determined power loss—configuration #HO-16-15 (homopolar)

Each of the stator poles is wound with 48 turns of #18 wire. The design bias current was 3 A resulting in a bias flux density of 0.47 T.

The rotor has bearing journals constructed from 0.356 mm (0.014 in) thick M-15 grade silicon-iron laminations, the same material from the same manufacturing run as that used for the corresponding heteropolar bearing rotor. The outer diameter of the journal is 91.67 mm (3.609 in) and the axial length is 54.31 mm (2.138 in). The axial length of the homopolar journal was slightly longer than the heteropolar journal due to the total longer axial length of the stators but the total pole face area is the same in both bearing configurations. The polar moment of inertia of the homopolar rotor is 9.04 N-s^2-mm (8.0 $\times$ 10^{-2} lbf-s^2-in).

Heteropolar Bearing Geometry

The comparable heteropolar bearing tested has a total of 8 poles. The poles are wound in a NSNS configuration. For the purposes of this study, this bearing is designated #HE-8-15. A drawing of the stator design is given in Fig. 4. The inner diameter of the stator is 92.43 mm (3.639 in) and the total axial length of the poles is 43.56 mm (1.715 in). The radial air gap is 0.381 mm (0.015 in). Each stator pole has a leg width and length of 20.1 mm (0.79) and 31.8 mm (1.25 in), respectively. Each of the stator poles is wound with 94 turns of #18 wire. The design bias current was 1.5 A resulting in a bias flux density of 0.47 T.

The rotor has bearing journals constructed from 0.356 mm (0.014 in) thick M-15 grade silicon-iron laminations, the same material from the same manufacturing run as that used for the corresponding homopolar bearing rotor. The outer diameter of the journal is 91.67 mm (3.609 in) and the axial length is 43.6 mm (1.715 in). The polar moment of inertia of the heteropolar rotor is 8.02 N-s^2-mm (7.1 $\times$ 10^{-2} lbf-s^2-in).

The heteropolar and homopolar rotor-bearing configurations are identical except for the flux path and the associated slightly longer journal axial length of the homopolar bearing to accommodate windings between the two planes of poles.

Experimental Results—Homopolar Bearing

Figure 5 shows a typical set of four run down plots for the homopolar bearing with a bias flux density of $B = 0.4$ *T*. A total of 24 run down measurements were taken for bias flux density levels of 0.32 *T* (three runs), 0.34 *T* (five runs), 0.38 *T* (four runs), 0.40 *T* (four runs), 0.46 *T* (three runs), 0.50 *T* (three runs), and 0.64 *T* (three runs). The bias flux density values presented in this paper represent average flux density values determined from measuring the static flux density under all poles of each bearing with a Hall probe and taking an average measurement.

The total power loss was determined by the method described earlier in Eqs. 2–3. A plot of the total determined power loss in Watts versus rotor speed for the seven bias flux density levels are shown in Fig. 6. This determined power loss is the total power loss including electromagnetic power losses from the two radial magnetic bearings and windage losses along the entire length of the rotor. As shown in Fig. 6, when the flux density level is maximum at ~0.6 Tesla and the speed is on the order of 30,000 rpm that the total power loss for the homopolar rundown case is ~627 Watts.

The data for all 24 runs was separated into hysteresis losses, eddy current losses and windage losses with results presented in Kasarda (1997). By combining Eqs. 3 and 4, the rotor rundown characteristics (rpm/sec) can be presented analytically as a function of rotor speed as

$$\frac{dN}{dt} = h_h + h_e N + h_w N^{1.8}, \tag{5}$$

where h_h, h_e, and h_w are hysteresis, eddy current, and windage coefficients, respectively. It was desired to investigate the effect of the bias flux density, B, on the hysteresis coefficient, the eddy current coefficient, and the windage coefficient. For the hysteresis coefficient, the model for the effect of the flux density is

$$h_h = A_h B^{n_h}. \tag{6}$$

Taking the logarithm of this equation gives

$$\log (h_h) = n_h \log (B) + \log (A_h), \tag{7}$$

which is linear. The logarithmic plot of all of the homopolar data was obtained and curve fit with B to various values of n_h. A good curve fit resulted with the power of $n_h = 1.0$ for the hysteresis losses. The parameters for the curve fit are given in Table 1. The coefficient A_h had a mean value of -9.3 (rpm-s^{-1} $-$ T^{-1}), a standard deviation of 0.5 (rpm-s^{-1} $-$ T^{-1}), and a correlation coefficient of 0.969. The standard deviation value is very good and is approximately 5 percent of the mean value. The correlation

Table 1 Coefficient evaluation statistics—configuration #HO-16-15

	Hysteresis Coefficient, A_h	Eddy Current Coefficient, A_e	Windage Coefficient, h_w
Mean of Normalized Coefficients	-9.3 rpm-s^{-1}-T^{-1}	-6.2 x 10^{-3} s^{-1}-T$^{-1.4}$	-1.0 x 10^{-6} rpm$^{-.8}$-s^{-1}
Standard Deviation of Normalized Coefficients	0.5 rpm-s^{-1}-T^{-1}	3.3 x 10^{-4} s^{-1}-T$^{-1.4}$	5.7 x 10^{-8} rpm$^{-.8}$-s^{-1}
Correlation Coefficient, R	0.969	0.986	-0.922

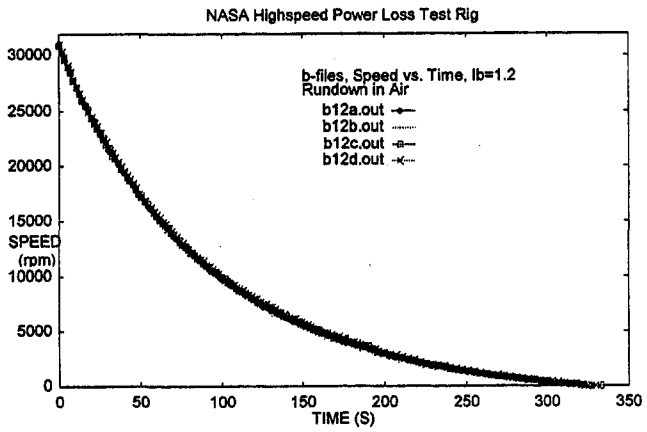

Fig. 7 Typical rundown data—configuration #HE-8-15-B = 0.32 T (heteropolar)

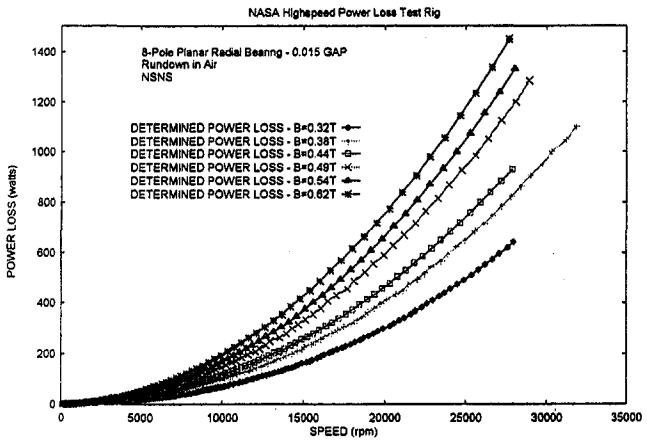

Fig. 8 Determined power loss—configuration #HE-8-15 (heteropolar)

coefficient is very near to 1.0 which indicates an excellent curve fit.

Using a similar approach for the eddy currents and a model of the form

$$h_e = A_e B^{n_e}, \tag{8}$$

the mean value, standard deviation, and correlation coefficient values are determined and also given in Table 1. The curve fit in this case resulted in a value of $n_e = 1.4$ for the best fit. Again, the standard deviation is approximately 5 percent of the mean value and the correlation coefficient is nearly 1.0 which indicates an excellent fit.

The windage power loss is not expected to be a function of the bias flux density. A curve fit of the windage coefficient h_w for the 24 experimental runs was evaluated and the parameters given in Table 1. The correlation coefficient of -0.922 indicates that there is a relatively large amount of negative correlation between the windage term and the bias flux density. The presence of unaccounted skin effects will most likely affect the windage coefficient since both are higher order terms which are expected to vary as speed to the power 4 (skin effects) and speed to the power 2.8 (windage). Recall, from Kasarda (1996b), that skin effects were excluded from the data regression model because while they are expected to be present, they are inseparable by current analysis methods. However, the absolute value of the unaccounted electromagnetic effects is very small in the homopolar bearing resulting in a small standard deviation in the actual windage coefficient on the order of 6 percent. Additional methods to separate the skin effect and windage term are underway but not addressed in this paper. Also, future data taken in a vacuum environment will eliminate the windage losses which will allow for the characterization of the skin effect power loss component.

Experimental Results—Heteropolar Bearing

Figure 7 shows a typical set of four run down plots for the heteropolar bearing with a bias flux density of $B = 0.32$ T. A total of 26 run down measurements were taken for bias flux density levels of 0.32 T (four runs), 0.38 T (four runs), 0.44 T (three runs), 0.49 T (five runs), 0.54 T (three runs), and 0.64 T (seven runs). Figure 8 shows a plot of the determined power loss value in Watts versus rotor speed for each of these flux density values. This determined power loss is the total power loss including electromagnetic power losses from the two radial magnetic bearings and windage losses along the entire length of the rotor. As shown in Fig. 8, when the flux density level is maximum at ~0.6 Tesla and the speed is on the order of 28,000 rpm the total power loss for the heteropolar rundown case is ~1544 Watts.

The data for all 26 runs was separated into hysteresis losses, eddy current losses and windage. It was desired to investigate the effect of the bias flux density, B, on the hysteresis coefficient, the eddy current coefficient, and the windage coefficient in Eq. 5. For the hysteresis coefficient, the model for the effect of the flux density was

$$h_h = A_h B^{n_h}. \tag{9}$$

Taking the logarithm of this equation gives

$$\log (h_h) = n_h \log (B) + \log (A_h), \tag{10}$$

which is linear. The logarithmic plot of all of the heteropolar data was obtained and curve fit with B to various values of n_h. A good curve fit resulted with the power of $n_h = 1.3$ for the hysteresis losses. The parameters for the curve fit are given in Table 2. The coefficient A_h had a mean value of -45.8 (rpm-s^{-1} $-$ $T^{-1.3}$), a standard deviation of 1.4 (rpm-s^{-1} $-$ $T^{-1.3}$), and a correlation coefficient of 0.996. The standard deviation value is approximately 3 percent of the mean value and the correlation coefficient is very near to 1.0 which indicated an excellent curve fit.

Using a similar approach for the eddy currents and a model of the form

$$h_e = A_e B^{n_e} \tag{11}$$

the mean value, standard deviation, and correlation coefficient values are determined and also given in Table 2. The curve fit in this case resulted in a value of $n_e = 2.0$ for the best fit. The standard deviation is approximately 7.5 percent of the mean value and the correlation coefficient is nearly 1.0 which indicates an excellent fit.

The windage power loss is not expected to be a function of the bias flux density. A curve fit of the windage coefficient h_w for the 26 experimental runs was evaluated and the parameters are given in Table 2. The correlation coefficient of -0.855 indicates that there is some correlation between windage and bias flux density.

Table 2 Coefficient evaluation statistics—configuration #HE-8-15

	Hysteresis Coefficient, A_h	Eddy Current Coefficient, A_e	Windage Coefficient, h_w
Mean of Normalized Coefficients	-45.8 rpm-s^{-1}-T$^{-1.3}$	-5.3 x 10^{-2} s^{-1}-T^{-2}	-7.0 x 10^{-7} rpm$^{-.8}$-s^{-1}
Standard Deviation of Normalized Coefficients	1.4 rpm-s^{-1}-T$^{-1.3}$	4.0 x 10^{-3} s^{-1}-T^{-2}	2.1 x 10^{-7} rpm$^{-.8}$-s^{-1}
Correlation Coefficient, R	0.996	0.998	-0.855

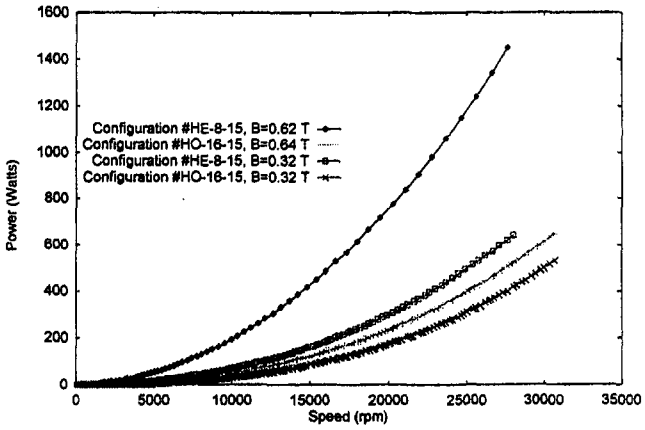

Fig. 9 Determined power loss—configuration #HE-8-15 and configuration #HO-16-15

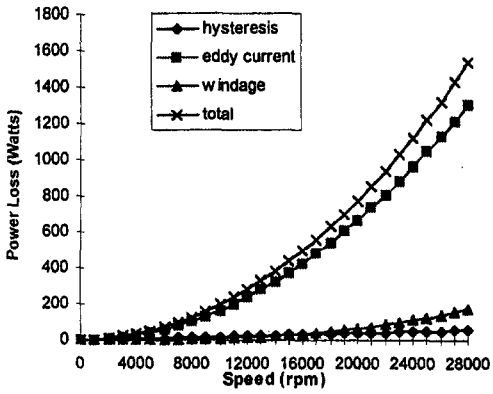

Fig. 11 Power loss components for heteropolar bearing; $B = 0.6$ T

As was the case with the homopolar data, the effect of unaccounted skin effects in the regression model may be appearing in the similarly higher order windage term. As shown in Table 2, the standard deviation for the windage coefficient is 30 percent of the mean value and skin effects are expected to be larger in this configuration than in the homopolar case. However, the overall magnitude of the power loss is dictated by the eddy current power loss component and the unaccounted skin effect has a small impact on the overall magnitude of the power losses.

Comparison of Homopolar and Heteropolar Results

It is very interesting to compare the power loss results from the homopolar and heteropolar configurations. Recall, that both the homopolar and heteropolar bearing have been designed with the same air gap length, tip clearance ratio, surface area under the poles, and bias flux level. The only major difference in the two bearing configurations are the direction of flux path as shown earlier in Fig. 1.

A comparison of the determined power losses of the two bearing configurations for two different flux cases is shown in Fig. 9. The homopolar bearing, #HO-16-15, was operated at $B = 0.32$ T and $B = 0.64$ T over the speed range while the heteropolar bearing, #HE-8-15, was operated at $B = 0.32$ T and $B = 0.62$ T. As seen in Fig. 9, for nearly the same bias flux density, the homopolar bearing configuration has considerably lower power losses than the heteropolar bearing configuration.

Another interesting comparison is made by separating the total power loss into each of the individual loss components. Shown in Fig. 10 is a plot of total power loss along with the hysteresis, eddy current, and windage loss components for the homopolar bearing when the flux density equals 0.6 T. As shown in this figure, the eddy current component of the homopolar configuration losses is approximately of the same magnitude as the windage loss for this speed range and these components make up the bulk of the power loss. The hysteresis component is very small for this test configuration.

The power loss components are also plotted in a similar manner for the heteropolar bearing when the flux density, $B = 0.6$ T, as shown in Fig. 11. This figure shows that the eddy current component is the dominant loss mechanism for the heteropolar case and is well above the magnitude of the windage loss component. Note that the actual magnitude of the windage power loss is very similar for both the homopolar and heteropolar cases (within 40 percent). As with the homopolar case, the hysteresis contribution is small for this test configuration.

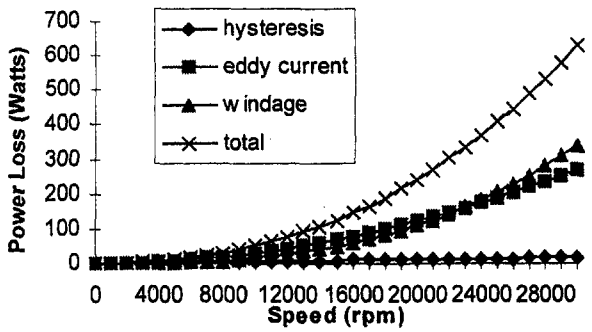

Fig. 10 Power loss components for homopolar bearing; $B = 0.6$ T

Conclusion

A radial heteropolar (radial flux path) and radial homopolar (mixed axial and radial flux path) bearing were designed to study the effect of flux path on rotating power loss. The test results demonstrate that, for these test bearings, the homopolar bearing showed significantly lower losses than the corresponding heteropolar bearing. The test bearings presented here were not designed to minimize power losses but to test the effect of the two different flux paths. It should be noted that all tests were run with the same rotor lamination thickness and that an alternative lamination thickness may result in different levels of variation in power losses for the two different configurations. It should also be noted that dynamic performance of the homopolar and heteropolar designs was not addressed in this study and differences may exist between the two configurations but are beyond the scope of this work. However, the results of this study do indicate that there is considerable promise for optimizing the radial magnetic bearing design for low rotor loss operation by utilizing the homopolar configuration.

Acknowledgment

This work was supported in part by NASA Lewis Research Center with Dr. Gerald Brown and Mr. Andrew Provenza as Project Monitors.

References

Allaire, P. E., Kasarda, M. E. F., Maslen, E. H., and Gillies, G. T., 1996, "Rotor Power Loss Measurements for Heteropolar and Homopolar Magnetic Bearings," Proceedings, Fifth International Conference on Magnetic Bearings, Kanazawa, Japan, August 28–30, Technomnic Publishing, Inc., Lancaster, PA, pp. 271–276.

Allaire, P. E., Kasarda, M. E. F., Maslen, E. H., Gillies, G. T., and Fujita, L. K., "Flux Density and Air Gap Effects On Rotor Power Loss Measurements in Planar Radial Magnetic Bearings," ASME Paper 97-GT-17.

Kasarda, M. E. F., Allaire, P. E., Maslen, E. H., and Gillies, G. T., 1994, "Design of a High Speed Rotating Loss Test Rig For Radial Magnetic Bearings," Proceedings, Fourth International Symposium on Magnetic Bearings, ETH Zurich.

Kasarda, M. E., and Allaire, P. E., 1996a, "Experimentally Measured and Improved Calculated Losses in Planar Radial Magnetic Bearings," *STLE Transactions*, Vol. 40, No. 2, pp. 219–226.

Kasarda, M. E. F., Allaire, P. E., Maslen, E. H., Brown, G. R., and Gillies, G. T., 1996b, "High Speed Rotor Losses in a Radial 8-Pole Magnetic Bearing, Part 1: Experimental Measurement," ASME Paper 96-GT-470.

Kasarda, M. E. F., Allaire, P. E., Norris, P. M., Maslen, E. H., Mastrangelo, C., 1997, "Comparison of Measured Rotor Power Losses in Homopolar and Heteropolar Magnetic Bearings," Proceedings, MAG '97, Alexandria, Va, August, 1997. pp. 323–333.

Meeks, C., 1989, "Trends in Magnetic Bearing Design," presented at Naval Sea Systems Command Magnetic Bearing Forum, Washington, D. C., July, 1989.

Rockwell, R. D., Allaire, P. E., and Kasarda, M. E. F., 1997, "Radial Planar Magnetic Bearing Analysis With Finite Elements Including Rotor Motion And Power Losses," ASME Paper 97-GT-503.

Sortore, C. K., Allaire, P. E., Maslen, E. H., Humphries, R. R., and Studer, P. A., 1990, "Permanent Magnet Biased Magnetic Bearings—Design, Construction, and Testing," Proceedings, Second International Symposium on Magnetic Bearings, Tokyo, Japan.

Studer, P. A., 1978, "Magnetic Bearings for Instruments in the Space Environment," NASA Technical Memorandum 78048.

Reduction of the Dynamic Load Capacity in a Squeeze Film Damper Operating With a Bubbly Lubricant

S. E. Diaz

L. A. San Andrés

Mechanical Engineering Department,
Texas A&M University,
College Station, TX 77843-3123

Squeeze film dampers (SFDs) are effective means to reduce vibrations and to suppress instabilities in rotor-bearing systems. However, at operating conditions while traversing critical speeds with large orbital whirl motions, ingestion and entrapment of air into the thin lands of SFDs generates a bubbly mixture (air in lubricant) that is known to reduce the dynamic film pressures and the overall damping capability. This pervasive phenomenon lacks proper physical understanding and sound analytical modeling. An experimental investigation to quantify the forced performance of a SFD operating with a controlled bubbly mixture is detailed. Tests are conducted in a constrained circular orbit SFD to measure the dynamic squeeze film pressures and journal motion at two whirl frequencies (8.33 and 16.67 Hz) as the air content in the mixture increases from 0 percent to 100 percent. The analysis of period-averaged film pressures reveals a zone of uniform low pressure of magnitude equal to the discharge pressure, independently of the mixture composition. The uniform pressure zone extends as the mixture void fraction increases. Radial and tangential film forces are estimated from the dynamic pressures at two axial locations of measurement. The tangential (damping) force decreases proportionally with the mixture volume fraction, while a radial hydrostatic force remains nearly invariant. The experimental results quantify effects previously known by qualitative description only, thus providing a benchmark towards the development of sound theoretical models.

Introduction

Current trends on the design of high performance turbomachinery demand for light and flexible rotors to operate at higher speeds within tighter clearances. Thus, the right amount of damping on the rotor supports is critical to control synchronous vibration levels and any subsynchronous instabilities associated with these operating conditions. Traditionally, squeeze film dampers (SFDs) have introduced the required viscous damping in aircraft jet engines. SFDs have also been used as retrofits in unstable turbomachines.

Squeeze film dampers consist of a lubricant film filling the space between a nonrotating journal, free to whirl, and a bearing housing. The (positive) squeezing of the film generates hydrodynamic pressures, which produce a damping force opposing the journal whirl motion. On the other hand, at the locations undergoing negative squeeze, i.e., increasing film thickness, suction pressures occur that may draw external air into the film. Classical lubrication theory considers a fluid as unable to sustain tension with an instantaneous phase change resulting in vapor cavitation. However, at high whirl speeds and with large journal vibration amplitudes, extensive practice and experimental research has revealed that air is ingested into the lubricant film and becomes entrapped. This phenomenon generates a bubbly (air in oil) mixture that resembles a foam (Hibner and Bansal, 1979; Walton et al., 1987; Zeidan and Vance, 1989, 1990a, b). This type of flow, intimately related to the kinematics of journal motion, flow rate and external conditions, is the one most commonly to appear in commercial applications of squeeze film dampers. Zeidan et al. (1996) in an extensive review of the state of the art in SFDs remark the importance of the phenomenon, as it considerably reduces the dynamic squeeze film forces and the overall damping capability of the SFD. Yet, to this date, there is not an accurate model addressing to the effects of air ingestion on SFD forced performance, or a relevant set of experimental measurements, which could aid in validating predictive tools.

Diaz and San Andrés (1997a) have recently measured the dynamic pressure fields in a SFD test rig operating with a bubbly mixture of air in oil. As the volume concentration of air in the mixture is increased, a constant pressure zone that interrupts the dynamic pressure raise from the minimum peak to the maximum peak appears. The extent of this region, named as the gaseous cavitation zone, is directly related to the air mixture volume fraction. For low concentrations of air, the gaseous cavitation extent is small and appears randomly in some of the cycles of journal motion (incipient regime). For larger amounts of air concentration, the uniform pressure zone appears in all the cycles of journal motion, with a notable reduction in the generation of squeeze film dynamic pressures (fully developed gaseous cavitation regime). Within the gaseous cavitation zone, the mechanical work done by the journal motion over the lubricant mixture goes into changing its specific volume, rather than in changing the film pressure.

The modeling of SFD dynamic fluid cavitation with bubbly mixtures is not a simple task. Many conceptual approaches have been considered, some of them very dissimilar to each other. Diaz and San Andrés (1997b) provide a more detailed discussion on this matter, though a cursory review of the most relevant literature follows.

SFDs are generally modeled with the classical fluid film Reynolds equation in conjunction with boundary conditions defining the onset and extent of the pure lubricant cavitation region. These are, for example, the π film, the Reynolds, or the Jakobsson-Floberg-Olsson models. However, in SFDs with bubbly mixtures, the air bubbles are dispersed within the squeeze film, even in the high-

Contributed by the International Gas Turbine Institute (IGTI) of The American Society of Mechanical Engineers for publication in the ASME Journal of Engineering for Gas Turbines and Power. Paper presented at the International Gas Turbine and Aeroengine Congress and Exhibition, Stockholm, Sweden, June 2–5, 1998; ASME Paper 98-GT-109.

Manuscript received by IGTI February 25, 1998; final revision received by the ASME Headquarters June 23, 1999. Associate Technical Editor: R. Kielb.

pressure zones, preventing the implementation of the conventional cavitation models. For simplicity, most models regard the bubbly mixture as a homogeneous medium and incorporate equivalent density and viscosity material parameters as functions of the pressure and mixture composition. However, no sound rationale exists for the appropriate correlations used, and in some cases their validity is questionable in lieu of empirical evidence (Braun and Hendricks, 1984; Fengh and Hahn, 1986; Pinkus, 1990).

Bubbly mixtures are not just confined to thin film lubrication-type flows. Bubble collapse damage along with cavitation erosion in water pumps is still a pervasive problem in industry. In this area of fluid mechanics, models for bubble dynamics based on the Rayleigh-Plesset equation have proven useful in cases where the dynamic changes of pressure affect the thermodynamic equilibrium between the two phases of the mixture (Plesset and Prosperetti, 1977; Hsie, 1988; Brennen, 1995).

More recently, the continuum theory of mixtures provides a more general formulation, though it still faces the closure problem since there are more unknowns than derived governing equations (Atkin and Crane, 1976; Rajagopal and Tao, 1995). Adequate rheological modeling thus requires of empirical correlations or constitutive equations, only attainable through careful experimentation. Nevertheless, several successful applications to steadily loaded hydrodynamic journal bearings and elasto-hydrodynamic contacts can be found in Al-Sharif et al. (1992), Wang et al. (1992), Chamniprasart et al. (1993), and Szeri (1996). Note that the issue of mixture component homogeneity seems to be well beyond the capabilities of current theoretical models.

The aim of this paper is to provide experimental evidence quantifying the reduction of the squeeze film damping forces due to air entrainment, and extending earlier work related to the measurements of squeeze film damper pressures in the same test rig (Diaz and San Andrés, 1996, 1997a). Air ingestion and entrapment are simulated with a controlled (air/oil) bubbly mixture that is fed into a SFD test rig. The air content is varied from 0 percent to 100 percent, emulating increasing degrees of severity for the air entrapped in an actual application. The test journal describes circular centered orbits within its bearing housing. Dynamic film pressures are measured at several locations around the damper circumference to verify the rotational symmetry of the ensemble-averaged dynamic pressure field. Then, dynamic SFD forces are estimated from integration of the measured film pressures at two whirl frequencies. The effects of air volume fraction in the notable reduction of the SFD tangential force are quantified for the first time. The measurements provide much needed experimental evidence to advance the state of the art in SFD modeling.

Experimental Facility

The circular centered orbit SFD test rig employed has served in the past to research different aspects of damper forced performance. A detailed description of the apparatus, shown in Fig. 1(*a*), can be found in Arauz and San Andrés (1993, 1996). The test section consists of a journal (length, $L = 31.1$ mm, outer diameter, $D = 129.4$ mm) mounted on a rigid shaft with an eccentric sleeve through a ball bearing (see Fig. 1(*b*)). Four anti-rotation pins prevent the journal from spinning, but allow it to whirl in a circular orbit. A variable speed electrical motor drives the shaft and makes the damper journal whirl at a frequency equal to the shaft speed. The damper radial clearance (C) is 0.343 mm (13.5 mils) and the nominal radius of the orbit (e) is 0.180 mm (7.1 mils), ($e/C = 0.53$), for a pressurized condition at 7.0 bars.

The bubbly mixture is produced at the sparger (mixer element) in the junction of (shop) air and oil lines (see Fig. 2). An ISO VG 68 pure lubricant is employed in the tests, and with a measured density (ρ) of 0.87 gr/cm^3 and viscosity (μ) equal to 77.5 and 25.8 centipoise at 28°C and 51°C, respectively. The lubricant is stored in a 114 liters (30 gallons) reservoir and delivered to the mixer with a gear pump. The oil condition is monitored through a transparent window. The (feed) static pressures for the pure lubricant and air are displayed in Bourdon type pressure gauges, PG_1 and PG_2, respectively. An additional gauge (PG_3) allows measurement of the mixture static pressure just before its entrance to the damper test section. A thermal mass flowmeter (0–100 *SLPM*) is employed to measure the airflow rate, and a positive displacement gear flowmeter (up to 4 *LPM*) for the oil volumetric flow rate. The lubricant inlet and outlet temperatures, the film temperature, and the air supply temperature are measured with K-type thermocouples (*TT*).

The bubbly fluid enters into the damper film through two holes 180 deg apart at the damper left end (location Z_o). An O-ring seals the damper journal on this side, thus forcing the flow to exit through the right end plenum (see Fig. 1(*b*)). The plenum or exit pressure is measured with a pressure gauge installed in the housing cap (see Fig. 1(*a*)). Two high-pressure transparent hoses serve to monitor the condition of the mixture at the inlet and outlet ports of the damper.

A photoelectric tachometer records the shaft speed and two orthogonally placed eddy current sensors (PP_X and PP_Y) measure the journal whirl motion. Four piezoelectric pressure transducers (*PT*) are flush mounted at the plane Z_2 (16.7 mm from the left end) on the circumferential locations 0 deg, 120 deg, 180 deg, and 240 deg, measured clockwise from the horizontal axis (see Figs. 1(*b*) and 2). The piezoelectric transducers are limited to measure dynamic variations of the pressure. Two strain gauge pressure sensors, flush mounted at 330 deg in the two different axial locations (Z_1 and Z_2), measure absolute film pressures. The location Z_1 (5.6 mm from the left end) is nearer to the sealed end of the *SFD*, and Z_2 is half way between Z_1 and the open end of the damper.

Nomenclature

C = SFD nominal radial clearance (0.343 mm)
D = journal diameter (129.4 mm)
e = nominal journal orbit radius or eccentricity (0.180 mm)
$f = f_r + if_t$, squeeze film force per unit length (at Z_j) (N/m)
f_r, f_t = radial and tangential components of squeeze film force (N/m)
$h = C + e\cos(\omega t)$. Local film thickness (m)
$i = \sqrt{-1}$, Imaginary unit
L = SFD journal length (31.1 mm)
LPM = liters per minute
n = number of full periods of journal motion
$P(t)$ = period-averaged or instantaneous film pressure at location (Z_j, θ) (Pa)
R = journal radius (64.7 mm)
r, t = radial and tangential coordinates
SLPM = standard liters per minute
t = time (sec)
t_o = time of minimum film thickness at 0° (sec)
$T = 2\pi/\omega$, Journal period of motion (sec)
$V_t = e\omega$, journal center tangential velocity (m/sec)
X, Y = horizontal and vertical coordinates of the journal center (m)
Z_j = axial location of pressure measurements (mm), Z_1 (5.16 mm), Z_2 (16.7 mm)
Z_0 = inlet SFD plane (0 mm)
Z_3 = discharge SFD plane (37.1 mm)
λ = mixture volume fraction (air volume/total volume)
ω = journal whirl frequency (rad/sec)
θ = angular location of pressure measurements (rad)

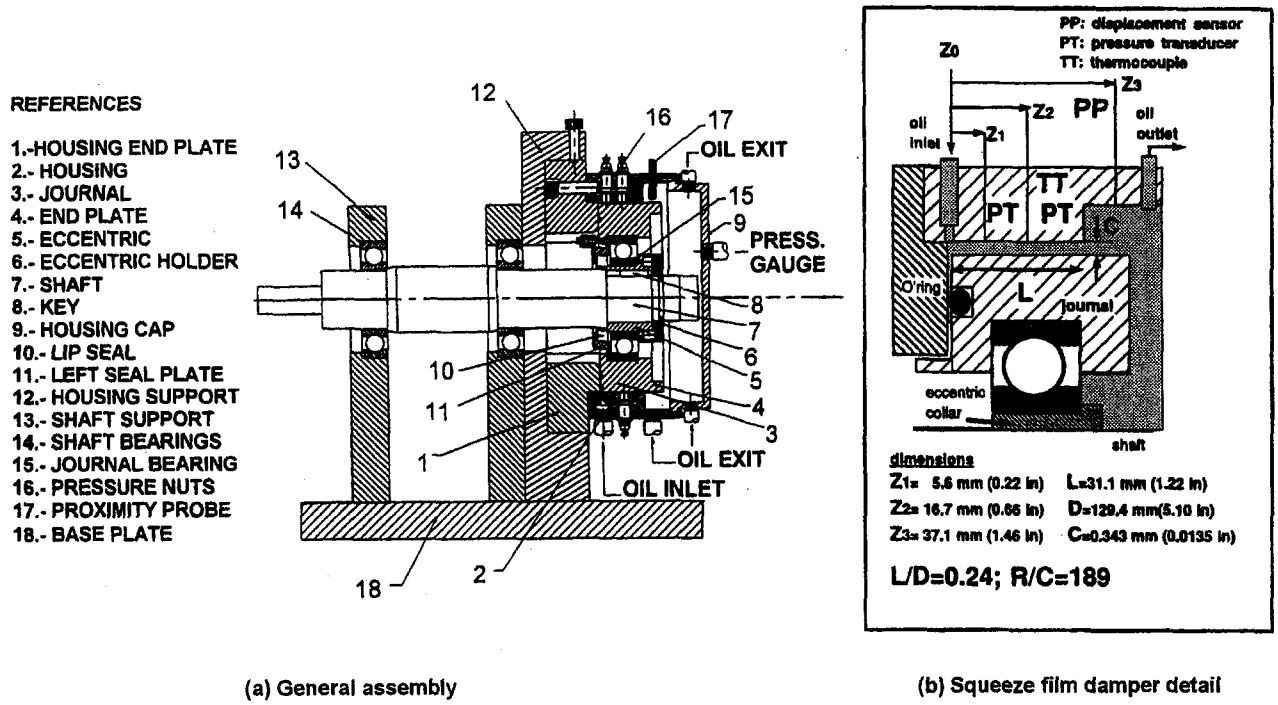

(a) General assembly

(b) Squeeze film damper detail

Fig. 1 Squeeze film damper test apparatus

Experimental Procedure

An uncertainty analysis and a calibration of the instrumentation are performed to verify manufacturer values for sensitivity and precision of the flowmeters, pressure gauges, and thermocouples. The individual calibration errors are: oil flow meter, 1 percent of measurement, air flow meter, 0.5 percent of full scale (100 *SLPM*), pressure gauges, 3 percent of full scale (150 psi), and thermocouples, 1 percent of full scale (200°F). These errors are propagated using the standard Kline and McClintock (1953) approach for simple sample experiments to estimate the uncertainty on the derived parameters. The film pressure measurement uncertainty is mainly due to the *A/D* conversion, and is on the order of hundredths of a bar. In the actual tests, however, a different source of uncertainty arises in the measurements. The nature of the bubbly mixture forced by the journal dynamic motion introduces temporal fluctuations in the squeeze film pressure that are estimated as two orders of magnitude larger than the instrumentation uncertainty, being the largest (worst case) on the order of one bar. This first-order uncertainty in dynamic measurements is thoroughly discussed by Moffat (1982).

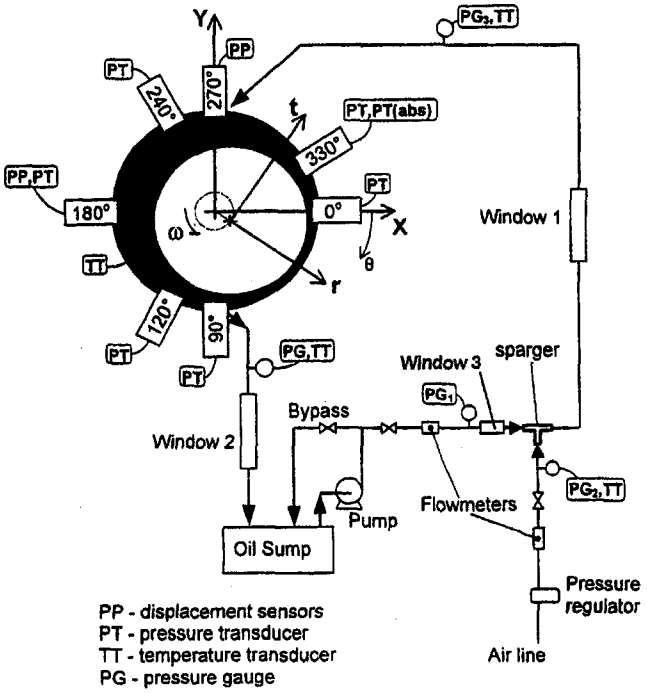

Fig. 2 Schematic of test rig and instrumentation

The bubbly mixture volume fraction is estimated as the ratio of the air volumetric flow rate and the total volumetric flow rate (air plus lubricant). The oil flow rate is obtained directly from the meter display, and the airflow rate is derived from the mass flow rate and the supply temperature and pressure. The estimated mixture volume fraction uncertainty is depicted with error bars on the corresponding graphs detailing the test results.

Measurements are performed at two shaft speeds, 500 rpm (8.33 Hz) and 1000 rpm (16.67 Hz). In both cases, the mixture volume fraction is increased from 0 to 1 (i.e., from pure oil to all gas condition). The air and oil supply pressures are kept constant at 6.8 bar (100 psi) to assure uniform mixing, and the mixture feed temperature is close to room temperature (25°C). The discharge or plenum pressure is kept to a constant value of 1.8 bar (26 psi). The mixture volume fraction, regulated by valves in the oil and air feed lines, requires some elapsed time to reach a uniform composition (usually less than 2 minutes). The power supply to the DC drive motor must be reset for each test mixture condition since this causes the shaft speed to vary, thus affecting greatly the SFD power consumption.

For each test case, the stationary values of the temperatures and feed pressures of air, oil, and mixture; the air and oil flow rates; and the journal speed are manually recorded. The dynamic film pressures and the horizontal (X) journal displacement sensor are acquired simultaneously at a rate of 500 samples per second, for a total of 1024 data points for each test (34 cycles of journal motion at 1000 rpm, and 17 cycles at 500 rpm). The tests performed at 500 rpm also include the film pressure at location Z_1 and the vertical

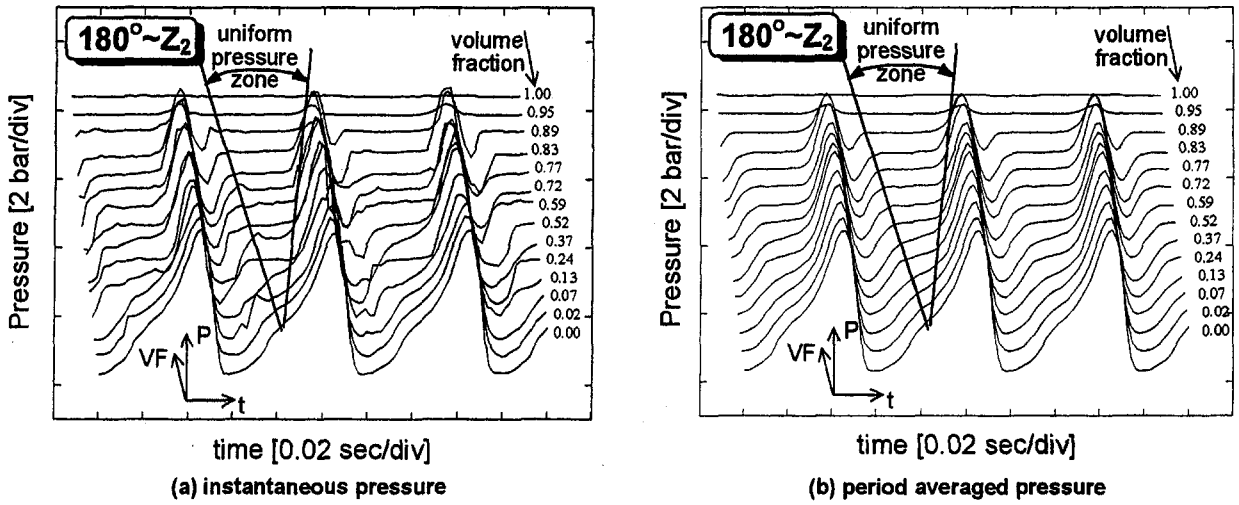

Fig. 3 Development of the pressure field and gaseous cavitation zone with the mixture volume fraction (VF) for a whirl frequency of 16.67 Hz at 180 deg

(Y) journal displacement. The digital data is stored for later analysis with a dedicated data processing software. The tests are conducted at all times with a pure lubricant available from the large reservoir and which is divided by a baffle preventing the mixing of aerated return oil with the fresh lubricant.

Results

Figure 3(a) shows a set of typical dynamic film pressures obtained with the bubbly mixture. The plot compiles the film pressures at the location (180 deg, Z_2) for a whirl frequency of 16.67 Hz, and over the whole range of mixture volume fractions. This waterfall-like plot depicts the pressure in the vertical axis, the time in the horizontal axis, and the mixture volume fraction in the in-plane axis. The most noticeable characteristic of the dynamic pressure field is its "noisy" nature. Pressure spikes and fluctuations on the peak-to-peak amplitude are intrinsic to the presence of bubbles in the lubricant (Diaz and San Andrés, 1996, 1997a). However, the implementation of a period averaging scheme results in a smooth pressure field in which the "noise" has been removed. This ensemble-averaging scheme consists of taking the entire pressure field recorded and dividing it into periods of journal motion (16 periods for 8.33 Hz, and 32 for 16.66 Hz). Then, each period is considered as an independent measurement and the time average of the whole set of "independent measurements" is computed. Figure 3(b) shows the period averaged field corresponding to the pressure measurements depicted in Fig. 3(a). The procedure shows that the pressure field can be represented by a periodic smooth function and that the pressure spikes (high frequency) need not be considered to describe the general behavior of the squeeze film damper. In the experiments, the temporal variations in the journal orbit amplitude (not shown here for brevity) range to a maximum 15 percent of the nominal value (0.180 mm). These changes are due to the frictional forces exerted by the external pressurization of the test apparatus and do not affect the test results hereby reported. Representative squeeze film forces can then be estimated from the period (ensemble) averaged pressure fields.[1]

The ensemble dynamic film pressure contains the main features common to all the measured periods in the pressure field. The occurrence of a zone of constant pressure that interrupts the pressure rise from its minimum value to its maximum peak is evident. The measurements thus confirm prior experiments of Zeidan and Vance (1990a, b) and Diaz and San Andrés (1996, 1997a). The constant pressure zone onset and extent are related to the amount of air present in the lubricant (Diaz and San Andrés, 1997a, 1997b). Figure 4 sketches a contour pressure plot of the surface generated by the curves depicted in Fig. 3(b). The graph presents the isobaric lines, at intervals of 0.61 bar, in the plane of mixture volume fraction and time. The local film thickness is displayed with the same time scale at the bottom of each figure. The uniform pressure zone develops around the time of maximum film thickness when going from negative film squeeze (increasing film thickness) to positive film squeeze (decreasing film thickness). The uniform pressure magnitude is independent of the mixture volume fraction and equal to the exit plenum pressure (1.8 bar). During a period of motion, the extent of the no-film pressure generation region increases (almost linearly) with the mixture volume fraction. The maximum peak pressure displaces towards the location of minimum film thickness when the mixture volume fraction increases, thus approaching the condition of an ideal gas. Similar conclusions are drawn from the measurements at all the other angular locations.

Diaz and San Andrés experiments (1997b) demonstrate the squeeze film pressures to be similar at the different angular locations of measurement, but shifted (in time) by a value equal to the angle between the circumferential locations of measurement divided by the whirl frequency (ω). In addition, the measurements

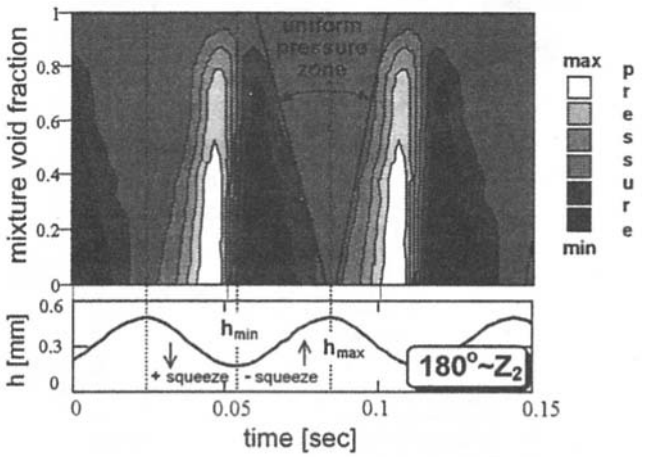

Fig. 4 Contour plot of the pressure field versus the mixture void fraction (VF) for a whirl frequency of 16.67 Hz at 180 deg

[1] The nature and importance of the high frequency, random pressure variations due to the bubbly-mixture is left out for future analysis. Such task of course requires a more complex methodology along with a more adequate theoretical foundation.

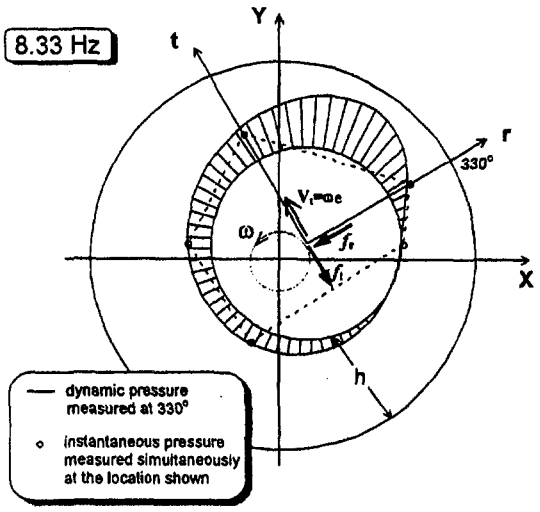

Fig. 5 Pressure profile around the journal damper from measurements at one fixed location over one cycle of motion and from simultaneous measurements at different angular locations at the plane of Z_2

show the peak-to-peak pressures to be nearly identical over the entire journal circumference. Nevertheless, the most convincing evidence of a rotating pressure field is shown in Fig. 5, where the circles denote film pressures measured simultaneously at the angular positions shown and at the journal position sketched. The continuous line depicts the dynamic pressure recorded at a fixed angular location (the one coinciding with the radial direction on the figure) over one period of journal motion. Note how the instantaneous pressure values coincide with the time varying pressure measurement at the fixed angle. Similar results are drawn from other measurements using the other transducers and at different mixture qualities than the ones presented in Fig. 5 (Diaz and San Andrés, 1997b, include in full these results). In sum, the dynamic pressure variations detected by a stationary observer (at a fixed angular location in the damper housing) have a unique correspondence to the values of the stationary pressure field as this rotates with an angular speed equal to the journal whirl frequency.

A test in which a pure oil is fed to the SFD at the nominal supply pressure (7.8 bar (115 psia)) and discharge pressure (1.8 bar (25 psia)) is performed for a nonwhirling journal. The shaft is manually (slowly) rotated and the film pressure variation is measured with the strain gauge pressure transducers. This hydrostatic pressure is depicted in Fig. 6 versus the angular location of the journal center measured from the transducer location (330 deg, Z_2). The local hydrostatic film pressure depends on the film thickness

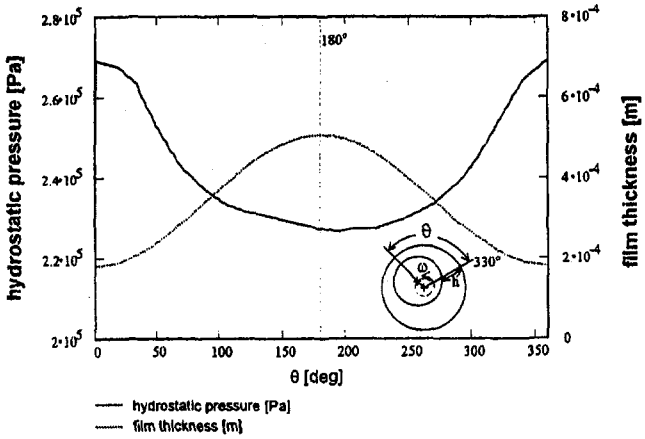

Fig. 6 Hydrostatic absolute pressure and local film thickness versus journal angular position at (Z_2, 330 deg)

constraining the local axial flow and the disposition of the feed holes acting as flow resistances. The hydrostatic pressure presents a maximum at the minimum film thickness, and a minimum at the maximum film thickness. Integration of this pressure field over the journal surface reveals (nearly) centering radial forces of 3372 N/m at Z_2 acting 6.4 deg from the radial direction, and 7275 N/m at Z_1 and 8.0 deg from the radial direction. The tests with journal whirl motion show that the dynamic pressure field is represented by the superposition of this hydrostatic pressure and the squeeze film generated pressure. The SFD forces presented next evidence this important conclusion.

A SFD describing circular centered orbits and with a stationary[2] pressure field (synchronous with the shaft) generates invariant forces in a radial and tangential coordinate system rotating with the same speed as the shaft. A pure tangential (−) force is distinctive of an ideal SFD since this force directly opposes any forward whirl force. Radial forces could be centering denoting a stiffness-like effect, or outwards implying a fluid inertia effect.

Dynamic damper forces (f_r, f_t) in the radial and tangential directions arise from integration of the pressure field around the journal surface. A kinematic relation between the stationary (though rotating) pressure field and the dynamic pressure field at a fixed location is used to transform the spatial integration around the journal circumference into integration in time. The relationship is

$$f_{(Z)} = (f_r + i \cdot f_t)_{(Z)} = \frac{-\omega \cdot \frac{D}{2}}{n} \cdot \int_{t_o}^{t_o + n \cdot T} P_{(t,Z)} \cdot e^{-i\cdot[\omega\cdot(t-t_o)+\theta]} dt. \quad (1)$$

Refer to the Nomenclature for a proper definition of all variables.

Figure 7 shows the estimated radial (f_r) and tangential (f_t) "forces per unit length" as a function of the mixture volume fraction (λ) at axial locations (Z_1, Z_2) and two whirl frequencies. Note that the magnitude of the forces is per unit length implying the discrete nature of the measurements in the axial direction. The similitude between the estimated forces using the pressures at different angular locations verifies (once more) the invariance of the dynamic pressure field in a rotating coordinate system. The ensemble-averaged forces, presented in the figures, also show good correlation with the forces from different angular locations. The estimates of the tangential (direct damping) force lay all within a narrow band around this ensemble average. The estimates of the radial (centering) force are also close to this ensemble average. However, the dispersion of the force estimates is a little larger for mixture volume fractions around 0.85.

The tangential force is largest for the condition of pure oil, while practically null for a volume fraction equal to one (pure air). The damping force presents a nearly linear variation with the air volume fraction, and thus, it evidences a reduction in the mixture viscosity and in the overall damping capability of the SFD. The radial (centering) force appears not to be greatly affected by the mixture composition, except at the largest air volume fractions where it rapidly drops to a null value ($\lambda > 0.85$). A closer scrutiny reveals that this force increases rapidly from the pure oil condition to mixtures with small amounts of air ($\lambda < 0.02$). As the air content increases, the radial force remains almost constant with a light tendency to increase. For both test speeds, the tangential force per unit length at the axial location Z_2 is larger than the radial force up to a mixture volume fraction, $\lambda \sim 0.70$. The radial force is larger above this value of λ. At the axial location Z_1, the tangential force is larger than the radial only up to a mixture volume fraction of about 0.40.

[2] Here the stationary qualification means an invariant pressure field relative to an observer positioned in the spinning shaft.

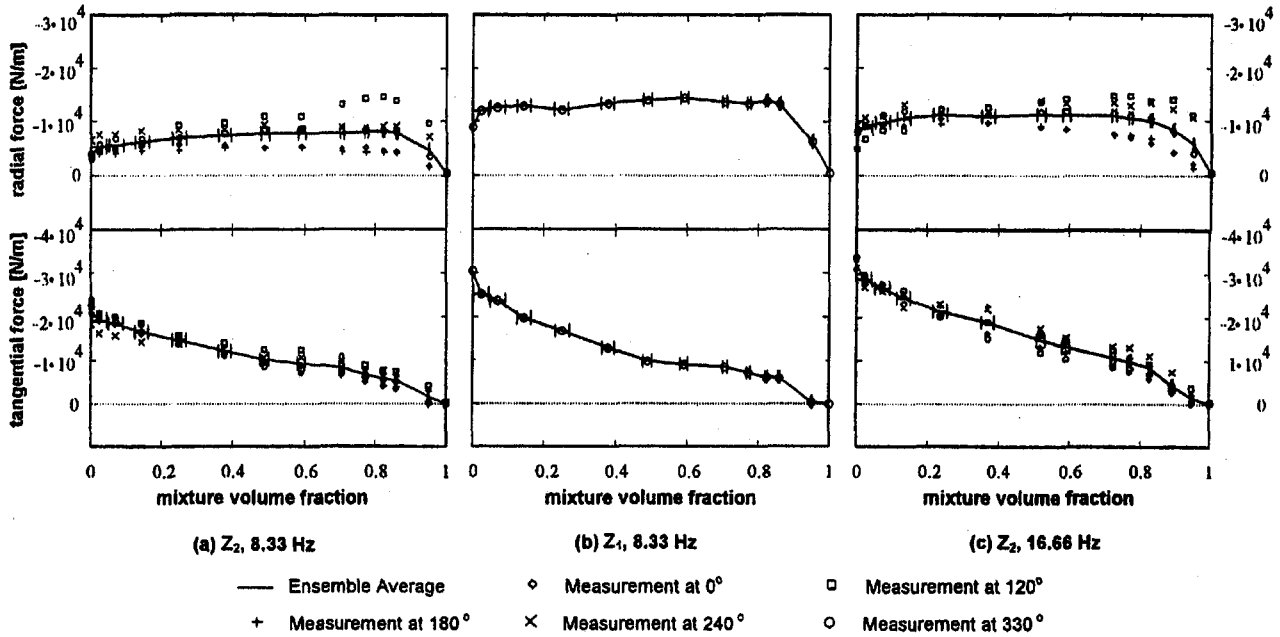

Fig. 7 Radial and tangential squeeze film forces at (*a*) *Z*1, 8.33 Hz; (*b*) *Z*2, 8.33 Hz; (*c*) *Z*2, 16.67 Hz

An incompressible fluid, full-film SFDs model would predict damper forces directly proportional to the lubricant viscosity, whirl frequency, and journal orbit radius. Thus, for a constant mixture composition (or at least for the pure oil condition) the forces at 16.67 Hz should be approximately twice their counterparts at 8.33 Hz. Yet, this is not the case in the present experiments. For the pure oil condition, the estimated total force at 16.67 Hz is less than 1.5 times the force at 8.33 Hz. In addition, it is well known that an uncavitated, oil lubricated SFD executing circular centered orbits renders a pure tangential (damping) force opposing the journal center speed. However, in all the test cases the radial forces have a nonzero value at a mixture volume fraction equal to zero (pure oil). This apparent inconsistency is due to two clearly identified factors.

First, the high supply pressure is enough to prevent fluid vapor cavitation at 8.33 Hz, but is not enough to prevent oil vaporization at 16.67 Hz for the lower mixture volume fractions (where the dynamic peak-to-peak pressures are larger). As a consequence, at 16.67 Hz and the pure oil test condition ($\lambda = 0$) the damper presents vapor cavitation. This possibly accounts for the lack of proportionality between the forces and the whirl frequency at the pure oil condition.

The hydrostatic pressure field is probably responsible for the radial (centering) force. Note how remarkably close are the estimates of radial force for pure oil at 8.33 Hz and those due to the hydrostatic pressure profile in both axial locations. The dynamic pressure measured is thus the superposition of the hydrodynamic pressure field produced by the squeezing motion and the hydrostatic pressure field induced by the external pressurization.

Conclusions

Most dampers operate with low levels of external pressurization allowing for lubricant vaporization or air entrapment while operating with large amplitude vibrations at high frequencies. Air ingestion leading to a bubbly mixture composition affects substantially the dynamic performance of squeeze film dampers. This complex phenomenon lacks adequate physical understanding and sound analytical modeling. Experimental measurements of dynamic squeeze film pressures and derived film forces in a SFD operating with a controlled bubbly mixture of air in oil are detailed. The tests are conducted at two different whirl frequencies (8.33 and 16.67 Hz) and over the full range of mixture volume fractions (from pure oil to pure air). The following are the most relevant conclusions:

1 A period averaging procedure is effective to eliminate random and "noisy" components of the dynamic film pressures, while preserving the most important features like shape, magnitudes, and periodicity of the pressure fields.
2 The existence of a pressure field rotating synchronously with the shaft is confirmed by the similitude of the pressure measurements around the damper circumference.
3 A zone of nearly constant pressure and of magnitude equal to the discharge pressure develops for increasing mixture volume fractions. The extent of this zone is directly related to the mixture composition.
4 The tangential component of the SFD force continuously decreases with the mixture volume fraction. However, the radial force component increases in the first instance and then remains almost constant up to a mixture volume fraction approximately equal to 0.85. Both force components drop to a null value for the pure air condition.
5 The radial (centering) force at the pure oil (uncavitated) condition is due to a hydrostatic pressure field arising from the feed mechanism and independent of whirl speed.

The test results provide experimental evidence of the paramount effect of air content in the lubricant on the dynamic performance of SFDs. The experimental results quantify parameters previously known by qualitative description only, thus providing a benchmark towards the development of sound theoretical models.

Acknowledgments

The support of the National Science Foundation and the TAMU Turbomachinery Research Consortium are gratefully acknowledged. The first author also likes to thank the support of CONICIT (Consejo Nacional de Investigaciones Científicas y Tecnológicas) and Universidad Simón Bolívar, Venezuela. Thanks to Mr. C. W. Karstens, undergraduate student, for his help in some aspects of the experimental work.

References

Al-Sharif, A., Chamniprasart, K., Rajagopal, K. R., Szeri, A. Z., 1992, "Lubrication with Binary Mixtures: Liquid-Liquid Emulsion," *ASME Journal of Tribology*, Vol. 115, pp. 46–55.

Arauz, G. L., and San Andrés, L., 1993, "Experimental Pressures and Film Forces in a Squeeze Film Damper," *ASME Journal of Tribology,* Vol. 115, No. 1, pp. 134–140.

Arauz, G. L., and San Andrés, L., 1996, "Experimental Study on the Effect of a Circumferential Feeding Groove on the Dynamic Force Response of a Sealed Squeeze Film Damper," *ASME Journal of Tribology,* Vol. 118, No. 4, pp. 900–905.

Atkin, R. J., and Craine, R. E., 1976, "Continuum Theories of Mixtures: Basic Theory and Historical Development," *Quarterly Journal of Mechanics and Applied Mathematics,* Vol. 29, pp. 209–244.

Braun, M. J., and Hendricks, R. C., 1984, "An Experimental Investigation of the Vaporous/Gaseous Cavity Characteristics of an Eccentric Journal Bearing," *ASLE Transactions,* Vol. 27, No. 1, pp. 1–14.

Brennen, C. E., 1995, "Cavitation and Bubble Dynamics," *Oxford Engineering Series 44,* Oxford University Press, New York.

Chamniprasart, K., Al-Sharif, A., Rajagopal, K. R., and Szeri, A. Z., 1993, "Lubrication With Binary Mixtures: Bubbly Oil," *ASME Journal of Tribology,* Vol. 115, pp. 253–260.

Diaz, S. E., and San Andrés, L. A., 1996, "Effects of Air/Oil Bubbly Mixtures on the Performance of Squeeze Film Dampers," TAMU Turbomachinery Research Consortium Progress Report, TRC-SFD-1-96, May.

Diaz, S. E., and San Andrés, L. A., 1997a, "Measurements of Pressure in a Squeeze Film Damper with an Air/Oil Bubbly Mixture," STLE PREPRINT 97-WTC-8.

Diaz, S. E., and San Andrés, L. A., 1997b, "Forced Response of SFDs Operating with a Bubbly (Air/Oil) Mixture," TAMU Turbomachinery Research Consortium Progress Report, TRC-SFD-1-April 1997.

Feng, N. S., and Hahn, E. J., 1986, "Density and Viscosity Models for Two-Phase Homogeneous Hydrodynamic Damper Fluids," *ASLE Transactions,* Vol. 29, No. 3, p. 361.

Hibner, D., and Bansal, P., 1979, "Effects of Fluid Compressibility on Viscous Damper Characteristics," Proceedings, Conference on the Stability and Dynamic Response of Rotors With Squeeze Film Bearings, University of Virginia, Charlottesville, VA, pp. 116–132.

Hsie, D. Y., 1988, "On Dynamics of Bubbly Liquids," *Advances in Applied Mechanics,* Vol. 26, Academic Press, Inc., San Diego, CA, pp. 63–133.

Kline, S. J., and McClintock, F. A., 1953, "Describing Uncertainties in Single-Sample Experiments," *ASME Mechanical Engineering,* Vol. 75.

Moffat, R. J., 1982, "Contributions to the Theory of Single-Sample Uncertainty Analysis," *ASME Journal of Fluids Engineering,* Vol. 104, pp. 250–260.

Pinkus, O., 1990, *Thermal Aspects of Fluid Film Tribology,* ASME Press, New York, pp. 317–326.

Plesset, M. S., and Prosperetti, A., 1977, "Bubble Dynamics and Cavitation," *Annual Review of Fluid Mechanics,* Vol. 9, pp. 145–185.

Rajagopal, K. R., and Tao, L., 1995, "Mechanics of Mixtures," *Series on Advances in Mathematics for Applied Sciences*—Vol. 35, World Scientific, Singapore.

Szeri, A. Z., 1996, "On the Flow of Emulsions in Tribological Contacts," *Wear,* Vol. 200, pp. 353–364.

Walton, J., Walowit, E., Zorzi, E., and Schrand, J., 1987, "Experimental Observation of Cavitating Squeeze Film Dampers," *ASME Journal of Tribology,* Vol. 109, pp. 290–295.

Wang, S. H., Al-Sharif, A., Rajagopal, K. R., Szeri, A. Z., 1992, "Lubrication with Binary Mixtures: Liquid-Liquid Emulsion in an EHL Conjunction," *ASME Journal of Tribology,* Vol. 115, pp. 515–522.

Zeidan, F. Y., and Vance, J. M., 1989, "Cavitation Leading to a Two Phase Fluid in a Squeeze Film Damper," *STLE Tribology Transactions,* Vol. 32, No. 1, pp. 100–104.

Zeidan, F. Y., and Vance, J. M., 1990a, "Cavitation Regimes in Squeeze Film Dampers and Their Effect on the Pressure Distribution," *STLE Tribology Transactions,* Vol. 33, pp. 447–453.

Zeidan, F. Y., and Vance, J. M., 1990b, "Cavitation and Air Entrainment Effects on the Response of Squeeze Film Supported Rotors," *ASME Journal of Tribology,* Vol. 112, pp. 347–353.

Zeidan, F. Y., Vance, J. M., and San Andrés, L. A., 1996, "Design and Application of Squeeze Film Dampers in Rotating Machinery," Proceedings, 25th Turbomachinery Symposium, Texas A&M University, College Station, TX, pp. 169–188.

Statistics of Response of a Mistuned Bladed Disk Assembly Subjected to White Noise and Narrow Band Excitation

D. Cha

A. Sinha

Department of Mechanical Engineering,
The Pennsylvania State University,
University Park, PA 16802

This paper deals with the statistics of the response of a mistuned bladed disk assembly subjected to random excitation. Analytical techniques are developed to compute this statistics for two types of random excitation: white noise and narrow band. The validity of the analytical methods has been established by comparison with the results from numerical simulations. The sensitivities of the response to mistuning have been examined as a function of the width of the frequency band of the random excitation, the dominant frequency of the random excitation and the structural coupling between adjacent blades.

1 Introduction

The forced response of a bladed disk assembly tends to be sensitive to small variations in the modal properties of individual blades. These variations in modal properties of blades, known as mistuning, are unavoidable in practice because of manufacturing tolerances. It has received a wide attention (Sogliero and Srinivasan, 1980; Griffin and Hoosac, 1984; Sinha, 1986; Wei and Pierre, 1988; Whitehead, 1996; Lin and Mignolet, 1997) in the existing literature because amplitude of the vibration of a blade in the mistuned bladed disk assembly can be significantly greater than that of a perfectly tuned system. However, except for the paper by Sogliero and Srinivasan (1980), all papers deal with deterministic and periodic excitation. Since variations in modal properties of blades are random in nature, there exists large number of possible sets of modal parameters that a bladed disk assembly may have. Hence, it is important to predict the statistics of forced response, particularly the probability that the maximum amplitude will exceed a critical value. Sinha and Chen (Sinha, 1986; Sinha and Chen, 1989; Chen and Sinha, 1992) have developed a technique to compute the statistics of the maximum amplitude when the excitation is deterministic and sinusoidal. This paper examines the impact of mistuning when the nature of excitation is random, which has been found to be true in many applications. Two types of random excitation have been considered in this paper: white noise and narrow band random excitation.

In the presence of random excitation, the mean and variance of the response are computed for a given system. Because of mistuning, these mean values and variances are random variables. Hence, the objective is to compute the statistics of mean and variance of the response, and then evaluate the impact of mistuning. For the computation of mean and variance of the response, modal decomposition methods are often used (Lubliner and Elishakoff, 1986). However, analytical calculation of the statistics of mean and variance of the response due to mistuning becomes complicated because elements of modal matrix are random variables (Yang and Griffin, 1997). When the excitation is white noise with zero mean, the mean value of the response is zero for each case of mistuning, and the variance of the response can be obtained by solving a Lyapunov equation (Lin, 1967). The same approach is valid for the case of the narrow band excitation also, because the narrow band excitation can be generated as an output of the band-pass filter with the white noise as an input. The solution of Lyapunov equation involves the solution of $2n(2n + 1)/2$ linear equations, where n is the number of second order differential equations. Since the number of linear equations to be solved for a system subjected to sinusoidal excitation is $2n$, computational efforts for Monte-Carlo simulation are going to be considerably higher when the excitation is random in nature. Consequently, it is necessary to develop an analytical technique to compute the statistics of the variance of a blade displacement. Sogliero and Srinivasan (1980) considered white noise excitation, and used the modal decomposition method to compute the mean square displacement. They computed the average value of this mean square displacement using Monte-Carlo simulations with only ten mistuned bladed disk assemblies.

In this paper, a general approach has been presented to compute the statistics of variance of a blade's displacement when the excitation is either white noise or narrow band. This approach is based on Lyapunov equation and Taylor series expansion. Numerical results are presented for a simple model of the bladed disk assembly (Fig. 1). In the presence of white noise excitation, it is shown that modal decomposition method leads to a very simple expression for the computation of the statistics of variance of the blade's displacement. The results from these analytical techniques are compared with those from Monte-Carlo simulations. The sensitivity of random response to mistuning is examined as a function of the frequency band of random excitation, the dominant frequency of random excitation and the structural coupling stiffness.

2 Formulation

Let M, K, and C be mass, stiffness, and damping matrices, respectively. The governing differential equation can be written as follows:

$$M\ddot{x} + C\dot{x} + Kx = F(t), \tag{1}$$

where the elements of the external excitation vector, $F(t)$, are random in nature. Furthermore, these random processes are assumed to be stationary with zero mean. It is assumed that the correlation matrix of external forces,

$$R_F(\tau) = E[F(t)F(t + \tau)^T], \tag{2}$$

is known.

Contributed by the International Gas Turbine Institute (IGTI) of THE AMERICAN SOCIETY OF MECHANICAL ENGINEERS for publication in the ASME JOURNAL OF ENGINEERING FOR GAS TURBINES AND POWER. Paper presented at the International Gas Turbine and Aeroengine Congress and Exhibition, Stockholm, Sweden, June 2–5, 1998; ASME Paper 98-GT-379.

Manuscript received by IGTI March 22, 1998; final revision received by the ASME Headquarters March 23, 1999. Associate Technical Editor: R. Kielb.

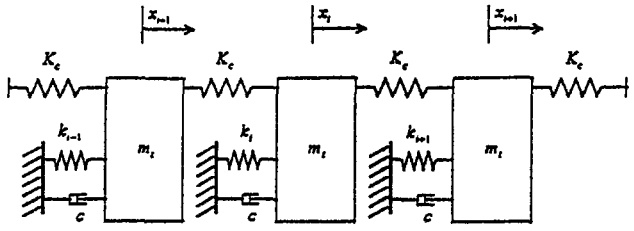

Fig. 1 Model of bladed disk assembly

The mistuning phenomenon is simulated by considering the perturbations in the stiffness matrix alone. If the stiffness matrix for the corresponding tuned system is K_0,

$$K = K_0 + \delta K, \tag{3}$$

where δK is the deviation in the stiffness matrix due to mistuning. It is assumed that the probability density function of each of the nonzero elements of δK is a linear combination of n independent Gaussian random variables with zero mean where n is the number of blades. In other words, one independent random variable, δK_i, is associated with each blade.

2.1 Computation of the Statistics of Response Via Modal Analysis. Let V be a normalized modal matrix. By the linear transformation,

$$x = Vy, \tag{4}$$

Eq. (1) can be changed to a system of n decoupled equations as follows:

$$\ddot{y} + 2\xi\omega_n\dot{y} + \omega_n^2 y = \Phi(t), \tag{5}$$

where

$$2\xi\omega_n = V^T C V = \text{diag}\,[2\xi_1\omega_{n1} \quad 2\xi_{n2} \quad \ldots \quad 2\xi_n\omega_{nn}] \tag{6a}$$

$$\omega_n^2 = V^T K V = \text{diag}\,[\omega_{n1}^2 \quad \omega_{n2}^2 \quad \ldots \quad \omega_{nn}^2] \tag{6b}$$

$$\Phi(t) = V^T F(t), \quad \xi_i = \frac{c}{2m_t\omega_{ni}}. \tag{6c, 6d}$$

Note that ω_n^2 and $2\xi\omega_n$ are diagonal matrices where ω_{ni} is the i^{th} natural frequency and ξ_i is the i^{th} modal damping ratio. Due to the orthonormality condition of normalized modal matrix,

$$V^T M V = I_n, \tag{6e}$$

where I_n is an identity matrix.

Next, the correlation matrix of transformed forces can be calculated as follows:

$$R_\Phi(\tau) = E[\Phi(t)\Phi(t+\tau)^T] = V^T R_F(\tau) V \tag{7}$$

where $E[\ ]$ is the expected value. The correlation matrix of modal response is then obtained (Papoulis, 1965) as

$$R_y(\tau) = E[y(t)y(t+\tau)^T]$$

$$= E\left[\left(\int_{-\infty}^{\infty} h(\lambda_1)\Phi(t-\lambda_1)d\lambda_1\right) \times \left(\int_{-\infty}^{\infty} h(\lambda_2)\Phi(t+\tau-\lambda_2)d\lambda_2\right)^T\right] \tag{8}$$

or component wise

$$R_{y_iy_j}(\tau) = E[y_i(t)y_j(t+\tau)]$$

$$= \int_{-\infty}^{\infty}\int_{-\infty}^{\infty} h_i(\lambda_1)h_j(\lambda_2)R_{\Phi_i\Phi_j}(\tau+\lambda_1-\lambda_2)d\lambda_1 d\lambda_2, \tag{9}$$

where $R_{\Phi_i\Phi_j}(\tau)$ is the correlation of transformed force and $h_i(t)$ is the unit impulse response of the ith modal system: i.e.,

$$R_{\Phi_i\Phi_j}(\tau) = E[\Phi_i(t)\Phi_j(t+\tau)] \tag{10}$$

$$h_i(t) = \frac{1}{\omega_{ni}\sqrt{(1-\xi_i^2)}} e^{-\xi_i\omega_{ni}t} \sin\left(\omega_{ni}\sqrt{(1-\xi_i^2)}t\right), \quad (t>0). \tag{11}$$

Using Eq. (4), the correlation matrix of physical response is obtained as below,

$$R_x(\tau) = V R_y(\tau) V^T. \tag{12}$$

The variance of the system response, σ_{xi}^2, is the diagonal elements of the correlation matrix of system response with $\tau = 0$: i.e.,

$$\sigma_{xi}^2 = E[x_i^2] = R_x(0)_{i,i} \tag{13}$$

2.2 Computation of the Statistics of Response Via State Space Analysis. Using the state space approach, the correlation matrix of the system response can also be calculated. Introducing the state variables, the system of second order differential Eq. (1) can be changed to the system of first order differential equations

Nomenclature

A = defined in Eq. (15b) and (24a)
B = defined in Eq. (15c) and (24b)
B_R = defined in Eq. (18)
C = damping matrix
c = damping coefficient of each blade
$D_{i,j}$ = defined in Eq. (39)
$E[\ ]$ = expected value
$F(t)$ = external force vector
$g(t)$ = narrow band excitation
$h_i(t)$ = impulse response of ith mode
I_n = identity matrix
K = stiffness matrix
k_0 = modal stiffness of each blade for the tuned system
k_i = modal stiffness of ith blade
M = mass matrix
m_t = modal mass of each blade
n = number of blades
P = correlation matrix of state variables
Q_0 = intensity of white noise excitation
$R_F(\tau)$ = correlation matrix of external force
$R_w(\tau)$ = correlation matrix of white noise excitation
$R_x(\tau)$ = correlation matrix of blade displacement
$R_y(\tau)$ = correlation matrix of modal displacement
$R_\Phi(\tau)$ = correlation matrix of transformed force
V = normalized modal matrix
$w(t)$ = white noise excitation
x_i = displacement of ith blade
y_i = ith modal displacement
z = state variables
δk = $k_i - k_0$
σ_{xi} = standard deviation of ith blade displacement
σ_R = defined in Eq. (28b)
μ_R = defined in Eq. (28a)
$\Phi(t)$ = transformed force vector
ξ_F = damping ratio of band-pass filter
ξ_i = damping ratio of ith mode
ω_F = resonant frequency of band-pass filter
ω_{ni} = natural frequency of ith mode

$$\dot{z} = Az + BF(t), \tag{14}$$

where z is the state vector, and matrices A and B are appropriately defined.

Case I: White Noise Excitation. If the element of the external excitation vector, $F_i(t)$, is assumed as an ergodic and Gaussian white noise, $w_i(t)$, then the state variables, system matrices A and B can be represented as

$$z^T = [x^T \dot{x}^T] \tag{15a}$$

$$A = \begin{bmatrix} 0 & I_n \\ -M^{-1}K & -M^{-1}C \end{bmatrix}, \quad B = \begin{bmatrix} 0 \\ M^{-1} \end{bmatrix}, \tag{15b, 15c}$$

and the correlation matrix of external forces is given as below.

$$R_w(\tau) = E[w(t)w(t+\tau)^T] = Q_0\delta(\tau)I_n, \tag{15d}$$

where Q_0 is the intensity and $\delta(\tau)$ is the dirac-delta function. Since $E[w_i(t)] = 0$, it has been shown that $E[z_i(t)] = 0$. Let P be the correlation matrix of state variables: i.e.,

$$P = E[z(t)z(t)^T] \tag{16}$$

then the correlation matrix P satisfies the following algebraic equation under steady state conditions (Sinha, 1990).

$$AP + PA^T = B_R, \tag{17}$$

where

$$B_R = -BQ_0B^T. \tag{18}$$

The equation (17) is called the Lyapunov equation which can be easily solved using MATLAB routine (MATLAB Manual, 1995) "lyap."

Case II: Narrow Band Excitation. If the external excitation, $F_i(t)$, is assumed as a narrow band excitation, $g_i(t)$, which can be generated from the white noise excitation, $w_i(t)$, by the band-pass filter: i.e.,

$$\ddot{g}_i + 2\xi_F\omega_F\dot{g}_i + \omega_F^2 g_i = \omega_F^2 w_i(t), \tag{19}$$

where ξ_F and ω_F are damping ratio and natural frequency of the band-pass filter.

Now, the governing differential equation is given by

$$M\ddot{x} + C\dot{x} + Kx = g(t), \tag{20}$$

where

$$g(t) = [g_1(t) \quad g_2(t) \quad \ldots \quad g_n(t)]^T. \tag{21}$$

If the state vector is selected as

$$z^T = [g^T \quad \dot{g}^T \quad x^T \quad \dot{x}^T] \tag{22}$$

then the Eq. (19) and (20) can be represented in the state space form as

$$\dot{z} = Az + Bw(t), \tag{23}$$

where

$$A = \begin{bmatrix} 0 & I_n & 0 & 0 \\ -\omega_F^2 I_n & -2\xi_F\omega_F I_n & 0 & 0 \\ 0 & 0 & 0 & I_n \\ M^{-1} & 0 & -M^{-1}K & -M^{-1}C \end{bmatrix} \tag{24a}$$

$$B = \begin{bmatrix} 0 \\ \omega_F^2 I_n \\ 0 \\ 0 \end{bmatrix} \tag{24b}$$

Therefore, Eq. (17) can now be used to calculate the correlation matrix P.

3 Analytical Computation of the Statistics of Variance of Displacement Due to Mistuning

Given M, K, C, and the nature of random excitation, the variance of the system response, σ_x^2, can be computed. However, because of mistuning, elements of stiffness matrix are random variables. As a result, σ_x^2 are random variables. Hence, it is desirable to predict mean and standard deviation of σ_x^2. In general, the modal decomposition method described in Section 2.1 can not be used to calculate mean and standard deviation of σ_x^2 because the modal matrix, V, can change significantly due to mistuning. Hence, the method based on the state space analysis is developed to calculate the statistics of σ_x^2.

Using the Taylor's series expansion, the solution of Eq. (17) can be approximated as follows:

$$P = P_0 + \sum_{i=1}^{n} \frac{\partial P}{\partial k_i}\delta k_i + \frac{1}{2!}\sum_{i=1}^{n}\sum_{j=1}^{n} \frac{\partial^2 P}{\partial k_i \partial k_j}\delta k_i \delta k_j, \tag{25}$$

where P_0 is the correlation matrix of the perfectly tuned system.

Note that the third and higher order terms of the Taylor's series expansion are neglected. $\partial P/\partial k_i$ is a solution of the following linear algebraic equation which is obtained by differentiating Eq. (17) with respect to k_i: i.e.,

$$A_0 \frac{\partial P}{\partial k_i} + \frac{\partial P}{\partial k_i} A_0^T = -\left(\frac{\partial A}{\partial k_i} P_0 + P_0 \frac{\partial A^T}{\partial k_i}\right). \tag{26}$$

Note that $\partial A/\partial k_i$ and $\partial A^T/\partial k_i$ can be calculated analytically. The matrix P_0 is known by solving Eq. (17) for a perfectly tuned system. Hence, the right hand side of Eq. (26) is known, and Eq. (26) is the Lyapunov equation which can be again solved by using the MATLAB routine "lyap." Similarly, the terms $\partial^2 P/\partial k_i \partial k_j$ can be calculated by the following algebraic equation which is obtained after differentiating Eq. (26) with respect to k_j: i.e.,

$$A_0 \frac{\partial^2 P}{\partial k_i \partial k_j} + \frac{\partial^2 P}{\partial k_i \partial k_j} A_0^T = -\left(\frac{\partial A}{\partial k_i}\frac{\partial P}{\partial k_j} + \frac{\partial P}{\partial k_i}\frac{\partial A^T}{\partial k_j} + \frac{\partial A}{\partial k_j}\frac{\partial P}{\partial k_i} + \frac{\partial P}{\partial k_j}\frac{\partial A^T}{\partial k_i}\right). \tag{27}$$

From the Eq. (25), the mean and standard deviation of response variance can be easily calculated as follows:

$$(\mu_R)_i = E[P_{i,i}], \quad (\sigma_R^2)_i = E[P_{i,i}^2] - (\mu_R)_i^2, \tag{28a, 28b}$$

where the expressions for $(\mu_R)_i$ and $(\sigma_R^2)_i$ are provided in appendix A.

4 Statistics of Response for a Given Model

In this section, a simple discrete model of a bladed disk assembly (Sinha, 1986; Sinha and Chen, 1989; Chen and Sinha, 1992) is chosen to study the effect of mistuning in the bladed disk system (see Fig. 1). The modal mass of each blade is considered to be identical and represented by m_i. And the modal stiffness of the i^{th} blade is represented by k_i. To study the phenomenon of mistuning, k_i is considered as a random variable. The mean value of k_i is equal to the modal stiffness k_0 of a blade in the perfectly tuned system. The standard deviation for the stiffness of each blade is chosen to be the same. Also, the distribution of k_i is assumed to be Gaussian and independent of each other. The mechanical coupling between adjacent blades due to the disk's flexibility has been represented by a spring with stiffness K_c. The intensity of white noise excitation, Q_0, is taken as unity because it acts as a scaling factor which equally affects the response of all blades.

In Section 4.1, the statistics of standard deviation of each

blade's response due to white noise excitation is calculated by the modal analysis whereas the results for narrow band excitation are obtained in the Section 4.2.

4.1 White Noise Excitation. The statistics of system response can be calculated from the state space analysis developed in Section 3. However, in this case, technique described in Section 2.1 leads to very simple expressions for computing the mean and standard deviation of σ_x^2. Because the modal mass of each blade is identical, the Eq. (6*e*) can be written as

$$V^T V = \frac{1}{m_t} I_n. \tag{29}$$

The correlation matrix of transformed forces can be calculated from Eq. (7) and (15*d*),

$$R_\Phi(\tau) = \frac{Q_0 \delta(\tau)}{m_t} I_n \tag{30}$$

The mean square value of modal response is obtained from Eq. (9) by setting $\tau = 0$,

$$R_{y_i y_j}(0) = \begin{cases} 0 & (i \neq j) \\ \dfrac{Q_0}{2c\omega_{ni}^2} & (i = j) \end{cases}. \tag{31}$$

The correlation matrix of modal response can be written as

$$R_y(0) = \frac{Q_0}{2c} (\omega_n^2)^{-1}, \tag{32}$$

where $(\omega_n^2)^{-1}$ is the inverse of the matrix ω_n^2.

It should be noted that, in the mistuned system, the correlation matrix of the modal response, $R_y(0)$, is also a diagonal matrix because the white noise excitations, $w_i(t)$, are uncorrelated. From Eq. (29), (32), (12), and (6*b*),

$$R_x(0)K = \frac{Q_0}{2c} I_n. \tag{33}$$

Therefore, the response correlation matrix is easily calculated as

$$R_x(0) = \frac{Q_0}{2c} K^{-1}. \tag{34a}$$

Using Eq. (3), $R_x(0)$ can be written as

$$R_x(0) = \frac{Q_0}{2c} (K_0 + \delta K)^{-1} = \frac{Q_0}{2c} (I_n + K_0^{-1}\delta K)^{-1} K_0^{-1}. \tag{34b}$$

Assuming that the higher order of $K_0^{-1}\delta K$ is small,

$$R_x(0) = R_{x0}(0) + \delta R_x(0), \tag{35}$$

where

$$R_{x0}(0) = \frac{Q_0}{2c} K_0^{-1}, \quad \delta R_x(0) = -\frac{Q_0}{2c} K_0^{-1}\delta K K_0^{-1}. \tag{36a, 36b}$$

Note that $R_{x0}(0)$ is the response correlation matrix of the perfectly tuned system and $\delta R_x(0)$ is the change of correlation matrix due to mistuning effect. The expression for each element of the correlation change matrix $\delta R_x(0)$ has the following form:

$$\delta R_x(0)_{i,j} = -\frac{Q}{2c} \sum_{l=1}^{n} \delta k_l (K_0^{-1})_{i,l} (K_0^{-1})_{l,j} \tag{37}$$

Since the mean of δk_i is zero, the mean of $\delta R_x(0)$ is also zero. Therefore, the mean of $R_x(0)$ is same as the response correlation of a perfectly tuned system. From the Eq. (37), the standard deviation of response variance, σ_R, can be easily calculated as follows:

Table 1 System parameters

$m_t = 0.0114kg$, $c = 1.45Ns/m$, $k_o = 430000N/m$, $K_c = 45430N/m$

$$(\sigma_R^2)_i = E[\delta k^2] \frac{Q_0}{2c} \sum_{l=1}^{n} (D_{i,l})^2, \tag{38}$$

where

$$D_{i,l} = (K_0^{-1})_{i,l} (K_0^{-1})_{l,i}. \tag{39}$$

Numerical Results. In order to verify the accuracy of this analytical technique, the results from numerical simulations are compared with those obtained analytically. The nominal values of modal parameters are chosen from the paper by Griffin and Sinha (1985), and are given in Table 1. The number of blades is selected to be equal to 10. The MATLAB command "randn" (MATLAB Manual, 1995) is used to generate the variations in the modal stiffness. It yields random numbers which have Gaussian distribution with zero mean and specified standard deviation.

The exact solution of σ_x^2 is obtained by solving Eq. (17) numerically, which is equivalent to solving Eq. (34*a*). The statistics of each blade's σ_x^2 are then generated by considering a large number (arbitrary chosen to be 1000) of bladed disk assemblies. The standard deviation of the blade's modal stiffness is chosen as 17200 N/m, which will correspond to about 2 percent mistuning in terms of ratio of standard deviation and mean values of the modal frequency of each blade.

First, the mean (μ_R) and standard deviation (σ_R) of each blade's σ_x^2 are calculated from the Monte-Carlo simulation and compared with the analytical results obtained from Eq. (38). The results are presented in Table 2 with three different coupling stiffness, K_c = 4300, 45430 and 107500 N/m. Note that the maximum and the minimum values of all blade's μ_R and σ_R are presented as simulation results in Table 2. The mean and standard deviation of each blade's σ_x^2 show good agreement with those from the analytical technique irrespective of the value of the coupling stiffness. On a Pentium P-75, the computation times required for numerical simulation and analytical technique are 10 min and 0.036 sec for each K_c, respectively. Consequently, analytical technique has been used to evaluate the effects of the coupling stiffness.

In Fig. 2, μ_R and the ratio σ_R/μ_R of each blade's σ_x^2 are obtained analytically as a function of K_c. The mean values and standard

Table 2 Statistics of σ_x^2 for white noise excitation

(a) μ_R : mean value of variance σ_x^2 (units: $\times 10^{-7} m^2$)

K_c = 4300 N/m	simulation	7.852 ~ 7.896
	analytical	7.863
K_c = 45430 N/m	simulation	6.730 ~ 6.745
	analytical	6.723
K_c = 107500 N/m	simulation	5.663 ~5.685
	analytical	5.670

(b) σ_R : standard deviation of variance σ_x^2 (units: $\times 10^{-8} m^2$)

K_c = 4300 N/m	simulation	2.951 ~3.240
	analytical	3.084
K_c = 45430 N/m	simulation	2.154 ~2.364
	analytical	2.254
K_c = 107500 N/m	simulation	1.532 ~1.682
	analytical	1.605

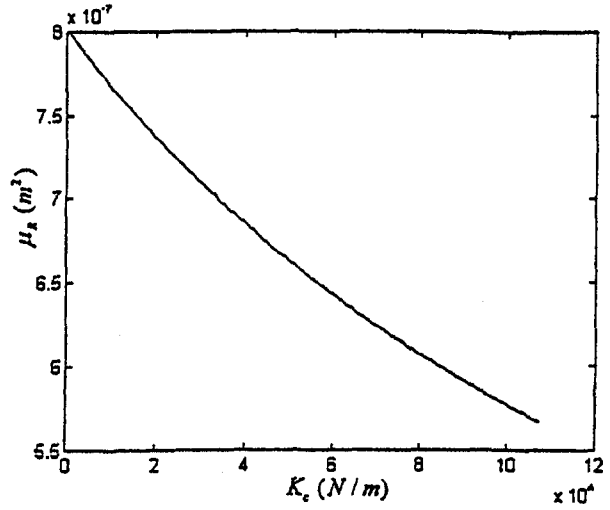

Fig. 2(*a*) μ_R versus K_c for white noise excitation

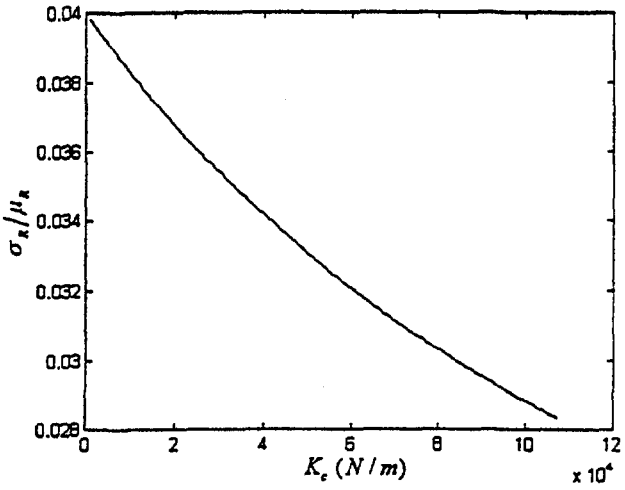

Fig. 2(*b*) σ_R/μ_R versus K_c for white noise excitation

deviations of σ_x^2 decrease with the increase of coupling stiffness K_c. Lastly, the ratio σ_R/μ_R is less than 0.04, which indicates that the system is not very sensitive to mistuning. This is reflected in Eq. (34*a*) as the elements of K^{-1} do not change significantly due to mistuning.

4.2 Narrow Band Excitation. For this case, formulation based on state space analysis is more convenient. Hence, the mean and standard deviation of σ_x^2 have been computed using Eq. (25) and (28).

Numerical Results. The band-pass filter is used to generate narrow band excitation and the numerical value for ξ_F is chosen as 0.001. The log-magnitude curve of band-pass filter is plotted in Fig. 3. The band-pass filter amplifies the white noise excitation at frequencies that are close to the resonant frequency of the filter ω_F. Therefore, the exciting force to the bladed disk system have dominant frequency band near the resonant frequency of the filter ω_F.

For the system with nominal parameters (Table 1), μ_R and the ratio σ_R/μ_R are plotted in the Fig. 4 as a function of the resonant frequency of the filter ω_F. These results are obtained analytically from Eq. (25) with only first order terms, and standard deviation of each blade's modal stiffness is taken to be 8000 N/m. The number of blades is again selected to be equal to 10. The results indicate that the system responses are very sensitive to the dominant frequency of the exciting force.

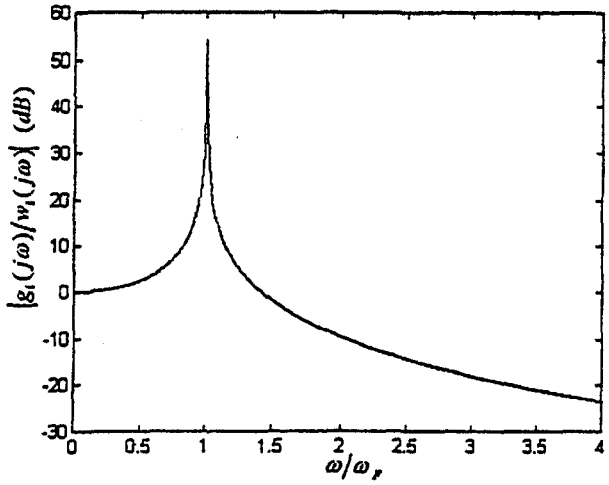

Fig. 3 Log-magnitude curve of the band pass filter

The number of peaks in plots for mean values (μ_R) and the standard deviations (σ_R) of σ_x^2 are related to the natural frequencies of the tuned system and the number of blades, respectively. These results are reflection of the fact that repeated natural frequencies of a tuned system split due to mistuning. This phenomenon becomes more obvious when the coupling stiffness is in-

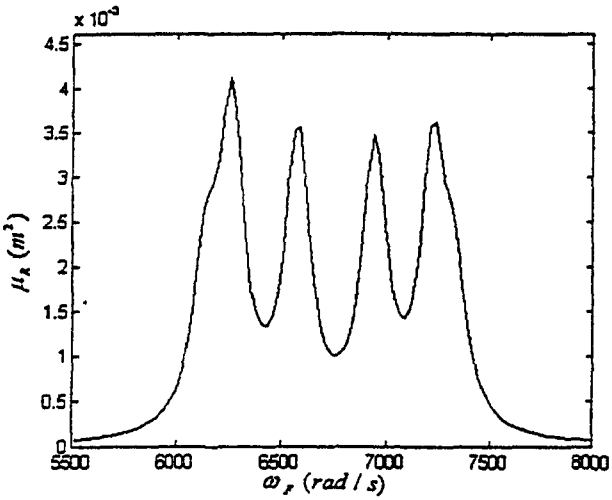

Fig. 4(*a*) μ_R as a function of ω_F (K_c = 45430 N/m)

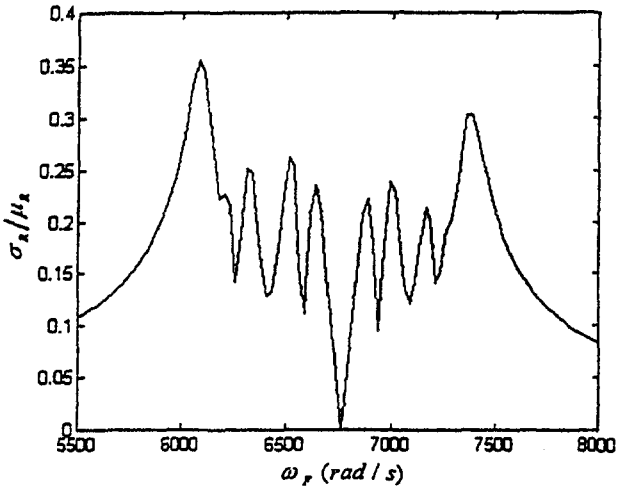

Fig. 4(*b*) σ_R/μ_R as a function of ω_F (K_c = 45430 N/m)

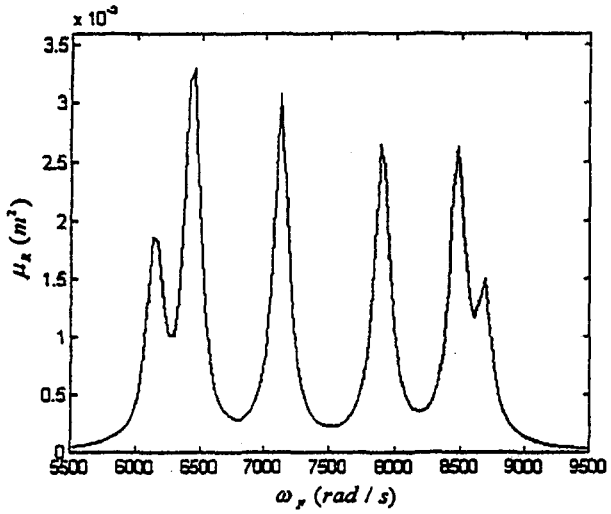

Fig. 5(*a*) μ_R as a function of ω_F (K_c = 107500 N/m)

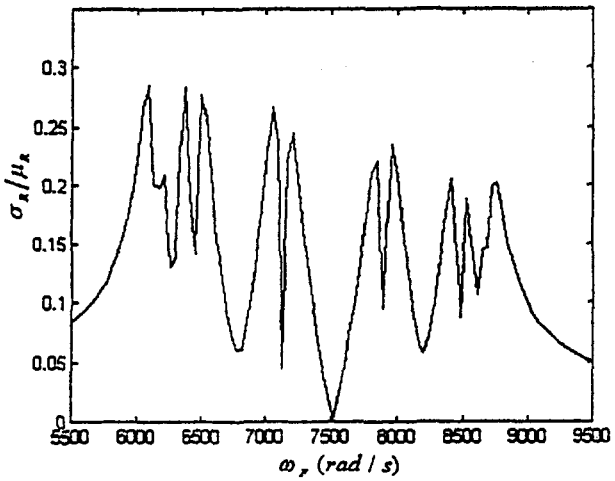

Fig. 5(*b*) σ_R/μ_R as a function of ω_F (K_c = 107500 N/m)

creased, Fig. 5 with K_c = 107500 N/m. In Fig. 5, there are six peaks in the plot for mean values, and ten peaks in the plot for standard deviations. Note that there are six distinct natural frequencies of the tuned system.

The analytical results obtained from Eq. (25) with first order terms only are compared with results from Monte-Carlo simulations. Three different cases, ω_F = 6260, 6760 and 7235 rad/s, are chosen for the system with nominal parameters because the μ_R have peaks at ω_F = 6260 and 7235 rad/s and the σ_R is very small at ω_F = 6760 rad/s. Results are presented in Table 3. Note that the maximum and the minimum values of all blade's μ_R and σ_R are presented as simulation results. The analytical results compare well with results from Monte-Carlo simulation except for σ_R at ω_F = 6760 rad/s. In this case, analytical results obtained from Eq. (25) with first and second order terms are quite accurate. On a Pentium P-75, the computation times required for numerical simulation and analytical technique with first order term are 42 min and 25.2 s for each ω_F, respectively. Consequently, the analytical technique has been again used to evaluate the effects of following parameters: K_c, ω_F, and ξ_F.

To study the effect of frequency band of exciting random force, μ_R and the ratio σ_R/μ_R are plotted in the Fig. 6 as a function of ω_F and ξ_F. These values are generated from Eq. (25) with only first order terms to keep the computational expense to be low. The system parameters are same as nominal parameters in Table 1. It is found that the mistuning effects are more severe when ξ_F is

Table 3 Statistics of σ_x^2 for narrow band excitation: K_c = 45430 N/m

(a) μ_R : mean value of variance σ_x^2 (units : $\times 10^{-3} m^2$)

ω_F =	simulation	3.713 ~ 3.786
6260 *rad / s*	analytical	4.106
ω_F =	simulation	1.033 ~ 1.035
6760 *rad / s*	analytical	1.006
ω_F =	simulation	3.374 ~ 3.449
7235 *rad / s*	analytical	3.624

(b) σ_R : standard deviation of variance σ_x^2 (units : $\times 10^{-4} m^2$)

ω_F =	simulation	5.780 ~ 6.193
6260 *rad / s*	analytical	5.837
ω_F =	simulation	0.436 ~ 0.472
6760 *rad / s*	analytical	0.009 (2nd order:0.402)
ω_F =	simulation	5.008 ~ 5.296
7235 *rad / s*	analytical	5.488

relatively small and ω_F is close to a natural frequency of the bladed disk assembly; i.e., when random forces have dominant frequencies near natural frequencies of the system. For large values of ξ_F, σ_R/μ_R is small and the variance of the response is not very sensitive to mistuning. The larger the value of ξ_F, broader is the band of random external excitation on blades. Hence, results for large values of ξ_F are consistent with results obtained for white noise excitation in this paper.

Next, μ_R and the ratio σ_R/μ_R are plotted in the Fig. 7 as a

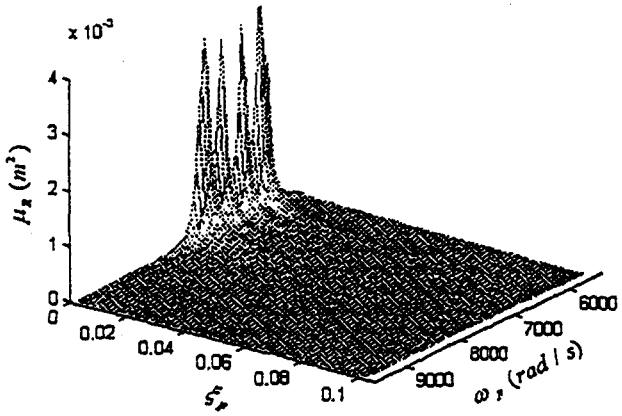

Fig. 6(*a*) μ_R as a function of ω_F and ξ_F (K_c = 45430 N/m)

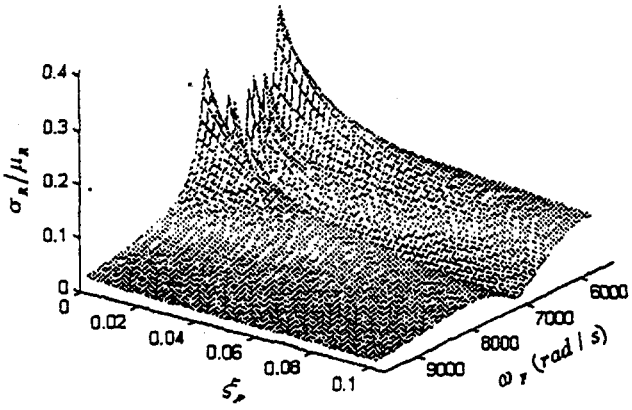

Fig. 6(*b*) σ_R/μ_R as a function of ω_F and ξ_F (K_c = 45430 N/m)

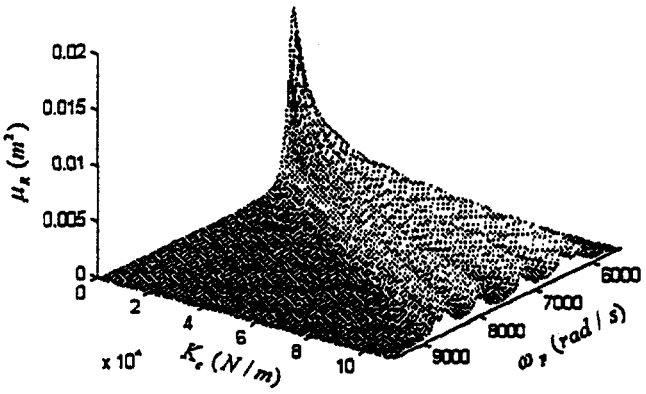

Fig. 7(*a*) μ_R as a function of ω_F and K_c (ξ_F = 0.001)

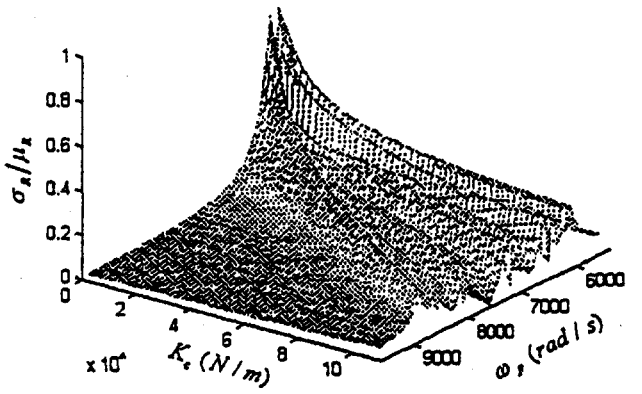

Fig. 7(*b*) σ_R/μ_R as a function of ω_F and K_c (ξ_F = 0.001)

function of coupling stiffness K_c and ω_F. It is found that the systems with small K_c have narrow band of resonant frequencies but the maximum values of both μ_R and the ratio σ_R/μ_R are considerably higher. It implies that the mistuning effect is more severe if the coupling stiffness is decreased. This result is similar to that for deterministic and purely sinusoidal excitation (Wei and Pierre, 1988). If the coupling stiffness is increased, the system resonance frequency band becomes larger because the natural frequency band of the tuned system is increased. The values of μ_R and the ratio σ_R/μ_R do not significantly change if the coupling stiffness is increased above the typical value, K_c = 45430 N/m.

It should be noted that results in Fig. 7 are obtained from Eq. (25) with first order terms only. The accuracy of these results has already been discussed when K_c = 45430 N/m. It has also been found that results are fairly accurate for large values of μ_R and σ_R when K_c = 12000 N/m, Table 4. However, accuracy of these results are not very high when K_c = 4300 N/m, Table 5.

Table 4 Statistics of σ_x^2 for narrow band excitation: K_c = 12000 N/m

(a) μ_R: mean value of variance σ_x^2 (units : $\times 10^{-3} m^2$)

ω_F =	simulation	5.784 ~ 6.114
6145 *rad / s*	analytical	6.263
ω_F =	simulation	6.284 ~ 6.353
6310 *rad / s*	analytical	6.405
ω_F =	simulation	5.632 ~ 5.914
6475 *rad / s*	analytical	5.991

(b) σ_R: standard deviation of variance σ_x^2 (units : $\times 10^{-3} m^2$)

ω_F =	simulation	2.136 ~ 2.271
6145 *rad / s*	analytical	2.850
ω_F =	simulation	0.893 ~ 0.979
6310 *rad / s*	analytical	0.025 (2nd order:1.005)
ω_F =	simulation	2.052 ~ 2.214
6475 *rad / s*	analytical	2.675

Table 5 Statistics of σ_x^2 for narrow band excitation: K_c = 4300 N/m

(a) μ_R: mean value of variance σ_x^2 (units : $\times 10^{-3} m^2$)

ω_F =	simulation	8.866 ~ 9.331
6130 *rad / s*	analytical	9.615
ω_F =	simulation	10.66 ~ 11.07
6205 *rad / s*	analytical	13.17
ω_F =	simulation	9.173 ~ 9.766
6265 *rad / s*	analytical	10.46

(b) σ_R: standard deviation of variance σ_x^2 (units : $\times 10^{-3} m^2$)

ω_F =	simulation	3.744 ~ 3.984
6130 *rad / s*	analytical	6.282
ω_F =	simulation	2.803 ~ 2.984
6205 *rad / s*	analytical	0.304 (2nd order:2.010)
ω_F =	simulation	3.508 ~ 3.709
6265 *rad / s*	analytical	6.082

5 Conclusions

A general analytical technique based on the state space approach has been developed to calculate the statistics of the variance of the response of a mistuned system subjected to a white noise and narrow band excitation. For a simple model of bladed disk assembly, the modal decomposition method also provides this information for the white noise excitation. The comparisons with the numerical simulation results indicate that the analytical techniques are fairly accurate for mistuning levels typical of those found in applications. It is observed that the impact of mistuning is not significant for white noise excitation. However, it can be significant for narrow band excitation if the random forces have dominant frequencies near the natural frequencies of system. This effect becomes more severe if the coupling stiffness between adjacent blades is small.

References

Chen, S., and Sinha, A., 1992, "Calculating the Statistics of Maximum Amplitude of Mistuned Bladed Disk Assembly Vibration," Proceedings, 33rd AIAA/ASME/AHS Structures, Structural Dynamics and Materials Conference, pp. 1296–1302.

Griffin, J. H., and Hoosac, T. M., 1984, "Model Development and Statistical Investigation of Turbine Blade Mistuning," ASME *Journal of Vibration, Acoustics, Stress, and Reliability in Design,* Vol. 106, pp. 204–210.

Griffin, J. H., and Sinha, A., 1985, "The Interaction Between Mistuning and Friction and the Forced Response of Bladed Disk Assemblies," ASME JOURNAL OF ENGINEERING FOR GAS TURBINES AND POWER, Vol. 107, pp. 205–211.

Lin, C.-C., and Mignolet, M. P., 1997, "An Adaptive Perturbation Scheme for the Analysis of Mistuned Bladed Disks," ASME JOURNAL OF ENGINEERING FOR GAS TURBINES AND POWER, Vol. 119, pp. 153–160.

Lin, Y. K., 1967, *Probabilistic Theory of Structural Dynamics,* McGraw-Hill, New York.

Lubliner, E., and Elishakoff, I., 1986, "Random Vibration of System With Finitely Many Degrees of Freedom and Several Coalescent Natural Frequencies," *International Journal of Engineering Science,* Vol. 24, No. 4, pp. 461–470.

MATLAB Manual, 1995, The MathWorks, Inc., Natick, MA.

Papoulis, A., 1966, *Probability, Random Variables and Stochastic Processes,* McGraw-Hill, New York.

Sinha, A., 1986, "Calculating the Statistics of Forced Response of a Mistuned Bladed Disk Assembly," *AIAA Journal,* Vol. 24, No. 11, pp. 1797–1801.

Sinha, A., and Chen, S., 1989, "A Higher-Order Technique to Calculate the

Statistics of Forced Response of a Mistuned Bladed Disk Assembly," *Journal of Sound and Vibration,* Vol. 130, No. 2, pp. 207–221.

Sinha, A., 1990, "Friction Damping of Random Vibration in Gas Turbine Engine Airfoils," *International Journal of Turbo and Jet Engines,* Vol. 7, pp. 95–102.

Sogliero, G., and Srinivasan, A. V., 1980, "Fatigue Life Estimates of Mistuned Blades Via a Stochastic Approach," *AIAA Journal,* Vol. 18, No. 83, pp. 318–323.

Wei, S.-T., and Pierre, C., 1988, "Localization Phenomena in Mistuned Assemblies with Cyclic Symmetry: Part I—Free Vibration; Part II—Forced Vibration," ASME *Journal of Vibration, Acoustics, Stress, and Reliability in Design,* Vol. 110, pp. 429–449.

Whitehead, D. S., 1996, "The Maximum Factor by Which Forced Vibration of Bladed Can Increase Due to Mistuning," ASME Paper 96-GT-125.

Yang, M. T., and Griffin, J. H., 1997, "A Normalized Modal Eigenvalue Approach for Resolving Modal Interaction," ASME JOURNAL OF ENGINEERING FOR GAS TURBINES AND POWER, Vol. 119, pp. 647–650.

APPENDIX A

Expressions for μ_R and σ_R^2

1 The Mean of Response Correlation: $(\mu_R)_i$.

$$(\mu_R)_i = E[P_{i,i}]$$

$$= E\left[P_{0i,i} + \sum_{l=1}^{n} \frac{\partial P_{i,i}}{\partial k_l}\,\delta k_l + \frac{1}{2!}\sum_{l=1}^{n}\sum_{m=1}^{n} \frac{\partial^2 P_{i,i}}{\partial k_l \partial k_m}\,\delta k_l \delta k_m \right]$$

$$= P_{0i,i} + \frac{1}{2!}\left(\sum_{l=1}^{n} \frac{\partial^2 P_{i,i}}{\partial k_l^2} \right) E[\delta k^2]$$

because

$$E\left[\sum_{l=1}^{n} \frac{\partial P_{i,i}}{\partial k_i}\,\delta k_l \right] = 0.$$

2 The Standard Deviation of Response Correlation: $(\sigma_R)_i$.

$$(\sigma_R^2)_i = E[P_{i,i}^2] - (\mu_R)_i^2$$

where

$$E[P_{i,i}^2]$$

$$= E\left[\left(P_{0i,i} + \sum_{i=1}^{n} \frac{\partial P_{i,i}}{\partial k_l}\,\delta k_l + \frac{1}{2!}\sum_{l=1}^{n}\sum_{m=1}^{n} \frac{\partial^2 P_{i,i}}{\partial k_l \partial k_m}\,\delta k_l \delta k_m \right)^2 \right]$$

$$= E[(P_0)_{i,i}^2] + E\left[\left(\sum_{i=1}^{n} \frac{\partial P_{i,i}}{\partial k_l}\,\delta k_l \right)^2 \right]$$

$$+ E\left[\left(\frac{1}{2!}\sum_{l=1}^{n}\sum_{m=1}^{n} \frac{\partial^2 P_{i,i}}{\partial k_l \partial k_m}\,\delta k_l \delta k_m \right)^2 \right]$$

$$+ 2E\left[P_{0i,i}\left(\sum_{i=1}^{n} \frac{\partial P_{i,i}}{\partial k_l}\,\delta k_l \right) \right]$$

$$+ 2E\left[P_{0i,i}\left(\frac{1}{2!}\sum_{i=1}^{n}\sum_{m=1}^{n} \frac{\partial^2 P_{i,i}}{\partial k_l \partial k_m}\,\delta k_l \delta k_m \right) \right]$$

$$+ 2E\left[\left(\sum_{l=1}^{n} \frac{\partial P_{i,i}}{\partial k_l}\,\delta k_l \right)\left(\frac{1}{2!}\sum_{l=1}^{n}\sum_{m=1}^{n} \frac{\partial^2 P_{i,i}}{\partial k_l \partial k_m}\,\delta k_l \delta k_m \right) \right]$$

and

(a) $E[(P_0)_{i,i}^2] = (P_0)_{i,i}^2$

(b) $$E\left[\left(\sum_{i=1}^{n} \frac{\partial P_{i,i}}{\partial k_l}\,\delta k_l \right)^2 \right] = E[\delta k^2] \sum_{l=1}^{n} \left(\frac{\partial P_{i,i}}{\partial k_l} \right)^2$$

(c) $$E\left[\left(\frac{1}{2!}\sum_{l=1}^{n}\sum_{m=1}^{n} \frac{\partial^2 P_{i,i}}{\partial k_l \partial k_m}\,\delta k_l \delta k_m \right)^2 \right]$$

$$= \frac{1}{2} E[\delta k^4] \sum_{l=1}^{n}\sum_{m=1}^{n} \left(\frac{\partial^2 P_{i,i}}{\partial k_l \partial k_m} \right)^2$$

$$+ \frac{1}{4} E[\delta k^4] \sum_{l=1}^{n}\sum_{m=1}^{n} \left(\frac{\partial^2 P_{i,i}}{\partial k_l^2}\,\frac{\partial^2 P_{i,i}}{\partial k_m^2} \right)$$

$$- \frac{1}{2} E[\delta k^4] \sum_{l=1}^{n} \left(\frac{\partial^2 P_{i,i}}{\partial k_l^2} \right)^2$$

(e) $$2E\left[P_{0i,i}\left(\frac{1}{2!}\sum_{l=1}^{n}\sum_{m=1}^{n} \frac{\partial^2 P_{i,i}}{\partial k_l \partial k_m}\,\delta k_l \delta k_m \right) \right]$$

$$= P_{0i,i} E[\delta k^2] \sum_{l=1}^{n} \left(\frac{\partial^2 P_{i,i}}{\partial k_l^2} \right)$$

(f) $$E\left[P_{0i,i}\left(\sum_{l=1}^{n} \frac{\partial P_{i,i}}{\partial k_l}\,\delta k_l \right) \right] = 0.$$

(g) $$E\left[\left(\sum_{l=1}^{n} \frac{\partial P_{i,i}}{\partial k_l}\,\delta k_l \right)\left(\frac{1}{2!}\sum_{l=1}^{n}\sum_{m=1}^{n} \frac{\partial^2 P_{i,i}}{\partial k_l \partial k_m}\,\delta k_l \delta k_m \right) \right] = 0.$$

Imbalance Response of a Rotor Supported on Open-Ends Integral Squeeze Film Dampers

O. de Santiago
Research Assistant

L. San Andrés
Associate Professor

Mechanical Engineering Department,
Texas A&M University,
College Station, TX 77843-3123

J. Oliveras
Professor
Universidad Simon Bolivar,
Caracas, Venezuela

Rotor vibration attenuation and structural components isolation in jet engines are achieved with squeeze film dampers, many of them supported on long elastic squirrel cages. Integral squeeze film dampers (ISFDs) are comprised of arcuate pads and wire-EDM webs rendering a compact viscoelastic support. An experimental study is conducted to evaluate the effectiveness of ISFDs in attenuating the imbalance response of a massive test rotor. Measurements of the damper structural stiffness and rotor natural frequencies are detailed. Impact tests on the test rotor supported on its dampers reveal the supporting structure to be very flexible, thus requiring the experimental evaluation of an equivalent stiffness for the damper and supports system. System damping coefficients extracted from impact load excitations vary with the lubricant viscosity and include a significant structural damping from the bearing supports. Rotor coast-down tests demonstrate the ISFDs to damp well the rotor response with peak vibration amplitude proportional (linear) to the imbalance. Viscous damping coefficients estimated from the amplitude response at the critical speeds agree reasonably well with predictions from a full-film, finite element model.

Introduction

Squeeze Film Dampers (SFDs) attenuate rotor vibrations and reduce transmitted forces in rotating machinery. SFDs are useful in aircraft engines, where damping from ball or roller bearings is small, and in process compressors as retrofit elements to suppress subsynchronous vibration. Integral squeeze film dampers (ISFDs) emerge as an alternative to conventional squirrel cage supported hydrodynamic dampers due to their reduced size and weight, low count part number, and allowance for easier assembly, inspection, and service (Zeidan, et al., 1996). However, widespread acceptance of this novel technology requires of adequate experimental verification of their damping capability along with a thorough validation of analytical models to predict their dynamic force performance.

SFDs supported on squirrel cages require a large axial space, three to four times longer than the damper itself, to provide enough flexibility and to allow for an effective viscous damping action. On the other hand, integral squeeze film dampers (ISFDs) are comprised of a number of arcuate segmented pads, and where thin wire EDM structural webs attach the pads to a ring acting as the flexible element of the damper. The thin gap between the sector pads and outer ring forms the squeeze film lands.

In general, the reaction forces developed by hydrodynamic dampers depend on the damper geometry (length, diameter, and clearance), lubricant viscosity, whirl frequency, and journal offset. Feeding grooves and/or holes, and end seals also affect the damper performance (Arauz and San Andrés, 1994). Numerous analyses note that SFD forces are nonlinear functions of the journal amplitude, and predict for sufficiently large imbalances, a bistable rotor response, jump phenomena and subsynchronous motions (Mohan and Hahn, 1974; San Andrés and Vance, 1988). Zeidan et al. (1996) provide an excellent summary of the state-of-the-art analysis and current technology of SFDs.

Contributed by the International Gas Turbine Institute and presented at the International Gas Turbine and Aeroengine Congress and Exhibition, Stockholm, Sweden, June 2–5, 1998. Manuscript received by the ASME Headquarters April 1, 1998. Paper No. 98-GT-6. Associate Technical Editor: R. Kielb.

Several test programs and field tests have been conducted to determine the effect of SFDs on the response of rotor-bearing systems and also aimed to validate analysis and computational predictions. In controlled imbalance test rigs, the synchronous rotor response is measured and peak amplitudes evaluated for extraction of damping ratios and identification of system damping coefficients. Thomsen and Andersen (1974) find that SFD direct damping coefficients are independent of the journal amplitude for motions below 25 percent of the radial clearance and show good correlation with a full film (uncavitated) model. Tonnesen (1976) presents impedance measurements of transmitted forces and which allow the identification of damping coefficients of a sealed SFD for both the concentric and the eccentric journal cases. SFDs operating eccentrically yield in general larger damping coefficients than centered dampers.

Kuzdzal and Hustak (1996) compare the effectiveness of five different SFDs (two o-ring centered, two spring centered, and one bottom resting) from rotor imbalance response measurements. The test results validate predictions where effective viscous damping coefficients raise as the journal center is statically offset. However, when a subsynchronous driving force is present as an excitation, off-centered and bottom resting dampers show larger levels of subsynchronous vibration than centralized SFDs. San Andrés and Lubell (1998) perform measurements of the rotor response due to imbalance for centered damper journals and increasing lubricant temperatures. The test cylindrical open-ends dampers are supported with long steel bars emulating a soft squirrel cage. The rotor responses demonstrate the rotor-SFD system to be well damped with amplification factors ranging from 1.6 to 2.1 while traversing cylindrical and conical critical speeds. The rotor amplitudes of motion are proportional to the imbalances for the first mode of vibration, and the damping coefficients extracted compare reasonably well to predictions based on the full-film SFD model. The measurements demonstrate an absence of non-linear behavior of the rotor-SFD apparatus for the range of imbalances tested.

Zeidan (1995) discusses successful applications of ISFDs in the petrochemical industry. Murphy et al. (1996) perform imbalance tests in a compulsator rotor supported on integral dampers with L-shaped EDM springs. The test rotor-ISFDs response is well damped, linear and without jumps, although criti-

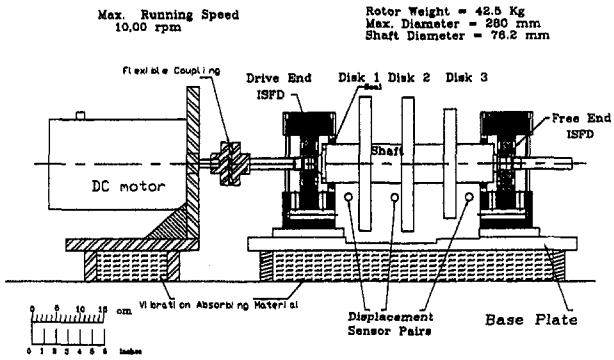

Fig. 1 View of test rig: rotor bearing supported on (integral) ISFDs

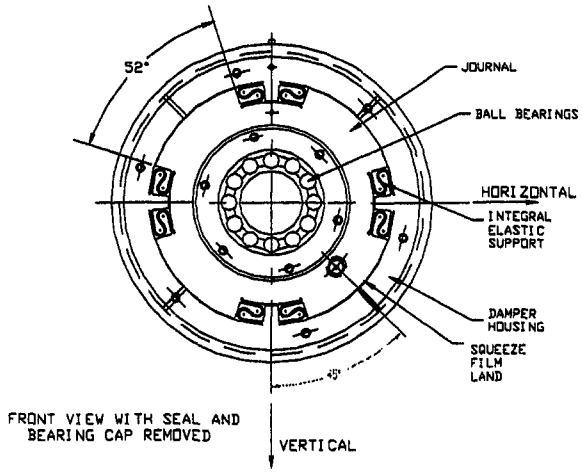

Fig. 2 Integral SFD tested on rotor-SFD test rig

cal speeds relocate due to the differences in theoretical and measured structural stiffnesses.

The objective of this paper is to present measurements of the stiffness and damping coefficients of a pair of ISFDs, to validate analytical predictions, and to demonstrate the dampers' effectiveness in attenuating the dynamic response of a massive rotor subjected to increasing levels of imbalance. The test apparatus and experiments to identify the rotor supports and dampers stiffnesses are detailed. Further experiments are conducted to identify the system damping coefficients from impact load excitations at null rotor speed. Measurements of coast-down rotor responses for various levels of rotor imbalance follow. Damping coefficients are extracted from the peak rotor responses while traversing the first critical speed and compared to predictions form a FEM analysis. The current work extends earlier measurements of the synchronous response of a rotor supported on conventional SFDs (San Andrés and Lubell, 1998).

The Test Rig and Integral Damper Description

San Andrés and Lubell (1998) provide a full description of the test rig shown in Fig. 1. A 7.5 kW DC motor drives the test rotor through a flexible coupling and a drawn cup roller. The rotor consists of a shaft 673 mm (26.5″) long and 76.2 mm (3″) in diameter, with three 25.4 mm (1″) thick disks shrunk fitted at evenly spaced intervals of 63.5 mm (2.5″). Two disks are 280 mm (11″) in diameter, and the third disk is 229 mm (9″). The rotor, with a weight of 42.5 kg (93.7 lb) including the coupling, is supported at a span of 406 mm (16″) on two pairs of high precision ball bearings which are themselves press-fitted inside each damper and provided with forced lubrication.

A lubrication system delivers oil (ISO VG 10) to the inlet damper ports and ball bearings from a 151 liter reservoir through a variable speed gear pump. Three pairs of eddy-current displacement sensors measure the rotor horizontal and vertical displacements at locations next to the middle disk and the inner side of the support housings, and piezoelectric accelerometers detect the supports' vibration. An optical keyphasor facing the shaft coupling detects the rotor speed. Type-*K* thermocouples and pressure gauges monitor the temperature and pressure at the dampers' feed and discharge planes.

The test integral damper depicted in Fig. 2 is composed of four independent 52 deg arcuate squeeze film pads and S-shape thin webs with a design radial stiffness (k_s) of 3.5 MN/m (20 klb/in). The squeeze film lands are machined at a diameter (D) of 96.52 mm (3.8″) with an axial length (L) equal to 23.0 mm (0.91″). The nominal film clearance (C) in operation should be close to 0.230 mm (0.009″). The top and bottom gaps have been machined to ~0.178 mm (0.007″) and ~0.305 mm (0.012″), respectively, so that under the rotor weight deflection they adjust to the desired nominal clearance. Each squeeze film pad is fed with lubricant through a 1.6 mm ($\frac{1}{16}$″) hole located at the center of each pad.

Experiments and Procedures

Controlled experiments are conducted to identify the fundamental rotor-bearing system parameters, to measure the imbalance response of the test rotor supported on ISFDs, and to

Nomenclature

c = nominal damper radial clearance (0.230 mm)
C_{crit} = Critical damping for first mode, $2(K_{eq}M_{eq})^{1/2}$, (N·s/m)
C_V, C_H = System damping coefficients (N·s/m)
C_{ISFD} = ISFD direct damping coefficient (N·s/m)
D = ISFD diameter (96.5 mm (3.8″)
e = Amplitude of rotor motion (μm)
f_{nV}, f_{nH} = First natural frequencies (Hz)
f_{nd} = natural frequency of integral damper (Hz)
k_s = damper structural stiffness (MN/m)
k_B = bearing support stiffness (N/m)
K_{Veq}, K_{Heq} = system equivalent stiffness coefficients (N/m)
L = ISFD length (23 mm (0.91″))
m = imbalance mass (gr)
M_{eq} = equivalent rotor mass for first mode (45.22 kg (99.7 lb))
Q = amplification factor at first critical speed
r = radius for location of unbalance mass (114.3 mm (4.5″))
u = imbalance displacement, $m \cdot r / M_{eq}$ (m)
ξ = system damping ratio, $C/C_{crit} = 1/2Q$

Subscripts

eq = equivalent for system at first mode
H, V = horizontal and vertical directions
D, F = drive end and free end of rotor

Table 1 Measured and computed free–free natural frequencies for test rotor, and rotor and coupling

Frequency		f_1(Hz)	f_2(Hz)	f_3(Hz)	f_4(Hz)
Rotor	test	620	930	1120	1410
	prediction	620	968	1295	--
Rotor & Coupling	test	250	920	1110	1410
	prediction	231	950	1184	1365

Uncertainty in measurements: +/- 4 Hz

extract the equivalent damping coefficients of the ISFDs from the peak rotor response at the first critical speed.

Identification of Rotor Free-Free Modal Frequencies. The rotor is hung with nylon ropes and is subsequently excited in the horizontal direction with a calibrated impulse hammer. The transient response is detected with a piezoelectric accelerometer (26.1 gr) installed through a magnetic base at different locations along the rotor. Table 1 presents a summary of the test natural frequencies along with predictions based on a 38 station-transfer matrix model using a commercial program (Murphy, 1995). The coupling in the rotor causes a sharp reduction of the first natural frequency since this is located at an antinode for the first elastic mode of vibration. The computed predictions are satisfactory and the model is taken to represent well the test rotor and coupling.

Measurement of Integral Damper Radial Stiffness. Precise knowledge of the dampers radial stiffness is needed for accurate prediction of the rotor-bearing system critical speeds. The damper design stiffness (k_s) is of similar magnitude to the squirrel cage SFDs tested by San Andrés and Lubell (1998). Each damper is mounted on a short steel shaft that is clamped on nearly rigid bushing supports. Static loads are applied with a crane to the damper outer rim and deflections of the shaft and rim are recorded with displacement sensors. The force is measured with a strain-gage load cell in series with the cable transmitting the load.

The damper stiffness is extracted as the slope of the applied load vs. displacement measurements on its linear range. Tests are conducted at 45 deg intervals, for loads directed towards a damper pad or in between pads. Regions of linear and nonlinear stiffness are identified, since a noticeable hardening of the damper occurs from progressive solid contact between the damper pads and lands. Figure 3 shows the applied load versus damper deflections for the two integral dampers designated as #1 (drive end side) and #2 (free end side). The plots depict results from tests along the vertical (⇓ gravity, 0 deg and 180 deg) and horizontal directions (90 deg and 270 deg). Note that the larger linear range occurs at 0 deg, when loads are applied towards the bottom damper pad which has the largest clearance (~0.305 mm). The test damper stiffness coefficients in the vertical and horizontal directions are equal to

$$\text{ISFD drive end: } k_{sDV} = 3.66 \text{ MN/m}, \; k_{sDH} = 3.80 \text{ MN/m}$$

$$\text{ISFD free end: } k_{sFV} = 3.50 \text{ MN/m}, \; k_{sFH} = 3.53 \text{ MN/m} \quad (1)$$

The standard error for 95 percent certainty in the measurements is just 149 N/m. The test stiffnesses are reasonably close to the design value, and the differences are attributed to machining inaccuracies. Each damper stiffness is also verified from its fundamental natural frequency in the free–free transverse mode and the estimated outer and inner ring masses from CAD draw-

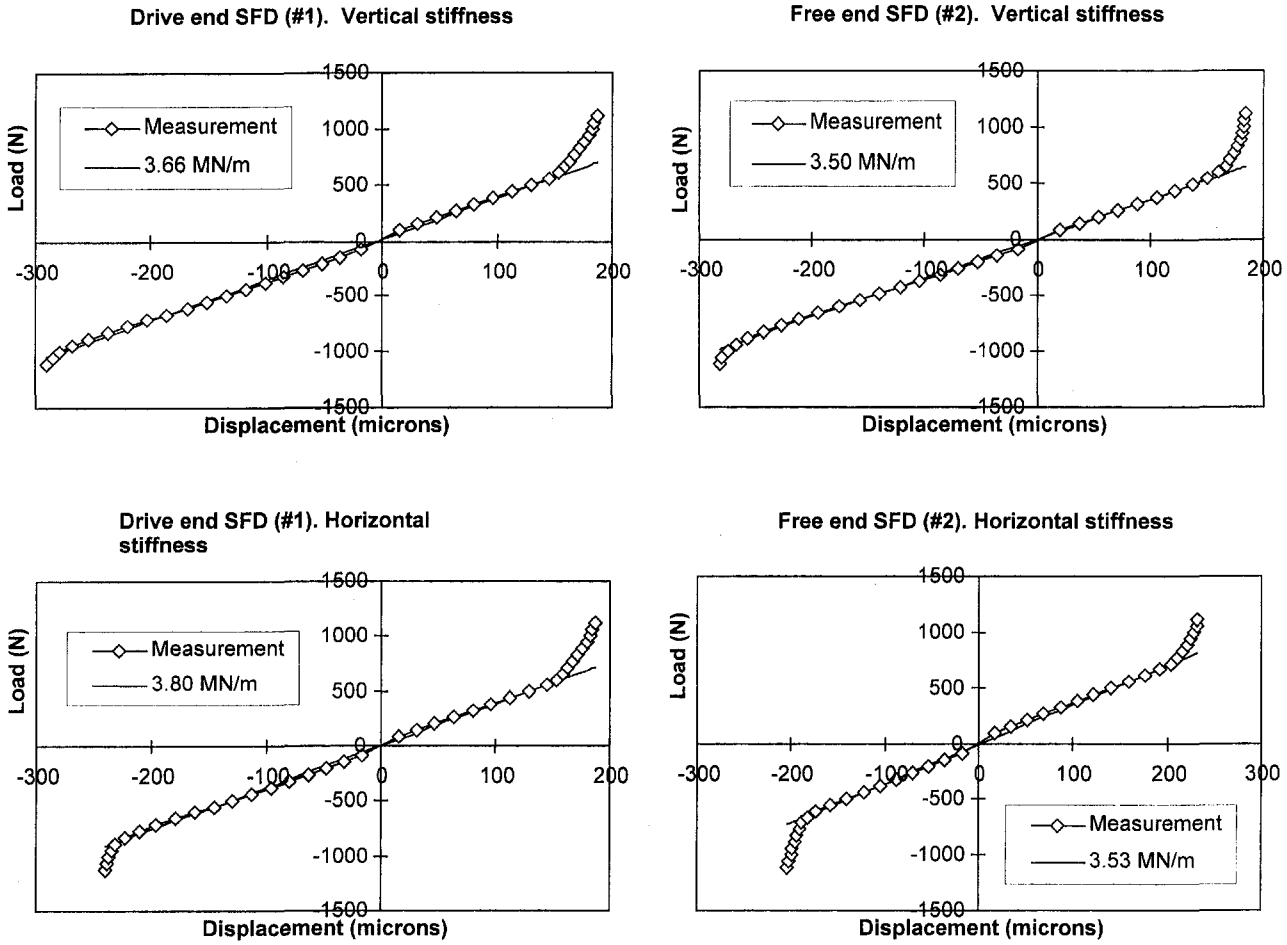

Fig. 3 Vertical and horizontal structural stiffness coefficients of integral dampers for drive-end and free-end supports

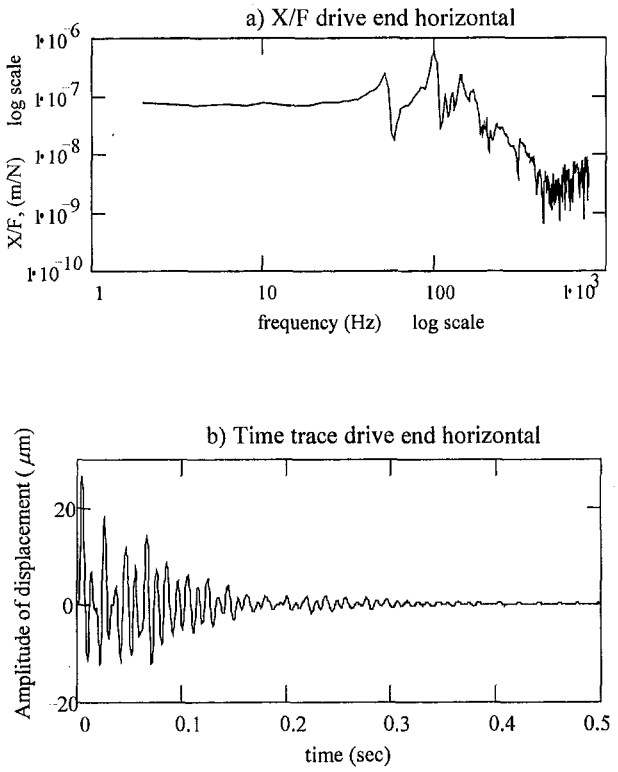

Fig. 4 Identification of drive end support stiffness from impact tests. Horizontal direction: (*a*) transfer function (displacement/load); (*b*) displacement versus time.

ings. See de Santiago et al. (1997) for further details on the tests conducted.

Natural Frequency of Test Rotor Supported on ISFDs. Rap measurements of the test-rotor supported on ISFDs are conducted to identify the system damped natural frequencies and the fundamental damping ratio. A calibrated impact hammer excites the rotor and an accelerometer magnetically attached to the middle-disk collects the rotor vibration at zero rotational speed. The fundamental (lowest) natural frequencies for the cylindrical rigid mode of vibration are f_{nH} = 52 Hz and f_{nV} = 56 Hz in the horizontal and vertical directions, respectively. These results denote (a) asymmetry in the support stiffness, and (b) equivalent support stiffnesses lower than those measured for the integral dampers alone.

An estimate for the equivalent stiffness of the rotor-bearing system is determined from the relationship $K_{eq} = M_{eq}(2\pi f_n)^2$, where ($M_{eq}$ = 45.2 kg) is the equivalent mass of the rotor-ISFDs system and f_n is the natural frequency for the first mode of rotor vibration on soft supports. The estimated equivalent stiffness (K_{eq}) along with the critical damping ($C_{crit} = 4\pi M_{eq} f_n$) for the fundamental mode of vibration are given below as

$$K_{eqH} = 4.82 \text{ MN/m}, \; C_{critH} = 29{,}942 \text{ NM.s/m}$$

$$K_{eqV} = 5.59 \text{ MN/m}, \; C_{critV} = 31{,}758 \text{ NM.s/m} \qquad (2)$$

These equivalent system stiffnesses are lower than the design value of $2 \cdot k_s$ = 7.0 MN/m, i.e., from the dampers' structural stiffness alone. The tests make evident that the bearing support structures are flexible.

Support Transfer Functions and Equivalent Impedance for Rotor-Bearing Model. Eddy current displacement sensors are rigidly attached to the test rig table to record the supports' horizontal and vertical motion resulting from impacts with a calibrated hammer. Figure 4 shows the measured support horizontal displacements and averaged (from 10 impacts) transfer functions for the drive end support. Coherence functions show a good correlation (>0.98), and, thus, the frequency response data allows expedient identification of the support flexibility. The tests show the bearing supports to be more rigid in the vertical direction as noted in Table 2. Most importantly, the vibration spectra shows structural resonances at around 50 Hz (due to the rotor) and ~100 Hz. The standard deviation for the measurement of the vertical (drive end) support stiffness indicates poor confidence for this test.

Table 2 Test bearing support stiffness (k_B) from impact tests

Stiffness	Vertical (MN/m)	Horizontal (MN/m)
Drive End support	30.66 ± 17.9	13.95 ± 0.72
Free end support	28.19 ± 5.5	10.10 ± 0.77
Equivalent drive end	3.17	2.82
Equivalent free end	3.11	2.76
Sum of free & drive ends	6.28	5.58
System from eqn. (2)	5.59	4.82

At each support, the bearings and integral dampers are in series, and consequently, equivalent bearing stiffness coefficients are easily obtained. The sum of the free end and drive end equivalent stiffnesses represents well the identified system stiffness given in Eq. (2).

Measurements of System Damping From Rap Tests. Rap tests of the test-rotor supported on ISFDs are conducted to identify the system damped natural frequencies and the fundamental damping ratio. A calibrated impact hammer excites the rotor and an accelerometer magnetically attached to the middle disk collects the vibration signatures from a number of impacts at zero rotational speed. Figure 5 shows a typical rotor acceleration time response to an impact excitation and the average (acceleration/load) transfer function from 10 impacts in the vertical direction. A similar procedure is carried out in the horizontal direction. The damping coefficients are extracted from least-

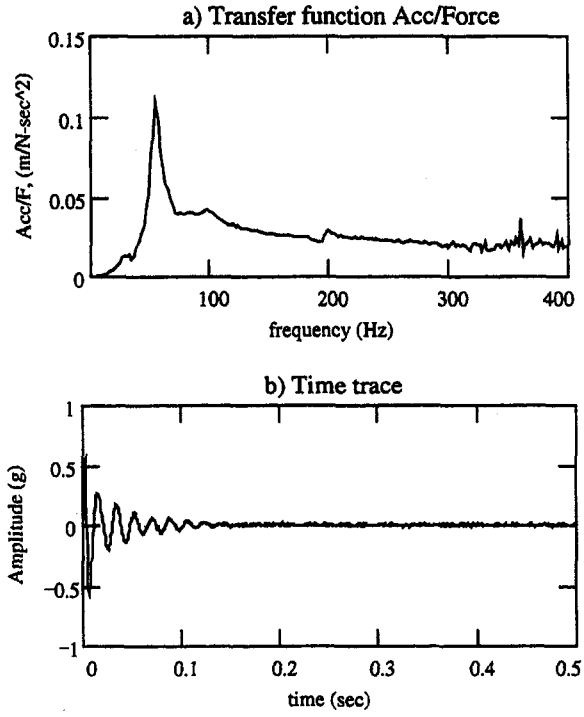

Fig. 5 Rotor acceleration response for impact tests at middle disk and at zero rpm with oil at 23°C. Vertical direction (*a*) Transfer function (acceleration/load) (*b*) Acceleration versus time.

Table 3 Identified system damping coefficients from RAP tests for increasing lubricant temperatures

Oil temperature (° C)	Viscosity (cp)	Damping Horizontal C_H (N.s/m)	Damping Vertical C_V (N.s/m)
22.8	16.7	2,560	2,749
23.7	16.2	2,388	2,821
24.7	15.5	2,115	2,809
29.5	13.0	1,903	2,709
37.7	9.57	1,731	2,555
DRY	(no oil)	950.4	1,687

f_{nH}=54 Hz, f_{nV}=58 Hz. Uncertainty in measurements ~ 175.3 N.s/m

square envelope fit and log decrement estimations from time domain decay responses and their respective transfer functions. The system damping coefficients given in Table 3 show a linear dependency on the oil viscosity. Note also the large (dry) structural damping coefficient in the test rig.

Test Rig Synchronous Imbalance Responses. The rotor is balanced by applying a least-square balancing technique to minimize its vibrations over the whole speed range, including the critical speeds. Small calibrated weights (m = 5, 10, 13, 17 gr) are inserted in the rotor middle disk at a radius r = 114.3 mm (4.5"), and corresponding to imbalance displacements (u) equal to 12.6, 25.2, 32.8, and 42.9 μm, respectively. In each test, the rotor is brought rapidly to a top speed of 10 krpm, the drive shut down, and the coast-down response measured. Each test is conducted twice at an average lubricant temperature of 23°C (73.5°F) and feed pressure equal to 0.70 bars (10 psig).

The measurements include six rotor displacements and the acceleration of each support pedestal. Figure 6 depicts the vertical and horizontal synchronous rotor responses near the middle disk for the various imbalances. These responses are slow-roll compensated at 500 rpm and the baseline (no imbalance) response is also subtracted at every speed. Very similar results are obtained at the rotor drive and free end planes (see, De Santiago et al., 1997). The rotor direct responses are mainly synchronous for all speeds, and with horizontal and vertical critical speeds excited at 3050 rpm (51 Hz) and 3300 rpm (55 Hz), respectively. The amplitudes of motion in the horizontal plane are typically larger than in the vertical plane, thus indicating smaller levels of damping in this direction and consistent with the lower support stiffness. Note that the rotor critical speeds do not shift as the imbalance increases, thus indicating the integral dampers do not generate any oil stiffness even for large rotor orbital motions.

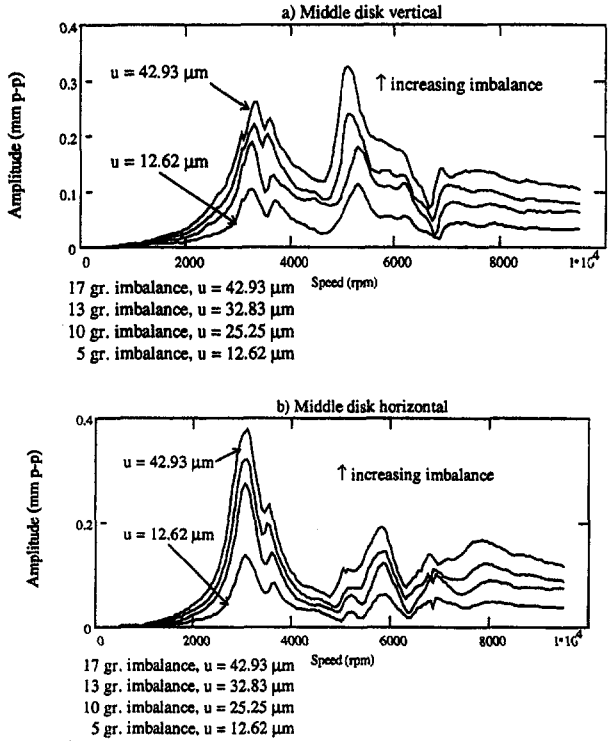

Fig. 6 Synchronous imbalance response near middle disk for various levels of imbalance displacements (*a*) vertical (*b*) horizontal

Table 4 Identified values of system damping ratio and damping coefficients from measurements at cylindrical mode critical speeds

imbalance u (μm)	Average amplitude (μm)	e/c	Amplification factor Q	Damping ratio ξ	*system* damping (C_V) N.s/m
12.62	53	0.231	4.20	0.119	3,790 ± 4.15%
25.25	95	0.415	3.76	0.133	4,233 ± 2.39%
32.83	115	0.502	3.50	0.143	4,550 ± 2.01%
42.93	140.5	0.614	3.27	0.153	4,874 ± 1.76%
			average	vertical	**4,362**

imbalance u (μm)	average amplitude (μm)	e/c	Amplification factor Q	Damping ratio ξ	*System* damping (C_H) N.s/m
12.62	64.5	0.282	5.11	0.098	2,893 ± 3.50%
25.25	128.5	0.561	5.09	0.098	2,906 ± 1.90%
32.83	152.0	0.664	4.63	0.108	3,194 ± 1.82%
42.93	180.0	0.786	4.19	0.119	3,519 ± 1.78%
			average	horizon	**3,128**

Estimation of ISFD Damping Coefficients and Comparison to Predictions. The amplification factor (Q) at the first critical speed is easily determined by the ratio of the rotor amplitude to the imbalance (u) while traversing the first critical speeds. From this result, estimates of the damping ratio (ξ = $1/2Q$) are also extracted. Finally, system-damping coefficients are calculated by multiplying ξ times the critical damping coefficients (C_{crit}) in each direction, vertical and horizontal. Table 4 summarizes the results with percent values noting the estimated uncertainty for each damping coefficient. The average peak amplitude divided by a nominal SFD radial clearance (c = 0.230 mm) intends to highlight the size of the journal whirl orbits within the clearance.

The system damping coefficients ($C_{H,V}$) increase with the magnitude of the imbalance, thus showing a dependency on the rotor amplitude of motion. Subtraction of the dry damping coefficients (Table 3) from the system damping values allows the estimation of the viscous damping coefficients due solely to the ISFDs[1]. In this procedure it is assumed both ISFDs provide identical amounts of damping and that the inherent structural (dry) damping does not vary with the amplitude of rotor motion.

A finite element program to model the squeeze film flow and forces from each pad of an ISFD allows the prediction of the viscous damping coefficients as a function of the operating fluid viscosity, whirl frequency, and amplitude of journal motion. The predicted and estimated ISFD damping coefficients from the imbalance measurements are depicted in Fig. 7. Computed results based on a full film model (no oil cavitation) correlate well with the test damping coefficients in the vertical direction.

[1] Of course this assumes the rotor-bearing system response to be linear. This argument is strongly supported by the measured responses.

However, the predicted damping values in the horizontal direction are larger than the estimations from the measurements since the rotor and journal displacements are larger in this direction. Note that the test damping coefficients show an approximate linear behavior with the journal amplitude, whereas the predictions are basically nonlinear. The experimental linear behavior of the ISFDs damping coefficients is also found in earlier tests with conventional SFDs (San Andrés and Lubell, 1997).

Support pedestal horizontal acceleration measurements indicate these to move significantly. Refer to De Santiago et al. (1997) for a full description of the measurements, the estimated amplitudes of motion and their magnitude relative to the rotor displacement measurements.

Computed predictions for the linear imbalance response of the rotor-ISFDs system are shown in Fig. 8 along with the measured response for the largest imbalance tested. The analysis assumes that each bearing support contributes $\frac{1}{2}$ the value of the estimated fundamental system damping. Note that the imbalance weights are inserted at the middle disk (very near to the rotor's transversal inertia axes), and consequently the excitation of any other mode but the cylindrical one should be insignificant. The predictions match very well the rotor response at the first critical speeds. However, the calculated responses fail to reproduce the measured large amplitudes of motion in the range of 5.5 to 6.5 krpm. Recall that support impedance measurements (Fig. 4) show a resonance around 95 Hz; thus explaining the large measured amplitudes over the referred speed range.

Conclusions

A test program to study the performance of integral squeeze film dampers is detailed. Application of integral dampers into aircraft jet engines could bring reductions in weight and length, accuracy of positioning, and a split configuration for easier assembly, inspection and retrofit.

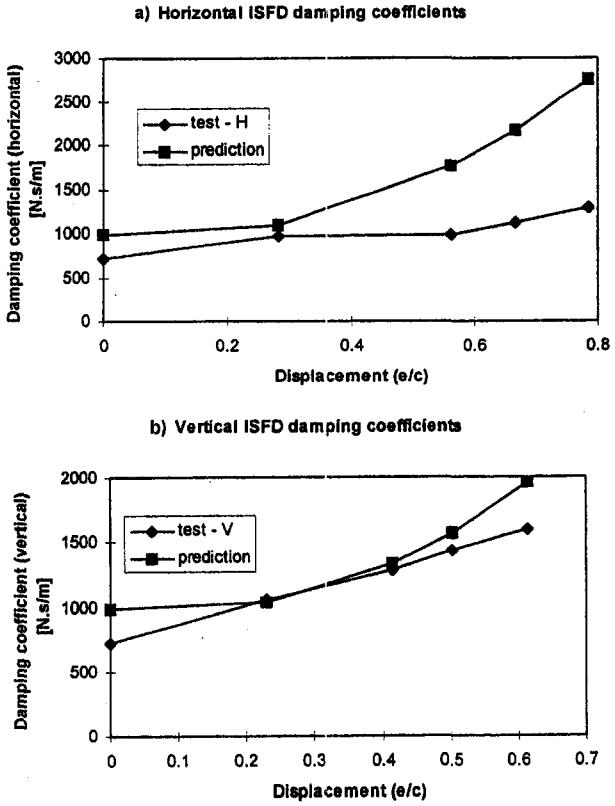

Fig. 7 ISFDs' damping coefficients estimated from imbalance tests and predictions versus average journal center displacement: (*a*) horizontal; (*b*) vertical

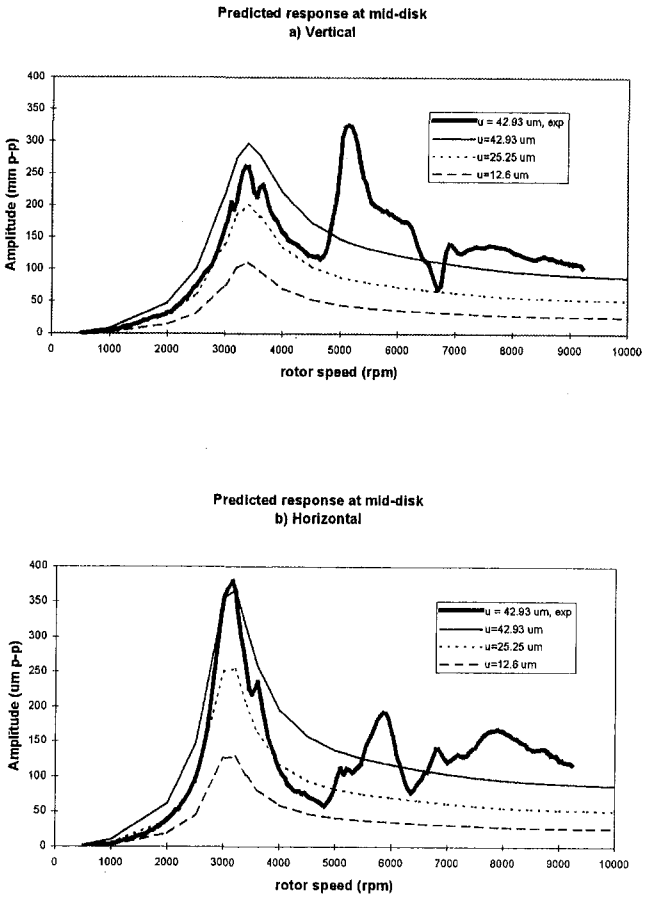

Fig. 8 Predicted synchronous imbalance responses at rotor middle disk for various levels of mass imbalance and experimental response for 17gr imbalance mass (compensated) (*a*) vertical (*b*) horizontal

The experiments are conducted on a massive, three-disk rotor supported on integral dampers. System damping coefficients extracted from impact rap tests increase with the lubricant viscosity, and include the contribution of the structural damping from the support pedestals. Measurements of the synchronous rotor response with increasing imbalance weights are performed in coast-down tests from 10 krpm.

The tests show the ISFDs to restrain well the rotor response for the cylindrical modes of vibration. Peak vibration amplitudes at the first critical speed are proportional (linear) to the magnitudes of applied imbalance. Large rotor whirl amplitudes up to 80 percent of the nominal ISFD clearance are measured, with no shifts of the first critical speed, thus denoting an absence of damper stiffness hardening. Computed imbalance responses predict well the passage through the first critical speed but fail to reproduce a support resonance at about 6 krpm.

The test system damping coefficients increase slightly with increases in the rotor whirl amplitude (larger imbalances). The identified ISFDs damping coefficients correlate favorably with predictions from a full hydrodynamic film, finite element model.

Acknowledgments

The support of National Science Foundation and the Texas A&M Turbomachinery Consortium are gratefully acknowledged. Thanks to KMC, Inc. for donation of the integral dampers.

References

Arauz, G., and San Andrés, L., 1994, "Effect of a Circumferential Feeding Groove on the Force Response of a Short Squeeze Film Damper," *ASME Journal of Tribology*, Vol. 116, No. 2, pp. 369–377.

De Santiago, O., Oliveras, J., and San Andrés, L., 1997, "Imbalance Response of a Rotor Supported on Integral Open Ends, SFDs," *Turbomachinery Research Consortium,* TRC-SFD-2-97, May, Texas A&M University, College Station, TX.

Kuzdzal, M. J., and Hustak, J. F., 1996, "Squeeze Film Damper Bearing Experimental vs. Analytical Results for Various Damper Configurations," Proceedings, 25th Turbomachinery Symposium, Houston, TX, pp. 57–70.

Mohan, S., and Hahn, E. J., 1974, "Design of Squeeze Film Dampers for Rigid Rotors," *ASME Journal of Engineering for Industry,* Vol. 96, pp. 976–982.

Murphy, B. T., 1995, *X LROTOR*, Rotating Machinery Analysis, Inc., Austin, TX.

Murphy, B. T., Manifold, S. M., and Kitzmiller, J. R., 1996, "Compulsator Rotordynamics and Suspension Design," Proceedings, 8th Electromotive Launcher Symposium, pp. 21–24.

San Andrés, L., and Lubell, D., 1998, "Unbalance Response of a Test Rotor Supported on Squeeze Film Dampers," ASME JOURNAL OF ENGINEERING FOR GAS TURBINES AND POWER, Vol. 120, No. 2, pp. 397–404.

San Andrés, L., and Vance, J. M., 1988, "Effect of Fluid Inertia on the Performance of Squeeze Film Damper Supported Rotors," ASME JOURNAL OF GAS TURBINES AND POWER, Vol. 110, pp. 51–57.

Thomsen, K. K., and Andersen, H., 1974, "Experimental Investigation of a Simple Squeeze Film Damper," *ASME Journal of Engineering for Industry,* Vol. 96, pp. 427–430.

Tonnesen, J., 1976, "Experimental Parametric Study of a Squeeze Film Bearing," *ASME Journal of Lubrication Technology,* Vol. 98, April, pp. 206–213.

Zeidan, F. Y., 1995, "Application of Squeeze Film Dampers," *Turbomachinery International,* Sept/Oct., pp. 50–53.

Zeidan, F. Y., San Andrés, L., and Vance, J. M., 1996, "Design and Application of Squeeze Film Dampers in Rotating Machinery," Proceedings, 25th Turbomachinery Symposium," Houston, TX, pp. 169–188.

Aerodynamically Induced Radial Forces in a Centrifugal Gas Compressor: Part 2—Computational Investigation

M. B. Flathers
Solar Turbines Inc.,
9330 Skypark Court,
San Diego, CA 92123

G. E. Baché
Advanced Scientific
Computing Corporation,
El Dorado Hills, CA

Radial loads and direction of a centrifugal gas compressor containing a high specific speed mixed flow impeller and a single tongue volute were determined both experimentally and computationally at both design and off-design conditions. The experimental methodology was developed in conjunction with a traditional ASME PTC-10 closed-loop test to determine radial load and direction. The experimental study is detailed in Part 1 of this paper (Moore and Flathers, 1998). The computational method employs a commercially available, fully three-dimensional viscous code to analyze the impeller and the volute interaction. An uncoupled scheme was initially used where the impeller and volute were analyzed as separate models using a common vaneless diffuser geometry. The two calculations were then repeated until the boundary conditions at a chosen location in the common vaneless diffuser were nearly the same. Subsequently, a coupled scheme was used where the entire stage geometry was analyzed in one calculation, thus eliminating the need for manual iteration of the two independent calculations. In addition to radial load and direction information, this computational procedure also provided aerodynamic stage performance. The effect of impeller front face and rear face cavities was also quantified. The paper will discuss computational procedures, including grid generation and boundary conditions, as well as comparisons of the various computational schemes to experiment. The results of this study will show the limitations and benefits of Computational Fluid Dynamics (CFD) for determination of radial load, direction, and aerodynamic stage performance.

Introduction

Aerodynamically induced radial forces in rotating machinery have been extensively studied and reported. Unfortunately, these studies have focused on centrifugal pumps. Modern industrial centrifugal gas compressors require an effective discharge system to meet aggressive efficiency and usable flow range objectives. To this end, single-tongue volutes are coupled with high efficiency impellers to maximize aerodynamic performance. These industrial centrifugal gas compressors can operate at very high suction pressures, nearly 1000 psi (6895 kPa) and higher, resulting in measurable radial forces. Double volutes, when properly designed, can reduce radial forces at off-design conditions, but the resulting casting will be quite complex and more difficult to manufacture. In the quest for improved aerodynamic performance, a compressor designer cannot lose sight of the rotordynamic behavior nor the producibility.

As observed in centrifugal pumps, nonuniform pressure distributions about the circumference of the impeller arise during off-design operation of the compressor. Guelich et al. (1986) reviewed, in some detail, the design parameters that affect radial force. A further summary of the applicable open literature can be found in de Ojeda and Flack (1992).

Stepanoff (1957) suggested that the radial force was a function of the discharge pressure, impeller tip diameter, impeller tip width, and a constant. The equation has the following form:

$$F_r = K_r P_e D_2 L \tag{1}$$

where K_r is a nondimensional radial load coefficient that varies with volume flow. This constant was experimentally derived and has the following form:

$$K_r = 0.36[1 - (Q/Q_n)^2], \tag{2}$$

where Q_n is the volume flow at the nominal design condition. It is evident from Eqs. (1) and (2) that rotational speed effects are not directly accounted for, and the radial force is zero at design flow and maximum at zero flow.

Agostinelli et al. (1960) completed an experimental investigation to understand the effects of specific speed and pump housing geometry on radial force. The authors concluded that low specific speed volute pumps had much flatter radial force characteristics than did higher specific speed volute pumps. In addition, the authors showed that the minimum force occurred at higher volume flows with higher specific speed pumps. The authors also proposed a new K value for Eq. (1) based on both specific speed and volume flow. Although 15 pumps were tested between an $Ns = 25$ and an $Ns = 112$, only one pump, an $Ns = 165$, was tested above an $Ns = 112$. No equation was derived from the data base to use in a design mode.

The objective of this paper is to use a commercially available CFD code to analyze the aerodynamic components of a high specific speed ($Ns = 180$) centrifugal gas compressor that affects radial load and direction, and compares them with the experimental findings. In addition, stage aerodynamic performance is extracted from the CFD solutions and compared with that available from PTC-10 testing.

Experimental Study

Part 1 of this paper (Moore and Flathers, 1998) detailed the experimental methodology to calculate the radial force and

Contributed by the International Gas Turbine Institute and presented at the 41st International Gas Turbine and Aeroengine Congress and Exhibition, Birmingham, United Kingdom, June 10–13, 1996. Manuscript received by the ASME Headquarters March 3, 1997. Paper No. 96-GT-352. Associate Technical Editor: J. N. Shinn.

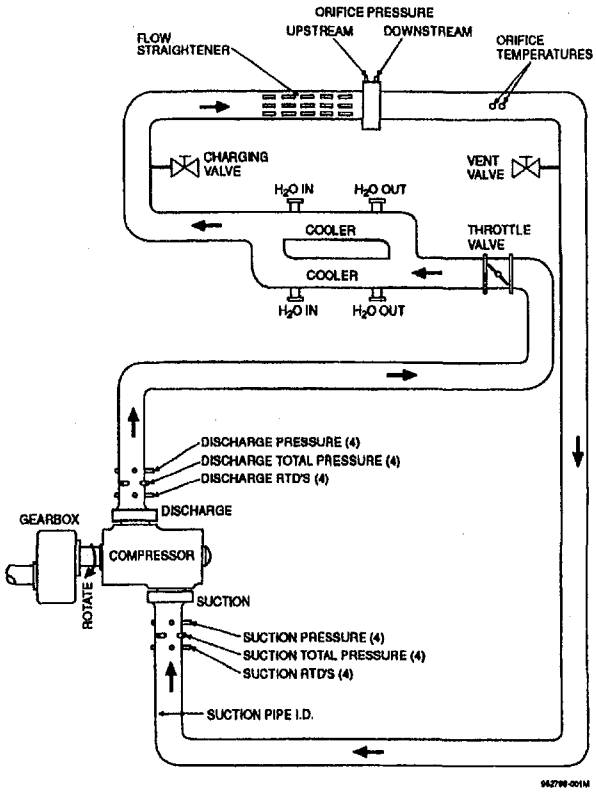

Fig. 1 Closed-loop test facility

direction by measuring the shaft centerline locus in the tilt-pad bearings, both in factory and field testing. Aerodynamic stage performance measurements were also acquired as part of closed-loop inert gas testing in accordance with ASME PTC-10 (1986) and PTC-19 (1959).

Test Facility. The test facility used in this study is a closed-loop arrangement capable of testing in accordance with PTC-10. A schematic of the closed-loop test facility is shown in Fig. 1. The test compressor is driven by a slave gas turbine engine capable of delivering greater than 3500 hp (2600 kW). A gearbox is also used to provide proper speed matching with the test compressor. Both the driven and compressor skids are fully instrumented for operation and control, as well as compressor mechanical and aerodynamic performance. Standard compressor instrumentation includes the following: temperature, pressure, flow, speed, vibration, and gas properties.

Temperature measurements include the following: four resistance temperature detectors (RTD's) at both compressor suction and discharge; two RTDs five diameters downstream of the orifice plate; one RTD for ambient conditions; two type-K thermocouples at both inlet and outlet for radial bearing lube oil; and two type-K thermocouples at both compressor suction and discharge for seal gas vent.

Pressure measurements include the following: four Kiel probes at both compressor suction and discharge; one delta-P across the orifice plate; and one static pressure upstream of the orifice plate.

Flow measurements include the following: compressor gas flow calculation with program FTAP from PTC-19 using orifice pressure, delta P and temperature as input; radial bearing lube oil flow at both suction and discharge ports with turbine flow meter; and seal gas vent flow at both suction and discharge ports with rotometers.

Gas properties are calculated from the gas composition. A continuous gas analyzer was used to measure the oxygen content in the nitrogen gas used for testing. All testing was conducted with pure nitrogen.

Vibration measurements include both X and Y probes for both suction and discharge radial bearings. The state-of-the-art data gathering employed a micro-Vax based data acquisition system and Bently-Nevada's ADRE for Windows vibration analysis system capable of performing both digital signal processing of the dynamic signal from the eddy-current proximity probes, as well as capturing DC probe gap voltage. Speed is measured using a Keyphasor.

Test Article. The subject compressor under evaluation is a single-stage centrifugal gas compressor for natural gas pipeline boosting (Fig. 2). The aerodynamic components include a radial inlet with radial inlet guide vanes, a mixed flow impeller, a vaneless radial diffuser, and a discharge volute. Further information on the performance of the radial inlet with radial inlet guide vanes can be found in Flathers et al. (1994). The 11-bladed mixed flow impeller is a high flow, low head design with a specific speed of 180 and diameter of 15.8 in. (401.3 mm). The design flow coefficient (ϕ) is 0.12 and the design head coefficient (ψ) is 0.75. The volute is sized for no pressure recovery from the radial vaneless diffuser exit to the volute throat at the design flow.

Test Procedure and Results. The compressor was operated for one hour prior to aerodynamic testing for heat soaking purposes. Testing was conducted at four rotational speeds (8275, 11,150, 12,340, and 14,300 rpm), from choke to surge, with a minimum of eight operating points per speed line. Steady-state conditions were typically reached 15 to 30 min after reaching the desired operating point. The test was run with primarily 300 psia (2068 kPa) suction pressure, although this was lowered to 150 psia (1034 kPa) at 14,300 rpm due to slave driver power limitations. Multiple data points at each flow/speed condition and repeat tests were conducted to ensure a data accuracy of approximately ±1 percent.

The nondimensional head versus flow results, including efficiency, are shown in Fig. 3 for the equivalent design speed. The inlet flow coefficient (ϕ) is defined as

$$\phi_1 = Q_1/[(\pi(D_2^2/4)]U_2, \quad (3)$$

Nomenclature

F = force (lbf)
K_r = nondimensional radial load coefficient
P = pressure (psia)
D = diameter (in.)
L = axial length of impeller (in.)
Q = volume flow (cfm)
Ns = specific speed (English units)
ϕ = inlet flow coefficient
U = impeller wheel speed (fps)
ψ = head coefficient
H = head (ft-lbf/lbm)
g = gravitational constant
η = efficiency
Pr = pressure ratio (P_e/P_i)
k = specific heat ratio
SG = specific gravity
Z = gas compressibility
Tr = temperature ratio (T_e/T_i)

Subscripts

n = nominal design flow
r = radial
1 = impeller inlet
2 = impeller exit
i = compressor inlet
e = compressor exit
is = isentropic

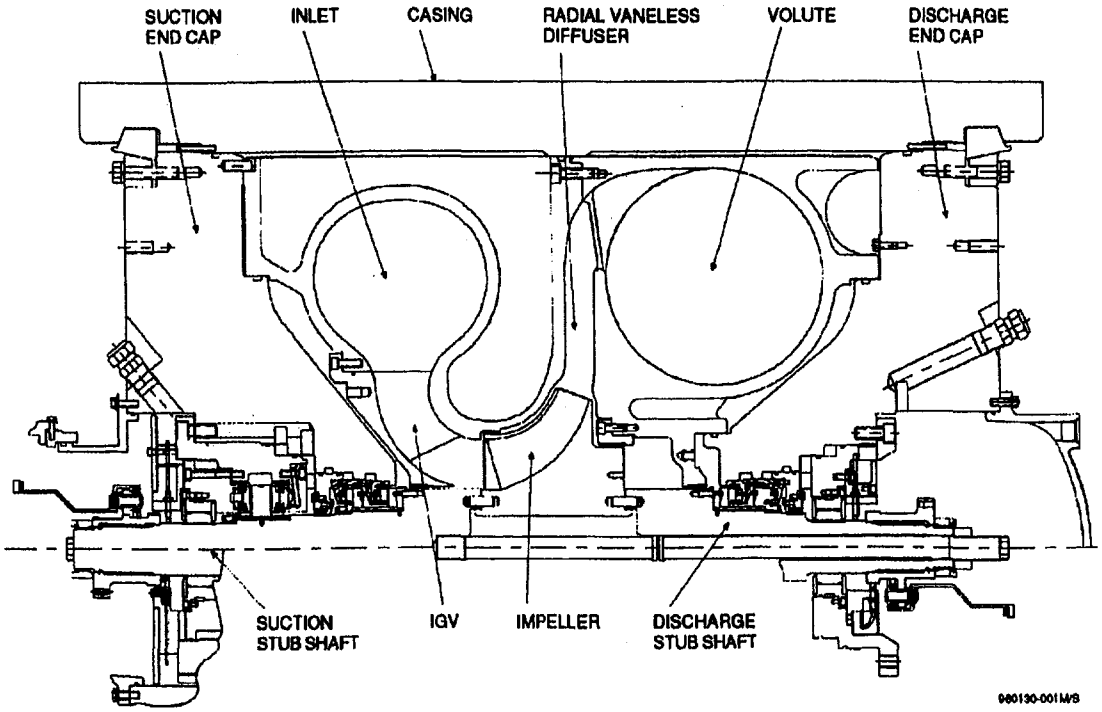

Fig. 2 Pipeline compressor cross section

the isentropic head coefficient (ψ_{is}) is defined as

$$\psi_{is} = H_{is}/(U_2^2/2g), \tag{4}$$

and the isentropic efficiency (η_{is}) is defined as

$$\eta_{is} = Pr^{k-1/k} - 1/(Tr - 1). \tag{5}$$

Although aerodynamic performance data were taken at four rotational speeds, radial load data were only taken at 14,300 rpm. However, radial load data at 11,150 rpm at higher suction pressures was taken during field testing of the same compressor.

Computational Methodology

The CFD code TASCflow (1994) was used for the numerical investigation. TASCflow solves the Reynolds stress averaged Navier-Stokes equations in primitive variable form, and is applicable to incompressible and compressible (subsonic, transonic, and supersonic) flows. The effects of turbulence were modeled using the standard k-ϵ turbulence model.

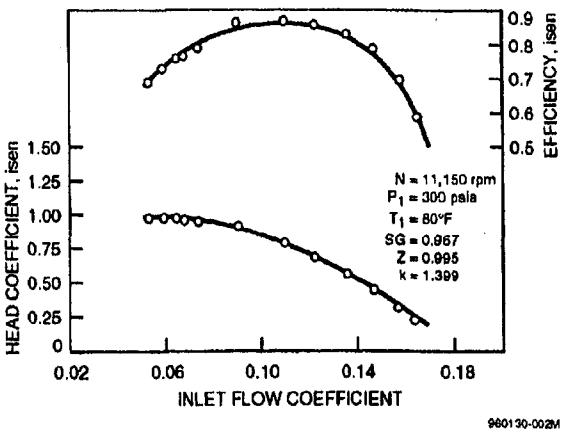

Fig. 3 Closed-loop test results

The code allows for modeling of extremely complex geometries, as is evident from the solutions presented in this report. A general nonorthogonal, boundary-fitted, structured grid is utilized. Often the domain of interest does not lend itself to subdivision by a single-structured mesh. For these situations, the code allows the user to connect simple blocks into a multiblock assembly. A convenient feature is that the grids are not required to match at the connection interface, and they need not even be contiguous. The preprocessor will make the necessary adjustments to ensure a "leak-proof" connection. Further modeling flexibility is possible through the ability to handle internal objects, pinched grids, and local grid refinement (also known as "grid embedding"). With the exception of grid embedding, each of the above capabilities was exercised by this numerical investigation and will be discussed in more detail in later sections.

The computational technique employs an element-based finite volume method. Pressure/velocity coupling is handled using a fourth-order pressure redistribution method that is standard for pressure-based (as opposed to density-based, time marching) codes. The domain is subdivided into hexahedral elements, which are the building blocks of the discretization. Volumes are constructed by the appropriate subdivision of the elements. The discretization scheme employed is second-order accurate. Its two key components are a directionally sensitive, upwind discretization scheme known as Linear Profile Skew upwinding (LPS), combined with a physically based correction term known as Physical Advection Correction (PAC) (Galpin et al., 1986; Schneider and Raw, 1986; Van Doormaal et al., 1987). Together, these schemes reduce solution errors that would naturally arise due to flow directionality and streamwise gradients. The result is a discretization scheme that exhibits very low levels of false total pressure loss, a property that is very important to the present investigation.

Another factor which is key to the feasibility of the scheme is the method used to solve the linearized algebraic equations. TASCflow uses an implicit, coupled-iterative solution method that is accelerated by a multi-grid method known as Additive Correction Multigrid (Van Doormaal et al., 1986; Hutchinson

and Raithby, 1986; Hutchinson et al., 1988). The strengths of this method, from the point of view of the user, are that it is very efficient and robust over a wide range of problems. It requires no user intervention, solution cost increases only linearly with increase in the number of nodes, and it can handle the wide range of control volume sizes and shapes commonly encountered in turbomachinery applications.

CFD techniques exist for predicting flows separately in rotating and stationary frames of reference. In many cases, single-component analysis is completely adequate. In other situations, as in this case, the impeller and volute must be solved for as a coupled system. If solved separately, the impeller would not feel the presence of the nonuniform circumferential pressure gradient produced by the volute, and the computed radial load would thus be zero at all flows. Two approaches were utilized during the analysis which allowed different frames of reference to contact each other, such that the solutions on either side of the interface are preserved in the appropriate frame of reference.

The first approach used was to analyze the impeller and volute as separate components sharing a common radial vaneless geometry. A coupled solution, one which models the impact of the impeller on the volute and the volute on the impeller, was achieved by performing manual iterations. This method will thus be referred to as "Manual Frozen Rotor." With this approach, frame change across the interface is allowed without relative position change over time and without any interface averaging. Steady, three-dimensional flow in the rotating frame of reference was first computed in the impeller. The full impeller (all blade passages) was modeled since modeling of a single passage was inadequate to compute radial load. Predicted impeller exit flow provided an inflow boundary condition for volute analysis. Steady, three-dimensional volute analysis in the stationary frame of reference followed. Results were used as an exit boundary condition for subsequent impeller analysis. This manual procedure, alternately solving the impeller and then the volute, was repeated until convergence was achieved.

The second approach used was to analyze the impeller and volute in a single-computational model. A sliding interface was established between the two components. Steady-State Multiple Frame of Reference (MFR) analysis was employed. Numerical details of this methodology are outlined in Galpin et al. (1995). Two steady-state MFR methods are available: stage and frozen rotor. For both MFR methods, frame change and communication across the interface is automatic but handled very differently. Stage methodology utilizes a conservative circumferential averaging at the sliding interface. This approach is inappropriate for the current study and was not used. The circumferential pressure gradient coming from the volute would be averaged out in the process of convergence; thus, integrated radial load would be zero. The other method, frozen rotor, achieves frame change across the interface without relative position change over time and without any interface averaging. This was the approach used and will be referred to as "coupled frozen rotor." Local flow features are allowed to transport across the interface; thus, pressure nonuniformities in the volute are allowed to propagate to the impeller which can result in radial load.

Both approaches, manual frozen rotor and coupled frozen rotor, neglect the true unsteady nature of the flow at the interface; thus, they represent steady solutions for the impeller/volute geometry at one fixed angular offset of the impeller trailing edge relative to the volute tongue. The coupled frozen rotor approach is obviously much preferred over the manual method. It requires much less user intervention. The manual approach only has value if the CFD code being used does not have MFR capability.

Grid Generation. The impeller grid was generated using TASCgrid with existing impeller grid generation templates. The volute grid was developed using TrueGrid (1994) with IGES files created in CADDS (1994).

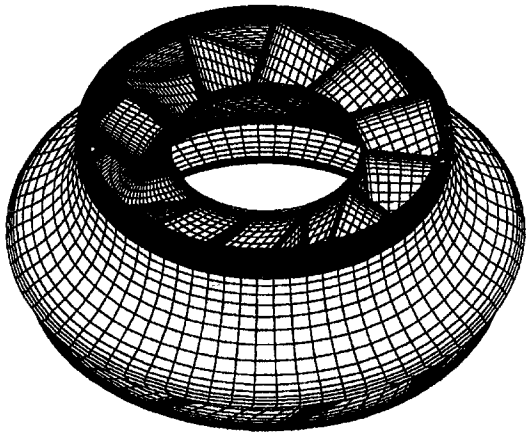

Fig. 4 Impeller model—manual analysis

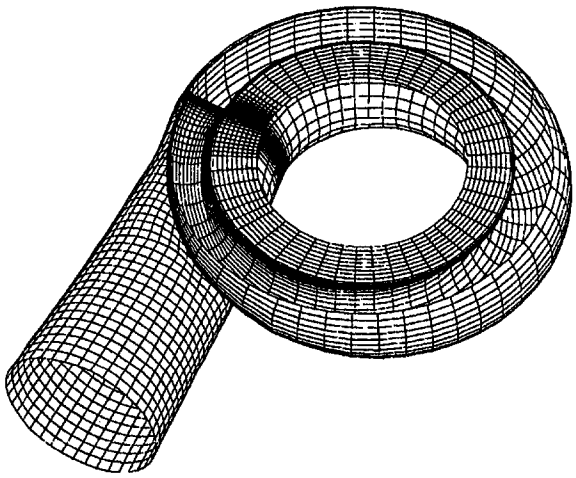

Fig. 5 Volute model—manual analysis

The computational models used for the manual frozen rotor method are shown in Figs. 4 and 5. Figure 4 shows the computational model of the impeller that was modeled using 65 streamwise nodes, 155 blade-to-blade nodes, and 11 hub-to-shroud nodes for a total of 110,825 nodes. Since a full 360 deg impeller model was required, this model represents a very coarse grid with only 10,075 nodes per impeller passage. Figure 5 shows the computational model of the volute that includes the upstream vaneless diffuser. This model contained six blocks with a total of 92,081 nodes. Impeller front and rear shroud cavities were also modeled to enhance radial load prediction capability. The cavities were modeled using an additional 42,087 nodes. The complete multi-block model of the impeller along with cavities had a total of 152,912 nodes and was made up of six sub grids. Total node count for entire geometry would be 244,993 for comparison to the coupled frozen rotor model.

The model used for the coupled frozen rotor computations is shown in Fig. 6. The model contained 14 subgrids including the impeller, the front and rear shroud cavities, the labyrinth seal, and the volute. The impeller contained 55,330 nodes, only 5030 per passage, the cavities were modeled with 33,507 nodes and the volute contained 52,314 nodes. Clearly, with a total node count of 141,151, the size of the coupled frozen rotor model would have to nearly double to obtain the same level of grid refinement as that used during manual frozen rotor analysis.

The impeller grid utilized a simple *H*-grid topology, while the volute utilized a multi-block arrangement to form what is referred to as a "butterfly" grid. A cross section of the volute

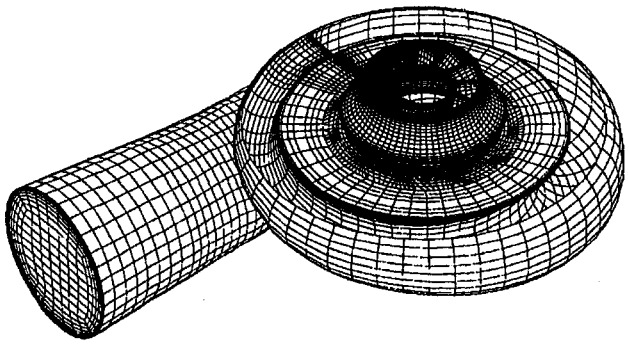

Fig. 6 141K model—coupled analysis

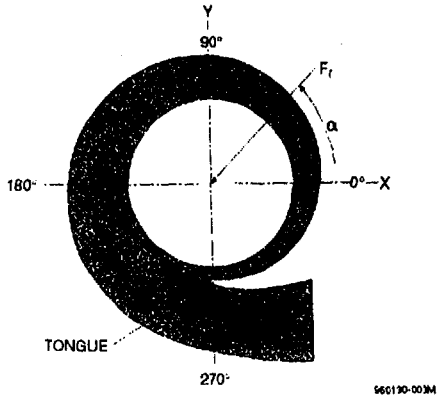

Fig. 8 Discharge volute convention

is shown in Fig. 7. A single-structured grid has been constructed by performing six internal grid connections. Precise grid control in the near wall region and improved overall grid orthogonality was achieved by using this "butterfly" mesh arrangement instead of the simpler *H*-type grid which is typically used.

The impeller grid was constructed using TASCgrid. A set of grid generation templates, specifically designed to produce meshes for bladed geometry, was used to automatically generate a single passage computational domain. This single passage was then replicated to form the full 360 deg model. The templates mentioned above import user-supplied blade pressure and suction surface coordinates to simplify the task of grid generation. Grid development took approximately one day.

The TrueGrid mesh generator was used to interactively generate the volute grids used in this study. It is capable of building multiple block structured parts and is designed to import CAD geometry. TrueGrid employs the projection method to mold a block mesh to the desired shape. The projection method automatically interpolates the edges of the grid and projects them to the required surfaces. Similarly, faces are interpolated and projected. Surface and curve geometry for the volute model was imported from the CADDS data base via several IGES files. Some of the surfaces were combined, forming composite surfaces, so that faces of the grid could smoothly transition from one surface to another. Many features were added to this basic grid. The distribution of the nodes with clustering near boundaries was carefully selected by interactive experimentation. The Thomas-Middlecoff (1980) elliptic solver was used extensively to position the surface nodes between edges, across composite surfaces, and throughout the interior of the grid. This method produced nearly orthogonal grid lines near the boundaries. A short session file was automatically saved and run later in batch mode. This made it easy to experiment with different node clustering, number of relaxation iterations, and the number of nodes used in the grid. The multi-block implementation allowed generation of each of the blocks within the same session. Grid output was in a form compatible with the TASCflow solver. Development took approximately 10 days.

Boundary Conditions. Full-scale simulations were performed over a wide range of flows. In general, the boundary conditions imposed when manual treatment of the interface was employed were the same as those imposed when coupled frozen rotor analysis was performed. The impeller, front shroud cavity, rear shroud cavity, and labyrinth seal were all modeled in the Rotating Frame of Reference (RFR). The vaneless diffuser and volute were modeled in the Stationary Frame of Reference (SFR). All 11 impeller passages were connected periodically between the first and last circumferential plane of nodes. To model the front shroud cavity and labyrinth seal, which connect the impeller exit with the impeller inlet, a periodic connection between the labyrinth seal grid and the impeller inlet grid section was made. Using a periodic connection, instead of a physical connection, prevented the high grid skewness which normally occurs as a result of impeller blade wrap. Inflow conditions (flow direction and turbulence levels) were obtained from a previous CFD analysis of the radial inlet and radial inlet guide vanes (Flathers et al., 1994). Walls were modeled as hydraulically smooth. Stationary walls were modeled as fixed in the SFR and counterrotating in the RFR.

Inflow and outflow boundary conditions for the two interface treatments were dissimilar as a necessary result of the analytical

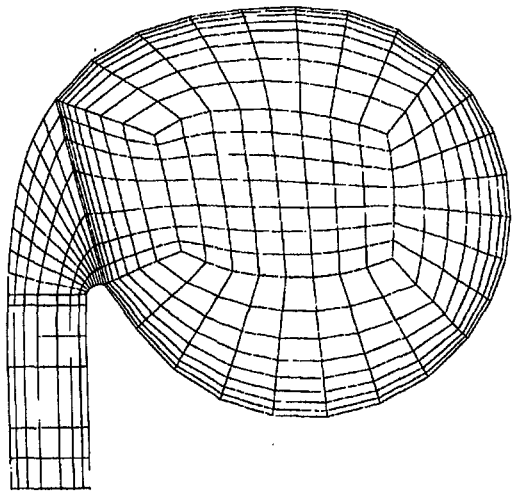

Fig. 7 Butterfly Grid in Volute Cross-Section

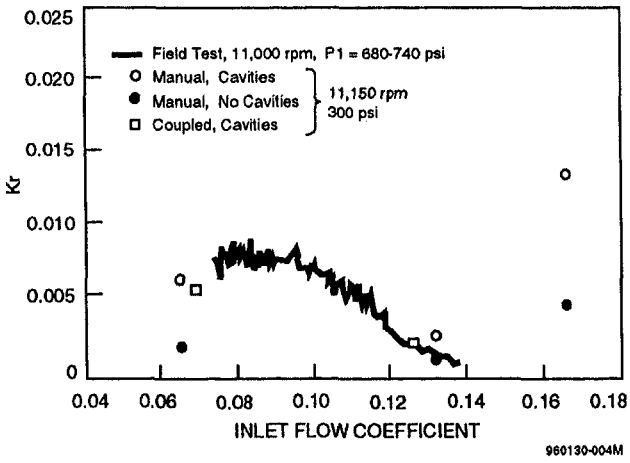

Fig. 9 Radial load comparison to field test data

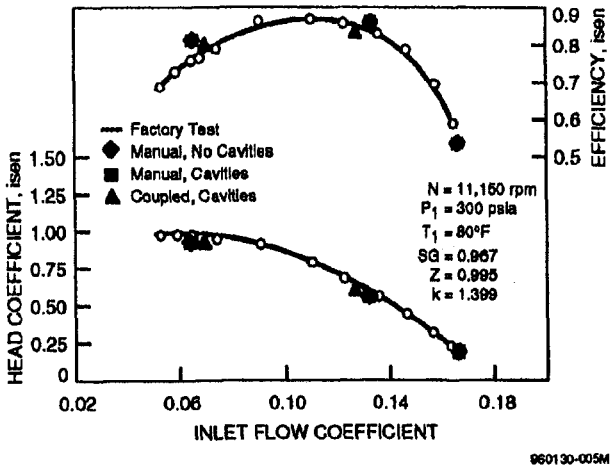

Fig. 10 Aerodynamic performance comparison to closed-loop test results

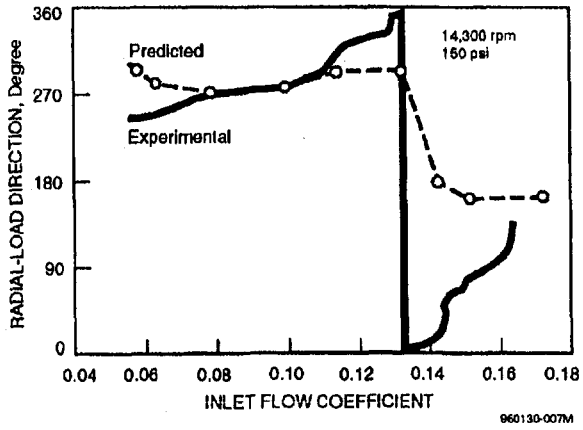

Fig. 12 Radial load direction in comparison to closed-loop test results

methodologies employed. During manual frozen rotor analysis, the inflow boundary conditions used for the impeller were mass flow, total temperature, turbulence intensity and length scale, and flow direction. The impeller outflow boundary condition used was static pressure based on profile from volute analysis. The inflow boundary conditions used for the volute were cartesian velocity, temperature, turbulent kinetic energy, and dissipation from the impeller analysis. The volute outflow boundary condition used was average static pressure. For coupled frozen rotor analysis, the inflow boundary conditions used were total pressure, total temperature, turbulence intensity and length scale, and flow direction. The outflow boundary condition used was mass flow. A frozen rotor, sliding interface boundary condition was used at the impeller exit (e.g., volute inlet). Specification of mass flow, rather than pressure ratio, offers a great advantage to the user. It significantly reduces the amount of time required to perform a given analysis. Iteration on pressure ratio to obtain a desired mass flow, which may take as many as three to five attempts, is not required.

Convergence. Solutions for each case were considered converged when the RMS residuals on all equations reached 1e-6 or less. Key performance parameters, including radial load and direction and isentropic head coefficient and stage efficiency, were also monitored to assure that they did not vary after the convergence criteria were met. Typically, initial guess solutions required about 120 iterations to converge, while restarts for different flowrates required about half as many. The coupled frozen rotor solutions with 141k nodes needed about 13 hours of CPU time for initial guess runs on an IBM R/S 6000 Model 590 workstation with 256 Mb of memory. Restarts for subsequent flowrates of interest required about 6 hours of CPU time. Limited coupled frozen rotor solutions with 245k nodes increased CPU requirements to 21 hours and 10 hours for initial guess runs and restarts, respectively, slightly better than a one-to-one relationship.

Results

Computations were performed at 11,150 rpm and 300 psia (2068 kPa) suction pressure and 14,300 rpm and 150 psia (1034 kPa) to match closed-loop test conditions. Radial loads were obtained by first computing the force acting on each element. Integration was performed over the entire surface of the impeller (hub, shroud, cavities, and blades). Integrating the force by components (x and y-direction loads) allowed computation of the load direction. Comparisons were made between prediction and experiment by plotting the dimensionless radial load coefficient (K_r) and the radial load direction against the compressor inlet flow coefficient. The convention used for radial load magnitude (F_r) and direction (α) is shown in Fig. 8. Radial load magnitude is shown acting on the shaft at an angular position that is measured from the x-axis, which is perpendicular to the compressor centerline. Using this convention, the volute tongue is positioned at 270 deg.

Manual Frozen Rotor. The manual frozen rotor method was run at 11,150 rpm and 300 psia (2068 kPa) suction pressure to match closed-loop conditions. Flow conditions at design flow, near stall, and near choke were investigated, with and without

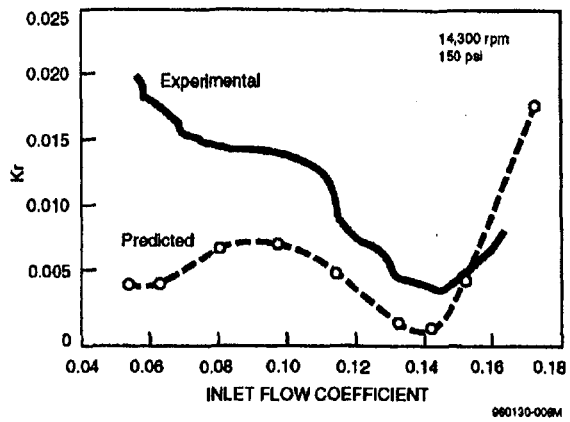

Fig. 11 Radial load comparison to closed-loop test results

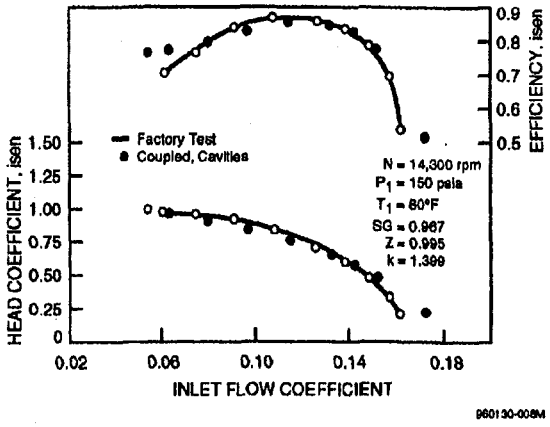

Fig. 13 Aerodynamic performance comparison to closed-loop test results

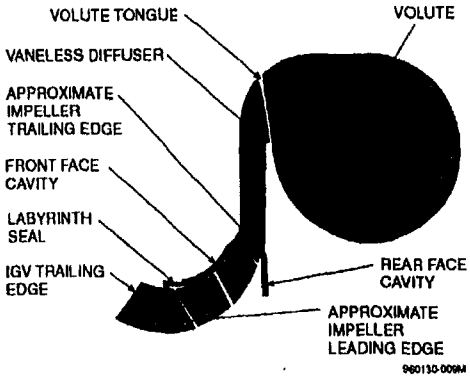

Fig. 14 Cross section of computational geometry

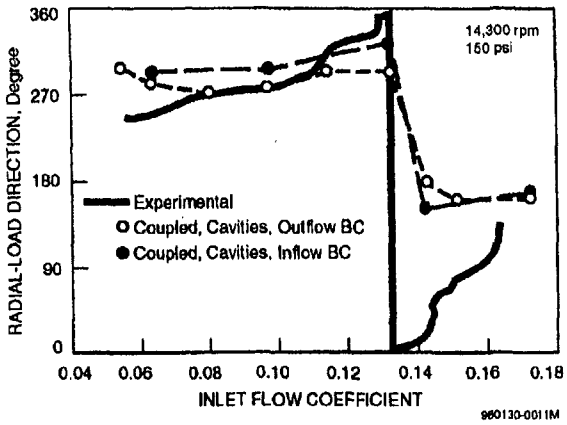

Fig. 16 Radial load direction comparison to closed-loop test results

front and rear face cavities. The computational results for nondimensional radial load are shown in Fig. 9, compared with field test data at 11,000 rpm and 700 psia (4826 kPa). Although no closed-loop radial load data were available at this speed, comparison to the field data at higher suction pressure should be valid because pressure effects are reduced out using K_r, as shown in Part 1 of this paper (Moore and Flathers, 1996). Clearly, the radial load is underpredicted at part-flow conditions when cavities are not included in the model; however, this is not unexpected considering the large surface areas that are excluded from the force integration. Agreement with field data at part flow improves significantly when cavities are included. No field data were available at higher than design flow to compare with the high radial loads calculated when cavities are included. Head coefficient and stage efficiency as a function of inlet flow coefficient are compared to the closed-loop test results in Fig. 10. Note that the agreement is very good, with or without cavities. Therefore, cavities need not be modeled if only aerodynamic performance is sought. Typically, three to five iterations were needed for the manual frozen rotor method at each flow rate investigated.

Coupled Frozen Rotor. The coupled frozen rotor method was run at both 11,150 rpm and 300 psia (2068 kPa) suction pressure and at 14,300 rpm and 150 psia (1034 kPa) suction pressure. The lower speed was analyzed to compare with the manual frozen rotor findings and the higher speed was analyzed because a complete experimental data set from closed loop testing, including radial load and aerodynamic performance, was available. The coupled frozen rotor analysis was completed at design flow and near stall flow for the lower speed case. Figure 9 shows the nondimensional radial load comparison of the two computational methods. The coupled frozen rotor method predicted a slightly lower radial load than the equivalent manual frozen rotor method. However, the agreement with field test was still reasonable. Both methods predict about the same head coefficient and stage efficiency as shown in Fig. 10.

Nine flow conditions from near stall to near choke were analyzed with the coupled frozen rotor method at 14,300 rpm and 150 psia (1034 kPa) suction pressure for comparison to factory test data. As can be seen in Fig. 11, the calculations significantly underpredict radial load, especially at lower flows. In fact, the nondimensional radial load levels were similar to the lower rotational speed results, which contradicts the speed effect measured experimentally. Nonetheless, the radial load direction is predicted fairly well as shown in Fig. 12. Figure 13 shows excellent agreement on head coefficient and stage efficiency.

Observations. Although all of the elements seemingly were in place to accurately compute radial load, the coupled frozen rotor method yielded poor results. The manual frozen rotor method, which is essentially equivalent to the coupled method, albeit more laborious, yielded good results. Upon further examination of the boundary conditions, it was noted that the coupled method used mass flow as an outflow boundary condition, while the manual method used mass flow as an inflow boundary condition. As stated earlier, mass flow is the preferred boundary condition, but location is typically a users option. However, the boundary condition mechanics between the impeller and the volute in the manual method require the user to specify mass flow at the impeller inflow boundary.

It is generally accepted and was most recently shown by Fatsis et al. (1995) that the effect of the circumferential pressure

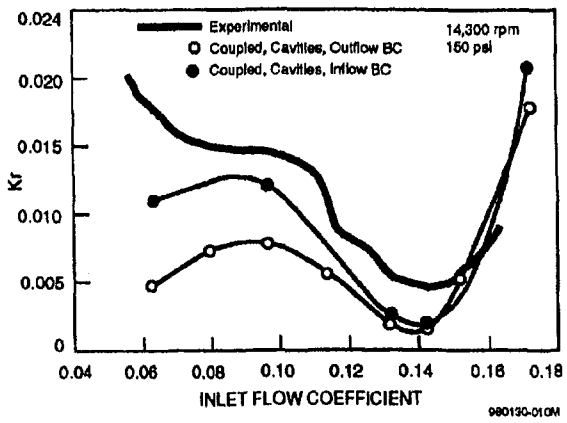

Fig. 15 Radial load comparison to closed-loop test results

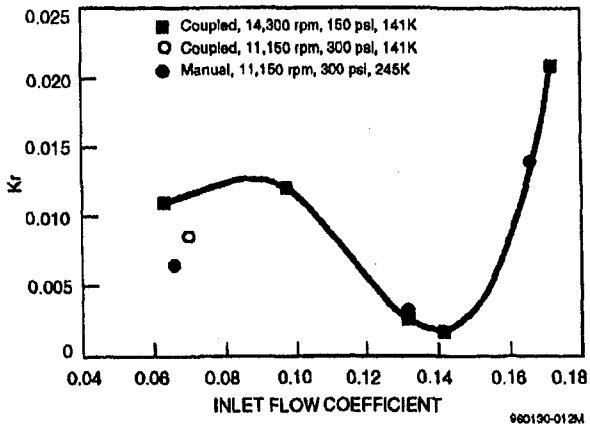

Fig. 17 Effect of speed and grid size predicted with inflow BC

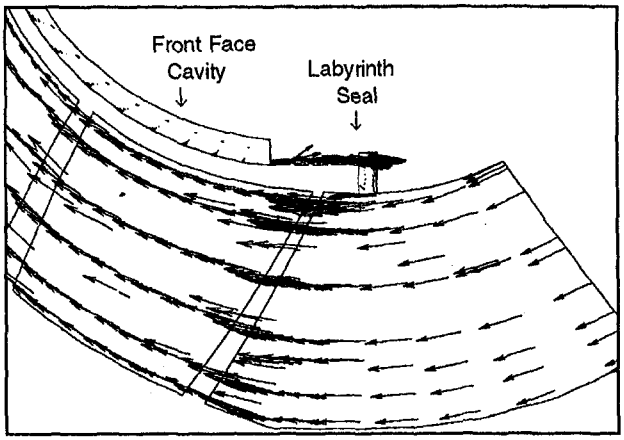

(a)

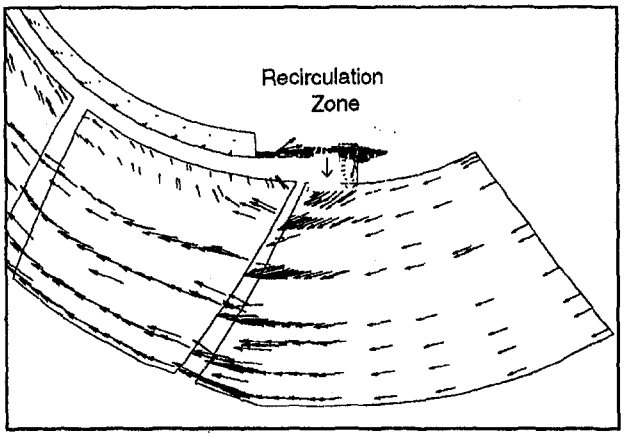

(b)

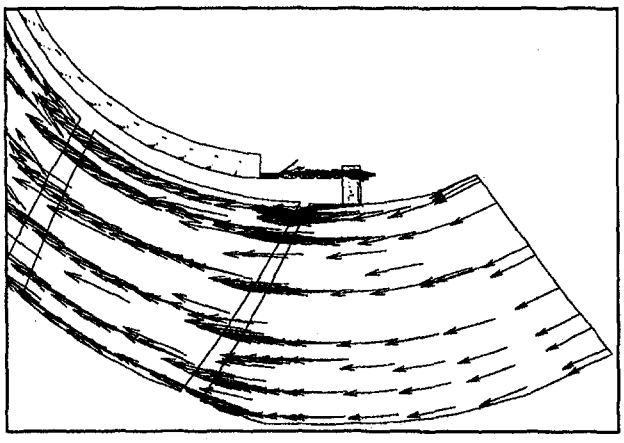

(c)

Fig. 18 (a) Inducer near design flow, (b) inducer near stall, (c) inducer near choke

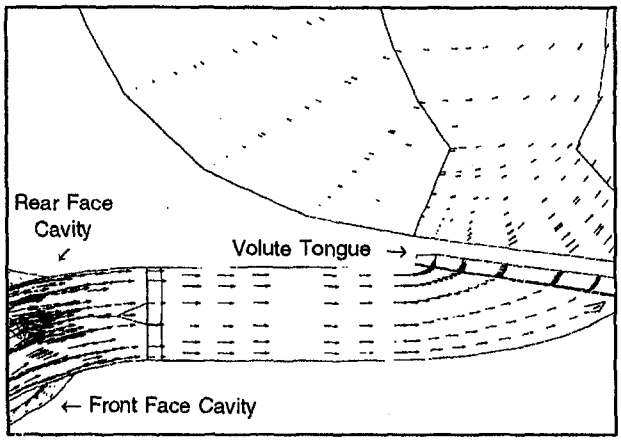

(a)

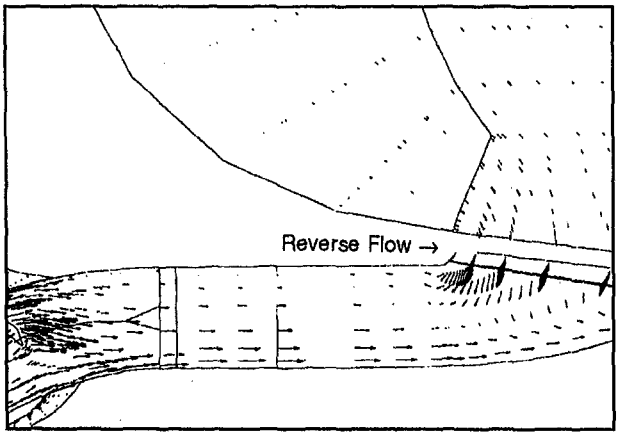

(b)

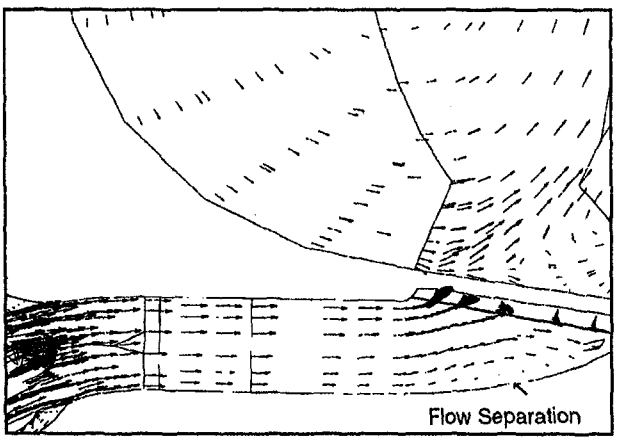

(c)

Fig. 19 (a) Exducer and diffuser near design flow, (b) exducer and diffuser near stall, (c) exducer and diffuser near choke

gradient at the impeller outlet can be seen upstream of the impeller. For this analysis, only a short flowpath extension upstream of the impeller leading edge was modeled. Figure 14 shows a cross section of the computational model at 270 deg. Note that the inlet boundary is relatively close to the impeller leading edge. In addition, the impeller shroud labyrinth seal is modeled, creating a potential flow disturbance close to the inlet boundary. Inlet flow recirculation in pumps at part flows has been documented by Graf (1993), which further illustrates that no boundary conditions should be imposed in this region. The upstream flowpath, which extends to the IGV exit, is acceptable at design flow. However, at off-design flows, elliptic effects interact with the inlet boundary condition, resulting in inaccu-

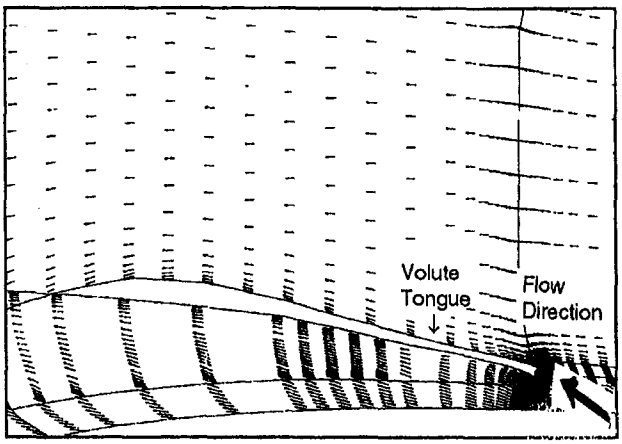

(a)

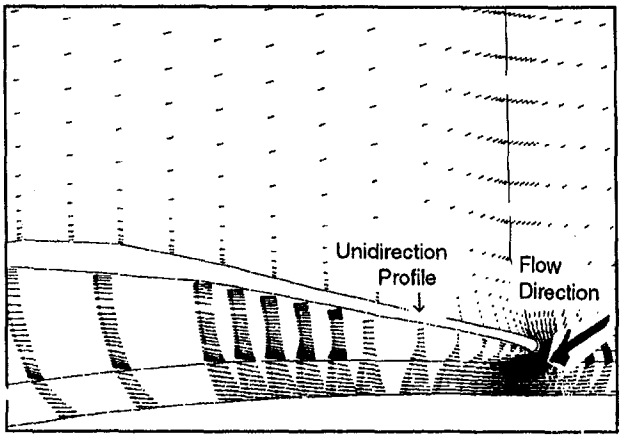

(b)

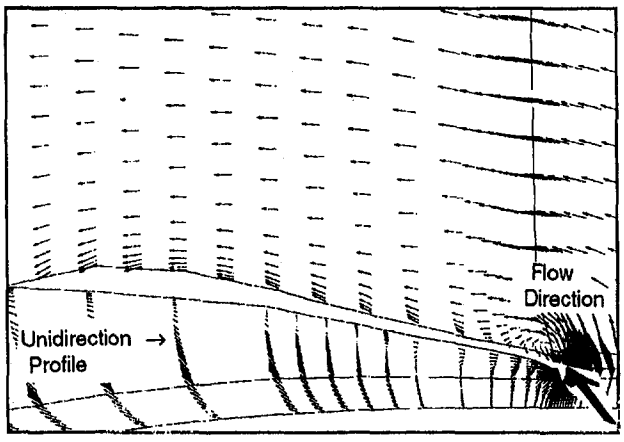

(c)

Fig. 20 (*a*) Volute tongue near design flow, (*b*) volute tongue near stall, (*c*) volute tongue near choke

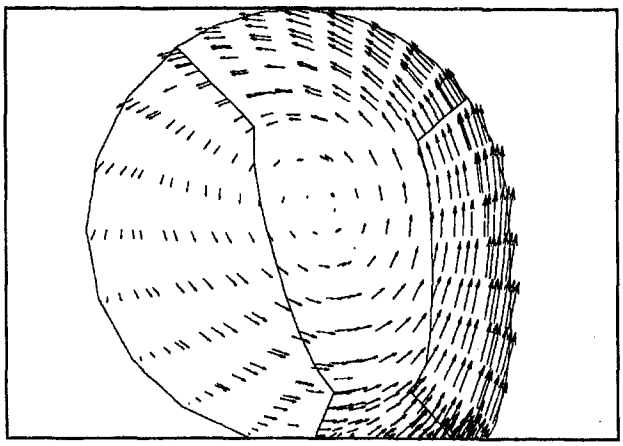

(a)

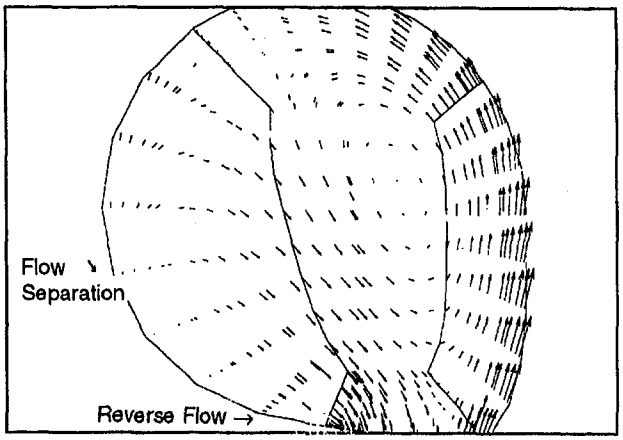

(b)

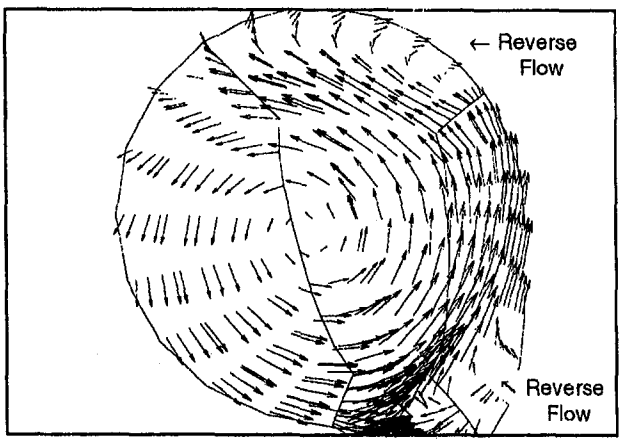

(c)

Fig. 21 (*a*) Volute near design flow, (*b*) volute near stall, (*c*) volute near choke

rate calculations. In fact, one could argue that the entire inlet system (Flathers et al., 1994) should be included.

Since the manual frozen rotor method provided reasonable agreement using a mass flow boundary condition at the inflow, it was decided to use the same boundary condition for the coupled method even though it was acknowledged that the upstream computational domain was most likely inappropriate at off-design flowrates. Initially, a flowrate near stall was repeated with the new boundary condition. The K_r more than doubled, while the load direction shifted about 10 deg, significantly improving the agreement with experiment. Four higher flowrates were then analyzed with the revised boundary condition and the K_r at design flow was essentially the same, while the K_r

near choke flow only increased about 15 percent. These results seem reasonable considering that the nonuniform circumferential pressure profile at the impeller exit, which may affect the inflow boundary, is most significant at off-design flowrates, especially near stall. The radial load and direction findings for all flowrates are plotted in Figs. 15 and 16, respectively, versus the experimental data and the initial computational results with the total pressure inflow boundary condition.

Figure 17 shows the calculations at 11,150 rpm compared with calculations at 14,300 rpm, both using a mass flow boundary condition at the inflow. When compared to lower rotational speed calculations, K_r increased by approximately the square of the speed increase, which is reasonably consistent with the experimental trend. The aerodynamic performance at all five flowrates was essentially unchanged from the original computations, indicating that stage head coefficient and efficiency are insensitive to inflow boundary condition selection.

Flowfield Features. Four regions of the flowfield are presented in Figs. 18 through 21 for near best efficiency, near stall, and near choke flow conditions. A circumferential position of 270 deg was selected to be consistent with the volute tongue location. The impeller leading edge region is shown in Fig. 18. Note the recirculation zone at the shroud leading edge, as well as the labyrinth seal effect for the near stall flowrate. Figure 19 shows the impeller trailing edge and vaneless radial diffuser region. The front and rear face cavity flow can be observed in this view. Note the large recirculation along the hub wall of the vaneless radial diffuser, that extends almost to the shroud wall at the volute entry for the near stall flowrate. At the near choke flowrate, note the shroud wall flow separation near the volute entry. The volute tongue is clearly shown in Fig. 20. Note the correct tongue angle near the best efficiency flowrate and the positive incidence near stall and the negative incidence near choke. It is also interesting to observe how quickly the flowfield structure recovers at stall, while the reverse flow zone near choke takes significantly longer to recover. Figure 21 shows the swirling nature of the flow in the volute cross section at 270 deg. Note the recirculation regions for both near stall and near choke flowrates.

Conclusions

The study presented above, to the best of our knowledge, is the first time that a fully three-dimensional viscous code has been applied to a centrifugal gas compressor stage, including a mixed flow impeller and a discharge volute, for the purposes of predicting radial force and direction and aerodynamic performance. The major conclusions are as follows.

Both the manual frozen rotor and the coupled frozen rotor methods yield reasonable agreement with the experimentally determined radial force and direction. Both methods also predict head coefficient and stage efficiency extremely well. Agreement with the experiment is particularly encouraging considering the low number of nodes per impeller passage. The coupled frozen rotor method is much less tedious than the manual frozen rotor method, and is therefore preferred.

Radial force is much more difficult to predict than aerodynamic performance using CFD. The inflow computational boundary relation to the impeller leading edge is critical for reasonable calculation of the radial force and direction. The authors feel that the addition of the radial inlet system would significantly improve the part-flow radial force prediction. Head coefficient and stage efficiency predictions proved insensitive to the computational method used, inclusion of cavities, and grid density.

The centrifugal gas compressor studied showed similarities to the pump literature presented except that rotational speed effects are observed that are not accounted for in typical pump theory. The authors speculate that this finding may be a function of the gas compressibility not present in liquid pumps.

It is obvious that CFD is capable of this type of complex analysis. Major flowfield features are captured and expected trends are well predicted. The computational methodology developed in the present work, although not truly practical in a design mode, can be used to study the worst case geometry in a given compressor frame size. Therefore, only one geometry needs to be modeled to ensure proper journal bearing sizing. In addition, once the geometry is modeled, CFD can be used as a numerical experiment, where possible design changes to minimize the radial force and improve the stage aerodynamic performance can be considered prior to hardware fabrication.

Acknowledgments

The authors would like to acknowledge the efforts of Jeffrey Moore who developed the experimental methodology reported in Part 1 of this paper (Moore and Flathers, 1996) and Bert Edlebeck who developed the conceptual design of the discharge volute. The authors would also like to thank Solar Turbines Incorporated for permission to publish this paper.

References

Agostinelli, A., Nobles, D., and Mockridge, C. R., 1960, "An Experimental Investigation of Radial Thrust in Centrifugal Pumps," ASME *Journal of Engineering for Power,* Volume 82, No. 2, pp. 120–126.

American Society of Mechanical Engineers, 1986, "Compressors and Exhausters—Power Test Code," PTC-10, 1965 ed., reaffirmed 1974 and 1986.

American Society of Mechanical Engineers, 1959, "Flow Measurements—Power Test Code," PTC-19, 1959 ed.

CAADS Version 5.0 Users Manual, 1994, Computer Vision, Bedford, MA.

de Ojeda, W., and Flack, R. D., 1992, "Experimental Pressures and Momentum Forces on the Impeller of Single and Double Volute Centrifugal Pumps," *ROMAC Report No. 338,* University of Virginia, Charlottesville, VA.

Fatsis, A., Pierret, S., and Van den Braembussche, R., 1995, "Three-Dimensional Unsteady Flow and Forces in Centrifugal Impellers with Circumferential Distortion of the Outlet Static Pressure," ASME Paper 95-GT-033, ASME Turbo Expo, Houston, TX.

Flathers, M. B., Baché, G. E., and Rainsberger, R., 1994, "An Experimental and Computational Investigation of Flow in a Radial Inlet of an Industrial Pipeline Centrifugal Compressor," ASME Paper No. 94-GT-134, 39th ASME Turbo Expo, The Hague, The Netherlands.

Galpin, P. F., Huget, R. G., and Raithby, G. D., 1986, "Fluid Flow Simulations in Complex Geometries," presented at the CNS/ANS Conference on Simulation Methods in Nuclear Engineering, Montreal, Canada.

Galpin, P. F., Broberg, R. B., and Hutchinson, B. R., 1995, "Three-Dimensional Navier Stokes Predictions of Steady State Rotor/Stator Interaction with Pitch Change," *CFD 95—CFD Society of Canada,* Banff, Alberta, Canada.

Graf, E., 1993, "Analysis of Centrifugal Impeller BEP and Recirculating Flows: Comparison of Quasi-3D and Navier-Stokes Solutions," *Pumping Machinery,* Vol. 154, ASME, NY.

Guelich, J., Jud, W., and Hughes, S. F., 1986, "Review of Parameters Influencing Hydraulic Forces on Centrifugal Impellers," organized by the Fluid Machinery Committee of the Power Industries Division of the Institution of Mechanical Engineers, London, England, pp. 1–16.

Hutchinson, B. R., Galpin P. F., and Raithby, G. D., 1988, "Application of Additive Correction Multigrid to the Coupled Fluid Flow Equations," *Numerical Heat Transfer,* Vol. 13, pp. 133–147.

Hutchinson B. R., and Raithby, G. D., 1986, "A Multigrid Method Based on the Additive Correction Strategy," *Numerical Heat Transfer,* Vol. 9, pp. 511–537.

Moore, J. J., and Flathers, M. B., 1996, "Aerodynamically Induced Radial Forces in a Centrifugal Gas Compressor: Part 1—Experimental Measurement," ASME, JOURNAL OF ENGINEERING FOR GAS TURBINES AND POWER.

Schneider, G. E., and Raw, M. J., 1986, "A Skewed, Positive Influence Coefficient Upwind Procedure for Control Volume-Based Element Convection-Diffusion Computations," *Numerical Heat Transfer,* Vol. 8, pp. 1–26.

Stepanoff, A. J., 1957, "Centrifugal and Axial Flow Pumps—Theory, Design and Application," 2nd ed., John Wiley & Sons Inc., New York.

TASCflow Version 2.4 Users Manual, 1994, Advanced Scientific Computing.

Thomas, P. D., and Middlecoff, J. F., 1980, "Direct Control of the Grid Point Distribution in Meshes Generated by Elliptic Equations," *AIAA Journal,* Vol. 18, No. 6, pp. 652–656.

TrueGrid Version 1.2.4 Users Manual, 1994, XYZ Scientific Applications, Livermore, CA.

Van Doormaal, J. P., Hutchinson, B. R., and Turan, A., 1986, "An Evaluation of Techniques Used to Accelerate Segregated Methods for Predicting Viscous Fluid Flow," AIAA Paper No. 86-1653, presented at the AIAA/ASME/SAE/ASEE 2nd Joint Propulsion Conference, Huntsville, Alabama.

Van Doormaal, J. P., Turan, A., and Raithby, G. D., 1987, "Evaluation of New Techniques for the Calculation of Internal Recirculating Flows," AIAA paper No. 87-0059, presented at the 25th Aerospace Sciences Meeting, Reno, Nevada.

N. Fueyo
School of Engineering,
University of Zaragoza, Spain,
Maria de Luna 3,
50015, Zaragoza, Spain

V. Gambón
LITEC,
Laboratory for Combustion Research,
Zaragoza, Spain

C. Dopazo
School of Engineering,
University of Zaragoza, Spain,
Maria de Luna 3,
50015, Zaragoza, Spain

J. F. González
Dirección de Ingeniería e I+D,
GRUPO ENDESA,
Madrid, Spain

Computational Evaluation of Low NOx Operating Conditions in Arch-Fired Boilers

In the present paper, a computational model is used to simulate the aero-dynamic, thermal, and chemical conditions inside an arch-fired coal boiler. The model is based on the Eulerian-Eulerian concept, in which Eulerian conservation equations are solved both for the gas and the particulate phases. A NO_x formation and destruction submodel is used to calculate the local concentration of NO. The model is used to simulate a range of operating conditions in an actual, 350 MW, arch-fired boiler, with the aim of reducing, using primary measures, the emissions of NO_x. The model results shed some light on the relevant NO_x-formation mechanisms under the several operating conditions. Furthermore, they correlate well quantitatively with the available field measurements at the plant, and reproduce satisfactorily the tendencies observed under the different operating modes.

1 Introduction

Arch fired boilers are often used in the power-generation industry for burning low-volatility coals, such as anthracites. The arch-fired configuration provides an environment with high residence times and high temperatures, which, while necessary for achieving flame stability and reasonable burnout of the coal particle, has the undesired side effect of promoting as well the formation of combustion-generated nitric oxides (NO_x).

The arch (or down) fired boiler is a geometrically complex boiler configuration, at least by comparison with the (more commonly encountered) wall and tangentially fired ones. The schematic of a typical arch-fired boiler, displayed in Fig. 1, shows a multiplicity of air and coal outlets, which increase the difficulty and cost of any multi-dimensional simulation of the boiler performance. Figure 1 (and the description that follows) relates to the boiler simulated in this paper; but is also typical of most down-fired boilers.

In the arch-fired boiler, the coal burners are mounted on the so-called burner arches (Fig. 1), and fire downwardly into the combustion chamber. On the arches, the burners are arranged in pairs. Each burner consists of four distinct outlets: a primary outlet, a vent, and two tertiary-air outlets that are concentric with the previous two. The primary outlet carries the coal and primary-air mixture into the combustion chamber. The primary outlet is in fact the exit from a cyclone, in which some of the carrying air is purged from the mixture of coal and particles, and subsequently injected separately into the combustion chamber through the vent located next to the burner, as shown in Fig. 1. The primary and vent outlets in each burner are surrounded by a ring through which a fraction of the combustion air is fed. This fraction is termed "tertiary air" in the operation terminology, and such denomination will be preserved in this paper.

However, the final fraction of the combustion air (the secondary air) is supplied through registers located on the chamber walls, and positioned below each burner. There are three registers for every burner (upper, middle, and lower), the middle one being split into two outlets. All the registers for all the burners are fed from a common wind box, but the air flow-rate through each register can be regulated independently from the others by means of dampers.

Therefore, the flame path starts near the burner mouth, whence it penetrates down into the combustion chamber, where the cross-stream flow of secondary air is mixed with the partially burned fuel and the combustion gases, and then turns upwards towards the chamber exit. (This flame path, in conjunction with corresponding one from the flame arising from the burner on the opposite arch, is the reason why this type of boiler is also known as U or W-fired.)

As with most boilers which were designed before the current environmental concern about the effect of combustion-generated pollutants (essentially NO_x), the operators of this arch-fired boiler are actively searching for ways of reducing the environmental impact without compromising boiler efficiency and availability. Among the several possibilities for NO_x abatement, primary measures (i.e., those that can be achieved by operating the boiler controls) are both cost-effective and within easy reach of the plant management. The multiplicity of burners and air outlets in the down-fired boiler results in endless combinations of operating possibilities, which need to be examined for both their NO_x-reduction potential and their impact on operating efficiency.

The simulation, using computational fluid dynamics (CFD) techniques, of the fluid-flow, combustion and heat transfer within the furnace is a well-known option for conducting such an exploration. CFD simulation of furnaces has been practiced since the early days of the discipline (Gibson and Morgan, 1970). The scientific literature has recorded several applications of CFD simulation to wall-fired and tangentially fired boilers (Fiveland and Wessel, 1988; Kjäldmann, 1993; Sargianos and Bergeles, 1993). Compared to CFD applications in other fields, coal-boiler simulation presents three additional challenges. The first is the tremendous complexity of the physical processes involved, which include multiphase flow, turbulence, chemical reactions, and radiation in an optically complex medium. The second is the uncertainty in the operating conditions: the furnace-wall conditions, the coal composition, the mass flow-rates through the several inlets to the combustion chamber are all either only approximately known or likely to depart with the operating time from the known conditions. Finally, the third is the disparity of length scales in the furnace,

Contributed by the Power Divison of THE AMERICAL SOCIETY OF MECHANICAL ENGINEERS for publication in the ASME JOURNAL OF ENGINEERING FOR GAS TURBINES AND POWER.

Manuscript received by the Power Divison February 2, 1998; final revision received by the ASME Headquarters April 1, 1999. Technical Editor: D. Lou.

which would require the use of very fine computational meshes to properly resolve all the processes of interest.

The present paper shows how, despite all the above limitations, CFD can be usefully employed to predict the performance of an arch-fired boiler under different operating conditions, with particular emphasis being placed on NO_x formation. A simplified, quasi-two-dimensional model will be used first to uncover the main features of the thermal and aerodynamic fields under different firing arrangements; and then the full three dimensional model will be used in order to compare predictions with existing measurements. It will be shown that the answers provided by the model are qualitatively correct, that they exhibit also the correct trends, and that their quantitative accuracy is in general acceptable.

2 Mathematical Model

The mathematical model used to represent the multiphase problem is of the Eulerian-Eulerian kind, in which both phases (gas and coal particles) are treated mathematically and numerically as Eulerian continua. The phases are treated as distinct but intermingling ones, each having their own properties (including velocities). The coexistence of the phases in the physical space causes the exchange of mass and other properties (such as momentum or heat). A model similar to the one used in this work has been described in sufficient detail elsewhere (Fueyo and Pérez, 1993; Fueyo et al., 1995), and, hence, only a brief summary will be provided here.

The model is based on the detailed modeling of all the coal-particle processes, including particle drag and turbulent dispersion, heat-up, drying, volatilization, and heterogeneous combustion. To this effect, the particle is characterized by its contents (as mass fractions) in moisture (water), raw coal, char (or the combustible residue left in the particle by the volatilization process), and ash. Therefore, the mathematical model consists of Eulerian conservation equations for each of these properties but one (since the fact that all the mass fractions add up to one can be used to obtain one of them from all the rest). Further equations are solved for each of the particle velocity components, for the particle specific enthalpy, for the local volume-fraction of the particulate phase, and for a special variable from which the mean particle size can be computed (Fueyo et al., 1997).

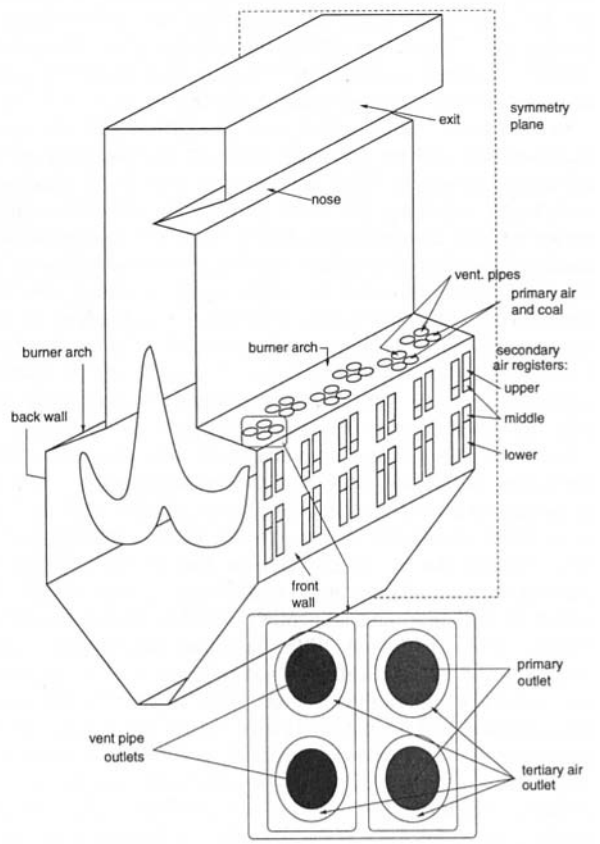

Fig. 1 Down-fired boiler geometry and burner positions. Only a half of the boiler is shown, the other half being symmetrical. Burners are symmetrically disposed on both arches.

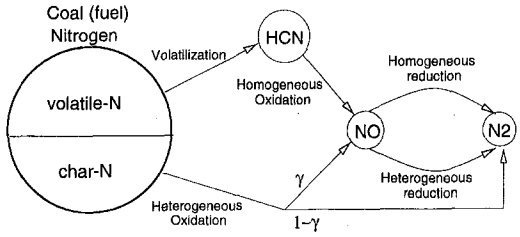

Fig. 2 Fuel-NO route

The gas phase is modeled as a multicomponent mixture, in which all the components (essentially N_2, O_2, H_2O, CO, CO_2, and CH_x, a general hydrocarbon which is the gaseous outcome of the particle pyrolysis) are accounted for by means of their mass fractions. Further equations need to be set up and solved for the velocity components, the phase specific enthalpy, the gas-phase local volume-fraction, the turbulent kinetic energy and its dissipation rate, and the three net radiation fluxes of six flux radiation model. For NO_x calculations, additional Eulerian transport equations are solved for the mass fractions of NO and HCN; but this is detailed in next section.

NO_x Formation Model. The main pollutants generated in coal boilers are nitrogen oxides (NO, NO_2, and N_2O), collectively referred to as NO_x. Because of the low concentrations of the species involved (typically under 1000 ppm), the NO_x models are considered not to contribute to the thermodynamic properties of the mixture, and, hence, are normally calculated in a post-processing run over the "frozen" results of the main combustion model. Such strategy is also used in the present work.

Among the nitrogen oxides just cited, N_2O is not an important pollutant in coal-firing conditions; and NO_2 is around 5 percent of all the NO_x formed in these conditions (Wall, 1987). Therefore, the main contribution is NO, which is formed through the following three distinct routes (Bowman, 1991; de Soete, 1990; Smoot, 1993): thermal NO, produced by the reaction of molecular nitrogen and oxygen at high temperatures; fuel NO, generated from the nitrogen contained in the coal; and prompt NO, which results from the reaction of molecular nitrogen with hydrocarbon radicals at the flame front. This latter route contributes with typically no more than 5 percent of the total NO production, and is usually neglected.

The thermal-NO mechanism used is the extended-Zeldovich one. A production rate for NO as a function of the concentrations of NO, O_2, and N_2 is derived by making several simplifying assumptions. These are essentially the following: a steady-state approximation for the atomic nitrogen; partial equilibrium for the reaction $O + OH \leftrightarrow O_2 + H_2$, neglecting the OH concentration; and partial equilibrium for the oxygen-dissociation reaction $O_2 \leftrightarrow 2O$. The model is similar to that employed in (Coelho and Carvalho, 1993), which can be consulted for details.

For the Fuel-NO route (a schematic of which is shown in Fig. 2), the coal-based nitrogen is presumed to evolve as the carbon, and at the same rates. Thus, coal nitrogen evolves both with the volatiles (volatile-N) and in heterogeneous oxidation (with the char, char-N), the split of the total nitrogen between these two processes being the same as for the carbon. Simpler models (Coelho and Carvalho, 1993; Kjäldmann, 1993), which consider the evolution of the whole of the coal nitrogen with the volatiles are unrealistic for anthracite combustion, given the low volatile contents of this type of coal.

Therefore, two different routes are considered in the present work for the fuel-NO_x formation, as detailed below.

The nitrogen released with the volatiles is assumed to evolve as HCN, with a rate of production proportional to the rate of volatiles release, $\dot{m}_{vol}$:

$$\dot{m}_{HCN} = K_{HCN}\dot{m}_{vol}. \quad (1)$$

This HCN is further oxidized to NO through the reaction (Kjäldmann, 1993):

$$4HCN + 5O_2 \rightarrow 4NO + 2H_2O + 4CO. \quad (2)$$

The reaction rate is given by

$$\frac{dy_{NO}}{dt} = K_v y_{O_2}^a y_{HCN}, \quad (3)$$

where K_v is an Arrhenius-type coefficient, and a is a constant.

The nitrogen remaining in the coal after devolatilization (char-N) is oxidized to NO in a heterogenous reaction with a rate of production proportional to the rate of consumption of char in heterogeneous combustion, $\dot{m}_{char}$. The conversion of char-N to NO has an efficiency factor γ typically between 0.1 and 0.2 for anthracites at high temperatures (Harding et al., 1996). A value of 0.15 is used in this work. The remaining char-N is reduced to N_2.

Thus,

$$\dot{m}_{NO} = -K_{NO}\gamma\dot{m}_{char}. \quad (4)$$

Nitrogen oxides can be, regardless of the formation route, reduced to N_2 through a homogeneous and a heterogeneous path.

The homogeneous path considered in the present model is (Kjäldmann, 1993):

$$4HCN + 6NO \rightarrow 5N_2 + 2H_2O + 4CO, \quad (5)$$

where the reaction rate is

$$\frac{dy_{NO}}{dt} = K_{hom}y_{NO}y_{HCN}, \quad (6)$$

and K_{hom} is an Arrhenius-type coefficient.

The heterogeneous-reduction route is through the reaction of NO on the particle surface (Levy et al., 1981). The reaction rate is:

$$\frac{dy_{NO}}{dt} = A_E\psi K_{het}P_{NO}, \quad (7)$$

where K_{het} is an Arrhenius-type coefficient, P_{NO} is the NO partial pressure, A_E is the particle surface area, and the multiplier ψ (taken here as $\psi = 1$) accounts for surface-increasing factors such as porosity and crevices.

Numerical Method. All the models described above were coded into the general-purpose CFD code PHOENICS (Spalding, 1981). PHOENICS uses a finite-volume, staggered-velocity scheme for the solution of the multiphase Eulerian transport equations. The IPSA algorithm (Spalding, 1980) is used to solve the pressure-velocity coupling.

The sources and sinks resulting from both the main combustion and some of the NO_x-formation processes are normally highly nonlinear; and this results in poor convergence behavior if the source terms are coded carelessly. Where possible, the source terms are therefore linearized; and when linearization is not possible, the source terms are relaxed linearly in a similar fashion to the relaxation used for some of the dependent variables.

The computational meshes used have typically about 14,000 cells (for the quasi-two-dimensional model) or about 200,000 (for the full three-dimensional model). The solution of the quasi-two-dimensional model has been checked to be grid-independent. Due to the long running times, a full grid-independency study has not been carried out for the three-dimensional model; but local, ad-hoc mesh refinements do not yield noticeable differences in the results.

Table 1 Mass flow rates for high and low-flame operating conditions

	High flame	Low flame
Coal mass-flow-rate (as fired)	17.611 Kg/sg	18.674 Kg/sg
Air mass-flow rate	164.568 Kg/sg	166.555 Kg/sg
Primary-air mass-flow-rate	25.544 Kg/sg	26.535 Kg/sg
Tertiary to secondary air ratio	0.85	2.0
Excess oxygen	4 %	2.5%

About 4000 iterations are needed for the the convergence of a main-combustion simulation of the full three-dimensional model, and about 500 additional ones for convergence of the NO_x post-processing simulation. The overall running time for the main-combustion simulation is about 271 CPU secs/iteration on an IBM RS6000/590 workstation.

3 Model Application and Results

The mathematical model outlined above has been employed to simulate the arch-fired boiler described in the introduction. The simulations covered a range of operating conditions, which can be nevertheless broadly classified in two operating modes that will be termed "high flame" and "low flame"

The "high flame" conditions correspond with the normal operating mode of the boiler. The tertiary-to-secondary air ratio (see introductory section for the meaning of this nomenclature) is close to one; and the excess oxygen is about 4 percent. The oxygen excess is sufficient to ensure an adequate particle-burnout level at the furnace exit.

An alternative operating strategy is to decrease the oxygen excess (thus increasing the boiler efficiency and hopefully reducing the formation of NO_x). To offset to some extent the adverse effect of the reduced air excess on the burnout levels, a longer residence time for the coal particle is provided in the furnace. This is achieved by increasing the tertiary-to-secondary air ratio to nearly two. This increases the momentum associated to the burner, and decreases the one in the cross-stream secondary air. The result is a deeper penetration of the flame into the furnace, and, hence, a longer residence time for the coal particles in the high-temperature region.

The coal-type is anthracite, with a volatile content of 8.86 percent (dry basis) and a lower heating value of 52.47 K cal/kg (dry basis). Table 1 lists the relevant operating conditions for both firing modes, corresponding to the boiler full-load (350 MW).

The Quasi-Two-Dimensional Model. The geometrical complexity of the actual boiler makes it rather difficult to identify, in a full three-dimensional simulation, the processes that are taking place in the combustion space, their relevance, and their interactions. Additionally, the meshing requirements are such that any exploratory run takes much longer than it is desirable. For this reason, it has been deemed appropriate to construct a reduced model, which takes into account the essential flow features but simplifies the geometry.

Such model consists of a vertical "slice" of the boiler which includes one burner, its venting outlet and its secondary-air registers as represented in Fig. 3. The computational domain does not include the furnace nose (shown in Fig. 1), and, hence, assuming that opposite burners are operated in the same way, the domain is symmetrical and only half of it needs to be simulated. The domain is not strictly two-dimensional, since the slice includes a full representation of the burner and of the space between burners, and, hence, it is termed quasi-two-dimensional here. The mesh distribution is $34 \times 5 \times 81$ (width, depth, height).

Because symmetry (no flux) boundary conditions are employed

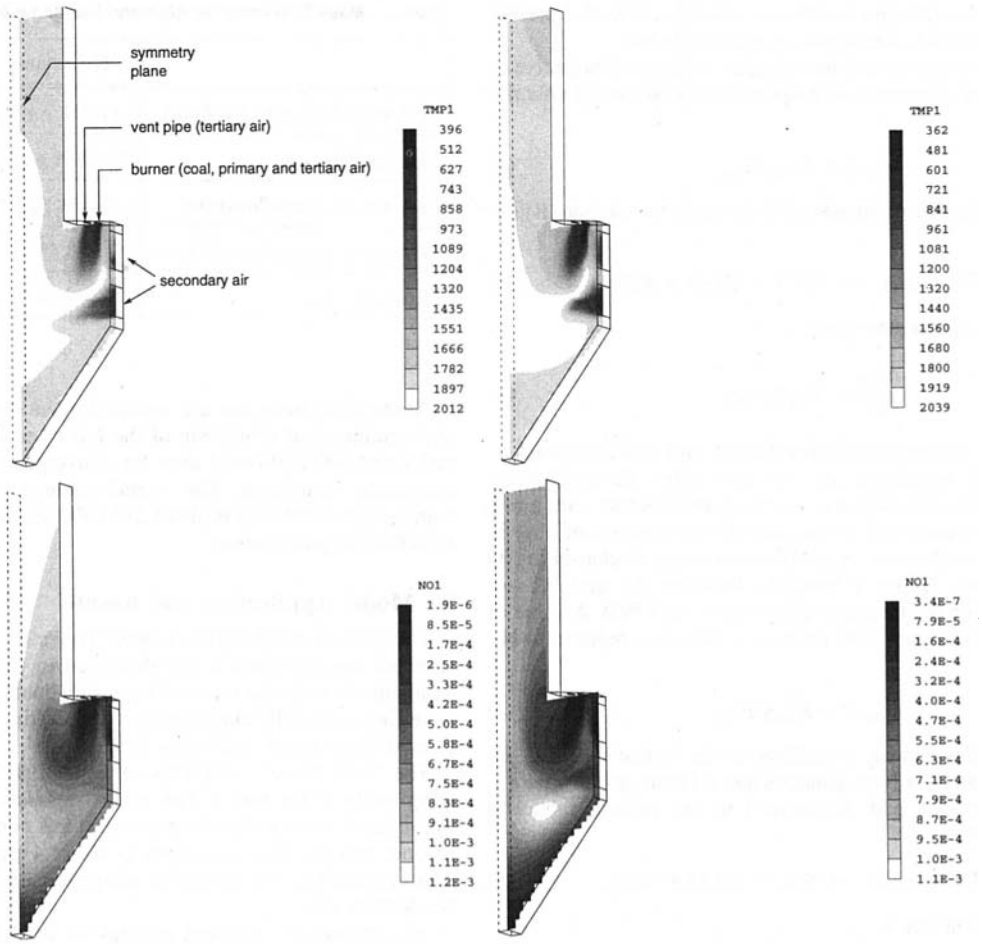

Fig. 3 Temperture (top, *K*) and NO_x concentration (bottom, mass fraction) on a burner plane (Quasi-two-dimensional model). High-flame (left) and low-flame (right) operating conditions.

for the "slicing planes", the situation simulated would correspond to the existence of an infinite number of similar slices next to each other. In the actual boiler, one of such slices would be representative of the situation in one of the central (hotter) burners, where the heat radiated to the lateral walls is minimum because such walls are the furthest away.

The top two graphics in Fig. 3 show the temperature fields resulting from the quasi-two-dimensional calculations of the high flame and low flame. The temperature fields in both cases are remarkably different, with the high flame showing higher temperature levels above the burner arch than the low flame. The reason for the shifting of the flame towards the burner arch in the high flame is the higher momentum of the cross-stream secondary-air, which reduces the penetration of the burner streams into the combustion chamber. A limited number of temperature measurements taken with optical pyrometers in the actual boiler confirm the qualitative difference just outlined.

The corresponding NO_x field for both flames is shown in the lower two graphics of Fig. 3. The consequence for NO_x formation of the situations depicted above is that for the high flame NO_x is formed above the burner arch, due to both the higher temperatures and also to the richer oxygen concentration for this flame configuration. In fact, the figure shows that the NO_x concentration increases above the burner arch towards the furnace exit. The picture for the low flame is quite different, and shows the maximum in NO_x concentration well below the burner arch, and an approximately constant level of NO_x above the burner arch. Measurements of NO just above the arch and at the furnace exit, taken at the plant by means of suction probes show precisely these two opposite trends for the high and low flames.

Further confidence in the correct qualitative behavior of the model can be gained by conducting a further test, in which the oxygen excess is varied with respect to the values used in the previous calculations. Specifically, the excess is decreased for the high flame and increased for the low one. The effect of such changes has also been measured at the plant, and the results of both simulations and field trials are summarized in Table 2. Of course, the comparison between computational and experimental results can only be qualitative, because the actual boiler is operated with slightly different firing-arrangements for the different burners, and these differences can be taken into account in the full three-dimensional model but not in the quasi-two-dimensional one. Nevertheless, Table 2 reveals that the trends are very well reproduced. It is remarkable that the outcome of the parametric change is an increase in NO_x both when the air excess is reduced in the high flame and when it is increased in the low one. For the high flame, a reduction in the air excess results in higher temperatures, and in a greater extent of the combustion process being shifted

Table 2 Air-excess influence: comparison of calculations and measurements

		O_2 excess change	$[NO_x]$ increase [a]	increase/change
High flame	Measurements	-18.0%	+21.5%	1.19
	Simulation	-19.2%	+18.4%	0.96
Low flame	Measurements	+37.2%	+13.9%	0.37
	Simulation	+51.5%	+21.6%	0.41

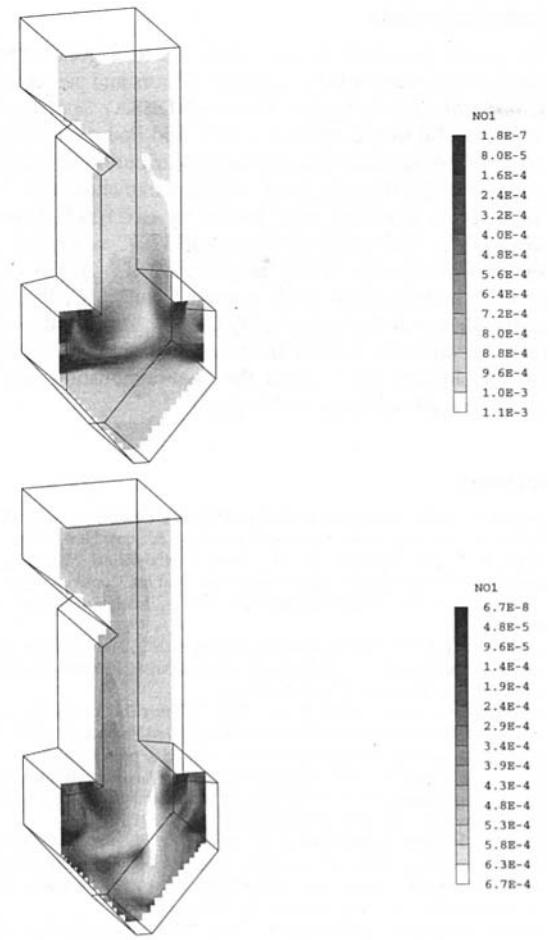

Fig. 4 NO_x concentration (mass fraction) on a burner plane (three-dimensional model). High-flame (top) and low-flame (bottom) operating conditions.

towards the zone above the burner arch. The first effect increases the thermal NO_x, while the second induces a release of the char-bound nitrogen in that region, where homogeneous reduction of NO by hydrocarbon radicals is much less likely. For the low flame, the increase in NO with a moderate increase in air excess is a frequently encountered and well-known effect, which in the present case can be attributed (as a detailed inspection of the simulation results reveals) both to slightly higher peak temperature (due to a more vigorous combustion) and to the wider availability of oxygen for the oxidation of the fuel and atmospheric nitrogen.

The 3D Model. While the quasi-two-dimensional model has been successful in both attributing causes to effects and in gaining some confidence in the model, a complete, three-dimensional boiler simulation is still needed for a comparison of model results with field measurements. This is so not only because the effects of the side walls may not be negligible, but also because different burners operate with different mass-flow rates, and some are even out of service. The furnace is nevertheless symmetrical (both geometrically and operationally), the symmetry plane being the one depicted in Fig. 1; hence, only half of the furnace is simulated. Therefore, the three-dimensional simulation is set up by discretizing not a single-burner slice but half of the boiler (the half shown in Fig. 1), with a total of 24 burners and their corresponding secondary-air outlets. The side wall is included with appropriate friction and thermal boundary conditions, and the symmetry plane is modeled with the customary no-flux conditions. In the course of parametric studies it was found that the boiler nose has some influence on the flow conditions in the vicinity of the burner arch, and, therefore, had to be included in the simulation. It was also

Table 3 Measured and computed NOx concentrations in high and low-flame operation

		Experimental data	Simulation results
High flame	NO_x (exit)	860 ppmm	943 ppmm
	NO_x (burner arch)	673 ppmm	780 ppmm
Low flame	NO_x (exit)	623 ppmm	581 ppmm
	NO_x (burner arch)	629 ppmm	599 ppmm

found that the (all-important) prediction of the primary-jet penetration was very much dependent on the fineness of the mesh in the burner and secondary-air regions, with coarser meshes providing less penetration. Consequently, the mesh was refined locally until further refinement did not result in noticeable differences. The resulting mesh is $54 \times 53 \times 67$ (width, depth, height).

Figure 4 shows the NO_x mass-fraction field on a typical vertical plane, for both the high flame (at the top) and the low one (at the bottom). The NO_x pattern in either case follows the trends outlined by the quasi-two-dimensional simulations. Thus, for the high flame the figure reveals that NO continues to be formed in the zone above the burner arch, while for the low flame most of the NO is formed below the burner arch. The quantitative comparison is shown in Table 3, which reports average values from measurements and calculations at two different heights: just above the burner arch and the furnace exit. Calculations are in reasonable agreement with measurements; and two different NO_x-formation patterns for the high and low flames are clearly evinced by the measurements.

Table 4 shows the relative weight of the several NO_x formation and destruction mechanisms for the two operating modes. The results reveal that much less NO_x of a thermal origin is produced in the low flame by comparison with the high flame. This is attributed to the lower oxygen levels. Heterogeneous reduction is increased for the low flame, due to the longer residence time of the char particle in the furnace.

The trial tests conducted at the plant included some further changes to the operating conditions. These changes were in general departures from the high-flame situation, since this was the normal operating mode at the plant. The changes affect essentially the burners which are placed out of service, the oxygen excess and the air distribution to the secondary-air registers.

Three of these cases have been studied computationally. These cases, and the relevant results, are described next. Table 5 is a summary of the main conclusions in respect of NO formation. The term "base case" refers from now to the high-flame case discussed above.

Case HF1 differs from the base case in the mill which is put out of service. In the base case, this is the E mill, which feeds some of the central burners, while in case HF1 it is the C mill, which feeds more external (closer to the walls) burners. Since more heat is generated in the hotter central part of the furnace, the temperature

Table 4 Contribution of the different NOx mechanisms to the global formation/reduction in high and low-flame operation

NO_x Mechanism	kg/seg		% formation or reduction	
	High	**Low**	**High**	**Low**
Thermal formation	0.0993	0.0323	51%	24%
Fuel-*NO* (volatile contribution)	0.0373	0.0416	19%	31%
Fuel-*NO* (char contribution)	0.0588	0.0589	30%	45%
Homogeneous reduction	0.0321	0.0308	95%	87%
Heterogeneous reduction	0.0016	0.0044	5%	13%

Table 5 Measured and computed NOx concentrations at the exit and thermal NOx mechanism production for the high flame operating conditions cases

	HF1	HF2	HF3
Simulation results (*ppmm*)	1156	792	773
Experimental measurements	958	795	700
Thermal NO_x production (kg/sg)	0.142 (60%)	0.078 (45%)	0.068 (41%)

increases, and so does the thermal-NO generation. Hence, the overall NO_x level is higher.

Case HF2 uses the same injection conditions as the base case, but the oxygen excess is increased to 5 percent. The additional air does not result in an increase in NO (as it is usually the case), but in a decrease. This can be traced to the lower thermal NO production (as can be seen in Table 5) as a consequence of the lower temperatures. The NO reduction is also predicted in the numerical simulation.

Case HF3 has the same excess air as the base case, and the same mill is put out of service. However, the secondary air is redistributed, so that more air is injected in the central (hotter) part of the furnace, thus reducing the temperature peaks in that region and in consequence the exit NO. The model correctly predicts this decrease with respect to the base case.

4 Conclusions

This paper has shown how a CFD model of a pulverised-coal furnace can provide valuable insight into the production of combustion-generated NO_x. The model is of the Eulerian-Eulerian type, and includes detailed submodels for all the relevant particle processes, as well as for the formation and reduction of NO_x through the thermal and fuel routes.

Even for a highly complex down-fired boiler, the model produces results that, by comparison with existing measurements, are of a sufficient accuracy for the model to be of use in the design of operation strategies for the boiler. Equally interesting is the ability of the model to predict the trends resulting from most common operational decisions.

The model has been used to study two main operating modes, and some variants of these. Both operating modes are essentially different in respect of the ratio of tertiary to secondary air. It is shown how, by increasing this ratio and reducing the overall air excess, the NO_x emissions can be significantly reduced. If the ratio is too high, a significant part of the combustion takes place above the burner arch, and fuel and thermal NO_x continue to be formed in this region. Higher tertiary-to-secondary-air ratios cause the flame to penetrate further into the furnace, which increases the residence time and thus makes it possible to operate the boiler with a lower excess air without compromising the boiler efficiency. This results in a lower thermal-NO_x contribution, while maintaining the homogeneous and heterogeneous reduction of NO to N_2 at the same levels.

Acknowledgments

The results presented in this paper are to a great extent the outcome of the interaction between the authors and personnel from the Compostilla Power Station (Grupo ENDESA). Specifically, we are very grateful to Messrs Pedro Otero and Pedro Gomez-Yague for their encouragement and for their contribution to our knowledge of the boiler through many technical explanations.

The research work has been funded by ENDESA. Further research work at University of Zaragoza/LITEC is funded by the European Commission, under project ESPRIT 20966 (MICA). One of the authors (VG) holds a grant from CSIC, the Spanish Scientific Research Council. Finally CHAM Ltd (London, UK) is thanked for allowing the use of their CFD code PHOENICS, in which the authors have coded the coal-combustion and NO_x-formation models outlined in this paper.

References

Bowman, C., 1991, "Chemistry of Gaseous Pollutant Formation and Destruction," *Fossil Fuel Combustion: A Source Book,* John Wiley & Sons, New York.

Coelho, P. J., and Carvalho, M. G., 1993, "Mathematical Modelling of NO Formation in a Power Station Boiler," Proceedings, 2nd Int. Conference on Combustion Technologies for a Clean Environment, Vol. 1, Instituto Superior Técnico, Lisbon.

de Soete, C. G., 1990, "Fundamental Chemistry of NO_x and N_2O Formation and Destruction," course notes, Third Flame Research Course, International Flame Research Foundation, IJmuiden, The Netherlands.

Fiveland, W. A., and Wessel, R. A., 1988, "Numerical Model for Predicting Performance of Three-Dimensional Pulverized-Fuel Fired Furnaces," ASME JOURNAL OF ENGINEERING FOR GAS TURBINES AND POWER, Vol. 110, pp. 117–126.

Fueyo, N., and Pérez, C., 1993, "Eulerian Models for Coal Combustion With NO_x Formation," Proceedings, Joint Meeting of the Italian and Spanish Sections of The Combustion Institute, The Combustion Institute, Pittsburgh, PA.

Fueyo, N., Ballester, J., and Dopazo, C., 1995, "An Eulerian-Eulerian Model of Coal Combustion, NOx Formation and Reburning," Proceedings, 12th Annual International Pittsburgh Coal Conference, S.-H. Chiang, ed., Center for Energy Research, University of Pittsburgh, Pittsburgh, PA, pp. 1113–1118.

Fueyo, N., Ballester, J., and Dopazo, C., 1997, "The Computation of Particle Size in Eulerian-Eulerian Models of Coal Combustion," *Int. J. Multiphase Flow,* Vol. 23, No. 3, pp. 607–612.

Gibson, M. M., and Morgan, B. B., 1970, "Mathematical Model of Combustion of Solid Particles in a Turbulent Stream With Recirculation," *Journal Institute of Fuel,* Vol. 43, pp. 517–523.

Harding, A. W., Brown, S. D., and Thomas, K. M., 1996, "Release of NO From the Combustion of Coal Chars," *Combustion and Flame,* Vol. 107, pp. 336–350.

Kjäldmann, L., 1993, "Numerical Simulation of Combustion and Nitrogen Pollutants in Furnaces," Ph.D. thesis, Helsinki University of Technology.

Levy, J. M., Chan, L. K., Sarofim, A. F., and Beér, J. M., 1981, "NO/char Reactions at Pulverizad Coal Flame Conditions," Proceedings, 18th Symp. (Int.) on Combustion, The Combustion Institute, Pittsburgh, PA, pp. 111–120.

Sargianos, N. P., and Bergeles, G., 1993, "Influence of Burner Angles on the Performance of a Lignite-Fuelled Utility Boiler: A Numerical Study," Proceedings, the 2nd Int. Conference on Combustion Technologies for a Clean Environment, Vol. 1, Instituto Superior Técnico, Lisbon.

Smoot, L. D., 1993, *Fundamentals of Coal Combustion for Clean and Efficient Use,* Elsevier, New York.

Spalding, D. B., 1980, "IPSA 1981: New Developments and Computed Results," Imperial College CFDU Report HTS/81/1, Imperial College, London.

Spalding, D. B., 1981, "A General Computer Program for Multi-Dimensional One and Two-Phase Flow," *Mathematics and Computers in Simulation,* Vol. 13, pp. 267–276.

Wall, T. F., 1987, "The Combustion of Coal as Pulverized Fuel Through Swirl Burners," Academic Press, London.

Fatigue Strength Reliability Analysis of Diesel Connecting Rod Based on Stochastic Finite Element Method

C. Yi

W. Mingwu

T. Ling

Shanghai Jiao Tong University,
Power and Energy Engineering School,
1954 Hua Shan Road,
Shanghai, 200030,
P. R. China

In this paper, stress of a diesel connecting rod (CR) is analyzed by the perturbation stochastic finite element method (PSFEM). A fatigue failure criterion of a diesel CR is also put forward with Corten-Dolan fatigue cumulative damage theory. Based on fatigue failure criterion and the results of stochastic stress analysis, the advanced first order second moment (AFOSM) method is used for fatigue strength reliability analysis. It is shown that PSFEM is efficient and accurate in stochastic stress analysis by comparing with Monte-Carlo simulation. The analysis shows that the reliability of a certain type of diesel CR is 0.99917, which coincides with the statistical data from the factory. It is also found that operating parameters such as combustion peak pressure and engine rotary speed have the greatest influence on CR reliability because of the large variances and high stress response sensitivity.

1 Introduction

In traditional diesel CR design, parameters such as structure size, material properties, external loads are often taken as determinate variables. In fact, when considering many uncertain factors in manufacture and usage, those parameters usually have uncertain characters. In order to account for the effects of uncertainty, the common measure is to apply a safety factor, but how to select the proper safety factor is difficult. When the safety factor is small, structures may be unsafe. When the safety factor is large, structures may be heavy. Other than the affects mentioned above, the safety factor cannot provide assistance for design improvements. In order to avoid any negative effects of the safety factor, reliability analysis is used in this paper.

In reliability analysis, Monte-Carlo simulation is often used (Astill et al., 1972). In order to get accurate results, a large number of samples must be obtained, which means enormous computing, especially in a high reliability structure. In this paper, a different method, PSFEM (Nakagiri and Hisada, 1982) combined with the AFOSM method (Hasofer and Lind, 1974), is used for fatigue strength reliability analysis of a diesel CR. In this analysis, combustion peak pressure, piston group mass, rotary speed of crankshaft, magnitude of interference between small-end bore and copper bushing, the transitive arc radius between small-end and shank, modulus of elasticity, and Poisson's ratio are taken as random variables. Mean, variance, and covariance of stress are obtained by PSFEM. These statistics are used in the reliability analysis by the AFOSM method. An example and experiment are provided to show the characteristics of this method.

2 Stochastic Stress Analysis

The conventional finite element solution for the nodal displacements $\tilde{U}$, strains $\tilde{\epsilon}$, and stresses $\tilde{\sigma}$, are expressed by

$$\tilde{U} = \tilde{K}^{-1}\tilde{F} \quad \tilde{\epsilon} = \tilde{B}\tilde{U} \quad \tilde{\sigma} = \tilde{D}\tilde{\epsilon}, \tag{1}$$

where "~" denotes a random variable, $\tilde{K}$ is stiffness matrix, $\tilde{F}$ is the nodal load vector, $\tilde{B}$ is the displacement-to-strain transformation matrix, and $\tilde{D}$ is elasticity matrix. $\tilde{U}$, $\tilde{\epsilon}$ and $\tilde{\sigma}$ are functions of basic input random vector $\tilde{X} = (\tilde{x}_1, \tilde{x}_2, \ldots \tilde{x}_n)$, which represents external loads, material properties and structure sizes. If the mean of $\tilde{X}$ is $\bar{X} = (\bar{x}_1, \bar{x}_2, \ldots \bar{x}_n)$, make

$$\alpha_i = \frac{\tilde{x}_i - \bar{x}_i}{\bar{x}_i} \quad i = 1, \ldots, n \tag{2}$$

whose mean and standard variance are

$$E(\alpha_i) = 0 \quad \hat{\alpha}_i = \frac{\hat{x}_i}{\bar{x}_i} \quad i = 1, \ldots, n, \tag{3}$$

where $\hat{x}_i$ is the standard variance of $\tilde{x}_i$. From Eq. (3), it can be seen that $A = (\alpha_1, \alpha_2, \ldots, \alpha_n)$ is a small perturbation vector. Expanding $\tilde{U}$, $\tilde{\epsilon}$, $\tilde{\sigma}$, $\tilde{K}$, $\tilde{F}$, $\tilde{B}$, and $\tilde{D}$ into a series at the mean of A, and neglecting items above the second order, because of A being a small perturbation, then the following equation can be derived:

$$\tilde{Y} = Y_0 + \sum_{i=1}^{n} Y_i\alpha_i + \frac{1}{2}\sum_{i=1}^{n}\sum_{j=1}^{n} Y_{ij}\alpha_i\alpha_j, \tag{4}$$

where $\tilde{Y}$ represent all random vectors and matrixes appearing in Eq. (1). Subscript 0 denotes at point $A = 0$, and i denotes first order perturbation with respect to α_i. ij denotes second order perturbation with respect to α_i, α_j. Taking Eq. (4) into Eq. (1), by center second order perturbation method (Chen and Liu, 1993a), we can get the following recursion equation sets:

$$\left.\begin{aligned} U_0 &= K_0^{-1}F_0 \\ \epsilon_0 &= B_0U_0 \\ \sigma_0 &= D_0\epsilon_0 \end{aligned}\right\} \tag{5}$$

$$\left.\begin{aligned} U_i &= K_0^{-1}(F_i - K_iU_0) \\ \epsilon_i &= B_0U_i + B_iU_0 \\ \sigma_i &= D_0\epsilon_i + D_i\epsilon_0 \end{aligned}\right\} \tag{6}$$

$$\left.\begin{aligned} U_{ij} &= K_0^{-1}(F_{ij} - K_jU_i - K_iU_j - K_{ij}U_0) \\ \epsilon_{ij} &= B_0U_{ij} + B_{ij}U_0 + B_iU_j + B_jU_i \\ \sigma_{ij} &= D_0\epsilon_{ij} + D_{ij}\epsilon_0 + D_i\epsilon_j + D_j\epsilon_i \end{aligned}\right\}. \tag{7}$$

Y_i, Y_{ij}, (Y denotes U, ϵ, and σ) can be computed by assembling partial derivative load vectors, stiffness matrices, geometry matri-

Contributed by the Internal Combustion Engine Division (ICE) of THE AMERICAL SOCIETY OF MECHANICAL ENGINEERS for publication in the ASME JOURNAL OF ENGINEERING FOR GAS TURBINES AND POWER.

Manuscript received by the ICE January 15, 1998; final revision received by the ASME Headquarters April 19, 1999. Associate Technical Editor: D. Assanis.

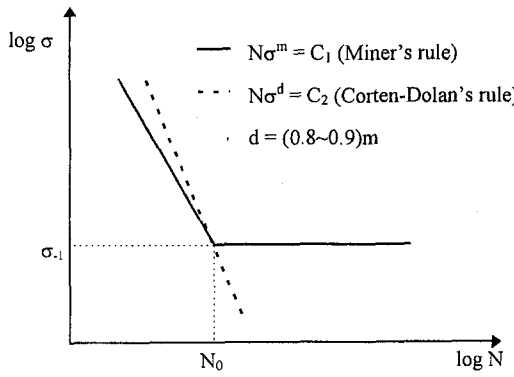

Fig. 1 σ-N curve for steels on log-log plot

ces, and elasticity matrices of all elements. It is important to note that this procedure requires no additional inversions of the stiffness matrix for computing Y_i, Y_{ij}. From Eq. (4), it is easily verified by Chen and Liu (1993b) that the statistical parameters of displacements and stresses are

$$E(y^p) = y_0^p + \tfrac{1}{2}\sum_{i=1}^{n}\sum_{j=1}^{n} y_{ij}^p E(\alpha_i\alpha_j) \tag{8}$$

$$\begin{aligned}\mathrm{COV}\,(y^p, y^q) = {} & \sum_{i=1}^{n}\sum_{j=1}^{n} y_i^p y_j^p E(\alpha_i\alpha_j) \\ & + \tfrac{1}{2}\sum_{i=1}^{n}\sum_{j=1}^{n}\sum_{k=1}^{n} y_{ij}^p y_k^q E(\alpha_i\alpha_j\alpha_k) + \tfrac{1}{2}\sum_{i=1}^{n}\sum_{j=1}^{n}\sum_{k=1}^{n} y_i^p y_{jk}^q E(\alpha_i\alpha_j\alpha_k) \\ & + \tfrac{1}{4}\sum_{i=1}^{n}\sum_{j=1}^{n}\sum_{k=1}^{n}\sum_{l=1}^{n} y_{ij}^p y_{kl}^q (E(\alpha_i\alpha_j\alpha_k\alpha_l) \\ & - E(\alpha_i\alpha_j)E(\alpha_k\alpha_l)),\end{aligned} \tag{9}$$

where y^p and y^q are the pth and qth components of nodal displacements or stresses.

3 Reliability Analysis

3.1 Failure Criterion of Diesel CR. Loads acting on the diesel CR are random variables, and the stress is variable amplitude stress. The cumulative fatigue damage theory is used in the life analysis. There are two classes of damage summing methods: linear damage theory and nonlinear damage theory. Miner's rule is a typical linear damage theory, while Corten-Dolan's rule is a typical nonlinear damage theory. As for steel material, life related to the stress equaling to or lower than endurance limit is infinite. If Miner theory is used, the effect of those low stress (equaling to or lower than endurance limit) is omitted. In fact, stress equaling to endurance limit or lower than endurance limit to some extend do affects component's life. Compared with Miner theory, Corten-Dolan theory considers the low stress effect. The difference of the two methods is shown in σ-N curve in Fig. 1 (Li et al., 1991). It can be seen from Fig. 1, Miner's theory do not consider the stress below the endurance limit, while Corten-Dolan theory considers. Diesel CR works at the low stress, high cycle condition, so the effect of low stress on life is important and must be considered. If Miner's rule is used, the predicted life will be longer than the real life. By reasons mentioned above, Corten-Dolan theory is used in this analysis. Corten-Dolan theory gives a damage formula for a given stress level (Corten and Dolan, 1956)

$$D = crn^a, \tag{10}$$

where D is "Damage", c is the number of damage sources, r is damage factor, n is the number of stress cycles, and a is constant. c, r, and a will change when stress level changes. By some experimental results and simplification, Corten-Dolan theory, used in multilevel loads, can be derived from Eq. (10) as follows:

$$N = \frac{N_l}{\sum_i \eta_i(\sigma_i/\sigma_l)^d}, \tag{11}$$

where N denotes the cycle life under multilevel stress cycles. N_l denotes the cycle life under maximum stress level σ_l. η_i denotes the ratio n_i/N. n_i is cycle number under stress level σ_i. d is material constant. By Mou (1988), Eq. (11) can also be expressed as

$$\left.\begin{aligned}\sum_i \frac{n_i}{N_i} &= 1 \\ N_i\sigma_i^d &= N_l\sigma_l^d\end{aligned}\right\}. \tag{12}$$

As for continuous stress spectrum, Eq. (12) is changed into

$$\int_{\sigma_{\min}}^{\sigma_l} \frac{n_t f(\sigma)}{N(\sigma)}\, d\sigma = 1, \tag{13}$$

where $\sigma_{\min}$ is the minimum stress level in cycles, n_t is the total amount of stress cycles, $f(\sigma)$ is the probability density function of stress amplitude σ, and $N(\sigma)$ is the cycle life under stress level σ. Thus, the failure criterion function g, is

$$g = N_l\sigma_l^d - n_t\int_{\sigma_{\min}}^{\sigma_l} f(\sigma)\sigma^d d\sigma, \tag{14}$$

where $g > 0$ denotes the safe state, $g = 0$ denotes the limit-state, and $g < 0$ denotes the failure state.

Equation (14) is applicable to a material bearing a symmetric stress cycle. Because the CR is working under an unsymmetrical stress cycle, additional explanations are essential. In a diesel engine, combustion peak pressure is high, which causes the mean stresses σ_m (defined in Eq. (20)) in danger points to be less than zero. From the Goodman diagram (alternating stress versus mean stress), the compressive mean stress has no effect on life, which means mean stress can be neglected in life analysis of the CR (Collins, 1987). The equation

$$g = N_l\left(\frac{\epsilon\beta}{k}\sigma_l\right)^d - n_t\int_{\sigma_{\min}}^{\sigma_l} f(\sigma)\sigma^d d\sigma \tag{15}$$

is used as fatigue failure criterion of the diesel CR. Where ϵ is size factor, β is surface factor, and k is stress concentration factor. The function $f(\sigma)$ can be a normal distributed function, log-normally distributed function, Weibull function, or other PDF.

3.2 Advanced First Order Second Moment Method. Because $g(x) > 0$ denotes the safe state, the reliability of the CR, then, is

$$R = P\{g(\tilde{X}) > 0\}, \tag{16}$$

where vector $\tilde{X}$ has been defined in section 2. For reliability analysis, it is convenient to transform the vector $\tilde{X}$ into the standard normal space

$$\tilde{Y} = Y(\tilde{X}), \tag{17}$$

where the elements of $\tilde{Y}$ are statistically independent and have the standard normal density. Then Eq. (16) is changed into

Table 1 Statistics of basic variables

Variable	Mean	SV
p_{max}, MPa	8.336	0.5002
n, rad/s	293.22	14.661
m, kg	1.318	0.04
δ, mm	0.0812	0.0087
r, mm	40	0.167
E, MPa	2.1×10^5	1.8×10^4
μ	0.3	0.0055

$$R = P\{g(\tilde{Y}) > 0\} = \int_{g(Y)>0} \phi(Y)dY, \tag{18}$$

where $\phi(\cdot)$ is the standard normal probability density function.

It is difficult to obtain the analytical solution of Eq. (18). Therefore, some approximate methods, such as AFOSM, are used. The basic idea of the AFOSM method is that the limit-state surface $g(\tilde{Y}) = 0$ is replaced by the tangent plane at the point with minimum distance from the origin. The first order estimate of the fatigue strength reliability of the CR is

$$R = \Phi(\beta), \tag{19}$$

where β, defined as the reliability index by Cornell (1969), is the minimum distance from the origin and $\Phi(\cdot)$ denotes the standard normal cumulative probability. There exist standard solution algorithms for finding the point which is the nearest to the origin (Liu and Der Kiureghian, 1986). According to these algorithms, computer code has been made for reliability analysis by the AFOSM method.

4 Calculation Results and Analysis

The methods previously mentioned are applied to the fatigue reliability analysis of a certain type of diesel CR.

4.1 The Result of Stress Analysis. In stress analysis, uncertainties of combustion peak pressure, p_{max}, rotary speed of crankshaft, n, mass of piston group (including piston and piston pin), m, interference between small-end bore and copper bushing, δ, the transitive arc radius between small-end and shank, r, modulus of elasticity, E, and Poisson's ratio, μ, are taken into consideration. Their mean values and standard variance (SV) are shown in Table 1.

In computing, two conditions were taken into account: maximum pull condition at TDC of the exhaust stroke and maximum pressure condition near TDC of expansion stroke. As an example, we only analyzed the stress of the small-end because it experienced the higher stress. Additionally, the calculation model is simplified in three aspects. First, external loads are symmetric to the CR axis under maximum pull and pressure conditions, then only half of small-end is used for calculation. Second, the contact force that the piston pin exerts on the small-end bore is assumed to be in cosine distribution. Distribution angle is 160 deg at the pressure condition, and 180 deg at the pull condition. Third, a plane stress model is used. The CR is taken as a two-dimensional object with a different thickness in a different part. In automatic finite element mesh generation, the CR is divided into many zones of varying thickness. Triangular mesh is generated in each of these zones by the advancing front technique (Peraire et al., 1987). Load distribution, along with FE mesh is shown in Fig. 2. According to the calculation, maximum stress amplitude is taken place at the outer boundary of CR transitive arc between small-end and shank. Points with large stress amplitude are pointed out in Fig. 2. These points are used for reliability analysis. Though the stress in CR is in a two-dimensional state, the stress of these "danger" points is in one-dimensional state. It is either compressive stress or tensile stress because "danger" points are situated at the free boundary of CR body. Stresses distributed on the surface of CR are shown in Fig. 3 and Fig. 4.

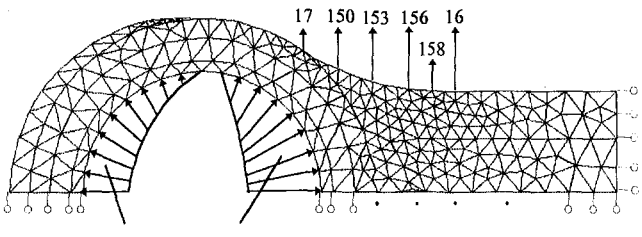

Fig. 2 Diagram of FE mesh, boundary constraint and loads

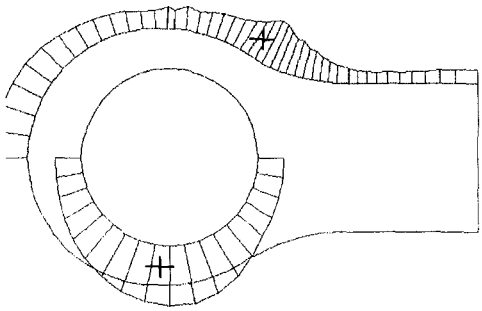

Fig. 3 Stress distribution of pull condition

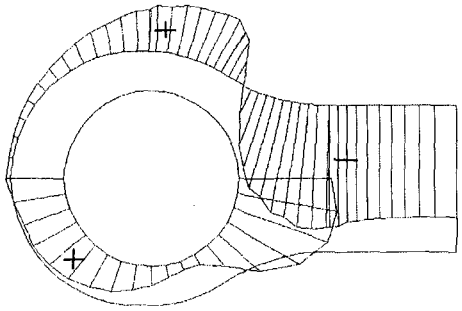

Fig. 4 Stress distribution of pressure condition

Monte-Carlo simulation was also carried out in order to compare with PSFEM. Statistics of stress for the two methods are shown in Table 2. It is shown that the results of the two methods are coincident with each other. However, Monte-Carlo simulation is very time consuming. When the number of samples is 200, time spent on Monte-Carlo simulation is twenty times longer than on PSFEM. Besides statistics of stress, PSFEM also provides stress response sensitivity with respect to every basic random variable. From Table 3, it can be seen that the stress is more sensitive to combustion peak pressure and rotary speed in the pressure condition. Because combustion pressure only exists in the pressure condition, the sensitivity of combustion peak pressure is zero in the pull condition.

Table 2 Statistics of stress in pressure condition

Node	PSFEM		Monte-Carlo	
	Mean	SV	Mean	SV
17	76.682	5.0893	76.138	5.1384
150	20.196	3.072	19.207	2.874
153	-121.19	9.5747	-126.05	9.859
156	-175.68	12.434	-179.58	12.636
158	-197.23	13.615	-199.57	13.632
16	-199.51	13.627	-200.8	13.657

Table 3 Stress response sensitivity of node 158

Sensi. (MPa)	pull condition	pressure condition
$\partial\sigma_e/\partial\alpha_p$	0	219.91
$\partial\sigma_e/\partial\alpha_n$	81.83	-53.83
$\partial\sigma_e/\partial\alpha_m$	40.91	-26.92
$\partial\sigma_e/\partial\alpha_\delta$	-2.49	2.73
$\partial\sigma_e/\partial\alpha_r$	11.74	-47.50
$\partial\sigma_e/\partial\alpha_E$	-0.46	0.52
$\partial\sigma_e/\partial\alpha_\mu$	-0.43	-6.53

4.2 Reliability Analysis. In Eq. (15), we take ϵ, β, σ_l, and stress amplitude σ as random variables. ϵ, β, σ_l, and related parameters given by Xu (1988) are shown in Table 4. Because danger points are in one-dimensional stress state, stress amplitude, σ, and mean stress, σ_m, are defined as

$$\sigma = \frac{\sigma_+ - \sigma_-}{2}$$

$$\sigma_m = \frac{\sigma_+ + \sigma_-}{2}, \tag{20}$$

where σ_+ is the tensile stress under maximum pull condition at TDC of the exhaust stroke, and σ_- is the compressive stress under maximum pressure condition near TDC of expansion stroke. σ_+ and σ_- are two relevant random variables. Mean, variance and covariance of σ_+ and σ_- can be determined by PSFEM. According to Eq. (20), the mean and standard variance of σ were derived and shown in Table 5. Because σ is affected by many random variables, such as p_{max}, n, m, r, δ, E, and μ, normal distribution assumption of σ is reasonable according to central limit theory of statistics. Therefore, the PDF, $f(\sigma)$ can be expressed as

$$f(\sigma) = \frac{1}{\sqrt{2\pi}\hat{\sigma}} \exp\left[-\frac{1}{2}\left(\frac{\sigma - \bar{\sigma}}{\hat{\sigma}}\right)^2\right], \tag{21}$$

where $\bar{\sigma}$ is the mean of σ, and $\hat{\sigma}$ is the standard variance of σ. Using computer code for reliability analysis with the AFOSM method, we obtained the fatigue strength reliability of some danger points on the CR, which is also shown in Table 5. It is shown that the point with the lowest reliability is situated in the joint of the transitive arc and shank, because of the large stress amplitude situated there. From Eq. (15), we can create the curve of reliability changing with cycle number n, Fig. 5. It can be seen that the reliability of the CR decreases sharply as the number of cycles increase.

5 Experiment

In reliability analysis of a CR, it is very important to accurately obtain the stress data. In this paper, the mean and variance of stress were obtained by PSFEM. In order to check the accuracy and reliability of this method, the CR deformation test was carried out by single beam laser speckle interferometry (Archibald et al., 1970). The experiment was carried out on a universal material test machine. Several pieces of the CR were tested. Locations of test points and loads are shown in Fig. 6. The displacements of the points received by calculation and by experiment are shown in Table 6. In order to eliminate the influence of rigid motion, points 1 and 2 are taken as constraint points and their displacements are zero. Because points 5 and 6 are symmetrical, only the mean value of their displacements are given. It is shown that the results of these two methods are similar, which confirms the reliability of PSFEM.

Table 4 Statistics of some parameters

Variable	σ_l, MPa	ε	β	k	d
Mean	421.7	0.7667	0.5353	1	5.846
SV	10.3	0.0749	0.0214	0	0

Table 5 Statistics of stress amplitude σ and reliability of danger points

Node No.	153	156	158	16
Mean of σ	91.517	110.61	116.06	112.01
SV of σ	4.9612	6.1422	6.6754	6.6639
Reliability	0.9^5812	0.9^3742	0.9^3169	0.9^3640

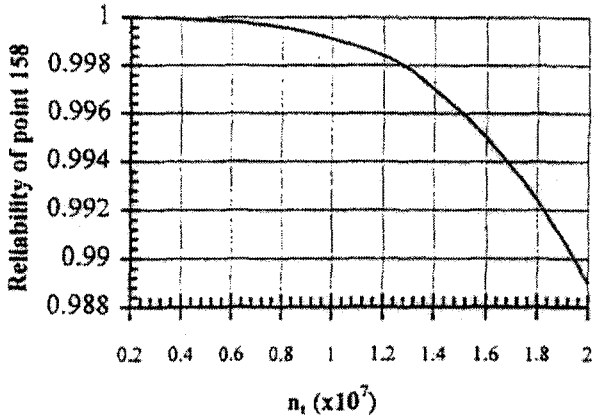

Fig. 5 The change of reliability

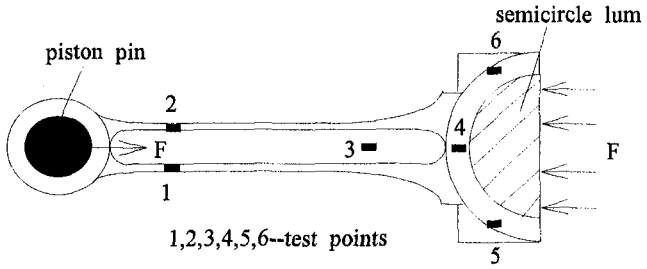

Fig. 6 Locations of test points and loads

6 Conclusion

The perturbation stochastic finite element method combined with the advanced first order second moment method is used for fatigue strength reliability analysis of a diesel engine connecting rod. The advantage of PSFEM is that the inversion of the stiffness matrix has to be done only once, which makes PSFEM very efficient. A fatigue failure criterion is given for the diesel CR. The criterion is derived directly from the Corten-Dolan theory, which has no relation to FE modeling. But, when stress is in a complicate state, such as in CR body (not surface), stress amplitude and stress mean must be substituted by effective stress amplitude and effective stress mean. More details can be found in the book of Surech (1991). By the criterion, we can not only analyze reliability under normal distributed stress but also reliability under any form of stress. Additionally, with the criterion, we can analyze how reliability changes with time. In this analysis, we find that stress is sensitive to combustion peak pressure, rotary speed, and the tran-

Table 6 Statistics of displacement (Unit: μm)

Test	Calculation		Experiment	
point	Mean	SV	Mean	SV
3	22.9	2.402	22.22	2.745
4	36.29	3.282	39.80	2.733
5, 6	37.8	3.342	42.54	3.832

sitive arc radius. Controlling the fluctuation of these parameters will improve the reliability of the CR.

References

Archibald, E., Burch, J. M., and Ennos, A. E., 1970, "Recording of in-Plane Surface Displacement by Double Exposure Speckle Photography," *Opt. Acta,* No. 17, pp. 883.

Astill, J., Nosseir, C. J., and Shinozuka, M., 1972, "Impact Loading on Structures with Random Properties," *Journal of Structure Mechanics,* No. 1, pp. 63–77.

Chen, Q., and Liu, X., 1993, *Stochastic Finite Element Method and Application in Engineering,* Southwest Jiaotong University Press, Chengdu.

Collins, J. A., 1987, *Material Failure Analysis, Prediction and Prevention in Mechanical Design,* Machinery Industry Press, Beijing.

Cornell, C. A., 1969, "A Probability Based Structure Code," *ACI J.,* Vol. 66, pp. 974–985.

Corten, H. T., and Dolan, T. J., 1956, "Cumulative Fatigue Damage," Proceedings, International Conference on Fatigue of Metals, I. Mech. Eng. and ASME Conf. Proc., ASME, New York, pp. 235–246.

Hasofer, A. M., and Lind, N. C., 1974, "An Exact and Invariant First-Order Reliability Format," *J. Engng. Mech. Div. ASCE 100 (EM1),* pp. 111–121.

Li, H. Z., Li, J., and Fang, H., 1991, "Reliability-Based Optimization of Crankshaft," *Transaction of ICE,* Vol. 9, No. 3, pp. 222–226.

Liu, P. L., and Der Kiureghian, A., 1986, "Optimization Algorithms for Structural Reliability Analysis," Report No. UCB/SESM-86/09, Department of Civil Engineering, Division of Structural Engineering and Structural Mechanics, University of California, Berkeley, CA.

Mou, Z. Z., 1988, *The Reliability Design of Mechanical Parts,* Machinery Industry Press, Beijing.

Nakagiri, S., and Hisada, T., 1982, "Stochastic Finite Element Method Applied to Structural Analysis with Uncertain Parameters," Proceedings, Int. Conf. on FEM, pp. 206–211.

Peraire, J., Vahdati, M., Morgan, K., and Zenkiewicz, O. C., 1987, "Adaptive Remeshing for Compressible Flow Computations," *Journal of Computational Physics,* Vol. 72, pp. 449–466.

Surech, S., 1991, *Fatigue of Materials,* Cambridge University Press, Cambridge.

Xu, H., 1988, *The Design of Fatigue Strength,* Machinery Industry Press, Beijing.

B. E. Lee[1]
Mem. ASME

C. A. J. Fletcher

M. Behnia
Mem. ASME

Center for Advanced Numerical Computation in Engineering and Science (CANCES), The University of New South Wales, Sydney 2052, Australia

Computational Prediction of Tube Erosion in Coal Fired Power Utility Boilers

Erosion of boiler tubes causes serious operational problems in many pulverized coal-fired utility boilers. A new erosion model has been developed in the present study for the prediction of boiler tube erosion. The Lagrangian approach is employed to predict the behavior of the particulate phase. The results of computational prediction of boiler tube erosion and the various parameters causing erosion are discussed in this paper. Comparison of the numerical predictions for a single tube erosion with experimental data shows very good agreement.

1 Introduction

Erosion of boiler tubes due to the impaction of fly ash particles causes serious financial problems in many pulverized coal-fired utility boilers. Therefore, such erosion has been of considerable concern to engineers in both the design and operation of utility boilers for several decades.

Many erosion models have been developed since Finnie (1960) proposed the first analytical erosion model in 1958 (Meng and Lumeda, 1995). Each model is based on one or two specific erosion mechanisms, and includes a wide variety of parameters that influence the erosion rate and pattern. Therefore, for an accurate prediction of erosion, the model should be developed and tested very carefully.

Erosion is the mechanical wear of the target metal by a stream of fluid carrying entrained solid particles. Therefore, each erosion model contains several parameters that are related to the motion of solid particles. For example, most models include the velocity and angle of impacting particles as important parameters. However, the measurement of the motion of the solid particles in a complex geometry, such as a boiler tube bank, is almost impossible without using CFD simulations.

There are basically two approaches commonly used to predict gas-particle flows: the Lagrangian and Eulerian formulations. The fundamental concepts of both approaches and their specific applications have been discussed and reviewed by Crowe et al. (1996) and Elghobashi (1994). The Lagrangian approach treats the fluid phase as a continuum and predicts the trajectory of a single particle in the fluid flow as a result of various forces acting on the particle. Therefore, the detailed physical behavior of the individual particles can be obtained directly. For this reason, the Lagrangian approach has been employed for the numerical prediction of erosion by many workers (Kitchen and Fletcher, 1989; Fan et al., 1991; Jun and Tabakoff, 1994).

In the present paper, computational predictions of boiler tube erosion using the Lagrangian approach in conjunction with a new erosion model are reported. The Lagrangian approach is employed to predict the behavior of the particulate phase. This paper discusses the results of computational prediction of boiler tube erosion and the various parameters causing erosion. The erosion rate provided by the Lagrangian approach is compared with the experimental data for a single tube.

2 Development of Erosion Model

It is generally agreed that the erosion of boiler tubes is mainly affected by such parameters as impact velocity, impact angle, particulate concentration (impact frequency), particle size, particle shape, mechanical properties of the particle, and the temperature of the target metal. Although about thirty general erosion models have been developed by many workers (see Meng and Ludema, 1995), none of them are completely suitable for the prediction of boiler tube erosion. This is because an erosion model should describe the following general features that occur in power utility boilers:

1 the erosion rate is a strong function of the particle shape
2 the dimensionless erosion rate varies as (impact velocity)^n where n is usually in the range of 2.2 to 2.8 (mean value of 2.4)
3 a maximum erosion rate of ductile metals occurs at an impact angle of 15 deg to 30 deg
4 erosion rate is controlled by particle size
5 erosion rate is proportional to particulate concentration (impact frequency)
6 the temperature of the target metal influences the erosion rate
7 mechanical properties of fly ash particles also influence the erosion rate

From the viewpoint of engineering design, it is desirable that an erosion model should be as simple as possible. It should be emphasized however that an erosion model must contain all important erosion parameters as separate variables and all excluded minor erosion parameters should be included in the erosion constant. The basic structure of the erosion model is organised to include the seven most important erosion parameters, as shown in Eq. (1):

$$E = \sum_{j=1}^{2} K_j \cdot C_{p_j} \cdot f(\beta_j) \cdot V^{n_j} \cdot g(d_p) \cdot h(T_h) \cdot \omega_j, \qquad (1)$$

where $j = 1, 2$ is the angular and spherical particle influence, respectively, K is the erosion constant, C_p is the particulate concentration term, $f(\beta)$ is the impact angle term, V^n is the impact velocity term, $g(d_p)$ is the particle size term, $h(T_h)$ is the temperature term, and ω is the chemical composition weight term. The significance of the parameters in Eq. (1) are discussed in chap. 3, calibrated in chap. 4, and tested in chap. 5.

3 Important Parameters Causing Erosion

There are many parameters which influence the extent of erosion. A fundamental understanding of various erosion parameters is essential in order to improve the life of boiler tubes. Several

[1] Current address: Senior Researcher, R&D Center of Hanjung, P. O. Box 77, Changwon, South Korea.

Contributed by the Power Division of THE AMERICAN SOCIETY OF MECHANICAL ENGINEERS for publication in the ASME JOURNAL OF ENGINEERING FOR GAS TURBINES AND POWER.

Manuscript received by the Power Division April 3, 1998; final revision received by the ASME Headquarters April 1, 1999. Technical Editor: D. Lou.

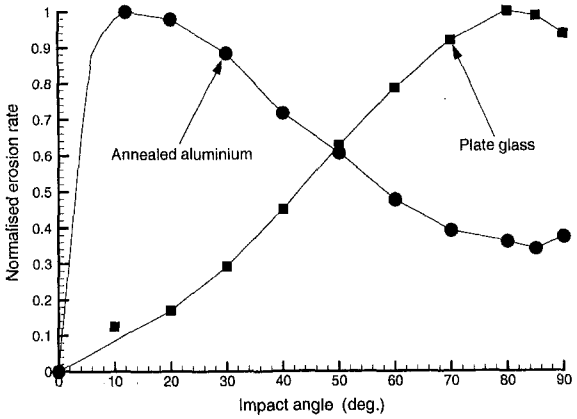

Fig. 1 Typical erosion curves for ductile and brittle materials as a function of particle impact angle (experimental data from Sheldon, 1970)

erosion parameters, which are involved in the erosion model, Eq. (1), are described for a better understanding of erosion.

3.1 Particle Shape. One of the most intriguing aspects of erosion is the influence of erodent particle shape which has been studied recently because of its severe effect on erosion rate. It has been observed by many investigators that angular particles produce a significantly higher erosion rate than spherical particles of the same size. For example, Raask (1969) found, in his erosion experiments on mild steel using relatively low velocities, that 100 μm sharp quartz particles were 10 times more erosive than glass spheres of the same size. Beckmann and Gotzmann (1981) also showed that the erosion rate increases linearly with shape factor they used.

Fly ash particles can be classified into two major shape groups: angular and spherical. In general, small fly ash particles have a spherical shape, while most large ones are irregularly shaped unvitrified quartz particles. According to Raask (1988) and Bauver et al. (1984), the rate of boiler tube erosion is a strong function of the unvitrified quartz content in fly ash. The fraction of unvitrified quartz is markedly influenced by the flame temperature, coal rank and particle sizes. The shape of fly ash particles is very difficult to characterise by a certain value. In addition, other erosion parameters, such as the angle of maximum erosion and the value of velocity exponent, are influenced by the particle shape.

In the present study an indirect method was developed to include the effect of particle shape. Firstly, it was assumed that all fly ash particles are classified into two shape groups: angular and spherical particles. Then, calibration of other erosion parameters could be obtained from experimental data of erosion by angular particles and spherical ones respectively. In this way, an explicit particle shape term in the erosion model is not required, as shown in Eq. (1).

3.2 Impact Velocity. It has been discovered empirically that erosion can be described by a power law of impact velocity. The velocity exponent (n, in Eq. (1)) depends on the physical characteristics of the materials involved and experimental conditions. Values of n for ductile materials range from 2.3 to 2.7; the range for brittle materials is from 2 to 4 (Humphrey, 1990). Thus, the erosion rate is strongly dependent on the impact velocity. For this reason, boiler designers have made an effort to reduce flue gas velocity in the convection pass (Vetterick et al., 1980).

3.3 Impact Angle. The effect of the impact angle on erosion is fairly well understood for both ductile and brittle materials. The curves shown in Fig. 1 are typical of materials having behavior that is ductile (e.g., steel, aluminium and copper) and brittle (e.g., glass and ceramic). In general, the erosion rate of ductile materials rises rapidly from zero to a maximum value as the impact angle increases from 0 deg to between about 15 deg and 30 deg, as shown in Fig. 1. It then decreases to one-quarter to one-half of the maximum erosion at 90 deg. In boiler tube erosion, impact angle varies almost linearly from 0 deg (near 90 deg from forward stagnation point) to 90 deg (forward stagnation point). Thus, the circumferential distribution of tube erosion is mainly determined by the impact angle.

3.4 Particle Size. It is important to establish the influence of particle size on the erosion rate of ductile materials, since fly ash particles have a broad size distribution. There are two interesting characteristics in conjunction with the effect of particle size: threshold size and saturation level (this is also called threshold effect). Tilly (1973) found that there was a threshold size, below which no erosion occurred. From a view point of aerodynamic influence, small particles may be deflected by the air flow so that they either fail to impact the target material or do so at modified angles and velocities. He also found that the erosion was independent of the particle size for particles larger than about 120 μm. As the erodent particle size increases at a fixed impact angle, the erosion rate increases but it tends to saturate at certain larger particle sizes. This effect is usually observed for ductile metals and considered to be a particle size threshold effect.

The behavior of erosion versus particle size can be formulated by the experimental function as follows:

$$g(x) = g(d_p/d_{\text{ref}}) = 1 - e^{-a(x-b)}, \tag{2}$$

where d_p is particle size, d_{ref} is reference particle size, a is a constant related to particle threshold effect, b is a constant related to threshold size, and x is the ratio of the threshold effect size to the reference particle size ($= d_p/d_{\text{ref}}$).

3.5 Particulate Concentration (Impact Frequency). Erosion increases linearly up to a certain point as particulate concentration increases, then it decreases because of particle-particle interactions. In other words, particle interference between incident particles and reflected particles is not an important factor in erosion until the particulate concentration is high enough. In general, particulate (fly ash) concentration in power utility boilers is 10–20 g/m^3 (Raask, 1969). On the other hand, Shida and Fujikawa (1985) showed that erosion rate increases linearly as the particle concentration increases in the particle concentration range of 20–120 g/m^3. Thus, it was assumed that the erosion rate of power utility boiler tubes increases linearly with increasing particulate concentration of flue gas.

3.6 Mechanical Properties of Particle. The major elements of fly ash particles are usually silica (SiO_2), alumina (Al_2O_3), and hematite (Fe_2O_3)—frequently called iron oxide. Kotwal and Tabakoff (1981) found that the magnitude of erosion caused by hematite is substantially less than that caused by the same size of alumina and silica particles. They note that the erosiveness of hematite is just 1 percent, based on 100 percent for alumina. Therefore, hematite was ignored in the present study. The calibration for the chemical composition of fly ash is given as follows:

$$\omega_1 = \text{a fraction of angular quartz particles by weight}$$

$$\omega_2 = 1 - \omega_1 - \text{a fraction of hematite by weight} \tag{3}$$

3.7 Temperature of Target Metal. It is well known that the erosion rate is significantly affected by the temperature of the target. An increase in temperature may increase or decrease erosion depending on the material involved. Shida and Fujikawa (1985) investigated the effects of temperature on the erosion rate of boiler tube materials. They found that the erosion rates increase with temperature, and are significantly different depending on the type of steel.

4 Summary of Calibration Results for the Erosion of 304 SS

4.1 The Values of Velocity Exponent.

$$n_1 = 2.5 \quad \text{and} \quad n_2 = 2.4,$$

where subscript 1 and 2 refer to angular and spherical particles, respectively.

4.2 Impact Angle.

$$f(\beta) = a + b\beta + c\beta^2 + d\beta^3 + e\beta^4 + f\beta^5$$

Table 1 Values of constants for impact angle term

	a	b	c	d	e	f	Interval
Angular	0.	13.448	−63.655	129.628	−121.287	42.451	0.≤β<.45
	9.056	−0.529	−0.355	0.413	0.0	0.0	.45≤β≤1
Spherical	0.	7.153	−16.081	11.703	−2.525	0.0	0.≤β ≤1

4.3 Particle Size.

$$g(x) = g(d_p/200) = 1 - e^{-17.387(x-0.025)}$$

4.4 Temperature of Target Metal.

$$h(T_h) = h(T/T_m) = 1 - 0.5633T_h + 7.8167T_h^2,$$

where T_h and T_m are the homologous temperature ratio and melting temperature, respectively.

5 Computational Prediction of Particulate Behavior Around a Single Tube in Cross Flow

Particulate behavior in particle-laden flows is important in many industrial fields especially those which suffer from severe erosion wear, such as pulverized coal-fired boilers, fluidized bed combustors, turbomachinery, and pneumatic systems. Information about particulate behavior in those systems is essential to the design and maintenance.

The commercial CFD code (FLUENT) is used for the simulation of turbulent gas-particle flow around a single tube in cross flow. An RNG k-ϵ turbulence model was chosen to simulate the gas turbulent fluctuations. A Lagrangian-formulated deterministic particle equation of motion is solved via an advanced Runge-Kutta method to predict particle velocities and trajectories once the gas flow field is obtained. FLUENT uses a stochastic calculation method which incorporates the instantaneous values of the fluctuating components of the continuous phase velocities appearing in the equations of motion.

A single tube was taken from the first row of the economizer section of a practical power station configuration which has a transverse pitch of 3 and tube diameter of 50.8 mm (2.0 in). Figure 2 illustrates the grid system for a single tube flow. The flue gas velocity of 30.5 m/s and particle size range of 10 to 150 μm, which coincide with the experimental conditions, were used in the numerical simulation.

The impact frequency, which can be defined as the number of impacting particles per unit area and unit time, is the most appropriate definition of the particulate concentration. This can be obtained directly using the Lagrangian approach since it predicts the trajectory of a single particle in the fluid flow as a result of various forces acting on it. Figure 3 shows the normalized particulate concentration in a single tube flow with a uniform inlet particulate concentration. General behaviour is quite similar with other results produced by many investigators (Fan et al., 1991; Schuh et al., 1989).

Figure 4 illustrates the circumferential distributions of the normalized impact velocity along a tube surface for various particle sizes. It can be seen that the impact velocity with normal impaction decreases as the particle size decreases because of the gas flow. Finally, very small particles come to rest at the front stagnation point of the tube, while large particles maintain their initial velocities because of their inertia. The incident particles are accelerated as the tube angle increases because the gas is also accelerated.

Figure 5 gives the impact angle of a particle on the tube for different Stokes numbers. It can be seen that the impact angle is

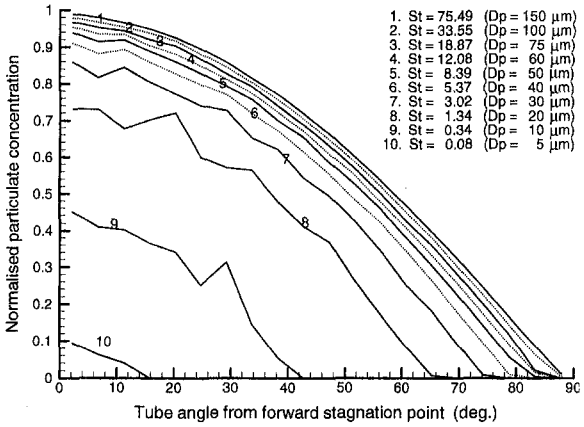

Fig. 3 Normalized particulate concentration

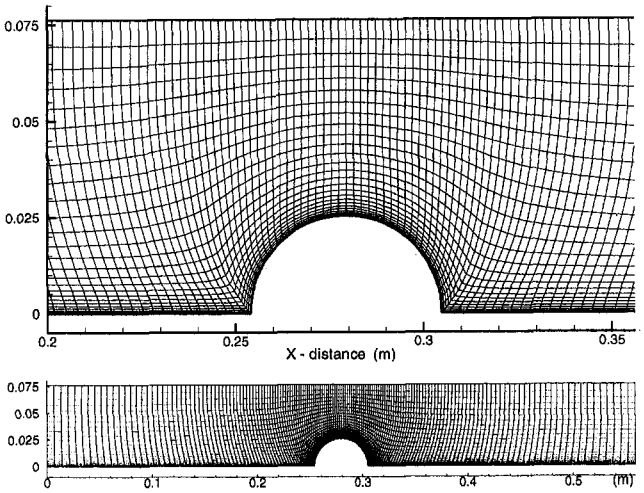

Fig. 2 Grid system for a single tube flow (161 × 26)

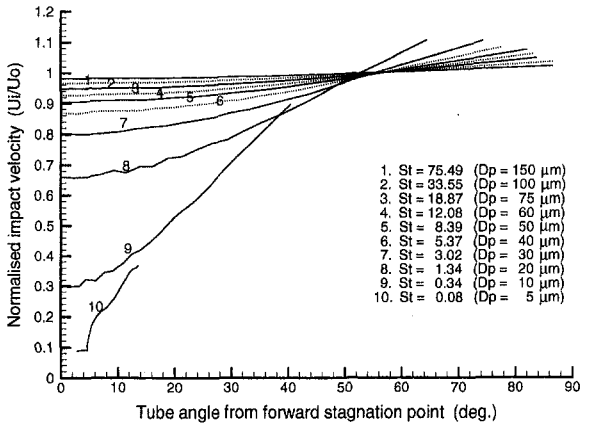

Fig. 4 Normalized impact velocity along the tube surface

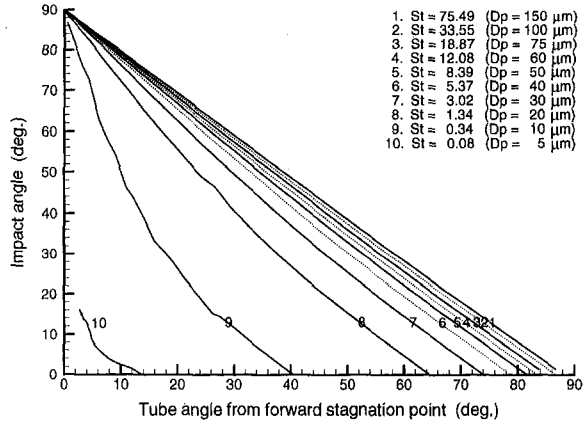

Fig. 5 Impact angle around a tube

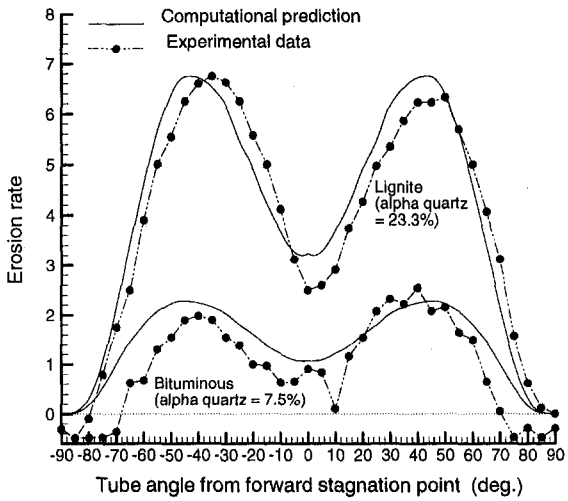

Fig. 7 Comparison of the erosion rate for different types of ash

largest at the front stagnation point of the tube, and decreases with increasing tube angle.

6 Computational Result and Discussion

Bauver et al. (1984) performed well controlled experiments for the prediction of boiler tube erosion in the Kreisinger Development Laboratory (KDL) of Combustion Engineering using the following two representative types of coal fly ash: lignite and bituminous. They produced detailed erosion data using an experimental test facility for boiler tube erosion. The computational predictions of erosion for a single tube are compared with their experimental data to test the accuracy of the erosion model developed in the present study.

Figure 6 illustrates the relative erosion rate for different particle sizes. The contribution of the particulate concentration, impact velocity, impact angle, and particle size are included in this figure. It can be seen that the maximum erosion occurs at between 40 deg and 45 deg from the forward stagnation point. It was already discussed that erosion rate reaches a plateau at a certain particle size (50 μm in the present study). However, one can see from Fig. 6 that the erosion rate increases as particle size increases. This result indicates that other erosion parameters also significantly influence erosion rate.

Figure 7 represents the erosion rates for a single tube caused by lignite and bituminous coal fly ashes that contain 23.3 percent and 7.5 percent alpha quartz, respectively. It can be seen from this figure that the computational predictions show quite good agreement with the experimental results. In the experimental data, the circumferential distribution of the erosion rate is not symmetric, and this may be due to the particle feeding system (see Fig. 1 of Bauver et al., 1984) as well as a short testing time. It should be noted that the erosion produced by lignite ash is approximately 3 times higher than that caused by bituminous ash. In general, the lignite ash is more erosive on the following two accounts: (1) because of its high quartz content and (2) because of the larger particle size.

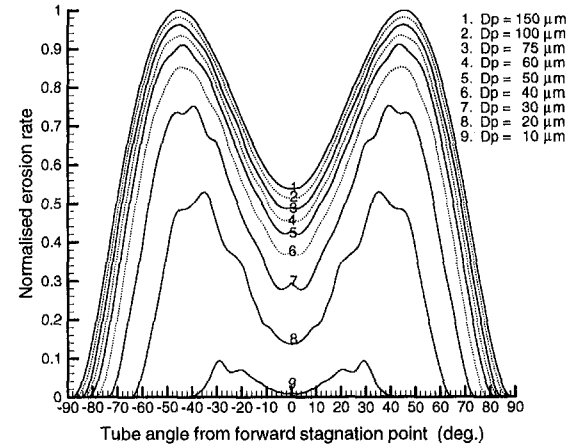

Fig. 6 Normalized erosion rate for different particle sizes

7 Conclusion

Computational prediction of erosion has been performed for a single tube flow. A new erosion model, which was developed for the prediction of power utility boiler tube erosion, has been successfully used to predict the erosion of a single tube due to the impaction of fly ash particles. From the present study, the following conclusions can be drawn:

1 particle shape, impact velocity, impact angle, particle size, impact frequency, and temperature of the target are the most important parameters in boiler tube erosion caused by the impaction of fly ash particles
2 the magnitude of erosion and the impact angle for maximum erosion are strongly influenced by the fraction of unvitrified angular quartz particles in the ash
3 the maximum erosion depth occurs at 40 deg from the forward stagnation point and the erosion depth has a symmetric shape for a single tube erosion
4 the maximum erosion tube angle increases with particle size

References

Bauver, W. P., Bianca, J. D., Fishburn, J. D., and McGowan, J. G., 1984, "Characterization of Erosion of Heat Transfer Tubes in Coal Fired Power Plant," ASME Paper 84-JPGC-FU-3.

Beckmann, G., and Gotzmann, J., 1981, "Analytical Model of the Blast Wear Intensity of Metal Based on a General Arrangement for Abrasive Wear," *Wear*, Vol. 73, pp. 325–353.

Crowe, C. T., Troutt, T. R., and Chung, J. N., 1996, "Numerical Models for Two-Phase Turbulent Flows," *Annu. Rev. Fluid Mech.*, Vol. 28, pp. 11–43.

Elghobashi, S., 1994, "On Predicting Particle-Laden Turbulent Flows," *Applied Scientific Research*, Vol. 52, pp. 309–329.

Fan, J., Zhou, D., Jin, J., and Chen, K., 1991, "Numerical Simulation of Tube Erosion by Particle Impaction," *Wear*, Vol. 142, pp. 171–184.

Finnie, I., 1960, "Erosion of Surfaces by Solid Particles," *Wear*, Vol. 3, pp. 87–103.

Humphrey, J. A. C., 1990, "Fundamentals of Fluid Motion in Erosion by Solid Particle Impact," *Int. J. Heat and Fluid Flow*, Vol. 11, No. 3, pp. 170–195.

Jun, Y. D., and Tabakoff, W., 1994, "Numerical Simulation of a Dilute Particulate Flow in Tube Bank," *J. Fluids Engng.*, pp. 770–777.

Kitchen, A. N., and Fletcher, C. A. J., 1989, "Computational Approach to the Prediction of Erosion in Economiser Tube Banks," Proceedings, Computational Techniques and Applications Conference, Brisbane, Australia.

Kotwal, R., and Tanakoff, W., 1981, "A New Approach for Erosion Prediction Due to Fly Ash," *J. Eng. Power*, Vol. 103, pp. 265–270.

Meng, H. C., and Ludema, K. C., 1995, "Wear Models and Predictive Equations: Their Form and Content," *Wear,* Vol. 181–183, pp. 443–457.

Pourahmadi, F., and Humphrey, J. A. C., 1983, "Modelling Solid-Fluid Turbulent Flows With Application to Predicting Erosive Wear," *PhysicoChemical Hydrodynamics,* Vol. 4, No. 3, pp. 191–219.

Raask, E., 1969, "Tube Erosion by Ash Impaction," *Wear,* Vol. 13, pp. 301–315.

Raask, E., 1988, "Erosion Wear in Coal Utilization," Hemishpere, New York.

Schuh, M. J., Schuler, C. A., and Humphrey, J. A. C., 1989, "Numerical Calculation of Particle-Laden Gas Flows Past Tubes," *AIChE J.,* Vol. 35, No. 3, pp. 466–480.

Sheldon, G. L., 1970, "Similarities and Differences in the Erosion Behavior of Materials," *J. Basic Eng.,* pp. 619–626.

Shida, Y., and Fujikawa, H., 1985, "Particle Erosion Behaviour of Boiler Tube Materials at Elevated Temperature," *Wear,* Vol. 103, pp. 281–296.

Tilly, G. P., 1973, "A Two Stage Mechanism of Ductile Erosion," *Wear,* Vol. 23, pp. 87–96.

Vettrick, R. C., Clessuras, G. L., Anacki, D. W., and Stockton, R. D., 1980, "A Boiler Manufacturer's Approach to Improving Operating Unit Availability," *Combustion,* September, pp. 38–42.

Analysis of Heat, Mass, and Momentum Transfer in the Rain Zone of Counterflow Cooling Towers

E. de Villiers

D. G. Kröger

University of Stellenbosch,
Department of Mechanical Engineering,
Stellenbosch, 7600,
South Africa

The rate of heat, mass, and momentum transfer in the rain zone of three counterflow cooling tower geometries is analyzed using simplifying assumptions and numerical integration. The objective of the analysis is to generate equations for use in a one-dimensional mathematical cooling tower performance evaluations. Droplet deformation is taken into account and momentum transfer is calculated from the air flow's mechanical energy loss, caused by air-droplet interaction. A comparison of dimensionless semi-empirical equations and experimental data demonstrates the method's capability to predict the pressure drop in a counterflow rain zone.

Introduction

A significant part of the total heat and mass transfer in large counterflow cooling towers occurs in the rain zone below the packing (or fill). Although some relations exist to describe these phenomena along with the rain zone pressure drop, they tend to be incorrect or limited to a narrow range of variables. Furthermore, finite-element methods that do accurately describe these occurrences (Benocci et al., 1986) are not often used in practice since they tend to be relatively costly and time consuming.

Hoffmann (1990), Šedina (1992), and Terblanche (1994) assume that the component forces on the droplets may be summed, and the resulting pressures added in vector form to find the pressure drop relative to the inlet and outlet sections of the rain zone. If one investigates the mechanics of the problem it becomes clear that droplet drag forces applied in such a manner will result in a nonphysical pressure value and not a pressure drop across the rain zone. The more correct approach would be to consider the rain zone pressure drop to originate from work done by the air stream on the falling drops. Zhenguo et al. (1992) employ this approach, but renege to fit an adequate equation to numerical data, with the result that the relation is only valid for a very narrow range of some of the primary variables. Most inquiries into rain zone characteristics also fail to incorporate the effects of droplet deformation.

The purpose of this paper is, thus, to derive a series of equations that are sufficiently accurate to describe the divergent data generated by a numerical analysis of the rain zones of various tower geometries (circular, rectangular, and counterflow). The coefficients produced by these equations are intended for use in a one-dimensional performance evaluation of the appropriate cooling tower.

To analyze the heat, mass, and momentum, transfer in the rain zone of a counterflow wet-cooling tower, the following simplifying approximations are made:

—no droplet agglomeration, collision or coalescence occurs (this is not strictly true; these phenomena do seem to have a variable effect on rain zone characteristics, but formulation of such a model is beyond the scope of this work)

—the water mass flow through the fill is evenly distributed and all droplet diameters are equal (in practice, an effective droplet diameter must be used)

—droplets enter the rain zone with zero absolute velocity (numerical tests show that variable droplet inlet velocities have a relatively small influence on overall performance if the drops enter the rain zone below 10 percent of terminal velocity)

—falling droplets have no effect on the velocity distribution of the air, nor the potential flow solution to the air flow

—there is no mutual interaction between droplets with regards to mass transfer and viscous drag

—both droplet and air physical properties change negligibly while traversing the rain zone (a study by Conradie (1993) indicates less than 1 percent overall variation of the transfer coefficient)

Air Inlet Section Velocity Field

Consider the air flow patterns in the inlet section of a circular counterflow cooling tower (Fig. 1). The flow is axi-symmetrical and if frictional effects can be neglected, a solution must be obtained for a two-dimensional cylindrical coordinate potential flow function, defined as $\phi(r, z)$. The radial and axial components, of the air velocity vector, are respectively given by

$$v_{ar} = -\partial\phi/\partial r \tag{1}$$

and

$$v_{az} = -\partial\phi/\partial z. \tag{2}$$

It can be shown that if ϕ is mathematically smooth enough, the criterion for irrotational flow is satisfied. The continuity equation for steady, axi-symmetrical, incompressible flow is

$$\frac{\partial v_{ar}}{\partial r} + \frac{v_{ar}}{r} + \frac{\partial v_{az}}{\partial z} = 0. \tag{3}$$

Substitute Eqs. (1) and (2) with their partial derivatives into Eq. (3) to find the equation of continuity written in terms of the potential function, ϕ.

$$\frac{\partial^2\phi}{\partial r^2} + \frac{1}{r}\frac{\partial\phi}{\partial r} + \frac{\partial^2\phi}{\partial z^2} = 0 \tag{4}$$

Hoffmann (1990) obtains a simple solution to the problem by assuming the air velocity through the fill to be uniform. Under such circumstances the following boundary conditions are applicable:

Contributed by the Power Division of THE AMERICAL SOCIETY OF MECHANICAL ENGINEERS for publication in the ASME JOURNAL OF ENGINEERING FOR GAS TURBINES AND POWER.

Manuscript received by the Power Division January 6, 1999; final revision received by the ASME Headquarters April 1, 1999. Associate Technical Editor: D. Lou.

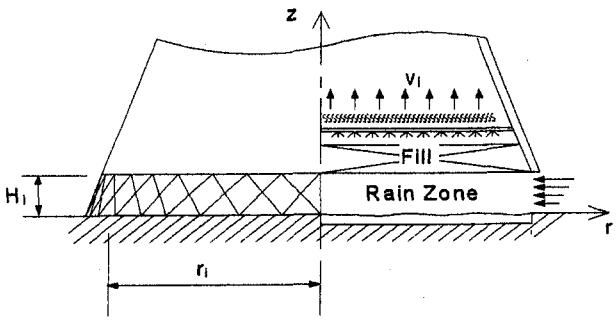

Fig. 1 Schematic representation of an inlet section of a circular counterflow cooling tower

$$v_{az}(r, 0) = \partial\phi/\partial z(r, 0) = 0; \quad \text{impervious surface}$$

$$v_{ar}(0, z) = \partial\phi/\partial r(0, z) = 0; \quad \text{symmetry axis (tower axis)}$$

$$v_{az}(r, H_i) = -\partial\phi/\partial z(r, H_i) = v_i; \quad \text{uniform flow through fill}$$

A fourth boundary condition is needed to complete the solution of Eq. (4). If the influx of ambient air at the tower inlet is considered purely radial the last boundary condition is obtained.

$$v_{az}(r_i, z) = -\partial\phi/\partial z(r_i, z) = 0$$

In practice such a flow field can only be achieved with a rounded inlet and in the absence of inlet inclined louvers and support struts, but the above boundary condition serves as an adequate approximation. The solution of Eq. (4) is found by separation of variables, with λ_n denoting the roots of $J_0(\lambda r_i) = 0$.

$$\phi(r, z) = \sum_{n=1}^{\infty} \frac{-2v_i}{\lambda_n^2 r_i} \frac{J_0(\lambda_n r)}{J_1(\lambda_n r_i)} \frac{\cosh(\lambda_n z)}{\sinh(\lambda_n H_i)} \tag{5}$$

The infinite series of Eq. (5) may be reduced to a finite number of terms, provided that the converged solution is approached. Adequate convergence is reached after 50 terms. Except for a small discontinuity at the upper edge of the tower inlet, the flow may be approximately described by simple linear representations of the vector components (axial and radial). The only deviation that the Bessel function solution shows from the simplified form, is near the tower's inlet radius, r_i. This region and the deviation are small enough to be ignored compared to the average flow field.

The linear model that satisfies Eq. (3) gives the radial air velocity as

$$v_{ar} = -0.5 v_i r/H_i \tag{6}$$

and the axial velocity as

$$v_{az} = v_i z/H_i, \tag{7}$$

where v_i is the average velocity of the air leaving the rain zone, i.e., $v_i \approx m_a/(\rho_a \pi r_i^2)$.

Droplet Velocity and Position

Using Eqs. (6) and (7), the velocity and displacement of the water droplets in the rain zone may be calculated. The total drag force acting on a droplet may be found from

$$\bar{F}_D = C_D A_d \rho_a \bar{v}_{ad}^2/2, \tag{8}$$

where v_{ad} is the velocity of the drop relative to the air flow,

$$|\bar{v}_{ad}| = \sqrt{(v_{az} - v_{dz})^2 + (v_{ar} - v_{dr})^2}, \tag{9}$$

with the relative angle $\theta_{ad} = \arctan[(v_{az} - v_{dz})/(v_{ar} - v_{dr})]$; C_D is the droplet's drag coefficient, and A_d it's cross-sectional area.

Photographic analysis by Muira et al. (1977) and others have shown that falling droplets are not spherical as most assume, but take on a flattened elliptical shape as they approach terminal velocity. This deformation has to be taken into account in the computation of the droplet's drag coefficient, C_D. The ratio of the drag coefficient of a deformed drop to that of a solid sphere is given by (Dreyer, 1994)

$$C_D/C_{Dsph} = 1 - 0.17185(1 - E) + 6.692(1 - E)^2 - 6.605(1 - E)^3, \tag{10}$$

where E is the droplet's deformation ratio that can be found from an analysis proposed by Dreyer (1994). The equation for the drag coefficient, C_{Dsph}, for solid spheres, is given by Turton and Levenspiel (1986).

Consider an accelerating droplet in the rain zone. If the buoyancy force on the drop is neglected, the forces acting on the drop are gravity and drag. The resulting force can be found from

$$|\bar{F}_d| = \sqrt{(\sin\theta_{ad}|F_D| - M_d g)^2 + (\cos\theta_{ad}|F_D|)^2}. \tag{11}$$

In differential form, the axial and radial acceleration of the droplet can now be described as

Nomenclature

A = area, m^2
a = dimensional coefficient; surface area per unit volume, m^2/m^3
C = coefficient
D = diffusion coefficient, m^2/s
d = diameter, m
E = droplet deformation ratio; mechanical energy, Nm
F = force, N
G = mass flow rate per unit area, kg/m^2s
g = gravitational acceleration, m/s^2
H = height, m
h_d = mass transfer coefficient, kg/m^2s
K = pressure drop coefficient
R = gas constant, J/kg K
S = surface area, m^2
M = mass, kg
m = mass flow rate, kg/s
n = number
p = pressure, N/m^2
r = radius, m
T = temperature, °C
v = velocity, m/s
W = width from center line, m
w = humidity ratio, kg/kg
z = axial co-ordinate, m

Greek Symbols

β = mass transfer coefficient, m/s
ϕ = potential function
μ = viscosity, Ns/m^2
θ = angle
ρ = density, kg/m^3
σ = surface tension, N/m

Subscripts

a = air
cv = control volume
D = drag
d = droplet
i = inlet, into the fill
L = length
o = outlet
r = radial
rz = rain zone
s = saturated
sph = sphere
t = terminal velocity
v = vapour
w = water
z = axial
μ = viscosity
ρ = density

$$dv_{dz}/dt = F_{Dz}/M_d - g \tag{12}$$

$$dv_{dr}/dt = F_{Dr}/M_d, \tag{13}$$

with starting values: $v_{dz} = v_{dr} = 0$ at $t = 0$. Drop velocity and displacement are found by integration of Eqs. (12) and (13) with respect to time. Using these discrete values, droplet velocity can then be found as a function of its position in the rain zone.

Pressure Drop Coefficient

Consider an annular control volume (CV) in the rain zone, the center at a point where the droplet velocity has been previously calculated. Let the sides of the annulus be parallel to the velocity vector of the droplet. Make the height, dz, and the width, dr, of the control volume small enough so that the change in droplet velocity through the control volume becomes negligible. The annulus now describes a streamtube for the droplets entering the control volume. Since the water flow rate through the fill is uniform, the water flow rate through subsequent vertical control volumes must also be uniform. Now the number of drops in a control volume, $dV_{cv} = 2\pi r dr dz$, at a given position can be found from,

$$n_{cv} = [6G_w/(\rho_w \pi d_d^3)]2\pi r dr dz/v_{dz}, \tag{14}$$

where G_w is the water mass flow rate per unit area.

The rate of change in the mechanical energy of the air, caused by drag on a single droplet in a control volume, is given by (for the radial and axial directions respectively)

$$dE_{ar}/dt = F_{Dr}v_{ar} \tag{15}$$

$$dE_{az}/dt = F_{Dz}v_{az} \tag{16}$$

The total pressure drop in the rain zone is found by summing the work done in all the control volumes and substituting it into the energy equation for a streamtube.

$$\Delta p_{rz} = \frac{\rho_a}{m_a}\int_0^{H_i}\int_0^{r_i} n_{cv}[F_{Dr}v_{ar} + F_{Dz}v_{az}] \tag{17}$$

In expanded simplified form, the dimensionless pressure drop coefficient, based on the fill frontal area, can be written as,

$$K_{rz} = 3\left(\frac{v_w}{v_i}\right)\left(\frac{H_i}{d_d}\right)\int_0^{H_i}\int_0^{r_i}\frac{C_D}{E^{0.666}}[v_{ad}^2]^{0.5}\Big/(v_{dz}v_i^2) \times (v_{ar}(v_{ar} - v_{dr}) + v_{az}(v_{az} - v_{dz}))rdrdz/(r_i^2 H), \tag{18}$$

where $v_w = m_w/(\rho_w \pi r_i^2)$.

It is obvious that only the integral need be solved numerically. By inspection of the source equations it is found that the integral in the pressure drop coefficient equation is dependent on the following variables, (d_d, r_i, H_i, v_i, ρ_a, ρ_w, μ_a, σ_w, g).

Utilizing dimensional analysis, these variables may be arranged to form dimensionless groups, thereby decreasing the active variables to six. The integral function can now be reduced to the following relation

$$I = f(a_L d_d,\ a_L r_i,\ a_L H_i,\ a_v v_i,\ a_\rho \rho_a,\ a_\mu \mu_a), \tag{19}$$

where the "a-" coefficients represent combinations of g, ρ_w, σ_w, and constants that make up each particular dimensionless group.

$$a_\mu = 3.06 \times 10^{-6}[\rho_w^4 g^9/\sigma_w]^{0.25};\quad a_L = 6.122[g\sigma_w/\rho_w]^{0.25}$$

$$a_v = 73.298[g^5\sigma_w^3/\rho_w^3]^{0.25} \quad \text{and} \quad a_\rho = 998.0/\rho_w \tag{20}$$

All these coefficients are equal to unity for $g = 9.8$ and $T_w = 22.72°C$. Since g, ρ_w, and σ_w never vary substantially, this particular arrangement allows greater freedom when fitting curves to the numerical data by removing the usual interdependence of the dimensionless groups.

The results of numerical integration produced the following correlation for the rain zone loss coefficient:

$$K_{rz} = 3a_v v_w\left(\frac{H_i}{d_d}\right)[0.22460 - 0.31467a_\rho\rho_a + 5263.04a_\mu\mu_a + 0.775526 \times [1.4824163\ \exp(71.5200a_L d_d) - 0.91] \times [0.39064\ \exp(2.1824 \times 10^{-2}a_L r_i) - 0.17] \times [2.0892(a_v v_i)^{-1.3944} + 0.14] \times \exp[(0.8449\ \ln(a_L r_i) - 2.312) \times (0.3724\ \ln(a_v v_i) + 0.7263) \times \ln[206.757(a_L H_i)^{-2.8344} + 0.43]]], \tag{21}$$

which is valid for $30 \le r_i \le 70$ m; $4 \le H_i \le 12$ m; $0.927 \le \rho_a \le 1.289$ kg/m^3; $1.717 \le \mu_a \le 1.92 \times 10^{-5}$ kg/ms; $0.002 \le d_d \le 0.008$ m; $0.0075 \le v_w \le 0.003$ m/s, and $1 \le v_i \le 3$ m/s.

Heat and Mass Transfer

Since the mass transfer coefficient is typically to be used in an analysis similar to that of Merkel (1925), it is unnecessary to calculate the heat transfer coefficient. This derives from Merkel's assumption that the Lewis factor, $(c_{pma}h_d)/h$, is equal to unity for wet-cooling towers.

In the absence of reciprocal droplet interaction, single drop correlations are applicable for heat and mass transfer applications in the rain zone. Ranz and Marshall (1952) propose the following semi-empirical correlation for the mass transfer coefficient for a single drop,

$$Sh = \beta d_d/D = 2 + 0.6\ \mathrm{Re}_d^{0.5}Sc^{0.33}, \tag{22}$$

where $\mathrm{Re}_d = \rho_a v_{ad} d_d/\mu_a$ and $Sc = \mu_a/(\rho_a D)$, and which is valid for $2 < \mathrm{Re}_d < 800$. However, Muira et al. (1977) show that this correlation accurately predicts their mass transfer data for Reynolds numbers of up to 2000. It is therefore, accepted that the correlation is accurate for the entire rain zone where the mean Reynolds number seldom exceeds 1500. Poppe (1984) derived the following relation between the mass transfer coefficient h_d and β for droplets larger than 1 mm:

$$h_d = (\beta p_a/R_v T_a)\ \ln\left[\frac{w_s + 0.622}{w + 0.622}\right]\Big/(w_s - w). \tag{23}$$

The Merkel number for an entire rain zone can be found from

$$h_{drz}a_{rz}H_i/G_w = 1\Big/(G_w\pi r_i^2)\int_0^{H_i}\int_0^{r_i} n_{cv}h_d S_d, \tag{24}$$

where $S_d = \pi d_d^2$ represents the mean surface area of the droplets.

The complete expanded version of the equation is found by substituting Eqs. (14), (22), and (23) into Eq. (24). By moving all the constants of integration to the left of the integral, the number of variables used in the empirical curve fitting will be greatly reduced and the accuracy of the equation will benefit from the similarity to the analytical model. After simplification and rendering in nondimensional form the relation has the following form:

$$\frac{h_{drz}a_{rz}H_i}{G_w} = 12\left(\frac{D}{v_i d_d}\right) \times \left(\frac{H_i}{d_d}\right) \times \left(\frac{p_a}{R_v T_a}\Big/\rho_w\right) \times \ln\left[\frac{w_s + 0.622}{w + 0.622}\right](w_s - w) \times \int_0^{H_i}\int_0^{r_i}\left(\frac{v_i}{v_{dz}}\right)(2 + 0.6\ \mathrm{Re}_d^{.5}Sc^{.33})\left(\frac{rdrdz}{r_i^2 H_i}\right). \tag{25}$$

From Eqs. (25) and (22) it clear that the integral is dependent upon the variables (d_d, r_i, H_i, v_i, ρ_a, ρ_w, μ_a, σ_w, g, and D). The diffusion coefficient, D, evidently has a much smaller presence in the integral (in Sc) than outside, and since it is a weak variable it is dropped from the list of dependants to simplify analysis. The variables may now be arranged in the same dimensionless groups as for the pressure drop coefficient (Eq. (21)). The integral is solved numerically and dimensional analysis and curve fittings of the results produce the following semi-empirical relation,

$$\frac{h_{drz}a_{rz}H_i}{G_w} = 12\left(\frac{D}{v_i d_d}\right)\left(\frac{H_i}{d_d}\right)\left(\frac{p_a}{R_v T_a}\Big/\rho_w\right) \times Sc^{0.33}$$
$$\times \ln\left[\frac{w_s + 0.622}{w + 0.622}\right]\Big/[w_s - w]$$
$$\times [0.90757a_\rho\rho_a - 30341.04a_\mu\mu_a - 0.37564 + 4.04016$$
$$\times [(0.55 + 41.7215(a_L d_d)^{0.80043})$$
$$\times (0.713 + 3.741(a_L H_i)^{-1.23456})$$
$$\times (3.11\exp(0.15a_v v_i) - 3.13)$$
$$\times \exp[(5.3759\exp(-0.2092a_L H_i))$$
$$\times \ln(0.3719\exp(0.003811a_L r_i) + 0.55)]]], \quad (26)$$

where the restrictions and "a-" coefficients are identical to those for the pressure drop coefficient equation and $R_v = 461.52$ J/kgK for water vapour.

Other Geometries

Using a similar approach, equations for rain zones with different geometries were also derived. For an induced draft rectangular tower the rain zone loss coefficient is given by

$$K_{rz} = a_v v_w \frac{3}{2}\frac{H_i}{d_d}\{0.219164 + 8278.7a_\mu\mu_a - 0.30487a_\rho\rho_a$$
$$+ 0.954153 \times [0.328467\exp(135.7638a_L d_d) + 0.47]$$
$$\times [26.28482(a_L H_i)^{-2.95729} + 0.56]$$
$$\times \exp[\ln[0.204814\exp(0.133036a_L W_i) + 0.21]$$
$$\times [3.9186\exp(-0.3a_L H_i)] \times [0.31095\ln(a_L d_d)$$
$$+ 2.63745]] \times [2.177546(a_v v_i)^{-1.46541} + 0.21]\}, \quad (27)$$

where the restrictions that differ from the circular tower are $1 \le v_i \le 5$ m/s; $2 \le H_i \le 8$ m; $2 \le W_i \le 20$ m (where W_i is the tower half-width), while all "a-" coefficients are identical. In an induced draft rectangular tower care must be taken to ensure that large water droplets are not entrained into the fill. This is done by obeying the following relation:

$$v_i \times [1 + (W_i/H_i)^2]^{0.5} \le v_t, \quad (28)$$

where, v_t, is the droplet terminal velocity. The equation for the Merkel number of a rectangular tower rain zone is,

$$\frac{h_{drz}a_{rz}H_i}{G_w} = 3.6\left(\frac{p_a}{R_v T_a}\Big/\rho_w\right)\left(\frac{D}{v_i d_d}\right)\left(\frac{H_i}{d_d}\right)Sc^{0.33}$$
$$\times \ln\left[\frac{w_s + 0.622}{w + 0.622}\right]\Big/[w_s - w] \times \{4.68851a_\rho\rho_a$$
$$- 187128.7a_\mu\mu_a - 2.29322 + 22.4121$$
$$\times [0.350396(a_v v_i)^{1.38046} + 0.09]$$
$$\times [1.60934(a_L H_i)^{-1.12083} + 0.66]$$

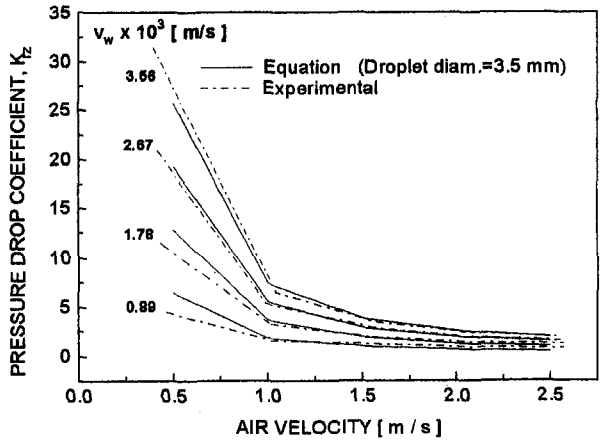

Fig. 2 Comparison of K_{rz} with experimental values from a pure counterflow tower

$$\times [34.6765(a_L d_d)^{0.732448} + 0.45]$$
$$\times \exp[7.7389\exp(-0.399827a_L H_i)$$
$$\times \ln[0.087498\exp(0.053238a_L W_i) + 0.85]]\}. \quad (29)$$

In the case of a purely counterflow rain zone the equations are somewhat simplified because of the system's one-dimensional nature. The loss coefficient in such a rain zone is calculated from,

$$K_{rz} = a_v v_w\{10645988a_\mu\mu_a - 130.7774a_\rho\rho_a - 32.6634$$
$$+ 888.6645 \times [2.45287(a_v v_i)^{-1.93315} + 0.34]$$
$$\times [4.03861\exp(-574.542a_L d_d) + 0.493]$$
$$\times \exp[(65.26215a_L d_d + 0.74827)$$
$$\times \ln[6.09836\exp(0.0767a_L H_i) - 6.1]]\} \quad (30)$$

with altered restrictions being $1 \le v_i \le 5$ m/s; $0.5 \le H_i \le 5.5$ m.

Figure 2 shows the comparison between pressure drop coefficients of an experimental test and Eq. (30). The tests were done in a section 1.52 m high, with a 1.5 × 1.5-m cross section and expanded metal sieves of decreasing density at the top of the rain zone. For the comparison a droplet diameter of 3.5 mm was used in the equation. The mass transfer coefficient in a counterflow rain zone is;

$$\frac{h_{drz}a_{rz}H_i}{G_w} = 3.6\left(\frac{p_a}{R_v T_a}\Big/\rho_w\right)\left(\frac{D}{v_i d_d}\right)\left(\frac{H_i}{d_d}\right)Sc^{0.33}$$
$$\times \ln\left[\frac{w_s + 0.622}{w + 0.622}\right]\Big/[w_s - w] \times \{5.01134a_\rho\rho_a$$
$$- 192121.7a_\mu\mu_a - 2.57724 + 23.61842$$
$$\times [0.2539(a_v v_{azo})^{1.6700} + 0.18] \times [0.83666(a_L H_i)^{-0.5299}$$
$$+ 0.42] \times [43.0696(a_L d_d)^{0.7947} + 0.52]\}. \quad (31)$$

Again restrictions are the same as for the pressure drop equation and global "a-" coefficients apply for both the loss and transfer coefficients. The counterflow equations are useful for calibrating effective droplet diameters.

Conclusion

The pressure drop and mass transfer coefficients for the rain zones of different cooling tower geometries are presented by simple expressions in terms of standard variables. These equations

are semi-empirical, incorporating both analytical and numerically derived expressions. In addition, data derived from the numerical model is not considered to be parallel on a normal or semi-log scale with regards to the second dimension variable for a specific curve fit as is normally done. Divergence of the data is taken into account by extra terms within each equation, specifically inside an $\exp^{[\ln]}$ term, giving the equations greater accuracy as multiple variables approach restriction values.

Experimentally obtained loss coefficients in a purely counterflow scenario agree well with the results for a drop diameter of 3.5 mm, and since exactly the same method was used for the other geometries it is reasonable to assume that they will perform equally well under similar conditions.

It must be noted that the expressions are curve fits of numerically generated data and that they will reflect any deficiency in the numerical analysis. In this regard, the effective drop diameter poses some questions. Although the counterflow experiment gives tentative evidence for a 3.5 mm drop, this may only be true for a specific fill type or water distribution system. An attempt must be made to accurately predict droplet size. Despite these deficiencies, the new equations overcome many of the defects inherent in previous methods of pressure drop and mass transfer prediction.

References

Beard, K. V., and Chuang, C., 1987, "A New Model for the Equilibrium Shape of Raindrops," *Journal of Atmospheric Sciences,* Vol. 44, No. 11, pp. 1509–1524.

Benocci, C., Buchlin, J. M., and Weinacht, P., 1986, "Prediction of the Air-droplet Interaction in the Inlet Section of a Natural Draft Cooling Tower," Proceedings, 5th IAHR Cooling Tower Workshop, Monterey, CA.

Conradie, C. F. G., 1993, "Die Verkoelingsvermoë van Nat Koeltorings en Droë/Nat Stelsels by Kragstasies," M. Eng. thesis, University of Stellenbosch, Stellenbosch.

Dreyer, A. A., 1994, "Modelling of Cooling Tower Splash Pack," Ph.D. dissertation, University of Stellenbosch, Stellenbosch.

Hoffmann, J. E., and Kröger, D. G., 1990, "Analysis of Heat, Mass and Momentum Transfer in the Rain Zone of a Natural Draft Counterflow Cooling Tower," Proceedings, 7th IAHR Cooling Tower and Spray Pond Symposium, Leningrad, USSR.

Merkel, F., 1925, "Verdunstungskühlung," VDI-Zeitschrift, Vol. 70, No. 70, pp. 123–128.

Muira, K., Muira, T., and Ohtani, S., 1977, "Heat and Mass Transfer to and from Droplets," *AIChE Symposium Series,* Vol. 73, No. 163, pp. 95–102.

Poppe, M., and Rögener, H., 1984, "Berechnung von Rückkühlwerken," *VDI-Wärmeatlas,* pp. Mh 1–Mh 15.

Ranz, W. E., and Marshall, W. R., 1952, "Evaporation from Drops," *Chemical Engineering Progress,* Vol. 48, No. 3, pp. 141–146.

Rish, R. F., 1961, "The Design of a Natural Draught Cooling Tower," Proceedings, 2nd International Heat Transfer Conference, Boulder, CO.

Šedina, M., 1992, "Heat and Mass Transfer and Pressure Drop in the Rain Zone of Cooling Towers," Proceedings, 8th IAHR Cooling Tower and Spray Pond Symposium, Karlsruhe, Germany.

Terblanche, J. E., 1993, "Inlaat Verliese by Koeltorings," M. Eng thesis, University of Stellenbosch, Stellenbosch.

Turton, R., and Levenspiel, O., 1986, "A Short Note on the Drag Correlation for Spheres," *Powder Technology,* Vol. 47, pp. 83–86.

Zhenguo, Z., Jingling, S., and Xiansong, C., 1992, "Study on Airflow Resistance in Natural Draft Cooling Towers," Proceedings, 8th IAHR Cooling Tower and Spray Pond Symposium, Karlsruhe, Germany.